

Design of Advanced Polymer Architectures by Tuneable Thermoresponsive LCST-UCST Copolymers

DISSERTATION

Zur Erlangung des Grades
eines Doktors der Naturwissenschaften
im Promotionsfach Chemie

vorgelegt von
M.Sc. Maximilian Felix Toni Meier

Eingereicht bei der Naturwissenschaftlich-Technischen Fakultät
der Universität Siegen
Siegen 2021

Doktorvater und Erstgutachter:

Prof. Dr. Ulrich Jonas
(Universität Siegen)

Zweitgutachter:

Prof. Dr. Holger Schönherr
(Universität Siegen)

Weitere Prüfungskommission:

Prof. Dr. Christian Gutt (Universität Siegen)
Prof. Dr. Sybille Krauss (Universität Siegen)
HDR. Dr. Tony Le Gall (Universität Brest)

Prüfungsdatum:

22. Februar 2022

Table of Contents

ACKNOWLEDGEMENTS.....	I
1. ABBREVIATIONS AND ANNOTATION.....	III
1.1. REGISTER OF ABBREVIATIONS.....	III
1.2. VARIABLES AND UNITS.....	V
1.3. STRUCTURES OF CHEMICALS.....	VI
2. ABSTRACT.....	XI
3. ZUSAMMENFASSUNG.....	XVII
4. GENERAL INTRODUCTION AND AIM OF THIS THESIS.....	1
5. STATE OF KNOWLEDGE.....	5
5.1. BRIEF INTRODUCTION TO CONTROLLED RADICAL POLYMERIZATIONS.....	6
5.2. REVERSIBLE ADDITION-FRAGMENTATION CHAIN TRANSFER POLYMERIZATION.....	6
5.3. INTRODUCTION TO THERMORESPONSIVE PROPERTIES.....	9
5.4. DUAL-THERMORESPONSIVE LCST-UCST BLOCK COPOLYMERS.....	17
5.5. IRON ION SENSITIVE MACROMOLECULAR COORDINATION LIGANDS.....	21
5.6. THERMORESPONSIVE COPOLYMERIC VECTORS FOR GENE DELIVERY.....	25
6. METHODS.....	33
6.1. DYNAMIC LIGHT SCATTERING.....	34
6.2. DIFFERENTIAL SCANNING CALORIMETRY.....	36
6.3. GEL-PERMEATION CHROMATOGRAPHY.....	38
6.4. UV-VIS SPECTROSCOPY.....	38
7. ADJUSTABLE UCST BY COPOLYMERIZATION OF AAM AND AN.....	43
7.1. INTRODUCTION TO COPOLYMERIZATION OF AAM AND AN.....	44
7.2. RESULTS AND DISCUSSION OF COPOLYMERIZATION OF AAM AND AN.....	45
7.3. SUMMARY AND CONCLUSION OF COPOLYMERIZATION OF AAM AND AN.....	61
8. PHOTO-CROSSLINKABLE NIPAAM-BASED LCST TERPOLYMERS.....	63
8.1. INTRODUCTION TO PHOTO-CROSSLINKABLE PNIPAAM TERPOLYMERS.....	64
8.2. RESULTS AND DISCUSSION OF PHOTO-CROSSLINKABLE PNIPAAM TERPOLYMERS.....	65
8.3. CONCLUSION AND OUTLOOK PHOTO-CROSSLINKABLE PNIPAAM COPOLYMERS.....	67
9. DOUBLE THERMORESPONSIVE LCST-UCST BLOCK COPOLYMERS.....	69
9.1. INTRODUCTION TO LCST-UCST BLOCK COPOLYMERS.....	70
9.2. RESULTS AND DISCUSSION OF LCST-UCST BLOCK COPOLYMERS.....	71
9.3. SUMMARY AND CONCLUSION OF LCST-UCST BLOCK COPOLYMERS.....	79

10.	THERMORESPONSIVE SWITCHING STATES IN NANOPORE MEMBRANES.....	81
10.1.	INTRODUCTION TO THERMORESPONSIVE SWITCHING STATES IN NANOPORES.....	82
10.2.	RESULTS AND DISCUSSION OF THERMORESPONSIVE SWITCHING STATES IN NANOPORES	84
10.3.	SUMMARY AND OUTLOOK OF THERMORESPONSIVE SWITCHING STATES IN NANOPORES	89
11.	IRON ION SENSITIVE MACROMOLECULAR COORDINATION LIGANDS.....	91
11.1.	INTRODUCTION TO MACROMOLECULAR COORDINATION LIGANDS	92
11.2.	RESULTS AND DISCUSSION OF MACROMOLECULAR COORDINATION LIGANDS.....	94
11.3.	CONCLUSION AND OUTLOOK OF MACROMOLECULAR COORDINATION LIGANDS	125
12.	THERMORESPONSIVE COPOLYMER VECTORS FOR GENE DELIVERY.....	127
12.1.	INTRODUCTION TO THERMORESPONSIVE COPOLYMER VECTORS	128
12.2.	RESULTS AND DISCUSSION OF THERMORESPONSIVE COPOLYMER VECTORS.....	130
12.3.	SUMMARY AND CONCLUSION OF THERMORESPONSIVE COPOLYMER VECTORS	142
13.	GENERAL CONCLUSION AND OUTLOOK OF THIS THESIS	145
14.	EXPERIMENTAL PART	149
14.1.	INSTRUMENTATION.....	150
14.2.	MATERIALS.....	154
14.3.	SYNTHESIS	155
15.	REFERENCES	197
16.	APPENDIX.....	205
16.1.	CHAIN TRANSFER AGENTS	206
16.2.	MONOMERS.....	216
16.3.	ADJUSTABLE UCST BY COPOLYMERIZATION OF AAM AND AN	224
16.4.	PHOTO-CROSSLINKABLE NIPAAAM-BASED LCST COPOLYMERS	237
16.5.	DOUBLE THERMORESPONSIVE LCST-UCST BLOCK COPOLYMERS	250
16.6.	THERMORESPONSIVE SWITCHING STATES IN NANOPORE MEMBRANES.....	255
16.7.	IRON ION SENSITIVE MACROMOLECULAR COORDINATION LIGANDS	259
16.8.	THERMORESPONSIVE COPOLYMER VECTORS FOR GENE DELIVERY	278

Acknowledgements

In the beginning, I want to express my gratitude to everybody, who received a share during the course of my dissertation and its success.

Firstly, I would like to thank particularly Prof. Dr. Ulrich Jonas for the opportunity and his supervision of my dissertation during the last four years in the Macromolecular Chemistry group in the University of Siegen. With the help of his inspiring discussions, scientific care and characteristic way of interpersonally relating to individuals, he is deserving of special gratitude.

Secondly, many thanks go to my cooperation partners from the attended projects.

I would like to thank Prof. Dr. Holger Schönherr for the collaboration with the Physical Chemistry group in the University of Siegen and the opportunity to participate in the interdisciplinary exchange between the Universities of Brest and Siegen *via* the PROCOP project. Besides, I was glad to exchange ideas and take part in the lively discussion with Dr. Stephanie Müller or M.Sc. Qasim Alhusaini within the common nanopores project.

Additionally, I want to thank Prof. Dr. Tristan Montier from the Medical Faculty of the University of Brest (F) for the common collaboration, the gained access and practical insights into his biological laboratories and the possibility of interdisciplinary as well as intercultural exchange. At this point, I also would like to especially thank Assistant Prof. Dr. Tony Le Gall for his time, effort and personal care. Dr. Yann Le Guen should be named as well for his scientific help and his great hosting.

Moreover, a special gratitude is owed to Dr. Franck Thetiot of the Inorganic Chemistry group in the University of Brest (F) for the great scientific work and shared time. With his effort, care and plenty of discussions, he had a great impact on my last four years. Besides, he variegated all my stays in Brest with his weekend trips and characteristic altruistic attitude. Thanks go as well to Dr. Narsimhulu Pittala for the synthesis of the triazole derivatives.

Furthermore, I would thank sincerely every single member of Macromolecular Chemistry Group for the support and the fantastic working atmosphere. Particularly, Dipl.-Lab.-Chem. Petra Frank is supposed to be mentioned here for her group organization, for her endless personal and technical support. As well, I want to thank all of my other colleagues, including M.Sc. Niklas Jung, M.Sc. Thorben Jaik, M.Sc. Clinton Richard Victor Thiagarajan, M.Sc. Fiona Diehl and M.Sc. Silvia Freese for the inspiring and helpful scientific environment and appreciated personal time. Additionally, Sandra Münker deserves my gratitude for her support. Particularly, I would like to thank all helpful correctors such as Dipl.-Lab.-Chem. Petra Frank, M.Sc. Clinton Richard Victor Thiagarajan, M.Sc. Sina Sarrafi and my brother

M.Sc. Till Meier for being my attentive glasses and gifting me a lot of their time for supporting critics and hints.

Last but not least, I want to express my most special gratitude to my family, my mum, my dad, my brother and my grandparents for their balancing love, continuous support and being my inspirational basis for all my deeds and progress in life. You all are and forever will be a part of me. Of course, one should not forget to honour my beloved girlfriend Anne, who supported and balanced me whenever it was possible. Lastly, I would like to thank all my friends for being a very important and colourful part of my life.

**„Die unterhaltendste Fläche auf der Erde für uns
ist die vom menschlichen Gesicht.“**

Georg Christoph Lichtenberg

1. Abbreviations and Annotation

1.1. Register of Abbreviations

The experiments are specified by the reaction code [MEM] and the corresponding experiment number, which are equal to the denomination in the lab journal. Besides that, following acronyms are used:

A.	Appendix
AA	Acrylic acid
AAm	Acrylamide
Abb.	Abbreviation
AN	Acrylonitrile
AIBN	2,2'-Azobis-2-methylpropionitrile
APAAm	<i>N</i> -(3-Aminopropyl) acrylamide
APTRZ	[1,2,4]-Triazole-1-yl-propylamine
APTRZMAAm	<i>N</i> -[3-(4 <i>H</i> -1,2,4-Triazol-4-yl)propyl] methacrylamide
AIPC	2,2'-Azobis[2-(2-imidazolin-2-yl)propane] dihydrochloride
BC	Block copolymer (in sample abbreviation)
BIT	2,2'-[Thiocarbonylbis(sulfanediyl)]-bis-(2-methylpropanoic acid)
BPAAm	<i>N</i> -(4-Benzoylphenyl) acrylamide
BP	Benzophenone (in sample code)
C/CP	Copolymer (in sample code)
CRP	Controlled radical polymerization
CryoTEM	Cryostatic transmission electronmicroscopy
CuAAC	Copper(I) catalyzed azide-alkyne cycloaddition reaction
CTA	Chain transfer agent
\bar{D}	Dispersity
DCM	Dichloromethane
DLS	Dynamic light scattering
DMAc	Dimethylacetamide
DMAP	<i>N,N</i> -Dimethylpyridin-4-amine
DMP	2-[[Dodecylthio]carbothioyl]thio}-2-methylpropanoic acid
DMP-APTRZ	1-[[3-(4 <i>H</i> -1,2,4-triazol-4-yl)propyl]amino}-2-methyl-1-oxopropan-2-yl)dodecyl carbonotrithioate
DMSO	Dimethylsulfoxide
DSC	Differential scanning calorimetry
EDC	3-(Ethyliminomethyleneamino)- <i>N,N</i> -dimethylpropane-1-amine
EMP	2-[[Ethylthio]carbothioyl]thio}-2-methylpropanoic acid
ESR	Electron spin resonance
EtBr	Ethidiumbromide
EtOAc	Ethyl acetate
Et ₃ N	Triethylamine
FRP	Free radical polymerization
Fig.	Figure
GPC	Gel-permeation-chromatography
HEAAm	<i>N</i> -(2-Hydroxyethyl) acrylamide
HPLC-MS	High performance liquid chromatography coupled to mass spectrometry
HTRZ	[1,2,4]-Triazole
HS	High-spin
IR	Infrared
Hex	Hexane
L/LC	LCST (co-)polymer (as sample abbreviation)

LCST	Lower critical solution temperature
LS	Low-spin
MAA	Methacrylic acid
MeCN	Acetonitrile
MeOH	Methanol
NIPAAm	<i>N</i> -Isopropyl acrylamide
NMR	Nuclear magnetic resonance spectroscopy
NHS	<i>N</i> -Hydroxysuccinimide
P	Homopolymer (in sample abbreviation)
PNIPAAm	Poly(<i>N</i> -isopropylacrylamide)
R	Reference (as sample abbreviation)
RAFT	Reversible-addition-fragmentation transfer polymerization
r.t.	Room temperature
ST	Spin-transition
SCO	Spin-crossover
SQUID	Superconducting quantum interference device
TGA	Thermogravimetric analysis
Tab.	Table
TBAS	Tetrabutylammonium hydrogensulfate
TEA	Triethylamine
THF	Tetrahydrofurane
TLC	Thin-layer chromatography
TRZ	[1,2,4]-Triazole moiety
UCST	Upper critical solution temperature
U/UC	UCST (co-)polymer (as sample abbreviation)
UV	Ultraviolet

1.2. Variables and Units

A	Absorption
[Å]	Angstroms
[a.u.]	Arbitrary units
[°C]	Degree Celsius
c	Concentration
D	Diffusion coefficient
d	Diameter
D_h	Hydrodynamic diameter
ϵ	Decadic extinction coefficient
[g]	Gram
[h]	Hour
[Hz]	Hertz
I	Present intensity
I_0	Intensity at time zero
[K]	Kelvin
k_B	Boltzmann constant
kb	Thousand base pairs (of DNA)
l	Length
[L]	Liter
[m]	Meter
m	Milli
M	Molar
μ	Micro
[min]	Minute
[MHz]	Mega Hertz
\bar{M}_n	Number average molar mass
\bar{M}_p	Molar mass of the peak maximum
\bar{M}_w	Weight average molar mass
n	Nano
η	Viscosity
p	Pico
pH	Power of hydrogen
$\langle r^2 \rangle^{1/2}$	End-to-end-distance
R_H	Hydrodynamic radius
rpm	Revolutions per minute
[s]	Second
$\langle s^2 \rangle^{1/2}$	Radius of gyration
S	Total spin
S_0	Ground state
S_x	Excited state
T	Temperature
T_c	Cloud point temperature
T_g	Glass transition temperature
T_m	Transition phase gel to liquid
[V]	Voltage
V	Volume
% Vol.	Percentage volume
wt%	Weight-percent
λ	Wavelength

1.3. Structures of Chemicals

Table I: The abbreviations, structures and names of the used monomers.

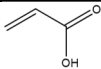
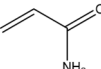
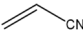
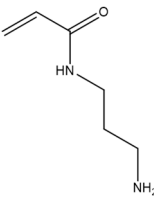
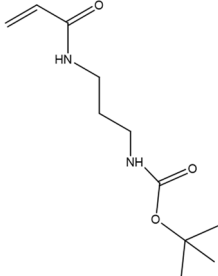
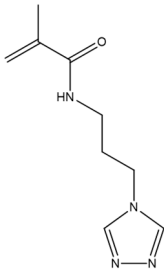
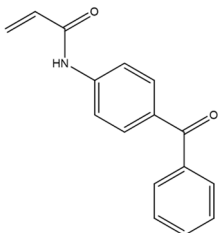
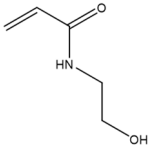
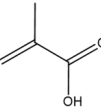
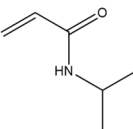
Abbreviation	Structure	Name
AA		Acrylic Acid
AAm		Acrylamide
AN		Acrylonitrile
APAAm		<i>N</i> -(3-Aminopropyl) acrylamide
APAAm-Boc		<i>tert</i> -Butyl (3-acrylamidopropyl) carbamate
APTRZMAAm		<i>N</i> -[3-(4 <i>H</i> -1,2,4-Triazol-4-yl)propyl] methacrylamide
BPAAm		<i>N</i> -(4-Benzoylphenyl) acrylamide
HEAAm		<i>N</i> -(2-Hydroxyethyl) acrylamide
MAA		Methacrylic acid
NIPAAm		<i>N</i> -Isopropyl acrylamide

Table II: Abbreviations, structures and names of the synthesized chain transfer agents.

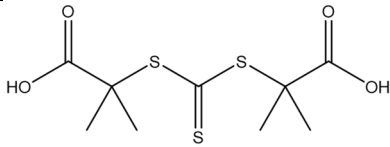
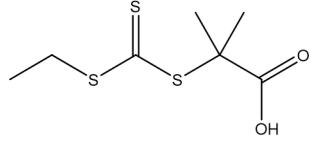
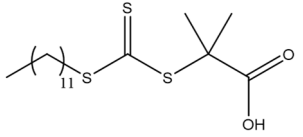
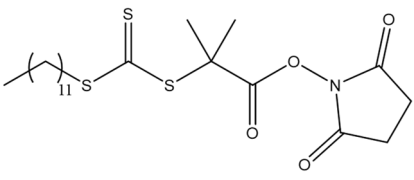
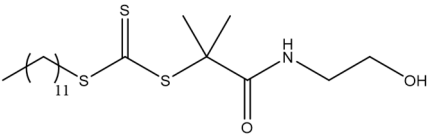
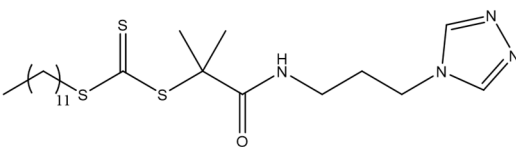
Abbreviation	Structure	Name
BIT		2,2'-[Thiocarbonylbis(sulfanediyl)]-bis-2-methylpropanoic acid
EMP		2-[[Ethylothio]carbothioyl]thio}-2-methylpropanoic acid
DMP		2-[[Dodecylthio]carbothioyl]thio}-2-methylpropanoic acid
DMP-NHS		2,5-Dioxopyrrolidin-1-yl 2-[[dodecylthio]carbonothioyl]thio}-2-methylpropanoate
DMP-EA		Dodecyl-{1-[(2-hydroxyethyl)amino]-2-methyl-1-oxopropan-2-yl} carbonotrithioate
DMP-APTRZ		1-[[3-(4H-1,2,4-Triazol-4-yl)propyl]amino]-2-methyl-1-oxopropan-2-yl dodecyl carbonotrithioate

Table III: The abbreviations, structures and targeted application of the synthesized (co-)polymers.

Abbreviation	Structure	App.
Poly(NIPAAm)-DMP		LCST system optimization
Poly(NIPAAm)-EMP		
Poly(NIPAAm-co-MAA-co-BPAAm)		
Poly(NIPAAm-co-AA-co-BPAAm)-DMP		
Poly(NIPAAm-co-MAA-co-BPAAm)-BIT		
Poly(NIPAAm-co-MAA-co-BPAAm)-DMP		
Poly(NIPAAm-co-AA-co-BPAAm)-DMP-EA		
Poly(NIPAAm-co-HEAAm-co-BPAAm)-DMP		

Table IV: The abbreviations, structures and targeted application of the synthesized (co-)polymers.

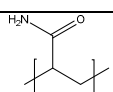
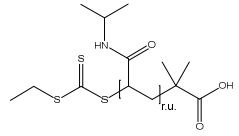
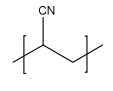
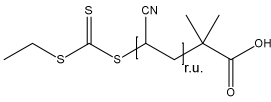
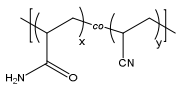
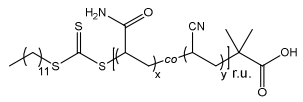
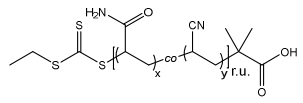
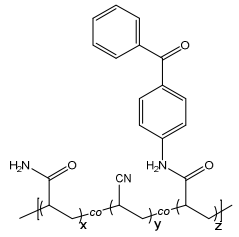
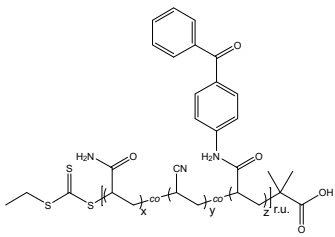
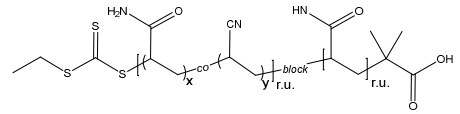
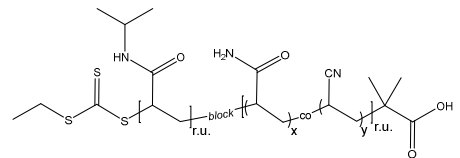
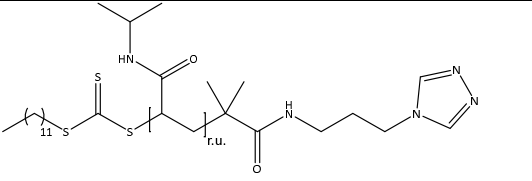
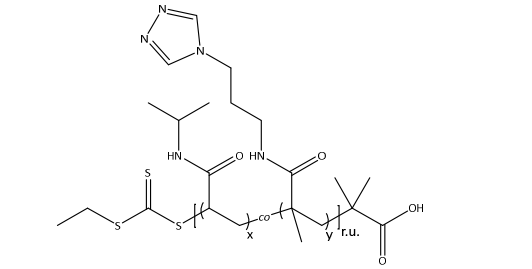
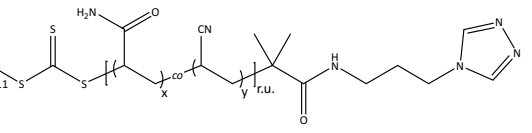
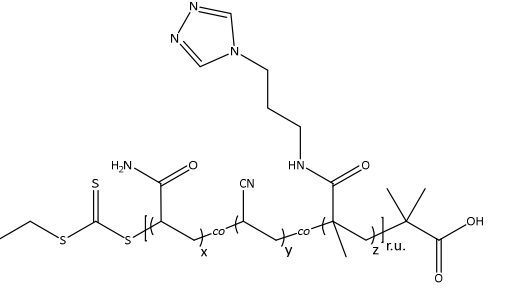
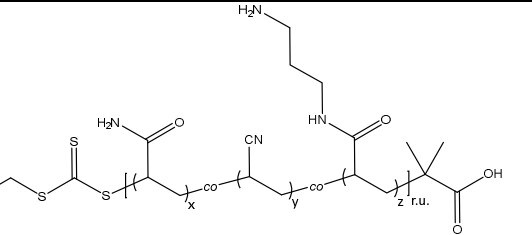
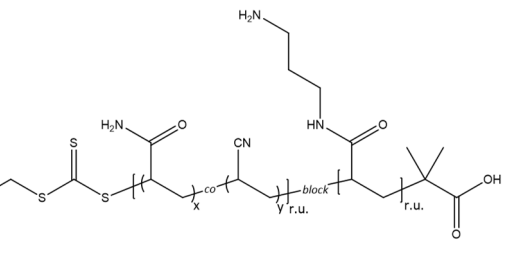
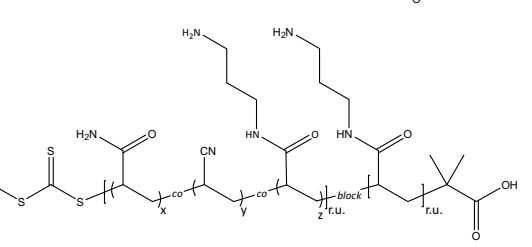
Abbreviation	Structure	App.
Poly(AAm)		UCST system optimization
Poly(AAm)-EMP		
Poly(AN)		
Poly(AN)-EMP		
Poly(AAm-co-AN)		
Poly(AAm-co-AN)-DMP		
Poly(AAm-co-AN)-EMP		
Poly(AAm-co-AN-co-BPAAm)		
Poly(AAm-co-AN-co-BPAAm)-EMP		
Poly[(AAm-co-AN)-block-(NIPAAm)]-EMP		
Poly[(NIPAAm)-block-(AAm-co-AN)]-EMP		

Table V: The abbreviations, structures, and targeted application of the synthesized (co-)polymers.

Abbreviation	Structure	App.
Poly(NIPAAm)-DMP-APTRZ		Iron ion sensitive macromolecular coordination ligand
Poly(NIPAAm-co-APTRZMAAm)-EMP		
Poly(AAm-co-AN)-DMP-APTRZ		
Poly(AAm-co-AN-co-APTRZMAAm)-EMP		
Poly(AAm-co-AN-co-APAAm)-EMP		Copolymer vector for gene delivery
Poly[(AAm-co-AN)-block-(APAAm)]-EMP		
Poly[(AAm-co-AN-co-APAAm)-block-(APAAm)]-EMP		

The following table (Table VI) gives an overview over the synthesized (co-)polymer samples, which are assigned to the certain research fields in this thesis. The abbreviations are related to the key properties of a sample as part of the corresponding experimental series. This table links the information of this work with the original data in the official laboratory journal (Macromolecular Chemistry, University of Siegen).

Table VI: The application fields of the samples, their used sample code in this dissertation and the corresponding reaction codes from the laboratory journal of the relevant (co-)polymers.

App.	Sample Code	Reaction Code	App.	Sample Code	Reaction Code
UCST optimization	FRP15%	A	LCST optimization	R1	MEM109 -
	FRP20%	B		FRP-MAA	MEM065 -
	FRP25%	C		CRP-AA	MEM083 -
	FRP30%	D		CRP-MAA-BIT	MEM088 A
	FRP35%	E		CRP-MAA	B
	FRP40%	F		CRP-AA-DMP-EA	MEM089 A
	FRP45%	G		CRP-HEAAm	B
	FRP50%	H		CRP-HEAAm10%16k	MEM093 -
	FRP-BP0.5%	A		CRP-HEAAm10%26k	MEM095 -
	FRP-BP1.0%	B		CRP-TRZ	MEM106 -
	FRP-BP1.3%1	E1	LCST-UCST block polymers	BC-LU	A3
	FRP-BP1.3%2	E2		BC-UL	C
	FRP-BP2.0%	C		BCU30.0%L	A
	FRP-BP5.0%	D		BCU32.5%L	B
	CRP25.0%	A		BCU35.0%L	C2
	CRP27.5%	B		BCU37.5%L	D
	CRP30.0%	C		BCU40.0%L	E
	CRP32.5%	D		BCU45.0%L	F
	CRP35.0%1	E		BCU50.0%L	G
	CRP35.0%2	E2		BCU55.0%L	H
	CRP37.5%	F	BC-U34L24	A	
	CRP40.0%	G	BC-U34L43	B	
	CRP41.0%	O	BC-U34L61	SCB077 C	
	CRP45.0%1	H	BC-U19L43	D	
	CRP45.0%2	H2	BC-U50L43	E	
	CRP50.0%	I	Macromolecular coordination ligands	P2k	A
	CRP55.0%	J		P4k	B
	CRP-BP0.5%	A		P7k	MEM017 C
	CRP-BP1.0%	B		P12k	D
	CRP-BP1.5%	C		P23k	E
	CRP-BP1.8%	D		P5k	MEM59 A
	CRP-BP2.0%	E		P25k	B
	R1CP	FRP		P3k	MEM063 -
	CRP3k	A		C4.9k10%	A
	CRP6k	B		C4.8k5%	MEM151 B
	CRP11k	C	C4.6k15%	C	
	CRP16k	D	UCP4k	A	
	CRP21k	E	UCP7k	B	
	CRP29k	F	UCP8k	LIR001 C	
	CRP0h	A	UCP16k	D	
	CRP1h	B	UCP27k	E	
	CRP2h	C	UCP11.6k2.5%	A	
	CRP4h	D	UCP14.9k5.0%	MEM153 B	
	CRP6h	E	UCP13.7k10.0%	C	
	CRP8h	F	Copolymer vectors	C10%	A
CRP24h	G	C10%AN		MEM148 A2	
R2AN-FRP	ZIL001 -	C20%		A22	
R3AAm-FRP	ZIL002 -	BC20		B2	
R4AN-CRP	ZIL003 -	C30%		A30	
R5AAm-CRP	ZIL004 -	C40%		A40	
		BC40		B40	
		BC60	B60		
		BC60AN	J2		
		BC20%40	C2		

2. Abstract

For advanced technical applications, the bio-inspired development of modern materials is of great importance and is *inter alia* encouraged by the discovery of liquid-liquid phase transitions, as main driving force for molecular structure formation of membrane-less organelles in living organisms. Motivated by this background, the present thesis is dedicated to the molecular design of advanced, modular polymer architectures based on versatile, thermoresponsive copolymer systems, bearing tuneable miscibility gaps in aqueous media in consequence of their lower or upper critical solution temperatures (LCST/UCST). These responses serve as external trigger to dynamically change “on-demand” the solvation properties of the macromolecular building blocks, which were exploited for several innovative applications in this thesis: (a) complex solution behaviours of dual-thermoresponsive LCST-UCST block copolymers, (b) characterization of thermally switchable membranes, (c) control of dynamic coordination structures in aqueous solution by thermoresponsive macromolecular coordination ligands and (d) non-viral copolymer vectors for gene delivery.

For this purpose, the LCST polymer poly(*N*-isopropyl acrylamide) (poly(NIPAAm)) and UCST analogue poly(acrylamide-co-acrylonitrile) (poly(AAm-co-AN)) are introduced as basic thermoresponsive systems, whose contrary solvation behaviours in aqueous polymer solutions are attributed by sharp and robust transitions, which can be monitored by turbidity measurements of their cloud points (T_c). The herein presented macromolecular structures are functionally designed by the choice of specific comonomers and were realized by the reversible addition-fragmentation chain transfer (RAFT) polymerization, which allows the fabrication of defined building blocks with variable end groups, controlled architectures and tuneable thermoresponsiveness.

The UCST system of poly(AAm-co-AN) was thoroughly studied to gain accurate knowledge about the prediction of the copolymer's thermoresponsive properties in free and controlled radical polymerization giving access to the subsequent research fields. In contrast to the literature, in which polar DMSO with high boiling point is used as solvent, the copolymer was synthesized in a mixture of water and 1,4-dioxane in order to simplify the common time-consuming purification (dialysis). Therefore, the polymerization parameters in terms of conversion and monomer incorporation were determined for the new reaction mixture in dependence of the reaction time to guarantee a suitable copolymerization behaviour of the monomers acrylamide (AAm) and acrylonitrile (AN). For the copolymers, the T_c could be synthetically adjusted by the choice of the proper acrylonitrile fraction in the monomer feed. An additional terpolymerization with the monomer *N*-(4-benzoylphenyl) acrylamide (BPAAm) provided access to the fabrication of photo-crosslinkable copolymers, which could be either covalently attached to surfaces or transformed to hydrogels by intramolecular network

formation *via* subsequent irradiation with UV light. These entire study results in an accurate prediction for the adjustment of desired cloud point temperatures within the copolymerization of AAm, AN and BPAAm, tremendously improving the applicability of this copolymer system. The already extensively-studied LCST system of poly(NIPAAm) was employed as robust thermoresponsive counterpart, which was copolymerized with BPAAm and hydrophilic comonomers to yield linear photo-crosslinkable copolymers with appropriate transition temperatures, enabling the subsequent fabrication of responsive hydrogels. These two main polymer systems were modified for the use in the following four application fields.

In the first research field, the contrary thermoresponsive systems above were combined in a dual-thermoresponsive LCST-UCST block copolymer by pursuing the sequential RAFT copolymerization pathway. This novel system of poly[(AAm-co-AN)-*block*-NIPAAm]-EMP showed a complex solvation behaviour in aqueous solution dependent to the adjustable hydrophobicity of its UCST block. While the thermoresponsiveness in previously reported systems is explained on basis of the simple behaviour of a homopolymer chain, here the analysis of the complex interdependent phase transitions also includes the intramolecular influence between both thermoresponsive blocks and their particular solvation state. The marked shift of the transition temperatures, when comparing the homoblocks with the corresponding block copolymers, is caused by the abrupt changes in the hydrophilicity during the coil-to-globule transitions for each block and therefore depends on the thermal history (heating or cooling cycle). Thus, the double-thermoresponsive copolymers were characterized with respect to their thermal behaviours, aggregate dimensions and calorimetric transitions *via* UV-Vis turbidity measurements, dynamic light scattering (DLS), and modulated differential scanning calorimetry (MDSC).

The second application demonstrated a successful combination of anodized aluminium oxide substrates (AAO) with thermoresponsive copolymers for the fabrication of thermally switchable nanopore membranes, to investigate reversibly alterable diffusion processes through nanoscopic channels by the external stimulus of temperature. While the inner pore surface of reported systems is usually functionalized with polymers *via* ATRP, here linear RAFT copolymers of characterized composition and thermoresponsiveness are deposited in adjustable quantities from solution, before they are photo-immobilized as hydrogels in the pores and forming highly defined membranes. The copolymer mass of the filling was quantified in thermogravimetric measurements with dynamic heating rate, while the thermoresponsive switching states in aqueous solution (in form of LCST transitions) could be evidenced inside the nanopores by MDSC for the first time.

In a third application, the reversible switchability of responsive polymer systems is married with the convenience of assembling highly defined molecular scaffolds by complexation of

metal ions with specifically tailored ligands. Novel macromolecular coordination ligands (MCLs) with LCST (published as: <https://doi.org/10.1039/D1PY00847A>) or UCST character in aqueous media have been designed by conjugation of thermoresponsive polymer systems poly(NIPAAm) or poly(AAm-co-AN) with 1,2,4-triazole coordination sites. These triazole units were integrated *via* the RAFT method into two fundamentally different MCL architectures following two synthetic strategies: (I) The customized chain transfer agent 1-[[3-(4H-1,2,4-triazol-4-yl)propyl]amino]-2-methyl-1-oxopropan-2-yl dodecyl carbonotrithioate (DMP-APTRZ) was employed for hemi-telechelic MCLs with a single triazole end group. (II) A tailored comonomer *N*-[3-(4H-1,2,4-triazol-4-yl)propyl] methacrylamide (APTRZMAAm) provides access to multidentate MCLs with a controllable number of triazole side groups along the polymer backbone. The thermally controlled variation of the MCL volume demand was exploited for reversible aggregate formation upon Fe²⁺ complexation with respect to their chain state in aqueous solution driven by the LCST or UCST behaviour. Thermal response was studied *via* UV-Vis turbidity measurements, aggregate dimensions were determined *via* DLS, while the aggregate morphology was analysed *via* customized transmission electron microscopy (TEM).

Finally, the copolymer system of AAm/AN was utilized for the first time in the scope of gene delivery research as basis of polycationic, non-viral vectors with UCST character. The RAFT methodology is suitable for the preparation of variable vector designs with a controlled integration of pDNA binding sites *via* the copolymerization with the known comonomer *N*-(3-aminopropyl) acrylamide (APAAm) to introduce free amine side groups to the polymer backbone. In contrast to the literature, which focuses on LCST polymers as thermoresponsive base, here the contrary thermoresponsiveness of UCST vectors allows the reverse switching of the solvation states from hydrophobic to hydrophilic chain behaviour in aqueous media upon external temperature stimuli, leading to dynamic interactions between vector and pDNA. Those synthesized vectors demonstrated marked abilities to complex pDNA and further transfect several cell strains (C2C12, A549 and HeLa) in strong dependence of their molecular composition and skeletal architecture: In the latter, the APAAm units were either distributed (I) randomly, (II) as concise end block, or (III) as hybrid-structure along the macromolecular chain.

3. Zusammenfassung

Für fortgeschrittene technische Anwendungen ist die bio-inspirierte Entwicklung moderner Materialien von großer Bedeutung und wird unter anderem durch die Entdeckung von Flüssig-Flüssig-Phasenübergängen als Hauptantriebskraft für die molekulare Strukturbildung membranloser Organellen in lebenden Organismen bestärkt. Von diesem Hintergrund motiviert, widmet sich die vorliegende Dissertation dem molekularen Design fortschrittlicher, modularer Polymerarchitekturen thermoresponsiver Copolymer-Systeme, die durch ihre kritischen unteren oder oberen Lösungstemperaturen (engl.: LCST/UCST) justierbare Mischungslücken im wässrigen Medium aufweisen. Dieses Verhalten dient als äußerer Impuls, um die Solvatationseigenschaften der makromolekularen Bausteine „nach Bedarf“ dynamisch zu ändern, die in dieser Arbeit für mehrere innovative Anwendungen genutzt wurden: (a) komplexes Lösungsverhalten von zweifach-thermoresponsiven LCST-UCST-Blockcopolymeren, (b) Charakterisierung thermisch-schaltbarer Membranen, (c) Kontrolle dynamischer Koordinationsstrukturen in wässriger Lösung durch thermoresponsive, makromolekulare Koordinationsliganden und (d) nicht-virale Copolymervektoren im Zuge des Gentransfers.

Zu diesem Zweck werden das LCST-Polymer Poly(*N*-isopropylacrylamid) (poly(NIPAAm)) und das UCST-Analogon Poly(acrylamid-co-acrylnitril) (poly(AAm-co-AN)) als grundlegende thermoresponsive Systeme vorgestellt, deren konträre Solvatationsverhalten in wässrigen Polymerlösungen scharfe und intensive Übergänge (engl.: T_c) aufweisen, die durch Trübungsmessungen ihres Phasenverhaltens beobachtet werden können. Die hier vorgestellten makromolekularen Strukturen wurden durch die Wahl spezifischer Comonomere konzipiert und durch die reversible Additions-Fragmentierungs-Kettentransfer-Polymerisation (engl.: RAFT polymerization) realisiert, welche die Herstellung definierter Bausteine mit variablen Endgruppen, kontrollierten Architekturen und einstellbarer Thermoresponsivität ermöglicht.

Das UCST-System Poly(AAm-co-AN) wurde tiefergehend untersucht, um genaue Kenntnisse über die Vorhersage der thermoresponsiven Eigenschaften des Copolymers in der freien und kontrollierten Radikalpolymerisation zu gewinnen und Zugang zu den nachfolgenden Forschungsgebieten zu gewähren. Im Gegensatz zur Literatur, in der als Lösungsmittel polares DMSO mit hohem Siedepunkt verwendet wird, wurde das Copolymer in einer Mischung aus Wasser und 1,4-Dioxan synthetisiert, um die übliche zeitaufwendige Reinigung (Dialyse) zu verkürzen. Daher wurden die Polymerisationsparameter hinsichtlich des Umsatzes und des Monomer-Einbaus in Abhängigkeit der Reaktionszeit für das neue Reaktionsgemisch bestimmt, um ein geeignetes Copolymerisationsverhalten der Monomere Acrylamid (AAm) und Acrylnitril (AN) zu gewährleisten. Bei den Copolymeren konnte der T_c

durch die Wahl des passenden Acrylnitril-Gehaltes in der Einwaage der Monomere synthetisch eingestellt werden. Eine zusätzliche Terpolymerisation mit dem Monomer *N*-(4-Benzoylphenyl)acrylamid (BPAAm) ermöglichte die Herstellung von photo-vernetzbaaren Copolymeren, die entweder kovalent an Oberflächen gebunden oder durch intramolekulare Netzwerkbildung mit anschließender UV-Bestrahlung in Hydrogele umgewandelt werden konnten. Diese Gesamtheit der synthetischen Studien erlaubte die Herleitung einer genauen Vorhersage zur Einstellung gewünschter Trübungspunkttemperaturen bei der Copolymerisation von AAm, AN und BPAAm, wodurch die Anwendbarkeit dieses Copolymerensystems enorm gesteigert werden konnte.

Das bereits umfassend untersuchte LCST-System Poly(NIPAAm) wurde als robustes, thermoresponsives Analogon verwendet, welches mit BPAAm und hydrophilen Comonomeren copolymerisiert wurde, um lineare photo-vernetzbaare Copolymere mit adäquaten Übergangstemperaturen zu synthetisieren und die anschließende Herstellung von responsiven Hydrogelen zu ermöglichen.

Diese zwei Polymersysteme wurden für den Einsatz in den folgenden vier Anwendungsgebieten modifiziert.

Im ersten Forschungsgebiet wurden die oben genannten gegensätzlichen thermoresponsiven Systeme in einem zweifach-thermoresponsiven LCST-UCST-Blockcopolymer kombiniert, indem eine sequentielle RAFT-Copolymerisation verfolgt wurde. Dieses neuartige System poly[(AAm-co-AN)-*block*-NIPAAm]-EMP zeigte ein komplexes Solvationsverhalten in wässriger Lösung in Abhängigkeit der einstellbaren Hydrophobie seines UCST-Blocks. Während die Thermoresponsivität in zuvor berichteten Systemen auf der Grundlage des einfachen Verhaltens einer Homopolymerkette erklärt wird, umfasst die vorliegende Analyse der komplexen voneinander abhängigen Phasenübergänge auch den intramolekularen Einfluss zwischen den beiden thermoresponsiven Einzelblöcken und ihrem jeweiligen Solvationszustand. Die deutliche Verschiebung der Übergangstemperaturen beim Vergleich zwischen Homoblock und des entsprechenden Blockcopolymeren zeigt, dass während der Knäuel-Globuli-Übergänge eine abrupte Änderung der Hydrophilie für jeden Block verursacht wird, weswegen sie daher von der thermischen Vorgeschichte abhängt (Heiz- oder Kühlzyklus). So wurden die doppelthermoresponsiven Copolymere hinsichtlich ihres thermischen Verhaltens, ihrer Aggregatdimensionen und kalorimetrischen Übergänge durch UV-Vis-Trübungsmessungen, dynamischer Lichtstreuung (engl.: DLS) und modulierte Differenzkalorimetrie (eng.: MDSC) untersucht.

Die zweite Anwendung stellte eine erfolgreiche Kombination von anodisierten Aluminiumoxidsubstraten (AAO) mit thermoresponsiven Copolymeren zur Herstellung von thermisch schaltbaren Nanoporenmembranen dar, um reversibel veränderbare Diffusionsprozesse durch nanoskopische Kanäle durch den externen Temperaturreiz zu

untersuchen. Während die innere Porenoberfläche der beschriebenen Systeme normalerweise mit Polymeren über ATRP funktionalisiert wird, werden hier lineare RAFT-Copolymere, charakterisierter Zusammensetzung und Thermoreaktion, in gewünschten Mengen aus Lösung abgeschieden, bevor sie als Hydrogele in den Poren photo-immobilisiert werden und hochdefinierte Membranen bilden. Die Copolymer-Masse der Füllung wurde in thermogravimetrischen Messungen mit dynamischer Heizrate quantifiziert, während die thermoresponsiven Schaltzustände in wässriger Lösung (in Form von LCST-Übergängen) erstmals innerhalb der Nanoporen durch MDSC nachgewiesen werden konnten.

In einer dritten Anwendung wird die reversible Schaltbarkeit responsiver Polymersysteme mit der Bequemlichkeit des Aufbaus hochdefinierter molekularer Gerüste durch Komplexierung von Metallionen mit speziell zugeschnittenen Liganden kombiniert. Neuartige, makromolekulare Koordinationsliganden (engl.: MCLs) mit LCST- oder UCST-Charakter im wässrigen Medium wurden durch Konjugation der thermoresponsiven Polymersysteme Poly(NIPAAm) (veröffentlicht als: <https://doi.org/10.1039/D1PY00847A>) oder Poly(AAm-co-AN) mit 1,2,4-Triazol-Koordinationsstellen versehen. Diese Triazol-Einheiten wurden über die RAFT-Methode in zwei grundlegend unterschiedliche MCL-Architekturen mittels zweier Synthesestrategien integriert: (I) Ein modifiziertes Kettenübertragungsmittel 1- $\{[3-(4H-1,2,4\text{-triazol-4-yl})\text{propyl}] \text{amino}\}$ -2-methyl-1-oxopropan-2-yl-dodecylcarbonotrithioat (DMP-APTRZ) wurde für hemi-telechele MCLs mit einer einzelnen Triazol-Endgruppe verwendet. (II) Ein maßgeschneidertes Comonomer *N*- $[3-(4H-1,2,4\text{-triazol-4-yl})\text{propyl}]$ methacrylamid (APTRZMAAm) bietet Zugang zu mehrzähligen MCLs mit einer kontrollierbaren Anzahl von Triazol-Seitengruppen entlang des Polymerrückgrats. Die thermisch-kontrollierte Variation des MCL-Volumenbedarfs wurde für eine reversible Aggregatbildung genutzt, bei der die Fe^{2+} -Komplexierung in Abhängigkeit von ihrem Kettenzustand in wässriger Lösung durch das LCST- oder UCST-Verhalten gesteuert werden konnte. Das thermische Verhalten wurde durch UV-Vis-Trübungsmessungen untersucht, während die Aggregatmessungen mittels DLS und die Aggregatmorphologie mittels individueller Transmissionselektronenmikroskopie (TEM) analysiert wurde.

Schließlich wurde das Copolymersystem aus AAm/AN erstmals im Rahmen der Gentransfer-Forschung als Basis polykationischer, nicht-viraler Vektoren mit UCST-Charakter genutzt. Die RAFT-Methodik eignet sich für die Herstellung eines variablen Vektordesigns mit einer kontrollierten Integration von pDNA-Bindungsstellen über die Copolymerisation mit dem bekannten Comonomer *N*-(3-Aminopropyl)acrylamid (APAAm), um freie Amin-Seitengruppen in das Polymerrückgrat einzuführen. Im Gegensatz zur Literatur, welche sich ausschließlich auf LCST-Polymere als thermoresponsive Grundlage fokussiert, ermöglicht hier die gegenteilige Thermoresponsivität von UCST-Vektoren das umgekehrte Umschalten der Solvatationszustände von hydrophobem zu hydrophilem Kettenverhalten im wässrigen

Medium bei externen Temperaturstimuli, was zu dynamischen Wechselwirkungen zwischen Vektor und pDNA. Diese synthetisierten Vektoren zeigten beachtliche Fähigkeiten, pDNA zu komplexieren und diverse Zellstämme (C2C12, A549 und HeLa) in starker Abhängigkeit ihrer molekularen Zusammensetzung und Skelettarchitektur zu transfizieren: In letzterer waren die APAAm-Einheiten entweder (I) zufällig (II) als definierter End-Block, oder (III) als beider Hybridstruktur entlang der makromolekularen Kette verteilt.

4. General Introduction and Aim of this Thesis

Natural processes are usually based on stimuli-driven, conformational and aggregational variations of proteins and other natural molecules.^{1,2} For several vital processes, liquid-liquid transitions emerged as recent mechanism for the formation of membrane-less organelles in living organisms.³⁻⁷ Such concepts also gain in importance for the bio-inspired development of modern materials and their implementation in advanced technical applications mimicking desired natural processes.^{8,9} This employed class of materials is known as “smart materials”, as those respond autonomously to environmental triggers by property changes.¹⁰

A key role in the development of smart materials play thermoresponsive polymers, which undergo property transformation upon temperature variation.¹¹ The temperature represents an external and non-invasive trigger to enhance originally static properties of a material by the introduction of dynamic responses. The sophisticated application of such materials is established by the target and reversible “on-demand” switching of alterable phase and volume transitions.¹²

In the current thesis, versatile sets of specialized smart materials with advanced architectures were designed by molecular engineering with respect to the targeted application field. The whole process for copolymers from the synthetic deliberations to their subsequent application in this thesis is illustrated in Figure 1.

Generally, the synthesized copolymers carry the key feature of retaining thermoresponsive properties. These properties are grouped into two classes: Lower critical solution temperature (LCST) and upper critical solution temperature (UCST). These systems undergo with miscibility changes in solution upon slight temperature changes. A demixing process upon heating indicates LCST behaviour, while UCST system demonstrate a miscibility change in the opposite temperature direction.^{13,14}

Poly(acrylamide-co-acrylonitrile) represents an prominent and cost-effective UCST system in aqueous medium. This example was chosen due to its advantageous and convenient properties. It offers a sharp transition, which is freely tuneable in the range of 0-100 °C due to varying monomer fractions of acrylamide (AAM) and acrylonitrile (AN) in the copolymer.¹⁵ Its non-ionic behaviour allows a notable tolerance against salts and pH variation. The LCST systems were based on poly(NIPAAm), as it represents an extensively studied and well-described polymer system, bearing highly robust and unsusceptible thermoresponsive properties around the human body temperature.^{16,17}

Those thermoresponsive components can be copolymerized with other comonomers to tune the cloud points *via* variation of the delicate hydrophilic-hydrophobic balance in the copolymer chain. Additionally, the versatile macromolecular basis can be equipped with specific properties for the use in the presented application fields by integrating other reactive units with desired functionalities such as photo-crosslinkability, metal ion complexation or DNA condensing functions.¹⁸⁻²⁰

In addition to the proper choice of features, such advanced applications require convenient fabrication pathways for the formation of defined building blocks. The utilized reversible addition-fragmentation chain transfer polymerization (RAFT) corresponds to the controlled synthetic approaches and is a powerful tool for the preparation of complex polymer structures with desired molar masses, narrow dispersities and introducible end group modifications. This process provides access to a variety of skeletal architectures, which has to be considered in each case regarding the optimization of the copolymer properties.²¹ For example, the RAFT mechanism allows sequential chain extension, which is favourable for the preparation of block copolymers.²²

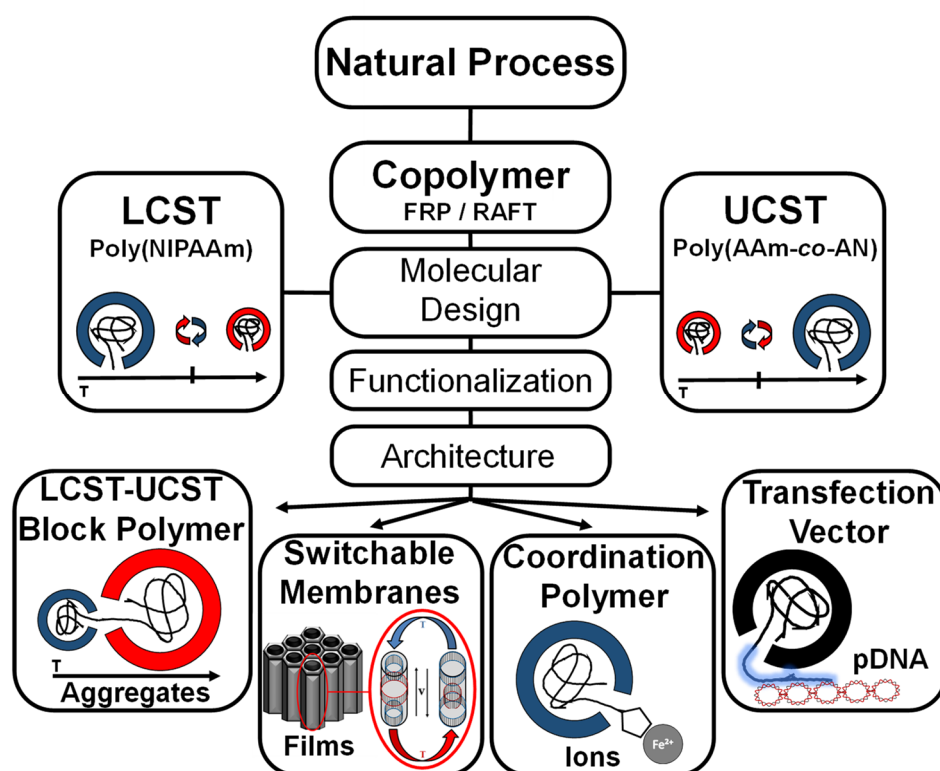


Figure 1: Flow chart illustrating the context of the current thesis. The synthesized and characterized thermoresponsive copolymer systems are based on poly(NIPAAm) and poly(AAm-co-AN) showing LCST and UCST behaviour. The systems were molecularly designed by the monomer composition, functionalized by the introduction of desired monomer units and fabricated in a target architecture specifically for the shown application fields.

In the course of this thesis, the noted general thermoresponsive systems were synthesized, characterized and modified for the particular research fields. The application of the copolymer sets dealt with study of the “schizophrenic” aggregation behaviour of dual-thermoresponsive LCST-UCST block copolymers (chapter 9, p.69), the thermoresponsive switching states in nanopore membranes (chapter 10, p.81), the coordinatively-driven aggregation behaviour of iron ion sensitive macromolecular coordination ligands (chapter 11, p.91) and the thermoresponsive non-viral vectors with UCST character for gene delivery treatments (chapter 12, p.127). These individual applications are briefly introduced in the respective chapters.

5. State of Knowledge

5.1. Brief Introduction to Controlled Radical Polymerizations

The free radical polymerization (FRP) is a popular chain polymerization method, which possesses a fundamental industrial impact. The risen exploitation is due to the potential employment of a variety of different polymerizable monomers.²³ Its facility, robustness towards impurities and enormous diversity of applicable monomers lead to a great commercial use.^{24,25} The restrictions are a broad size distribution, an uncontrolled polymerization process and limited polymer architectures.^{23,26,27} A broad Schulz-Flory-like distribution of the molar mass with large dispersity affect glass-, melting- and crystallization temperature and may result in undesired material properties. A completely homogenous polymer behaviour requires a narrow weight distribution.²⁸

A variety of methodologies were developed to combine a living-like polymerization character with the advantages of a free radical polymerization. In radical polymerizations, controlled conditions are achieved by the reduction of active chain ends and the corresponding termination processes. The active chain end reduction is accomplished by capturing the free radicals or effective chain transfer mechanisms in the simultaneous propagation step of all chains.²⁹ These strategies are grouped in the terminology controlled radical (or quasi-living) polymerization (CRP).²⁹

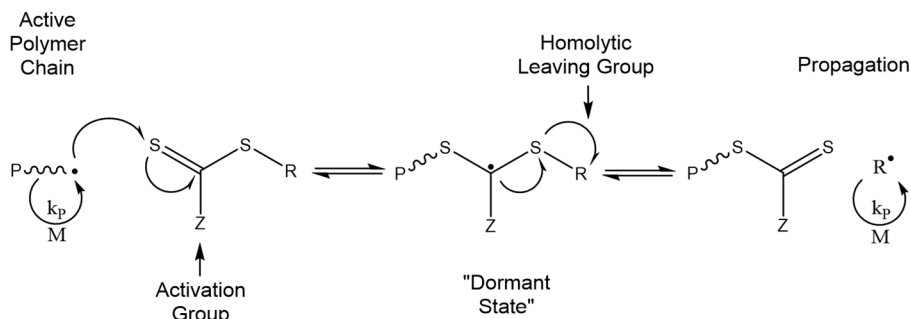
Nitroxide-mediated radical polymerization (NMP) or atom transfer radical polymerization (ATRP) belongs to the common pathways, as they lead to a capturing of the active chain ends.^{30,31} Reversible-addition-fragmentation chain transfer polymerization (RAFT) proceeds *via* effective chain transfer and produces a dormant state for an uniform chain propagation.³² The main issue is a highly controlled polymerization process with a narrow dispersity (Poisson-like distribution) and a potential polymer end-functionalization.³³

5.2. Reversible Addition-Fragmentation Chain Transfer Polymerization

The RAFT polymerization belongs, as mentioned previously, to the class of controlled radical polymerizations and is obtained by a conventional free radical polymerization in presence of a highly active chain transfer agent (CTA), leading to an effective chain transfer mechanism between active radicals and CTA (lowering probability of termination). The mechanism bears a high control over the chain growth process and effects a narrow molar mass distribution with enabled adjustment of the molar mass.³⁴

Utilizing RAFT mechanism, the CTA constitutes a facile pathway for the introduction of functional end groups to the subsequent polymer chain. The modification of the CTA opens an enormous variety of accessible synthetic routes for macromolecular engineering and the formation of complex polymer architectures. Potentially targeted properties like surface grafting *via* introduced anchor groups or molecular end group labelling, post-synthetic coupling reactions *via* functional groups (e.g. click chemistry, NHS esterification, disulfide

bridging of polymer chains *via* aminolysis of macroCTA or hetero-Diels-Alder cycloaddition), widespread accessible architectures (brushes, dendrimers, block and star polymers) and other post-synthetic approaches (e.g. grafting from the backbone or grafting to particle surfaces) are realized by this technique.^{34–37}



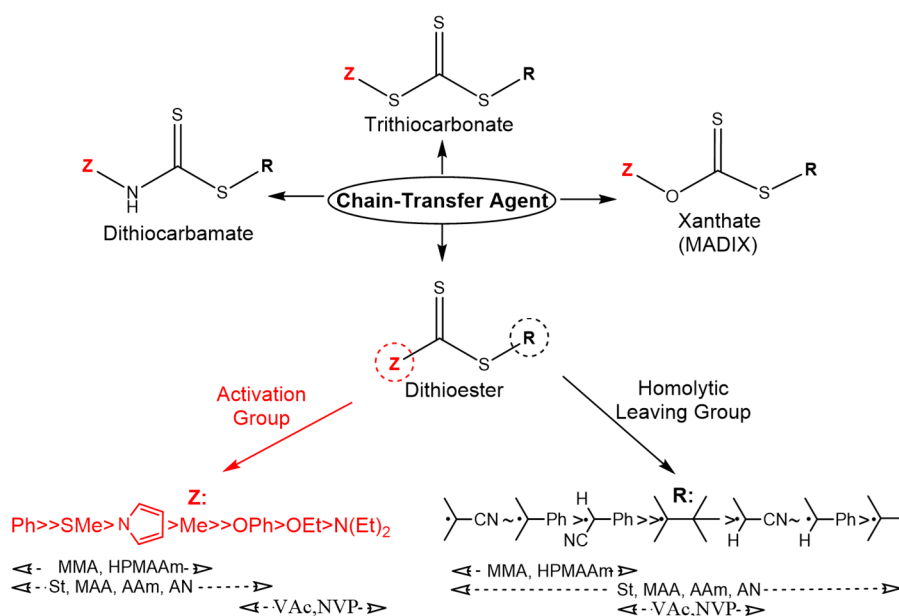
Scheme 1: The mechanism of RAFT polymerization with its main equilibrium of the chain transfer between chain propagation and dormant state.

The controlled conditions are achieved by addition-fragmentation equilibria caused by the chain transfer agent. It is commonly based on xanthate, dithioester, trithiocarbonate or trithiocarbamate derivatives and has to be chosen in accordance to the nature of the monomer.^{38–40} For instance, trithiocarbonates suit for the RAFT polymerizations of styrenes, acrylates and acrylamides, while thiocarbonates support vinyl ester and -amide polymerizations.⁴¹

The CTA represents a highly reactive thiocarbonylthio compound and consist of an activating Z- and homolytic leaving R-group. The interplay of Z- and R-group determines the reactivity of the CTA, which has to be adjusted to the choice of polymerized monomers.⁴² The initiation is induced by the decomposition of the initiator as source of radicals (thermally- and photo-induced, or *via* redox system). A radical chain end adds to the thiocarbonylthio species ($P^{\bullet} + R-SC(Z)=S$) and forms the dormant state ($R-SC(Z)-S-P$). Its fragmentation results in a released radical ($S=SC(Z)-P + R^{\bullet}$), which is able to propagate. The rapid equilibrium between the active radical species (P^{\bullet} and R^{\bullet}) and the dormant state leads to a rapid de- and activation of the propagation step *via* predominating chain transfer, which leads to a consistent, equal but intermittently chain growth. The molecular mass increases linearly with conversion, until the monomers are consumed. The isolated polymer species carries still the reactive chain transfer agent moiety, which can be re-initiated and used as macroCTA, further modified or removed.^{37,43}

The Z-group stabilizes the radical and its intermediate state. It influences both, the fragmentation and propagating process in the dormant state, which is represented in the radical addition and fragmentation rate. A strong stabilization renders the polymerization processes due to reduced propagation rates.

The R-group is supposed to be a good leaving group. It is responsible for the re-initiation of the propagation step and allow the free exchange of the active polymer chain end (RM_x^\bullet), which is affected by the interplay of the leaving group R and the reactivity of the Z-group.⁴² The homogeneous propagation among all chains correlates with a high transfer-constant (C_{tr}). The control of the polymerization increases along the value of the transfer constant, so that an initiation of a new polymerization reaction is preferred. Ideally, the released radical R^\bullet exhibits a similar reactivity as the propagating species (RM_x^\bullet), so that an efficient chain transfer occurs and leads to the small dispersity ($\mathcal{D} = 1.0-1.3$) and linearly growth of the polymer.^{42,44} This mechanism with its main equilibrium is briefly depicted in Scheme 1, while common classes of CTAs are shown below in Scheme 2.



Scheme 2: Chemical structure of the most common CTA classes for RAFT polymerization with general reactivity series of activation (Z) and homolytic leaving groups (R) with respect to potential polymerizable monomers. Concept schematics partially based on Keddie et al.⁴²

The living-like character of the RAFT polymerization enables the adjustment of the degree of polymerization and the corresponding approximate averaged molecular mass. Experimentally, it is defined as the molar fraction of monomer and CTA. The number averaged molar mass (\bar{M}_n) is determined by product of the molar mass of the monomer (M_M), the molar fraction of the feed ratio of (weighted) monomer ($[M]_0$) and chain transfer agent ($[CTA]_0$) in dependence of the conversion (ρ) including the molar mass of the CTA (M_{CTA}). Commonly, the CTA is applied in five- to tenfold excess according to the initiator.²¹

$$\bar{M}_n = M_M \cdot \frac{[M]_0}{[CTA]_0} \cdot \rho + M_{CTA} \quad (1)$$

The result of the molar mass prediction can be determined by gel-permeation chromatography or ^1H NMR measurements (via comparison of characteristic repeat unit

signals with respect to a single end group).⁴⁵ The ¹H NMR analyses delivers satisfying reliabilities exclusively for small molar masses ($\bar{M}_n < 10 \text{ kg}\cdot\text{mol}^{-1}$) due to the diffusion broadening of the end group signals.

The RAFT process combines the overcome limitations with the advantages of a free radical polymerization. Its simplicity, the tolerance to several solvents (even water) or impurities, and diversity of applicable monomers is expanded by the potential introduction of targeted functional moieties, the molecular engineering of complex structures and formation of sophisticated architectures.³⁹

For industrial and biomedical applications, the removal or transformation of the CTA moiety is of great interest and has been studied to avoid undesired coloration and potential harmfulness of the material. The removal of the trithiocarbonyl moiety from the polymer chain is proceeded *via* radical-induced reduction of the thiocarbonyl group or transformed *via* aminolysis.^{37,43,46}

5.3. Introduction to Thermoresponsive Properties

5.3.1. Thermoresponsive Properties of Polymer Solutions

Thermoresponsive polymer behaviour is characterized by drastic solubility changes of polymer solutions upon variation in temperature. As the temperature represents an external trigger to switch the original (static) properties of a polymer, the class belongs to the smart or stimuli-responsive materials.¹² The temperature change allows a unique manipulation of characteristic properties such as solubility⁴⁷, E-modulus⁴⁸, optical density^{49,50}, aggregation sizes, hydrophilicity^{51,52} or certain volume changes in polymer films⁵³. Due to the dynamic self-altering, thermoresponsive polymers are emerged in promising smart systems in the field of bio-separation, hydrogels, liquid chromatography, sensors, biomedical applications, gene therapy, tissue engineering or in drug delivery.^{54–58}

The general class of thermoresponsive polymers is divided into the two subclasses of lower critical solution temperature (LCST) and upper critical solution temperature (UCST) polymers.⁵⁹ When the demixing process (or loss of solubility) of a polymer solution occurs upon heating, a lower critical solution temperature is present.¹³ An upper critical solution temperature is indicated by a miscibility change in the contrary temperature direction.¹⁴

The thermodynamic origin of demixing deviates in between LCST and UCST, so that they are not ordinary inversions. While the lower critical solution temperature is predominantly enthalpically-driven, the upper critical solution temperature is referred to entropically events.^{60–62} Generally, the transition temperatures are caused by a delicate balance between polymer-polymer and polymer-solvent and solvent-solvent interactions. The phase separation process, based on the Gibbs free energy of mixing for polymer solutions, is detailed described by Flory-Huggins theory (in detail in chapter 5.3.2).^{28,63} In the miscible

regime, the polymers are solubilized *via* dipole-dipole interactions and hydrogen bonding of the polar groups, while a cage of water molecules is arranged around nonpolar segments (hydrophobic hydration).⁶² Due to the changes in temperature, the Gibbs free energy of mixing turns positive and a coil-to-globule-transition occurs (in the phase diagram of Figure 2).^{28,63}

Taking LCST polymers as example, they are homogeneously dissolvable below the critical solution temperature, maintaining a high degree of solvent-polymer interaction. Above, the cooperative dehydration of the polymer chains takes place, and the polymer coil collapses (globular state). The polymer chains and chain segments predominantly develop intra- and intermolecular interactions. It leads to larger aggregates and results in the appearance of a cloud point.^{49,64–66} UCST polymer solutions behave *vice versa* and proceed the coil-to-globule transition out of the miscible regime upon cooling.

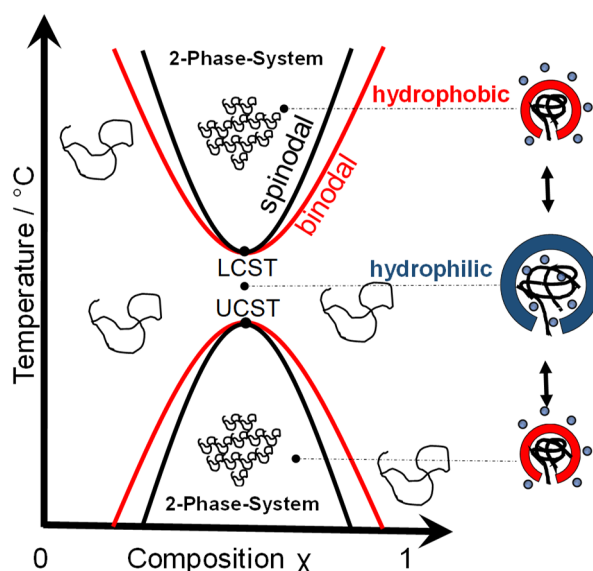


Figure 2: Schematic temperature-composition diagram of thermoresponsive polymer systems bearing LCST or UCST behaviour with corresponding indication of the hydrophobic and hydrophilic coil states during the coil-to-globule transitions in aqueous solution.⁶⁴

The behaviour of thermoresponsive materials in solutions is visualized in a phase diagram (or T- χ -diagram) (shown in Figure 2). It illustrates the composition dependent demixing of thermoresponsive polymer solutions, hereby combined for LCST and UCST systems. The demixing processes from a homogeneous polymer solution into the immiscible phase occurs crossing the binodal and spinodal curves. The area between both curves is declared as metastable region. The spinodal characterizes the transition to the complete immiscible two-phased system. It is important to note that the LCST or UCST is defined as the temperature minimum or maximum of the corresponding curves (allowing a direct inter-phased de-/mixing transition). Thus, they are characteristic points referred to a specific polymer concentration, which are resulted from the intercept of the spinodal and binodal curves. The unspecified demixing temperatures (independently from the concentration) proceed *via* co-existing phase

and is specified as cloud point or turbidity temperature with respect to its turbid appearance originating of larger scattering objects.

The detection of the clouding is performed *via* temperature dependent light absorbance measurements at a fixed wavelength and (commonly) 1.0 wt% concentration.^{57,67} The thermodynamic and kinetic approach of the transition can be detected additionally *via* modulated differential scanning calorimetry.^{60,66–68}

5.3.2. Thermodynamic Aspects of Coil-to-Globule Transitions

The coil-to-globule mechanism (Figure 3) of thermoresponsive polymers occurs in (aqueous) solution. The polymer is solubilized in the miscible regime *via* dipole-dipole interactions and hydrogen bonding. The swollen state of the polymer coils reduces the van-der-Waals interactions of the backbone. The surrounding water molecules possess a high structuration due to their strong hydrogen bonding.^{62,66} The dissolving of polymer perturbs the solvent's structure due to the introduction of polar and apolar polymer groups in the solvent. The water molecules prefer self-interactions instead of hydrophobic moieties, so that the nonpolar groups are surrounded by cages of solvent molecules, which is called hydrophobic hydration. A growth of the hydrophobic fraction leads to a breakage of the cages, which result in a demixing of the polymer.^{62,66} The co-play of hydrophobic (e.g. polymer backbone, *N*-isopropyl or nitrile moieties in accordance to Figure 3) and hydrophilic components (e.g. amide groups) affect the delicate balance of the specific miscibility behaviour.

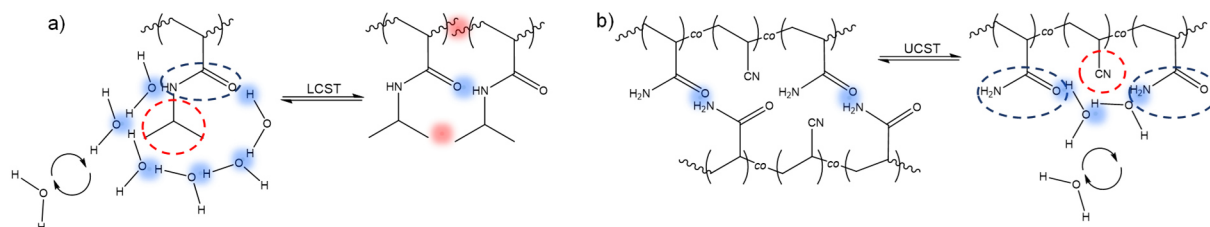


Figure 3: Schematic illustration of the coil-to-globule transition *via* LCST and UCST processes by the means of a) poly(NIPAAm) and b) poly(AAm-co-AN). The colour code indicates hydrophilic (blue) and hydrophobic (red) impacts (dashed) and interactions (solid). While the exemplary LCST polymer bears a hydrophilic and hydrophobic component within a single monomer unit (NIPAAm), the UCST system is copolymerized of separated hydrophilic (AAM) and hydrophobic units (AN).⁶⁴

The thermoresponsive behaviour of polymer solutions is established in the thermodynamic perspective of LCST or UCST and is theoretically further described by the Flory-Huggins. In this theory, the ordinary Gibbs free energy of mixing (ΔG_M) is enhanced by the assumption of a lattice model for the description of the thermodynamics in polymer solutions.^{28,63}

$$\Delta G_M = \Delta H_M - T\Delta S_M \quad (2)$$

It is expressed by term of enthalpy (ΔH_M) and thermally dependent entropy ($-T\Delta S_M$). While the process of demixing turns the value of Gibbs free energy positive ($\Delta G_M > 0$), the

dissolution delivers negative values ($\Delta G_M < 0$). The partial term of entropy (ΔS_M) possesses a positive value due to the risen number of potential arrangements in the dissolution process, while the enthalpy correlates with the energy liberation (exothermic) and consumption (endothermic) of the occurring processes. Followingly, this approach is derived from the interplay of polymer-polymer, polymer-solvent and solvent-solvent interactions. For ideal conditions, those interactions are equally contributed and result in a neglectable enthalpy of mixing ($\Delta H_M \sim 0$). These conditions are defined as theta conditions (showing an ideal freely-jointed polymer chain behaviour).^{28,63}

In the theory of Flory-Huggins, both solvent molecules and polymer segments can occupy an arbitrary free volume in the lattice, in which they are able to arrange randomly.⁶⁹ The enhancement of that theory is the Flory-Huggins parameter (χ), which implements a quantity for the interaction of solvent and polymer in a mixing process for one mole of lattice sites (hereby mole of chain segments) at a certain temperature (T) with the gas constant (R). The volume fractions of solvent and polymer are denoted by $\Phi_1 = n_1/(n_1 + x \cdot n_2)$ and $\Phi_2 = x \cdot n_2/(n_1 + x \cdot n_2)$.^{28,63}

$$\Delta G_M = RT[\Phi_1 \cdot \ln\Phi_1 + \left(\frac{\Phi_2}{x}\right) \cdot \ln\Phi_2 + \chi \cdot \Phi_1 \cdot \Phi_2] \quad (3)$$

The first two terms originate from the combinatorial entropy of mixing (negative value), which supports the miscibility. The final term is based on the contact interaction of both lattice sites (positive value) promoting a demixing. The final interplay of those contributions is governed by the temperature and the Flory-Huggins parameter, which finally determines the critical miscibility state of a polymer solution.^{28,63} In equilibrium of the phase transition, the Gibbs free energy is zero ($\Delta G_M = 0$), which allows the expression of the cloud point in relation of the entropy and enthalpy of mixing.^{59,62}

$$T_c \sim \left(\frac{\Delta H_M}{\Delta S_M}\right) \quad (4)$$

Upon heating of LCST polymer solutions, the hydrogen bonds become weaker due to rising temperatures. The hydrogen bonds between the polymer and water molecules break and the water is released ($T > T_c$). The hydrophobic segments associate inter- and intramolecularly via van-der-Waals interaction ($\Delta S_M > 0$) - the polymer solution demixes ($\Delta G_M > 0$).⁶² The enthalpy of the process is endothermic.^{60,70} During the demixing of UCST polymer solutions ($T < T_c$), the hydrogen bonds breaks between the polar units, which provoke the demixing of the polymer ($\Delta G_M > 0$). The exothermic breakage of hydrogen bonds is replaced by the formation of intermolecular hydrogen bonds, so that the overall enthalpy of the process is low.⁶²

The differentiation of the mechanisms LCST and UCST is not completely clarified, yet, so that experimental experiences are usually consulted to accomplish the theoretical approach.

Commonly, the thermoresponsive behaviour of LCST polymers is less susceptible than those of UCST conjugates (under assumption of almost identical conditions). The cloud point changes for LCST polymers are less volatile, regarding slight changes in molecular mass, concentration and introduction of hydrophobic/hydrophilic moieties.^{61,62,71–73} In consequence, it is assumed that the hydrophobic effect and the corresponding change of entropy (ΔS_M) figures the predominating impact, as enthalpic contributions of hydrophobic groups are usually neglectable.⁵⁹ According to the relation of $\Delta H_M/\Delta S_M$, the different sensitivities of LCST and UCST are referred to variant enthalpies of mixing for both processes ($\Delta H_{M,LCST} \gg \Delta H_{M,UCST}$). This assumption is supported by calorimetric investigations, which revealed heat flow differences between LCST ($\Delta H_M \sim 50 \text{ J}\cdot\text{g}^{-1}$ for PNIPAAm) and UCST transitions ($\Delta H_M \sim 0.7 \text{ J}\cdot\text{g}^{-1}$ for PNAGA) by two orders of magnitudes.^{60,61}

Two promoting examples are denoted below to support the assumptions above based on the experimentally found data. Firstly, the copolymerization of NIPAAm with 0.8 mol% acrylic acid (AA) causes a rise in the cloud point by 3 K, whereas 0.2 mol% AA in PNAGA vanishes the complete thermoresponsive behaviour.^{61,71} It illustrates the fragile process of UCST. Secondly, the cloud point of the UCST system poly(AAm-co-AN) is dependent on the fraction of the hydrophobic component AN in the copolymer. Slight changes of $\Delta[\text{AN}] = 4 \text{ mol}\%$ leads to an increase of the cloud point by $\Delta T_c = 25 \text{ K}$, although the number acrylamide units in the chain, which illustrates the potential number of hydrogen bonds (enthalpy of mixing) is not varying dramatically. Therefore, the hydrophobic effect (and not the enthalpic formation/breakage of hydrogen bonds) has the predominating impact on the cloud point.

5.3.3. Lower Critical Solution Temperature Polymers in Aqueous Solution

In the recent decades, LCST polymers are highlighted in many researches and are widely applied. Their phase transition near the human body temperature (Table 1) catches a high attraction in medical applications. Depending on the polymer system and physical properties like molar mass, skeletal architecture, number of repeat units inside the chain and the thermoresponsive behaviour are tuneable effectively. The most common polymers (Figure 4 and Table 1) belongs to the class of poly(*N*-acrylamide)s, poly(*N*-vinyl amide)s, poly(ether)s, poly(vinyl ether)s or poly(oxazoline)s.^{11,57}

The most investigated example for this class of biocompatible polymers is poly(*N*-isopropylacrylamide). It is easily synthesized *via* free or controlled polymerization. Its cloud point around 32 °C makes it favourable and benefiting towards biomedical applications e.g. controlled release of drugs in field of oral delivery of calcitonin and insulin or non-viral vector for gene-delivery applications.^{58,74} It usually shows sharp transitions with a high independence to the chain length and concentration of polymer in solution.⁷⁵ The transition

range becomes tuneable by the modifications with hydrophilic or hydrophobic end groups or comonomers.^{13,76,77}

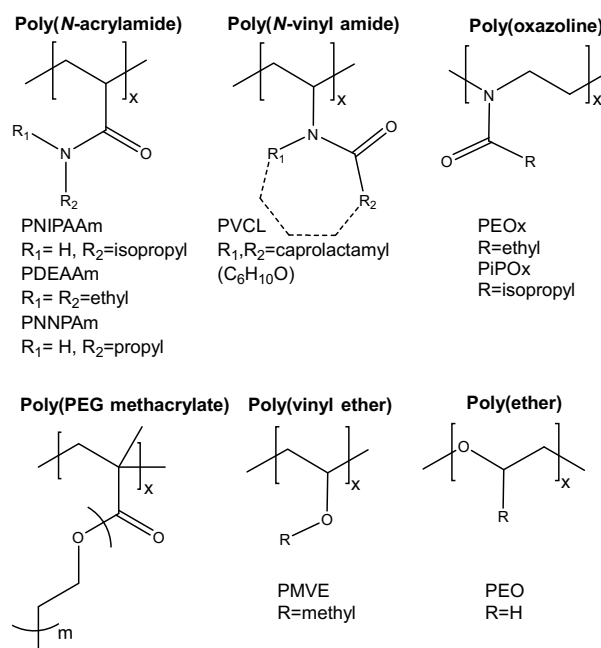


Figure 4: Overview of the most common thermoresponsive polymers bearing LCST behaviour.

By contrary, the cloud point of poly(*N*-vinylcaprolactam), as part of the class of poly(*N*-vinyl amide)s, differs strongly with variation of the molar mass.⁷⁸ It is an amphiphilic polymer, which consists of a seven-membered rings with a polyethylene backbone a hydrophobic vinyl chain connected to a hydrophilic cyclic lactam. Poly(oxazoline)s and poly(methyl vinyl ether)s are prepared by cationic polymerizations, which are sensitive to slight impurities of reagents and traces of nucleophiles e.g., water, alcohols or amines. It represents a limitation of the potential of these LCST systems.⁷⁴ Though, their cloud point exhibits an abrupt transition. Poly(ether), or interchangeably called poly(ethylene glycol), offers a high cloud point, which increases with length of the side-group. Especially, PEG-methacrylate provides a thermoresponsive behaviour exclusively with a PEO-side chain length shorter than 10 ethylene oxide units. The molar mass and the architecture possess a major impact the T_c .⁵⁷

Table 1: Common LCST polymers according their polymer class and with the corresponding abbreviation and cloud point.^{11,57}

Class	Example	Abbreviation	$T_c / ^\circ\text{C}$
Poly(<i>N</i> -acrylamide)	Poly(<i>N</i> -isopropylacrylamide)	PNIPAAm	~32
	Poly(<i>N,N</i> -diethylacrylamide)	PDEAAm	25-33
	Poly(<i>N-n</i> -propylacrylamide)	PNNPAm	10
Poly(<i>N</i> -vinyl amide)	Poly(<i>N</i> -vinylcaprolactam)	PVCL	25-35
Poly(oxazoline)	Poly(2-ethyl-2-oxazoline)	PEOx	62-65
	Poly(2-isopropyl-2-oxazoline)	PiPOx	36
Poly(vinyl ether)	Poly(methyl vinyl ether)	PMVE	35-36
Poly(ether)	Poly(ethylene glycol)	PEG/PEO	~85
Poly(acrylate)	Poly(ethylene glycol methacrylate)	PEGMA	60-90

The thermoresponsive properties of LCST systems are tuneable by many synthetic approaches and conditions such as composition^{13,79}, the pH-value⁸⁰, salts⁸¹, the molar mass distribution and the end groups (polymers with $\bar{M}_n < 30 \text{ kg}\cdot\text{mol}^{-1}$)¹⁷. The cloud point of polymer solutions is raised due to enhanced dipole-dipole interactions with the solvent, hydrophilic end groups, comonomers and short plasticizing chains.^{82,83} These impacting parameters has to be considered for each targeted application of the polymers.

5.3.4. Upper Critical Solution Temperature Polymers in Aqueous Solution

UCST polymers correspond to the class of thermoresponsive polymers, and their solution behaviour bears a miscibility gap upon cooling (in contrast to LCST systems). Although they belong to the same class of polymers, a misbalance between UCST systems and their conjugates is existent in the literature. The examples of polymers, showing an UCST behaviour in aqueous solution, represent a side note in the research.⁶¹ As already discussed in chapter 5.3.2, the process of UCST is predominantly driven by entropic effects^{59,62}, which provokes a tremendous influence of the polymer concentration in solution, the polymer's molar mass and the impact of hydrophobic/hydrophilic moieties in the macromolecule onto the thermoresponsive properties (or cloud point).^{14,73,84} Presumably, the high susceptibility of the thermoresponse and the lower synthetic reproducibility of UCST polymers is hampering the search of appropriate conditions for distinct applications.⁶² Followingly, their use is often less convenient than for example in case of PNIPAAm.

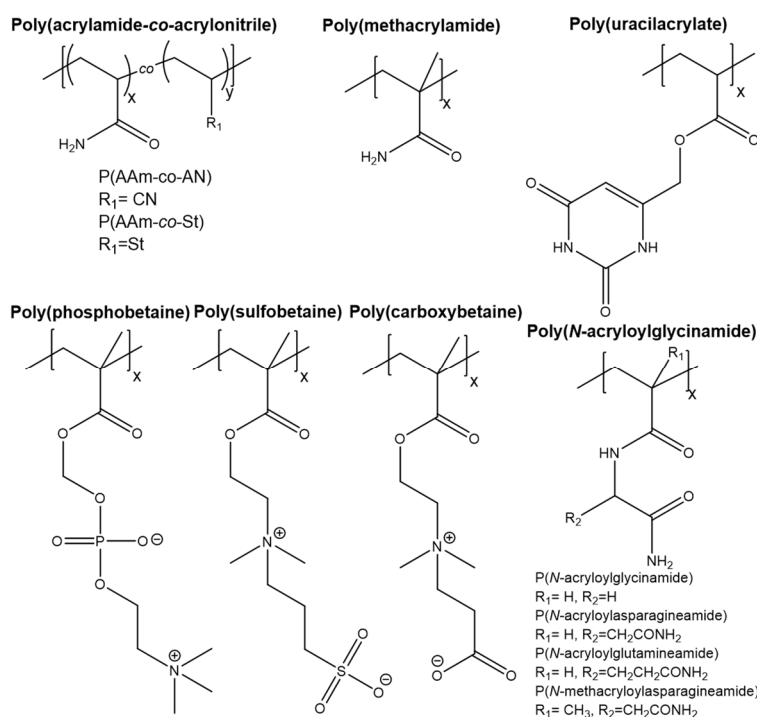


Figure 5: Overview of the most common thermoresponsive polymers bearing UCST behaviour.

The most common (co-)polymers are exemplary shown in Figure 5. They belong to the chemical class of poly(acrylamide)s, poly(uracilacrylate)s, poly(sulfobetaine)s, poly(phosphobetaine)s, poly(carboxybetaine)s and poly(*N*-acryloylglycinamide) (PNAGA) derivatives.

The most studied UCST polymer system is represented by poly(NAGA). It is polymerizable *via* both free and controlled radical polymerizations (RAFT and ATRP) and shows a thermoresponsive behaviour in aqueous solution ($T_c=14-24$ °C in 1.0 wt% aqueous solution⁶¹). The thermoresponsive properties are obtained by non-ionic interactions of the side groups *via* hydrogen bonding, tuneable in both directions *via* copolymerization with hydrophilic or hydrophobic monomers. While hydrophobic monomers like butyl acrylate or styrene increase the cloud point (hydrophobic effect), the value is lowered by hydrophilic monomers units like *N*-acetyl-acrylamide.^{61,62}

Table 2: Common UCST polymers according to their polymer class with the corresponding abbreviation and reported cloud points. The sensitive cloud points are denoted as potential temperature ranges (according to corresponding literature) due to the major impact of the measurement's conditions like variable polymer concentration, molar masses, and end groups.

Class	Example	Abbreviation	$T_c /$ °C	Ref.
Poly(acrylamide)	Poly(acrylamide- <i>co</i> -acrylonitrile)	P(AAm- <i>co</i> -AN)	20-67	18,73
	Poly(acrylamide- <i>co</i> -styrene)	P(AAm- <i>co</i> -St)	49-62	90
	Poly(methacrylamide)	PMAAm	41-57	14
Poly(uracilacrylate)	Poly(uracilacrylate)	PAU	60	59
Poly(<i>N</i> -acryloylglycinamide)	Poly(<i>N</i> -acryloylglycinamide)	PNAGA	10-20	14
	Poly(uracilacrylate- <i>co</i> -styrene)	P(NAGA- <i>co</i> -ST)	10-85	14
	Poly(uracilacrylate- <i>co</i> -butyl acetate)	P(NAGA- <i>co</i> -BA)	10-60	14
	Poly(<i>N</i> -acryloylasparagineamide)	PNAAAm	22	14
	Poly(<i>meth</i> acryloylasparagineamide)	PNMAAAm	13	14
	Poly(<i>N</i> -acryloylglutamineamide)	PNAGAAm	2 ^[a]	14
	Poly(<i>N,N'</i> -dimethyl (methacryloylethyl)ammonium propanesulfonate)	PSDMAPS	0-43	86
Poly(sulfobetaine)	Poly[<i>N</i> -(3-sulphopropyl)- <i>N</i> -methacryloxyethyl- <i>N,N</i> -dimethyl ammonium betaine]	PSPE	5-60	84
	Poly{[2-(Methacryloyloxy)ethyl] dimethyl(3-sulfoethyl)-ammonium hydroxide}	PSBMA	15	91
	Poly[2-(methacryloyloxy)ethyl phosphorylcholine]	PMPC	-	62
Poly(carboxybetaine)	Poly[2-Carboxy- <i>N,N</i> -dimethyl- <i>N</i> -(2'-methacryloyloxyethyl) ethanaminium inner salt]	PCBMA	-	91

^[a] No cloud point in aqueous solution, detected in $40 \cdot 10^{-3}$ M Tris-HCl, pH=8.

Another promising system is the non-ionic copolymer poly(AAm-co-AN) consisting of purely hydrophilic and hydrophobic components.^{14,73} It owns the benefits of being a low-cost copolymer with robust thermoresponsive properties even under physiological conditions. It offers a freely adjustable and sharp cloud point in the range between 0-100 °C with respect to the hydrophilic-hydrophobic balance, which correlates with the acrylonitrile fraction in the copolymer.^{14,15,73,85} Although, the robust solution properties are sustainable under a broad range of conditions (e.g. co-solvents, salts, buffers, varied pH values) for days. But it is important to note, that ongoing hydrolysis may decrease the cloud point due to the formation of ionic side groups.^{15,85}

Poly(MAAm) offers an intramolecular hydrophilic-hydrophobic balance, which exhibits an intrinsic, non-ionic UCST behaviour. The monomer unit bears a cloud point in aqueous solution caused by the hydrophobic effect of the methyl group in the backbone. Even though, its thermoresponsive behaviour is kinetically hindered, so that the hysteresis between the cloud points derived from the heating and cooling curves is enormous ($\Delta T_c=16$ K).^{14,62}

Poly(sulfobetaine)s, poly(phosphobetaine)s and poly(carboxybetaine)s correspond to the zwitterionic representatives, which exhibit a UCST behaviour relying on intra- and intermolecular Coulomb interactions. Their miscibility gap is generally tremendously affected by the molar mass of the polymers and concentration in solution.^{84,86} Due to the intramolecular charges, the thermoresponsive properties react highly sensitive to ions in solution. The cloud points are lowered or even completely vanished by the occurring screening effect of charges in the presence of ions.^{84,87} Especially, poly(sulfobetaine)s are known disregarding their thermoresponsive properties as ultra-low fouling materials with excellent biocompatibility.^{88,89}

5.4. Dual-Thermoresponsive LCST-UCST Block Copolymers

5.4.1. Synthetic Aspects of Block Copolymers

Block copolymers (BCs) correspond to a specific copolymer class, in which distinct blocks of monomer units are grouped along the chain. These can be configured into branched (graft- or star polymer), linear and cyclic architectures, which are accessible *via* different synthetic strategies.²² Mainly, the employed strategies follow the sequential polymerization approach of defined blocks, which is proceeded in living or controlled polymerizations (detailedly discussed in chapter 5.1) or by coupling of activated chain ends (e.g. click chemistry).^{22,92}

The controlled radical polymerization represents versatile route for the synthesis of block copolymers. The benefits are the simple synthesis route, the high tolerance towards solvents and impurities, and the variety of applicable monomers. An important representative is the RAFT polymerization (detailedly described in chapter 5.2), which can be utilized for block copolymerizations.⁹³ The chain transfer agent owns a key role in that strategy, which is

illustrated in Figure 6. It enforces the final skeletal architecture of the block copolymer. While a conventional CTA allows a linear polymer, a conjugate with multiple thiocarbonyl groups leads to a rather star-shaped polymer. Additional functionalization widens the field of further architectures and properties as surface anchor groups for grafting-from or grafting-to pathways and reactive chain ends for post-synthetic couplings or modifications.⁹⁴

Generally, the RAFT block copolymerization is further sub-classed by the R- and Z-group approach. The Z-group approach occurs *via* a pre-modified chain transfer agent carrying a macromolecular tail as Z-group. Finally, the thiocarbonyl moiety is located between both polymer blocks. The disadvantage of this method is the destruction of the targeted skeletal architecture by the hydrolysis/aminolysis of the (sensitive) chain transfer agent. The R-group approach proceeds *via* propagation between the thiocarbonyl group and the macromolecular leaving R-group. The homolytic properties are influenced by the macromolecular chain and leads to potential side reactions or slower diffusion processes.⁹³

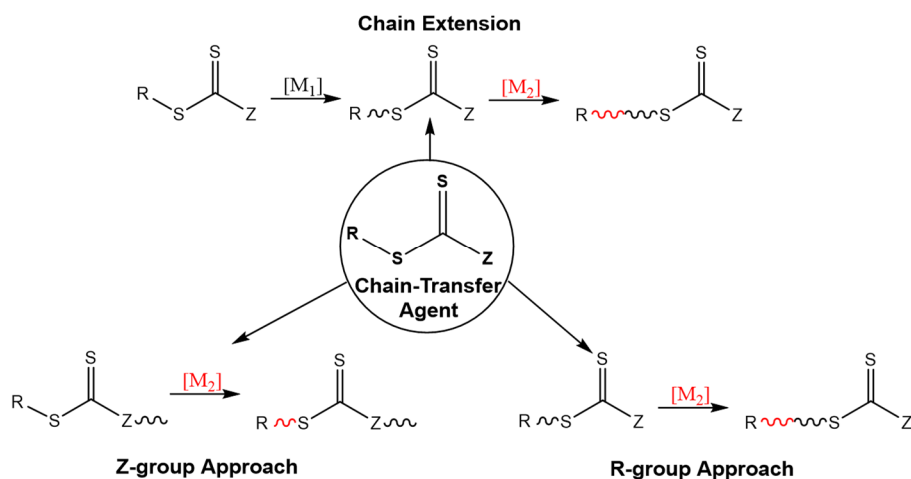


Figure 6: General approaches for the synthesis of block copolymers *via* RAFT polymerization. Concept schematics partially based on Barner et al.⁹³

The simplest and facile synthetic route for block copolymers is allowed *via* iterative chain extension. Each RAFT polymer product represents a discrete macroCTA, as it carries still the reactive thiocarbonyl species. After each initiation another propagation step can occur, so that the latest polymer block is formed between the thiocarbonyl moiety and macromolecular R-group.^{93,94} In that case, the blocks are covalently bound. It is important to note that both the macroCTA, the monomers of the recent propagating step and the initiator, as well as the block copolymer product has to provide solubilities in a common reaction mixture to realize an efficient polymerization.⁹⁴

5.4.2. Dual-Thermoresponsive Block Copolymers

Stimuli-responsive materials possess distinct solution properties responding to external triggers. Concerning potential applications, smart materials are supposed to exhibit

adjustable and well-defined responses. Some thermoresponsive block copolymers show temperature-controlled amphiphilic characters in solution combining the properties of LCST and UCST. This behaviour is also denoted as schizophrenic. This copolymer class was firstly reported by Arotcarena et al. who copolymerized NIPAAm with the zwitterionic monomer 3-[*N*-(3-methacrylamidopropyl)-*N,N*-dimethyl]ammonio propane sulfonate (SPP) *via* chain extension RAFT copolymerization.⁹⁵ In certain temperature regimes, such block copolymers start to self-assemble *via* inversion of their micellar aggregation structure.^{96,97} The dual-thermoresponsive properties provide a complex solution behaviour with respect to the composition and architecture of the blocks^{95,98,99}, which can be further fine-tuned *via* additional triggers like pH, salts, gases or fluorescent markers.^{100–102}

This unique demixing behaviour attracts the attention to be utilized in biomedical researches for the construction of three-dimensional aggregation structures and mimicked natural proteins or viruses.¹⁰³ The exemplary poly(OEGMA-*block*-NIPAAm) carrying a biotin end group was demonstrated to feature a temperature-controlled binding process to immobilized streptavidin surfaces. It represents a valid concept for stimulus-controlled binding approaches of biopolymers onto protein surfaces.¹⁰⁴ Other potential applications of dual-thermoresponsive block copolymers could be drug release systems with low cytotoxicity⁸⁵, switchable enzyme bioactivity systems¹⁰⁵ and human blood purification and preservation.¹⁰⁶ The architecture of the block copolymers affects the final structuration of the aggregates and subsequently, as well, the physicochemical properties. Upon the trigger of temperature variation, the conformation of the dual-thermoresponsive block polymer is switchable externally. The UCST-LCST di-block polymers provide the following combinational aggregation states (illustrated in Figure 7).

Here, the thermoresponsive behaviour of the block copolymers is sketched by the coloured symbols for both contrary thermoresponsive chains to explain the phase transitions of the block copolymers on the molecular and colloidal level. The switching of the thermoresponsive chains occurs on the molecular level of a single chain and leads in the ensemble picture to colloidal scattering objects by forming micellar aggregates from several chains. In the illustrated ideal case, the coil-to-globule transitions of the single blocks are proceeding independently of each other, so that just two different thermoresponsive combinations are possible (UCST < LCST and LCST < UCST). Such thermoresponsive transition leads to an abrupt block behaviour change from the hydrophobic globule to the hydrophilic coil state upon cooling for LCST and upon heating for UCST polymer blocks. The hydrophobic/hydrophilic properties of the distinct blocks result in attractive or repulsive forces among the polymer chains and chain segments in solution *via* the interplay of polymer-polymer (intra- and intermolecular aggregation) and polymer-solvent interactions (dissolution processes).^{95,103,107}

The first combination is set by a lower cloud point of the UCST block with respect to the LCST conjugate. The UCST block lies in the hydrophobic state, so that the block copolymer owns an amphiphilic character at lower temperatures. The hydrophobic segments form the core of the micelles above a critical micelle concentration (cmc) due to attractive chain-chain interactions. Upon heating, the UCST transition is executed, and the block copolymer is nearly molecularly dissolved. Above the cloud point of the LCST system, the corresponding block turns hydrophobic and assembles in inverse micellar structures (above cmc).¹⁰³

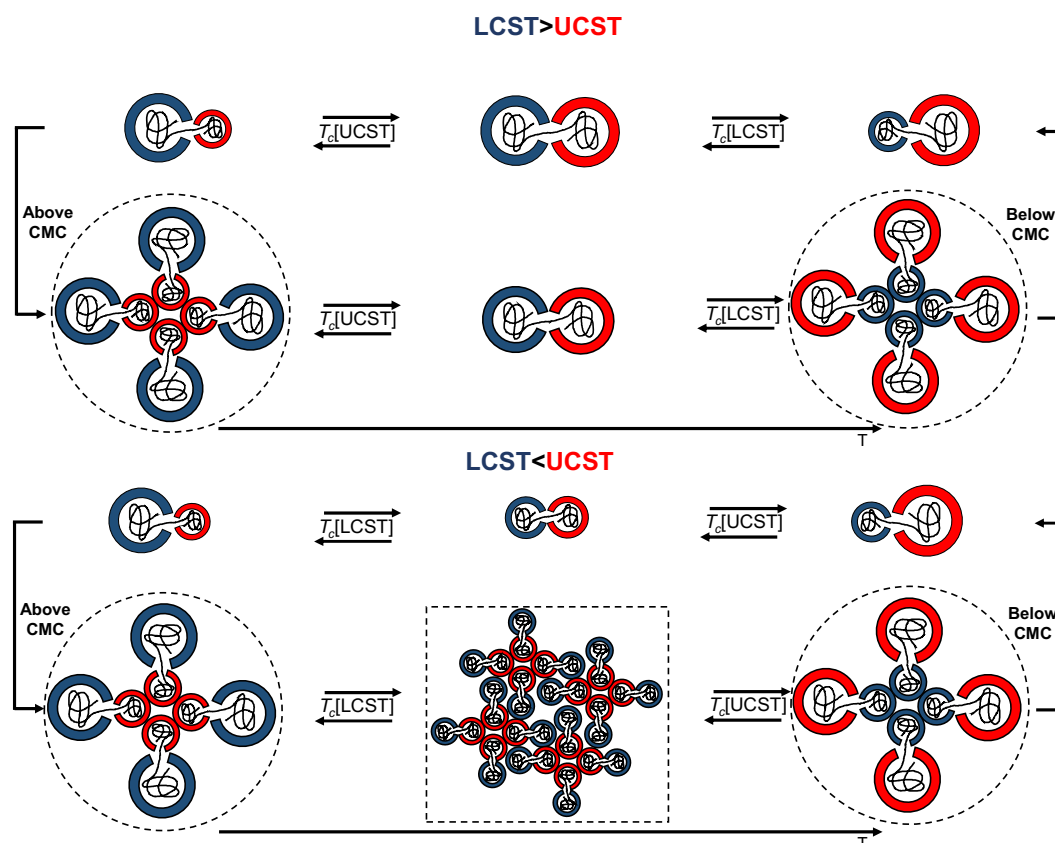


Figure 7: Two aggregation states of dual-thermoresponsive UCST-LCST di-block polymers with respect to the temperature and the polymer concentration below/ above cmc in aqueous solution as single chain or intermolecular aggregate. The UCST block is denoted in red, while LCST equivalent in blue. Micellar aggregation is indicated by dashed spheres and colloidal precipitates by dashed rectangles. Concept schematics partially based on Kotsuchibashi et al.¹⁰³

In the opposite block combination (with a lower LCST cloud point), the identical dissolution state is present initially at lower temperatures. Upon heating, the complete block copolymer becomes hydrophobic, which results in strong attractive forces among the chains, so that a complex aggregational structuration takes place and a crude precipitation process is supported. When the temperature is raised above the cloud point of the UCST block, the chain behaves hydrophilic and an inverse micelle is generated due to the aggregation of the hydrophobic block tails.¹⁰³

This ideal process description becomes more complicated, when mutual influences of the distinct LCST and UCST blocks are considered. Due to the coil-to-globule transition of single

thermoreponsive segments, their hydrophilic strengths change and impact the dissolution behaviour of the secondary block, which causes interdependent and reversible thermoresponsive switchable states. This behaviour leads to altering of the cloud points in dependence of the heating/cooling direction. It is also reported by Can et al. in terms of “cross-influences” in the dissolution behaviour of the LCST-UCST block copolymer poly(methyl acrylate-*block*-diethylene glycol ethyl ether acrylate) *via* thermoresponsively linked switching states.¹⁰⁸

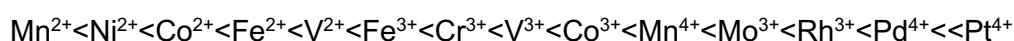
5.5. Iron Ion Sensitive Macromolecular Coordination Ligands

5.5.1. General Aspects of Coordination Processes

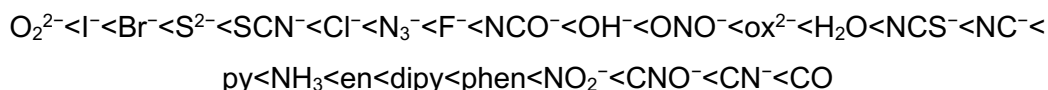
Coordination processes are performed *via* non-covalent, ionic bonding arrangements consisting of ligands surrounding a central ion. These complexes are based on electron donor-acceptor systems (Lewis acids/bases). Commonly, the central ion corresponds to elements of the transition metal group with vacant *d*-orbitals. The binding properties of the ions are denoted in the nomenclature for transition metals (d^1 - d^{10}) with respect to the number of electrons present in the outer shell.¹⁰⁹ This number of valence electrons is defined by the specific element and its oxidation state. The ligand, the central ion and its oxidation state determines the formation, type and stability of a complex.¹¹⁰

The interplay of distinct central ion and ligand type impacts the strength of the ligand field. The ligand field force causes the total crystal field splitting (Δ) in the molecular orbital, which leads to changes in the optical, magnetic, physical and chemical behaviors. A systematic spectroscopic study of crystal fields led to the spectroscopic chemical series with respect to both central ions and ligands.¹¹⁰ The series are applicable for the practical approximation of the crystal field splitting energy (CFSE) and allows qualitative prediction of the electronic complex arrangement.

The transition metal ion radius contracts with higher oxidation state, which rises the electron density and strength of the crystal field splitting between central ion and ligand. In the spectrochemical series for central ions, the elements are ordered with increasing electrostatic repulsion between metal ion and ligand. The formation of low-spin states (LS) becomes more probable for a larger crystal field splitting.¹⁰⁹



Ligands differ in charge, steric demand and number of denticities so that variable ligand field strengths are produced.¹⁰⁹ In the spectrochemical series, the strength of the ligand field and the resulting crystal field splitting increases from left (weak field) to right (strong field).¹¹⁰



The free ion exhibits a degeneration of the d-orbitals (Figure 8). The coordination number determines the symmetry of crystal field e.g., octahedral (Δ_O) or tetrahedral (Δ_T). The total crystal field splitting causes a breakage of the electronically degenerated molecular orbital states. In the case of d^4 - d^7 element ions, two potential states can be occupied. These varying electronic states are called high-spin (HS) and low-spin (LS). The magnitude of the crystal field splitting settles the electronically favored state and the corresponding total spin number (S).¹¹¹ The spin state refers to the strength of the ligand-field. Strong ligands (e.g., CN^- , CO) affect LS-states causing a great crystal field, so that its energy (Δ) is higher than the spin pair energy (P) (Figure 8). This leads to an occupation of lower orbitals, which causes variation of the total spin number (S).

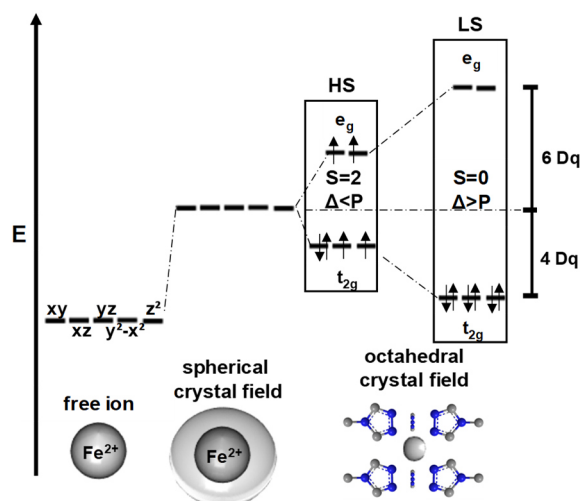


Figure 8: Schematic energy state diagram of the d^6 element Fe^{2+} indicating the two potential occupiable electronic states of high- and low-spin.¹¹²

The Fe^{2+} ion belongs to the d^6 elements and is an example for being existent in both high- and low-spin states (Figure 8). While the LS is the ground state (1A_1) in the corresponding electronic configuration t_{2g}^6 , the HS state is energetically slightly unfavored ($t_{2g}^4e_g^2$). The energy differences allow an external switching between diamagnetism ($S=0$) and strong paramagnetism ($S=2$).¹¹³ Such processes are detectable *via* electron spin resonance (ESR), Mößbauer spectroscopy, UV-Vis absorption spectroscopy or magnetic balances.^{114,115} The selective switching between both electronic states can be potentially used in applications for the memory devices, detection techniques, sensor devices, opto-electronic displays and as liquid crystals.^{112,114,116}

5.5.2. Macromolecular Coordination Ligands

In accordance with the overall development in research, interdisciplinary investigations attract rising attention. The linkage between the macromolecular and coordination chemistry seems to be originally contrary, but is faced in the field of macromolecular coordination ligands (MCLs) or interchangeably chelating polymeric ligands (CPLs).¹¹⁷ The introduction of macromolecular ligands opens up a wide variety of accessible properties. The molecular design accesses the synthesis of very expedient chelating agents towards their desired application. Different chelating functionalities, skeletal architectures and numerous additional properties (e.g. biological, catalytic, electrical, magnetic, or optical) lead to beneficial use as multidimensional nanostructured materials.^{117,118}

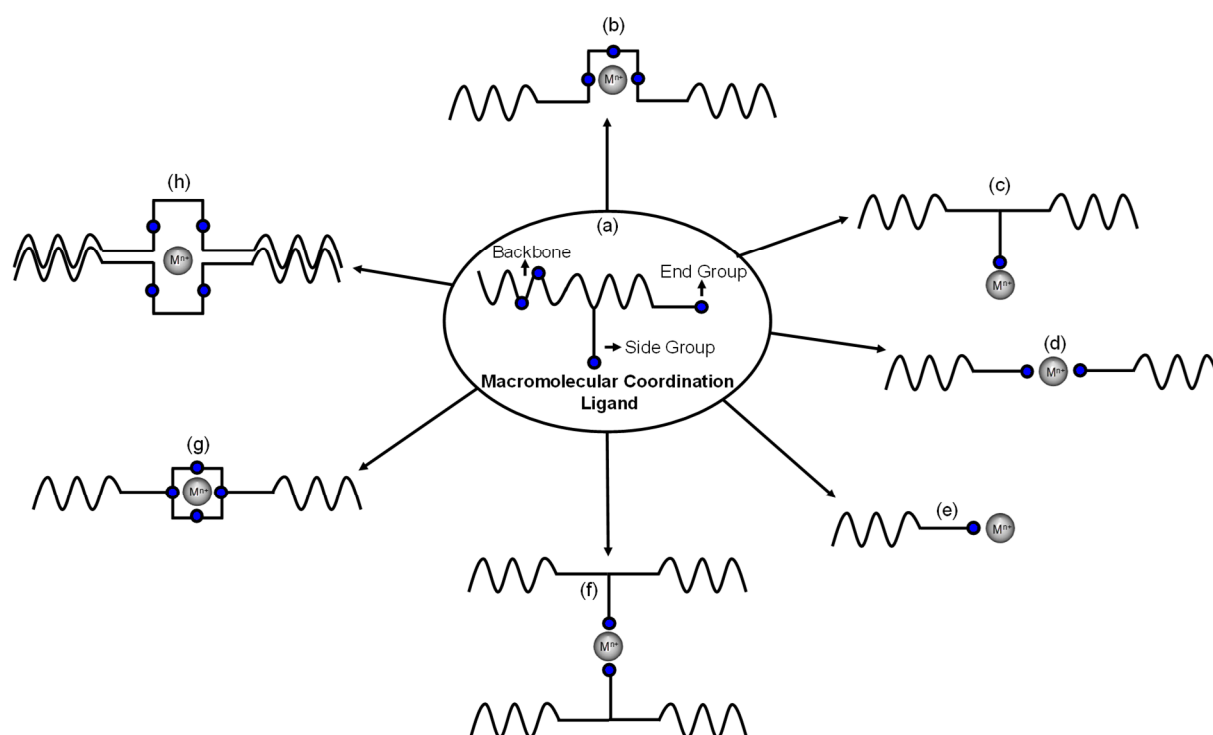


Figure 9: Schematic coordination structures (b-h) formed in a coordination process with metal ion M^{n+} (grey) by macromolecular coordination ligands with differing architectures and molecular location of the ligand motif (blue). The coordination site is carried in the backbone (b, g, h), in the side group (c, f) or in the end group (d, e). Concept schematics partially based on Aziz et al.¹¹⁹

Facing the main problems^{118–120} like macromolecular architecture, corresponding reactivity, specificity and competing of complexation processes, MCLs are applicable as catalysts, polymer light-emitting diodes (PLEDs)^{121,122}, sensors^{122,123}, biomedical metal-carrier molecules, biosensors¹²², drugs¹²⁴, antidotes¹²⁵ and bioimaging agents^{126,127}. Such MCLs gives access to more complex arrangements and supramolecular structuration processes.^{118,127–129} Common coordination structures are often formed irreversibly. The irreversible behaviour can just be interchanged by ligand exchange processes *via* addition of strong chelators (e.g. EDTA, HEEDTA).^{130,131}

In rare cases, the implementation of external stimuli results in more dynamic polymer-metal complex systems, which exploit for example redox or pH active responses.^{123,132,133} Especially, the use of thermoresponsive polymer ligands offers a reversible switching of the dynamic complex arrangements by external trigger of temperature variation.^{20,127,134,135}

The polymer ligands (sketched in Figure 9a) deliver an opportunity to carry the chelating motifs in different positions of the macromolecules either directly in the backbone (Figure 9b,g-h) or pendent to the backbone as side (Figure 9c/f) or end group (Figure 9d/e). These motifs are classified with respect to the number of binding sites as mono-, di-, tri- or polydentate site. The formed type of complex structure is received in a coordination process in dependence of the mutual co-play between the macromolecular architecture, the character of the binding site, the metal centre and the applied synthetic conditions. The binding sites capture metal ions along the linear polymer chain or act as crosslinking sites among two or more chains. The complexation can be employed as synthetic introduction of distinct properties by the choice of metal ions or as driving force for structurally self-assembly processes of highly complex building blocks. Potential structures could be either a linkage between two reaction partners *via* coordinative chain extension or *via* multiple metal bridging partners in an one-dimensional coordination structure mode or *via* multi-chelating ligands in random coordination networks.¹¹⁹

The coordination of metal ions can be performed *via* chemical groups like (heterocyclic) amines, carboxylic acids, thiols, imines, amides, esters or phosphoric acids.¹³⁶ Most commonly, bi- or terpyridines and other close derivatives are applied as coordination moiety in polymeric chelators.^{20,129,137} Other important motifs are based on substructures like imidazoles, metallocenes, phthalocyanines, porphyrin or triazoles.^{136,138,139}

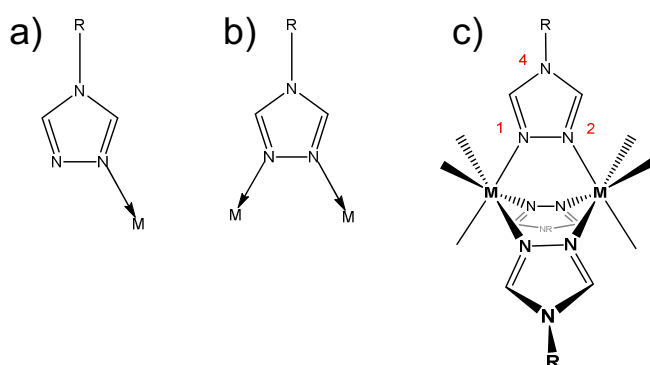


Figure 10: Representation of a) a monodentate, b) bidentate and c) stable triple N^1, N^2 -triazole bridging binding mode of the coordination motif 4-substituted 1,2,4-triazoles.¹¹²

Triazoles are known to be efficient ligands for various metal ions. An important representative of this class is 1,2,4-triazole. The thermal and chemical stability, the synthetical variability of the modifiable 4-position and the unique coordination properties leads to divers beneficial applications.^{138–140} In particular, 1,2,4-triazole attends attraction due

to the characteristic one-dimensional complexation structure in presence of divalent iron ions. This structuration occurs by iterative octahedral N^1, N^2 -bridging of the triazole being bound between two metal centers (illustrated in Figure 10c). The formed structures may offer additionally switchable spin-crossover properties caused by the labile electronic spin states of divalent iron (HS-LS). In addition to the stable and ridged one-dimensional binding state, also the mono- and bidentate binding modes are observed.¹¹²

1,2,4-Triazoles are usually known as building blocks in the conventional field of coordination chemistry, but possess a minor significance for MCLs. Solely, the modified monomer 3-substituted vinyl-1,2,4-triazole by Kilic et al. was found as applicable precursor.¹⁴¹

5.6. Thermo-responsive Copolymeric Vectors for Gene Delivery

5.6.1. Basic Aspects of Gene Delivery Process

Gene therapy is an intercellular delivery process of genomic material used for therapeutic treatments of genetic abnormalities and defects to restore the original gene function. The gene carrying mutations has to be identified primary in the treatment process. Then, the healthy conjugate is cloned, which is denoted further as transgene. Once the transgene is produced, it has to diffuse inside the mutant cell. To support this process, the transgene is transported to the cell nucleus often by the help of carrier molecules, the so-called vectors (in detail for chemical vectors in chapter 5.6.2).¹⁴²

The first human gene transfer experiment was performed for the treatment of tumour-infiltrating lymphocytes in 1989, while the first complete gene therapy was conducted in 1990 as treatment for patient with severe combined immunodeficiency defect (SCID).^{143,144} Nowadays, the gene therapy research is focusing on diseases like cystic fibrosis (CS), adenosine deaminase severe combined immunodeficiency defect (ADA-SCID), emphysema, retinitis pigmentosa, sickle cell anaemia, phenylketonuria, haemophilia, Duchenne muscular dystrophy (DMD), some other autosomal dominant disorders or even different cancer forms.¹⁴⁵ By the emerging pandemic of coronavirus 2, the gene delivery method abruptly entered the daily life of billion people through the accelerated development of modern mRNA vaccines.^{146–148}

The gene therapy is divided into two major classes. The germline gene therapy provides an enormous potential, but is ethically forbidden, as it deals with the manipulation of sperm cells, nuclei, egg cells or embryonic stem cells. The somatic conjugate was investigated and developed actively over the last decades. Here, the genetic material can be delivered in various pathways. The *ex vivo* delivery occurs *via* explanting of the target tissue, which is cultivated, further manipulated and transduced, before it is replaced again. This procedure exhibits a minimum of immunologic drawbacks.¹⁴⁵ The *in situ* delivery succeeds *via* administration of the genetic material following different pathways to reach target tissues.¹⁴⁵

The *in vivo* therapy demands a proper carrier molecule for the delivery to the target location in the tissue. The target located application of the genetic material is one of the key problem of this method and can be faced by the development of optimized vectors.¹⁴⁵

The gene delivery process of non-viral polymeric vectors undergoes several distinguishable mechanistic steps (shown in Figure 11). The polycationic vectors interfere with the transgenic DNA *via* electrostatic interaction with its negatively charged backbone, resulting in a condensation to sub-micrometer complexation objects – known as polyplexes (regarding to polymeric vectors). In these polyplexes the genetic material is stored in a compacted state consisting of numerous DNA molecules.¹⁴⁹ The loaded material is protected by the vector shell against physiological conditions or degradation processes (like e.g. enzymatic degradation) and gives the access to the inner cell improving the cell membrane permeability. These condensed particles are able to interact with the anionic cell surface *via* transmembrane proteins. The entering of the cells occurs *via* receptor-mediated endocytosis (for particles below $d \sim 200$ nm, otherwise micropinocytosis or phagocytosis¹⁵⁰), which results in the development of endosomal vesicles.¹⁴⁵

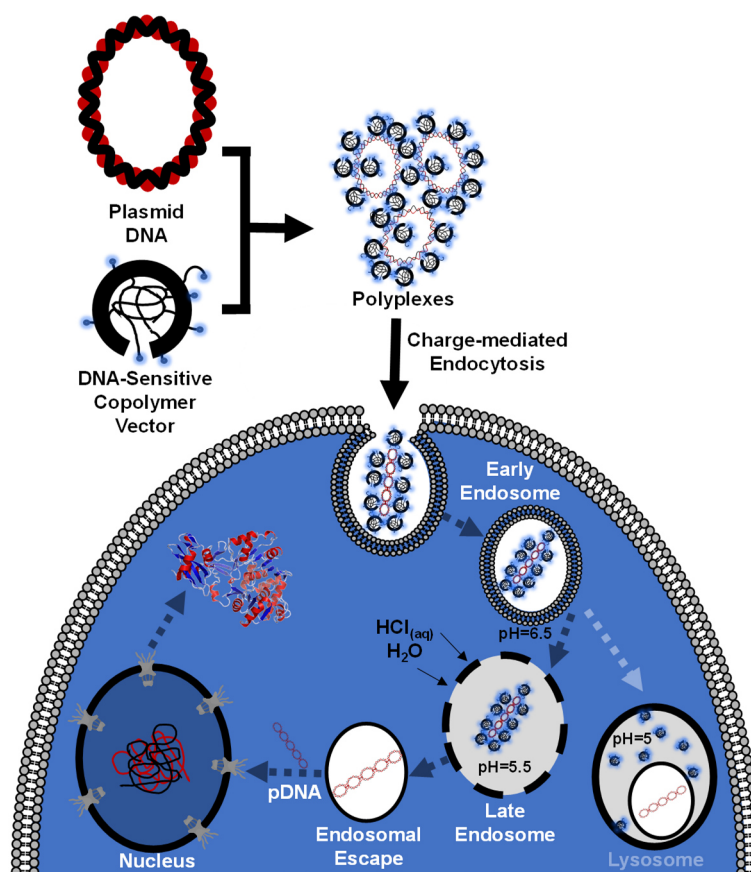


Figure 11: The gene delivery process of non-viral cationic vectors illustrated by the mechanistic steps of polyplex formation, proceeded endocytosis, endosomal acidification, endosomal escape and final transcription in the nucleus. Concept schematics partially based on Shen et al.⁵⁸

The maturing from the early to the late endosome is accompanied by an endosomal acidification by the ATPase enzyme (pH=5-6).¹⁵¹ The late endosomes release the genetic

material in the cytoplasm of the cell, then the nucleic acids diffuse through the latter, before to be translocated to the nucleus, where they are expressed. If the genetic material is not released properly to the cytoplasm, it will be degraded rapidly. It is assumed, that the endosomal release of polycationic polymeric vectors occurs due to the undergone proton-sponge effect. The cationic vectors become protonated by the acidification in the endosomes, which lead to the induced influx of further protons and corresponding counterions. The enlarged number of present ions in the endosome is balanced by aqueous endosomal dilution and results in an osmotic swelling followed by a subsequent rupture.¹⁵¹ After the endosomal escape, the DNA is able to stay 50-90 min in the cytoplasm. The compaction of the condensed DNA is enhancing the mobility and prevents a degradation on the way into the nucleus. The transcription of the genetic material occurs by a translation process of the native machinery by the help of certain promoters, so that the mutant cell function is restored or designed.¹⁵¹

5.6.2. General Overview of Potential Vector Types

Gene delivery treatments require an efficient transportation procedure of the genetic material through the cell membrane. This transportation is promoted by certain carrier molecules, which are denoted as vectors and ferry the DNA into the target cell type. First of all, these vectors are classified into viral and non-viral vectors (Figure 12).

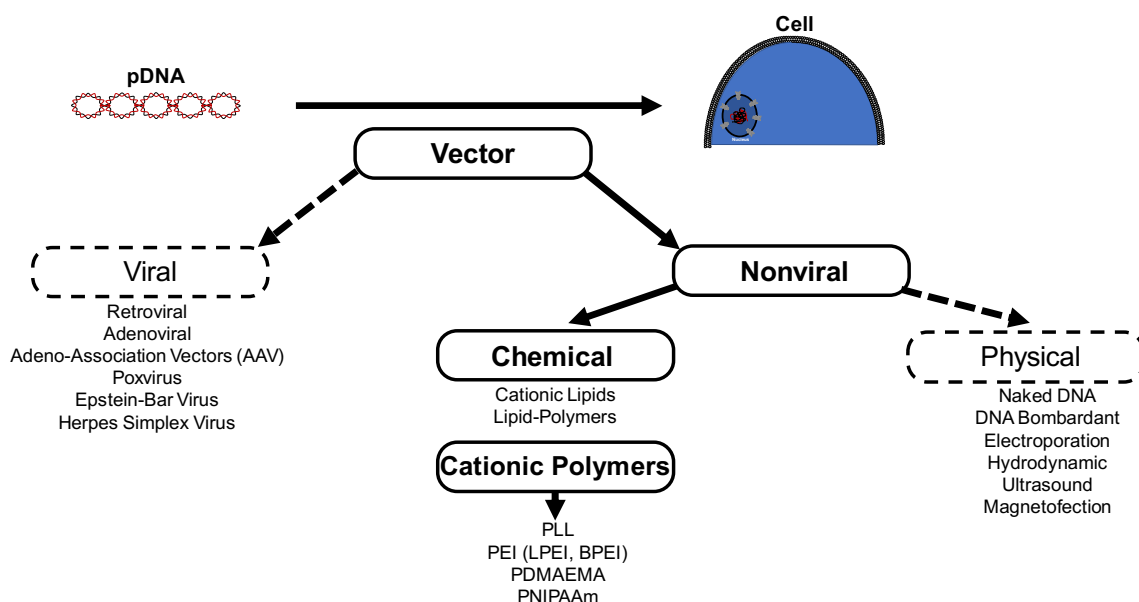


Figure 12: The gene delivery pathway into the cell is promoted *via* vectors. The overview summarizes the common subclasses.¹⁴⁵ The bold font denotes the focused class in the scope of the recent thesis.

The viral vectors represent a successfully therapy system exploiting engineered virus devoid of virulence and pathogenic genes. Despite the high potential transduction efficiencies, the viral vectors own the drawback of marked immunogenicity resulting in an induction of the immune system (e.g., impossible re-administration of vector, degeneration of tissue, toxin

production). Most frequently, retroviral systems are employed in gene transfer, as they allow a transfection process of the host genome from dividing cells being able to pass through mitotic cells. These vectors have been applied for the treatment of X-SCID or familial hyperlipidaemia.¹⁴⁵ Adenoviral conjugates allow the transport of large DNA particles. Their clinical tests evidenced serious side effects. Adeno-associated vectors (AAV) feature similar desired properties and possess additionally a deficiency in the replication and pathogenicity (more viable). The vector possesses a great size limitation of the transgene (5 kb). Poxvirus vectors offer a high stable insertion capacity as advantageous feature, so that it has been applied in therapies for prostate, colorectal, breast and lung cancer.¹⁴⁵

Compared to the viral equivalents, the non-viral class generally exhibits a lowered transfection efficiency. However, the reduced induction of the immune system, the simple and cost-effective preparation constitutes an advantageous system for potential gene delivery therapies. The non-viral approach overcomes the size limitation of the transgene, which can be freely adjusted (in contrary to viral conjugates).^{145,152} This class is subdivided into physical and chemical methods, which also can be combined to synergize the effect of the treatments. The physical approaches are used both *in vitro* and *in vivo*.

A safe method with a low transfection efficiency represents the administration of the naked DNA of specific sizes (2-19 kb), which is able to transfect a gene by itself being applied in the skin, thymus, cardiac muscle and skeletal muscle administered *via* syringe. The limitation of intramuscular treatment is represented by the area, where the transgene is expressed. The pathway of DNA particle bombardant employs a gene gun, which fires focused pDNA-coated particles ($d=1-3\ \mu\text{m}$) with high velocity on target tissue cells. Electroporation processes exploit electrodes for the destabilization of the cell membrane, which allows the DNA penetration from the surrounded medium. The low efficiency (0.01%) and the damages, originated from the high voltage, are hampering the expansion of the application field. The hydrodynamic method is based on transfection process *via* administration of water-soluble compounds and particles. The magnetofection combines the beneficial properties of non-viral biochemical and physical systems (being viable and efficient) by the use of a focused magnetic field to concentrate particles in the target volume of the tissue.¹⁴⁵

The chemical non-viral vectors are widely spread and of higher importance than the physical equivalents. These vectors effect the formation of nanoscopic complexes by the interaction of poly-negatively charged DNA backbone and contrarily charged ligands. The formed complexes are termed either lipo- or polyplexes with respect to the ligand type (condensed by cationic liposomes or polymers). The interaction of polycationic polymers leads to the formation of stable polyplex particles, which hinder the degradation of the DNA and enable the entering of the cells *via* undergone endocytosis. The non-viral chemical vectors are denoted by an usually high viability.¹⁴⁵

This class is consisting of cationic lipids, lipid-polymers and cationic polymers. The cationic lipids are carrying polar fatty acid groups, with alkyl tails and positively charged heads. They correspond to the polycationic systems and attract attention due to their capability of various drugs, high viability and absence of immune system reactions. The reticuloendothelial response leads to degradation of the lipids, so that the liposomes are commonly surface-modified by hydrophilic polymers (*via* PEGylation) to prevent that process and interaction with serum. The cationic lipid vectors are applied in the lung, spleen, kidney, liver, heart and skin.^{145,153} The last subclass of non-viral polymer vectors are described more precisely in the following chapter.

5.6.3. Conventional and Thermo-responsive Non-Viral Polymer Vectors

In the scope of this thesis, the cationic polymeric vectors are of major interest. The polymeric vectors are designed for a delicate counterbalance between high gene delivery efficiency and corresponding low cytotoxicity. The design depends on the charge density, the type of charge centre, the macromolecular mass of the vector, the grafting functionality and the final stability of the polyplexes in the surrounding medium.¹⁵¹ The number of charges is controllable in the synthetic pathway of the vectors by the introduction of coordinating side groups or by the adjustment of the chain length. The charged centre is characterized by the binding site type (primary, secondary, tertiary or quaternary nitrogen) and determines the resulting binding strength indicated by the pK_a . The molecular mass and its distribution (dispersity) affects the formation of the polyplexes and represents a major impact for the cytotoxicity. The functionalization of the vector is used for the tuning of the polyplex stability, the cellular uptake and intracellular escape with respect to the vectors hydrophobic-hydrophilic balance, architecture, potential stimuli response or further introduction of therapeutics.¹⁵¹

The first reported polymeric vectors are based on polylysine (PLL), synthesized by basic polycondensation of lysine in aqueous medium.¹⁵⁴ The length of the polymer chain determines the number of positive charges of the resulting vector. The more charges are available, the tighter the DNA strand is bound and the more stable the subsequent polyplex becomes. The binding strength provokes a contrary interplay of rising transfection efficiency and lower viability. This was reported by studies, which investigated the molecular mass dependent transfection by PLL vectors with varied chain lengths of $\bar{M}_n=3.97\text{-}233.2$ kDa ($X_n=19\text{-}1116$).¹⁴⁵ Due to the hampered cellular uptake *in vitro* or the endosomal escape *in vivo*, the pure PLL shows a low efficiency and is boosted *via* attachment of hydrophilic components to avoid plasma protein binding.¹⁴⁵

The most important and studied cationic polymer is polyethyleneimine (PEI), which represents a highly dense cationic macromolecule, prepared *via* cationic ring opening polymerization (CROP) of ethylenimine. Mostly, the architectures of linear (LPEI) and

branched PEI (BPEI) are investigated. The linear architecture offers more efficient and viable transfection properties. Commonly, PEI shows an improved activity for *in vitro* experiments compared to *in vivo* applications. PEI-DNA polyplexes produce a stable toroidal arrangement of defined aggregation sizes, which exhibit a high resistance against physiological influences such as buffer and pH variations. Unfavourably, the PEI is not biodegradable and followingly cytotoxic for *in vivo* experiments.^{155,156} The notable factors like delivery efficiency and viability are counterplay of each other and has to be defined for every distinct system. The highest efficiency is found for molar masses of 25k for BPEI and 22k for LPEI.¹⁴⁵

The third relevant vector class is illustrated by polymethacrylates. The main representative is poly[2-(dimethylamino)ethyl methacrylate] (PDMAEMA), which possesses an efficient gene delivery due to its ability to destabilize endosomes and being able to dissociate from the plasmid after proceeded delivery in the cytosol. The focus of current research is located in the development of polymethacrylates carrying biodegradable cationic side chains to boost the beneficial properties of the system with respect to obtain an improved targeted and viable release of the DNA.¹⁵⁷ Recent polymer systems provide biodegradable and biocompatible properties by themselves and use chitosan, β -dextrines, dextrans or schizophyllan backbones. Further exemplary classes are poly(4-hydroxy-l-proline ester)s, poly[α -(4-aminobutyl)-l-glycolic acid]s (PAGA) or poly(amino-ester)s.^{142,157}

The gene delivery research aims to find potential vectors fulfilling the contradictive demands of a high transfection efficiency combined with a low cytotoxicity. This is referred to the interplay of coordinative strength in the polyplexes (improving the cellular uptake and guarding against undesired enzymatic degradation of the transgene) and the target intracellular release of the genetic material with a high biodegradability of the vector (no activated immune response). The process of polyplex formation, cellular uptake and endosomal release are requiring specific hydrophilic impacts of the vector to be optimized for distinct cellular mechanisms. As conventional non-viral polymeric vectors deliver just static hydrophilic-hydrophobic properties, the implementing of additional responses like thermoresponse or pH response are tested to overcome these deficiencies by thermally switchable hydrophilic-hydrophobic polymer behaviours.⁵³ The changes in the hydrophilic behaviour of thermoresponsive polymers is accompanied by variation of aggregational dimensions (detailedly described in chapter 5.3.1), which may be adjustable for target polyplex magnitudes. It is important to note that the stimuli-responses are supposed to occur under physiological conditions (e.g., pH, salt) and applicable concentrations. Common explored polymer systems are applying poly(*N*-isopropylacrylamide), poly(*N,N*-diethylacrylamide), poly(methyl vinyl ether), poly(*N*-vinylcaprolactam) or poly(AAm-co-AAc).¹⁵⁸

These smart vectors show an optimized formation-dissociation behaviour of the polyplexes specifically for each cellular process in dependence of the temperature. The gene expression

control has been successfully shown by Kurisawa et al. employing a terpolymeric vector with varying composition of NIPAAm, DMAEMA and BMA (butylmethacrylate).¹⁵⁹ The control *via* temperature altering was evidenced by several works.⁵⁸ This facility opened up another great synthetic variety applicable in the gene delivery research field. Highly developed vectors are accessible due to the investigation of novel monomer and polymer systems, modified polymerization techniques and several different skeletal architectures.^{19,158,160}

6. Methods

The following chapter gives a brief introduction to the method of operation of the used equipment (DLS, DSC, GPC, and UV-Vis). Though, the nuclear magnetic resonance spectroscopy (NMR), thermogravimetric analysis (TGA) and the infrared spectroscopy (IR) are excluded, as they belong to the basic characterization methods in the macromolecular chemistry and are not explained further. Other techniques like TEM, high performance liquid chromatography coupled mass spectrometer (HPLC-MS), gel electrophoresis and field emission scanning electron microscope (FESEM) are of minor importance for the present work.

6.1. Dynamic Light Scattering

Dynamic light scattering (DLS) is a useful technique for the study of the macromolecular diffusion behaviour in solution and the corresponding aggregation size distributions of colloidal systems. In the present work, the method was employed for the study of thermoresponsive properties of copolymers and aggregation behaviour of ion-sensitive macromolecular coordination ligands.

The measuring setup (shown in Figure 13) consists of a monochromatic laser with lenses, which is focused on a cuvette filled with dissolved or dispersed analyte, which scatters the light. The scattered light is detected by a photomultiplier detector set in a defined angle. The used instrument was set in the $\phi=173^\circ$ backscattering mode.¹⁶¹ The backscattering detection enables the measurement of concentrated samples, as the light does not have to pass through the entire cuvette. Additionally, large dust contaminants scatter in forward direction, which avoids the detection of such contaminants.¹⁶²

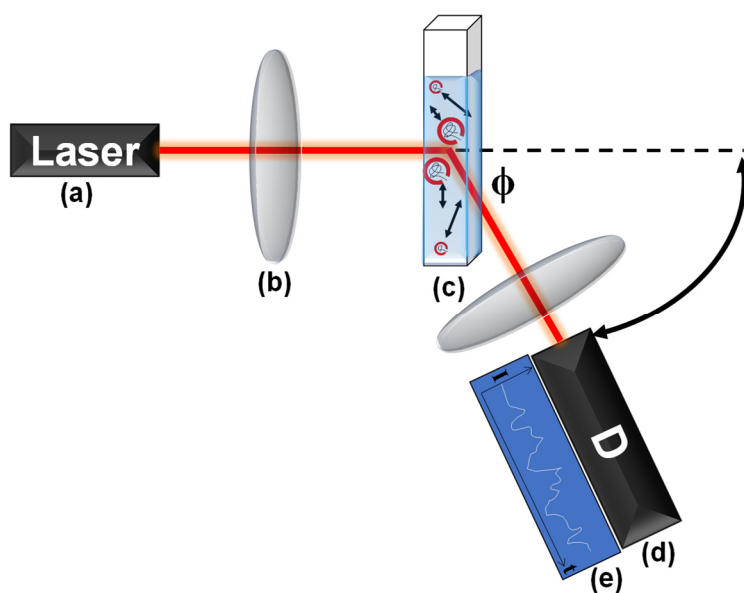


Figure 13: Schematic setup of a dynamic light scattering consisting of a) a laser light source, b) system of lenses, c) cuvette filled with polymeric solution, d) detector and e) the resulting raw data.

Generally, the interaction of light and molecules is spectroscopically described by Raman. Light irradiation impacts an inelastic energy level change of the molecule with respect to the translational, rotational, vibrational or electronic degree. The technique of DLS deals with the elastic change of translational and rotational degree, which is dedicated to the Rayleigh scattering of particles much smaller than the wavelength of light ($D_h < 1/10 \cdot \lambda_{ex}$, otherwise Mie scattering occurs).¹⁶¹ The electric field of the irradiated light causes an oscillating polarization of the electrons from a molecule. The electrons are forced to move in a direction and induce a dipole, which is a source of electromagnetic radiation independently of the direction (elastic scattering process).⁶³ The Rayleigh scattering equation formulates the relation between the scattering intensity and particle diameter. It is described by the initial intensity (I_0) in the distance (R) around the angle (Θ) in dependence to the refractive index (n), the diameter of the particle (d) and at the time (τ).

$$I = \frac{I_0}{R^2} \cdot \frac{1 + \cos^2 \theta}{2} \cdot \left(\frac{2 \cdot \pi}{\tau}\right)^4 \cdot \left(\frac{n^2 - 1}{n^2 + 2}\right)^2 \cdot \left(\frac{d}{2}\right)^6 \quad (5)$$

The intensity of the scattered light is influenced strongly by the size of bigger particles, which affects a potential covering effect of the intensities of smaller species in a broad mixture, so that their determination usually becomes imprecise.¹⁶¹

The principle of the method is based on different velocities of particles. According to their hydrodynamic radius, the molecules are diffusing heterogeneously in solution driven by the Brownian motion. Smaller molecules diffuse faster than bigger scattering objects. The velocity differences cause a variation of the scattering intensity and result in a Doppler broadening of the scattering light - it interferes destructively or constructively. In the case of constructive interference, a detectable signal is produced. The interplay of object size, Brownian motion and light interference provokes a time-resolved fluctuation of the intensity. This fluctuation is analysed by the autocorrelation function and refers the diffusion behaviour to the size of the aggregates.¹⁶²

The analysis is performed by a normalization of the autocorrelation function ($g_2(\tau)$), which is expressed by the integrals of the intensity at time t and delayed time ($t + \tau$).¹⁶²

$$g_2(\tau) = \frac{\langle I(t) \cdot I(t+\tau) \rangle}{\langle I(t) \rangle^2} \quad (6)$$

For a practical application, the general autocorrelation function was further modified by its expression as electric field function (particle diffuse relatively), the Siegert relation of a homodyne process (accessible detection of exclusively scattered light in Gaussian distributions) and the implementing of Bagg's law (wave vector diffusion). It results in the final mathematical description of the particle motion by the coherence factor (β) (correlation with

the detector area and scattering properties of the macromolecule), the parameter (q) (proportional to the refractive index of the solvent) and the diffusion coefficient (D).¹⁶²

$$g_2(\tau) = 1 + \beta \cdot e^{-2Dq^2} \quad (7)$$

The diffusion coefficient is linked by the Stokes-Einstein equation to the size of the particles in solution and is mathematically dependent on the Boltzmann constant (k_B), the temperature (T), the dynamic viscosity of the solvent (η) and the hydrodynamic radius (R_H). It is used for the calculation of the hydrodynamic radius. This equation demands the requirement of temperature dependent solvent viscosity and refractive index of the macromolecule for the performance of a measurement.

$$D = \frac{k_B \cdot T}{6 \cdot \pi \cdot \eta \cdot R_H} \quad (8)$$

The correlation curve is fitted *via* two approaches to evaluate the aggregation size and homogeneity of an analyte. Firstly, monomodal distributions could be investigated by the cumulant fit due to its reliable and easy data treatment found by Koppel.¹⁶³ It allows the extraction of predominantly Gaussian-like distributions of averaged diffusion coefficients and polydispersity indices. Secondly, the non-monomodal distributions are derived by the non-negative least squares (NNLS) method of Morrison for polydisperse systems.¹⁶⁴ As it does not consider certain type of distribution, it represent a proper method for broad and multimodal distributions.

6.2. Differential Scanning Calorimetry

Differential scanning calorimetry (DSC) corresponds to the thermal analysis techniques and is a powerful tool for the physical characterization of polymers¹⁶⁵, widespread of inorganic and organic materials^{166–168}, pharmaceuticals¹⁶⁹, biological approaches¹⁷⁰ and even foods¹⁷¹. It possesses a wide variety of applications in the field of research and economy due to the simplicity and universality of this method.¹⁷² It provides qualitative and quantitative information about endothermic and exothermic processes. General thermal properties of liquids, gels and solids can be studied in terms of heat flow and capacity without a specified time-consuming sampling.¹⁷²

In the field of macromolecular chemistry, it provides an insight into the glass transition, crystallization and melting processes, internal stress of solids, kinetic investigations of polymerizations, as well as the coil-to-globule transition of thermoresponsive polymer solutions.^{60,165,173,174} In the present thesis, DSC analysis was applied for the determination of glass transition temperatures of copolymers with various monomer fractions, the study of double thermoresponsive properties of UCST-LCST block copolymers and the detection of

thermoreponsive properties of photo-crosslinked hydrogels inside nanoporous aluminium oxide membranes.

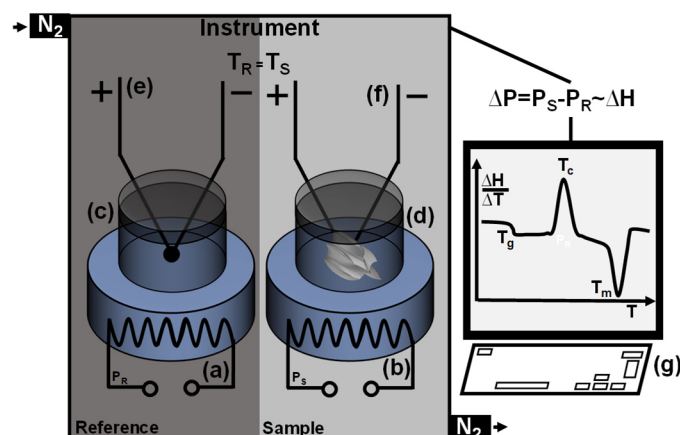


Figure 14: Schematic setup of a differential scanning calorimeter consisting of two independent heaters (a-b), the pans for reference (empty) and sample (polymer) (c-d), the corresponding thermocouples (e-f) and the resulting measurement of a semi-crystalline polymer sample (g).

The measurement allows the monitoring of enthalpic processes under thermal and isothermal conditions and is performed in (hermetic) aluminium pans (shown in Figure 14). Both reference (commonly empty) and sample pan are placed in the measuring cell with nitrogen flux on independently acting heaters with thermocouples. During the measurement both pans are held on the identical temperature. While the empty pan consumes exclusively the energy of the pan's heat capacity, the sample in the other pan undergoes additionally thermal transitions, which consume (endothermic) or liberate (exothermic) certain portions of energy. The differences in electrical power used of the independent heaters can be resolved time- or temperature-wise and correlate with the transitions' magnitude of enthalpy.^{63,175}

First order processes (with a heat flow curve maximum/minimum) are typically depicted by exothermic polymerizations and crystallization of polymers or endothermic melting processes.¹⁷⁵ The glass transition is based on a continuous change of the heat capacity and belongs to a transition of a second order (gradual heat flow change).^{63,175}

Despite the high number of advantageous features, the methodology includes certain limitations. If multiple transitions occur in a narrow time range, they might be difficult to interpret and assign.¹⁷² Weak transition could be accentuated by increasing either the mass of analyte (restricted by the pan size) or the scan rate due to the reduced signal-to-noise ratio (sensitivity). However, larger scan rates provoke a signal overlapping of closely occurring transitions due to an artificial broadening of the signal. The improved sensitivity is always in expense of the resolution, which proves beneficial to apply modulated differential scanning calorimetry (MDSC).¹⁷²

In the MDSC, the total heat flow, which corresponds to the signal of a conventional DSC measurement, is split up into a reversing (thermodynamically-driven) and non-reversing

(kinetically-driven) component. The separation of the processes is accessible *via* sinusoidal modulation of the heating rate, which oscillates periodically around its linear value (Figure 15a). The total heat flow (dH/dt) consists of the reversing heat flow ($C_p \cdot dT/dt$) and a kinetic, non-reversing signal ($f(T,t)$).^{165,176}

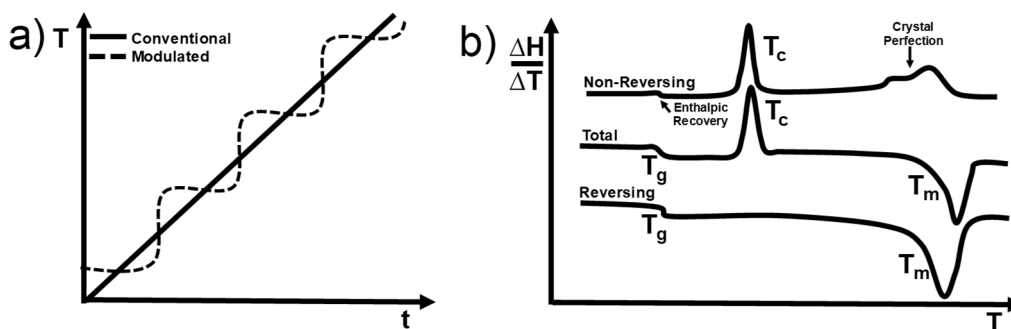


Figure 15: a) Schematic temperature ramp of a conventional (solid) and modulated (dashed) DSC measurement. b) An illustrated modulated DSC measurement of a semi-crystalline polymer indicating the separation of processes into the total, reversing and non-reversing heat flow signal.

The different calorimetric components are derived from the three parameters of time, modulated temperature and modulated heat flow. While the total heat flow is calculated by the average of the modulated conjugate, the heat capacity (C_p) is determined by the periodic variation of the heating rate. It is determined *via* discrete Fourier-transformation of the ratio of modulated heat flow amplitude and modulated heating rate amplitude. The heat capacity is referred to the negative heating rate (dT/dt) to obtain the resulting reversing heat flow. The kinetic component is the arithmetic difference of the reversing and total heat flow.^{165,172}

$$\frac{dH}{dt} = C_p \cdot \frac{dT}{dt} + f(T, t) \quad (9)$$

The glass transition and melting process belongs mainly to the heat capacity events and is monitored in the reversing heat flow, while enthalpic relaxation, crystallization and curing are detected in the non-reversing counterpart (sketched in Figure 15b).¹⁷² The process of critical solution temperatures is more complicated, as it owns a variety of overlapping processes like hydrogen bond breakage and formation (reversing processes), nonpolar dehydration, conformational chain movements or aggregation of hydrophobic groups (non-reversing processes).^{60,66,68,70} Additionally, the frequency of the modulated measurement is inconsistently influencing the sensitivity of the reversing and non-reversing signals, which leads to a deviating frequency dependent signal ratio.⁶⁶

6.3. Gel-Permeation Chromatography

The gel-permeation chromatography (GPC) belongs to the porosimetric techniques of size exclusion chromatography (SEC) and represents a powerful tool for the analysis of polymers. In the present thesis, the method was employed for the determination of the dispersity and

molar mass distribution of the polymers and to study the homogeneity of the performed polymerizations.

The terminology is based on the use of soft organic gels as original column packings. Initially, the size exclusion was developed in 1956 by G. H. Lathe and C. R. J. Ruthven with starch as column packing.¹⁷⁷ The technique is used for the characterization of soluble natural and synthetic polymers (with linear, branched or star-shaped architecture) in terms of the determination of the dispersity, the averaged molar mass and molar mass distribution.¹⁷⁸

The setup (shown in Figure 16a-g) is comparable to a high-performance liquid chromatography system and consists of a reservoir of eluent (proper for the dissolution of the polymer), an isocratic pump, an injector, a packed column and a detectors (commonly UV- and RI- detectors) connected to a user interface.¹⁷⁸ Common eluents are DMAc, THF, toluene, DMF, aqueous solutions of electrolytes and buffers.¹⁷⁸ The column material illustrates the stationary phase consisting of a granular and porous material nowadays often based on porous silica, crosslinked poly(divinyl benzene) or poly(hydroxy methacrylate) with a diameter of 5-30 μm with different pore sizes in the range of 5-10⁵ nm.^{63,178} The column packing is supposed to show pure entropy-controlled separation, as interaction between analyte and column material leads to undesired retention time deviations.

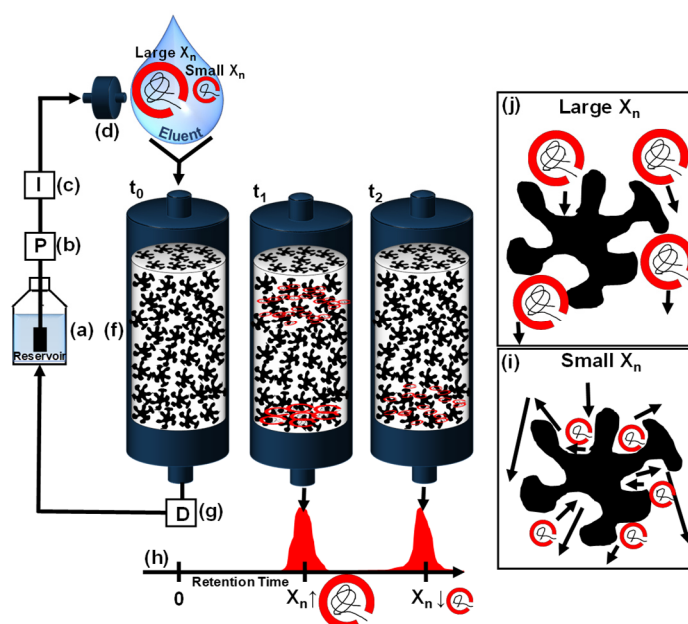


Figure 16: Schematic setup of a gel-permeation chromatograph consisting of a) an eluent reservoir with reflux, b) isocratic pump, c) injector, d) pre-filter, f) column and g) detectors (e.g., UV, RI). with h) resulting elugram. The working concept is illustrated by the mean of analyte mixture with differing polymer masses i) and j) at elution times (t_0 - t_2).

The principle of this method is established by the fractionation of a polymeric analyte along the pathway through the column according to its corresponding size in solution (hydrodynamic radius). The retention time of an analyte in the column decrease with molar mass due to the reduced accessible pathway inside the pore volume of the column packing

(shown in Figure 16h-j). Polymers of larger masses are unable to diffuse inside the pores and possess consequently a shorter retention time than smaller molecules.

The technique itself belongs to the relative methods, as a calibration correlates the elution volume and the molar mass of a detected species. The calibration is performed *via* elution time determination of a series of polymer standards with varying but exact and narrow mass distributions. A proper standard should be similar to the analyte regarding the composition, structure and degree of polymerization to mimic potential (undesired) interactions with the column packing (non-entropic fractioning).⁶³ By the mean of the calibration curve the elugram is transferred to the molar mass distribution, which delivers number averaged (\bar{M}_n), mass averaged (\bar{M}_w) molecular masses, the maximum of the molecular mass signal (\bar{M}_p) and the corresponding dispersity (\mathcal{D}).¹⁷⁸

The detection is usually performed *via* concentration dependent UV and RI detectors. Absorption or refractive index variations are indicating the analyte concentration with respect to the elution time. The precise concentration of the analyte has to be known for subsequent determinations of species fractions in the analyte. It is important to note that UV detection is applicable exclusively for wavelengths out of the range of the intrinsic absorptions of the eluent.¹⁷⁹ The coupling of RI and UV detectors allows the proof of the availability of certain UV-active moieties (e.g. comonomers, end groups or photo-crosslinking moieties) as part of the polymeric chains to value the homogeneity of the analyte. Other systems like viscosity or dynamic/static light scattering (DLS/SLS) detectors are molar mass sensitive detection methods. The coupling of RI and DLS allows the simultaneous determination of the precise molar mass and species fractions within the analyte mixture.^{63,178}

6.4. UV-Vis Spectroscopy

UV-Vis spectroscopy belongs to the spectro-photometrical analysis methods and is based on the determination of the absorbance in the range of visible to ultraviolet light (200-800 nm).⁶³ The incoming light causes transitions of the outer electrons into different electronic levels. For organic molecules the excitation occurs for bonding electrons (mostly) from the highest occupied bonding molecular orbital (HOMO) to the lowest unoccupied molecular orbital (LUMO).⁶³ Especially, $\sigma \rightarrow \sigma^*$ transitions (high energy, $100 \text{ nm} < \lambda < 200 \text{ nm}$), $\pi \rightarrow \pi^*$ transitions and weak forbidden $n \rightarrow \pi^*$ lone pair transitions (near/middle UV, $200 \text{ nm} < \lambda < 400 \text{ nm}$) or chromophores (visible light, $400 \text{ nm} < \lambda < 700 \text{ nm}$) are detectable.⁶³ The energy difference between the states represent the absorbance at certain wavelengths so that study of the occurring excited states is accessible. The broad application field of this technique allows the characterization of both inorganic and organic compounds as well as complexes and quantitative analysis of molecules, polymeric moieties, radicals and ions.¹⁸⁰ In present thesis,

it is mainly used for studies of the thermoresponsive behavior of polymers and their cloud point (T_c).⁸³

This measurement (shown in Figure 17) is carried out in cuvette of a specific length, in which the analyte is filled. The incoming light I_0 is passing the cuvette and is reflected, scattered and absorbed by the sample, which leads to a loss of the initial intensity of light. The decadic logarithm of the ratio of initial and detected light represents the absorbance. This relation is given in the Bouguer-Lambert-Beer law.

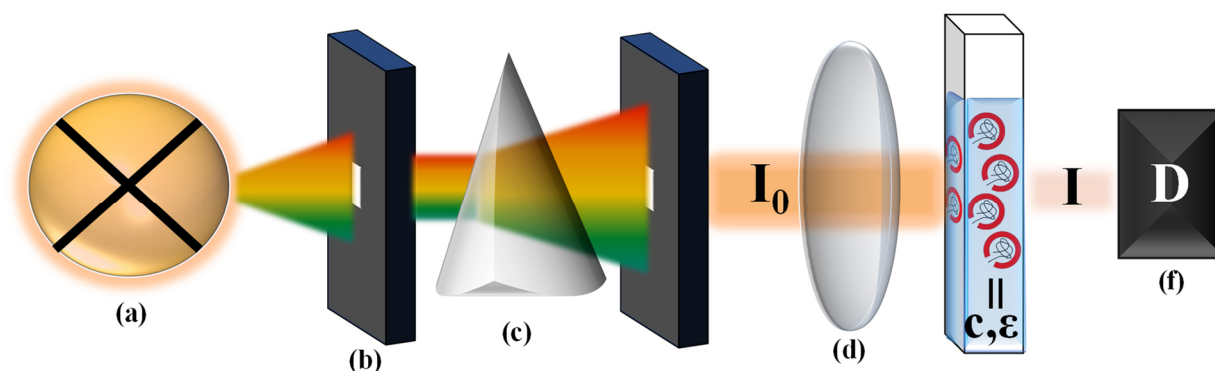


Figure 17: Schematic setup of a UV-Vis spectrometer consisting of the a) light source, b) system of slits, c) monochromator, d) system of lenses, e) cuvette filled with polymeric solution and the f) detector.

The absorbance (A) correlates with the absorption coefficient (ϵ), the pathlength of the light through the medium (d) and the concentration of the sample. This relation is restricted for diluted systems ($[c] < 0.01M$), irradiated with monochromatic light featuring a strictly linear correlation of the absorbance. The characteristic coefficient (ϵ) describes the potential of an analyte to show a certain transition and increases with higher intensity of transition.¹⁸¹ The excitation of an electron out of the ground state S_0 to an excited state S_x belongs to a specific difference of energy and allows the assignment of absorption to specific transitions.

$$A = \lg\left(\frac{I_0}{I}\right) = \epsilon \cdot c \cdot d = E_{S_x} - E_{S_0} \quad (10)$$

In the present thesis, UV-Vis spectroscopy was employed for the investigation of thermoresponsive polymers in an aqueous solution, monitoring their optical clouding during the coil-to-globule transition. In the globular solvation state, the thermoresponsive polymer separates from homogeneous solution, yielding in a strong aggregation. During this coil-to-globule-transition, the detected light is reduced by the formation of larger scattering objects, which leads to higher absorbances. The cloud point is defined as the inflection point of the turbidity transition curve.¹⁸² In this way, the measurement of absorption at fixed wavelength with temperature variation is used to investigate the cloud point and corresponding kinetics.¹⁸³ The wavelength exhibits a minor influence on the detection of the cloud point, but is supposed to be adjusted beyond the structural absorption of polymer functionalities (e.g., dithiocarbonates, trithiocarbonates, chromophores).⁶⁷

7. Adjustable UCST by Copolymerization of AAm and AN

7.1. Introduction to Copolymerization of AAm and AN

The development of intelligent materials requires steady progression in the field of stimuli-responsive polymer systems to develop an accurate switching process, entirely suitable for the applied demands of advanced applications. Thermoresponsive polymers allow targeted control of their properties by the variation of the temperature, which represents a reversible and non-invasive remoting process. In the literature, the polymer systems, bearing UCST behaviour in aqueous solution, are still underrepresented in comparison to their LCST conjugates.⁶¹ The widespread applicability of thermoresponsive systems depends on general demands such as cost-effectiveness, reliability and highly controllable thermoresponsive properties. In comparison to other famous UCST representatives like poly(NAGA), poly(MAM) and the zwitterionic poly(betaines), the present system of acrylamide and acrylonitrile shows a unique set of substantial benefits.

The copolymerization of the low-cost monomers AAm and AN allows the synthesis of tuneable UCST copolymers supported by their comparable copolymerization parameters ($r_1=0.86$, $r_2=0.81$, $r_1r_2=0.697$).^{14,184} The poly(acrylamide) possesses an original UCST character in aqueous solution below 0 °C, which can be shifted to higher values by copolymerization with hydrophobic components.⁵⁹ This property is referred to non-ionic solvent interactions of the acrylamide moiety *via* reversibly formed hydrogen bonding, which results in a high tolerance toward the presence of salts/ions and pH variation compared to other UCST systems.^{15,59,73} The delicate hydrophilic-hydrophobic counterbalance in poly(AAm-co-AN) is set by the fraction of the monomers (illustrated in Figure 18) and can be utilized for the synthetical adjustment of the thermoresponsive behaviour in the temperature ranges of 0-100 °C, which represents an advantageous key property for prospective application fields.¹⁴

Several other parameters have to be considered, which influence the cloud point like the molecular mass (Figure 18h/c), hydrophilic/hydrophobic units (Figure 18f/g), copolymer concentration in solution (Figure 18b), end group (Figure 18e) and copolymer architecture (as such random, block or graft copolymer).^{18,73,85,185}

The reported syntheses are commonly performed in DMSO under free or controlled radical conditions and allow the copolymerization with other responsive monomers such as acrylic acid (AA) and BPAAm to obtain additional pH-sensitive or photo-crosslinkable behaviours.^{18,85} Generally, the thermoresponsiveness of the system is reported in rough dependence of the acrylonitrile fraction in the copolymer, without providing an accurate approach to synthetically adjust the target phase transition temperature.^{14,18} Due to the high boiling point of the polar solvent DMSO, the purification of the products is done *via* dialysis or vacuum drying at higher temperatures, as contamination of remaining solvent leads to a shift of the cloud point and increase of copolymer toxicity. Despite the choice of the solvent, the

product purity is often provided by ^1H NMR spectra in DMSO-d_6 , which do not even allow the monitoring of remaining DMSO residues.^{14,85,185}

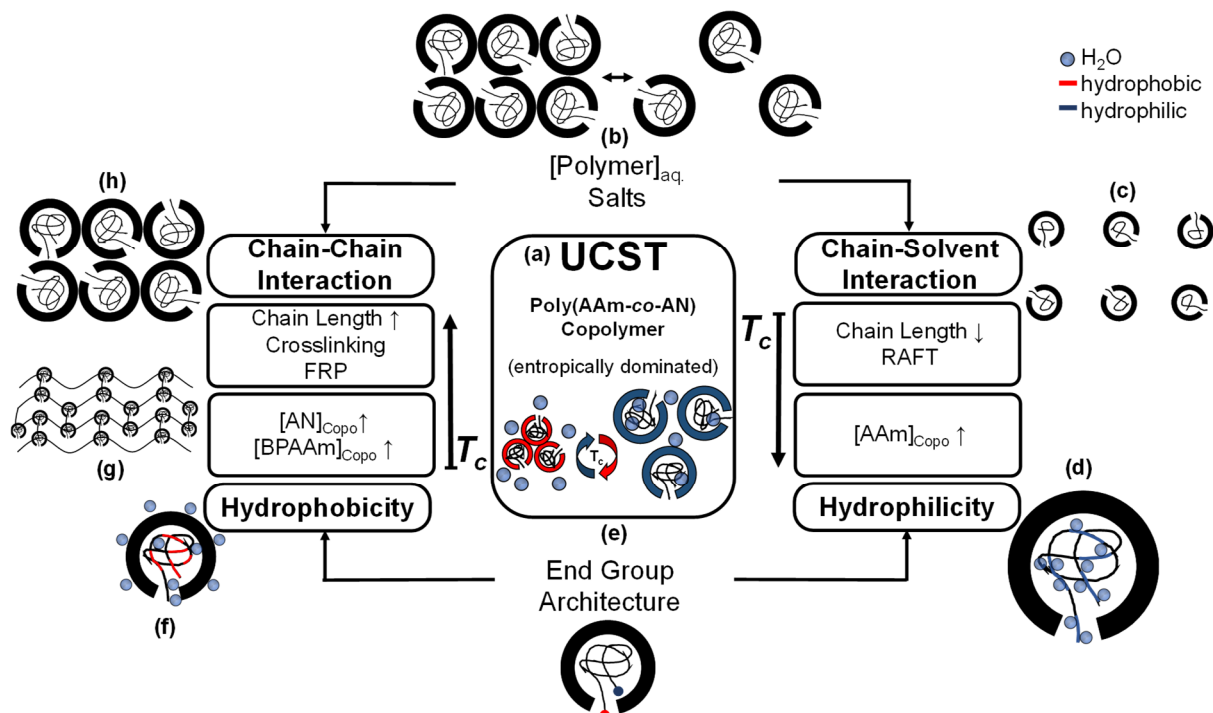


Figure 18: The overview of the investigated parameters influencing the thermoresponsive UCST behaviour of poly(AAm-co-AN) copolymers.

Thus, the following chapter demonstrates the enhanced convenience in the synthesis of tuneable UCST copolymers, employing the monomers AAm, AN and the photo-crosslinkable BPAAm, by simplifying their time-consuming workup and improving their thermoresponsive properties. Therefore, experimental series were designed with particular focus to establish a reliable prediction method for the synthetical adjustment of desired clouding temperatures in aqueous solution.

The fabricated copolymers of this section were also used in the following sections dealing with dual-thermoresponsive LCST-UCST copolymers (in chapter 9) and the filling of the thermally switchable nanopore membranes (in chapter 10). The cloud point estimation was successfully applied on further functionalized copolymers for the application of iron ion sensitive macromolecular coordination ligands (in chapter 11) and the thermoresponsive non-viral vectors for gene delivery (in chapter 12).

7.2. Results and Discussion of Copolymerization of AAm and AN

7.2.1. Optimization of Reaction Conditions and Characterization Methods for Poly(AAm-co-AN)

In literature, the general synthesis of poly(AAm-co-AN) is performed in DMSO, which requires the usual workup procedure of precipitation followed by dialysis to properly remove contaminations due to the high boiling point of the very polar solvent. In order to simplify this

purification pathway, the copolymerization was supposed to be performed in aqueous medium as another polar solvent. To suppress the occurring thermoresponsive properties, a reaction mixture of water and dioxane was applied, because 1,4-dioxane turned out as most suitable cosolvent. Upon the stepwise addition of 1,4-dioxane (0-15 vol%) to an aqueous copolymer solution (1 wt%), the cloud point dropped the most between turbidity measurements in comparison to several other water-mixable solvents (like acetonitrile, DMSO, ethanol and methanol).

The fraction of dioxane was adjusted to the solubility of the used educts offering a homogeneous reaction mixture for all components. The free radical polymerization was performed in water/dioxane (35:65). As the overall polarity of the reaction mixture limits the solubility and, thus, also maximum molar mass of the polar polymer products, the RAFT copolymerization was carried out in a more polar mixture of water/dioxane (60:40), which represents the solubility limitation for the given system with respect to the hydrophobic components such as CTA and BPAAm. The developed standard purification procedure consisted of a twofold precipitation step in cold methanol (re-dissolved in H₂O), followed by a lyophilization cycle in water to ensure a complete removal of the solvents proper for even biomedical applications. The synthesized samples showed thermoresponsive properties in aqueous solution and were investigated by turbidity measurements with UV-Vis spectroscopy ([c]=1 wt%, λ_{abs} =650 nm).

The formation of the target copolymer is confirmed *via* ¹H NMR measurements, which are exemplary shown Figure S17a/b (appendix). The spectra demonstrate satisfying purity of the samples. The ¹H NMR spectra were recorded either in a mixture of D₂O/MeCN-d₃ (85:15) or in dry DMSO-d₆. The measurements in DMSO-d₆ allowed the determination of the relative acrylamide fraction in the product by the integral ratio of acrylamide and backbone protons, which are exemplary indicated as "A" and "B" in the mentioned figure. The standard measurement was performed in D₂O/MeCN-d₃ (85:15) to evaluate exclusively the purity of the products and calculate the chain length of the RAFT conjugates (see equation on page 224).

For the determination of the molar mass distribution, gel permeation chromatography measurements were performed on a PSS Suprema column for aqueous eluents, calibrated with pullulan standard. A mixture of water/acetonitrile (85:15) with NaNO₃ (0.1 mol·L⁻¹) and NaN₃ (0.011 mol·L⁻¹) was used, which allowed the suppression of the thermoresponsive properties by a shift of the phase transition below ambient temperature, which allowed a complete solubility of the copolymers with T_c up to 60 °C during the measurement. Besides, the screening of the analyte's charges was accomplished by the salts avoiding the interaction with the stationary phase in the column. In principle, the measurements delivered reliable values conformed to the theoretical values (see appendix, Table S5). The samples, bearing

cloud points above 50 °C, tend to show artificially shrank molar masses due to different coiling behaviours caused by the increased hydrophobicity in the copolymer. It is expected that the target molar masses were reached in accordance with the data derived from the RAFT conjugates (see appendix, Table S3 and Table S5).

The setup of the analytical methods enabled the systematic study of the copolymerization of acrylamide and acrylonitrile with respect to a precise control of the UCST behaviour.

7.2.2. Characterization of Poly(AAm-co-AN) Synthesized *via* Free Radical and RAFT Copolymerization

Variation of the Acrylonitrile Fraction

The thermoresponsive behaviour of poly(AAm_x-co-AN_y) was studied in dependence of the molar fraction of acrylonitrile in the reaction mixture feed under free radical and RAFT conditions. The copolymers were applied as macroCTA in the project of dual-thermoresponsive LCST-UCST copolymers (in chapter 9). The developed synthesis route was successfully applied for further functionalized copolymers in the application of iron ion sensitive macromolecular coordination ligands (in chapter 11) and the thermoresponsive non-viral vectors for gene delivery (in chapter 12).

The free radical copolymerization of acrylamide and acrylonitrile was performed varying the AN content from 15 to 50 mol% using the thermal initiator AIBN at 70 °C in water/dioxane (35:65). The sample code (FRP_%) denotes the molar feed ratio of AN in the reaction mixture.

The DSC traces illustrate a second order transition in the range between $T_g=150.9$ °C to 177.1 °C and corroborate the formation of a single copolymeric species. The glass transition temperature is linearly reduced with increasing acrylonitrile fraction in the copolymer and matches with the theoretical model of thermal copolymer behaviours (Table 12). The molar masses and compositions of the copolymers were investigated by ¹H NMR measurement in the mixture D₂O/MeCN-d₃ (85:15) or DMSO-d₆, which matches with the desired values. The GPC elugrams show unimodal molar mass distributions with a broad dispersity, typical for free radical conditions ($D=2.28-3.99$). Surprisingly, the molar masses are uncommonly small in the range of $\bar{M}_n=17.7-24.5$ kg·mol⁻¹, which may refer to limited solubility of the copolymer in the apolar reaction mixture leading to inhomogeneity among the polymerization processes. The cloud points, measured in 1 wt% aqueous solution, raise with increasing content of AN. For FRP15% and FRP20%, the cloud point lays below 0 °C, while it increases to 74 °C for equimolar composition of FRP50%. Satisfying yields between 48 and 63% were obtained for all copolymers. Spectra, GPC elugrams, TGA and DSC traces are exemplary shown in (Figure 23) and in the appendix, Figure S17 (p.224) and Figure S18 (p.225). The corresponding synthetic and physical data are summarized in Table 12 (p.170) and in the appendix, Table S3 (p.225).

The RAFT copolymerizations were performed with varying the AN content from 25 to 55 mol% in presence of the trithiocarbonate EMP in water/dioxane (60:40) with a constant ratio of $[\text{monomers}]/[\text{CTA}]/[\text{initiator}]=200:1:0.1$ using the thermal initiator 2,2'-azobis[2-(2-imidazolin-2-yl)propane]dihydrochloride (AIPC) at 55 °C. The sample code (CRP_%) denotes the molar feed ratio of AN in the reaction mixture.

In the ^1H NMR spectra, the CTA moiety is detectable in the copolymers, which reinforces the RAFT mechanism and allows the chain length determination of the copolymers. As previously mentioned, the molar acrylamide fraction of the obtained RAFT conjugates suits to the feed values in the reaction mixture. The GPC elugrams confirms the targeted molar masses in the range of $\bar{M}_n=11.1\text{-}14.1\text{ kg}\cdot\text{mol}^{-1}$ with a narrow unimodal distribution ($D=1.34\text{-}1.43$), corroborating the control over the polymerization process with EMP according to the mechanism of RAFT. The molar masses determined *via* ^1H NMR and GPC align to their theoretical values. As mentioned in 7.2.1, the copolymers with high molar fraction of $[\text{AN}]>45$ mol% tend to reduced molar masses caused by minored solvent-polymer interactions and resulted shrinking coiling states. The DSC traces show a second order transition. The glass transition temperature of the copolymers is increasing from 152.7 °C to 162.9 °C with decreasing AN fraction in the copolymer. In comparison to the FRP products, the values are lowered due to the smaller molar mass. The cloud points of a 1 wt% aqueous solution (UV-Vis, at 650 nm) are covering ranges from 2 °C to 79 °C with 30 to 55 mol% AN in the copolymer. The copolymers were obtained in good yields between 58 and 83%, indicating an efficient copolymerization and purification process.

Spectra and GPC elugrams are exemplary shown in the appendix, Figure S18 (p.225), Figure S19 (p.226) and Figure S23 (p.230). The corresponding synthetic and physical data are summarized in Table 13 (p.171) and in the appendix, Table S5 (p.230). The thermoresponsive properties of all copolymers are discussed separately in detail in chapter 7.2.5.

Variation of the Chain Length

The cloud points were studied in dependence of the chain length of the copolymer. The copolymers were synthesized in accordance to the previously introduced RAFT procedure with a constant molar feed ratio of $[\text{AN}]=37.5$ mol% in the reaction mixture. The RAFT process was utilized to adjust the molar mass of the copolymers by variation of the molar ratio of $[\text{M}]/[\text{CTA}]/[\text{I}]=[\text{M}]:1:0.1$ with $[\text{M}]=50\text{-}400$ in the reaction mixture. The ^1H NMR spectra align to the shown example and are not specified further. The elugrams verify differing chain lengths in molar mass ranges of $\bar{M}_n=2.7$ to $28.7\text{ kg}\cdot\text{mol}^{-1}$ showing narrow molecular mass distributions ($D=1.20\text{-}1.40$), which attest again an effective control over the polymerization. The experimental molar masses extracted from ^1H NMR and GPC measurements displayed the desired values. The cloud points measured in 1 wt% aqueous solution raise with

increasing molar mass and corresponding chain length from 10 °C to 36 °C. The obtained yields lie in accordance with previous experiments between 50% and 57%.

Spectra and GPC elugrams are exemplary shown in the appendix, Figure S19 (p.226), Figure S24A (p.231) and Figure S25 (p.232). The corresponding synthetic and physical data are summarized in Table 14 (p.172) and in the appendix, Table S6 (p.232). The thermoresponsive properties of all copolymers are discussed separately in detail in chapter 7.2.5.

7.2.3. Characterization of Poly(AAm-co-AN-co-BPAAm) Synthesized via Free Radical and RAFT Terpolymerization

The thermoresponse of the photo-crosslinkable poly(AAm-co-AN-co-BPAAm) was studied for free radical and RAFT copolymerized conjugates with respect to the molar fraction of the hydrophobic monomer *N*-(4-benzoylphenyl)acrylamide in the terpolymer. Additionally, the photo-crosslinking properties of the terpolymers were qualitatively tested to determine a critical fraction of BPAAm, which allows the formation of stable films of crosslinked hydrogel networks for the application in the thermal switchable nanopore membranes (in chapter 10).

The free radical terpolymerization of AAm, AN and BPAAm was performed varying the BPAAm content from 0.5 to 5 mol% at a fixed molar ratio of [AAm]/[AN]=70:30 in the reaction mixture using the thermal initiator AIBN at 70 °C in water/dioxane (35:65). The sample code (FRP-BP_%) denotes the molar feed ratio of BPAAm in the reaction mixture.

The ¹H NMR spectra attest an efficient incorporation of BPAAm in the terpolymer. The relative BPAAm fraction in the product composition is calculated by the equation on page 233, which correlates the proton integral ratios of the benzophenone side groups and the backbone indicated as “B” and “A” in the ¹H NMR spectra (appendix, Figure S26). The incorporation of BPAAm is less complete with its rising fraction and cloud point. The elugrams verify unimodal broad distributions with $D=2.60-3.15$ in the molar mass range of $\bar{M}_n=15.6-17.6 \text{ kg}\cdot\text{mol}^{-1}$, which is typical for free radical conditions. The monomer BPAAm seems to act as weak retarding agent, as the molar mass of the copolymer is slightly lowered with its increasing fraction. The film stability was tested qualitatively by the optical impression of the film behaviour such as dissolution, swelling and thermoresponsive collapse under temperature variation. A molar fraction of [BPAAm]>1.3 mol% in the copolymer is sufficient for the formation of an optically stable crosslinked network. DSC traces show second order transition belonging to the glass transition temperature, which is fluctuating between the temperatures of 171.6 °C and 175.2 °C without remarkable trend. The cloud point increased from 9 °C to >90 °C with percentual incorporation of BPAAm. The terpolymers were obtained in sufficient yields between 42% to 68%, which conform to previous values from the original copolymerization.

Optical film impressions, spectra and GPC elugrams are exemplary shown in the appendix, Figure S19 (p.226) and Figure S27 (p.234). The corresponding synthetic and physical data are summarized in Table 15 (p.173) and in the appendix, Table S7 (p.211). The thermoresponsive properties of all copolymers are discussed separately in detail in chapter 7.2.5.

For the RAFT terpolymerization of AAm, AN and BPAAm, a constant molar ratio of $[AAm]/[AN]=70:30$ was chosen varying the BPAAm content from 0.5 to 5 mol% as for the radical copolymerization. In correspondence to previous procedures, the molar mass was adjusted by the ratio $[monomers]/[CTA]/[initiator]=200:1:0.1$ in presence of the trithiocarbonate EMP using the initiator AIPC at 55 C° in water/dioxane (60:40). The sample code (CRP-BP_%) denotes the molar feed ratio of BPAAm in the reaction mixture.

As shown before, the CTA end groups allow the chain length determination of the terpolymers *via* 1H NMR spectroscopy and the integrals of the aromatic protons enable the calculation of the BPAAm content. The elugrams prove unimodal molar masses in the range of $\bar{M}_n=8.8-13.7 \text{ kg}\cdot\text{mol}^{-1}$ with a narrow distribution ($D=1.27-1.41$), corroborating the control over the polymerization process with EMP according to the mechanism of RAFT. The molar mass drops with increasing BPAAm content in the product, which evidences a gradual retarding effect of the monomer. This behaviour is intensified by the lower coil sizes in the medium due to the high cloud points of the copolymers, which lead to deviations in the molar mass for 1H NMR (broadening of end group signal) and GPC measurements (globular chain conformation). The compositional fraction of BPAAm conforms to the feed ratios in the reaction mixtures for terpolymers with fraction of $[BPAAm]\leq 1.5 \text{ mol}\%$. Higher contents inhibit the complete incorporation of the apolar BPAAm into the terpolymers, which may be reasoned by the low solubility in the polar solvent mixture water/dioxane (60:40).

Compared to the FRP conjugates, higher fractions of photo-crosslinker $[BPAAm]\geq 2.0 \text{ mol}\%$ are required for the formation of stable films, which is referred to smaller degree of polymerization and the corresponding lower number of benzophenone side groups per macromolecule. The yields were obtained between 58 and 75%, which promote an efficient copolymerization and purification procedure. The yields are improved compared to the FRP products, which may be caused by reduced losses during the purification pathway due to differing solution behaviours of end functionalized RAFT copolymers.

Spectra and GPC elugrams are exemplary shown in the appendix, Figure S19 (p.226) and Figure S28 (p.235). The corresponding synthetic and physical data are summarized in Table 16 (p.174) and in the appendix, Table S8 (p.236). The thermoresponsive properties of all terpolymers are discussed separately in detail in chapter 7.2.5.

7.2.4. Kinetics of the RAFT Copolymerization of Poly(AAm-co-AN)-EMP

The copolymerization of acrylamide and acrylonitrile is affected by the reactivities of the monomer components under the given synthetic conditions. The free radical synthesis performed in DMSO is reported to bear similar copolymerization parameters ($r_{AN}=0.86$, $r_{AAm}=0.81$, $r_{AN}r_{AAm}=0.697$) and Q/e values (AAm: 1.18/1.20 and AN: 0.60/1.20), promoting a statistical free radical copolymerization between both monomers.^{14,184} Advanced applications of smart materials demand highly controllable and tuneable properties, which require the kinetic description of each individual reaction medium to ensure the proper copolymerization progress.

To prove the applicability of the optimized synthesis conditions, the RAFT copolymerization, performed at 55 °C in presence of the chain transfer agent EMP and the initiator AIPC, was investigated in the reaction mixture of D₂O/dioxane (60:40) at different reaction times to monitor the monomer consumption, the copolymeric growth and the incorporation ratios of the individual monomers for achievement of the kinetic description. For the study, the feed ratios of [monomers]/[CTA]/[initiator]=200:1:0.1 in the reaction mixture with a constant molar monomer ratio of [AAm]/[AN]=60:40 were chosen.

The study of the copolymerization was performed *via* ¹H NMR and GPC measurements from the reaction mixtures at different times between 1 and 24 hours. The solvent mixture of H₂O/dioxane (60:40) was exchanged by D₂O/dioxane (60:40), which was supposed to minimize the perturbation of the water signal in the subsequent ¹H NMR spectra. Undeuterated dioxane was used as internal standard for the integral normalization of the spectra, allowing a comparability in between all measurements of the aliquots, which became independent of the analyte volume taken from the reaction mixture. The reaction was performed simultaneously under identical conditions in separated reaction tubes with added reaction mixture from stock solution, to avoid the contamination by taking several aliquots. After the degassing by three freeze thaw cycles, the reactions were started simultaneously in a common and preheated sample holder. After completion of the desired reaction times, the reaction was quenched and analysed *via* ¹H NMR and GPC.

The monomer consumption was determined by the integrals originated from the individual double bond protons AAm (6.35 ppm) and AN (6.39 ppm), which is illustrated in the appendix, Figure S20a-c. The chain propagation could be observed by the growth of the backbone signal (1.50-3.50 ppm) in reference to the fixed integral ratio of the internal standard 1,4-dioxane (3.76 ppm) and the end group of the CTA (1.36 ppm) at t=0 hours (in the appendix, Figure S21a). This ratio was compared to the molar mass obtained from the recorded GPC elugrams (in the appendix, Figure S22). The conversion of the copolymerization was calculated by the experimental chain lengths analysed at certain reaction times in correspondence to the target value of $X_n=200$ repeat units. The composition

of the copolymer samples was analysed *via* ^1H NMR measurements from the purified products in dry DMSO-d_6 quantifying the fraction of AAm in the macromolecule.

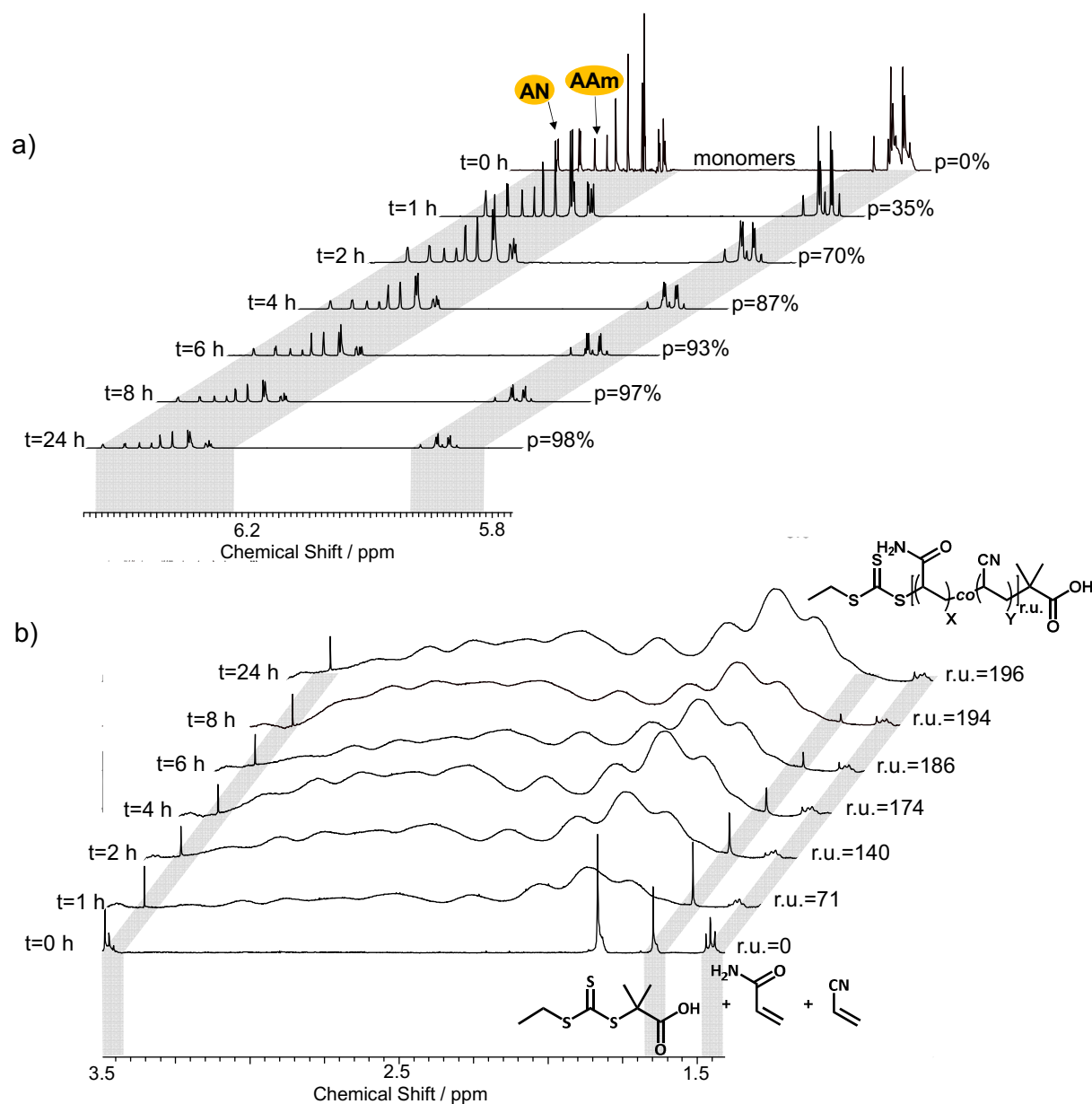


Figure 19: Time resolved ^1H NMR spectra (0-24 h) from the reaction mixture of the copolymerization of acrylamide and acrylonitrile during RAFT copolymerization of poly(AAm-co-AN)-EMP in D_2O /dioxane (60:40), recorded in D_2O . The spectra show a) the consumption of the monomers acrylamide and acrylonitrile and b) the growth of the polymer chain (r.u.) at various reaction times.

The initial and final state of copolymerization is visualized in the ^1H NMR spectra presented in the appendix, Figure S21. The monomer integrals decreased with their progressing consumption during the copolymerization. The progress of the monomer consumption is illustrated in Figure 19a with respect to the denoted rising conversion. Before initiation, the present chain transfer agent EMP can be detected in the reaction mixture (1.32 ppm, t, 3H and 3.36 ppm, s, 6H). With rising reaction time, the copolymer backbone (1.50-3.50 ppm) is growing between the end group signals of EMP indicated as "A" and "B" in the appendix,

Figure S21. The steady growth from the bare CTA to the final copolymer is visualized with the denoted degree of polymerization in Figure 19b. The chain growth is reinforced by the increasing molar mass, extracted from the corresponding elugrams (shown in the appendix, Figure S22). The time-resolved development of the molar mass, the corresponding degree of polymerization and the dispersity is summarized for ^1H NMR and GPC in the appendix, Table S4. Both analysis methods prove identical molar masses. The chain growth corroborates the enormous velocity of the RAFT process. The molar mass increased mainly within the first 4 hours ($\bar{M}_n=11.1 \text{ kg}\cdot\text{mol}^{-1}$) in good correlation to the product conversion of $p=87\%$, which converges to the adjusted value ($\bar{M}_n=13.1 \text{ kg}\cdot\text{mol}^{-1}$ and $p=98\%$) along the reaction time.

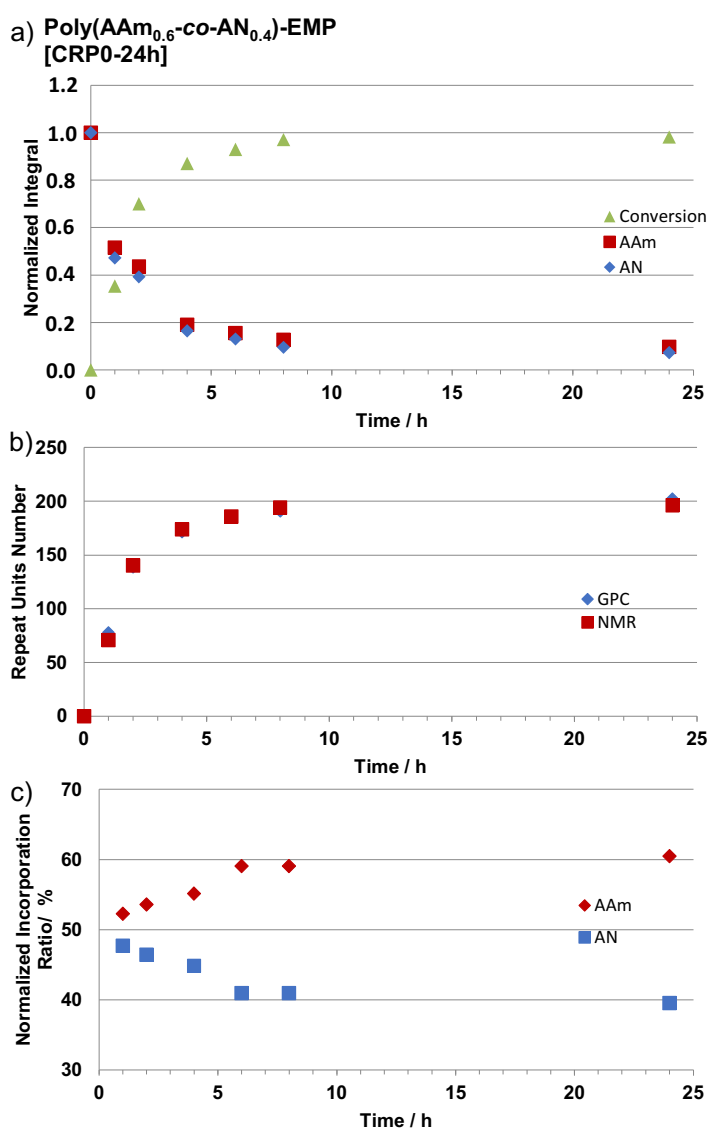


Figure 20: The results of the time resolved ^1H NMR measurements for the determination of the kinetics of the RAFT copolymerization of the poly(AAm_{0.6}-co-AN_{0.4})-EMP. a) The normalized consumption of the monomers with respect to the original feed of AAm/AN (60:40 mol%) with the resulting conversion. b) The calculated repeat unit number of the copolymer chains determined by the analyses of GPC and ^1H NMR. c) The incorporation ratio of the monomers acrylamide and acrylonitrile in poly(AAm-co-AN)-EMP at different reaction times.

The extracted data of the previously shown measurements are presented in detail below. The broadening of the bands clearly indicates the formation of polymer species. The conversion shows a linear growth within the first 2 hours of reaction time, until it converges slowly to its final value (Figure 20a). All individual consumptions of both monomers correlate with their initial feed ratio of $[AAm]/[AN]=60:40$. After the complete reaction time of 24 hours, the monomers are consumed apart from small residuals (7.2-9.7%). Due to the mechanism of RAFT, the chain growth proceeds fast until the final chain length of $X_n=196$ r.u. is accomplished (Figure 20b). In Figure 20c, a slight copolymerization drift ($\Delta=10\%$) was observed, which is balanced during the reaction so that the desired composition of the copolymer feeds was maintained in the overall macromolecule.

The proceeded RAFT copolymerization in D_2O /dioxane (60:40) follows an approximatively random copolymerization with a slight initial copolymer drift, so that longer reaction times are recommended. This study delivers the confirmation of a highly controllable copolymerization process between AAm and AN in the modified reaction mixture, which provides access to a risen applicability of the investigated UCST copolymer system for the denoted projects.

7.2.5. Adjustable Thermoresponsive Properties of Poly(AAm-co-AN) Copolymers

The previous subchapters dealt with the synthetic approach for the preparation of a highly defined and versatile building block based on the UCST copolymer system poly(AAm-co-AN) to provide access to various advanced applications. The experimental series were designed with particular regards to establish a reliable prediction method for the thermoresponsive behaviour. The cloud point was supposed to be tuneable by the compositional design of the copolymer. In order to achieve a predictable cloud point, the influences of the comonomers, the molar mass and the polymer concentration in aqueous solution were systematically studied for free radical and RAFT copolymerized products.

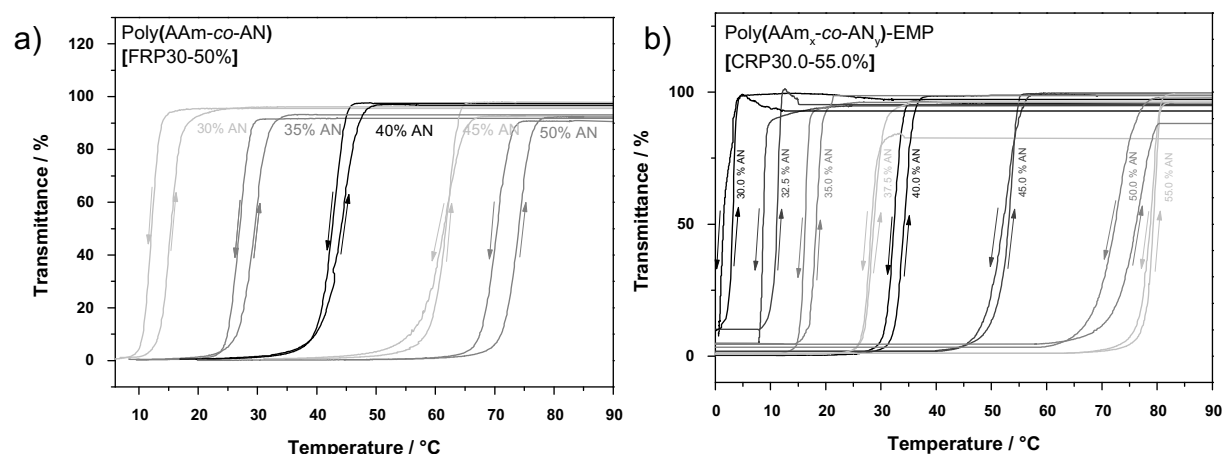


Figure 21: Cloud point determination of the tuneable UCST copolymer a) poly(AAm-co-AN) (FRP30%-50%) and b) poly(AAm-co-AN)-EMP (CRP30.0%-55.0%) with various acrylonitrile fractions, recorded from 1.0 wt% aqueous solution (at $\nu=650$ nm).

As previously remarked, the copolymer compositions conform to the feed ratios in the reaction mixture and bear the desired physical properties. The thermoresponsive properties were characterized *via* turbidity measurement of a 1 wt% aqueous solution (if not specified otherwise) and are indicated by the occurring cloud points, which could be freely adjusted synthetically in the temperature window of $T_c=0-100$ °C. The synthesized copolymers were responsive upon slight variation of temperature - homogeneously dissolving at high temperatures and demixing upon cooling. The tuneability of the cloud point was accomplished by the delicate intramolecular hydrophilic-hydrophobic counterbalance achieved by the compositional ratio of acrylamide and acrylonitrile. The transitions proceeded sharply and led to a complete clouding of the copolymer solution. The denoted cloud points were derived from the cooling curves (if not specified) due to the way out of the homogenous single-phase regime. Upon heating, the values are affected by additional kinetic dissolution processes ($T_{c,heat} > T_{c,cool}$), which lead to a hysteresis between the turbidity curves of the heating and cooling cycle ($\Delta T_c = 1.0-3.0$ K).

Free radical polymerized poly(AAm-co-AN) was prepared by using molar acrylonitrile fractions between 15 and 50 mol%. The products exhibited detectable thermoresponsive behaviour in aqueous medium for molar fractions higher than $[AN] > 25$ mol% ($T_c < 6$ °C for FRP25%). The transition temperature raised consistently with increasing AN content in the copolymer to cloud points up to $T_c = 73.8$ °C for a fraction of $[AN] = 50$ mol%.

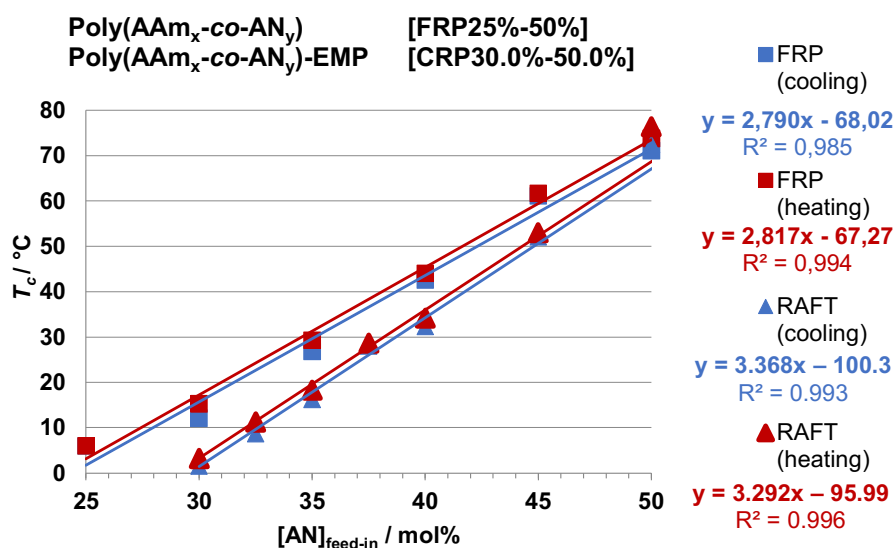


Figure 22: Acrylonitrile fraction correlated cloud points of poly(AAm-co-AN)-EMP (CRP25%-50%) in comparison to poly(AAm-co-AN) (FRP25%-50%).

The RAFT conjugates were synthesized with molar fraction of acrylonitrile between 30 to 55 mol% in the reaction mixtures feeds covering the temperature ranges of $T_c = 1.6$ to 78.8 °C. In comparison to the FRP products, the phase transitions of the RAFT equivalents with identical compositions tend to occur at lower temperatures, which is reasoned in the smaller molar

masses and the introduced hydrophilic moieties of the polar CTA, which increases the solvent-copolymer interactions.

The dependency between the monomer fraction of the hydrophobic component AN in the reaction feed and the resulting cloud point is highlighted for the heating and cooling cycle separately (Figure 22). The cloud points of the copolymers rise linearly with increasing AN content for both FRP and RAFT products ($\Delta T_c = 2.8$ K/mol% and 3.4 K/mol%) (values summarized in Table 12 on p.170 and Table 13 on p.171). The data allow the use of a linear fit, as denoted for the individual curves in Figure 22. The coefficients of determination from the linearization curves ($R^2=0.984-0.996$) and the number of samples promote a sufficient reliability and reproducibility of the present data set.

The mathematical fitting *via* linearization offers the possibility of an approximate prediction of the cloud point by the synthetic adjustment of compositional feed ratio between AAm and AN in the reaction mixture. The prediction is proved by some duplicates and delivered remarkable results ($\Delta T_c \pm 2.5$ K) under the given synthetic conditions.

In Figure 23, the thermal properties of the copolymers with varying AN fraction are shown. The exemplary thermogram (FRP35%) indicates a thermal stability up to $T=220$ °C for the neat copolymer, which is representative for both FRP and RAFT copolymers. The temperature of complete decomposition is mentioned hereby ($T=700$ °C), as this value was important for the application in the switchable nanopore membranes. A complete decomposition was necessary, in order to determine the mass of the copolymer pore coating and to confirm a proper purification process of the outer membrane surface.

The copolymers bear defined glass transition temperatures, which emphasizes the presence of a single copolymeric species. The variation of the glass transition temperature follows the theoretical thermal behaviour of copolymers.⁶³ Figure 23c-d (p.57) confirms a consistent linear correlation between the T_g and molar fraction [AN]. Increasing glass transition temperatures of the neat products provoked lower cloud points of the copolymers in solution. The comparison between the FRP ($T_g=150.9-177.1$ °C for [AN]=15-50 mol%) and RAFT copolymers ($T_g=152.7-162.9$ °C for [AN]=30-45 mol%) promotes the expected molar mass dependency of the glass transition temperature (values summarized in Table 12 and Table 13 on p.170 and 171). The linearization of the T_g gives access to the determination of the acrylonitrile content in the copolymer for a given system with defined chain length *via* differential scanning calorimetry measurements. As both the glass transition temperature and the cloud point are correlated to the compositional fraction of the monomer acrylonitrile in the linear manner, the thermoresponsive properties of the copolymers are cross-related linearly to the T_g as well (as indicated in Figure 23e-f). The introduced AN decrease the number of available hydrogen bonding in the macromolecules, which reduces both the chain-chain interaction in the neat solid (lowering T_g) and the chain-solvent interactions in aqueous

solution (raised T_c). The simple fabrication and the freely adjustable cloud point represent a key property of the highlighted UCST system of poly(AAm-co-AN).

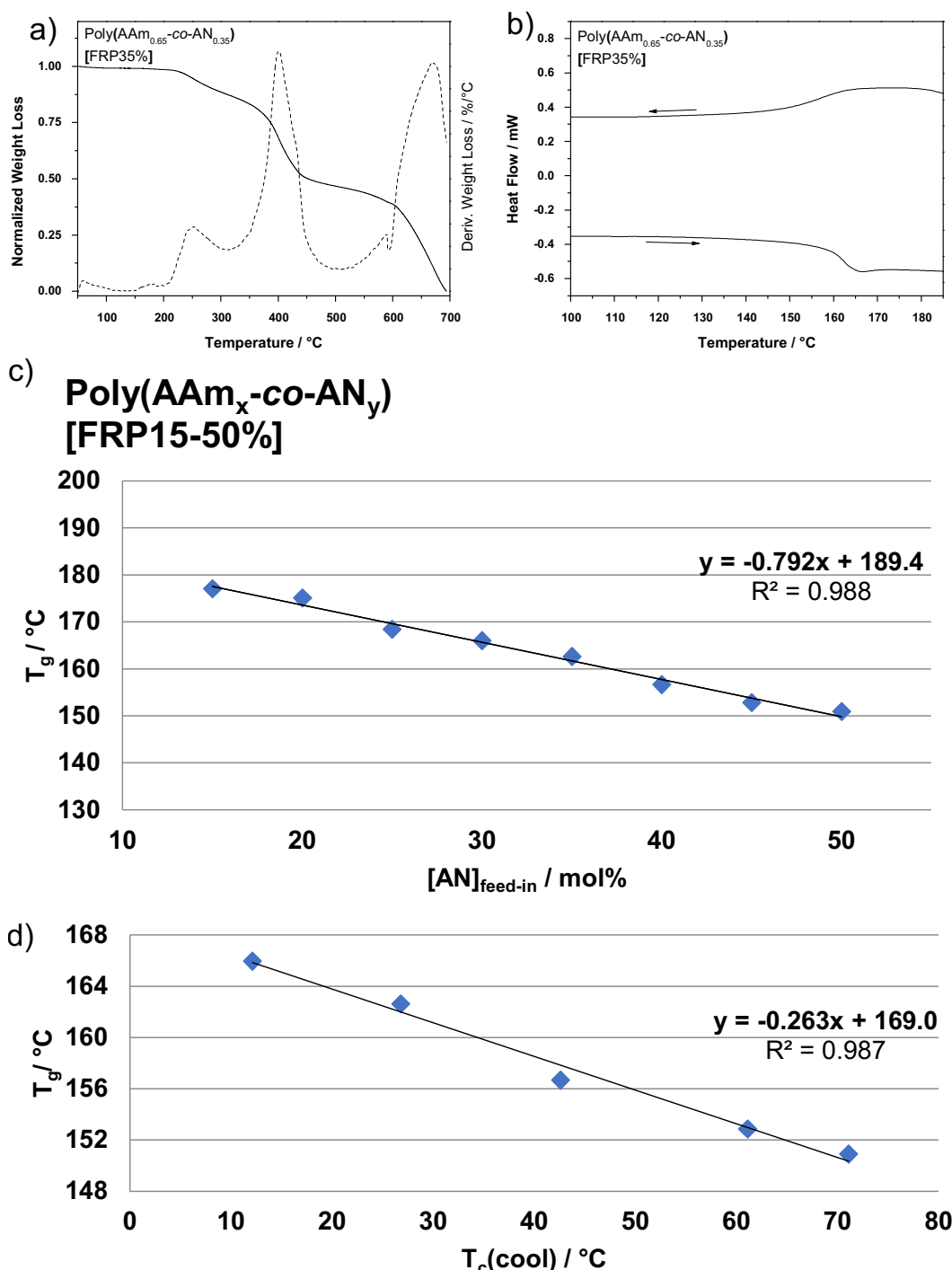


Figure 23: a) Thermogram and b) determination of glass transition temperature from the UCST copolymer poly(AAm-co-AN) (FRP35%). Acrylonitrile fraction dependence of the glass transition temperature of c) poly(AAm-co-AN) (FRP15%-50%) and d) poly(AAm-co-AN)-EMP (CRP30%-45%). Correlation of the cloud point in aqueous solution (1.0 wt%) with the glass transition temperature of the neat copolymer e) poly(AAm-co-AN) (FRP30%-50%) and f) poly(AAm-co-AN)-EMP (CRP30%-50%).

In accordance with the glass transition temperature, also the thermoresponsive properties are dependent to the molar mass of the copolymers. As previously mentioned (5.3.2), the UCST is kinetically dominated, which results in a tremendous sensitivity of the cloud point

regarding slight changes of the molar mass. The UCST is based on the intramolecular hydrophilic-hydrophobic balance of the copolymers in aqueous medium. Hydrophobic interactions enhance the polymer-polymer interactions resulting in an increased cloud point. The molar mass of the copolymers enlarges the number of chain segments present in the given solvent volume, which rises the polymer-polymer interaction and the corresponding phase transition temperature. In Figure 24a, these theoretical assumptions are corroborated by the increasing cloud points from 9.5 °C to 34.8 °C with growing molar mass from 2.7 to 28.7 kg·mol⁻¹ and chain length from 50 to 400 repeat units for the copolymer poly(AAm_{0.625}-co-AN_{0.375})-EMP (see appendix, Figure S24a). Below a critical molar mass of $\bar{M}_n=6.1$ kg·mol⁻¹ ($X_n=100$), the relative impact of the hydrophilic chain transfer EMP becomes enormous causing a remarkable drop of the cloud point ($\Delta T_c=13.7$ K).

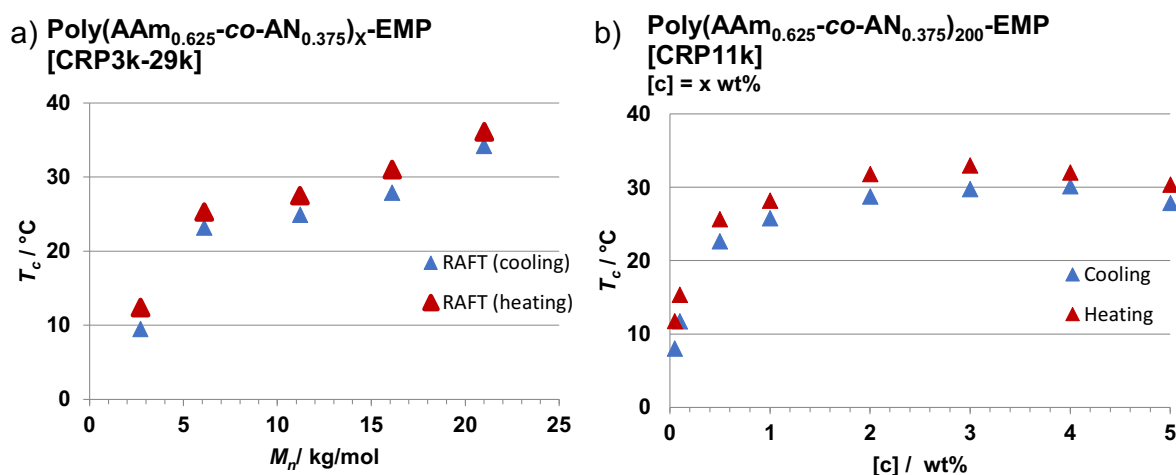


Figure 24: a) Molar mass dependence of the cloud point of the UCST copolymer poly(AAm-co-AN)-EMP (CRP3k-22k) and b) the phase diagram of CRP11k from 0.05-5 wt% aqueous solution.

The copolymer concentration in aqueous solution causes an increase of the absolute molecule number per volume, which impacts dramatically the entropically-driven UCST transition. In Figure 24b, the phase diagram of poly(AAm_{0.625}-co-AN_{0.375})₂₀₀-EMP with $\bar{M}_n=11.2$ kg·mol⁻¹ is presented in ranges of 0.05 to 5.00 wt% and lies in accordance to the theoretical background (5.3.1). The system bears an intense optical UCST behaviour with strong clouding in even very diluted media ([c]=0.05 wt%, see in the appendix, Figure S24), which is contrary to the common LCST example PNIPAAm (exemplary diagram in the appendix on p.244, Figure S39b-c). The cloud point temperature drops tremendously by 17.5 K in the diluted regime between 0.05 and 1.00 wt%, which has to be considered for certain applications. The characteristic UCST of the system is represented with $T_c \sim 33.0$ °C at the concentration of roughly 3 wt%. The variety of applicable concentrations in aqueous solution influenced by the strong non-ionic hydrogen bonding is a quite advantageous benefit for advanced application and represent an unique critical dissolution behaviour for the common UCST systems.

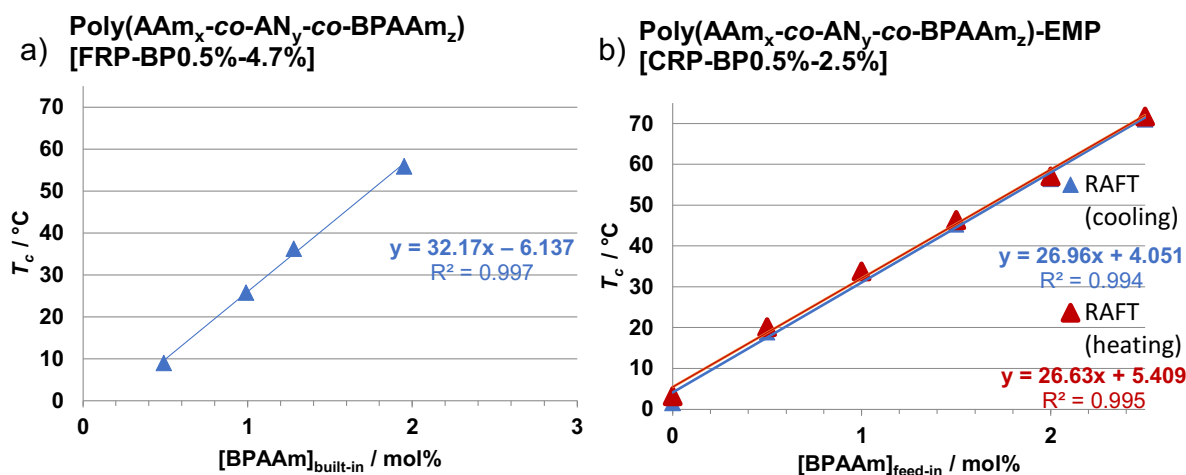


Figure 25: BPAAm fraction dependent correlation of the cloud point of a) free-radical polymerized poly(AAm-co-AN-co-BPAAm) (FRP-BP0.5%-2.5%) and b) the RAFT conjugates poly(AAm-co-AN-co-BPAAm)-EMP (CRP-BP0.5%-2.5%) with AAm/AN (70:30). The heating curves of the FRP products is not plotted due to kinetically-driven inconsistencies of samples with higher cloud points (see Figure S27).

The introduction of a photo-crosslinking unit gives access to the preparation of a thermoresponsive hydrogel bearing tuneable UCST behaviour. For that purpose, *N*-(4-benzoylphenyl)acrylamide (BPAAm) was applied in a mutual terpolymerization with AAm and AN, whose products can be crosslinked subsequently.

The benzophenone side group has a strong hydrophobic effect, so that its influence on the thermoresponsive properties was studied with the molar BPAAm fraction from 0 to 5.0 mol% in FRP and RAFT terpolymers with a fixed compositional ratio AAm/AN=70:30 (as shown in Figure 25). In the case of the FRP products, the cloud points of poly(AAm-co-AN-co-BPAAm) are shifted linearly with a percentual increase per molar BPAAm content to much higher temperatures ($\Delta T_c=32$ K/mol%). Above the molar fraction of [BPAAm]>5 mol% in the reaction feed, the cloud point lies beyond the detectable scale in water as shown in the appendix, Figure S27. The thermoresponsive properties of the RAFT conjugates are slightly less sensitive regarding percentual increase of the photo-crosslinking monomer ($\Delta T_c=27$ K/mol%). Based on the linearization, the theoretical BPAAm content of [BPAAm]=3.6 mol% represents the upper proportion, which enable a measurable cloud point of poly(AAm-co-AN-co-BPAAm)-EMP. If an application requires a higher crosslinking density in combination with an ambient cloud point, the acrylonitrile content in the copolymer could be reduced in the synthesis, to balance the overall hydrophobic effect.

These synthetic deliberations led to the creation of a mathematical prediction method, which enables the adjustment of thermoresponsive properties utilizing a proper monomer feed ratio in the reaction mixture. The extracted linearization of the fraction series of AN (Figure 22) and BPAAm (Figure 25) gives access to a synthetic control of the UCST behaviour of poly(AAm-co-AN-co-BPAAm) in solution. The percental incorporation of the monomer fractions in the macromolecule cause a certain cloud point shift (ΔT_c). In the case of RAFT

products, this percental shifts are represented by the individual slopes of the linearization curves for the monomers AN ($\Delta T_c=3.4$ K/mol%) and BPAAm ($\Delta T_c=27.0$ K/mol%).

The copolymerization between AAm, AN and BPAAm allow an accurate cloud point adjustment with the defined composition of poly(AAm_x-co-AN_y-co-BPAAm_z)₂₀₀-EMP by varying just the monomer fractions. For less defined systems with deviating comonomers (e.g., aminopropyl acrylamide) and molar masses, the synthesis of a comparative sample with defined composition, molar mass and detectable thermoresponsive behaviour is necessary to enable an estimation of the cloud point. The thermoresponse of the comparative sample can be refined to the desired value in a following synthesis step by re-adjusting the copolymer's composition. With increasing complexity of the system, the accuracy of the prediction for the T_c is diminished.

The mathematical prediction of the cloud point is illustrated below in equation 11. The final UCST copolymer, showing the desired cloud point (T_c), is related to the general composition of poly(AAm_{100%-y-z}-co-AN_y-co-BPAAm_z)_{r.u.}-EMP. In comparison to the cloud point of the comparative sample ($T_{c,0}$), each variation of the copolymer composition causes a relative cloud point shift (ΔT_c), which is based on the relative change in the percental fraction of [BPAAm]_{mol%} or [AN]_{mol%}. The desired thermoresponsive properties can be subsequently finetuned, considering even the absolute cloud point shifts originating from non-linear processes like differing copolymer concentration in solution ($\Delta T_{[Copolymer]_{wt\%}}$) (derived from Figure 24b) and the molar mass ($\Delta T_{\bar{M}_n}$) (derived from Figure 24a). These correlations can be used as basis for the additive refinement of the desired T_c under present conditions.

$$T_c = T_{c,0} + \Delta T \frac{^{\circ}C}{mol\% BPAAm} \cdot \Delta[BPAAm]_{mol\%} + \Delta T \frac{^{\circ}C}{mol\% AN} \cdot \Delta[AN]_{mol\%} \pm \Delta T_{\bar{M}_n} \pm \Delta T_{[Copo]_{wt\%}} \quad (11)$$

$$\text{e.g. } T_c = 32 \text{ } ^{\circ}C + 27.0 \frac{^{\circ}C}{mol\%} \% \cdot 1 mol\% - 3.4 \frac{^{\circ}C}{mol\%} \% \cdot 8 mol\% + 0 \text{ } ^{\circ}C + 0 \text{ } ^{\circ}C = 32 \text{ } ^{\circ}C \quad (12)$$

The example above (equation 12) shows the applied procedure for the cloud point refinement of a RAFT copolymer by the help of the comparative sample. The copolymer was supposed to own a similar thermoresponsive behaviour like the initial sample, but combined with a higher BPAAm content, which allows an improved photo-crosslinking behaviour for the subsequent hydrogel formation. The exemplary comparative sample showed the initial composition of poly(AAm_{0.693}-co-AN_{0.297}-co-BPAAm_{0.01})₂₀₀-EMP. The strong hydrophobic impact of the BPAAm fraction onto the cloud point ($\Delta[BPAAm]_0+1$ mol%) is balanced by a reduction of the AN content ($\Delta[AN]_0-8$ mol%), which adjusts the compositional design of the copolymer. Enhancing the fraction of BPAAm, the overall fractions of all repeat units are adjusted, yielding the required composition of poly(AAm_{x+8%=0.773}-co-AN_{y-8%=0.217}-co-BPAAm_{z+1%=0.02})₂₀₀-EMP.

The introduction of further specified functionalities to the macromolecule leads to deviating thermoresponsive behaviours due to undefined hydrophobic/hydrophilic entities. As discussed, such cases demand the procedure of an initial comparative sample preparation. This pathway was successfully applied for the setting of target T_c in copolymerization with functional monomers APTRZAAM (ion sensitive) and APAAM (pDNA binding) (see chapter 11 and 12).

7.3. Summary and Conclusion of Copolymerization of AAm and AN

In the current chapter, the known copolymer system poly(AAm-co-AN) was investigated for the versatile use as a cost-effective product for advanced applications.

In comparison to the literature, the usual laborious purification for the removal of solvent contaminations in the products could be simplified by the synthesis in a reaction mixture of water/dioxane instead of the original solvent DMSO, which avoids a dialysis step due to the much lower boiling point of water. This mixture allowed the successful preparation of copolymers by free radical and RAFT copolymerization using the monomers acrylamide and acrylonitrile. Under these conditions, the RAFT copolymerization was confirmed to produce nearly statistical copolymers by time-dependent investigations of the polymerization parameters using ^1H NMR and GPC measurements, which allowed the simultaneous monitoring of the monomer consumption, conversion, chain growth and intramolecular monomer composition in the copolymer. The chosen conditions provide access to a full control over the RAFT polymerization with its characteristic fast conversion ($t=8$ h, $p=97$ %). The reactions should be performed towards high conversions to receive homogeneous copolymer compositions equal to the initial monomer feed, as the copolymer composition drifted slightly from an AAm-rich to an AN-rich chain in the end during this reaction.

The fraction of the hydrophobic component acrylonitrile in the reaction mixture allows a synthetical adjustment of the phase transition temperatures for the investigated copolymer system due to the reduction of the solvent-polymer interactions in water. The copolymerization with the monomer BPAAm effected an enormous hydrophobic impact on the copolymer chain, which responds with a marked shift of the cloud points to higher temperatures. Such photo-crosslinkable copolymer could be covalently attached to surfaces or transformed to thermoresponsive hydrogels by intramolecular network formation *via* subsequent irradiation with UV light, as it was required for thermally switchable membranes in chapter 9 (p.69).

In this study, the main objective was to improve the handling of this copolymer system with UCST behaviour, by fabricating copolymers with highly controllable thermoresponsive properties. These comprehensive synthetic studies result in an accurate prediction method for the adjustment of desired cloud point temperatures during the copolymerization of AAm, AN and *N*-(4-benzoylphenyl) acrylamide (BPAAm), which tremendously enhance the

applicability of this system. This method was quite accurate for the systems of varying molar compositions conforming to poly(AAm-co-AN) and poly(AAm-co-AN-co-BPAAm). For less defined systems with more uncertainties (such as differing comonomers), the ill-defined phase transition temperature of the initial product could be shifted to the target value by re-adjusting the proper monomer feed composition in the reaction mixture of a second synthesis step.

While the synthesis of FRP products may be affected by several factors such as degassing pathway, reaction tube architecture, heat capacity of the preheated sample holder, the mechanism of RAFT allows to overcome most of the current limitations *via* efficient chain transfer leading to a highly tuneable system for advanced applications.

In that way, the presented system combines the expected benefits and represents a convenient representative for the class of UCST copolymers. The systematic studies helped to overcome the initial weaknesses of the system, yielding to UCST copolymers with very controlled and reproducible thermoresponsive properties, which may open the access to more versatile application fields. In the following, several exemplary applications are discussed dealing with the schizophrenic solution behaviour of double-responsive LCST-UCST block copolymers in chapter 9 (p.69), with iron ion sensitive aggregation behaviour of thermoresponsive macromolecular coordination ligands in chapter 11 (p.91) and thermally switchable non-viral copolymer vectors for gene-delivery, which clearly demonstrates the benefits of the developed poly(AAm-co-AN) copolymers.

8. Photo-Crosslinkable NIPAAm-Based LCST Terpolymers

8.1. Introduction to Photo-crosslinkable PNIPAAm Terpolymers

In the previous chapter, an UCST copolymer system was discussed in detail for subsequent applications presented in this work. The requirements for advanced applications demand the flexible use of thermoresponsive copolymers, utilizing their unique solution behaviours in both temperature directions. While the UCST systems show their phase transition upon cooling, the LCST conjugates perform their demixing process upon heating.⁶²

The most famous representative is poly(NIPAAm), which is a commercially available polymer system being extensively studied and well-described. Its applicability is reasoned with its stable and highly controllable thermoresponsive properties.^{16,17} It exhibits highly robust thermoresponsive properties near the body temperature ($T_c \sim 32^\circ\text{C}$), which make the polymer beneficial for diverse biomedical applications.^{58,74} The thermoresponse is based on hydrogen bonds, which usually causes sharp phase transitions with a high tolerance regarding varied chain lengths and concentrations in solution.⁷⁵ The transition temperature becomes slightly tuneable *via* modifications with hydrophilic or hydrophobic end groups or comonomers.^{13,76,77} In the recent thesis, the thermoresponsive LCST behaviour of linear poly(NIPAAm) has been exploited for double-responsive LCST-UCST block copolymers in chapter 9 and for iron ion sensitive aggregation behaviours of thermoresponsive macromolecular coordination ligands in chapter 11.

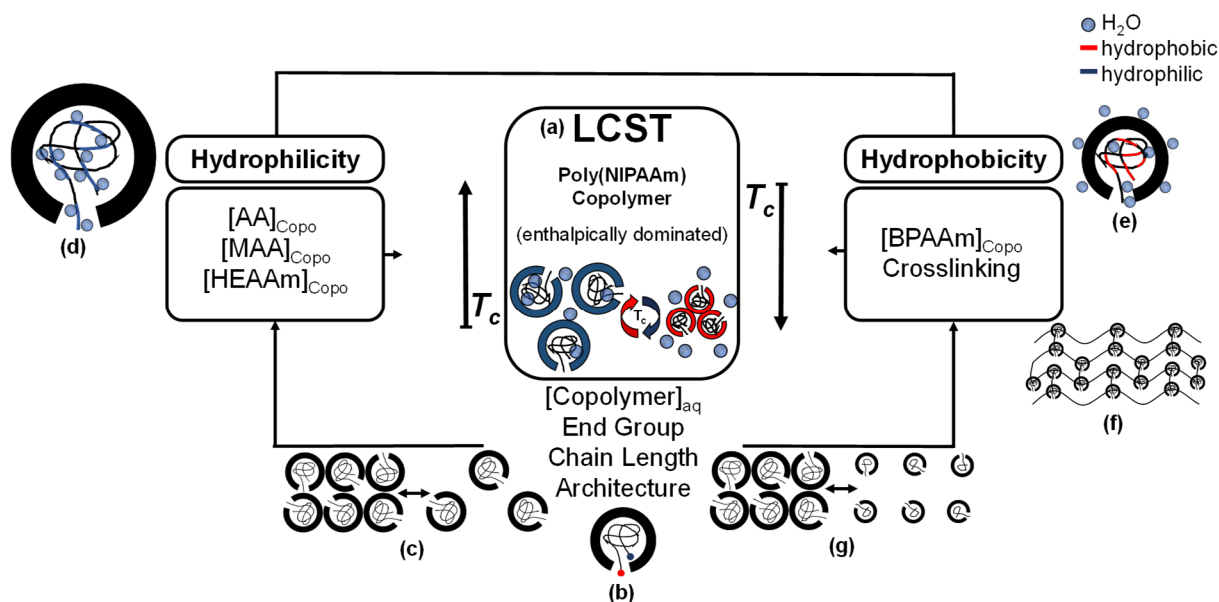


Figure 26: The overview of the investigated parameter influencing the thermoresponsive LCST behaviour of poly(NIPAAm) copolymers.

Generally, hydrogels are formed by hydrophilic polymer networks, which are able to swell under absorption of enormous quantities of water, so that they are used regularly in medical applications as wound dressing¹⁸⁶, tissue engineering¹⁸⁷ and drug delivery systems.¹⁸⁸ To yield thermoresponsive hydrogels, the already reported photo-crosslinkable adhesion

copolymer poly(NIPAAm_{0.94}-co-MAA_{0.05}-co-BPAAm_{0.01}) served as thermoresponsive base, which was modified by copolymerizing with other comonomers in presence of varying chain transfer agents.^{189,190} Here, the transition temperatures of the copolymer system was fine-tuned, considering many parameters such as the molecular balance of hydrophilic/hydrophobic units (Figure 26d-e), the concentration behaviour in solution (Figure 26c), the end group (Figure 26b), the molecular mass (Figure 26g) and copolymer architecture.^{13,17,79-81}

In the scope of the present work, the copolymers were synthesized mainly *via* RAFT copolymerization to obtain highly controlled macromolecular building blocks with defined molar masses. This allowed the homogenous coating of the inner pore walls from diluted copolymer solutions, which was enabled by a controlled diffusion process of suiting coil sizes into the nanoscopic channels of anodized aluminium oxide membranes (AAO), where the linear poly(NIPAAm) copolymers were transformed to copolymer networks upon irradiation with UV light. Their LCST behaviour implemented an external response into the network structure to swell and collapse the hydrogels under uptake and release of water, which was subsequently exploited as thermoresponsive films inside nanoporous membranes to yield thermally switchable nanochannels in chapter 10.

As this LCST system is already well-established, the useful exploitation of poly(NIPAAm) copolymers is just briefly discussed in the present thesis.

8.2. Results and Discussion of Photo-crosslinkable PNIPAAm Terpolymers

8.2.1. Brief Characterization of Poly(NIPAAm) Copolymers Synthesized *via* Free Radical and RAFT Terpolymerization

In this chapter, the thermoresponsive behaviour of photo-crosslinkable LCST copolymers was studied. As the cloud point is undesirably affected by the introduction of hydrophobic BPAAm units, it has to be balanced by an implementation of hydrophilic counterparts. Here, the RAFT homopolymer poly(NIPAAm)-EMP was synthesized as reference, which displayed its characteristic cloud point of $T_c=33.0$ °C. As side note, the experimental cloud points are extracted from the heating cycles of the turbidity measurement.

For the original adhesion copolymer based on poly(NIPAAm_{0.94}-co-MAA_{0.05}-co-BPAAm_{0.01}), the clouding proceeds just *via* gentle drop in the transmittance at $T_c\sim 32$ °C in aqueous solution with an 1 wt% copolymer concentration.¹⁹⁰ In order to enhance the intensity of the clouding for the simplified detection inside the thermally switchable nanopore membranes (in chapter 10), a set of hydrophilic monomers were tested for the copolymerization with NIPAAm as such acrylic acid, methacrylic acid and hydroxyethyl acrylamide.

The photo-crosslinking monomer BPAAm was incorporated efficiently in all copolymers and is not discussed further. As reference, the classical adhesion copolymer (FRP_MAA) was repeated successfully in a free radical terpolymerization with the monomer ratio

[NIPAAm]/[MAA]/[BPAAm]=94:4:1 in 1,4-dioxane using AIBN at 70 °C. The GPC elugram shows a large molar mass with $\bar{M}_n=138 \text{ kg}\cdot\text{mol}^{-1}$ and a broad unimodal distribution with $\bar{D}=2.23$, typically for a free radical copolymerization. The product was obtained with satisfying 66% yield and showed a cloud point in 1 wt% aqueous solution at 33.6 °C.

The RAFT copolymerizations were performed successfully, varying either the hydrophilic monomer component such as AA, MAA or HEAAm or the type of chain transfer agent (BIT, DMP or DMP-EA). The reactions were performed in 1,4-dioxane using the thermal initiator AIBN at 70 °C with a constant ratio of [monomers]/[CTA]/[initiator]=100:1:0.1, if not specified otherwise. The sample code (CRP-_) denotes the interchanged parameter in the reaction mixture.

The molar masses and compositions of the copolymers were investigated *via* ^1H NMR measurement in CDCl_3 , which match sufficiently with the theoretical values. The elugrams show unimodal molar mass distributions in ranges of $\bar{M}_n=10.3\text{-}26.1 \text{ kg}\cdot\text{mol}^{-1}$ with a narrow dispersity, revealing efficient RAFT conditions ($\bar{D}=1.10\text{-}1.26$). The cloud points, measured in 1 wt% aqueous solution, lie between 25.3 °C and 33.6 °C. Satisfying yields between 61 and 77% were obtained for all copolymers.

The spectra of the individual copolymers are collected in the appendix, from Figure S30 to Figure S48 (p.239-249). The GPC elugrams are exemplary shown in the appendix, Figure S29 (p.237). The corresponding synthetic and physical data are shown in subchapter 14.3.4 (p.175) and the results are summarized in Table S9 (p.238). The thermoresponsive properties of all copolymers are discussed separately in detail in the following chapter 8.2.2

8.2.2. Thermoresponsive Properties of Photo-Crosslinkable Poly(NIPAAm) Terpolymers

The desired application as thermoresponsive filling inside thermally switchable nanopore membranes (discussed in chapter 10), requires a locally defined crosslinking mechanism inside the operation site. Therefore, the original adhesion copolymer poly(NIPAAm-*co*-MAA-*co*-BPAAm) (FRP-MAA) was employed and modified.

Dissolved in water, the linear copolymer shows highly reproducible thermoresponsive properties being constant for many cycles (in the appendix, Figure S33). In comparison to the homopolymer, the clouding of the copolymer solution is substantially attenuated by the incorporation of the polar acrylic acid side groups, which may hamper the sensitive detection of the thermoresponsive properties inside the pores.

During the filling process of the anodized aluminium oxide membranes, the proper diffusion inside the pores was ensured following the RAFT mechanism, which controls the molar mass and, thus, the coiling size of the copolymers in solution. The RAFT product (CRP-MAA) responded to the reduced molar mass with a slight shift of the cloud point to lower temperatures ($T_c=28.5 \text{ °C}$) and led to a more intense clouding down to 20% transmission.

The concentration dependency of the cloud point and the corresponding phase diagram is shown in range of $[c]=0.1$ to 5.0 wt% in the appendix, Figure S39 (p.244). In water, lower concentrations ($[c]<1.0$ wt%) lead to a decreased clouding intensity of the solution, which stays in contrast to the previously discussed UCST system. The estimated specific value of LCST lies at 25.0 °C near 4 wt% concentration, which is corroborated additionally by the T_1/T_2 NMR studies, indicating the binodal and spinodal mixing behaviours (in the appendix, p.245, Figure S40).

The exchange of the component MAA by the even more hydrophilic monomer acrylic acid resulted in a neglectable raise of the cloud point ($T_c=29.1$ °C) with a comparable absorption. The copolymerization with HEAAm (CRP-HEAAm) induced a comparable thermoresponsive behaviour ($T_c=27.7$ °C), but displayed a complete clouding of the solutions ($T_\lambda=0$) in comparison to the previous examples. Here, the cloud points were raised slightly with increasing molar fraction of HEAAm ($T_c=28.8$ °C) and molar mass of the copolymer ($T_c=30.6$ °C). All other synthesized copolymers showed similar thermoresponsive properties with similar dissolution behaviours in water.

8.3. Conclusion and Outlook Photo-Crosslinkable PNIPAAm Copolymers

All synthesized copolymers were suitable for the filling of the nanopore membranes. The RAFT copolymerizations of NIPAAm with the photo-crosslinker BPAAm and other comonomers were successful for all tested CTAs. The reached temperature variations were insignificant for the employed fraction ranges of the hydrophilic components. In the synthesis of the photo-crosslinkable copolymers, the monomer BPAAm applies an enormous hydrophobic effect on the macromolecular chain in solution, which has to be balanced by copolymerization with hydrophilic comonomers to yield appropriate phase transition temperatures.

When much increasing cloud points are required, higher molar contents of the hydrophilic components have to be considered with $[M]>10$ mol%. The upper limit of applicable comonomer quantities in the copolymers is restricted by the experimental fraction of NIPAAm units, which is necessary to maintain the thermoresponsive behaviour of in copolymer chain in solution. With special regards to the monomer series, the choice of HEAAm featured the most beneficial copolymerization properties, leading to an improved tuning of the clouding temperatures accompanied by highly intensive phase transitions.

To form stable hydrogels, the synthesis of larger molecules is recommended for prospective applications, which could fulfil the required absolute number of BPAAm units per chain, necessary for a proper crosslinking process of stable films, without lowering the LCST transition too much due to higher fractions of hydrophobic monomer in the feed.

Here, particularly the RAFT representatives CRP-AA-DMP-EA and CRP-HEAAm (in congruence Table S9) were applied in chapter 10 (p.81) in comparison to the reference

copolymer FRP-MAA, while the basic LCST behaviour of linear poly(NIPAAm) has been also utilized in the following for double-responsive LCST-UCST block copolymers in chapter 9 (p.69) and for iron ion sensitive aggregation behaviour of thermoresponsive macromolecular coordination ligands in chapter 11 (p.91).

9. Interdependent Switching States of Double Thermoresponsive LCST-UCST Block Copolymers in Aqueous Solution

9.1. Introduction to LCST-UCST Block Copolymers

The development of intelligent materials requires continuous improvements in the field of thermoresponsive polymer systems bearing distinct and controllable dissolution behaviours. The temperature-induced response provoke dynamic variations of the aggregation magnitudes in aqueous media.^{12,62,98} The previous chapters focused on copolymer systems possessing either LCST or UCST behaviour. When those two thermoresponsive properties are combined in an unique dual responsive system, advanced systems with more complex solution behaviours can be yielded. An common synthesis of defined block copolymers exploits the effective chain extension pathway *via* stepwise RAFT block copolymerization.⁹³ Such complex solution behaviours are demonstrated for already published block copolymer systems such as poly[(NIPAAm)-*block*-(SPP)]^{95,191}, poly[(PDMAEMA)-*block*-(PSBMA)]¹⁰², poly[(PEO)-*block*-(NAGA)]¹⁹², poly[(AAM-*co*-AN)-*block*-(PDMAEMA)]¹⁰⁷ or poly[(AAM-*co*-AN)-*block*-(PEG)]⁹⁸. Other block copolymers exhibit even lower cytotoxicity and seem to be promising candidates for advanced drug release applications for specialized conditions.⁹⁸ Such LCST-UCST block copolymers usually feature an inside out core-corona inversion with an unimolecular dissolution process in between the critical solution temperatures upon slight thermal variations (insoluble-soluble-insoluble).¹⁰² While the soluble phase is caused by a double hydrophilic chain state, the insoluble phases are dominated by hydrophobic microdomains, which produces an amphiphilic character of the block copolymer in analogy to macrosurfactants.¹⁹³ Hereby, the hydrophobic chain segments form the inner core of the aggregates surrounded by the hydrophilic corona of the hydrophilic conjugates. This switchable and complex aggregation behaviour is influenced by the block composition and length, the molar mass, salts and the pH.¹⁰²

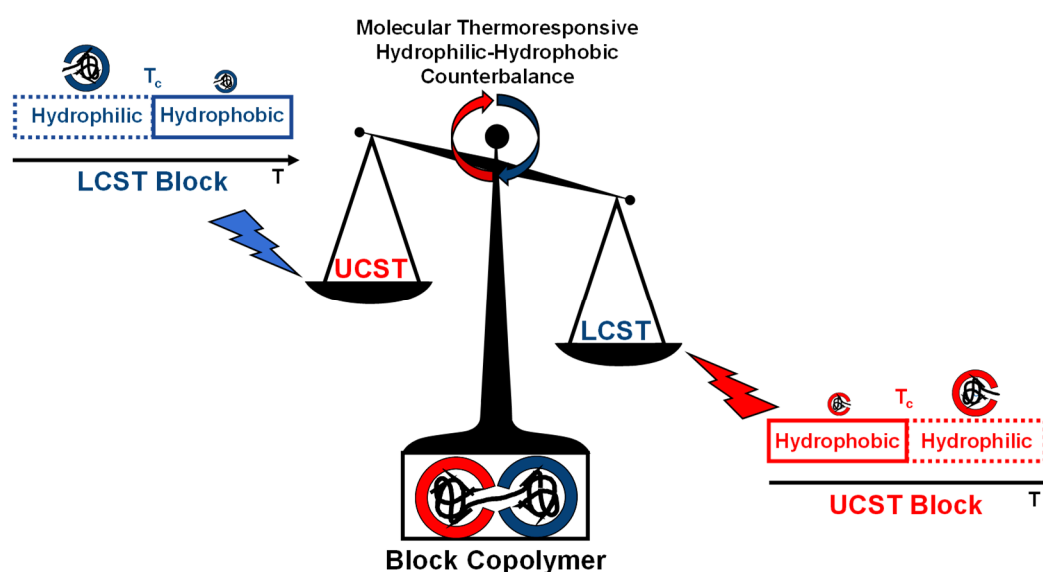


Figure 27: The individual thermoresponsive transitions of each block tune the delicate hydrophilic-hydrophobic balance of the entire macromolecule causing a temperature related interdependence of LCST-UCST switching states in double thermoresponsive block copolymers.

LCST-UCST block copolymers exhibit a double thermoresponsiveness originating from the covalently linked blocks. In the field of thermoresponsive block copolymers, the occurring events of LCST and UCST are often discussed independently of each other.¹⁹⁴ For mono-thermoresponsive systems, these phase transitions are commonly investigated with respect to induced hydrophilic/hydrophobic effects, which are introduced by single moieties and comonomers.^{59,79} In double thermoresponsive block copolymers, the analysis is supposed to become more complex due to the block-wise phase transition from hydrophilic to hydrophobic and *vice versa*, inducing an intramolecular influence on the neighbouring block, which results in a shift of the original phase transition temperature of the chain segments (in accordance to an end group). Such cross-influence is briefly discussed for the solution behaviour of poly[(diethylene glycol ethyl ether acrylate)-*block*-(methyl acrylate)] copolymers in water/ethanol by Can et. al.¹⁰⁸ While thermoresponsiveness in previously reported systems is explained on basis of the simple behaviour of the homopolymer chain, here the analysis of the complex interdependent phase transitions also includes the intramolecular influence between both thermoresponsive blocks and their particular solvation states, which are triggered by the coil-to-globule transitions of each block and thus their thermal history. This effect causes an interdependent interference of occupied LCST and UCST chain states in aqueous media so that a cooperative dissolution behaviour is maintained for double thermoresponsive block copolymers.

In the present chapter, the complex aggregation behaviours of the novel block copolymer system poly[(AAm-*co*-AN)-*block*-(NIPAAm)]-EMP, providing constant LCST but tuneable UCST properties, was investigated with special focus on the interdependent switching states.

9.2. Results and Discussion of LCST-UCST Block Copolymers

9.2.1. Characterization of Poly[(AAm-*co*-AN)-*block*-(NIPAAm)]-EMP Block Copolymers Synthesized *via* MacroCTA Chain Extension

To obtain double thermoresponsive block polymers, the synthetic chain extension pathway *via* sequential RAFT copolymerization was utilized as denoted in Figure 28. Here, the UCST block was employed as macroCTA (pathway 1) to allow an initial characterization of the tuneable starting block, before the product was realized by the block copolymerization with NIPAAm. Thus, the thermoresponsive properties between of the starting block and product could be compared in order to abstract the novelty of the solution behaviour for the block copolymers in aqueous media.

For the fabrication of such block copolymers, the synthetic pathway 1 was chosen, as purification along pathway 2 was hampered. Here, the dissolution behaviours of the side product poly(AAm-*co*-AN) and product did not enable a complete separation *via* precipitation. The received solvation behaviours are characterized with respect to block copolymers with equal molecular block contributions with $X_n[\text{UCST}] = X_n[\text{LCST}]$ dependent to varying phase

transition temperatures of the UCST blocks, which could be adjusted by acrylonitrile fractions in the macroCTA.

The thermoresponsive behaviours of the synthesized poly[(AAm_x-co-AN_y)₂₀₀-block-(NIPAAm)₂₀₀]-EMP block copolymers were studied dependent to the composition of the UCST precursors with differing cloud points. For the block synthesis, the chain extension pathway *via* two-step RAFT block copolymerization was employed, utilizing the tuneable precursor poly(AAm-co-AN)-EMP as macroCTA. The initial cloud point of the starting block was tuned by the molar acrylonitrile fraction in the reaction mixture feed, synthesized under RAFT conditions in accordance with chapter 7 (p.43).

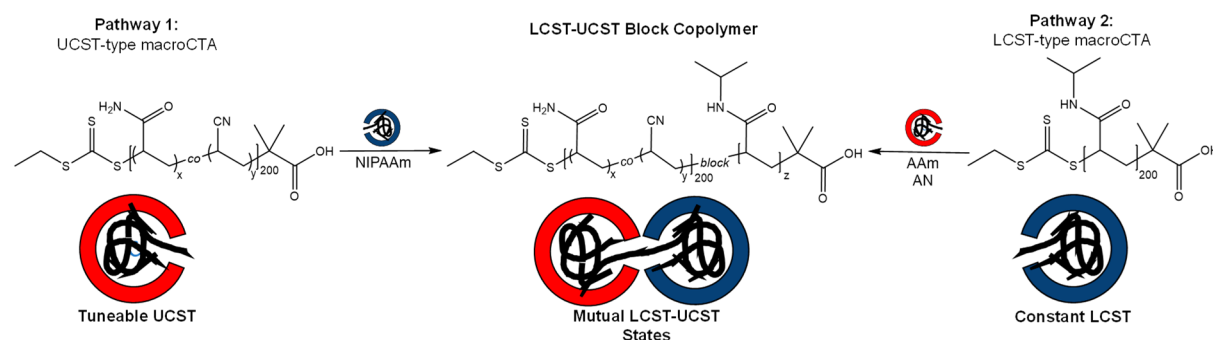


Figure 28: The two synthetic chain extension pathways for the preparation of LCST-UCST block copolymers *via* RAFT copolymerization utilizing a macroCTA species.

The obtained macroCTA was purified to prohibit side reactions in the subsequent block copolymerization. As the polymerizations of both individual systems can be performed in presence of the trithiocarbonates, the chain transfer agent EMP was used. The reaction was performed in the reaction mixture of water/dioxane (60:40) with AIPC as initiator at 40 °C to avoid potential LCST transitions under the given synthetical conditions. A fixed feed ratio NIPAAm/macroCTA/initiator=200:1:0.2 was employed for all samples. The precipitation in a fortyfold excess of EtOAc (100 mL) enabled the uptake of the water from the reaction mixture and allowed the selective isolation of the product from other potential NIPAAm species.

The comparative ¹H NMR spectra of both neat LCST and UCST systems and the double responsive product confirms the formation of the desired block copolymer. The product shows all cooperative characteristics of both individual blocks such as the Z-group of the macroCTA precursor and the isopropyl group of NIPAAm unit as noted with “B” and “D” in the appendix, Figure S49c (p.250). The length of the UCST block was calculated in accordance to the equation in the appendix, chapter 16.3.2 (p.226), while the LCST equivalent is determined by the number of isopropyl units in the final block copolymer.

The GPC elugrams show a substantial growth of the molar mass compared to their macroCTA precursors. The unimodal mass distributions between $\bar{M}_n=31.3$ and 43.9 kg·mol⁻¹ exhibit narrow dispersities ($\bar{D}=1.15$ -1.44) and match with their corresponding theoretical values, which corroborates the formation of block copolymers under controlled conditions *via*

the mechanism of RAFT. The GPC elugrams of product and macroCTA could not be recorded in the same eluent due to fundamental solubility variations of the polymer systems, so that exclusively the magnitudes of molar masses are compared. The block copolymers were obtained in good yields between 69% to 87%.

Successful block copolymerizations altered the solubilities and the thermoresponsive behaviours of products. In dependence of the composition of the UCST block and correlating phase transition temperature, the block copolymers vary their solvation behaviour in aqueous solution dramatically. The thermoresponsive behaviour of all block copolymers are discussed separately in detail in the following chapter 9.2.2.

All spectra, GPC elugrams and DSC traces are exemplary shown in Figure 29 (p.75) and in the appendix, Figure S49 (p.250), Figure S50 (p.251), Figure S51 (p.252) and Figure S52 (p.253). The corresponding synthetic and physical data are summarized in Table 18 (p.180) and in the appendix, Table S10 (p.254).

9.2.2. Complex Double Thermoresponsive Behaviour of LCST-UCST Block Copolymers in Water with Varying UCST

Advanced applications for thermoresponsive polymer systems require convenient fabrication pathways and a high control of their responses in solution. As synthetic parameters like composition, block chain lengths and end group could be controlled previously *via* the mechanism of RAFT, the thermoresponsiveness is investigated for potential applications like for example drug release systems. The present block copolymer system combines the properties of LCST and UCST on molecular level. Both transition types were individually introduced in the previous chapters 7 (p.43) and 8 (p.63) referred to the examples of poly(AAm-co-AN) and poly(NIPAAm). This chapter deals with the mutual interplay of both transitions in a cooperative system, which possesses fixed LCST, but tuneable UCST properties.

Generally, such thermoresponsive transitions are accompanied by molecular changes in hydrophilicity, which render the solvation forces inducing either predominantly polymer-solvent or polymer-polymer interactions. Due to the covalent linkage between LCST and UCST blocks, such switching from hydrophilic to hydrophobic and *vice versa* has to affect the thermal response of the neighbouring blocks in correspondence to the published knowledge about the analysis of thermoresponsive homopolymers by the simple picture of a single chain. In consequence, both thermoresponsive switching states of both blocks (LCST and UCST) are interdependent and interfere with each other, and thus have to be taken into account simultaneously. The coil-to-globule transitions in such LCST-UCST block copolymers can provoke four hypothetical coiling states offering either double hydrophilic, double hydrophobic or the two amphiphilic states with one block hydrophilic and the other hydrophobic. Those states are analysed *via* turbidity measurement as function of the

temperature dependent transmission value. Here, the complex thermoresponsive property of block copolymers are impacted by both the molecular phase transition in a single block on the single chain level and the optical transitions as result of the ensemble structure formation in colloidal aggregates from multiple (individual) chains. Thus, the discussion of the complex solvation behaviours encompasses both dimensional levels for analysis.

In Figure 29, the turbidity curves of the block copolymer series are presented with respect to the tuneable UCST block with varying composition from low to high clouding temperatures in ranges of 2 °C to 79 °C, which is synthetically defined by the molar fraction of acrylonitrile from 30 to 55 mol% (as denoted in the sample code). The original cloud points of the individual blocks are indicated in the turbidity spectra as triangles for the assumed, constant LCST (blue) and pre-characterized UCST block (red) at their specific temperature values. The chain states are sketched by cartoons illustrating the coil expansion or shrinkage dependent on the single chain picture. The heating and cooling curves are accentuated by arrows clarifying the temperature direction of the measurement. The presented turbidity curves demonstrated different curve shapes, which were grouped and discussed together in detail. In accordance to the published knowledge, the LCST transition is anticipated to take place at a constant temperature of 32-34 °C, while the UCST equivalent was characterized by the cloud point from the macroCTA precursor.¹⁹⁵ The measurements were performed in an 1 wt% aqueous solution. The cuvette surface was flushed in the spectrometer with nitrogen and checked visually at low temperature to ensure a clean cuvette (fogging).

The optical data were supplemented by thermal properties determined *via* modulated differential scanning calorimetry, which allow the differentiation between both phase transition types. As discussed in chapter 5.3.2 (p.11), the process of UCST produces weak kinetic signals, while the LCST transition is indicated by distinct enthalpic changes. In the appendix, Figure S51 (p.252), the MDSC traces of the synthesized block copolymers show a significant first order transition in the non-reversing component around the expected LCST-typed transitions. The reference homopolymer of poly(NIPAAm)-DMP (Figure S51f) confirms the matching of the turbidity curve with the data from the non-reversing component in the MDSC traces. These thermal data were used to refer the occurring block copolymers transitions to their thermoresponsive origin. All samples showed at least one transition, which can be attributed to the process of LCST. If two phase transitions were existent, the LCST analogous occurred consistently at higher temperature, so that the MDSC data are not specified further.

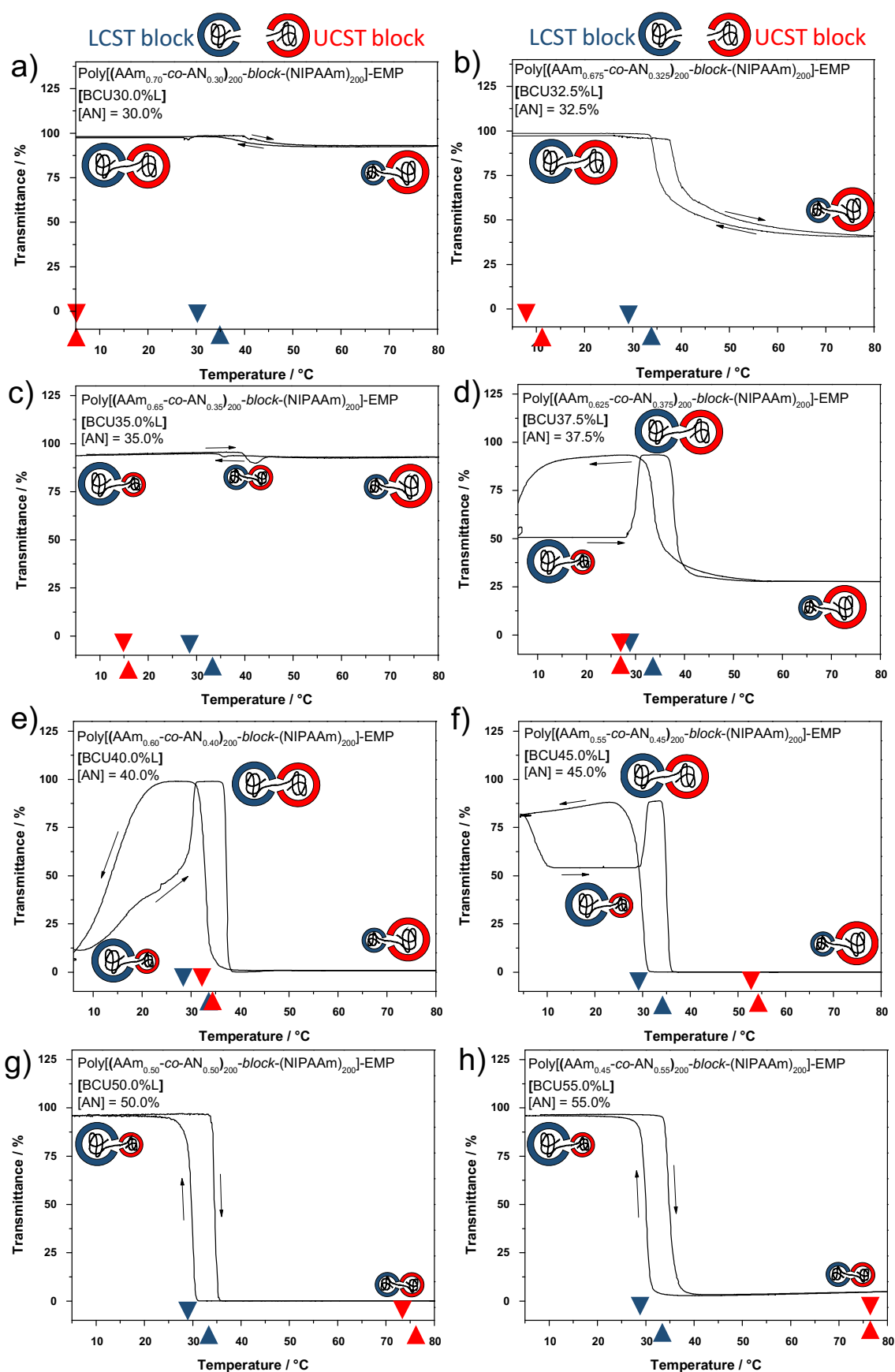


Figure 29: The cloud point determination of the double thermoresponsive LCST-UCST-block copolymers poly[(AAm-co-AN)₂₀₀-block-(NIPAAm)₂₀₀]-EMP with varied molar fraction of AAm/AN a) (70.0:30.0), b) (67.5:32.5), c) (65.0:35.0), d) (62.5:37.5), e) (60.0:40.0), f) (55.0:45.0), g) (50.0:50.0) and h) (45.0:55.0) in the starting block, recorded from 1.0 wt% aqueous solution (at $v=650$ nm). The triangles indicate the cloud points of the heating (\blacktriangle) and cooling (\blacktriangledown) cycles of the individual starting blocks. The copolymer symbols illustrate the anticipated solvation state of the single chains and not the resulting aggregate structure.

In Figure 29a-b, a single transition with LCST-shape is detected for the samples between 30.0 to 32.5 mol% AN in the UCST chain resulting in an initial cloud point of 1.6 to 8.7 °C. Thus, the clouding temperature of the pure UCST block is much lower than the LCST conjugate (UCST \ll LCST). The hydrated poly(NIPAAm) block introduces a marked hydrophilic effect on the total block copolymer, which forces the UCST transition below the measurable temperature range of 0 °C.

At low temperatures, the block copolymer occupies a dual hydrophilic solvation state, which shifts the LCST transition in the heating cycle to higher temperature. Above the LCST cloud point, the corresponding block collapses and produces an amphiphilic macromolecule, leading to the formation of micelles with associated hydrophobic segments in the core and a surrounding corona of a hydrophilic tails. With increasing AN content, the hydrophobicity of the block copolymers rises and enhances the optical intensity of their clouding. The transmission is reduced by the very defined formation of micellar scattering objects of larger aggregation magnitudes ($D_h=57$ and 332 nm), which are characterized by an unimodal decay of the correlation times (as shown in the appendix, Figure S52a-b, p.253). The clear solution at 20 °C is characterized by multiple scattering species between 9 and 487 nm. As the signal intensity depends tremendously on the aggregation size ($I\sim D_h^6$), the smallest aggregates with hydrodynamic diameters between $D_h=9$ to 11 nm are underrepresented and lead to a low scattering intensity, so that the solution is rather clear in the turbidity measurement. The hydrophobic effect of higher AN content lowered the interaction with the solvent water and, thus, the LCST transition temperature from 39.5 °C to 36.1 °C.

The sample with an acrylonitrile content of [AN]=35.0 mol% in the UCST block showed two weak transitions with LCST and UCST behaviour (Figure 29c). Compared to the previous samples, the difference between both solution temperatures is reduced (UCST $<$ LCST). The increased overall chain hydrophobicity leads to an interdependent interference between both blocks, which causes a nearly synchronized sequence of both transitions between 35 and 37 °C. At low temperatures, the amphiphilic chain with solvated LCST block and collapsed UCST chain induces the formation of micellar aggregation. The intramolecular counterbalance of hydrophobic and hydrophilic moieties lifts the UCST transition temperature, but concurrently lowers the LCST equivalent, which results in a tight time window between both molecular transitions. Between both phase transitions ($T\sim 36$ °C), the di-hydrophobic block copolymers start aggregating for a short time and form larger scattering sizes, which slightly reduces the transmittance. Then, the sudden solvation of the UCST chain induces micellar aggregates with poly(NIPAAm) chains in the core.

In Figure 29d-e, the turbidity curves for the block copolymers with 37.5 and 40.0 mol% AN in the UCST block (with the original cloud point of $T_{c,CTA}=28.0$ and 32.3 °C) display two intense transitions owning both LCST- and UCST-shape. In these cases, the initial clouding

temperature of the pure UCST block is equivalent to the LCST analogous (UCST~LCST). As shown for the cooling cycle, the UCST chain becomes more hydrophobic with increasing AN content, which leads to a lowering of the LCST transition temperature from 34.2 to 32.9 °C and to higher UCST analogues from 7.5 to 15.6 °C in the block copolymers.

At low temperatures, the UCST block is dehydrated, which generates an amphiphilic chain character forming micellar aggregates. Upon heating above the UCST transition, the whole chain is well-solvated and produces a complete dissolution of the aggregates. Due to further heating, the LCST segment turns hydrophobic, the inverse of the primary amphiphilic chain state is developed with collapsed LCST and swollen UCST segments. In DLS, the collapse of the LCST block leads to very defined aggregates. The contrary schizophrenic chain behaviour with collapsed UCST block produces at low temperature ($T=20$ °C) less stabilized aggregates composed of two main species (in the appendix, Figure S52c-d, p.253). This hydrophilicity of the hydrated LCST block improves the solvation of the ensemble aggregate species, which leads in average to smaller scattering sizes ($D_h=11-646$ nm) than for the contrary chain behaviour, resulting in higher transmission. Here, the chain state at higher temperatures generates very defined micellar scattering objects ($D_h=305$ and 634 nm), which is expressed in the transmittance difference between both contrary schizophrenic states ($\Delta T_\lambda \sim 12-25$ %).

In dependence of the thermal history, the different shapes of the heating and cooling curves demonstrate the existence of interdependent states of the single chains. The temperature direction of the measurement plays a significant role for the transition temperatures of the thermoresponsive block copolymers. The molecular solvation state of one block affects the transition temperature of the neighbouring block and induces varying clouding of the polymer solution by forming ensemble aggregates. In the cooling cycle at high temperatures, the dehydrated LCST block turns during its transition hydrophilic and induces a hydrophilic effect onto the sensitive entropy-driven poly(AAm-co-AN) block, which responds with a tremendous drop of its transition temperature. While heating, the UCST block is dehydrated and becomes hydrophilic upon its globule-to-coil transition. The double hydrophilic solvation state of the block copolymer enhances the polymer-solvent interaction and shifts the LCST transition to higher temperatures.

In Figure 29f, the turbidity curve of the product with 45 mol% AN in the UCST chain and an original clouding point of 52.1 °C exhibits a divergent shape for the heating and cooling cycle. The heating cycle shows two transitions plus one additional kinetic relaxation process in the measurable temperature range, while the cooling cycle displays just a single one. For the first time, the original cloud point of UCST is higher than the LCST analogous (UCST>LCST). The risen AN content in the UCST block enhances the hydrophobic impact and leads to a very fragile counterbalance between hydrophobic and hydrophilic interactions.

In the heating cycle at low temperatures, the hydrated poly(NIPAAm) tail reduces the clouding temperature of the UCST conjugate. The amphiphilic solvation state with collapsed UCST block forms scattering objects of medium aggregation sizes leading to a partial clouding of the solution. The increasing hydrophobicity of the UCST block shifts the LCST transition to lower temperatures (compared to the previous BCU40.0%L) so that the temperature window for a double hydrophilic chain with an optical clear solution is narrowed to $\Delta T \sim 4$ K. During further heating, the LCST block collapses molecularly and results in a schizophrenic chain character, whose ensemble transition yields a complete optical clouding due to larger aggregation dimensions.

Upon cooling from this temperature, a single LCST-typed transition takes place at molecular level by expansion of the poly(NIPAAm) block, which results in smaller scattering objects due to the double hydrophilic solvation state of the block copolymers (at low temperature), leading to a clear solution. The strong hydrophilic impact and the kinetic hindrance of the aggregation state disturb micellar arrangements by an increase of the solvent-polymer interaction, which forces the cloud point of the UCST chain below the measurable detection range of 0 °C.

The differing curve shapes of the heating and cooling cycle reinforce the vast sensitivity of the phase transition to external conditions, which is accompanied by a metastable kinetic relaxation process in the heating from the completely hydrated chain state (mentioned above) to the amphiphilic chain behaviour with a dehydrated UCST chain at low temperatures ($T = 10$ °C). In context of other internal researches on poly(sulfobetaine-*block*-NIPAAm) block copolymers (Dissertation, Cleiton Kunzler), this defined shape of the third transition in the heating cycle may also suggest a doubled re-entrance mechanism, dealing with the crossing of two coexisting insolubility gaps in closed-loop shaped phase transition diagrams, which could explain the occurrence of three visible phase transition for a double responsive system of UCST-LCST block copolymers. As the provided data set of this research could not clearly confirm this hypothesis, they are just discussed on the denoted basis of single and ensembled chain pictures. For the shown turbidity curves, the corresponding DLS displays very defined aggregation species for all temperature steps, which illustrate these data as snapshot of the equilibrated temperatures and not of the dynamic solvation system. Here, the scattering sizes may fit to the solution behaviour of the block copolymers from the heating cycle, as only large and defined object dimensions of both schizophrenic chain behaviours are monitored with collapsed UCST and hydrated LCST block or *vice versa*, but not of the double hydrophilic chain state as visible in the appendix, Figure S52e, p.253.

The block copolymers in Figure 29g-h own an acrylonitrile content of $[AN] \geq 50$ mol% ($T_{c,CTA} = 72.5-78.8$ °C). The clouding temperature of the pure UCST block is much higher than

the LCST conjugate (UCST \gg LCST). The turbidity curves possess an identical shape as shown for the opposite analogous with lowest AN fraction. The UCST block exhibits an enormous hydrophobicity, so that its transition occurs above the measurable temperature range, so that exclusively the LCST-typed transition is visible (like for A and B). At low temperatures, the high UCST transition temperature generates an amphiphilic chain character with hydrophobic UCST segment. On the molecular view, the block copolymer completely dehydrates upon the heating due to the additional collapse of the LCST block. In the ensemble picture, the initial objects of small scattering dimensions provoke a slight clouding of the solution in the schizophrenic state, while the colloidal phase separation occurs as consequence of the strong chain attraction of both hydrophobic segments.

The present subchapter confirmed the hypothetical existence of interdependent switching states on molecular and colloidal level for the present dual-thermoresponsive block copolymer system bearing LCST and UCST behaviours. The cooperative interferences between both covalently linked blocks in poly[(AAm-co-AN)-*block*-(NIPAAm)]-EMP were corroborated by the optical thermoresponsive clouding underpinned by the thermal properties from MDSC traces and the aggregational study *via* DLS.

9.3. Summary and Conclusion of LCST-UCST Block Copolymers

In the current chapter, the successful preparation of new dual-thermoresponsive LCST-UCST block copolymers was described, utilizing the sequential RAFT copolymerization pathway. Complex aggregation behaviours of poly[(AAm-co-AN)-*block*-(NIPAAm)]-EMP block copolymers with equimolar block chain length was studied for a set of copolymers with constant LCST and tuneable UCST behaviour. In comparison to the literature, the thermoresponsiveness of LCST-UCST block polymers was analysed on the basis of i) the molecular level from a single chain by occurrence of coil-to-globule transitions and ii) the ensemble view on aggregating (individual) macromolecules. For the present system, the thermal switching of one molecular block influenced the transition temperature of the neighbouring segment, inducing an aggregation process of multiple chains, which could be monitored as function of the optical clouding in aqueous solution.

Different thermoresponsive behaviours could be induced by the variation of the acrylonitrile fraction in the UCST block of poly(AAm-co-AN). Dependent on the temperature and the intramolecular hydrophilic-hydrophobic balance, the investigated system could occupy in aqueous solution four different chain solvation states, such as double hydrophilic, double hydrophobic and two additional amphiphilic chain behaviours with dehydrated LCST and solvated UCST segments or *vice versa*. The thermal switching of block copolymers confirmed the molecular existence of interdependent solvation states between both distinct thermoresponsive blocks (LCST and UCST), whose responses entailed varying complex aggregation behaviours on the colloidal observation level.

The block copolymers with a content of 37.5 to 45.0 mol% AN in the UCST block showed a dual-thermoresponsive behaviour featuring both transitions of LCST and UCST. The dissolution behaviour was significantly impacted by the temperature direction of the measurement (heating/cooling), confirming the interdependence of solvation states through a mutual hydrophilic/hydrophobic influence on the phase transition temperatures of neighbouring block. The optical data were underpinned by the thermal and aggregational solution behaviours determined *via* MDSC and DLS measurements. In prospective works, the distinct molecular orientation of the single chains in the overall aggregates could be further investigated by *via* T_1/T_2 NMR or two-time correlated small angle neutron scattering studies (TTC-SANS).

This unique solution behaviour can be potentially employed for advanced applications, which require more defined clouding temperature windows in solution. The narrow solubility ranges near the body temperature could attract attention for the utilization in advanced drug release systems. Another promising application could be the research field of gene delivery, as chapter 12 (p.127) already attests a high viability and a marked gene transfer rate for pure poly(AAm-co-AN)-EMP being copolymerized with a pDNA binding monomer. Such advanced applications require a comprehensive control over the synthetic parameter and solution temperature.

Thus, prospective researches have to investigate the influence of further parameters such as the total chain length, ratio between the LCST and UCST blocks, concentration in solution, pH, salts or physiological conditions to evaluate certain restrictions. On this basis, the implementations of other functionalities could be realized by the copolymerization with other comonomers.

10. Thermoresponsive Switching States in Nanopore Membranes

10.1. Introduction to Thermoresponsive Switching States in Nanopores

The continuous progress in the vast field of smart materials leads to a fast development of novel thermoresponsive polymer systems. Their application in advanced objectives requires a versatile and commercially available polymer system, allowing a comprehensive control over the synthetic and thermoresponsive properties. The polymer responds to the external trigger of temperature variation, which can be exploited to mimic natural materials and processes.¹⁰³ The temperature represents a non-invasive remote control to artificially switch the most important physicochemical properties of the thermoresponsive polymer such as hydrophilicity^{51,52}, solubility⁴⁷, E-modulus⁴⁸, optical density^{49,50}, aggregation sizes¹⁹⁶ or specific volume of polymer films⁵³. This unique behavior attracts a special attention for the fabrication of smart composite materials.¹⁹⁷ Upon slight temperature variations, the thermoresponsive polymer coatings enable the tuning of the surface properties from hydrophilic to hydrophobic or *vice versa*.^{51,52} An additional copolymerization with the monomer *N*-(4-benzoylphenyl) acrylamide (BPAAm) provided access to the fabrication of photo-crosslinkable copolymers, which could be covalently attached to surfaces such as AAO walls and transformed to hydrogels by intramolecular network formation *via* subsequent irradiation with UV light.^{198,199} Such polymer systems can further functionalize porous materials for the preparation of intelligent membranes by the endowment with additional responses to control the pore permeability.²⁰⁰

One example of such porous materials is anodized aluminum oxide substrates (AAO). Those rigid substrates provide a highly ordered arrangement of hexagonal pores with synthetically tuned diameter and length.^{197,201} By controlling their anodization conditions, the corresponding parameter can be precisely adjusted in the ranges between 10–400 nm for pore diameter, 50–600 nm for interpore distance, a thickness of the porous layer from 10–150 nm and porosity from 5–50%.^{197,202–204}

In the literature, poly(*N*-isopropylacrylamide) is commonly grafted from or to the pore walls to introduce a thermoresponse to the inner membrane site upon the variation of temperature or pH.^{200,205,206} The combination of nanoporous AAO membranes and thermoresponsive polymers enable the fabrication of intelligent nanopore membranes, which can be reversibly switched by the external stimulus of temperature. The coil-to-globule transition of such thermoresponsive copolymer induces an abrupt change of the polymer's hydrophilicity in aqueous solution, which alter the volume demand of the macromolecules in the nanochannels as consequence of varying solvent interactions.^{49,205}

In Figure 30, two main concepts are illustrated for the fabrication of thermally switchable nanopore membranes with open backsides, which allow the study of reversibly alterable diffusion processes through nanoscopic channels in aqueous solution. The functionalization of AAO channels with thermoresponsive copolymers with LCST behaviour (Figure 30a) can

be utilized for an on-off switching of the membrane's permeability and, thus, enables the control of the solvent flux through the membrane.²⁰⁵ Going one step further, the iterative incorporation of alternating LCST and UCST copolymer layers may provide access to the control of more complex processes, such as peristaltic nano-pumping (Figure 30b), which is based on the simultaneous volume contraction and expansion of the thermoresponsive layers with contrary solvation behaviors. Such smart membranes could mimic biometric ion channels, which are of great importance for many physiological processes.^{205,207–209} Further potential application fields are ultrafiltration²¹⁰, desalination²¹¹, DNA-sequencing²¹², biosensing²¹³, functional properties^{214,215} and many other applications.

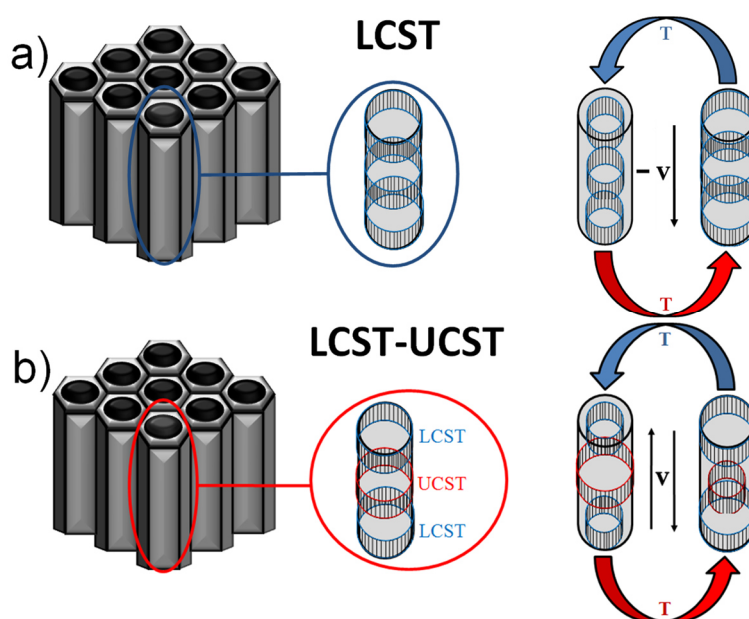


Figure 30: Conceptual approach for the fabrication of thermally switchable anodized aluminium oxide nanopore membranes with a) LCST copolymer filling for alterable “on-off” diffusion behaviours through nanoscopic channels and b) with alternating LCST-UCST copolymer layer filling for peristaltic pumping processes in aqueous medium upon external temperature stimulus.

In the following section, the thermoresponsive switching of the hydrogels inside nanoscopic AAO channels was studied for the prospective development of peristaltic nanopores. In contrast to pores of reported systems, which are usually functionalized with polymer *via* grafting-from polymerizations such as ATRP, we deposited linear RAFT copolymers of characterized composition and thermoresponsiveness from solution for their subsequent photo-immobilization as hydrogels, which accesses highly defined membranes by the adjustment of desired copolymer quantities and phase transition temperatures.

Those photo-crosslinkable copolymers were based on poly(NIPAAm) and exploited for the formation of hydrogels as responsive inner-pore coating, which was investigated optically *via* field emission scanning electron microscopy (FESEM) and quantitatively *via* thermogravimetric measurements with dynamic heating rate and (hi-res mode TGA). To the best of my knowledge, the thermoresponsive switching of hydrogels inside such nanoporous

AAO membranes was investigated in dependence of the temperature for the first time *via* modulated differential scanning calorimetry (MDSC) in aqueous surrounding and compared to the original solvation behaviour of the copolymers.

For the preparation of the target peristaltic membranes, photo-crosslinkable UCST and LCST copolymers were previously synthesized for the formation of hydrogels as described in chapter 7 (p.43) and 8 (p.63). The following chapter of the bio-inspired membranes with LCST behaviour discusses just the validation of the membrane filling and relates thereto suitable characterisation methods.

10.2. Results and Discussion of Thermoresponsive Switching States in Nanopores

10.2.1. Quantification of the Copolymer Filling inside the Nanopores

Before the thermoresponsive properties of the hydrogels inside the AAO membranes and the function of the total valve is demonstrated, the filling characteristics of the copolymer inside the nanopores had to be studied. Confer to chapter 8 (p.63), the terpolymer with the structure of poly(NIPAAm_{0.94}-CO-HEAAm_{0.05}-CO-BPAAm_{0.01}) was synthesized and chosen for the preliminary filling tests. Its physicochemical properties are summarized in the appendix, Table S11 and Table S12 (p.255). For initial tests, the application of photo-crosslinkable LCST copolymers were studied, as the polar UCST conjugates would hamper the subsequent purification and characterization pathways of the membranes due to their limitation to very polar solvents with high boiling points.

The AAOs were coated with thermoresponsive copolymers inside the pores by dipping in an ethanolic copolymer solution of 0.1 to 3.0 wt% concentration and drying under reduced pressure. The outer substrate surfaces were cleaned by manual wiping with an ethanol-soaked tissue after drying. Finally, the copolymer was immobilized in the nanopores by photo-crosslinking of the linear chains under laser light irradiation and transformed to a hydrogel coating, which is able to swell and collapse upon temperature variation in aqueous medium. The homogeneity of the pore filling and the purity of the outer AAO surface were checked optically *via* FESEM and quantitatively *via* thermogravimetry. The architecture of the thermoresponsive valve is sketched in Figure 31 and characterized by FESEM images.

The exemplary shown membrane exhibits a porous layer thickness of 75 to 85 μm (green frame), an interpore distance of 0.4 μm and a pore diameter of around 100 nm (blue frame). The images confirm the successful purification procedure of the outer surfaces, as the wiping removed the copolymer layer efficiently, which is shown by the almost entirely visible pore entrances in the images from the AAO surface (blue frame). The side-faced view from the bottom (red frame) visualizes that the copolymer solution penetrates the whole depth of the pores and forms a homogeneous coating of the inner pore walls after drying. It has to be noted, that a membrane with closed backside is exemplary shown here. In all other

experiments, the backside was previously removed to receive an open membrane. Further synthetic details and strategies for the AAO membrane fabrication and the corresponding filling will not be discussed here, as they were discussed in the corresponding theses of the collaboration partners Dr. Stephanie Müller, Qasim Alhusaini, and Rafael Trivella Pacheco da Silva from the physical chemistry group of Prof. Dr. Holger Schönherr in the university of Siegen.

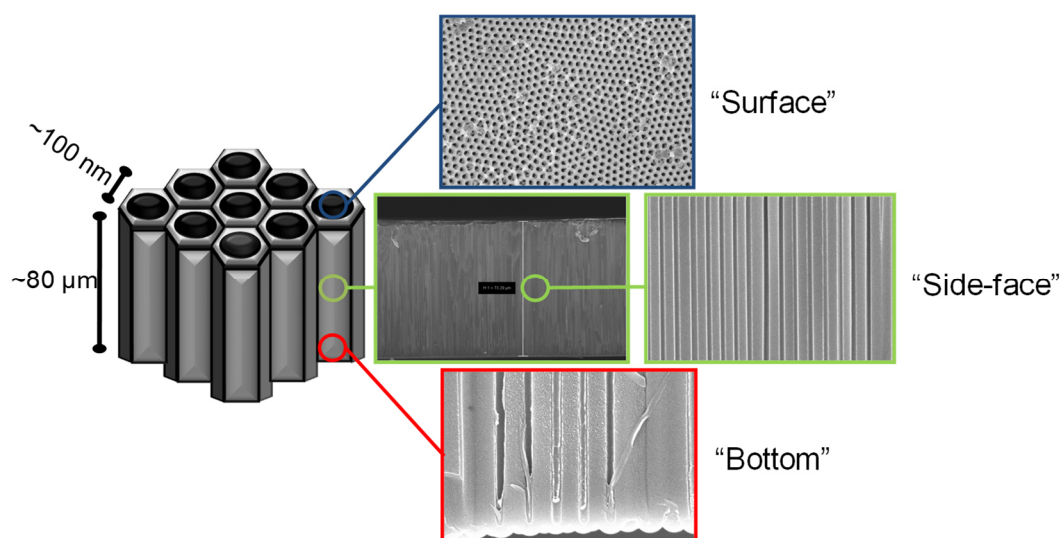


Figure 31: SEM images of the nanopore membrane filled with poly(NIPAAm-co-HEAAm-co-BPAAm)-DMP (94:5:1) (CRP-HEAAm) from different views.

To quantify the amount of copolymer inside the substrate, the copolymer was decomposed in a TGA experiment with dynamic heating rate (Hi-Res mode). The setup allows the determination of very small weight losses.²¹⁶ The AAOs were treated with copolymer concentrations between 0.1 to 3.0 wt%. In order to avoid the melting of the aluminium and contamination of the TGA pan holder at high temperatures, the backsides of the AAO substrates were removed previously. The TGA measurement of the membranes was performed in two heating cycles. In the first cycle, the total weight loss of the filled AAO was detected. The second cycle was used to determine the mass fluctuations of the same but bare substrate, whose weight loss was used as blank value after decomposing the entire copolymer. The extracted weight loss of the filled membrane received in first cycle is corrected by the value of blank conjugate from the second cycle (in the appendix, Table S14, p.256).

The isothermal pre-treatment at 90 °C for 120 min represent a proper drying step favouring a reproducible and homogenous measurement of the substrates. The comparison of the weight losses between a cleaned and uncleaned membrane verified major differences, which proved the success of the purification procedure in alignment to the FESEM images from Figure 31. This analysis method validates the purity of the membrane surface. It turned out,

that the sensitivity of the instrument is not sufficient to detect weight losses of samples, which were treated with polymer solutions below 1 wt%.

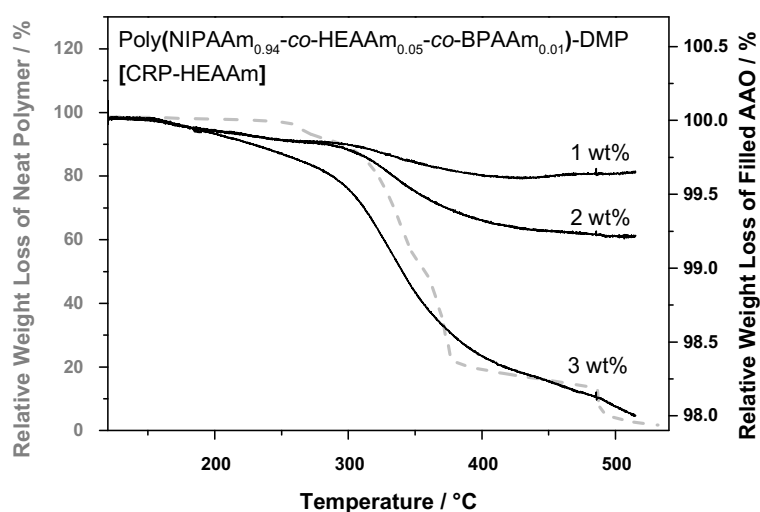


Figure 32: Comparative weight loss (in %) of differing polymer-concentrations filled nanopores in comparison to the thermogram of the neat polymer poly(NIPAAm-co-HEAAm-co-BPAAm)-DMP (94:5:1) (CRP-HEAAm) (dashed grey).

Therefore, the TGA measurements are presented in Figure 32 only for the concentrations of the AAO filling solutions between 1.0 to 3.0 wt% of copolymer. The shape of the weight loss curve for a filled AAO membrane (black) conforms to the analogous originated from the neat copolymer (dashed, grey), which attests the complete degradation of the copolymer until the upper measurement temperature of 550 °C ($\Delta m=98.3\%$). The total mass loss of the membranes is markedly depending on the copolymer concentration in solution. The extracted weight losses are similar to the theoretical values, which are based on the hypothetical inner pore volume, the determined AAO porosity and density of the used copolymer solutions (0.79-0.80 g·cm⁻³). The calculation are noted in the appendix, chapter 16.6.1 and summarized in Table S13 (p.256).

Table 3: The experimental weight losses of the copolymer filled AAOs (CRP-HEAAm) in comparison with the theoretical values in dependence of the concentration from the copolymer filling solution.

[c] / wt%	Measured Weight Loss / μg	Theoretical Weight Loss / μg
1	13.5	16.0
2	40.4	32.1
3	50.8	48.3

The results of the corrected weight losses are presented below in Table 3, which underline a satisfying match of the experimental and theoretical dimensions within the tested concentration range. The values demonstrate that the mass of the deposited coating inside the pores can be adjusted during the filling process by the choice of the copolymer fraction in

solution. That opens the opportunity to fill the substrates systematically with the desired amount of copolymer.

The photo-crosslinkable copolymer system allows the controlled deposition and transformation of pre-characterized copolymers as immobilized hydrogel networks onto the inner membrane walls. The combined analyses *via* FESEM and TGA represent a reasonable analysis pathway for the description of the thermoresponsive AAO membranes. For all tested samples, the differences between theoretical and experimental mass losses are about 25% or less, which represents a good approximation taking the detection limits of technique into account.

10.2.2. Thermoresponsive Switching of Copolymer Films inside the Nanopores

As the copolymer deposition inside the smart membranes was detailly characterized in the previous subchapter, the investigation of the inner pore switching caused by the thermoresponsive copolymer coating is of major interest on the way to the fabrication of a peristaltic nano-pump.

To yield thermoresponsive hydrogels with LCST character in aqueous media, photo-crosslinkable copolymers were synthesized on the basis of poly(NIPAAm) integrating *N*-(4-Benzoylphenyl)acrylamide side groups. As previously discussed in chapter 5.3.2 (p.11), the thermoresponsive transition of the copolymer inside the nanopores is accompanied by thermodynamic and kinetic processes, which can be displayed by DSC measurements.^{49,172,217} In the following, the technique of MDSC is used for the determination of the phase transition temperature inside the pores and not for more detailed analyses.

For the measurements, the coated membranes were crushed coarsely, filled inside the DSC pans and hydrated in water. The mass of the free copolymer exposed from the fracture's edges is neglectable for the measurement, as its intensity lays far beyond the detectable copolymer concentration.

In analogy to Figure S51 (p.252), the MDSC traces allow the investigation of the thermoresponsive properties for poly(NIPAAm) homopolymers in water, which represent an improved analysis of thermoresponsive switching states inside the nanopores. Hereby, two copolymers out of chapter 8 (p.63) are used with the structure of poly(NIPAAm-co-MAA-co-BPAAm) (FRP-MAA) and poly(NIPAAm-co-AA-co-BPAAm)-DMP-EA (CRP-AA-DMP-EA). The proof of principle is established experimentally by the study of thermoresponsive membranes, which are filled with photo-crosslinked copolymers possessing different cloud points as aqueous copolymer solution. Thus, the phase transition temperatures inside the pores of different copolymers are calorimetrically determined in comparison to the turbidity measurements of the corresponding copolymer solutions (1 wt%) by UV-Vis spectroscopy. As shown in the appendix, Figure S53 (p.257) and Figure S54 (p.258), the recorded signals

could be clearly attributed to the thermoresponsive switching of the hydrogels inside the membranes for both exemplary copolymers.

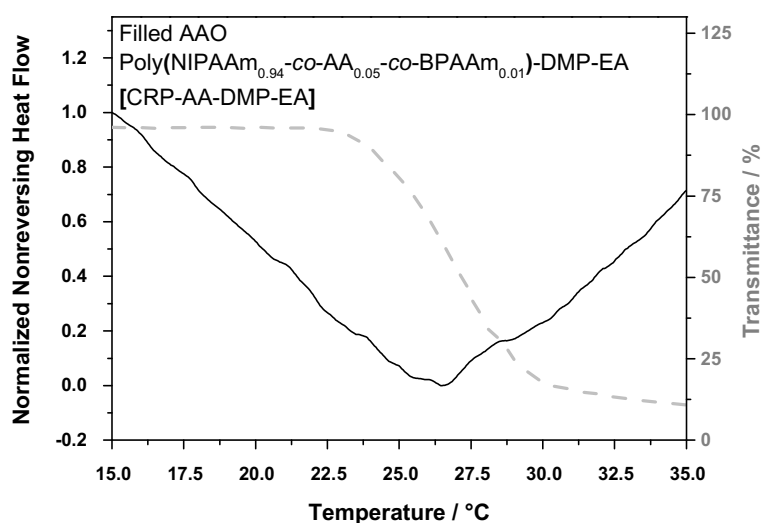


Figure 33: LCST determination in the nanopores *via* modulated DSC (black) of poly(NIPAAm-*co*-AA-*co*-BPAAm)-DMP-EA (94:5:1) (CRP-AA-DMP-EA) in comparison with the corresponding turbidity-measurement (dashed grey) in solution (1.0 wt%).

The MDSC traces of such hydrated membrane (Figure 33) visualize a remarkable endothermic transition of a first order in the non-reversing heat flow trace at 26.8 °C (solid, black), which matches with the recorded optical turbidity curve in solution (dashed, grey). The transition is visible exclusively in the non-reversing heat flow, which indicates a breakage of hydrogen bonding between copolymer and water, caused by the dehydration of the copolymer network as enthalpic event due to the proceeded phase transition of LCST.²¹⁷ The temperature of the thermoresponsive transition was monitored as apparent value so that the calorimetric data are not analysed further.

Table 4: The determination of the thermoresponsive properties, the used copolymers (FRP-MAA and CRP-AA-DMP-EA) *via* UV-Vis spectroscopy and MDSC in polymeric solution and in filled AAO.

Copolymer System		FRP-MAA	CRP-AA-DMP-EA
Turbidity ^[a]	$T_{c,heat}$ / °C	33.6	27.0
Calorimetric [in Solution]	$T_{c,heat}$ / °C	31.2	28.7
Calorimetric [in AAO]	$T_{c,heat}$ / °C	32.4	26.8

^[a] Values determined in solution (1 wt%) *via* UV-Vis spectroscopy.

As summarized in Table 4, the measurement of the membranes with varying LCST cloud point are delivering consistent and reproducible results in good agreement between calorimetric determination inside the pores and the optical clouding of the copolymers in solution (1 wt%). The established method allows the reliable detection of the phase transition temperatures from the investigated copolymer systems inside nanoscopic AAO membranes.

The recorded data are matching well with the supplemental results, obtained by white light interferometry and small-angle neutron scattering experiments from the cooperation partners in the physical chemistry group of Prof. Dr. Schönherr and the X-ray science group of Prof. Dr. Gutt, whose results are noted in the related theses associated to the project of nanopores.

The shown analysis methods complete the characterization pathway for thermally switchable nanopore membranes and provide access to the prospective preparation of more advanced systems, such as the desired peristaltic nano-pump. For that issue, the deposition and purification process of the AAO substrates have to be adapted for the incorporation of the UCST copolymer system of poly(AAm-co-AN), which may hamper the cleaning of the AAO surface due to its high polarity, which restricts the wiping process to warm water (above the phase transition of the used copolymer). Due to the entropic driven transitions of UCST copolymers, the corresponding calorimetric detection of their thermoresponsive switching inside the pores may be handicapped by much lower signal intensities in DSC.

10.3. Summary and Outlook of Thermoresponsive Switching States in Nanopores

In this chapter, nanoporous AAO substrates could be successfully combined with thermoresponsive poly(NIPAAm) copolymers for the fabrications of thermally switchable AAO membranes. Upon the external stimulus of temperature, those substrates demonstrated reversibly switching behaviours in aqueous media for the study of controlled diffusion processes through nanoscopic channels.

For the fabrication of such smart membranes, photo-crosslinkable copolymers with defined molar masses and architecture are deposited inside nanopores of the used anodized aluminium oxide substrates, where they can be immobilized *via* irradiation with UV laser light. The copolymer residues on outer membrane surfaces are successfully removed by manual wiping with an ethanol-soaked tissue, before the originally linear copolymers has been transformed to a hydrogel coating of the inner nanopore.

The homogeneity of the hydrogel coating at inner pore walls could be confirmed optically by FESEM images. The deposited copolymer mass inside membranes is controlled precisely by the synthetical choice of the copolymer concentration between 1.0 to 3.0 wt% in ethanolic solution during the deposition process, which could be displayed *via* two-cycled thermogravimetric experiments with dynamic heating rates. For the first time, the thermal switching processes of thermoresponsive copolymer hydrogels is reproducibly monitored in nanochannels *via* temperature dependent MDSC measurements in water. The calorimetric detection clearly evidences that the inner-pore transition temperatures match with the optical clouding of pure copolymer solutions. In contrast to the applied characterization methods in recent publications, where the thermoresponse is analysed indirectly as function of the

conductance or water flux through the substrate, the calorimetry represents a beneficial method for the direct proof of the thermoresponsive phase transition inside such smart membranes. Additionally, the utilization of very defined and pre-characterized RAFT copolymers, which can be transformed to thermoresponsive hydrogel coatings inside the pores, and the precise control of the deposited copolymer mass gives access to a highly controlled membrane architecture.

In prospective works, the investigated procedures of the copolymer deposition in the pores and the cleaning of the outer membrane surfaces have to be refined to yield similarly defined membranes. Such UCST copolymer systems like poly(AAm-co-AN-co-BPAAm)-EMP are usually highly polar and thus only soluble in pure water or polar organic solvents with high boiling points, which hamper the filling and also removal of copolymer residues from the outer surfaces. Furthermore, the measurement of the UCST phase transition is kinetically-driven and weakly detectable in MDSC measurements. To overcome this weakness, other non-calorimetric detection techniques such as the supplemented white-light interferometry or SANS could be potentially employed, which indicate slight variations of the local density. For the ambitious fabrication of the desired peristaltic membrane, the contrary copolymer systems owning LCST and UCST are deposited in defined alternating layers. This copolymer alternation requires a highly focused laser beam for the precise photo-immobilization in concrete layers, so that the excessive copolymer beyond that target layer thickness can be washed out, before the contrary copolymer analogue is iteratively filled in again.

11. Thermoresponsive Polymers as Macromolecular Coordination Ligands: Complexation-Dependence of Thermally Induced Aggregation in Aqueous Solution

11.1. Introduction to Macromolecular Coordination Ligands

A reversible structure formation at the molecular and supramolecular level is of fundamental relevance for vital processes in living organisms, as currently investigated in liquid-liquid phase transitions of dissolved proteins in membrane-less organelle formation.^{3-5,7} Such concepts also play an increasing role for the bio-inspired development of modern materials and their implementation in advanced technical applications. The involved reversible transitions are driven by the variation of intermolecular interactions in dependence of system conditions (such as temperature), as exemplified by the aggregation behaviour of thermoresponsive polymers or ligand-central ion bonding strength in coordination complexes.^{65,138}

The corresponding coordination process is determined by an electron-donor-acceptor arrangement (Lewis acid-base pair) between ligands and central metal ion.²¹⁸ The repetitive occurrence of inorganic or organometallic coordination motifs as backbone-forming elements along an extended macromolecular structure is termed coordination polymer.^{219,220} In contrast, the term metallopolymer is defined as macromolecular structures with an organic backbone, that integrates metal complexes in the molecular framework.²²¹⁻²²³

If a single coordination site is localized at one end of the polymer chain the particular architecture is referred to as hemi-telechelic. This structural concept was one of the two main strategies pursued in the present publication. The second architectural strategy is targeting macromolecular structures with multiple coordination sites distributed along the polymer backbone, termed here as multidentate ligands. Upon coordination with a metal centre the corresponding complexes can act as network junctions, resulting in molecular scaffolds known as metal-organic coordination-networks.²²⁴ The introduction of polymeric building blocks for the afore mentioned coordination structures provides an elegant possibility to tune the architectural details by the design of the macromolecular framework (such as the chain lengths determined during synthesis).¹²⁹

Three examples demonstrating the versatility of polymeric ligands as building blocks to enable complex functions are provided by the recent literature: 1) mechanochromic sensors utilizing reversible metal-ligand dissociation of telechelic coordination polymers,²²⁵ 2) self-healing polymers based on reversible triazole coordination,²²⁶ 3) metallopolymer networks with designable multicoloured photoluminescence.²²⁷

Going one step further and endowing the polymer with thermoresponsive behaviour yields the additional feature to dynamically control the structural dimensions by an external temperature stimulus. Such thermoresponsive control over the swelling behaviour in a polymeric host-guest system was demonstrated by a reversible

complexation/decomplexation process of a cyclodextrin copolymer *via* molecular recognition.^{134,135} Yet, no analogous example was described in the literature for metal coordination systems with thermoresponsive polymeric ligands, to the best of our knowledge.

Based on this lack, we have chosen to study dynamic structure formation of a novel thermoresponsive metal-polymer complexes featuring LCST- or UCST-phase transitions in water in dependence of temperature.

For this purpose, a [1,2,4]-triazole unit was conjugated with thermoresponsive poly(*N*-isopropylacrylamide) (PNIPAAm) or poly(acrylamide-*co*-acrylonitrile) (poly(AAm-*co*-AN)) to yield LCST- or UCST-type macromolecular coordination ligands (MCLs) bridgeable *via* Fe²⁺ complexation. Functionalized triazole derivatives offer strong coordinative interactions with numerous metal ions such as Fe²⁺, Cu²⁺, Zn²⁺, Ag⁺ and surfaces of nanoparticles.^{228–230} They can be utilized as antibacterial-, antitumoral- and anti-fouling agents, pesticides, herbicides, dyes, analytical reagents and lubricants, beyond their SCO properties.^{139,140,231–233}

In iron complexes, particularly [1,2,4]-triazoles exhibit preferred coordination modes including the monodentate, bidentate and the more stable triple *N*¹,*N*²-bridging mode: In this latter geometry, the octahedrally coordinated iron ions are bridging the metal-centres by triazole units forming an extended 1D-coordination structure, which reduces the electrostatic repulsion of the central ion (Figure 35i (p.105)) and may lead to far unprecedented SCO properties depending on the specific details of counterions and the ligand structure.¹³⁸ Furthermore, a flexible synthetic modification of the ligand in its 4-position and allows convenient tuning of the coordination properties, as documented for [1,2,4]-triazole-1-yl-propylamine (APTRZ) (in the appendix, Figure S55a-b (p.259)).²³⁴

In our present work, the triazole coordination site was modified with a thermoresponsive polymer to empower dynamic control over the complexation behaviour. The solvation state of the responsive chain in aqueous solution can be reversibly switched by the external stimulus of temperature, inducing a coil-to-globule transition.²³⁵

The thermal response is commonly grouped into lower and upper critical solution temperature behaviour, which involve a phase separation of the polymer solutions upon heating (LCST) or cooling (UCST).^{14,62} These groups entail numerous polymer classes commonly based on poly(*N*-acrylamides), poly(*N*-vinyl amides), poly(oxazolines) or poly(ethers) for LCST polymers,^{236,237} and poly(acrylamide-*co*-acrylonitrile), poly(*N*-acyloylglycinamides) or poly(sulfobetaines) for UCST systems^{59,62}. Amongst these, the most studied example poly(NIPAAm) provides a

robust LCST character in water with the phase transition near body temperature (32 °C), while its comparative UCST system poly(AAm-co-AN) benefits a robust and freely-adjustable phase transition temperature between 0-100 °C even under physiological conditions.^{14,73,238} Both thermoresponsive systems are well-accessible *via* similar synthetic routes,^{73,238} which realize the target design of common ligand architectures.

For that purpose, the reversible addition-fragmentation chain transfer polymerization (RAFT)^{15,21,73} represents a powerful method to fabricate very defined ligands with controlled molar mass and desired end group.²³⁹ Here, a [1,2,4]-triazole end group was introduced *via* the chain transfer agent (CTA) by performing the RAFT polymerization in presence of 1-[[3-(4*H*-1,2,4-triazol-4-yl)propyl]amino]-2-methyl-1-oxopropan-2-yl dodecyl carbonotrithioate (DMP-APTRZ).

For these thermoresponsive MCLs based on NIPAAm and AAm/AN, the solution- and coordination behaviours were studied for LCST and UCST character in presence of iron(II) ions *via* UV-Vis spectroscopy, DLS and cryo-TEM. Particularly, a structure-property relationship was established for the two distinct architectures: the hemi-telechelic and multidentate design. The here presented LCST-typed MLCs were published as “Thermoresponsive Polymers as Macromolecular Coordination Ligands: Complexation-Dependence of Thermally Induced Aggregation in Aqueous Solution”.²⁴⁰

11.2. Results and Discussion of Macromolecular Coordination Ligands

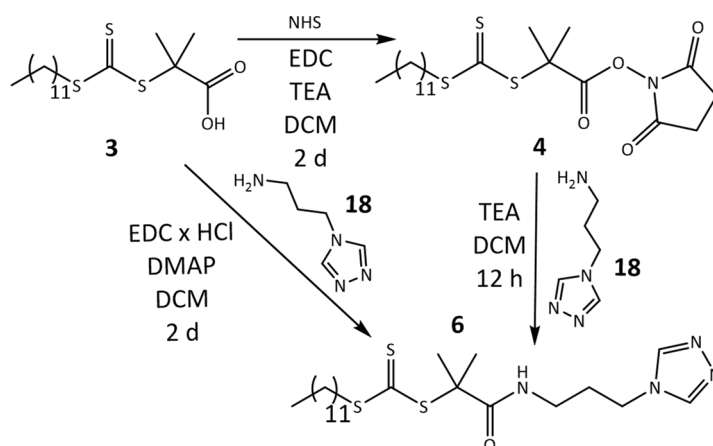
11.2.1. Synthetical Aspects

The syntheses of the coordinating chain transfer agent (DMP-APTRZ) and the MCLs poly(NIPAAm)-DMP-APTRZ with LCST character (P3k-P25k) were already developed in the previous Master's thesis (2016). As brief introduction, the fundamental pathways are sketched in the following, as they improve the understanding of the recent results. The complex results were further analysed in the recent thesis and set into the context of the novel hemi-telechelic ligands based on poly(AAm-co-AN)-DMP-APTRZ bearing UCST behaviour (UCP4k-UCP27k). The synthesis of the coordination monomer *N*-[3-(4*H*-1,2,4-triazol-4-yl)propyl]acrylamide (APTRZAAm) was refined, as its previous procedure led to an undesired side reaction, presented in chapter 14.3.2 (p.162) and in the appendix chapter 16.2.3 (p.219). The improved synthetic pathway for the novel triazole monomer APTRZMAAm is denoted below. The associated copolymer sets either bearing LCST or UCST behaviour were prepared and applied as multidentate MCLs.

Preparation of the Triazole CTA by Coupling of DMP with APTRZ

The successful RAFT polymerization of acrylamides such as poly(NIPAAm) or poly(AAm) with 2-dodecylsulfanylthiocarbonylsulfanyl-2-methyl propionic acid (DMP)

was already reported in the literature.²³⁸ In order to introduce a coordination site for Fe^{2+} ions, the carboxylic group of DMP **3** was modified here by [1,2,4]-triazole-1-yl-propylamine (APTRZ **18**) as bidentate ligand for the application as sketched in Figure 34 (p.103) and in the appendix, Figure S55 (p.259). Two different coupling strategies were compared: (1) a two-step approach *via* the DMP-NHS ester with total yield of 58 % (referenced to DMP) and (2) direct EDC coupling with a yield of 95 % (see Scheme 3).



Scheme 3: End-functionalization of the chain transfer agent DMP **3** by APTRZ **18**.

The molecular structure of the product was confirmed by ^1H and ^{13}C , COSY and HMBC NMR measurements (in the appendix, Figure S5 - Figure S7 (p.210-212)) with the presence of the characteristic signals for the [1,2,4]-triazole group (^1H : 2 H, s, 8.23 ppm; ^{13}C : 143.0 ppm) and the amide proton (^1H : 1H, t, 6.71 ppm). Direct EDC coupling was preferred over the NHS route based on the good yield of product **6** and the convenience of the reaction.

The functionalized chain transfer agent was employed in the RAFT polymerizations of the poly(NIPAAm) and poly(AAm-*co*-AN) yielding in coordination ligands with LCST or UCST behaviour.

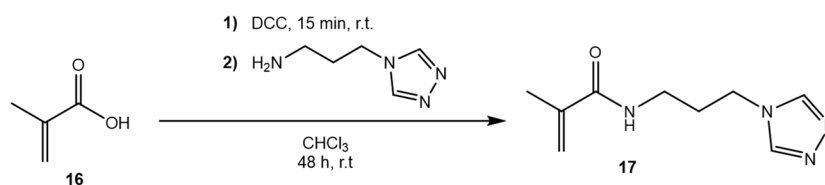
Preparation of the Triazole Monomer APTRZMAAm

While the triazole CTA above provides a coordination site at the chain end of the polymer ligand, a triazole-substituted monomer would allow the introduction of multiple coordination sites along the backbone, which is sketched in Figure 40 (p.118) and in the appendix, Figure S55c/e/g (p.259). The resulting graft architecture is expected to have a substantial influence on the coordination behaviour upon the interaction with Fe^{2+} ions.

An acrylamide derivative of APTRZ would be a desired monomer, as the copolymerization parameters are expected to be very close to AAm and NIPAAm.

Unfortunately, the coupling attempts of APTRZ to acrylic acid by various synthetic strategies failed, which is described in detail in chapter 14.3.2 (p.162) and the appendix 16.2.3 (p.219). Instead, side reactions *via* Michael addition are expected to be suppressed for methacrylic acid by the steric hindrance of the methyl group adjacent to the double bond and is confirmed in the appendix by Figure S11 and Figure S12 (p.217-218).

Finally, the APTRZ-modified methacrylamide monomer *N*-[3-(4*H*-1,2,4-triazol-4-yl)propyl]methacrylamide (APTRZMAAm) is synthesized by a direct coupling of methacrylic acid to the primary amine group of APTRZ with *N,N'*-dicyclohexylcarbodiimide (DCC) in the absence of an auxiliary base to obtain the product in 43% yield after workup (Scheme 4). The synthetic strategy using DCC is preferred over EDC or CDI as condensation agent, since the workup is facilitated due to the insolubility of the formed *N,N'*-dicyclohexylurea in water, while the other reagents and products are readily soluble under given conditions.

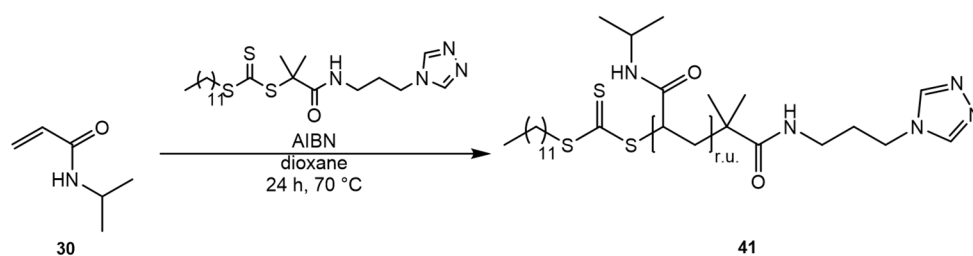


Scheme 4: Synthesis of the coordination monomer APTRZMAAm **17**.

It is worthwhile to note that after purification by extraction of water (product phase) with chloroform the product **17** may not be isolated as a neat compound, since it becomes difficult to dissolve after extended periods of drying (brownish resin, only very slowly soluble in a solvent mixture of H₂O/MeOH=1:1). Thus, the aqueous product solution was only partially concentrated by incomplete freeze drying and stored as a concentrated stock solution in the freezer. The purity of the chiefly dried product was confirmed by TLC measurements, HPLC-MS (shown in the appendix, Figure S12 (p.218)), ¹H- and ¹³C-NMR measurement (shown in the appendix, Figure S11 (p.217)). The chemically equivalent methylene groups characteristic for the [1,2,4]-triazole moiety (¹H: 8.26 ppm, s, 2H; ¹³C: 142.9 ppm), the protons of the amide functionality (¹H: 6.76 ppm, br. s, 1H; ¹³C: 169.1 ppm) as well as those of the methacrylate double bond (¹H: 5.36 ppm, 1H; 5.74 ppm, 1H; ¹³C: 120.0 ppm and 139.9 ppm) all confirm the target structure **17**.

RAFT Homopolymerization of Hemi-Telechelic Poly(NIPAAm)-DMP-APTRZ

The RAFT homopolymerization of NIPAAm was performed with the novel CTA DMP-APTRZ in dioxane in analogy to the literature procedure, but with AIBN initiation at 70 °C.²³⁸



Scheme 5: RAFT polymerization of NIPAAm **30** by the chain transfer agent DMP-APTRZ **6** for different monomer-CTA ratios.

The ^1H NMR spectrum (shown in the appendix, Figure S57 (p.262)) confirms the presence of the terminal CTA-moiety in the polymer (characteristic triazole signal at ca. 8.5 ppm). The isolated hemi-telechelic polymers are characterized by narrow molar mass distributions ($\mathcal{D}=1.12\text{--}1.34$) and possess the targeted chain lengths ($\bar{M}_n=3.1\text{--}24.8\text{ kg}\cdot\text{mol}^{-1}$), corroborating full control over the polymerization process with DMP-APTRZ according to mechanism of RAFT as shown in the appendix by the elugrams in Figure S58 (p.263).

Table 5: Theoretical and experimental number-average molar mass (\bar{M}_n), degree of polymerization (X_n), cloud point (T_c), dispersity (\mathcal{D}) and sample code of the hemi-telechelic MCLs with triazole end groups.

[NIPAAm] ₀ : [CTA] ₀ : [I] ₀	$\bar{M}_{n,theo}$ / $\text{kg}\cdot\text{mol}^{-1}$ (X_n)	$\bar{M}_{n,exp}^{[a]}$ / $\text{kg}\cdot\text{mol}^{-1}$ (X_n)	$T_c^{[b]}$ / $^{\circ}\text{C}$	\mathcal{D}	Yield / %	Sample Code
15: 1: 0.1	2.2 (15)	3.1 (21)	34.7	1.38	68	P3k
25: 1: 0.1	3.3 (25)	3.9 (30)	33.4	1.27	94	P4k
50: 1: 0.1	6.1 (50)	6.9 (57)	32.9	1.38	92	P7k
100: 1: 0.1	11.8 (100)	12.3 (104)	34.1	1.34	87	P12k
150: 1: 0.1	17.5 (150)	23.3 (199)	34.8	1.12	86	P23k
150: 1: 0.1	17.5 (150)	24.8 (212)	- [c]	1.19	60	P25k

[a] Values determined by GPC measurement.

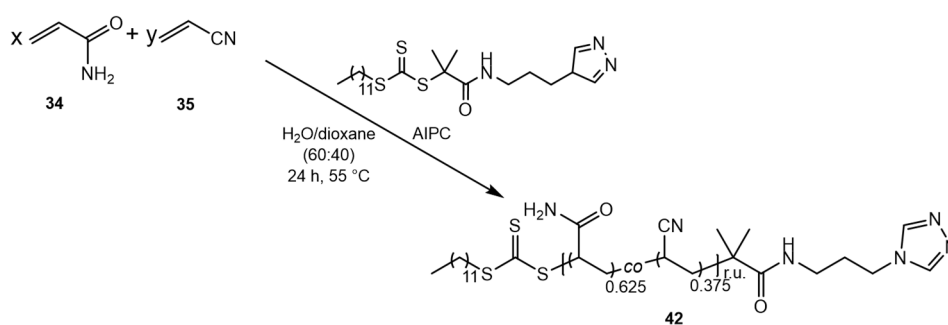
[b] Cloud point determined from the heating cycle of the turbidity measurement by UV-Vis spectroscopy

[c] Values not determined.

The corresponding physical data, like monomer:CTA:initiator feed ratios, experimental ($\bar{M}_{n,exp}$) and theoretical molar mass ($\bar{M}_{n,theo}$), degrees of polymerization (X_n), cloud points (T_c), dispersities (\mathcal{D}) and yields are summarized in Table 5. All poly(NIPAAm) samples (P3k–P25k) show the typical thermoresponsive behaviour in aqueous solution and the transition temperature is only slightly affected by the triazole end group (32.9–34.8 $^{\circ}\text{C}$), as illustrated in the appendix, Figure S59 (p.264).

RAFT Copolymerization of Hemi-Telechelic Poly(AAm-co-AN)-DMP-APTRZ

The RAFT copolymerization of acrylamide and acrylonitrile was performed in presence of the CTA DMP-APTRZ in water/dioxane (60:40) in accordance with the procedure of chapter 7 (p.43) with AIPC initiation at 55 $^{\circ}\text{C}$.



Scheme 6: RAFT copolymerization of AAm **34** and AN **35** by the chain transfer agent DMP-APTRZ **6** for different monomer-CTA ratios.

The ^1H NMR spectrum (shown in the appendix, Figure S65 (p.268)) confirms the presence of the terminal CTA-moiety in the polymer (characteristic triazole signal at ca. 8.64 ppm). The isolated hemi-telechelic polymers are characterized by rather narrow molar mass distributions ($D=1.36\text{--}1.72$) and exhibit the targeted chain lengths ($\bar{M}_n=4.2\text{--}26.8\text{ kg}\cdot\text{mol}^{-1}$), corroborating sufficient control over the polymerization process as indicated by the elugrams in Figure S66 (p.268). In comparison to the previous LCST analogous, the RAFT process seems to be hampered, which may be reasoned by the limited solubility of the chain transfer agent in given reaction mixture. For the copolymerizations, DMP-APTRZ was used still as CTA, as it allows the fabrication of comparative ligands with the desired molecular mass variation, an identical architecture and the required UCST behaviour. The yields are lowered for low molecular mass copolymers, as the precipitation is compromised. The corresponding physical data, like monomer:CTA:initiator feed ratios, experimental ($\bar{M}_{n,exp}$) and theoretical molar mass ($\bar{M}_{n,theo}$) degrees of polymerization (X_n), cloud points (T_c), dispersities (D) and yields are summarized in Table 6.

Table 6: Theoretical and experimental number-average molar mass (\bar{M}_n), degree of polymerization (X_n), cloud point (T_c), dispersity (D) and sample code of the hemi-telechelic MCLs with triazole end groups.

[NIPAAm] ₀ : [CTA] ₀ : [I] ₀	$\bar{M}_{n,theo}$ / $\text{kg}\cdot\text{mol}^{-1}$ (X_n)	$\bar{M}_{n,GPC}^{[a]}$ / $\text{kg}\cdot\text{mol}^{-1}$ (X_n)	$\bar{M}_{n,NMR}$ / $\text{kg}\cdot\text{mol}^{-1}$ (X_n)	$T_c^{[b]}$ / $^{\circ}\text{C}$	$D^{[a]}$	Yield / %	Sample Code
30: 1: 0.1	2.4 (30)	4.2 (53)	4.5 (56)	11.5	1.36	37 ^[d]	UCP4k
60: 1: 0.1	4.3 (60)	6.5 (91)	8.3 (116)	– ^[c]	1.44	46 ^[d]	UCP7k
100: 1: 0.1	6.9 (100)	8.4 (122)	8.8 (127)	18.8	1.63	51	UCP8k
200: 1: 0.1	13.3 (200)	15.6 (232)	15.4 (232)	19.9	1.72	73	UCP16k
400: 1: 0.1	26.2 (400)	26.8 (409)	21.2 (324)	34.8	1.52	60	UCP27k

^[a] Values determined by GPC measurement.

^[b] Cloud point determined from the cooling cycle of the turbidity measurement by UV-Vis spectroscopy

^[c] Values below the measurable temperature range of $T < 0\text{ }^{\circ}\text{C}$.

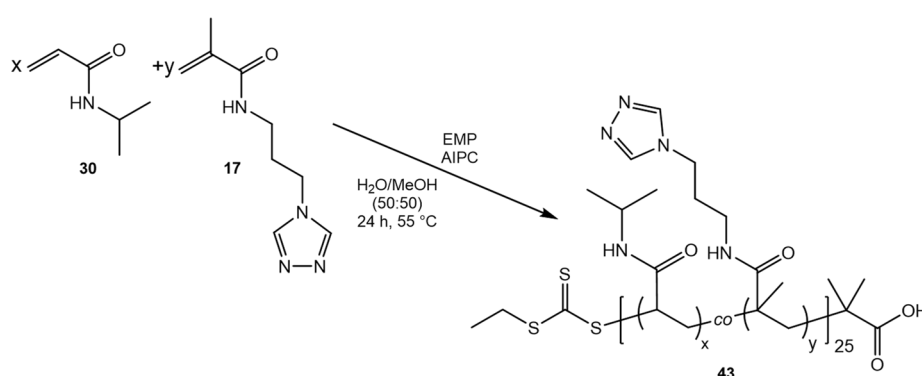
^[d] Yields reduced due to the losses during precipitation process the amphiphilic character of low molecular mass copolymers.

All ligands of poly(AAm-co-AN)-DMP-APTRZ (UCP4k–UCPP27k) show the typical thermoresponsive behaviour of an UCST in aqueous solution, which transition

temperatures (11.5–34.8 °C) are highly affected by the interplay of molar mass (as discussed in chapter 7.2.5, p.54) and the triazole end group as illustrated in the appendix, Figure S67 (p.269).

RAFT Copolymerization of Multidentate Poly(NIPAAm-co-APTRZMAAm)-EMP

The triazole monomer APTRZMAAm could be successful copolymerized with *N*-isopropylacrylamide (depicted in Scheme 7) enabling the introduction of a precise ratio of coordination sites between 5 to 15 mol% along the polymer backbone.



Scheme 7: RAFT copolymerization of NIPAAm **30** and APTRZMAAm **17** with the chain transfer agent EMP with varying monomer ratios.

The reaction was performed in a mixture of water/MeOH (1:1v/v) to allow homogeneous dissolution of all reaction partners, including the very polar APTRZMAAm and the less polar CTA EMP. Here, EMP was chosen over DMP due to the shorter alkyl chain, which provides solubility in the polar reaction medium.

Table 7: Feed and incorporation ratios of APTRZMAAm monomer, theoretical and experimental number average molar mass (\bar{M}_n), degree of polymerization (X_n), cloud point (T_c), dispersity (\mathcal{D}) and sample codes for the multidentate copolymer ligands with varying amounts of triazole side chains.

[APTRZMAAm] / mol%		$\bar{M}_{n,theo}$	$\bar{M}_{n,exp}^{[b]}$	$T_c^{[c]}$	\mathcal{D}	Yield	Sample Code
Feed	Incorporated ^[a]	/ kg·mol ⁻¹ (X_n)	/ kg·mol ⁻¹ (X_n)	/ °C		/ %	
5.0	4.1	3.2 (25)	4.8 (36)	36.6	1.07	69	C4.8k5%
10.0	7.6	3.3 (25)	4.9 (33)	39.1	1.08	60	C4.9k10%
15.0	13.8	3.4 (25)	4.6 (33)	44.7	1.10	55	C4.6k15%

^[a] Determined by ¹H-NMR.

^[b] Determined by GPC measurement.

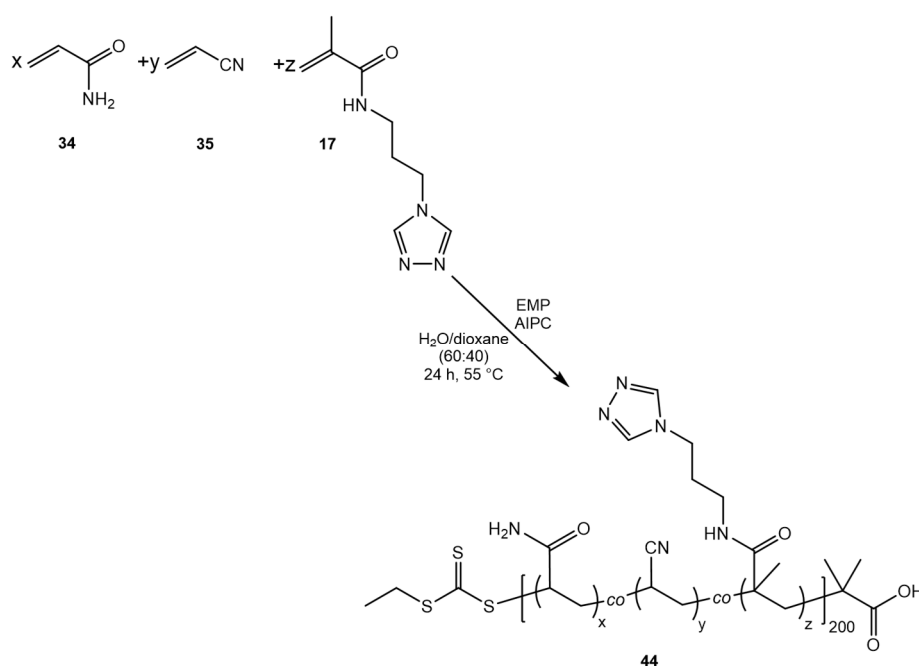
^[c] Cloud point determined from the heating cycle of the turbidity measurement by UV-Vis spectroscopy.

The yields for the copolymerization with EMP are in the range of 55-69%, similar to the homopolymerization of NIPAAm with the CTA DMP-APTRZ. The analysis by gel permeation chromatography indicated a successful copolymerization with the CTA EMP *via* a RAFT mechanism by a unimodal, narrow molar mass distribution (\mathcal{D} =1.07-1.10, shown in Table 7).

The presence of the characteristic signals for the triazole group in the ^1H NMR spectra (in the appendix, Figure S70, (p.272)) confirms a successful copolymerization of APTRZMAAm (8.55 ppm for triazole and 6.52 ppm for amide) with NIPAAm. The experimentally found ratios of the incorporated triazole repeat units are within acceptable ranges of the theoretically expected values. In dependence of their incorporation ratios, the hydrophilic repeat units of APTRZMAAm systematically raise the coil-to-globule transition temperature in aqueous solutions (*cf.* Figure 41 (p.121)) in comparison to the typical value of $T_c \sim 32$ °C.

RAFT Terpolymerization of Multidentate Poly(AAm-co-AN-co-APTRZMAAm)-EMP

In addition, the triazole monomer APTRZMAAm could be successfully included in a terpolymer with acrylamide and acrylonitrile (depicted in Scheme 8) allowing a precise ratio of coordination sites between 2.5 to 10.0 mol% along the copolymer backbone. The reaction was performed in a mixture of water/dioxane (60:40) in order to allow a homogeneous dissolution of all polar components poly(APTRZMAAm) and AAm as well as the less polar CTA EMP. The molar ratio of AAm and AN was set to 50:50 for all samples guaranteeing cloud points within detectable temperature ranges. Here, EMP was chosen to mimic the architecture of the LCST conjugates.



Scheme 8: RAFT terpolymerization of AAm **34**, AN **35** and APTRZMAAm **17** with the chain transfer agent EMP with varying monomer ratios.

The molecular mass analysis by gel permeation chromatography indicates a successful copolymerization with the chain transfer agent EMP *via* the mechanism of RAFT suggested by unimodal, narrow molar mass distributions ($\mathcal{D}=1.11-1.24$, shown in Table 8). The analysis was affected by the polarity changes of the terpolymers, as

their eluent quality (in DMAc) was reduced with an increasing incorporation of the polar monomer APTRZMAAm. Hence, the molar mass derived from the ^1H NMR measurements were more reliable. The presence of the characteristic signals for the triazole group in the ^1H NMR spectra (in the appendix, Figure S72, (p.275)) confirms successful terpolymerization of APTRZMAAm (8.55 ppm for triazole and 6.52 ppm for amide) with the UCST segments of AAm and AN.

Table 8: Feed and incorporation ratios of APTRZMAAm monomer, theoretical and experimental number average molar mass (\bar{M}_n), degree of polymerization (X_n), cloud point (T_c), dispersity (\mathcal{D}) and sample codes for the multidentate copolymer ligands with varying amounts of triazole side chains.

[APTRZMAAm] / mol%		$\bar{M}_{n,theo}$ / $\text{kg}\cdot\text{mol}^{-1}$ (X_n)	$\bar{M}_{n,GPC}^{[b]}$ / $\text{kg}\cdot\text{mol}^{-1}$ (X_n)	$\bar{M}_{n,NMR}^{[a]}$ / $\text{kg}\cdot\text{mol}^{-1}$ (X_n)	$T_c^{[d]}$ / $^{\circ}\text{C}$	$\mathcal{D}^{[b]}$	Yield / %	Sample Code
Feed	Incorporated ^[a]							
2.5	2.5	13.3 (200)	12.2 (184)	11.6 (175)	50.5	1.11	65	UCP11.6k2.5%
5.0	4.4	13.9 (200)	8.3 ^[c] (119)	14.9 (214)	45.2	1.21	61	UCP14.9k5.0%
10.0	7.4	15.6 (200)	6.4 ^[c] (82)	13.7 (176)	35.6	1.24	58	UCP13.7k10.0%

^[a] Determined by ^1H -NMR.

^[b] Determined by GPC measurement.

^[c] Molar masses determined *via* gel-permeation chromatography affected by varying coiling of copolymers in eluent DMAc.

^[d] Cloud point determined from the cooling cycle of the turbidity measurement by UV-Vis spectroscopy.

The experimentally found ratios of the incorporated triazole repeat units are within acceptable ranges of the theoretically expected values. In dependence of their incorporation ratios, the hydrophilic APTRZMAAm repeat units systematically lower tremendously the coil-to-globule transition temperature for aqueous solutions of the terpolymers (Figure 42 (p.124)). Similar to the copolymerization of NIPAAm and APTRZMAAm in presence of EMP, the yields for the recent terpolymerization are within the range of 58-65%.

11.2.2. Morphology Switching of Hemi-Telechelic Thermoresponsive Fe^{2+} -Polymer Coordination Systems

The present hemi-telechelic polymers with triazole end group and varying chain length bearing LCST- or UCST-character may serve as bulky ligands with thermally switchable steric demand for iron ion (Fe^{2+}) coordination in aqueous solution as presented in Figure 34 (p.103) (or detailed in the appendix, Figure S55d/f (p.259)). Before discussing the experimental details of the complexation studies, the hypothetical model is introduced first, considering the potential interaction motives between the respective molecular components. Such interactions encompass the following components:

(1) The pivotal feature for structure formation is the attraction based on the coordinative bond between the Fe^{2+} centre and the triazole nitrogen, as sketched in Figure 35i (p.105) or Figure 38i (p.112).

(2) Secondly, repulsion by steric demand of the polymer chain is a function of the degree of polymerization X_n (Figure 34a/h) and of the temperature-dependent swelling state (LCST or UCST volume transition), represented in the schemes of Figure 34c-d, l-m, f-e and j-k.

(3) In addition, the steric repulsion of the more hydrophilic, solvated polymer chains in the swollen state (below the LCST or above the UCST) can be thermally switched to an attraction of the more hydrophobic chain segments in the collapsed state (above the LCST or below the UCST), illustrated in Figure 34c-d, f-e, j-k and l-m with the accompanying coil-to-globule transition.^{49,65}

(4) Lastly, van der Waals attraction exists between the hydrophobic dodecyl substituents from the CTA units at the polymer chain ends, (Figure 34b/g/i/n). In essence, the solution behaviour is the result of the temperature-dependent balance of these various types of interactions.

In the following section, the hypothetical structure models and morphology changes in Figure 34 are discussed individually for the small and large polymer ligands in the context of the various interaction motives for LCST and UCST chain behaviour, respectively. The shown architectures represent the elemental structural unit that serve as building blocks for the larger scattering objects. This hypothetical picture is corroborated by the experimental data (DLS, UV-Vis, TEM) discussed in the following chapters individually in detail for ligands either with LCST or UCST behaviour. Followingly, the overview figure for hemi-telechelic polymer ligands (Figure 34) is presented repeatedly with special focus on the transition type in the corresponding sections of Figure 35 (p.105) for LCST and Figure 38 (p.112) for UCST ligands. The synthetic and analytic context for the whole work is sketched in the appendix, Figure S55 (p.259) to providing a comprehensive overview of the study.

The small polymer ligands with LCST and UCST behaviour ($\bar{M}_n \leq 4 \text{ kg}\cdot\text{mol}^{-1}$; Figure 34a) with a low number of repeat units ($X_n < 25$) possess a pronounced amphiphilic character due to the hydrophobic dodecyl group of the CTA on one end and the hydrophilic triazole head group on the other chain end. In Figure 34b/g, the micellar aggregation of the small ligands in aqueous solution present in the hydrated chain state below the T_c at 22 °C for LCST copolymers and above the T_c at 50 °C for UCST conjugates is depicted. The dodecyl chains form the hydrophobic core due to their van der Waals attraction and the hydrophilic triazole head groups residing at the surface of the micelles in contact with the water phase. The existence of such aggregates is

supported by the DLS data of LCST and UCST ligands shown in Figure 36 (p.108) and Figure 39 (p.113) (black traces).

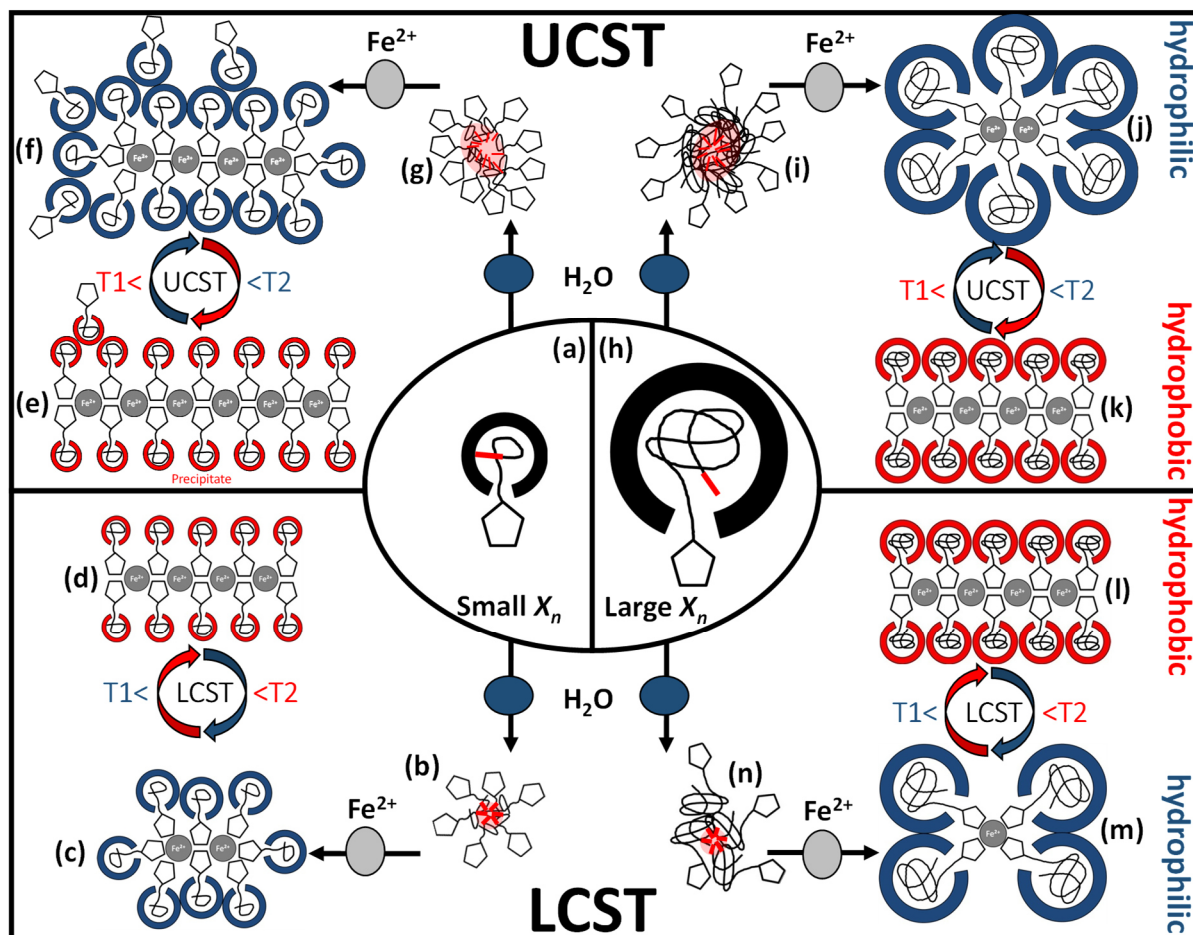


Figure 34: Overview of the proposed structural organization for short (a-g) and long (h-n) MCLs with LCST (P3k-25k) and UCST chain behaviour (UCP4k-UCP27k) with respect to iron ion coordination and thermal variation of the solvation state. These architectures represent the elemental structural unit, of which many may assemble to form the larger scattering objects observed in DLS. The triazole units are schematically represented by pentagons and the C12 alkyl chain as short red line.

The larger aggregates of the iron-polymer complexes in Figure 34b/g are formed after addition of iron (II) tetrafluoroborate to the polymer ligands below the T_c at 22 °C for LCST polymers and above the T_c at 50 °C for UCST conjugates. The increase in aggregation size is driven by attractive forces due to complex formation between the iron ions and multiple triazole head groups, which brings multiple chain ends together. Again, such substantial morphology change is supported by the DLS data from LCST and UCST ligands shown in Figure 36a (p.108) and Figure 39a (p.113) (red traces).

The exact structure of coordination sphere is currently not known for the studied polymer ligands. But based on the known complexation motives of [1,2,4]-triazoles an extended 1D-coordination structure *via* a triple N^1, N^2 -bridging mode with octahedrally coordinated iron ions is possible, at least as subunits in the larger scattering objects, as sketched in Figure 35i (p.105) or Figure 38i (p.112).¹³⁸ Such a potential 1D association is depicted in Figure 34d/e for the collapsed, dehydrated polymer ligands at 35 °C for

LCST polymers (above the T_c) and 2 °C for UCST copolymers (below the T_c) with a reduced steric demand. This is further enhanced by the hydrophobic attraction between the polymer chain segments. Such hydrophobic attraction may lead to further aggregation of these 1D elements into larger scattering objects, as observed in the DLS data (red curve) of Figure 36 (p.108) for LCST ligands and Figure 39 (p.113) for UCST analogous. Eventually, this leads also to the precipitation of the short chain samples.

An analogous picture can be drawn for the larger polymer ligands ($\bar{M}_n > 4$ up to 27 kg·mol⁻¹) of Figure 34h. For LCST ligands below the T_c and for UCST above the T_c , the longer polymer chain is well hydrated and thus reduces the relative influence of the hydrophobic dodecyl end group, leading to an overall weaker amphiphilic character. Still, these chains lead to micellar aggregation, as seen from the DLS trace in Figure 36 (p.108) for LCST and Figure 39 (p.113) for UCST ligands (black curve).

Upon addition of iron salt, the triazole head groups are expected to coordinate with the metal centres, as sketched in Figure 34j/m. But due to the higher steric demand of the longer polymer ligand, only few chains can associate *via* complex formation in the core. The DLS data in the appendix, Figure S61b (p.265) and Figure S69d (p.271) illustrate exactly this point, as no remarkable difference of aggregate dimensions is visible with or without iron ions at 22 °C. As for shorter chains, an extended 1D coordination structure can be envisioned for the large polymer ligands above the T_c at 35 °C for LCST polymers and below the T_c at 2 °C for UCST copolymers, shown in Figure 34k/l. This binding motive *via* the triple N^1, N^2 -bridging mode (Figure 35i (p.105) or Figure 38i (p.112)) may become possible by the reduced volume demand of the collapsed, dehydrated chains and their hydrophobic attraction. Overall, this morphology change is apparent in the DLS measurements of Figure 36 (p.108) for LCST and Figure 39 (p.113) for UCST ligands (red trace).

The hypothetical structure models provided here are referenced to the experimental data in the following sections.

11.2.3. Steric Demand Dependent Aggregation of the Hemi-Telechelic LCST Ligand Poly(NIPAAm)-DMP-APTRZ with LCST Character

To investigate the thermal response of the metal-polymer complex in aqueous medium, polymer solutions with a concentration of 0.1-1.0 wt% were combined with ten times higher amounts of $\text{Fe}(\text{BF}_4)_2$ with respect to triazole end groups and traces of ascorbic acid in water.

The polymer ligands P3k and P4k with lower molecular mass precipitated at room temperature upon addition of the Fe^{2+} salt, but as the iron polymer complexes do not crystallize, they are unfortunately not suitable for X-ray diffraction analysis. The Fe^{2+} -polymer

systems with higher molar mass (P7k, P12k, and P23k) were fully soluble at low and precipitated at elevated temperatures. For all samples, the variation of the temperature-dependent aggregation behaviour in solution was studied by turbidity measurements, DLS and TEM.

Turbidity measurements

The turbidity measurements (*cf.* appendix, Figure S59 (p.264)) deliver information about the temperature-dependent aggregation process of the thermoresponsive polymer ligands by increasing turbidity due to intra- and intermolecular chain aggregations caused by the coil-to-globule transition.⁶⁵ The complex shape of the turbidity curves below the transition is attributed to kinetic effects during the reorganization process of the colloidal structures upon polymer aggregation.

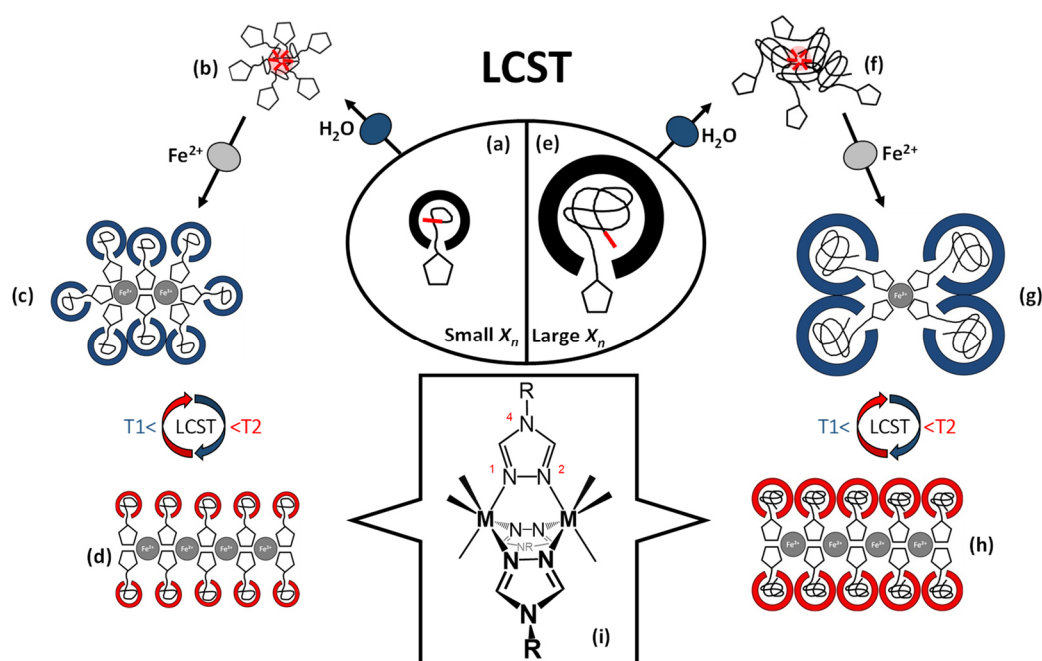


Figure 35: Schematics of the proposed structural organization for short (a-d) and long (e-h) polymer ligands P3-25k bearing LCST character with respect to iron ion coordination and thermal variation of the solvation state. These architectures represent the elemental structural unit, of which many may assemble to form the larger scattering objects observed in DLS. Under ideal conditions, a N^1, N^2 -bridging¹³⁸ of [1,2,4]-triazoles in one-dimensional divalent iron-polymer complexes is illustrated in the chemical structure (i). The triazole units are schematically represented by pentagons and the C12 alkyl chain as short red line.

The cloud point temperatures determined by the inflection points in the turbidity curves (summarized in the appendix, Table S15 (p.263)) reveal the influence of the APTRZ triazole end group. This moiety is hydrophilic and leads to a slightly raised cloud point in pure water by stronger polymer-solvent-interactions.²⁴¹ Upon addition of the divalent iron salt $\text{Fe}(\text{BF}_4)_2$, the shorter polymer ligands ($\bar{M}_n < 3 \text{ kg}\cdot\text{mol}^{-1}$, $X_n < 15$) precipitate abruptly independent of the temperature. The larger polymer ligands form homogenous, clear solutions in the presence of Fe^{2+} below the cloud point. Above the

T_c , polymer phase separation causes clouding of the solution, apparently by attractive coordination force that leads to a substantial growth of the scattering objects.

Generally, coordination of the APTRZ moieties with Fe^{2+} ions decreases the cloud point temperature. The difference between aqueous medium with and without present iron ions rises with decreasing molar mass of the polymers (depicted in the appendix, Table S15; $\Delta T_{H_2O/Fe(II)}=0.9\text{--}4.5$ K). These results suggest that in the hydrated state at lower temperatures the shorter chains can more efficiently participate in an extended coordination structure with the Fe^{2+} ions, which also leads to their preferential precipitation.

DLS measurements

DLS of 0.1 wt% polymer solutions was employed to indirectly follow complex formation by variation of the aggregation state upon addition of Fe^{2+} ions as before with a tenfold molar excess of $\text{Fe}(\text{BF}_4)_2 \cdot 6\text{H}_2\text{O}$. The here reported average dimensions serve predominantly as indicator for structural changes of the scattering objects, since exact values depend on the specific experimental conditions and may be subject of variation due to kinetic effects. The data for the short ligand P4k and the long ligand P23k are depicted in Figure 36, while the complete data set for all polymer samples including the chain lengths in between are provided in the appendix, Figure S61 (p.265). The size distribution analysis is based on a mathematical fit assuming a spherical aggregate shape, which may not be realistic for the complex aggregate morphologies observed in TEM measurements (Figure 37 (p.110)) for some samples. Thus, mainly the relative changes between different experimental conditions are considered.

In Figure 36a, the DLS curves are shown at low temperature (22°C) for the short polymer ligand P4k ($\bar{M}_n < 4$ kg·mol⁻¹, $X_n < 25$) in pure water (black curve) and iron solution (red curve). In pure water the broad decay of the autocorrelation curve indicates the presence of several coexisting aggregation species with substantially different dimensions (thus, for this case no size distribution is included in the inset - refer to the appendix, Figure S62 (p.266) for such details). Even for the smallest scattering species, the diameter is typically between $D_h=15\text{--}21$ nm (in the appendix, Figure S61 (p.265) and Figure S62 (p.266)), which suggests for the given experimental degrees of polymerization in the range of $X_n=20\text{--}200$ the presence of micellar aggregates composed of several polymer chains. Such micellation is supported by the asymmetric chain structure with one end carrying a hydrophobic dodecyl chain located in the micelle core, while the other end features a hydrophilic triazole unit at the micelle periphery, as discussed above in section 11.2.2 (p.101) and sketched in Figure 35b.

Upon addition of Fe^{2+} ions, the DLS trace (Figure 36a, red curve) exhibits an additional slow mode at higher correlation times corresponding to larger scattering objects. At the same time an insoluble precipitate is forming (in particular for the shortest polymer ligand). Under these conditions, the system is not in thermodynamic equilibrium and thus DLS is not appropriate to determine absolute object dimensions, but such measurements are used as indicator for the aggregation tendency. Apparently, the attractive forces between the triazole units upon iron ion complexation lead to a reorganization of the aggregate architecture with the complex units in a core cluster, as sketched in Figure 35b-c. Such complex clusters may serve as building blocks for the larger aggregates formed over time. As precipitation is commonly observed for Fe^{2+} complexation with triazoles that carry no or only small substituents,²⁴² the shorter polymer chains (P3k and P4k) below the cloud point temperature seem to have a sufficiently small space requirement even in their swollen state to allow an unconstrained N^1, N^2 -bridging coordination (Figure 35i).

In Figure 36b the DLS traces for the largest polymer ligand P23k below the T_c in water (black) and Fe^{2+} solution (red) show no significant difference. Both are characterized by a fast process with a single-exponential decay indicating well-defined micellar aggregates consisting of a few polymer chains (illustrated in Figure 35f) with unimodal size distribution of $D_{h,22^\circ\text{C}} \sim 20$ nm. This is in contrast to the short polymer ligands P3k and P4k that shows a change of aggregation size upon iron addition. For the larger ligands P7k and above no effect of Fe^{2+} ions on aggregate size is observed in DLS (in the appendix, Figure S61b (p.265)).

In pure water below the cloud point, the large ligand possesses a strong hydrophilic character that induces steric repulsion between neighbouring polymer chains. As schematically shown in Figure 35f, the associated larger coil volume in comparison to the small dimensions of the hydrophobic dodecyl end group in the micelle core allow only the formation of spherical micelles with smaller aggregation number (detailed DLS analysis in the appendix, Figure S62 (p.266)).

Addition of iron salt potentially leads to a reorganization of the aggregates induced by the complexation with the triazole end groups, now in the centre of the micelle (Figure 35g-h). Again, the steric demand of the large polymer coil is responsible for the small number of chains per micelle, which also prevents the formation of extended 1D coordination structures *via* N^1, N^2 -bridging. When heating the polymer solutions above the transition temperature T_c , the chains undergo a volume transition and compact while solvent molecules are expelled from the polymer coil.

Figure 36c shows a single exponential decay for the DLS curves of the shorter polymer P4k in pure aqueous solution above the cloud point temperature T_c . The induced coil-

to-globule transition leads to a narrowing of the size distribution resulting in scattering objects with well-defined dimensions. When adding the divalent Fe^{2+} ions at $T=35^\circ\text{C}$, the autocorrelation curve with mono-exponential decay shifts to longer correlation times, indicating increased dimensions of the scattering objects. Apparently, the attractive forces between the collapsed chains are further enhanced by the coordination processes, leading to a growth of the aggregates from $D_{h,\text{H}_2\text{O}}=315$ nm in pure water to $D_{h,\text{Fe}}\sim 1400$ nm for P4k.

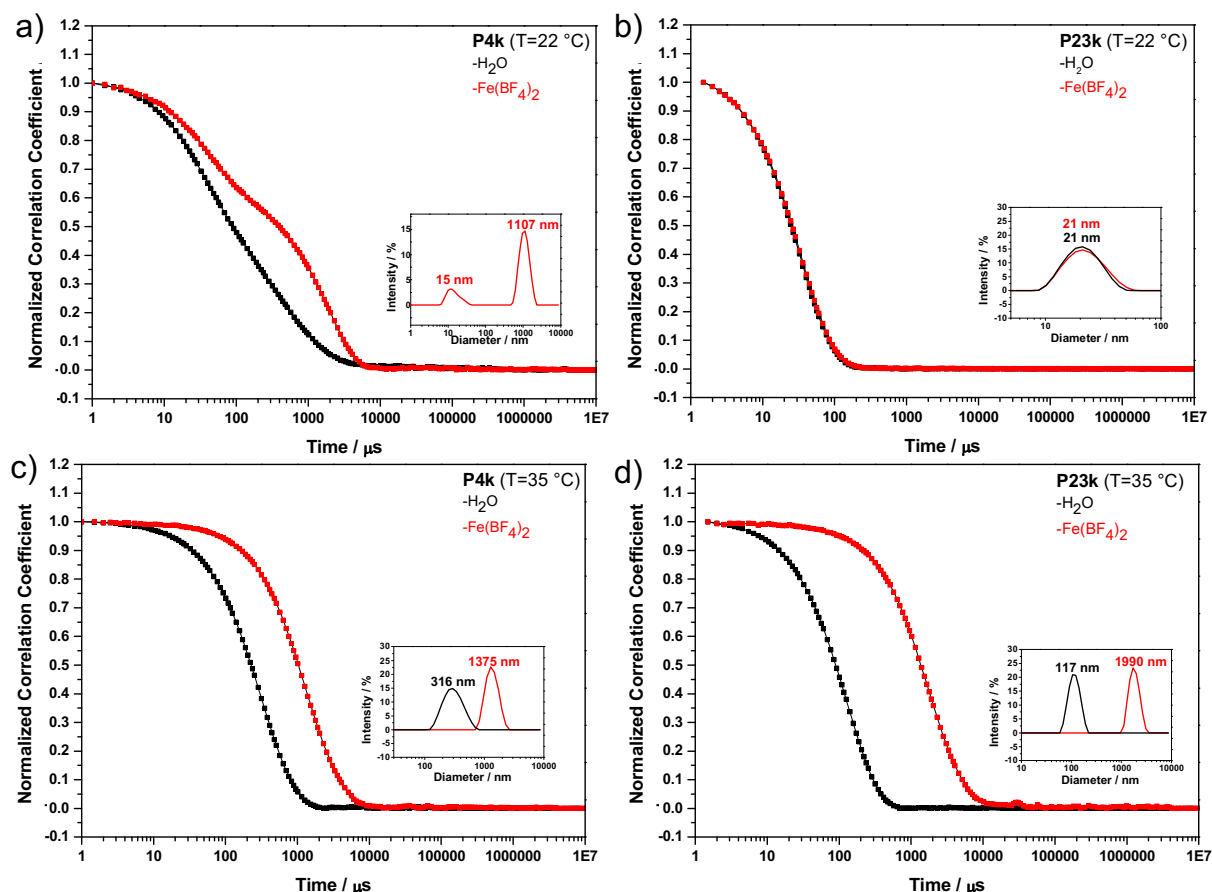


Figure 36: Iron ion-sensitive aggregation behaviour of the hemi-telechelic polymer ligand with LCST behaviour illustrated for the short chain length P4k (a-b) and long chain length P23k (c-d) carrying a TRZ end group with their (apparent) hydrodynamic diameter below (a, b) and above (c, d) the T_c of a 0.1 wt% solution. The aggregation sizes are analyzed by intensity.

The mono-exponential correlation curves of the DLS measurements for the larger polymer ligand P23k above the T_c are presented in Figure 36d. In pure water the aggregated dimensions substantially increase upon heating from $D_{h,22^\circ\text{C}}=20$ nm to $D_{h,35^\circ\text{C}}=117$ nm due to the increased attraction of the collapsed, hydrophobic polymer chains. Interestingly, when comparing to the aggregate dimensions of the shorter polymer ligand P4k under identical conditions ($D_{h,\text{H}_2\text{O}}=315$ nm in pure water above T_c), the longer polymer ligand possesses only about half the aggregate diameters. This effect may be explained by the increased coil volume of the longer polymer chains, which are organized with their triazole end groups at the micelle periphery. The

hydrophobic dodecyl end groups are presumably localized in the micelle centre, but steric crowding with increasing polymer chain length leads to smaller aggregate numbers (in the appendix, Figure S61c (p.265)). In agreement with the literature^{65,243}, a lower degree of polymerization reduces the flexibility of the chain segments, which results in an enhanced segment interaction and thus the aggregation cluster size increases.¹⁹⁶

The addition of iron salt shifts the DLS trace (Figure 36d) to longer correlation times, indicating a coordination-induced growth of the aggregate dimensions to an apparent diameter of around $D_h=1400\text{--}2600$ nm. The temperature-dependent aggregation process of the iron-coordinated polymer ligand P23k is reversible upon thermal cycling in the appendix, Figure S60b (p.264), which further supports the schematic switching between the coordination structures in Figure 35g/h due to a volume transition of the ligands.

In the attractive force state at 35 °C, the sample P23k assembles in presence of Fe^{2+} -ions to large aggregates ($D_{h,35^\circ\text{C}}=2200$ nm; according to Figure 35h). The aggregates dissociate by the ligand-growth due to the voluminous coil-state and cooling the polymeric solution below the temperature of turbidity ($D_{h,22^\circ\text{C}}=21$ nm; according to Figure 35g). The temperature triggered change of the hydrophilicity of the thermoresponsive backbone delivers the option to tune the structural assembly of the longer polymer ligands.

TEM measurements

The effect of the coordination processes (Figure 35c-d/g-h) on the aggregation structure was additionally investigated with a specialized TEM method utilizing trehalose as immobilization matrix and staining with uranyl acetate. This method allows to image structures from aqueous solutions in analogy to cryo-transmission electron microscopy in order to validate visually the results from DLS (Figure 36 (p.108) and in the appendix, Figure S61 (p. 265)) and UV-Vis-spectroscopy in the appendix, Figure S59 (p.264)).

The shortest and longest end-functionalized polymers (P3k in Figure 37 and P23k in the appendix, Figure S64 (p.267)) were chosen for the TEM investigation, as they provided the most distinct thermoresponsive coordination behaviour.

The short polymer P3k (Figure 37a) showed in pure water ($T=22$ °C) below the T_c spherical/elliptical aggregates with dimensions of about 20–30 nm, in overall agreement with the DLS data ($D_h=15$ nm, referred to Figure 36 (p.108)). The aggregates are randomly distributed throughout the hydrophilic trehalose matrix, while the aggregates prefer to localize at the hydrophobic carbon surface of the TEM grid at higher temperature of $T=40$ °C above T_c (Figure 37b), indicating their increased

hydrophobic character. A noteworthy peculiarity under these conditions is the internal lamellar structure of the aggregates with a width of 30 to 90 nm and an average periodicity of 5-10 nm (Figure 37b). Again, the data are in accordance with the DLS observations (overall scattering object dimensions: TEM: 150-400 nm and DLS: 316 nm).

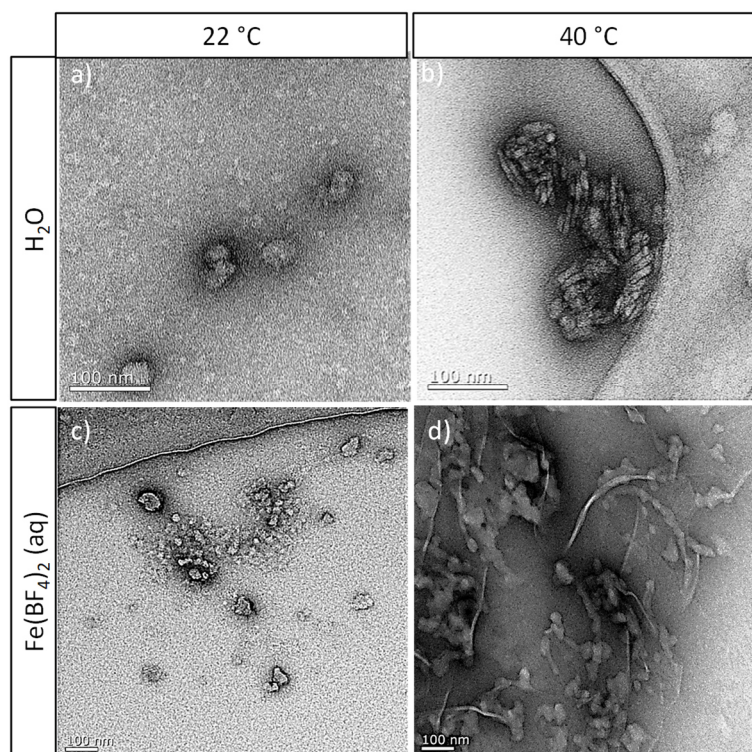


Figure 37: TEM images of the short LCST-typed hemi-telechelic MCL (P3k) prepared in a trehalose matrix and dried from a 0.1 wt% aqueous solution without (a-b) and with iron ions (c-d) in a tenfold excess, below (a, c) and above (b, d) the T_c .

Besides smaller, less defined structures, an increase of the P3k aggregate dimensions to 50-100 nm with irregular shape is observed upon addition of Fe^{2+} to the aqueous medium at low temperature ($T=22\text{ }^\circ\text{C}$). The increased aggregation tendency upon Fe^{2+} addition is again in agreement with the multiple scattering species observed in the DLS measurements (compare to Figure 36a (p.108)) and suggests formation of triazole-iron complexes. When the temperature of the P3k- Fe^{2+} system is raised above T_c to $40\text{ }^\circ\text{C}$ (Figure 37d), yet another substantial reorganization becomes evident in the TEM images with a combined formation of extended, interconnected globular and fibrillar structures. Also, here, these observations are congruent with the DLS data (Figure 36c (p.108)) and support the hypothesis of extended 1D coordination structures.

The TEM images of the long polymer ligand P23k are provided and discussed in detail in the appendix, Figure S64 (p.267). The visualized aggregate structures under the

different experimental conditions are again in good agreement with the results from the DLS measurements and fit the hypothetic models outlined in Figure 35 (p.105).

11.2.4. Steric Demand Dependent Aggregation of the Hemi-Telechelic Poly(AAm-co-AN)-DMP-APTRZ with UCST-Character.

In agreement with the previous chapter dealing with the aggregation behaviour in aqueous solution of hemi-telechelic polymer ligands with LCST character, the thermal response of the metal-polymer complex of the UCST conjugates were investigated in polymer solutions with a concentration of 1.0 wt% with ten times higher amounts of $\text{Fe}(\text{BF}_4)_2$ and traces of ascorbic acid in water.

All triazole copolymers (UCP4k-UCP27k) precipitated upon addition of the Fe^{2+} salt below their cloud points at room temperature. The copolymer ligand UCP4k ($\bar{M}_n < 4.2 \text{ kg}\cdot\text{mol}^{-1}$, $X_n < 56$) with lowest molecular mass precipitated independently of the temperature in presence of Fe^{2+} ions. As before, the iron polymer complexes do not crystallize, so that they are not suitable for X-ray diffraction analysis.

The hemi-telechelic UCST ligands showed the desired reverse chain behaviour of the previous LCST analogues. The Fe^{2+} -copolymer system with higher molar mass (UCP7k, UCP8k, UCP16k and UCP27k) were fully soluble above their cloud points at high temperature (all $< 43 \text{ }^\circ\text{C}$) forming homogenous, clear solutions in the presence of Fe^{2+} and precipitated upon cooling at lower temperatures. For all samples, the variation of the temperature-dependent aggregation behaviour in solution was studied by turbidity measurements and DLS.

Turbidity Measurements

In comparison to the thermoresponsive properties of the reference sample with carbonic acid end group and equivalent molar composition of AAm/AN=50:50 ($T_c = 72.5 \text{ }^\circ\text{C}$; referring to data from the appendix, Table S5 (230)), the triazole functionalization has a strong hydrophilic impact, which tremendously lowers the cloud point of the UCST copolymers in pure water by stronger polymer-solvent-interactions (*cf.* appendix, Figure S67 (p.269)).^{14,59}

The cloud points of the larger copolymers (UCP7k-UCP27k) drop systematically with decreasing molar mass from $T_c = 28.0 \text{ }^\circ\text{C}$ to $T_c < 0 \text{ }^\circ\text{C}$ due to minimized chain-chain interactions in solution. The copolymer (UCP4k) possesses a dominating relative impact of hydrophobic dodecyl rest with respect to the short macromolecular chain ($X_n = 56$), which leads to a divergent solvation behaviour in form of an existing optical clouding in pure water. Upon the addition of iron salt, the phase separation causes a precipitation of the copolymer ligands due to the enhanced attractive force of the coordination process, that lead to a substantial growth of the scattering objects. In all

cases, the coordination of the APTRZ moieties with Fe^{2+} ions enlarges the cloud point temperature tremendously, which is shown in appendix, Table S17 and Figure S67 (p.269).

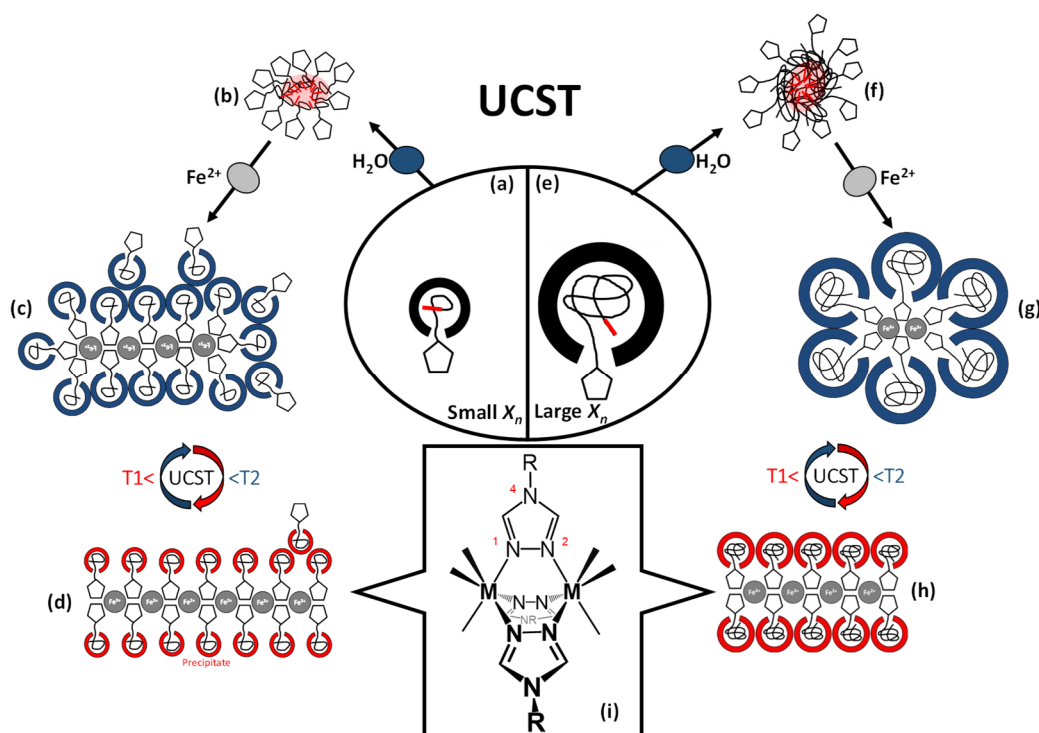


Figure 38: Schematics of the proposed structural organization for short (a-d) and long (e-h) polymer ligands UCP4-27k bearing UCST-character with respect to iron ion coordination and thermal variation of the solvation state. These architectures represent the elemental structural unit, of which many may assemble to form the larger scattering objects observed in DLS. Under ideal conditions, a N^1, N^2 -bridging¹³⁸ of [1,2,4]-triazoles in one-dimensional divalent iron-polymer complexes is illustrated in the chemical structure (i). The triazole units are schematically represented by pentagons and the C12 alkyl chain as short red line.

The differences between the cloud temperatures, measured in aqueous solution with and without present Fe^{2+} ions, decreases with growing molar mass of the copolymers (depicted in the appendix, Table S17 (p.269); $\Delta T_{\text{H}_2\text{O}/\text{Fe(II)}} = 2.2\text{--}9.7$ K). This tendency suggests that the shorter chains in the hydrated state at higher temperatures can more efficiently participate in an extended coordination structure with Fe^{2+} ions, which also leads to their preferential precipitation.

DLS measurements

In analogy to the LCST ligands, the DLS of 1.0 wt% copolymer solutions was employed under identical conditions to indirectly visualise complex formation of the UCST analogues *via* variation of the aggregation state upon addition of Fe^{2+} ions. As the size distribution of the DLS analysis may not be realistic for the non-spherical complex aggregate morphologies, mainly the relative changes between different experimental conditions are considered in agreement to the previous chapter. In presence of Fe^{2+} ions, the strong colloidal aggregation of the copolymers does not

allow the analysis of the size distributions, as they are not in kinetic equilibrium. In the following, the data for the short copolymer ligand UCP4k and the long conjugate UCP27k are depicted in Figure 39, while the complete data set for all copolymer samples, including the chain lengths in between, are provided in the appendix, Figure S69 (p.271).

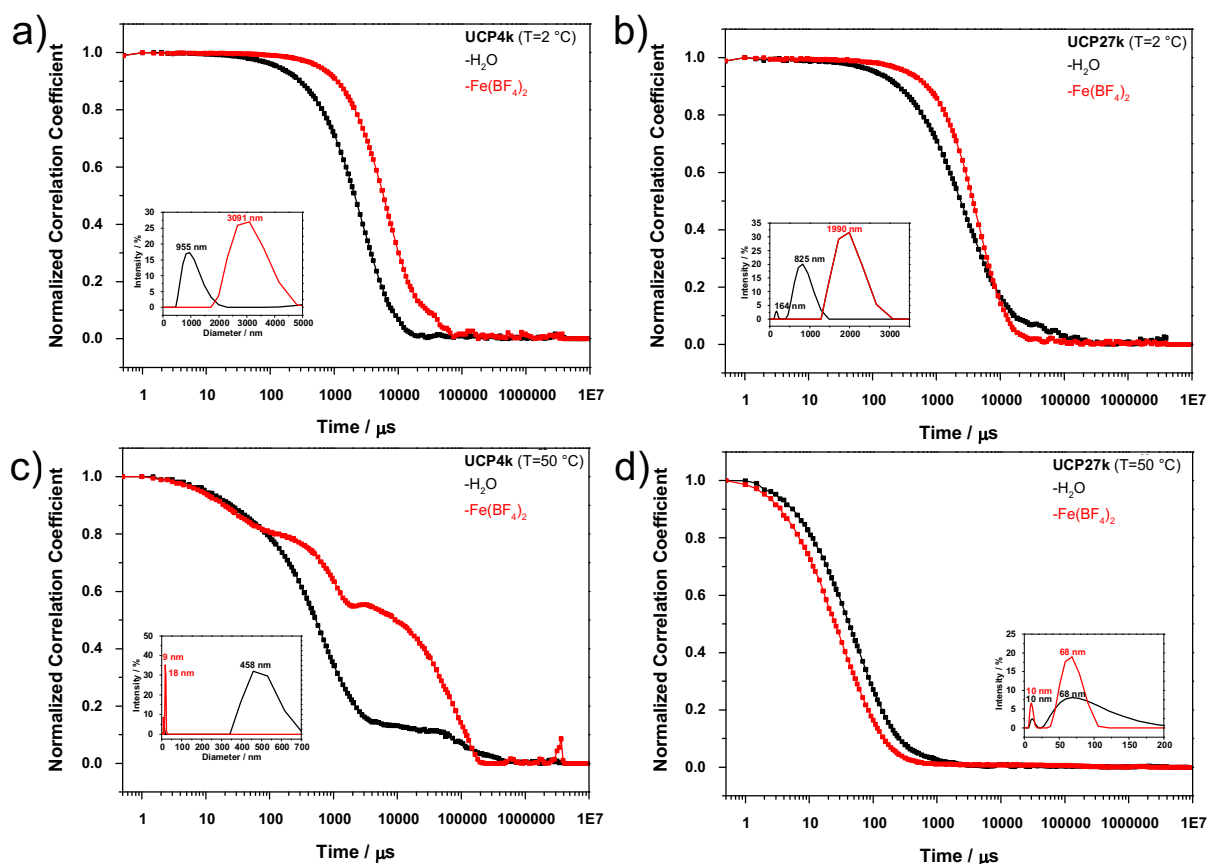


Figure 39: Iron ion-sensitive aggregation behaviour of the hemi-telechelic polymer ligand with UCST behaviour illustrated for the short chain length UCP4k (a-b) and long chain length UCP27k (c-d) carrying a TRZ end group with their (apparent) hydrodynamic diameter below (a, b) and above (c, d) the T_c of a 1.0 wt% solution. The aggregation sizes are analyzed by intensity and are, as such, not representative in presence of iron ions.

In Figure 39a, the DLS data of the short copolymer ligand UCP4k ($\bar{M}_n=4.2 \text{ kg}\cdot\text{mol}^{-1}$; $X_n=53$) are presented at low temperature (2 °C) in pure water without (black curve) and with added iron salt (red curve). For both cases, the autocorrelation curve shows a single exponential decay below the cloud points of the UCST ligands. In pure water, the copolymer forms defined colloidal aggregates of remarkable dimensions, which is characteristic for the dehydrated system of poly(AAm-co-AN), suggesting a strong interactions between the collapsed and hydrophobic chains localized in the centre of the aggregates (as discussed in subchapter 12.2.3 (p.134)).

Upon addition of Fe^{2+} ions, the DLS trace of UCP4k (red curve) show a slowing of the modes at higher correlation times. According to the comparative ligands with LCST behaviour, also the UCST analogues form an insoluble precipitate in the collapsed chain state at the same time. Again, it has to be noted, that the system is not in

thermodynamic equilibrium under these conditions and thus DLS is inappropriate to determine absolute object dimensions, even though the measurements are used as indicator for the aggregation tendency.

Apparently, the addition of iron ions acts as attractive driving force leading to extended complexes (as sketched in Figure 38b-c (p.112)) *via* N^1, N^2 -bridging mode forming 1D coordination structures consisting of numerous macromolecular ligands (Figure 38i (p.112)).¹³⁸ The coordination process may lead to a reorganization of the aggregates induced by the available iron ions in presence of the triazole end groups, which now occupy the centre of the micelles with grafted thermoresponsive coils along the coordination backbone (Figure 38c-d).

In Figure 39b, the autocorrelation curves are illustrated for the largest copolymer ligand UCP27k ($\bar{M}_n=26.8 \text{ kg}\cdot\text{mol}^{-1}$; $X_n=409$) below its T_c at low temperature (2 °C) in pure water without (black curve) and with added iron salt (red curve). In pure water, the copolymer shows a broader correlation curve composed of two decay times indicating corresponding species of aggregates. The first distribution with the lowest intensity ($D_{h,2^\circ\text{C}}=164$) is supposed to be the main species according to the number analysis fit. As before, the dehydrated chain state induces the formation of colloidal aggregate clusters with remarkable sizes.

In comparison to the amphiphilic behaviour of the smaller ligand, the ratio between longer hydrophobic backbone and polar triazole head is enlarged for high-molecular mass ligands, which apparently results in a stabilization of smaller, colloidal aggregation clusters ($D_{h,27k}=164$, $D_{h,4k}=955 \text{ nm}$). Based on the Figure S69 (p.271) in the appendix, the scattering sizes of the main species (in numbers) tend to decrease with increasing molar mass of the ligands from $D_{h,2^\circ\text{C}}=955$ to 164 nm for the synthesized degrees of copolymerization of $X_n=53$ to 409.

Upon the addition of Fe^{2+} salt, the mono-exponential correlation curve (red) is shifted to higher times, suggesting even larger dimensions of well-defined scattering objects. The apparent coordination process results in a substantial growth of the species' magnitude (apparent value of $D_{h,\text{H}_2\text{O}}=165 \text{ nm}$ and $D_{h,\text{Fe}}\sim 2000 \text{ nm}$). In agreement the LCST conjugates, the reduced steric demand of the larger copolymer coils in the collapsed state provides at elevated temperatures the required space for the formation of extended 1D complexes (as sketched in Figure 38f-g (p.112)).

In Figure 39c, the DLS traces for the smallest polymer ligand UCP4k show significant differences at high temperature (50 °C) above the T_c . in water (black) and Fe^{2+} solution (red). Both are characterized by several processes with a multi-exponential decay, indicating the presence of several coexisting aggregation species of tremendously different magnitudes. In pure water, two species are visible with a broad

aggregation size distribution belonging to numerous small micellar and few bigger colloidal structures ($D_{h,H_2O}=13$ and 458 nm). Such micellation agrees on the data, derived from the low molecular mass ligands with LCST character in the hydrophilic chain state, as discussed above in section 11.2.4 and sketched in Figure 38b (p.112).

In the presence of Fe^{2+} ions, the correlation curve becomes more distorted, as multiple processes indicating an inconsistent but substantial growth of the aggregates. The curve shape comes along with observed precipitate formation, which turns the DLS to an inadequate method, as the aggregation behaviour is not in the thermodynamic equilibrium. The smallest ligands offer even in the well-hydrated chain state sufficient steric space to associate numerous triazole ligands around the metal centres in larger 1D complex structures, which gain significantly in size, so that they produce settling precipitates (Figure 38d (p.112)).

In Figure 39d, the correlation curves for the largest copolymer ligand UCP27k show above its T_c at high temperature (50 °C) no significant difference in pure water without (black curve) and with present iron ions (red curve). In both cases, the DLS traces visualize fast processes with di-exponential decays of the autocorrelation curves, which indicate very broad distributions of two sizes (with maxima at $D_{h,50\text{ °C}}=10$ and 68 nm). Although the correlation curves are slightly shifted to each other, the available species suggest the presence of identical averaged aggregation sizes. This effect is observed in the DLS traces under similar conditions for the reference copolymer (UCP14COOH) with carbonic acid as end group comparing the aggregation behaviours with and without present iron ions (in the appendix, Figure S68 (p.270)). The slight changes in the aggregation behaviours are apparently based on the salt effect, which is related to the Hofmeister series⁸¹.

Above the clouding temperature, the large ligand leads to an enhanced steric repulsion between neighbouring polymer chains as sketched in Figure 38f (p.112). In relation to the small dimensions of the aliphatic dodecyl end group in the micelle's core, the associated larger thermoresponsive coil enables only the association of smaller aggregation numbers (detailed DLS analysis in the appendix, Figure S69 (p.271)).

Addition of iron ions may lead to a reorganization of the aggregates induced by the complexation with the triazole end groups, now in the centre of the micelle (Figure 38g-h). As before, the enlarged ligand volume of the hydrated chain in solution above the cloud point is responsible for the small number of chains per micelle, which prevents the arrangement of extended 1D complexes.

The investigation of the novel set of MCLs bearing UCST-character successfully supports the results obtained from their LCST analogues and underpinned the drawn

hypothetic picture of chapter 11.2.2 outlined in Figure 34 (p.103). In dependence of the reverse thermoresponsive behaviour, their aggregation behaviours conform to each other in the expected contrary manner. The UCST ligands showed the molar mass dependent aggregation process, which promotes the desired interactions between Fe^{2+} ions and triazole functionalized copolymers. The volume changes between the different thermoresponsive chain states could be used to reversibly switch “on demand” the structure of the complexes in solution.

11.2.5. Consistent Aggregation Behaviours of Hemi-Telechelic Macromolecular Triazole Ligands with LCST and UCST

In the previous subchapters 11.2.3 and 11.2.4, the individual aggregation behaviours of thermoresponsive hemi-telechelic ligands were studied for both phase transitions with respect to the LCST and UCST processes in order to confirm the autonomous attractive interactions between iron ions and triazole end group independently of the polymer system. Besides, the hypothetical picture for the aggregational behaviour of the ion sensitive polymer ligands in solution, as drawn in subchapter 11.2.2, seems to be verified based on the agreement of the consistent data from both tested synthetical series.

Both series showed identical molar mass dependent aggregation behaviours, whose dimensions match in the reversed temperature direction due to the contrary phase transitions of LCST and UCST. Therefore, only the common chain states as such hydrophilic (at $T=22\text{ }^{\circ}\text{C}$ for LCST and $T=50\text{ }^{\circ}\text{C}$ for UCST ligands) or hydrophobic (at $T=35\text{ }^{\circ}\text{C}$ for LCST and $T=2\text{ }^{\circ}\text{C}$ for UCST ligands) are compared.

In agreement to the sketched hypothesis in Figure 34 (p.103), the ligands possess similar dimensions and morphologies of scattering objects in dependence of the occupied chain states. While the DLS traces are shown for the small and large ligands in Figure 36 (p.108) for LCST and in Figure 39 (p.113) for UCST copolymers.

The classification of small and large ligands referred to Figure 34a/h (p.103) is chosen with respect to the present aggregation behaviour in solution. While the smaller macromolecules respond to available iron ions independently of the occupied chain state (Figure 34c-d and e-f), the larger conjugates enable the formation of growing aggregation structures only for the hydrophobic character of the collapsed chain (Figure 34j-k and l-m).

For both thermoresponsive polymer systems, the change of this characteristic aggregation behaviours is observed for critical molar masses below $7\text{ kg}\cdot\text{mol}^{-1}$, as apparently the iron-triazole complexes may offer only a limited volume in their coordination structure available for each ligand (summarized in the appendix, Table S16 (p.265) and Table S18 (p.270)), which is predefined by the metal distance in the

N^1, N^2 -bridging mode of the triazole end groups. Too large ligand rests of the grafted macromolecular tails induce strain in the complex structures, which suppresses their extensive growth.

In the hydrophilic chain state, the small ligands (P4k and UCP4k) bear micellar aggregation behaviours consisting of multiple species (Figure 34b/g). Upon the addition of Fe^{2+} ions, the reduced space requirement of the low number of repeat units allows an association of numerous ligands in an extended coordination structure (Figure 34c/f), while the hydrophobic regime induces colloidal aggregates of defined dimensions. The coil volume of the small ligands is further reduced, which improves the formation of extended and defined complex structures in presence of iron ions (Figure 34d/e).

In the hydrophilic chain state, the larger ligands (P23k and UCP27k) show small micellar structures in pure water (Figure 34i/n). The enlarged space requirements of the well-hydrated chains with higher degree of polymerization prevent the formation of enlarged complexes upon the addition of iron salt (Figure 34j/m). In the hydrophobic regime, the voluminous copolymer coils collapse and offer sufficient enough space for the coordinative association in enlarged clusters with defined dimensions (Figure 34k/l).

Amidst the published knowledge of iron-triazole complexes, the matching of the DLS data of both series suggests the process of coordination as main driving force for the tremendous growth of the aggregates in the presence of Fe^{2+} ions and strengthens the hypothetical picture of the drawn ligand size dependent aggregation process.

11.2.6. Morphology Switching of Multidentate Thermo-responsive Fe^{2+} Copolymer Systems

A comparative study of the solution- and iron(II) ion coordination behaviour was conducted for two fundamentally different polymer architectures: the hemi-telechelic design discussed in chapter 11.2.2 (p.101) *versus* a multidentate copolymer ligand with triazole side chains. The particular benefit of this synthetic approach lies in the control over the number of triazole units per chain segment by the comonomer composition in the polymerization reaction feed in accordance with section 11.2.1 (p.94).

In contrast to the hemi-telechelic polymer ligand with a single triazole unit at one chain end, the multidentate design provides the possibility for multiple physical crosslinks between different chains by iron(II) ion coordination, which leads to a polymer network architecture. The thermal response should be maintained even in the coordination network with the chain segments between the crosslink points swelling or collapsing upon the phase transition.

The formation of such structures is mainly dependent to the percentual incorporation of the triazole monomer in the macromolecule but not much to their molar mass. As UCST copolymers of low molecular mass respond sensitively to slight changes in their composition, a higher degree of polymerization had to be synthesized (than for the LCST conjugates). Again, the hypothetical architectures show just the elemental structural unit that may represent an excerpt of larger scattering objects.

In Figure 40, the hypothetical aggregation behaviour of the multidentate copolymer ligands is sketched in aqueous solution exhibiting either LCST (C4.8k5%-C4.6k15%) or UCST chain characters (UCP11.6k2.5%-UCP13.7k10.0%).

The ligands show a strong micellar aggregation with a high number of copolymer coils. The carboxylic acid end group may be protonated by the slightly acidic MilliQ water (pH~5-6) causing a strong assembling of the copolymer chains with the dimethyl propanoic acid group located in the centre and the hydrophilic triazole head groups towards the outer surface of the aggregates (confering to Figure 40b/e).

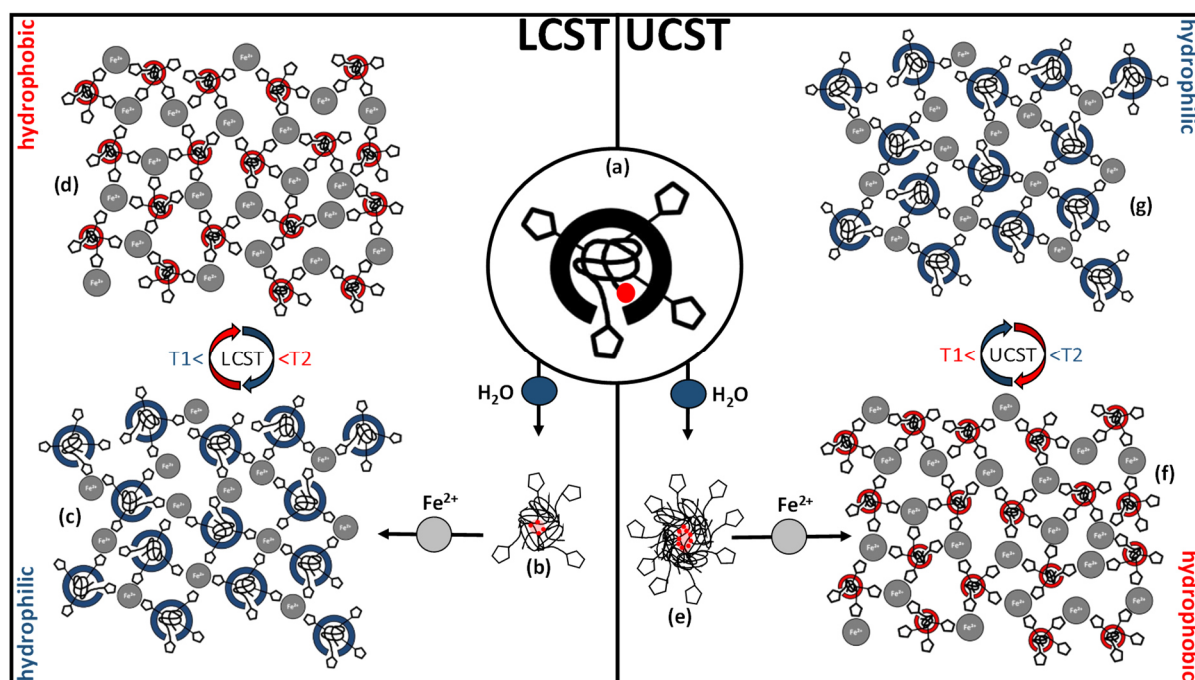


Figure 40: Overview of the proposed structural organization for the multidentate coordination copolymer ligands with LCST (C4.8k5%-C4.6k15%) and UCST chain behaviour (UCP11.6k2.5%-UCP13.7k10.0%) with respect to iron ion coordination and thermal variation of the solvation state. These architectures represent the elemental structural unit, of which many may assemble to form the larger scattering objects observed in DLS. The triazole units are schematically represented by pentagons and the C2 alkyl chain as short red circle.

Upon the temperature variations, the coil-to-globule transition switches between hydrophilic and hydrophobic behaviour of the thermoresponsive chain. In pure water, the ligands form smaller aggregates in the hydrophilic state due to the well hydrated chain (below T_c for LCST and above T_c for UCST), while they show a strong assembling upon the hydrophobic character of the collapsed copolymeric chain

(above T_c for LCST and below T_c for UCST). Although the dimensions of the aggregates of LCST and UCST ligands are comparable, the UCST conjugates tend to larger scattering objects, what may be reasoned in the higher degree of polymerization indicated by the DLS results presented in the appendix, Figure S71a/c (p.273) for LCST and Figure S73a/c (p.276) for UCST analogues.

The addition of iron (II) salt induces an enhanced association due to the attractive forces between the iron ions and the triazole head groups, which bring various chains and chain segments together (Figure 40c/f) so that larger aggregates of iron-copolymer complexes are produced, as sketched in Figure 40b-c and e-f below the T_c at 20 °C for LCST copolymers and above the T_c at 70 °C for UCST conjugates. Due to the strong association, the coordination system may respond with precipitation to the addition of iron ions (as denoted in the appendix, Table S20 (p.274) for LCST ligands and Table S22 (p.277) for UCST conjugates). In such cases, the DLS analyses is not appropriate.

Referred to the published knowledge of likely complexation motives for the class of [1,2,4]-triazoles (indicated in Figure 35i (p.105)), the coordination between triazole groups and ions may induce the association of multiple ligands to larger coordination networks and scattering objects.¹³⁸

Higher triazole fractions in the chain provoke stiffer coordinational networks with increased crosslink densities. In the hydrophilic chain state, the thermoresponsive chain segments between two coordinated triazole units are well-hydrated and swells the entire complex network. Despite the multiple triazole units, the interactions between hydrophilic chain and water represent a repulsive force, which can affect a lower assembling with smaller scattering objects in comparison to the hydrophobic chain behaviour as observed by the comparative DLS traces in the appendix, Figure S71b/d (p.273) for LCST and Figure S73b/d (p.276) for UCST. The variation of temperature interchanges the chain behaviour to the hydrophobic state, which produces an association of the formed complexes followed by a simultaneously contraction of the network loops (sketched in Figure 40c/d and g/f).

The hypothetical structure models provided here are referenced to the experimental data in the following sections.

11.2.7. Coordination Site Fraction Dependent Aggregation Behaviour of Multidentate Poly(NIPAAm-co-APTRZMAAm)-EMP with LCST Character

In the following, the solution- and coordination behaviour is compared for the designs of poly(NIPAAm)-DMP-APTRZ *versus* the multidentate copolymer ligand: Poly(NIPAAm-co-APTRZMAAm)-EMP carries multiple triazole units in the side chain and provides as such the possibility for multiple physical crosslinks between different

chains by iron(II) ion coordination leading to a metallopolymer (*cf.* 11.2.2 (p.101)). The anticipated structure formation of the multidentate ligand in aqueous solution (1 wt%), as outlined in Figure 40 (p.118), follows the behaviour of the hemi-telechelic system, which is an increase of the chain aggregate dimensions, when raising the temperature above the T_c in absence of iron ions. In presence of Fe^{2+} ions, the scattering objects further grow, as the multidentate design provides the possibility for numerous physical crosslinks between neighbouring chains *via* ion coordination of the triazole side groups, which structurally results in an extended coordination network architecture characteristic for a metallopolymer. The thermal response should be maintained even in the coordination network with the chain segments between the crosslink points swelling below or releasing water above the phase transition (*cf.* Figure 40c/d (p.118)).

Turbidity measurements

In order to investigate the effect of the overall polymer architecture, a novel copolymer of NIPAAm with a triazole-containing monomer (APTRZMAAm) was synthesized (as described in section 11.2.1 (p.94)), which carries multiple triazole coordination sites along the polymer backbone. As an interesting side note, the as synthesized copolymer in water had to be first heated above the phase transition and cooled down in order to obtain a clear solution. This suggests a kinetic hindrance of the solvation process by strongly interacting chains in the dry state.

The copolymers C5k5%-C4k15% contain a content of the hydrophilic triazole comonomer APTRZMAAm between 5 to 15 mol%, which provoke a strong shift of the cloud points from 36.6 to 44.7 °C in contrast to the hemi-telechelic poly(NIPAAm) homopolymers (in the appendix, Figure S59 (p.264)). This shift indicates the expected influence of the polar monomer, which increases the overall hydrophilicity (Figure 41a).

By the addition of salt $\text{Fe}(\text{BF}_4)_2 \cdot 6\text{H}_2\text{O}$, the T_c is lowered in correlation to the rising triazole content present in the ligand ($\Delta T_{c,H_2O/Fe} = 0.6\text{--}12.7$ K, Table 9 and Figure 41a-b). All samples responded by forming precipitates above their T_c . For C4.2k15% with the highest triazole content of 15% in the copolymer, precipitation was observed even below the cloud point (20 °C). The ill-defined turbidity curves for 10% and 15% APTRZMAAm content are attributed to larger flakes of polymer precipitates circulating through the light beam in the stirred cuvette. The observed behaviour clearly indicates the increased attraction between the copolymer chains with higher triazole ligand content in the presence of Fe^{2+} ions.

DLS measurement

In accordance with the previous aggregation studies of the hemi-telechelic polymer ligands, the DLS of 1.0 wt% copolymer solutions was performed to indirectly monitor

the formation of complex structures upon addition of $\text{Fe}(\text{BF}_4)_2 \cdot 6\text{H}_2\text{O}$ salt at different temperatures. Again, the relative changes of the correlation curves are contrasted between comparative measurement conditions. The data are shown in Figure 41c-d for the triazole-rich copolymer ligand C4.2k15%, while the complete data set is depicted for molar triazole contents of $[\text{APTRZAAm}] = 5\text{-}15 \text{ mol}\%$ in the appendix, Figure S71 (p.273). The here reported average dimensions serve predominantly as indicator for structural changes of the scattering objects, since exact values depend on the specific experimental conditions and may be subject of variation due to kinetic effects.

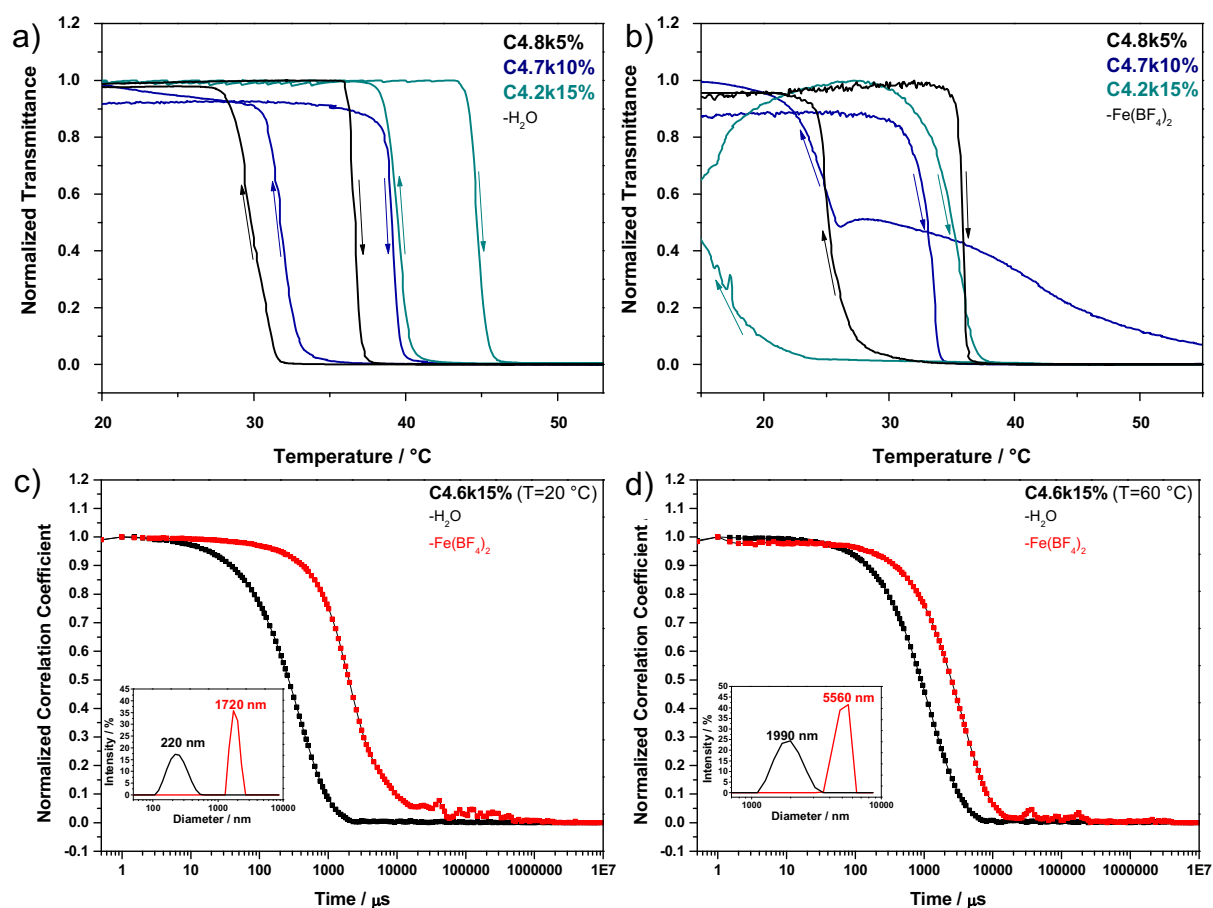


Figure 41: Cloud point determination of the macromolecular multidentate ligands (C4.8k5%-C4.6k15%) with LCST behaviour with varied fractions of the triazole monomer APTRZMAAm in the chain as 1.0 wt% aqueous a) solution without ($\lambda = 550 \text{ nm}$) and with iron ions ($\lambda = 740 \text{ nm}$) by UV-Vis spectroscopy. Iron-ion-dependent aggregation behaviour of the multidentate ligand C4.6k15% with its (apparent) hydrodynamic diameter below (c) and above (d) the T_c of a 1.0 wt% solution. The aggregation sizes are analysed by intensity.

In Figure 41c, the DLS curves are illustrated at low temperature ($20 \text{ }^\circ\text{C}$) in pure water (black curve) and iron solution (red curve). Below the cloud point in pure water, the copolymer forms faster and defined scattering objects with a monoexponential decay of the black trace ($D_h = 220\text{-}459 \text{ nm}$, Table 9). This magnitude indicates a micellar aggregation structure with a high number of associating copolymer coils. The carboxylic acid end group may be protonated by the slight acidic MilliQ water ($\text{pH} \sim 5\text{-}6$) causing a strong assembling (Figure 40b (p.118)). Even below their T_c at 20°C , all

copolymer ligands responded sensitively to the addition of iron salt by growing dimensions (red curve, $D_h=1400-1700$ nm; Figure 41c). This significant growth suggests a strong attraction between the chains by the formation of coordination networks in alignment to Figure 40c (p.118).

Upon raising the temperature to 60 °C above the cloud point, the DLS traces (black curve) of the aqueous copolymer solutions in Figure 41d shows an increase of the aggregate dimension (apparent value of $D_h=2000-3100$ nm, summarized in Table 9). Under these conditions, the copolymers turn hydrophobic and assemble into colloidal scattering objects, which tend to smaller sizes with increasing number of hydrophilic triazole units per polymer chain (*cf.* appendix, Figure S71 (p.273)).

Upon the addition of iron salt (red curve), the colloidal aggregates further accumulate ($D_h\sim 4800-9500$ nm, Table 9) and an insoluble precipitate is formed for all ligands refer to Figure 40. Due to the precipitation, the DLS data becomes inadequate, as the system is not in thermodynamic equilibrium under these conditions. Even though the measurements are used as indicator for the aggregation tendency.

Table 9: Aggregation and thermoresponsive behaviour in terms of molar mass \bar{M}_n , the cloud point (T_c), hydrodynamic diameter at 20 and 60 °C of the coordination copolymer poly(NIPAAm-co-APTRZMAAm)-EMP. Aggregation in Fe^{2+} -solution described as apparent values.

Sample Code	$\bar{M}_n / \text{kg}\cdot\text{mol}^{-1}$	H ₂ O			Fe ²⁺ _{aq}		
		$T_{c, \text{heat}}^{[b]} / \text{°C}$	$D_{h, 20 \text{ °C}} / \text{nm}$	$D_{h, 60 \text{ °C}} / \text{nm}$	$T_{c, \text{heat}}^{[b]} / \text{°C}$	$D_{h, 20 \text{ °C}} / \text{nm}$	$D_{h, 60 \text{ °C}} / \text{nm}$
C4.8k5%	4.8	36.6	459 106	3090	35.9	1420	9450 ^[a]
C4.9k10%	4.9	39.1	255	2670	33.1	1480	5560 ^[a]
C4.6k15%	4.6	44.7	220	1990	32.4	1720 ^[a]	4800 ^[a]

^[a] Precipitation occurred.

^[b] The values were extracted from the heating cycle

As the copolymers yield very large aggregates upon Fe^{2+} salt addition and partially precipitate, no TEM investigations were attempted. The obtained results for the multidentate ligand poly(NIPAAm-co-APTRZMAAm)-EMP show a marked response of the aggregation and thermal behaviour upon the addition of iron salt. This extreme change in properties is associated with the hypothetical picture of a coordination network sketched in Figure 40 (p.118).

11.2.8. Coordination Site Fraction Sensitive Aggregation Behaviour Multidentate Poly(AAm-co-AN-co-APTRZMAAm)-EMP with UCST-Character

In agreement with the previous chapter, the thermal response of the UCST conjugates were investigated in copolymer solutions with a concentration of 1.0 wt% under identical conditions. As sketched in Figure 40 (p.118), the aggregation of the multidentate ligand poly(AAm-co-AN-co-APTRZMAAm)-EMP with UCST-character matches with the reverse behaviour of the contrary thermoresponsive system poly(NIPAAm).

Turbidity measurements

Compared to their LCST analogues, the solution behaviour of multidentate ligands UCP11.6k2.5%-UCP13.7k10.0% behaves in the expected reversed manner. The measured temperatures of turbidity demonstrate again the great influence of the hydrophilic monomer APTRZMAAm (2.5-10.0%) onto this value compared to the poly(AAm_{0.5}-co-AN_{0.5})₂₀₀-EMP copolymer with identical degree of polymerization and AAm/AN ratio (in the appendix, Table S5 (p. 230)). With increasing incorporation of the triazole monomer, the cloud point temperature drops from 50.5 to 35.6 °C (Figure 42a (p. 124)).

After the addition of the iron salts, the T_c rises slightly with increasing triazole fraction in the copolymer ($\Delta T_{c,H_2O/Fe}$ =1.2-13.1 K, in Figure 42a-b and in the appendix, Table S21 (p.275)). All samples responded by forming precipitates even above their cloud points in the hydrated chain state at 70 °C. The turbidity measurements indicate fluctuations in the copolymer solutions by formed macroscopical coordination clusters leading to complex curve shapes with significant deviations between heating and cooling cycle. This behaviour indicates a tremendous growth of the aggregates driven by the addition of iron ions and the subsequent formation of extended complex structures.

DLS measurements

As for the multidentate LCST ligands, DLS measurements of 1.0 wt% copolymer solutions were performed to contrast relative changes of aggregation behaviours between comparative measurement conditions. The data are shown in Figure 42c-d for the triazole-rich copolymer ligand UCP13.7k10.0%, while the complete data set is depicted for molar triazole contents of [APTRZAAm]=2.5-10.0 mol% in the appendix, Figure S73 (p. 276). The measurements with and without iron ions were specifically measured in aqueous solution below and above their UCST (T_1 =20 °C; T_{2,H_2O} =60 °C and $T_{2,Fe}$ =70 °C).

In Figure 42c, the DLS traces are shown for the multidentate ligand poly(AAm-co-AN-co-APTRZMAAm)-EMP with the highest triazole content (10 mol%) at low temperature (20 °C) in pure water (black curve) and iron solution (red curve). Below their cloud point, the copolymer forms very slow but defined scattering objects with a monoexponential decay in pure aqueous solution, indicating significant scattering sizes (D_h =3100-4800 nm; Table 10), which were driven by the strong attraction between the dehydrated chains.

After the addition of iron salt, the ligand responded sensitively by forming insoluble, macroscopic precipitates. Under these conditions, the system does not represent the thermodynamic equilibrium, so that the DLS data becomes inappropriate. The trace

(red curve) is illustrated even though, delivering an important indicator for the described aggregation tendency. In presence of Fe^{2+} ions, the multidentate copolymer ligands precipitate promoting the tremendous growth of the aggregates due to the formation of extended complex structures. In comparison to the aggregation behaviour of the hemi-telechelic polymer ligands with UCST-character (described in chapter 11.2.4 (p.110)), the coordination process *via* multiple triazole unites seems to be the dominating component for the determined attractive chain interaction.

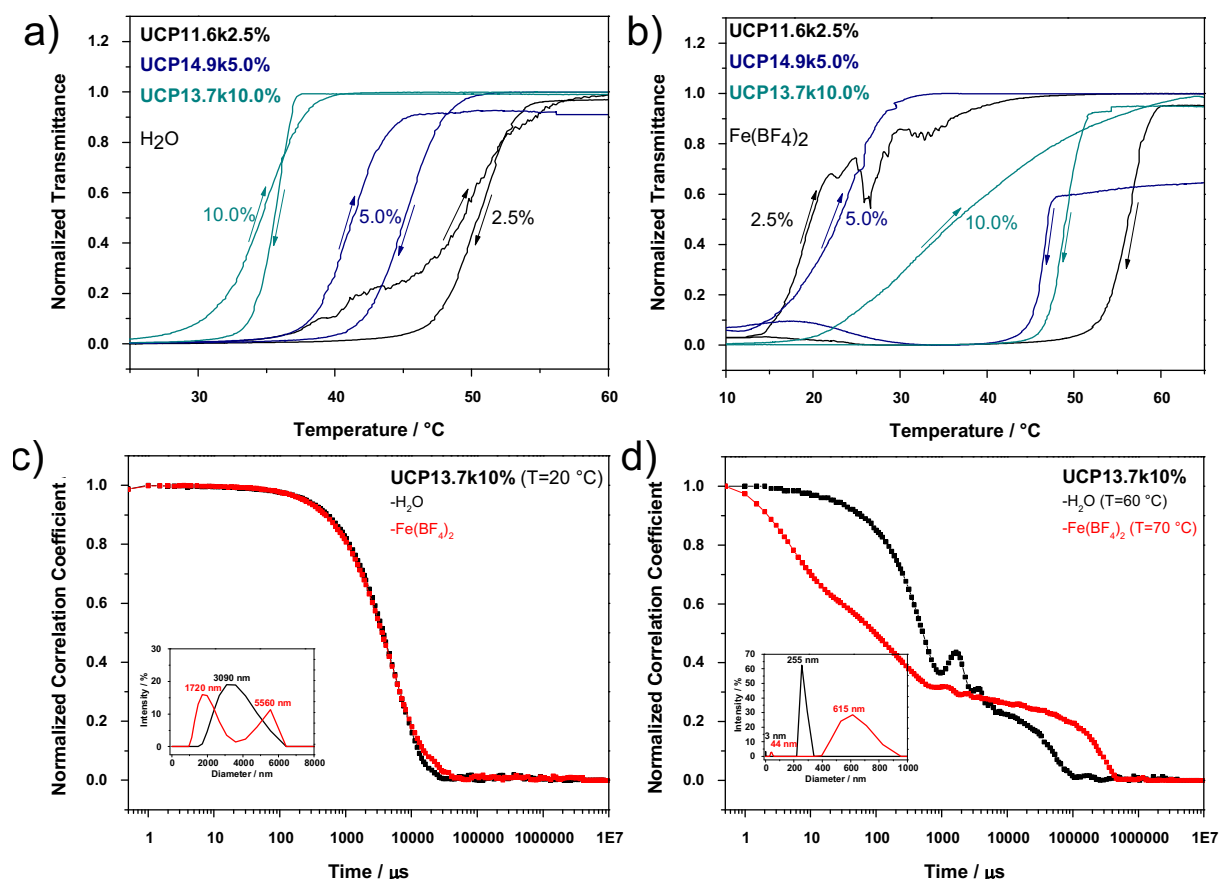


Figure 42: Cloud point determination of the macromolecular multidentate ligands (UCP11.6k2.5%-UCP13.7k10.0%) with UCST behaviour with varied fractions of the triazole monomer APTRZMAAm in the chain as 1.0 wt% aqueous solution without ($v=550$ nm) and b) with iron ions ($v=740$ nm) by UV-Vis spectroscopy. Iron-ion-dependent aggregation behaviour of the multidentate ligand UCP13.7k10% with its (apparent) hydrodynamic diameter below (c) and above (d) the T_c of a 1.0 wt% solution. The aggregation sizes are analyzed by intensity and represent, as such, a snapshot of kinetical precipitation processes in presence of iron ions.

In Figure 42d, the DLS measurements are illustrated above the point of turbidity at 60 °C in aqueous solution (black curve) and 70 °C in iron solution (red curve). In water, the copolymer chain is well-hydrated and forms multiple aggregates species (black curve, $D_h=3$ and 255 nm; summarized in Table 10). While the smallest species may belong to single chains, the large species indicate a micellar assembling.

The addition of iron salt leads to a tremendous growth to colloidal aggregates followed by precipitation. The DLS trace (red curve) confirms the change of the aggregation behaviour by a shift of the broad size distribution to slightly higher correlation times

and is not discussed further. The precipitation leads to the temporal observation of the aggregation behaviour during the DLS measurement, which is beyond the thermodynamic equilibrium. As before, all copolymer ligands precipitated even above the T_c upon the addition of iron salt.

Table 10: Aggregation and thermoresponsive behaviour in terms of molar mass \bar{M}_n , the cloud point (T_c), hydrodynamic diameter at 20 and 60 °C/ 70 °C of the coordination copolymer poly(AAm-co-AN-co-APTRZMAAm)-EMP. Aggregation in Fe^{2+} -solution described as apparent values.

Sample Code	$\bar{M}_n / \text{kg} \cdot \text{mol}^{-1}$	H ₂ O			Fe ²⁺ _{aq}		
		$T_{c, \text{cool}}^{[b]} / \text{°C}$	$D_h, 20 \text{ °C} / \text{nm}$	$D_h, 60 \text{ °C} / \text{nm}$	$T_{c, \text{cool}}^{[b]} / \text{°C}$	$D_h, 20 \text{ °C} / \text{nm}$	$D_h, 70 \text{ °C} / \text{nm}$
UCP11.6k2.5%	11.6	50.5	(712) 4800	122 615	56.2	5560 ^[a]	255 ^[a]
UCP14.9k5.0%	14.9	45.2	3090	5 615	46.2	5560 ^[a]	(4) 342 ^[a]
UCP13.7k10%	13.7	35.6	3090	(3) 255	48.2	1720 5560 ^[a]	(44) 615 ^[a]

^[a] Precipitation occurred.

^[b] The values were extracted from the cooling cycle.

The precipitation of the multidentate ligand independently of the thermoresponsive properties corroborate the expected picture illustrated in Figure 40e-g (p.118) and confirms the coordination as main driving force for the observed assembling. The present ligands with UCST character show the expected reverse aggregation behaviour compared to the LCST conjugates. The more sensitive respond to iron ions may be reasoned in higher degree of polymerization of the UCST ligands, which enlarged just the absolute number of triazole units per macromolecular chain.

11.3. Conclusion and Outlook of Macromolecular Coordination Ligands

The proposed strategy (in the appendix, Figure S55 (p.259)), to introduce thermoresponsiveness to ion-coordinating building blocks, could be successfully demonstrated with two macromolecular architectures based on a hemi-telechelic and a multidentate ligand promoted by their fundamentally deviating aggregation behaviours. To reach these architectures, the coordination site 3-(4H-1,2,4-triazol-4-yl)propan-1-amine served as functionalization of the chain transfer agent DMP (by introduction of a single triazole unit) and an acrylamide monomer (by incorporation of several triazole units per chain).

The RAFT polymerization of NIPAAm or AAm/AN in presence of the triazole coupled CTA DMP-APTRZ enabled the synthesis of thermoresponsive hemi-telechelic ligands with LCST or UCST behaviour. The controlled conditions were exploited to vary synthetically the steric demand of the polymer ligands in the complexes, which could be further tuned non-invasively upon variation of the temperature due to their volume transitions.

The hemi-telechelic ligands with either LCST- or UCST-characters, showed in presence of iron ions and identical chain state (hydrophilic/ hydrophobic) similar aggregation behaviours dependent to their molar mass, so that they were further analysed with respect to their

specific aggregation behaviours for ligands with small ($\bar{M}_n < 7 \text{ kg}\cdot\text{mol}^{-1}$) and large steric requirements ($\bar{M}_n \geq 7 \text{ kg}\cdot\text{mol}^{-1}$). Short polymers suggested enormous attractions between chains and iron ions independently of the temperature, leading to a substantial growth of the aggregates, which is attributed to extended complex formation. The larger conjugates allowed an external regulation of the aggregation behaviour inducing a reversible assembly-disassembly of the complexes in dependence of the temperature due to the thermoresponsive volume transformation of the ligands, which supports the denoted hypothetical aggregation behaviour. Presumably, such behaviour could be applied for reversible coordinative coatings of metal particles and surfaces, for purification issues, thermoresponsive sensing- and ion-catch-release devices (related to literature¹³⁴).

In comparison to the hemi-telechelic ligands, a triazole monomer offered the opportunity to introduce multiple coordination triazole units to the macromolecular chain for a multidentate design, which serve as physical crosslinks between different chain segments resulting in the formation of a polymer network architecture according to a metallopolymer.

All multidentate ligands with UCST or LCST behaviour show for both a temperature increase and iron salt addition a growth in aggregate dimension. The assumed network formation upon iron complexation is corroborated by the fact that the systems precipitate above the phase transition. The multidentate ligands with the highest triazole content (10 to 15 mol%) precipitates even at lower temperatures, evidencing a denser network.

Consequently, this iron-sensitive polymer system revealed another promising tuneable opportunity of the coil-to-globule transition, which might also be suitable as stable selective coordination anchor for coating of metal ions, particles and surfaces. Additionally, the application as potential molecular ion sensor could be enabled in correspondence to recent literature.²⁴⁴

12. Molecular Design of Thermoresponsive Non-Viral Vectors for Gene Delivery: Variable Composition and Skeletal Architectures by RAFT Copolymerization with AAm

12.1. Introduction to Thermoresponsive Copolymer Vectors

Nowadays, gene therapy gains in importance as a promising pathway in the scope of advanced medicine.^{151,245,246} By the emerging pandemic of coronavirus 2, the gene delivery method abruptly entered the daily life of billion people through the accelerated development of modern mRNA vaccines.^{146–148} Generally, the efficiency of such therapy depends tremendously on the design of the carrier molecules.^{19,158,247} These vectors mostly possess a viral nature: Although they exhibit remarkable transfection efficiencies, their viral character may cause immunogenic or pathogenic issues.¹⁴⁵ Another class is represented by non-viral vectors based on cationic lipids or polymers, which overcome the mentioned drawbacks, but tend to lower transfection efficiencies.^{142,150}

Compared to their lipidic analogues, polymeric vectors feature a very defined size distribution, a high stability against the enzyme nuclease and a tuneable hydrophilicity.¹⁵⁷ Therefore, cationic polymers continue receiving close attention for gene delivery purposes.²⁴⁸ The polymeric vectors give access to an adjustable counterbalance between high gene delivery efficiency and simultaneous low cytotoxicity, which depends on many parameters such as charge density in the molecule, the chemical type of charge centre, the macromolecular mass of the vector, the grafting functionality and the final stability of the polyplexes in the surrounding medium.¹⁵¹ The number of charges is controllable in the synthetical pathway of the vectors by the introduction of DNA-binding side groups.⁵⁸ The molecular mass and the dispersity of its distribution affect the formation of the polyplexes and represent a major impact for the undesired cytotoxicity.^{249–252}

The first reported polymeric vectors were based on polylysine (PLL), which is generally synthesized by basic polycondensation of lysine in aqueous medium.¹⁵⁴ Polyethylenimine (PEI) is another common polymer vector, which is a lead representing compound demonstrating good transfection activity in different types of cells, thanks to both high charge density and endosomal pH buffer capacity.^{253,254} The transfection performance of these polymer vectors depends on their macromolecular structure as well as the molecular mass, in which 25 kDa branched PEI (hereafter denoted as bPEI) and 22 kDa linear PEI (IPEI) have turned out to be the best. Followingly, bPEI was applied as gold standard for non-viral gene transfection.¹⁴⁵ Unfavourably, the PEI is not biodegradable and followingly cytotoxic both *in vitro* and *in vivo*.^{155,156}

The gene delivery research aims to find potential vectors fulfilling the contradictive demands of a high transfection efficiency combined with a low cytotoxicity, which are referred to the interplay of coordinative strength in the polyplexes (cellular uptake and enzymatic degradation of the transgene) and the proper intracellular release of the genetic material with a high biodegradability of the vector.¹⁵¹ These processes are requiring specific vector hydrophilicities for each step to undergo efficiently distinct cellular mechanisms.¹⁵¹ As

conventional non-viral polymeric vectors deliver just static hydrophilic characters, the implementing of an additional thermoresponsive chain behaviour is tested to overcome these deficiencies.⁵³

Thermoresponsive polymers in water generally exhibit a reversible abrupt change in hydrophilicity, which can be characterized by the clouding temperature of the polymer solution, in response to the external trigger of temperature. Depending on the system, the polymer proceeds this change at a critical temperature from hydrophilic to hydrophobic (lower critical solution temperature (LCST)) or reverse (upper critical solution temperature (UCST)).⁶² The use of such polymers for "temperature-sensitive gene delivery" has been reported in different contexts.^{58,255–258} Common explored polymer systems are applying poly(*N*-isopropylacrylamide), poly(*N,N*-diethylacrylamide), poly(methyl vinyl ether), poly(*N*-vinylcaprolactam) or poly(AAm-co-AAc).^{19,158}

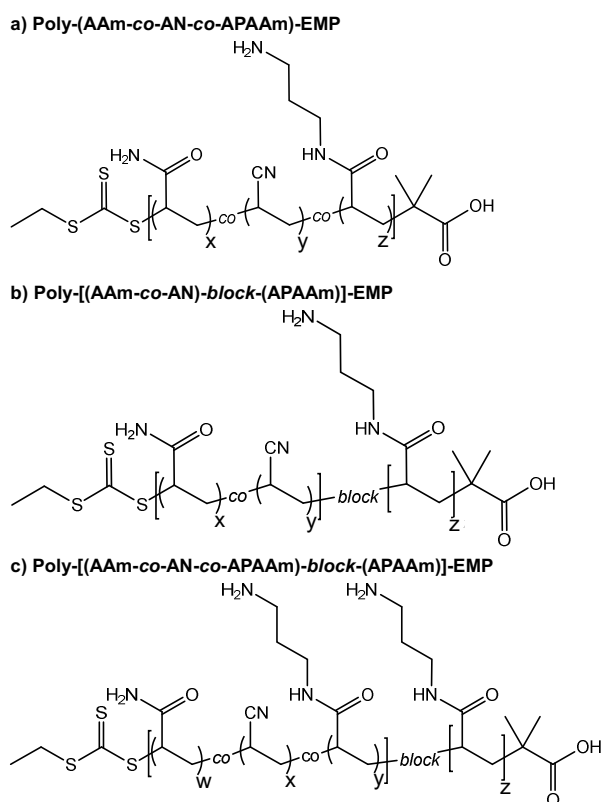


Figure 43: General chemical structures of the tested copolymer vectors a) poly(AAm-co-AN-co-APAAM)-EMP, b) block copolymers poly[(AAm-co-AN)-block-APAAM]-EMP and c) hybrid block copolymer poly[(AAm-co-AN-co-APAAM)-block-APAAM]-EMP reported in this study.

These smart vectors show an intelligent formation-dissociation behavior of the polyplexes in dependence of the temperature variation, which is enabled by the internal coil-to-globule transition of the thermoresponsive chains in solution. Such transfection process, which is triggered by the stimuli of temperature, has been successfully demonstrated in the literature.^{58,159} This facility opened up another great synthetic variety applicable in the gene delivery research field. Highly developed vectors are accessible driven by the investigation of

novel polymer systems, modified polymerization techniques and several different skeletal architectures.^{19,158,160}

Hereby, the synthesis, thorough characterization, as well as the evaluation as DNA carriers is introduced for gene transfection purposes in various *in vitro* cellular contexts utilizing a consistent series of thermoresponsive copolymers (denoted in Figure 43). The tuneable UCST copolymer poly(AAm-co-AN) is copolymerized under RAFT conditions related to chapter 7 (p.43) in different skeletal architectures with varying fractions of the cationic monomer aminopropyl acrylamide (APAAm), which was synthesized according to a modified procedure and referred to an innovative copolymer system in the literature.^{19,259} The study employs non-viral cationic vectors, whose dynamic transfection properties can be adjusted by the intramolecular hydrophilic-hydrophobic balance in the monomer composition.

12.2. Results and Discussion of Thermoresponsive Copolymer Vectors

12.2.1. Composition and Architecture of the Copolymers

The transfection properties were investigated in relation of the copolymer composition and the structural architecture. A copolymer system based on the copolymerization of acrylamide and acrylonitrile with robust and adjustable thermoresponsive UCST properties was chosen for the application as copolymer vectors by the copolymerization with the cationic monomer aminopropyl acrylamide. The bare UCST system poly(AAm-co-AN) is expected to deliver biocompatible properties.^{260–262} Its UCST behaviour allows the reversible and instant change from a hydrophilic to hydrophobic chain behaviour along the coil-to-globule transition in aqueous solution by the external trigger of temperature.⁵⁹ The composition of the monomers affects the hydrophilic-hydrophobic balance of the total copolymer and shifts its transition temperature, which is indicated by optical clouding of the polymer solution.

As the general transfection experiments are performed under standard conditions, the influence of the thermal switching onto the transfection process cannot be monitored. The diluted working concentration of the vectors in the cell tests provoke a lowering of their cloud point below the temperature of the experiment so that all copolymers occupied the hydrophilic chain state. These conditions allow the focused investigation of the compositional and structural vector properties independent of thermoresponsive processes. Besides, the experimental conditions are defined/adjusted for the study of the thermoresponsive impact on the processes like DNA condensation and transfection.

The set of samples was collected to comprehensively study the influences of the specific moieties and substructures present in the different vectors, which are sketched in Figure 43c. Hereby, the copolymers from AAm and AN without any binding site for pDNA were applied as references. Terpolymers with different fractions of the comonomer aminopropyl acrylamide, carrying a primary amine side group, were employed for the formation of active

vectors in dependence of their differing architecture. In the terpolymers, the APAAm repeat units are either randomly distributed over the whole macromolecule, present in a second homoblock in the end of the macromolecule, or forming a hybrid structure of both. The precise composition between AAm, AN and APAAm, as well as the corresponding sample code is denoted for each vector in Table 11, which indicates additionally the localization of APAAm in the macromolecule.

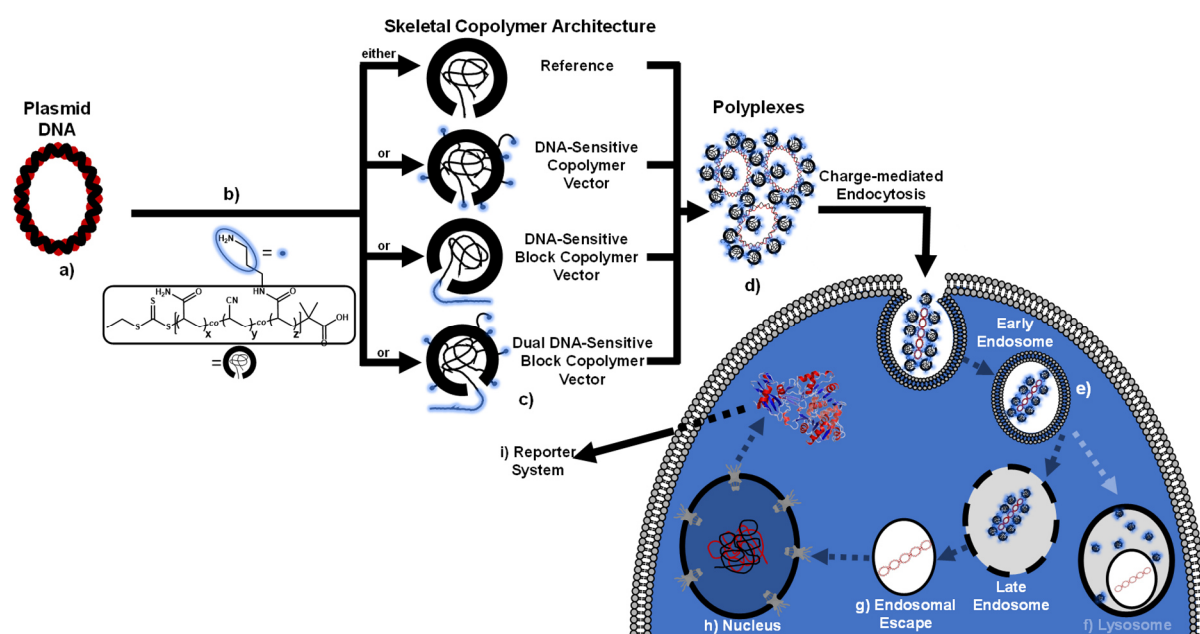


Figure 44: Exemplary illustration of the gene delivery process of a non-viral copolymeric vector in dependence of the investigated thermoresponsive copolymer architectures. The plasmid DNA a) is condensed by the cationic side groups (blue) in the copolymer vector b), which possesses one of the tested architectures c). After the formed polyplexes d) enters the cell *via* charge-mediated endocytosis, the early endosome e) undergoes different potential intercellular processes *via* undesired lysosome f) or target endosomal escape g) to deliver the genetic material to the cytoplasm, where it can be translocated to the nucleus h), which can express the DNA i).

Based on the knowledge of chapter 7 (p.43), the set of copolymers was prepared in RAFT copolymerizations to control efficiently the molar mass and dispersity leading to very defined vectors. The viability of the thermoresponsive basis was studied using pure poly(AAm-co-AN) copolymers without amine functionalities as reference, in order to evaluate the unlikely formation of polyplexes along acrylamide side groups. To exclude a potential cytotoxicity of the trithiocarbonate group, which introduced by the CTA in the RAFT copolymerization, two analogous copolymers with and without CS₃ functionalization were synthesized utilizing the synthesis strategies of FRP (denoted as R1) and RAFT copolymerization (denoted as R2-R4). For the RAFT copolymers, the biochemical role of acrylonitrile was investigated by using different fractions of 32.5 to 45.0 mol% in copolymer poly(AAm-co-AN)-EMP.

The condensational strength between cationic comonomer APAAm and the negatively charged pDNA is investigated for a set of terpolymers with different compositions and architectures.¹⁹ To optimize the concentration of APAAm, its fraction is varied between 10 to 40 mol% in the random terpolymers with the structure of poly(AAm-co-AN-co-APAAm)-EMP

holding the ratio between the other monomers AAm and AN constant. The structural impact of the macromolecular architecture was examined by the comparison of random copolymers (denoted as C10%-C40%), block copolymers featuring a binding site block (BC20-BC60) and hybrid copolymers with primary amines in both blocks (denoted as BC20%40). The block polymer system poly[(AAm-co-AN)-*block*-(APAAm)]-EMP possesses a pDNA-sensitive end block. While the composition of the thermoresponsive starting block is kept constant, the number of APAAm repeat units in the chain of the end block is varied from 20 to 60 repeat units (denoted as BC20-BC60). The block polymer BC60AN has a higher AN content (42.3 mol%) and consequently enhanced cloud point in solution. The block copolymer poly[(AAm-co-AN-co-APAAm)-*block*-(APAAm)]-EMP represents a hybrid architecture with an amine-rich (20 mol%) terpolymeric starting block and an additional APAAm chain as end block (40 r.u.). For this sample, the terpolymer with the vector with sample code of C20% was used as precursor.

Table 11: Feed ratio composition of the non-viral copolymer vectors indicating their differing structural properties relating to the total chain or the single building blocks.

Sample Code	Type	Total Vector				Start Block	End Block
		X_n / r.u.	[AAm] / mol%	[AN] / mol%	[APAAm] / mol%	[APAAm] / X_n (mol%)	[APAAm] / X_n (mol%)
R1 ^[a]	Reference ^[b]	- ^[a]	65.0	35.0	0	-	-
R2		200	67.5	32.5	0	-	-
R3		200	59.0	41.0	0	-	-
R4		200	55.0	45.0	0	-	-
C10%	Copolymer ^[c]	200	41.0	49.0	10.0	20 (10.0)	-
C10%AN		200	31.0	59.0	10.0	20 (10.0)	-
C20%		200	28.0	52.0	20.0	40 (20.0)	-
C30%		200	24.5	45.5	30.0	60 (30.0)	-
C40%		200	21.0	39.0	40.0	80 (40.0)	-
BC20	Block Copolymer ^[d]	220	59.1	31.8	9.1	-	20 (9.1)
BC40		240	54.1	29.2	16.7	-	40 (16.7)
BC60		260	50.0	26.9	23.1	-	60 (23.1)
BC60AN		260	34.6	42.3	23.1	-	60 (23.1)
BC20%40 ^[e]		240	23.4	43.3	33.3	40 (16.7)	40 (16.7)

^[a] Number of repeat units of the FRP product poly(AAm_x-co-AN_y) (R1) not determinable *via* ¹H NMR.

^[b] Reference samples are based on pure poly(AAm_x-co-AN_y)-EMP (R2-R4).

^[c] Copolymer samples are based on poly(AAm_x-co-AN_y-co-APAAm_z)-EMP (C10%-C40%).

^[d] Copolymer samples are based on poly[(AAm_w-co-AN_x)₂₀₀-*block*-(APAAm)_z]-EMP (BC20-BC60AN).

^[e] Copolymer samples are based on poly[(AAm_w-co-AN_x-co-APAAm_y)₂₀₀-*block*-(APAAm)_z]-EMP (BC20%40).

12.2.2. Synthetic Approach of the Copolymer Vectors

All cationic copolymer vectors were prepared on basis of the previous experiences derived from the synthesis of bare poly(AAm-co-AN) copolymers, which were discussed in chapter 7.2.2. The novel vectors were received from RAFT terpolymerizations between AAm, AN and

APAAM, which were inspired by the general published knowledge.^{19,259} The synthetic properties of the copolymers are summarized below and discussed briefly.

As the free amine functionality of the monomer APAAM is hampering the RAFT copolymerization, a *tert*-butyloxycarbonyl protection group (Boc) was introduced to the monomer before its use in a subsequent polymerization process. It allows an efficient synthesis of the vectors without further side reactions and aminolysis of the CTA. After the polymerization, the primary amine side groups are recovered by cleaving off the protection group in acidic media (water/TFA 50:50). The successful cleavage is indicated by the disappearing singlet signal (9H, (CH₃)₃-C-NH-R) in the exemplary ¹H NMR spectra assigned as “H” in the appendix, Figure S76 (p.284). For random terpolymers, the deprotection process required several days (3-4 d), while block architectures accelerated this process significantly (1-2 d). The free amine functionality was maintained after the deprotonation with weakly basic anion exchanger in aqueous solution (1d). Exemplarily, the vectors C30% and BC40 were analysed before and after the deprotection process of the APAAM side groups as illustrated in the appendix, Figure S76 (p.284) and Figure S77 (p.285)).

The utilized RAFT mechanism offers the possibility to adjust the molar mass of the copolymers bearing a narrow size distribution. The products were obtained in satisfying yield between 45% to 86%, which indicates proper conditions during the synthesis and an accurate work-up, which consists of dialysis and iterative freeze-drying cycles. For all copolymers, which allowed an analysis *via* GPC and ¹H NMR measurements, the experimental molar masses in the range of $\bar{M}_n=10.9\text{-}24.3\text{ kg}\cdot\text{mol}^{-1}$ match with their theoretical values. The GPC elugrams show unimodal molar mass distributions with corresponding dispersities complying with the expectations of the chosen synthesis routes, such as FRP ($\bar{D}=2.62$) and RAFT copolymerization ($\bar{D}=1.20\text{-}1.50$). These measurements reinforce the suitable control in all reactions *via* both the neat CTA in random copolymerizations and the macroCTA in block copolymerizations.

For some samples, thermoresponsive properties were observed between 3.5 and 58.2 °C in aqueous solution with 1 wt% concentration. The terpolymerization with the hydrophilic APAAM led to a lowering of the cloud points, so that copolymers with higher fractions tend to show no detectable clouding (C20%-C40% and BC40-BC60). Compared to the cloud temperatures of random terpolymers, the analogous of block copolymers is more resistant towards the hydrophilic impact of APAAM, which allows the fabrication of vectors with competitive amine contents and high cloud points by enhancing the AN fraction in the thermoresponsive chain (as for sample BC60AN).

The compositions of the vectors are analysed concerning the fractions of AAM and APAAM, which were determined *via* ¹H NMR in accordance to the calculations presented in the appendix, subchapters 16.8.7 and 16.8.8 (p.287-288). Due to the limiting solubility of the

products in water, the acrylamide fraction could be determined only for the less polar Boc-protected precursors, which was performed only for some exemplary vectors. The measurements confirmed a complete incorporation of AAm in accordance to previously shown data from the basic system of poly(AAm-co-AN) in the appendix, chapter 16.3.2 (p.226). The incorporation of the aminopropyl acrylamide monomer, matches with the feed ratio of APAAm in the reaction mixture. The first time, the preparation was successfully demonstrated for such defined cationic copolymer vectors based on poly(AAm-co-AN) copolymers in a comprehensive set of samples maintaining the desired compositional and structural properties.

Spectra and GPC elugrams are exemplary shown in the appendix, Figure S74 (p. 282), Figure S75 (p.283), Figure S76 (p.284), Figure S77 (p.285) and Figure S78 (p.286). The corresponding synthetic and physical data are summarized in the appendix, Table S23 (p.280) and Table S24 (p.281).

12.2.3. Hypothetical Impact of the Macromolecular Composition and Architecture onto the Interaction between Vector and pDNA

In the following section, the potential synthetic parameters are discussed in detail to facilitate the understanding of the interplay between macromolecular moieties and design of the tested cationic copolymer vectors (sketched in Figure 44 (p.131)) dependent to the subsequently achieved transfection abilities.

As expected, the basic copolymer system of poly(AAm-co-AN)-EMP delivers exclusively thermoresponsive properties without any DNA-binding ability. The molecular composition and the varied structural architecture of the DNA sensitive terpolymer from AAm, AN and APAAm have major influence on the transfection activity of the vectors with respect to different cell lines, as indicated in Figure 47 (p.131). Hence, the activity of the vectors can be tuned synthetically by several parameters.

Firstly, a cationic functionality is required in the structure of the vector to produce a proper interaction with the pDNA strands. The monomer APAAm is introducing an amine side group to the copolymer, which plays a key role for the gene delivery process in the given system referred to the results of Figure 47 (p.131). The fraction of APAAm determines the number of amine side groups in the macromolecule. Many amine units in the vector strengthen the condensation of the pDNA, which improves the transfection efficiency, but lowers the desired viability of the vectors due to a hampered DNA release and higher number of potential cytotoxic metabolites. Therefore, the optimal fraction of APAAm in the terpolymer composition has to be found.

Secondly, the hydrophilic-hydrophobic balance of the copolymeric vector has to be adjusted to tune the interaction between vector and pDNA during the partial subprocesses of the transfection. During the entering of the cell, the endocytosis requires stabilized polyplexes

bearing a certain hydrophobicity improving the interaction with the lipophilic cell walls. In contrast, the endosomal release of the pDNA occurs more efficient for polar vectors with higher solvent interactions. The design of the thermoresponsive chain delivers the option to refine the hydrophilicity of the chain by tuning the composition between hydrophobic (e.g., AN) and hydrophilic components (e.g., AAm, APAAm). Besides, the hydrophobicity of the vectors changes the copolymer-solvent interaction due to a shift of the coil-to-globule transition temperature, leading to varying aggregation behaviour in the surrounding medium, which affects the formation and growth of the polyplexes during the condensation process. The size of the vectors influences the aggregation dimensions of the final polyplexes, which are of great importance for the proceeding pathway of the endosomal uptake.

Thirdly, the architecture of the copolymer (see Figure 44c) impacts the process of the polyplex formation and their resulted colloidal aggregation structure. Randomly copolymerized vectors possess distributed amine anchors along the total backbone, which achieve an effective pDNA interaction by locally lower binding probabilities. The random copolymer vectors do not show any thermoresponse due to the induced high hydrophilic shift of the cloud point caused by the potent APAAm fraction, which are required to provide an effective transfection efficiency (see Figure 47).

The block copolymers carry the reactive amine moieties as concentrated end block. This architecture enables the local separation of the functionalities as thermoresponse and pDNA binding sites. Block copolymers may keep the thermoresponsive behaviour, despite potent amine doses in the polymer vectors, as hydrophilic impact of the APAAm end block on the UCST chain is minimized. Here, it is assumed that the APAAm block binds to the DNA while the thermoresponsive coil of poly(AAm-co-AN) sticks out of the polyplexes. These coils show a stable abrupt thermoresponsive behaviour in dependence of the temperature trigger and represents an external switch for the hydrophobic and hydrophilic chain states. Below the critical temperature, the thermoresponsive chain is hydrophobic and develops a strong inter- and intramolecular chain interaction between chains or chain segments causing a colloidal aggregation. Above the critical temperature, the thermoresponsive block turns hydrophilic and supports the interaction between the vector and solvent.

12.2.4. DNA Complexation Assays

Before the study of the transfection, the interaction between the copolymer vectors and pDNA was investigated in dependence to the vector's composition and the architecture to set the results in a comprising biochemical context. To monitor the condensation state between the DNA and copolymer, ethidium bromide (EtBr) was employed as DNA intercalator, which emits a fluorescence once inserted between two DNA strands. The fluorescence measurements of such complexation assays display the exchange of the intercalator vectors leading to a fluorescence drop upon tightly binding vectors in dependence of different mass

ratio between copolymer and pDNA. In Figure 45, the results of the copolymer vectors are presented mixed with pDNA in HEPES at r.t. ($T \sim 25^\circ\text{C}$) and stained with EtBr. In all these tests, bPEI was used as a reference.

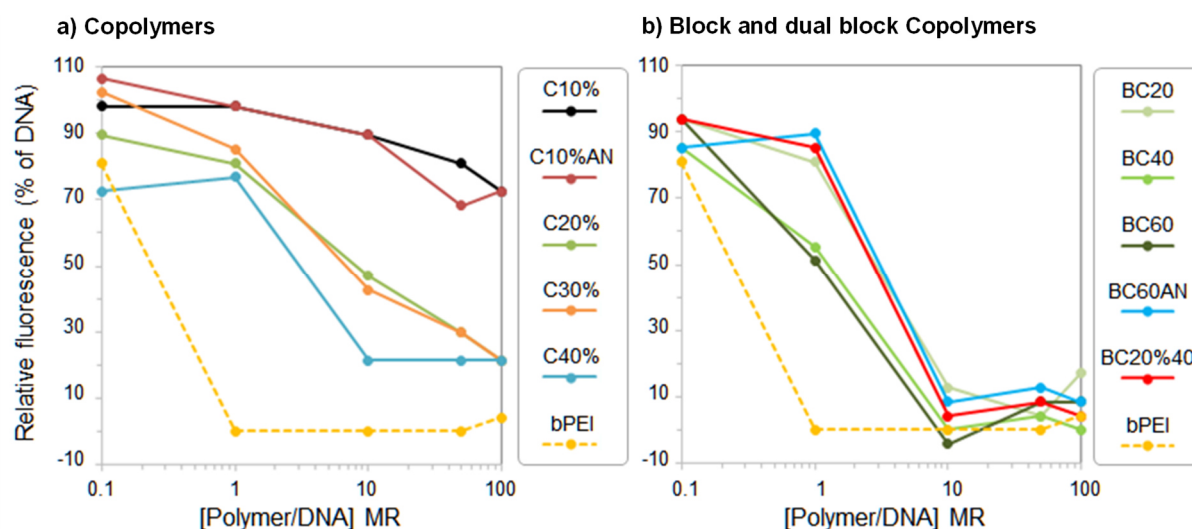


Figure 45: Relative fluorescence of DNA stained with EtBr when mixed with a) random copolymers or DNA-sensitive block and b) dual DNA-sensitive block copolymers. Polyplexes were prepared in 20 mM HEPES. MR 0.1, 1, 10, 50 and 100 correspond to polymer concentrations of 1, 10, 100, 500 and 1000 $\mu\text{g/mL}$, respectively. Intensities are expressed relative to the fluorescence of naked (i.e., free, non-condensed) stained DNA set to 100% (% of DNA). Polyplexes formed at mass ratios between vector and pDNA with MR 1, 10, 50 and 100 were also assayed by agarose gel electrophoresis (in the appendix, Figure S79).

The copolymers exhibited diverse abilities for the condensation of DNA, ranging from poorly interacting to strongly compacting reagents. The results obtained from the fluorescence measurements (Figure 45) and agarose gel retardation assay (in the appendix, Figure S79 (p.289)) were mostly compatible and indicated a clear correspondence.

Considering the residual fluorescence at the mass ratio of MR10 (Figure 45a), three groups of copolymers could be distinguished: 1) weakly efficient: C10% and C10%AN (fluorescence $\geq 70\%$), 2) intermediate: C20%, C30% and C40% (fluorescence between 10% and 70%) and 3) efficient: all others copolymers (fluorescence $\leq 10\%$).

This highlights the ability of the tested copolymers to interact with DNA in dependence of both their APAAm fraction and their skeletal architecture. Exclusively, the reference copolymers of the structure poly(AAm-co-AN) demonstrated no abilities to interact with DNA due to the absence of free amine groups in the macromolecule (results not shown). Thus, any ability of the acrylamide unit or the chain transfer agent moieties could be excluded for the coordination of DNA and the formation of polyplexes. The copolymers owning higher APAAm fractions show the tendency to improve the binding strength of the DNA along the risen number of available amine moieties.

Similarly, the copolymer architecture offered a major impact onto the condensation, as the block copolymers gained a higher efficiency to interact with the DNA than random copolymers. It might be caused by the locally higher amine concentration in comparison of

the randomly distributed analogous (higher number of contact points). At a mass ratio of MR10, the block copolymers were as efficient as bPEI, for which MR1 was sufficient to produce an optimal DNA condensing ability.

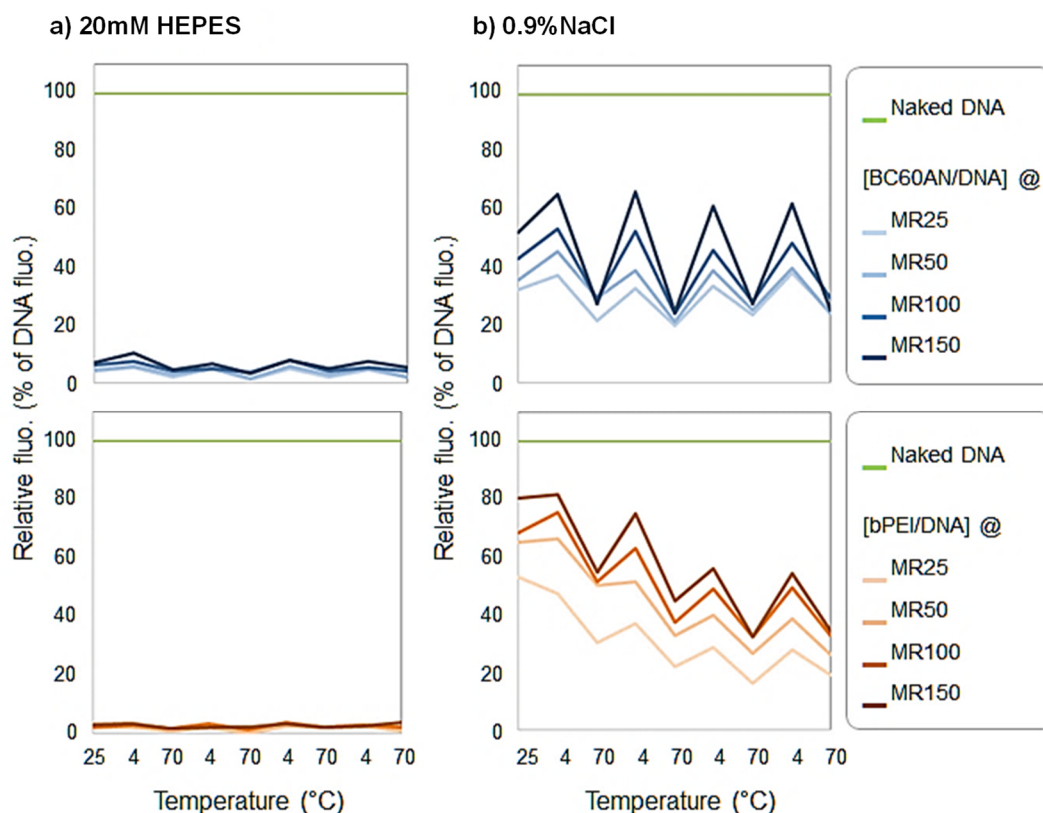


Figure 46: Relative fluorescence of polyplexes prepared either in a) 20 mM HEPES or b) 0.9% NaCl following successive rapid heating and cooling cycles. MR 25, 50, 100 and 150 correspond to copolymer concentrations of 250, 500, 1000 and 1500 $\mu\text{g}/\text{mL}$, respectively. Intensities are expressed relative to the fluorescence of naked (i.e., free, non-condensed) DNA stained with EtBr (% of DNA).

As the ability of DNA condensation was tested previously under standard conditions (i.e., at r.t. in HEPES), they were further investigated with temperature variations and using different buffer solutions, such as HEPES or saline. For this purpose, the sample BC60AN was selected, which possessed the most suitable thermoresponsive properties for this experiment owning a high clouding temperature of $T_c(0.1 \text{ wt}\% \text{ polymer})=58 \text{ }^\circ\text{C}$ in water or $T_c(0.1 \text{ wt}\% \text{ polymer})=65 \text{ }^\circ\text{C}$ in 0.5X PBS, as denoted in the appendix, Table S23 (p.280). Each polymer such as BC60AN and bPEI was mixed with DNA either in a physiological buffer (HEPES) or in an ionic saline solution (NaCl).

The corresponding fluorescence measurements illustrate a lower intensity at higher temperatures, which indicates a more efficient coordination process between copolymer and DNA. Presumably, the change in hydrophilicity of the thermoresponsive vector causes a varying DNA-interaction reasoned in the switching between hydrophobic chain state at low and hydrophilic chain state at high temperature ($T > T_c$: hydrophilic state, improved DNA interactions).

In HEPES, the fluorescence was not intense for both copolymers, although a slight temperature dependent alteration of the intensity of 2 to 5% could be observed in case of BC60AN, indicating the altering thermoresponsive coordinative modes. In saline, the temperature-induced switching states developed higher recoverable amplitudes of nearly 40 %, when sequentially tuning the temperature from 4 to 70 °C. In case of BC60AN, this effect was reinforced by high copolymer concentrations due to the corresponding raised cloud points (entropic effect). The standard reference bPEI showed a similar alternating fluorescence, but with progressively dropping intensity indicating a gradual improvement of the DNA condensation. The copolymer BC60AN possessed a more intense fluorescence at lower temperatures (4 °C) (than at 70 °C) with a highly reproducible temperature profile (in Figure 46), while the intensity of the standard bPEI decreased with each detecting cycle. Consequently, the DNA-sensitive block copolymer BC60AN showed the ability to reversibly condense DNA by the external trigger of temperature variation between 70 °C (hydrophilic, $T > T_c$) and 4 °C (hydrophobic, $T < T_c$) specifically in saline.

The varying amplitudes between the aqueous HEPES and saline solution evidence different binding strengths between DNA and vector. The higher overall intensity in saline correlates with weaker condensation of the DNA, which is based on a stronger shielding effect of the side groups by the sodium chloride ions.

A potential error might be the thermoresponsive clouding of the copolymer solution, which would lead to an opposite result at low temperatures with an increased absorption due to bigger scattering objects, which lower the intensity of fluorescence. Furthermore, the varying mass ratio (MR) between pDNA and vector intrinsically supports the thermal switching of the thermoresponsive vector BC60AN in the temperature-dependent complexation assay. Experimentally, the different mass ratios correlate with the vector concentration in solution, which tremendously impacts the thermoresponsive properties of UCST copolymer system in accordance to previous data, presented in corresponding section 7.2.5 (Figure 24b, p.58). Lower mass ratios result in decreasing copolymer concentration in solution and reduce the entropic polymer-polymer interactions so that the phase transition temperature of the vector drops significantly. Under the particular experimental conditions, only the mass ratios 150 ($[c]=0.15$ wt%) and MR=100 ($[c]=0.1$ wt%) can respond to temperature, which may explain the larger variations of the fluorescence between these mass ratios and MR50 or MR25.

The terpolymer vectors providing amine side groups are proved to condense pDNA effectively at higher mass ratios compared to the reference bPEI. The interaction between the thermoresponsive vectors and pDNA are shown to be temperature dependent, which represents a primarily target on the way to the intelligent vector. Prospectively, this data could be underpinned by temperature-dependent DLS studies to confirm the switchable complexation process between pDNA and thermoresponsive vector. The thermoresponse

was applied to modify the hydrophobicity of the copolymer vectors during the treatment in order to investigate this switchable DNA-catch-release process for the application in the field of targeted smart gene-delivery systems. As the formation of the polyplexes is sufficiently studied, the set of vectors is applied in gene-delivery experiments for the investigation of *in vitro* transfection tests.

12.2.5. Transfection Assays

The transfection properties of various copolymers were investigated in relation of the represented cell lines from diverse human and animal, organs and tissues, such as A549 (human lung cancer), C2C12 (mouse muscle) and HeLa (cervical cancer). For this purpose, the luminescence, which is delivered by the expression of the luciferase reporter gene from the pDNA, informed about the transfection ability of the copolymer. For this purpose, the luminescence (resulting from the expression of the luciferase reporter gene produced by the pDNA) allowed to evaluate the ability of the copolymer to deliver DNA determining the content of adenosine triphosphate (ATP) and to measure the cell viability during the transfection experiments. As before, the standard polymer bPEI was used as positive control due to its distinct gene transfection efficiency for the considered cell lines. This procedure allowed to unveil the potential effect of gene transfer under standard conditions in dependence of the chemical composition and structural architecture of various copolymers.

The copolymer vectors showed very different transfection efficiencies, which differ over almost 4 logs of magnitude as derived from Figure S82 (p.291). Some investigated derivatives proved to be efficient transfection reagents for gene transfer of human or animal derived cell lines. Generally, higher copolymer doses of vectors were needed in comparison to the reference bPEI to obtain noticeable transfection efficiencies.

The optimal dose is represented by the transfection maximum reached at a specific mass ratio (MR) between vector and pDNA. This relative ratio can be translated into comparable N/P values, which represent a ratio between available cationic amine binding sites in the vector and negatively-charged phosphate units in the DNA backbone. These values are calculated in the appendix, Table S25 (p.292) and Table S26 (p.293). In the following, solely experimental N/P values are denoted, which are based on the synthetical data from the copolymers (referred to experimental molar mass and composition).

As summarized in Figure 47, some copolymers were found to be as efficient as the standard bPEI, while exhibiting an equivalent or better biocompatibility, which was assessed through their corresponding cell viability measurements. The copolymers confirmed the expectations to be highly viable independently of the CTA functionalization and acrylonitrile fraction in the macromolecule. An excellent safety profile could be demonstrated at very high mass ratio ranging from MR=64 to 128 for the different cell lines in exemplary microscope images from the block copolymer vector BC20 in comparison with the standard bPEI in Figure S81(p.290).

The viability tended to shrink with increasing content of amine functionalities originating from the monomer APAAm.

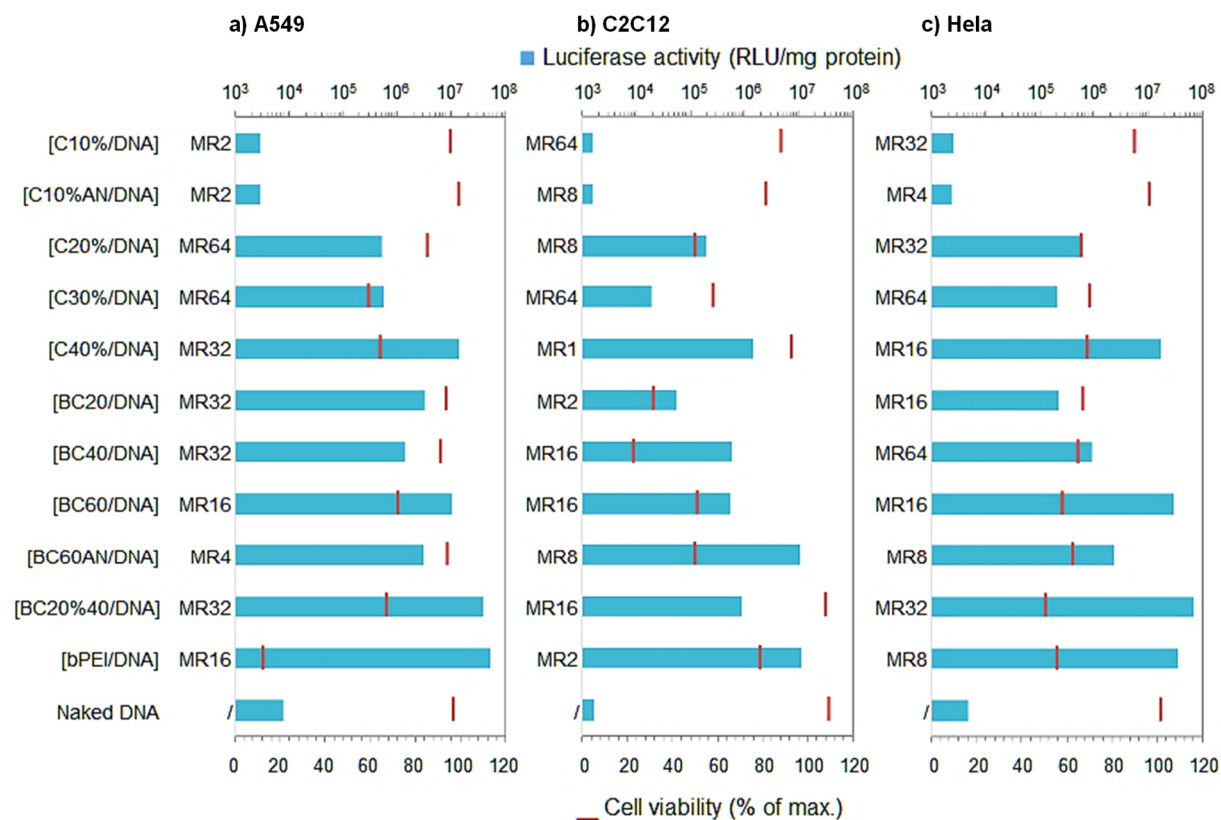


Figure 47: Maximum of transfection efficiency and associated cell viability using copolymers or block polymers in a) A549, b) C2C12 and c) HeLa. Polyplexes were prepared by mixing copolymers and DNA in 20 mM HEPES before depositing into the culture medium of cells. For each cell line and copolymer, the MR at which the peak of efficiency is reached is indicated. For the results obtained at all MR tested (i.e., from 1 to 128) see appendix Figure S82 (p.291).

Irrespective of the considered cell line, the investigated copolymer vectors could be grouped in three main classes with respect of their maximal efficiencies to deliver DNA: 1) ineffective: C10% and C10%AN, 2) intermediate: C20%, C30%, BC20 and BC40, 3) good (same order of magnitude as bPEI): C40% and BC20%40 (Figure 47). Others (BC60 and BC60AN) delivered intermediate or good results, which varied depending on the corresponding cell line. The inefficiency of C10% and C10%AN highlighted the requirement of a minimal amine content for DNA interaction and delivery into cells. In the following, the vectors are analysed in detail with respect to the specific cell lines.

In Figure 47a, the block copolymers seemed to be effective vectors for the tested cell line A549 showing intermediate to good efficiency as for example BC60 (MR16, N/P=15.6), BC60AN (MR4, N/P=3.9) and BC20%40 (MR32, N/P=15.6). The overall percental fraction of APAAm lies between 26.9 to 34.0 mol% provoking even higher transfection efficiencies than for the random copolymer C40% with 38.8 mol% APAAm. The lower amine concentration resulted in an improved viability and a tendency to minor optimal doses (mass ratio). The dual sensitive block copolymer BC20%40, containing propyl amine side groups in both

blocks, seemed to be nearly as efficient as the standard bPEI with an improved viability (MR32 and N/P=43.1, in comparison to PEI with MR16 and N/P=125.7). Its hybrid block architecture guarantees a potent interaction between vector and DNA by both the thermoresponsive mediator block and the concentrated head block. The head block forms a locally higher amine concentration and provides an effective DNA condensation process.

The cell line C2C12 (Figure 47b) underlined the previous results and displayed a positive impact of the block architecture onto the gene transfer, although the transfection efficiencies were lowered by 1 log of magnitude compared to the results from the previous cell line. The block copolymer vectors possessed broader ranges of the intermediate transfection efficiencies for the vectors BC40, BC60 and BC20%40, while BC60AN exhibited good transfection properties. Randomly copolymerized vectors with high APAAm contents (e.g., C40%) showed a medium efficiency, which was reached at an already very low mass ratio (MR1 corresponds to N/P=1.4). The optimal doses tended to lower mass ratios corresponding to N/P values between 1.4 to 21.5. The hydrophobic block copolymer BC60AN with higher acrylonitrile concentration of [AN]=42.3 mol% delivered the best transfection values at MR=8 or N/P=7.7 in ranges of the standard PEI (MR=2, N/P=15.7). The vectors with increased hydrophobicity were more effective as their hydrophilic analogous, so that for this cell line a hydrophobic chain may improve the pDNA transport through the lipophilic cell membrane and soften the binding strength between copolymer vector and pDNA.

In Figure 47c the results of the transfection assay are shown for the HeLa cell line. The vectors were divided into intermediate (C20%, C30%, BC20, BC40 and BC60AN) and good conjugates (C40%, BC60 and BC20%40). The vectors with highest fraction of the amine sites underwent the most efficient transfection processes such as C40% at a mass ratio of MR16 or N/P=22.9, BC60 at MR16 or N/P=15.6 and BC20%40 at MR32 or N/P=43.1. The dual pDNA-sensitive block copolymer BC20%40 indicated an even more efficient transfection process than the standard bPEI at MR8 (N/P=62.9). Within the given data set, the more hydrophilic vectors (with highest [APAAm] and lowest [AN]) revealed higher transfection efficiencies illustrated by the exemplary comparison of vectors BC60 and BC60AN. The tested vectors showed an enhanced transfection tendency with rising APAAm contents and slightly increased N/P ratios number, so that the number of APAAm repeat units per chain seems to play the key role for the fabrication of specialised vectors for the recent cell line.

The data attested high viabilities and transfection efficiencies by the non-viral cationic vectors based on the UCST system of poly(AAm-co-AN), which could even compete with the gold standard bPEI. The transfection efficiency and the attested impact of the thermoresponsive properties on the DNA condensation represented a first milestone on the way to the target

fabrication of smart vectors for gene delivery purposes. The influence of thermoresponse has to be investigated more details by several analysis methods and specific transfection protocols allowing the monitoring of temperature variation influence. Partially, the corresponding experiments have been started, but are not sufficiently advanced to be evaluated in the recent thesis.

12.3. Summary and Conclusion of Thermoresponsive Copolymer Vectors

The synthesis of non-viral polycationic copolymer vectors was successfully demonstrated by the RAFT terpolymerization between the thermoresponsive basis of acrylamide and acrylonitrile with the amine-containing monomer *N*-(3-aminopropyl) acrylamide in order to combine a robust UCST behaviour in aqueous solution with the ability to condense pDNA through free amine side groups along the polymer's backbone. Here, the vectors were investigated dependent to varying molar compositions and three fundamentally different architectures, in which the amine side groups could be integrated I) randomly in the copolymer chain, II) in a distinct end block of the macromolecule or III) in a mutual hybrid structure.

The thermoresponsiveness of vectors has been used in complexation assays to alter the interaction between vector and pDNA by the external trigger of temperature. This thermal trigger represents the basis to dynamically influence the solubility of the vectors by changing the chain state from hydrophobic to hydrophilic, which solve the problem of the schizophrenic requirements of vectors, which has to interact with both polar pDNA strands and also lipophilic cell membranes.

All vectors belonging to structure of poly(AAm-co-AN-co-APAAM)-EMP were attributed by defined composition, controlled molar mass and narrow dispersity, while being equipped with desired architecture and tuneable thermoresponse in aqueous media. While random terpolymers were studied with 10 to 40 mol% of intramolecular amine side groups in the chain, the block copolymer architecture was encompassed by an amine tailing of 20 to 60 units (9 to 23 mol%). The hybrid structure combined the previous arrangements with 20 mol% of amine groups in the random chain and additional 40 units as end block (overall 33 mol%). These were characterized in a series of complexation and transfection assays, unveiling structure-activity relationships.

The bare reference poly(AAm-co-AN), as synthesized in the previous chapter 7 (p.43), turned out to be highly biocompatible, even though, carrying a trithiocarbonyl group from the CTA. A decrease in cell viability could be observed for cationic vectors with raising fractions of amine side groups. As expected, their presence in the macromolecular chain turned out to be the key factor for a successful pDNA condensation and thus for the transfection process. All types of vectors featured distinct condensation properties depending on the amine content and architecture: In comparison to the random vectors, the block copolymer

conjugates demonstrated a significant enhancement of the pDNA complexation ability, which suggests an improved coordination process by more specific anchor segments with locally higher amine concentrations in the APAAm-rich end block.

These data were accompanied by marked transfection properties for all tested cell lines (A549, C2C12, and HeLa) with magnitudes in the range of the standard bPEI. In contrast to the complexation assay, here in particular the fraction of the monomer APAAm and secondary the vector architecture played an important role for the transfection process. While only high amine contents in random copolymers provoked notable efficiencies, just moderate quantities were required for the case of other architectures. Notably, the thermoresponsive behaviour of random polymers was disturbed by enhanced solvent-polymer interactions as consequence of the polar monomer units, which were distributed over the macromolecular chain so that only the block copolymers could maintain their UCST character under given experimental conditions. Here, the transfection efficiencies of the vectors varied among the cell lines, which indicates the importance of characteristic vectors of specific composition and architecture yielding in optimal results for specific cell types.

All these results further consolidate the large potential of the UCST copolymer system poly(AAm-co-AN) as basis for polycationic copolymer vector in the development of advanced gene delivery applications with a sophisticated switchability for reversible polyplex formation processes.

Although the tested copolymer system bears promising fundamental qualities, many parameters have to be refined, such as the molar mass of the vectors, other aliphatic spacers in the amine acrylamide side chain (e.g., C4 to C12 side chain) or other structural intramolecular arrangements (e.g., star polymers). These parameters could further enhance the considerable effect of the presented highly versatile and cost-efficient copolymer system for the fabrication of cationic vectors. It should be focused on the purposeful benefit of the thermoresponsive UCST character to non-invasively switch on-demand the vector properties in the inner of the cells. To confirm this switchability, also temperature dependent DLS measurements could be exploited to evidence concrete changes of the polyplex dimensions in solution by condensation of the pDNA upon the external stimulus of temperature. Last but not least, a well-established protocol has to be developed for the reliable investigation of the transfection process under temperature variation, enabling a particular comparability of the results gained under ideal standard conditions and thermal alteration, which may mask the influence of the vector's thermoresponsiveness by amended internal processes and viability of living cells.

13. General Conclusion and Outlook of This Thesis

In this thesis, smart materials were designed in order to mimic natural processes by introducing specific responses to the artificial macromolecules in analogy to proteins and other natural compounds, which are autonomously responding to changes of surrounding conditions. The thermoresponse was exploited to attribute intelligent behaviours to the polymer structures, which undergo certain property transformation upon external temperature variations. Polymers with lower and upper critical solution temperatures in aqueous solution were studied to facilitate the desired phase transitions in both contrary temperature directions specialized for each application. Therefore, poly(NIPAAm) and poly(AAm-co-AN) were utilized for versatile sets of smart materials, which could be synthesized in advanced architectures in order to fulfil the specific requirements of the concerned application fields.

In particular, the UCST system of poly(AAm-co-AN) was investigated in detail to guarantee a full control over the synthesis and the adjustable thermoresponsive properties. Complete sets of copolymers were investigated with special focus on the cloud point tuned by parameters like varying AN-fractions, molar masses and polymer concentrations in solution, as well as the incorporation of photo-crosslinkable monomer units (BPAAm). By this knowledge, the basis of poly(AAm-co-AN) represents an immensely versatile UCST system, which opens up a variety of potential application fields. In addition to that, the well-studied poly(NIPAAm) was employed as robust LCST counterpart to expand the portfolio of thermoresponsive polymers showing their typical transformations in both temperature directions. Both polymer systems could be set in new and advanced research contexts by endowing previously static systems with dynamic thermoresponses. In this thesis, the switchability of solvation states was exploited for complex aggregation behaviours of LCST-UCST block copolymers, smart diffusion control through nanoscopic channels of thermal switchable nanopore membranes, dynamic complex formation in aqueous media by iron ion sensitive macromolecular coordination ligands or switchable pDNA condensation by thermoresponsive cationic non-viral vectors for gene-delivery.

In the first research field, double thermoresponsive LCST-UCST block copolymers with the structure of poly[(AAm-co-AN)-*block*-(NIPAAm)]-EMP showed in aqueous media multiple aggregation behaviours dependent to the tuneable hydrophobic character of the UCST block. On molecular level, the phase transition of one block could be influenced by an altered solvation state of the neighbouring block changing from hydrophilic to hydrophobic or *vice versa*. This molecular change induced in the ensemble picture a complex aggregation behaviour of associating individual chains as function of their interdependent switching states triggered by the thermal history of copolymers in solution (heating/cooling cycle).

In the second application, both copolymer systems were applied as thermoresponsive inner-pore coating of inorganic nanopore substrates producing thermally switchable membranes with controllable diffusion behaviour. The distinct immobilization of the photo-crosslinkable

poly(NIPAAm) copolymers as hydrogels was achieved inside the nanoscopic pores, whilst their deposited molar mass and thermoresponsive switching could be controlled and detected even inside the substrates.

Thirdly, a novel concept was demonstrated by endowing both thermoresponsive polymers with LCST or UCST character with an Fe^{2+} -coordinating 1,2,4-triazole unit to thermally switch the complex structure of these macromolecular coordination ligands (MCL) in aqueous solution. Such smart building blocks are inspired by two macromolecular architectures based on a (I) hemi-telechelic MCL with triazole end group and (II) a multidentate MCL with multiple triazole substituents along the polymer backbone. The thermoresponsive polymer segments can change their solvation state and interactions in solution upon temperature variation, which consequently alters the overall chain conformation and volume demand. This thermal trigger presents the basis to dynamically influence the complexation behaviour *via* the switchable coil dimensions of the polymer.

For the last application of cationic non-viral vectors, poly(AAm-co-AN)-EMP was copolymerized in varying skeletal architectures with a DNA-sensitive monomer to incorporate free amine side groups to the backbone. The terpolymeric vectors showed thermally switchable condensation strength of DNA and delivered promising *in vitro* transfection abilities for a different set of cell lines in the range of the standard bPEI. As side note, also an excellent safety profile could be attested in particular for the thermoresponsive copolymer system, which may open up a broad range of application fields.

The studied smart materials have demonstrated their beneficial qualities on the basis of the accomplished application fields, which profit the key properties of offering tuneable thermoresponsive properties, being multiply deployable and cost-effective. The executed projects delivered promising results, bearing vast potentials for further continuation with respect to fine-tune the explored systems to further boost their efficiency for the corresponding application.

Especially, the fields of thermoresponsive cationic copolymer vectors and thermally switchable nanopore membranes might still serve space to achieve further sophisticated innovations leading to more effective systems, which move closer to the ambitious targets of the certain project. The fundamental knowledge about the thermoresponsive iron-sensitive copolymers and dual-responsive schizophrenic LCST-UCST block copolymers can be adopted for more purposeful and advanced applications, which require more complex solvation behaviours or further responses. Also, the concept to incorporate metal ions to a polymer backbone could be applied for the development of antibacterial and non-fouling materials. Last but not least, the substantial synthetic improvements of poly(AAm-co-AN) produced a highly controlled and reliable UCST copolymer system overcoming several initial

drawbacks, so that it may be able to reduce the imbalance in prospective works to the prominent LCST counterpart of poly(NIPAAm).

14. Experimental Part

14.1. Instrumentation

ATR-FTIR Spectroscopy: The ATR-FTIR was recorded by using the FTIR spectrometer of the type Bruker Tensor 27 equipped with an ATR unit. The measurements were performed with 32 scans average and the evaluation of the spectra was undergone with the software OPUS and plotted in Origin.

Differential Scanning Calorimetry (DSC): The standard characterization of the thermal properties was performed on a TA Instruments Q 1000 V9.9 Build 303 with temperature controller TC H03 under inert conditions (N_2 : 50 ml/min) with 10 K/min in TA Instruments hermetic aluminium pans.

The determination of the thermoresponsive properties and the general assignment of kinetic and thermodynamic thermal processes was performed *via* modulated DSC measurements in the heat-only mode with a periodicity of 15 s and with an amplitude of ± 0.099 K and heating rate of $2.5 \text{ K}\cdot\text{min}^{-1}$ using TA Instruments Tzero hermetic aluminium pans (if not specified otherwise). The cloud points of the double-thermoresponsive block copolymers were measured in usual hermetic aluminium pans from TA Instruments.

The thermoresponsive properties were determined from a 1.0-3.0 wt% polymer solution (40-50 μL , empty pan as reference). The sample was equilibrated for at least 30 min below the critical solution temperatures. For the LCST determination inside nanopores, the polymer filled AAO without aluminium backside ($d=10$ mm, 2nd anodization: 24h, 195 V, 0.1 M phosphoric acid, 1.0 wt% polymer) was crushed and stacked in the pan. Distilled water (10 μL) was added to the pan repeatedly with each AAO-stack. The samples were equilibrated 90 min at 2°C and analysed between $2\text{-}40^\circ\text{C}$. The calibration was performed with indium. The transition temperatures were obtained by the fitting of the heat flow curve minima.

Dynamic Light Scattering (DLS): The aggregation studies were performed with the Malvern Zetasizer Nano ZS at different temperatures in disposable PMMA and PS cuvettes. A 4 mW He-Ne laser (633 nm) was used as light source. The hydrodynamic radius was calculated at 173° angle using the intensity mode. The editing and fitting of the raw data were carried out using the software Malvern Zetasizer. By default, polymer solutions with a concentration of 0.1 wt% were applied. For sensitive copolymeric systems with major concentration dependency, the concentration of the previous characterization methods was chosen. Multi distributional aggregation (md) sizes are analyzed by intensity, but the corresponding sizes are exclusively used indicatively not as precise values.

Gel-Permeation-Chromatography (GPC): The molar mass distributions and the dispersities of the DMAc-soluble polymers were measured by a GPC-system. It

consists of a PSS-SECcurity system Agilent Technologies 1260 infinity, equipped with a PSS GRAM 100Å column and a 10 µm particle size pre-column. A solution of DMAc with 0.1% LiBr was used as eluent. A sample volume of 20 µL was injected at temperature of T=60 °C. A flow rate of 1 mL/min was adjusted. The calibration curve was generated with PMMA standards (Polymer Standard Service, Mainz) and the molar mass of the polymers was calculated using the Mark-Houwink-Constants.

The molar mass distributions and the dispersities of the water-soluble polymers were measured by a PSS-SECcurity system Agilent Technologies 1200 Series, equipped with a PSS Suprema 3000 Å column and a 10 µm particle size pre-column. A solution mixture of water/MeCN (85:15 vol%) with NaNO₃ (0.1 mol·L⁻¹) and NaN₃ (0.011 mol·L⁻¹) was used as eluent. A sample volume of 20 µL was injected at temperature of T=30 °C. A flow rate of 1 mL/min was adjusted. The calibration curve was generated with pullulan standards (Polymer Standard Service, Mainz) and the molar mass of the polymers was calculated using the Mark-Houwink-Constants.

The elugrams of block copolymers are shown in a common figure, although not recorded in the identical eluent due to complimentary solubilities of starting block and final block copolymer or strong interaction with the column material. Despite the same flow rate (1 mL/min), the elution times are not comparable precisely and are used indicatively to prove the success of the block copolymerization.

High-Performance Liquid Chromatography Mass Spectrometry (HPLC-MS): The precise molar mass of the compounds was determined by a HPLC-MS system. It consists of an Agilent 1100 system equipped with auto sampler, binary pump, InfinityLab poroshell column (Agilent, 120 EC-C18, 4.6 x 50 mm, 2.7µm) and photodiode array detector connected to an Agilent G1946D quadrupole mass spectrometer (m/z=100-650) with an electrospray ionization source in the positive mode (70 V). A solution of water/acetonitrile (95:5) with 0.1 vol% TFA was used as eluent. A sample volume of 5 µL was injected at temperature of T=20 °C. A flow rate of 0.4 mL/min was adjusted. The editing of the raw data was carried out using the software ChemStation and Origin.

NMR Measurements: The NMR spectra were recorded by a Bruker Avance 400 and/or Jeol ECZ 500 spectrometer. While the ¹H NMR measurements were carried out with a frequency of 300 MHz, 400 MHz and 500 MHz the ¹³C NMR measurements were done at a frequency of 101 MHz and 125 MHz. All spectra were recorded at room temperature T=20 °C. As internal standard, the signals of the non-deuterated solvents (CDCl₃: ¹H: 7.26 ppm, ¹³C: 77.2 ppm, DMF: ¹H: 2.75 ppm, 2.92 ppm, 8.03 ppm, D₂O: ¹H: 4.75 ppm, DMSO-d₆: ¹H: 2.50 ppm, ¹³C: 39.52 ppm, MeOD: ¹H: 3.31 ppm, ¹³C: 49.0

ppm) were used. The chemical shifts were reported in parts per million (ppm). The signals were assigned using the MestReNova and ACD/Labs software software.

Qualitative Swelling Tests: The hydrogels were prepared photochemically from aqueous 1.0 wt% polymer solution under irradiation inside an UVP CL-1000 Ultraviolet Crosslinker at a wavelength of $\lambda=365$ nm ($1 \text{ h}=13.0 \text{ J/cm}^2$) for 15 min and checked visually with respect to film stability, swelling and turbidity point.

Synthesis Conditions: The syntheses were performed with dry glassware under inert conditions (Ar) at room temperature (if not specified otherwise).

Transmission Electron Microscopy (TEM): For the TEM investigations, great importance was paid to the structure-preserving preparation. Instead of the shock freezing of cryo-TEM preparation, here, the samples were embedded in a thin, amorphous matrix of trehalose in order to minimize the changes to the sample structure. For this purpose, the dispersion was applied to a holey carbon film and mixed with a solution of trehalose and uranyl acetate. Excess solution was blotted off with a filter paper to leave a thin film of trehalose spanning the holes in the carbon film. TEM micrographs were acquired with a Tecnai F20 operated at an acceleration voltage of 200 kV.^{263,264}

Thermogravimetric Analysis (TGA): The standard measurement was performed with a TGA Q 500 unit (TA-Instruments) in the conventional mode with a linear temperature gradient ($\Delta T=10$ K/min, if not specified otherwise).

The measurement of minor weight differences was performed in the high-resolution mode. The mode was applied for the determination of polymer filling fraction of AAO pores. The polymer filled AAO substrates without aluminium backside was crushed and placed inside the platinum pan. The high-resolution method (sens.=4, res.=4) was used between 120-530 °C with an averaged heating gradient of 10 K/min after the drying step for 90 min at 120 °C. A gas change from nitrogen to oxygen was performed at 500 °C. A second cycle of the empty “burnt” AAO was measured as blank. The subtracted weight losses of both measurements were defined as mass of the polymer in the pores.

Turbidity Measurements: The lower critical solution temperature (point of turbidity) was measured on an UV-Vis spectrophotometer Thermo Fisher Scientific Evolution 220 equipped with a water-cooled Peltier element and an automatic sample changer with stirring bar. Quartz cuvettes (10.0 x 10.0 mm²) were used as measuring cells. By default, a 1.0 wt% polymer in de-ionized water with 1 K/min with at wavelength of $\lambda=650$ nm was used, if not specified otherwise. For measurements in presence of Fe²⁺ (due to slight absorption) a higher wavelength of 740 nm was adjusted. The editing

and fitting of the raw data were carried out using the software Origin, with a non-linear curve Boltzmann fit. The turbidity points were determined from the heating cycle for LCST- and from cooling cycle for UCST polymer systems, respectively.

Biochemical Experimental Part: The descriptions, instrumentation, materials and procedures of the biochemical experiments for the thermoresponsive copolymer vectors performed in the laboratories of Prof. Dr. Tristan Montier from the university of Brest (F) are described in the appendix (according to 15.8.1).

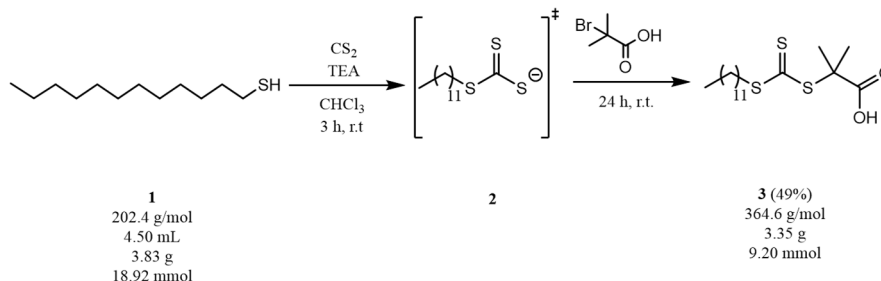
14.2. Materials

Water was deionized with a MilliQ filtration unit ($\sigma=18.2 \text{ M}\Omega\cdot\text{cm}$). The employed solvents hexane, diethyl ether (Arcos, 99.5%), chloroform, dichloromethane (DCM), 1,4-dioxane (< 98%, Roth chemicals, dried over sodium and freshly distilled), ethanol, ethyl acetate, methanol (MeOH) (99.4%, VWR) and tetrahydrofuran (THF) (99.9%, Fisher Scientific) of technical purity of university supplier unless specified otherwise. Absolute ethanol (99.9%, Sigma Aldrich), $\text{Fe}(\text{BF}_4)_2\cdot 6\text{H}_2\text{O}$ (99%, Sigma Aldrich) were stored under inert conditions. Aqueous ammonia (25%, Roth Chemicals), *L*-ascorbic acid (99%, Alfa Aesar), 2-bromo-2-methylpropionic acid (>98%, Alfa Aesar), 2-bromo-2-methylpropionic acid (>98%, Alfa Aesar), carbon disulfide (>99%, Sigma Aldrich), 4-(dimethylamino)-pyridine (99.9%, Acros Organics), *N,N'*-dicyclohexylcarbodiimide (99%, Sigma Aldrich), 1-dodecanethiol (>98%, Sigma Aldrich), 3-(ethyliminomethyleneamino)-*N,N*-dimethylpropane-1-amine (EDC) (99%, Roth Chemicals), *N*-hydroxy succinimide (NHS) (98%, Alfa Aesar), phthalimide (99%, Alfa Aesar) and triethylamine (99%, Alfa Aesar, distilled and stored over mole sieve 4 Å) were used as received. Acrylic acid (AA) (Merck, 99%), acrylamide (AAm) (99%, Merck, recrystallized from acetone), acrylonitrile (AN) (99%, Merck, destabilized via column chromatography, aluminium oxide, neutral), 3-aminopropan-1-ol (99%, Alfa Aesar), 2,2'-azobis[2-(2-imidazolyl)propane] dihydrochloride (AIPC) (98%, Wako Chemicals), 2,2'-azobis(2-methylpropionitrile) (AIBN) (99%, Acros Organics, recrystallized from methanol), diisopropyl azodicarboxylate (DIAD) (94%, Alfa Aesar), formic hydrazide (98%, Alfa Aesar), hydrazine monohydrate (>98%), hydroxyethyl acrylamide (HEAAm) (Sigma Aldrich, 97%), 2-methacrylic acid (MAA) (Merck, 99%), *N*-isopropylacrylamide (NIPAAm) (99%, Acros Organics, recrystallized from hexane/toluene [1:4]), triethyl orthoformate (98%, Alfa Aesar), triphenylphosphine flakes (99%, Alfa Aesar) and trifluoroacetic acid (TFA) (99.9%, Roth Chemicals) were stored under inert conditions in a dark place at 0-4 °C. *tert*-Butyl-(2-acrylamidopropyl)carbamate (APAAm-Boc)²⁵⁹, benzophenone acrylamide (BPAAm)²⁶⁵, dodecyl {1-[(2-hydroxyethyl)amino]-2-methyl-1-oxopropan-2-yl}carbonotrithioate (DMP)²⁶⁶, dodecyl-{1-[(2-hydroxyethyl)amino]-2-methyl-1-oxopropan-2-yl}carbonyl ethanolamine (DMP-EA) and 2-[[[(ethylthio)carbothioyl]thio]-2-methylpropanoic acid (EMP)²⁶⁶ were synthesized and checked by TLC, ¹H- and ¹³C NMR. The CTAs and AIBN were stored cooled in the dark. The weakly basic anion exchanger (Lewatit MP62, Bayer) was freshly regenerated, the dialysis membrane (Spectra/Por 6, pre-wetted RC tubes 1 kDa, Roth Chemicals) washed and stored for 30 min in distilled water before use.

14.3. Synthesis

14.3.1. Chain Transfer Agents

Carboxyl-terminated Asymmetric Chain Transfer Agent 2-[[[(Dodecylthio)carbothioyl]thio]-2-methylpropanoic Acid (DMP)



Scheme 9: The synthesis of the chain transfer agent DMP 3.

2-[[[(Dodecylthio)carbothioyl]thio]-2-methylpropanoic acid (DMP) was synthesized according to a modified procedure of Postma et al.²⁶⁶

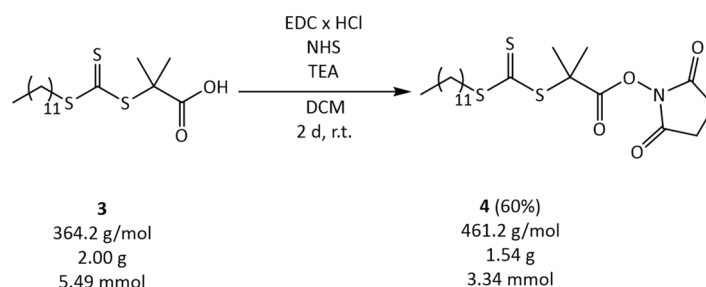
1-Dodecanethiol (3.83 g, 18.9 mmol, 4.5 mL) was dissolved in chloroform (50 mL) until TEA (2.85 g, 28.2 mmol, 3.9 mL) was added. The mixture was stirred for 20 minutes, before CS₂ (3.40 g, 37.6 mmol, 2.7 mL) was added through a septum forming a yellowish reaction mixture. After another 3 hours reaction time, α-bromoisobutyric acid (3.15 g, 18.9 mmol) was added to the reaction mixture. The product was obtained after 24 hours reaction time and threefold extraction with 1M HCl (100 mL) and water (100 mL). The product was dried over anhydrous sodium sulfate and concentrated to dryness. The product was recrystallized twice in cold hexane. The reaction status was monitored using the TLC (silica gel, EtOAc:Hex=1:2, R_f(DMP)=0.40, iodine indicator and CHCl₃:MeOH:NH₃=13:6:1, R_f(DMP)=0.28, iodine indicator).

Yield: 3.35 mg (50%)

¹H NMR (400 MHz, CDCl₃, shown in the appendix, Figure S1a), δ ppm: 0.89 (t, 3H, J=7.0 Hz, -CH₂-CH₃), 1.26 - 1.39 (m, 18H, -(CH₂)₉-CH₃), 1.68 (p, 2H, J=7.3 Hz, -CH₂-CH₂-(CH₂)₉-), 1.73 (s, 6H, -C-(CH₃)₂) and 3.29 (t, 2H, J=7.3 Hz, -CS₃-CH₂-).

¹³C NMR (101 MHz, CDCl₃, shown in the appendix, Figure S1b), δ ppm: 14.1 (-CH₂-CH₃), 22.7 (-CH₂-CH₃), 25.2 (-C-(CH₃)₂), 27.8 (-CH₂)₈-, 29.0 (-CH₂)₈-, 29.1 (-CH₂)₈-, 29.4 (-CH₂)₈-, 29.5 (-CH₂)₈-, 29.6 (-CH₂)₈-, 29.6 (-CH₂)₈-, 31.9 (-CH₂-CH₂-CH₃), 37.2 (-CS₃-CH₂-), 55.5 (-CS₃-C-(CH₃)₂-COOH), 178.9 (-COOH) and 220.8 (-CS₃-).

Ester Activated Chain Transfer Agent 2,5-Dioxopyrrolidin-1-yl-2-[[[(dodecylthio)carbothioyl]thio]-2-methylpropanoate (DMP-NHS).



Scheme 10: The active ester of the chain transfer agent DMP **4**.

Previously, 2-[[[(dodecylthio)carbothioyl]thio]-2-methylpropanoic acid (DMP) was synthesized according to a modified procedure of Postma et al.²⁶⁶

NHS (1.27 g, 11.00 mmol) was added to a solution of DMP (2.00 g, 5.50 mmol), EDC (1.28 g, 8.25 mmol) and TEA (0.56 g, 5.50 mmol) in DCM (100 mL) under inert atmosphere with rigorous stirring in a two-neck flask and further stirred for 48 hours at room temperature. The reaction status was monitored using the TLC (silica gel, CH₂Cl₂:CHCl₃:MeOH:NH₃=80:13:6:1, R_f(DMP-NHS)=0.3, iodine indicator). The reaction mixture was concentrated, and the crude product was purified by column chromatography (silica gel, EtOAc) to obtain the yellowish solid after drying.

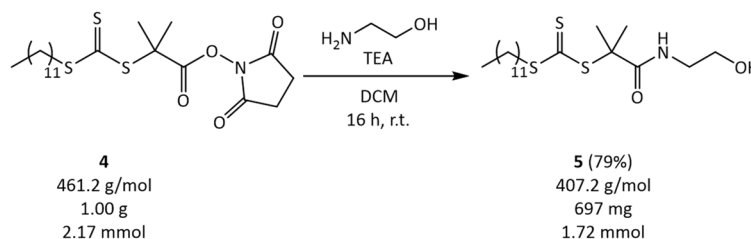
Yield: 1.54 mg (60%).

¹H NMR (400 MHz, CDCl₃, shown in the appendix, Figure S2a), δ ppm: 0.89 (t, 3H, J=7.0 Hz, -CH₂-CH₃), 1.26 - 1.39 (m, 18H, -(CH₂)₉-CH₃), 1.69 (p, 2H, J=7.3 Hz, -CH₂-CH₂-(CH₂)₉-), 1.88 (s, 6H, -C-(CH₃)₂), 2.82 (br. s, 4H, -NHS) and 3.31 (t, 2H, J=7 Hz, -CS₃-CH₂-).

¹³C NMR (101 MHz, CDCl₃, shown in the appendix, Figure S2b), δ ppm: 14.1 (-CH₂-CH₃), 22.7 (-CH₂-CH₃), 25.8 (-NHS), 25.8 (-CS₃-C(CH₃)₂-COO-NHS), 27.7 (-(CH₂)₈-), 29.0 (-(CH₂)₈-), 29.1 (-(CH₂)₈-), 29.4 (-(CH₂)₈-), 29.5 (-(CH₂)₈-), 29.6 (-(CH₂)₈-), 29.6 (-(CH₂)₈-), 31.9 (-CH₂-CH₂-CH₃), 37.2 (-CS₃-CH₂-), 54.3 (-CS₃-C-(CH₃)₂-COO-), 168.9 (-COO-, -CONH-) and 218.7 (-CS₃-).

IR (shown in the appendix, Figure S3): 1734 cm⁻¹ and 1777 cm⁻¹ (5- membered imide ring).

Hydroxy End-functionalized Chain Transfer Agent Dodecyl-{1-[(2-hydroxyethyl)-amino]-2-methyl-1-oxopropan-2-yl}carbonotrithioate (DMP-EA).



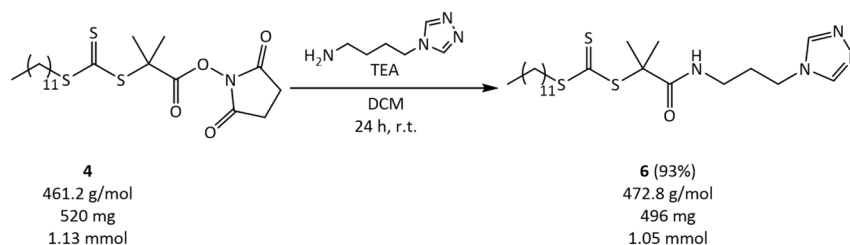
Scheme 11: The end-functionalization of the chain transfer agent DMP-EA with ethanolamine **5**.

The ethanolamine (EA) was freshly distilled. DMP-NHS (1.00 g, 2.17 mmol) and EA (0.15 g, 2.38 mmol, 144 μ L) were dissolved in DCM (50 mL). TEA (0.22 g, 2.17 mmol, 300 μ L) was added. The reaction was stirred for 16 hours at room temperature. The reaction status was monitored using the TLC (silica gel, EtOAc, R_f (DMP-EA)=0.66, iodine indicator). The impurities of DMP were removed by column chromatography (silica gel, EtOAc:hexane=1:2) and the pure product was obtained by an eluent-change (silica gel, CHCl_3 :MeOH: NH_3 =13:6:1, iodine indicator). The product phase was concentrated to dryness.

Yield: 697 mg (79%).

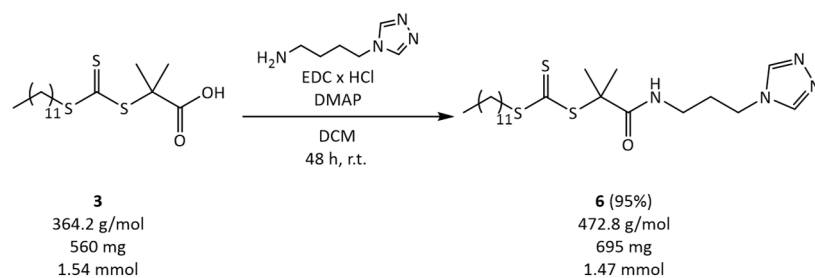
^1H NMR (400 MHz, CDCl_3 , shown in the appendix, Figure S4a), δ ppm: 0.89 (t, 3H, $J=7.0$ Hz, $-\text{CH}_2-\text{CH}_3$), 1.26 - 1.39 (m, 18H, $-(\text{CH}_2)_9-\text{CH}_3$), 1.67 (p, 2H, $J=7.6$ Hz, $-\text{CH}_2-\text{CH}_2-(\text{CH}_2)_9-$), 1.72 (s, 6H, $-\text{C}(\text{CH}_3)_2-$), 2.27 (br. t, 1H, $-\text{CH}_2-\text{CH}_2-\text{OH}$), 3.29 (t, 2H, $J=7.3$ Hz, $-\text{CS}_3-\text{CH}_2-$), 3.40 (q, 2H, $J=7.3$ Hz, $-\text{CONH}-\text{CH}_2-\text{CH}_2-\text{OH}$), 3.70 (q, 2H, $J=7.3$ Hz, $-\text{CONH}-\text{CH}_2-\text{CH}_2-\text{OH}$) and 6.88 (t, 1H, $J=7.3$ Hz, $-\text{CONH}-\text{CH}_2-\text{CH}_2-\text{OH}$).

^{13}C NMR (101 MHz, CDCl_3 , shown in the appendix, Figure S4b), δ ppm: 14.1 ($-\text{CH}_2-\text{CH}_3$), 22.7 ($-\text{CH}_2-\text{CH}_3$), 25.8 ($-\text{CS}_3-\text{C}(\text{CH}_3)_2-\text{CONH}-$), 27.7 ($-(\text{CH}_2)_8-$), 29.0 ($-(\text{CH}_2)_8-$), 29.1 ($-(\text{CH}_2)_8-$), 29.4 ($-(\text{CH}_2)_8-$), 29.5 ($-(\text{CH}_2)_8-$), 29.6 ($-(\text{CH}_2)_8-$), 29.6 ($-(\text{CH}_2)_8-$), 31.9 ($-\text{CH}_2-\text{CH}_2-\text{CH}_3$), 37.2 ($-\text{CS}_3-\text{CH}_2-$), 43.2 ($-\text{CONH}-\text{CH}_2-\text{CH}_2-\text{OH}$), 57.1 ($-\text{CS}_3-\text{C}(\text{CH}_3)_2-\text{COO}-$), 61.9 ($-\text{CONH}-\text{CH}_2-\text{CH}_2-\text{OH}$), 173.6 ($-\text{CONH}-$) and 221.1 ($-\text{CS}_3-$).

Triazole End-functionalized Chain Transfer Agent 1-{[3-(4*H*-1,2,4-Triazol-4-yl)-propyl]amino}-2-methyl-1-oxopropan-2-yl-dodecyl-carbonotrithioate (DMP-APTRZ).**Procedure 1:** Indirect coupling *via* active ester.**Scheme 12:** The end-functionalization of the chain transfer agent DMP with the coordination moiety APTRZ **18** *via* active ester **4**.

DMP-NHS (520 mg, 1.13 mmol) and APTRZ (142 mg, 1.13 mmol) were dissolved in dry dichloromethane (50 ml) in a two-neck flask under argon atmosphere. TEA (114 mg, 1.13 mmol, 156 μ L) was added to the above solution and the reaction mixture was continued to stir for 24 hours. The TEA-salts were removed by extraction with water (50 mL) and the organic phase was concentrated under reduced pressure. The impurities of DMP were removed by column chromatography (silica gel, EtOAc:hexane=3:1) and the pure product was obtained by an eluent-change (silica gel, CH₂Cl₂:CHCl₃:MeOH:NH₃=80:13:6:1, R_f(DMP-APTRZ)=0.44, iodine indicator). The product phase was concentrated to dryness.

Yield: 417-497 mg (78-93%).

Procedure 2: Direct coupling *via* EDC.

Scheme 13: The end-functionalization of the chain transfer agent DMP with the coordination moiety APTRZ **18** *via* direct EDC coupling.

The triazole derivative APTRZ (175 mg, 1.39 mmol) was added to the dichloromethane (150 mL) solution containing excesses of 66% EDC (358 mg, 3.08 mmol) and 10% DMP (560 mg, 1.54 mmol) in a two-neck flask under argon flux. The 4-(dimethylamino)-pyridine (186 mg, 1.54 mmol) was then added to the reaction mixture with continuous stirring for 48 hours at room temperature. The salts of 4-(dimethylamino)-pyridine were removed by threefold extraction from 1M HCl (150 mL), water (150 mL) and 1M NH₃ (150 mL), and the organic phase was concentrated under reduced pressure. The uncoupled conjugate DMP was removed by short-column chromatography (silica gel, EtOAc:hexane=3:1) and the dark yellowish solid was obtained by an eluent change (CHCl₃:MeOH:NH₃=13:6:1, iodine indicator, R_f(DMP-APTRZ)=0.26). The product phase was concentrated to dryness.

Yield: 695 mg (95%)

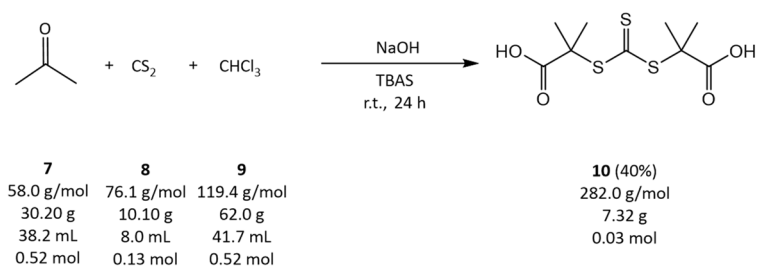
¹H NMR (400 MHz, CDCl₃, shown in the appendix, Figure S5a), δ ppm: 0.89 (t, 3H, J=7.0 Hz, -CH₂-CH₃), 1.26-1.39 (m, 18H, -(CH₂)₉-CH₃), 1.67 (p, 2H, J=7.3 Hz, -CH₂-CH₂-(CH₂)₉-), 1.71 (s, 6H, -C-(CH₃)₂), 1.99 (m, 2H, J=6.7 Hz, -CH₂-CH₂-TRZ), 3.28 (m, 4H, -CH₂-CS₃-, -CH₂-(CH₂)₂-TRZ), 4.08 (t, 2H, J=7.0 Hz, -CH₂-TRZ), 6.72 (br.t, 1H, J=6.2 Hz, -CONH-) and 8.24 (s, 2H, -TRZ).

¹³C NMR (101 MHz, CDCl₃, shown in the appendix, Figure S5b), δ ppm: 14.1 (-CH₂-CH₃), 22.6 (-CH₂-CH₃), 25.7 (-C-(CH₃)₂), 27.6 (-(CH₂)₈-), 28.9-29.6 (-(CH₂)₈-), 31.3-31.8 (-CH₂-CH₂-CH₃, -CH₂-CH₂-TRZ), 36.9 (-CH₂-CS₃-), 37.2 (-CH₂-(CH₂)₂-TRZ), 43.0 (-CH₂-TRZ), 57.1 (-C-(CH₃)₂), 142.8 (-TRZ), 173.2 (-CONH-) and 221.0 (-CS₃-).

TGA: T_{dec} =389 K

DSC: T_g =287 K (2 J/g), T_m =331 K (86 J/g).

Carboxyl-terminated Symmetrical Chain Transfer Agent 2,2'-[Thiocarbonyl-bis-(sulfanediyl)]-bis-(2-methylpropanoic Acid) (BIT).



Scheme 14: The synthesis of the chain transfer agent BIT **10**.

2,2'-[Thiocarbonylbis(sulfanediyl)]-bis-(2-methylpropanoic acid) (BIT) was synthesized according to a modified procedure of Lai et al.^{267,268}

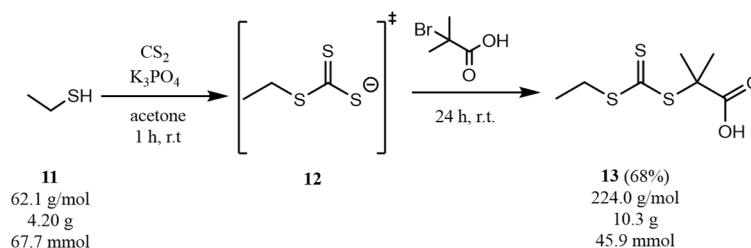
Carbon disulfide (10.10 g, 0.13 mol), chloroform (62.00 g, 0.52 mol), acetone (30.20 g, 0.52 mol) and tetrabutylammonium hydrogen sulfate (TBAS) (0.88 g, 26.0 mmol) were dissolved in hexane (20 mL). A 12.8 M aqueous NaOH solution (73.0 mL) was added dropwise to the cooled reaction mixture. The reaction status was monitored using the TLC (silica gel, EtOAc, $R_f(\text{BIT})=0.55$, iodine indicator). After 24 hours the reaction mixture was diluted with distilled water (300 mL) and acidified with concentrated aqueous HCl (60 mL). After 30 minutes the precipitate was filtrated and recrystallized twice in CCl_4 . The product was dried under reduced pressure.

Yield: 7.32 g (40%).

^1H NMR (400 MHz, DMSO-d_6 , shown in the appendix, Figure S8a), δ ppm: 1.59 (s, 12H, $\text{HOOC-C}(\underline{\text{C}}\text{H}_3)_2\text{-CS}_3^-$) and 12.91 (s, 12H, $\underline{\text{H}}\text{OOC-C}(\text{CH}_3)_2\text{-CS}_3^-$).

^{13}C NMR (101 MHz, DMSO-d_6 , shown in the appendix, Figure S8b), δ ppm: 24.9 ($\text{HOOC-C}(\underline{\text{C}}\text{H}_3)_2\text{-CS}_3^-$), 56.2 ($\text{HOOC-C}(\text{CH}_3)_2\text{-}\underline{\text{C}}\text{S}_3^-$), 173.1 ($\text{HOOC}\underline{\text{C}}\text{-C}(\text{CH}_3)_2\text{-CS}_3^-$) and 219.0 ($\text{HOOC-C}(\text{CH}_3)_2\text{-}\underline{\text{C}}\text{S}_3^-$).

Carboxyl-terminated Asymmetrical Hydrophilic Chain Transfer Agent 2-[[Ethylthio)carbothioyl]thio]-2-methylpropanoic Acid (EMP).



Scheme 15: The synthesis of the chain transfer agent EMP **13**.

2-[[Ethylthio)carbothioyl]thio]-2-methylpropanoic acid (EMP) was synthesized according to a modified procedure of Schmidt et al. and Postma et al.^{266,269}

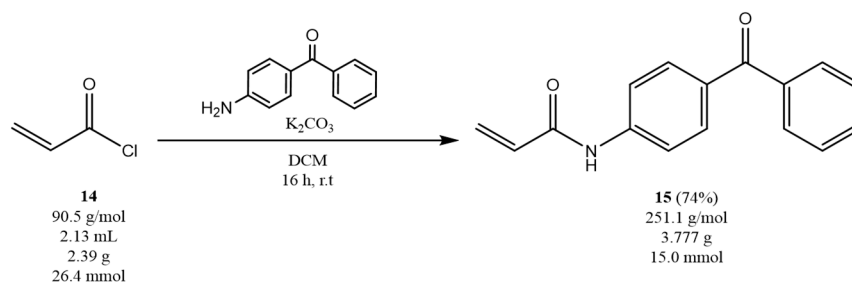
Ethanthiol (4.20 g, 67.7 mmol) and $\text{K}_3\text{PO}_4 \cdot \text{H}_2\text{O}$ (14.40 g, 67.7 mmol) were added to acetone (250 mL). After 30 minutes carbon disulfide (4.20 g, 67.7 mmol) and after another 30 minutes 2-bromoisobutyric acid (9.40 g, 56.4 mmol) were added under vigorous stirring. After 24 hours the reaction mixture was neutralized with aqueous 1M HCl (200 mL) and extracted trice with DCM (150 mL). The combined organic phase was washed trice with saturated aqueous NaHCO_3 (150 mL), with distilled water (150 mL) and dried over anhydrous MgSO_4 . After filtration and concentrating to dryness, the obtained product was recrystallized trice in *n*-hexane.

Yield: 10.28 g (68%).

^1H NMR (500 MHz, CDCl_3 , shown in the appendix, Figure S9a), δ ppm: 1.34 (t, 3H, $\text{J}=7.4$ Hz, $\text{CH}_3\text{-CH}_2\text{-CS}_3^-$), 1.73 (s, 6H, $-\text{CS}_3\text{-C}(\text{CH}_3)_2\text{-COOH}$), 3.30 (q, 2H, $\text{J}=7.4$ Hz, $\text{CH}_3\text{-CH}_2\text{-CS}_3^-$) and 10.99 (br. s, 1H, $-\text{COOH}$).

^{13}C NMR (125 MHz, CDCl_3 , shown in the appendix, Figure S9b), δ ppm: 12.6 ($\text{CH}_3\text{-CH}_2\text{-CS}_3^-$), 24.9 ($-\text{CS}_3\text{-C}(\text{CH}_3)_2\text{-COOH}$), 31.1 ($\text{CH}_3\text{-CH}_2\text{-CS}_3^-$), 55.3 ($-\text{CS}_3\text{-C}(\text{CH}_3)_2\text{-COOH}$), 178.9 ($-\text{COOH}$) and 220.3 ($-\text{CS}_3^-$).

14.3.2. Monomers

Photo-crosslinkable Monomer *N*-(4-Benzoylphenyl)acrylamide (BPAAm).

Scheme 16: The synthesis of the photo-crosslinkable monomer BPAAm **15**.

N-(4-Benzoylphenyl)acrylamide (BPAAm) was synthesized according to a modified procedure of Nash et al.²⁶⁵

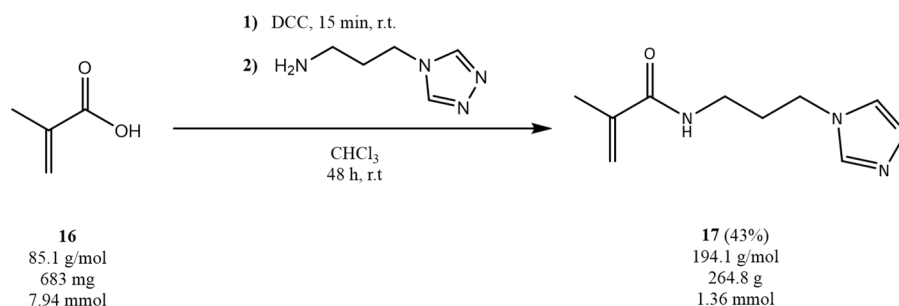
In a two necked flask equipped with magnetic stirring bar, dropping funnel and argon flux, 4-aminobenzophenone (4.00 g, 20.3 mmol) was dissolved in CH₂Cl₂ (50 mL) containing K₂CO₃ (2.80 g, 20.3 mmol). Prop-2-enoyl chloride (2.39 g, 26.4 mmol, 2.13 mL) was dissolved in CH₂Cl₂ (50 mL) and transferred to the dropping funnel. The solution was added dropwise to the cooled reaction mixture under vigorous stirring. The conversion was investigated by TLC (silica gel, CH₂Cl₂:EtOAc=6:1, R_f(BPAAm)=0.78, iodine indication). After 16 hours the mixture was extracted three times with water (100 mL) and concentrated *via* rotary evaporation. The product was recrystallized twice in cold dichloromethane. Afterwards the slightly brownish solid was dried.

Yield: 3.77 g (74%).

¹H NMR (400 MHz, CDCl₃, shown in the appendix, Figure S10a), δ ppm: 5.82 (dd, 1H, J=1.2/10.2 Hz, H₂C=CH-CONH-), 6.34 (dd, 1H, J=10.2/17.0 Hz, H₂C=CH-CONH-), 6.47 (dd, 1H, J=1.5/17.0 Hz, H₂C=CH-CONH-), 7.48 (m, 2H, -CONH-arom.), 7.59 (m, 1H, J=7.4 Hz, -CONH-arom.), 7.75 (m, 6H, J=7.4 Hz, -CONH-arom.) and 8.14 (br. s, 1H, -CONH-arom.).

¹³C NMR (101 MHz, CDCl₃, shown in the appendix, Figure S10b), δ ppm: 119.1 (-CONH-arom.), 129.1 (-CONH-arom.), 129.6 (H₂C=CH-CONH-), 130.7 (-CONH-arom.), 131.7 (-CONH-arom.), 132.4 (-CONH-arom.), 133.2 (H₂C=C_H-CONH-), 133.9 (-CONH-arom.), 137.7 (-CONH-arom.), 141.9 (-CONH-arom.), 163.9 (-CONH-) and 196.9 (-CONH-arom.-C=O-arom.).

Ion Sensitive Coordination Monomer *N*-[3-(4*H*-1,2,4-Triazol-4-yl)propyl]methacrylamide (APTRZMAAm).



Scheme 17: The synthesis of the ion sensitive coordination monomer APTRZMAAm **17** via DCC coupling.

MAA (0.68 g, 7.94 mmol) and DCC (1.97 g, 9.52 mmol) were dissolved in chloroform (10 mL) and stirred for 15 min. A solution of APTRZ (0.40 g, 3.18 mmol), prepared in chloroform (10 mL), was added dropwise to the reaction mixture within 10 minutes under vigorous stirring. The conversion was monitored *via* TLC (silica gel, EtOH, $R_f(\text{APTRZMAAm})=0.8$, FeBr_2 or bromocresol green indication). After 48 hours the mixture was concentrated *via* rotary evaporation and extracted fivefold with water (5x 10 mL). The combined aqueous phase was washed three times with CHCl_3 (150 mL), concentrated by freeze drying (not to dryness) and further applied as aqueous stock solution. The shown recorded spectra were from a completely dried sample.

Yield: 0.26 g (43%).

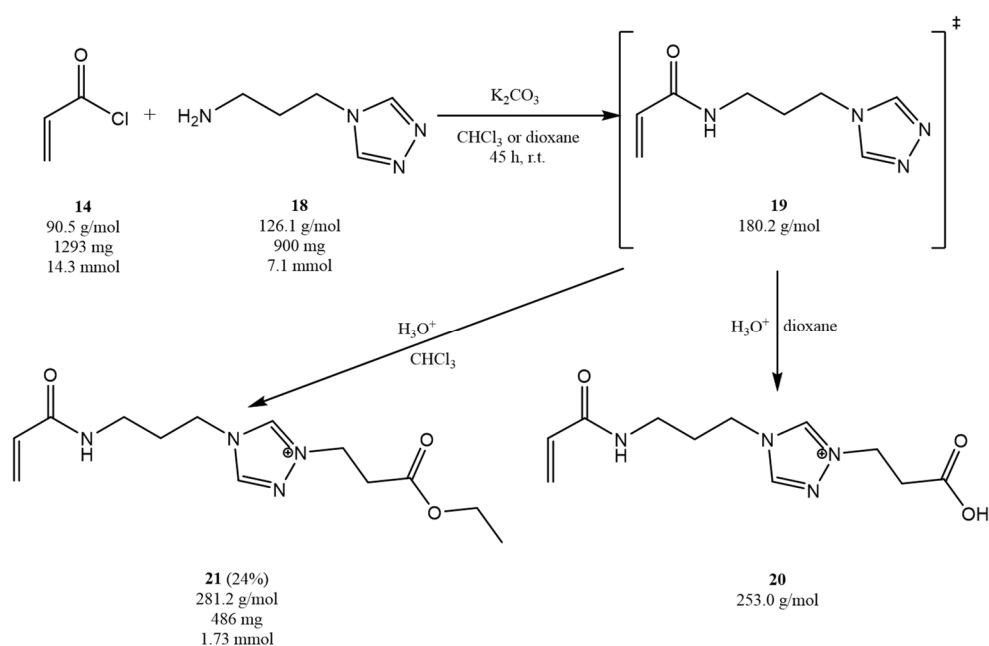
HPLC-MS (water/acetonitrile (95:5), shown in the appendix, Figure S12): 4.76 min, $M[+H]=195.1$ g/mol.

^1H NMR (500 MHz, CDCl_3 , shown in the appendix, Figure S11a) δ ppm: 1.97 (s, 3H, $\text{H}_2\text{C}=\text{CR}-\underline{\text{CH}}_3$), 2.08 (quin, $J=6.7$ Hz, 2H, $-\text{CH}_2-\underline{\text{CH}}_2-\text{CH}_2-\text{TRZ}$), 3.37 (q, $J=6.2$ Hz, 2H, $-\text{CONH}-\underline{\text{CH}}_2-\text{CH}_2-$), 4.11 (t, $J=6.9$ Hz, 2H, $-\text{CH}_2-\underline{\text{CH}}_2-\text{TRZ}$), 5.35 (s, 1H, $\underline{\text{H}}_2\text{C}=\text{CR}-\text{CH}_3$), 5.74 (s, 1H, $\underline{\text{H}}_2\text{C}=\text{CR}-\text{CH}_3$), 6.80 (br. s., 1H, $\text{H}_2\text{C}=\text{C}-\text{CH}_3-\text{CONH}-\underline{\text{H}}-\text{CH}_2-$) and 8.30 (s, 2H, $-\text{CH}_2-\underline{\text{TRZ}}$).

^{13}C NMR (125 MHz, CDCl_3 , shown in the appendix, Figure S11b), δ ppm: 18.7 ($\text{H}_2\text{C}=\text{CR}-\underline{\text{C}}\text{H}_3$), 31.2 ($-\text{CH}_2-\underline{\text{C}}\text{H}_2-\text{CH}_2-\text{TRZ}$), 36.4 ($-\text{CONH}-\underline{\text{C}}\text{H}_2-\text{CH}_2-$), 43.0 ($-\text{CH}_2-\underline{\text{C}}\text{H}_2-\text{TRZ}$), 120.0 ($\text{H}_2\underline{\text{C}}=\text{CR}-\text{CH}_3$), 139.6 ($\text{H}_2\text{C}=\underline{\text{C}}\text{R}-\text{CH}_3$), 142.9 ($-\text{CH}_2-\underline{\text{TRZ}}$) and 169.1 ($\text{H}_2\underline{\text{C}}=\text{C}-\text{CH}_3-\underline{\text{C}}\text{ONH}-\text{CH}_2-$).

Unsuccessful Pathways within the Syntheses of Ion Sensitive Coordination Monomers.

Pathway 1: Acrylation via Acryloyl Chloride



Scheme 18: The unsuccessful synthesis of the ion sensitive coordination monomer APTRZAAm **19** via acryloyl chloride **14** coupling with its solvent dependent formed side product.

APTRZ (0.90 g, 7.1 mmol) was dissolved in CHCl_3 (40 mL) containing K_2CO_3 (4.44 g, 32.1 mmol). Prop-2-enoyl chloride (1.29 g, 14.29 mmol) was dissolved in CHCl_3 (40 mL) and transferred to the dropping funnel. The solution was added dropwise to the cooled reaction mixture under vigorous stirring. The conversion was investigated by TLC ($\text{Al}_2\text{O}_3\text{-N}$, CH_2Cl_2 : $\text{MeOH}:\text{NH}_3=45:7:1$, $R_f(\text{APTRZAAm})=0.69$, iodine indication). After 45 hours the mixture was concentrated *via* rotary evaporation and under vacuum. The remaining gel was diluted in DCM and filtered to remove the K_2CO_3 and concentrated to dryness. Afterwards the slightly brownish oil was dissolved in water and freeze dried. The acrylic acid impurities were removed by column chromatography (cellulose MN 2100, hexane) and the targeted product was supposed to be obtained by an eluent change (cellulose MN 2100, $\text{THF}:\text{AcOH}=28:1$, $R_f(\text{APTRZAAm})=0.81$, iodine indicator). The product phase was concentrated to dryness. The targeted product (APTRZAAm) could not be obtained.

Yield: 0.49 mg (24%).

HPLC-MS (water/acetonitrile (95:5), shown in the appendix, Figure S13): 7.108 min, $M[M^+]=281.2$ g/mol.

^1H NMR (400 MHz, CDCl_3 , shown in the appendix, Figure S13a), δ ppm: 1.23 (t, $J=7.3$ Hz, 3H,

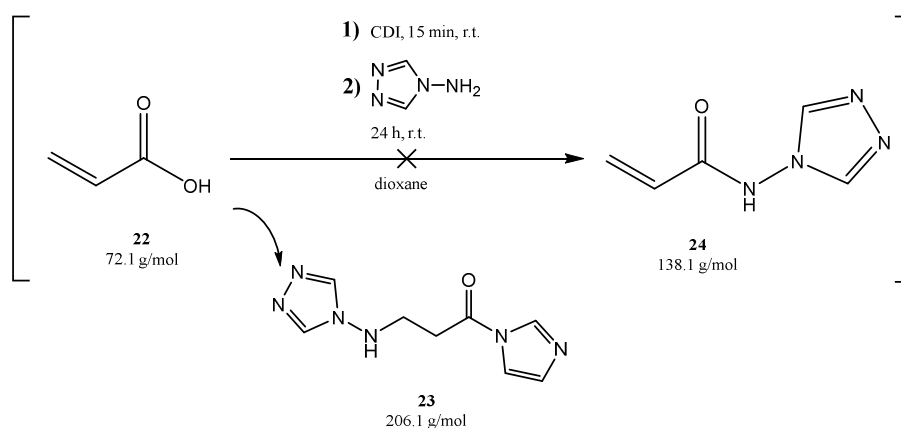
R-COO-CH₂-CH₃), 2.25 (p, $J=5.6$ Hz, 2H, R-CONH-CH₂-CH₂-CH₂-R), 3.04 (t, $J=6.4$ Hz, 2H, R-CH₂-CH₂-COO-R), 3.35 (q, $J=5.6$ Hz, 2H, R-CONH-CH₂-CH₂-CH₂-R), 4.12 (q, $J=7.3$ Hz, 2H, R-COO-CH₂-CH₃), 4.59 (t, $J=6.4$ Hz, 2H, R-CONH-CH₂-CH₂-CH₂-TRZ), 4.73 (t, $J=6.4$ Hz, 2H, R-TRZ-CH₂-CH₂-R), 5.67 (dd, $J=1.8/10.2$, 1H, HCH=CH-CONH-R), 6.23 (dd, $J=1.8/17.3$ Hz, 1H, HCH=CH-CONH-R), 6.38 (dd, $J=10.2/17.0$, 1H, H₂C=CH-CONH-R), 8.62 (br. t, 1H, H₂C=CH-CONH-R), 9.24 (s, 1H, R-TRZ-R) and 10.43 (s, 1H, R-TRZ-R).

^{13}C NMR (101 MHz, CDCl_3 , shown in the appendix, Figure S13b): δ ppm 14.0 (R-COO-CH₂-CH₃), 29.8 (R-TRZ-CH₂-CH₂-R), 32.4 (R-CONH-CH₂-CH₂-CH₂-R), 35.4 (R-CONH-CH₂-CH₂-CH₂-R), 46.3 (R-CONH-CH₂-CH₂-CH₂-TRZ), 48.1 (R-TRZ-CH₂-CH₂-R), 61.5 (R-COO-CH₂-CH₃), 126.2 (H₂C=CH-CONH-R), 131.0 (H₂C=CH-CONH-R), 143.9 (R-TRZ-R), 144.6 (R-TRZ-R), 166.9 (H₂C=CH-CONH-R) and 169.6 (R-CH₂-COO-CH₂-CH₃).

The isotope synthesis applied in dioxane was not purified. The yield was not determined. The NMR (not shown) supported the existence of a product mixture of the targeted compound APTRZAam and the described side-product.

HPLC-MS (water/acetonitrile (95:5), shown in the appendix, Figure S14): 3.727 min, $M[M^+]=253.0$ g/mol.

Pathway 2: CDI Coupling



Scheme 19: The unsuccessful synthesis of the ion sensitive coordination monomer equivalent TRZAAM **24** via CDI coupling with its formed side product **23**.

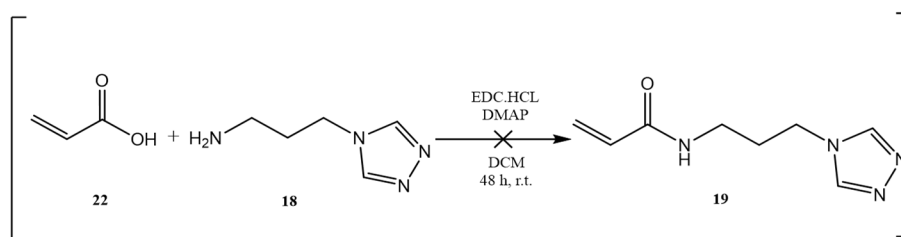
CDI (925.6 mg, 5.70 mmol) was dissolved in distilled dioxane (20 mL) containing AA (342.8 mg, 4.78 mmol). TRZ-NH₂ (200.0 mg, 2.38 mmol) was added to the reaction mixture after 15 minutes under vigorous stirring. A whitish precipitate was obtained after short time. After 24 hours the solid was filtered and washed several times with distilled dioxane. The product was dissolved in little amount of distilled water and precipitated in EtOAc. The analyses revealed the formation of a side product.

Yield: - mg (-%) (Not analysed)

HPLC-MS (water/acetonitrile (95:5), shown in the appendix, Figure S15b/c): 3.409 min, $M[M+H^+]=207.1$ g/mol.

¹H NMR (400 MHz, DMSO-d₆, shown in the appendix, Figure S15a), δ ppm: 2.79 (t, J=6.7 Hz, 2H, TRZ-NH₂-CH₂-CH₂-CO-TRZ), 3.45 (br. s, 1H, TRZ-NH-CH₂-CH₂-CO-TRZ), 4.27 (t, J=6.7 Hz, 1H, TRZ-NH-CH₂-CH₂-CO-TRZ), 6.90 (s, 1H, TRZ-NH-CH₂-CH₂-CO-TRZ), 7.17 (s, 1H, TRZ-NH-CH₂-CH₂-CO-TRZ), 7.62 (s, 1H, TRZ-NH-CH₂-CH₂-CO-TRZ) and 8.57 (s, 2H, TRZ-NH-CH₂-CH₂-CO-TRZ).

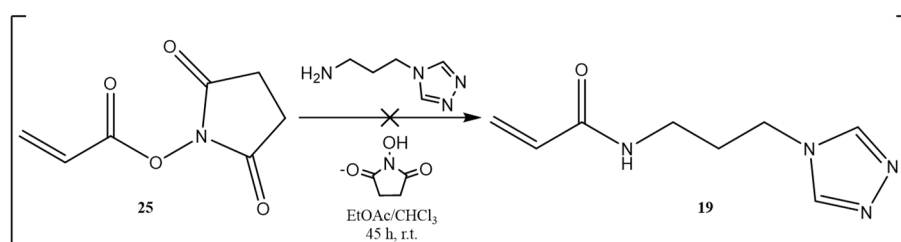
Pathway 3: EDC Chemistry/Active Ester Coupling



Scheme 20: The unsuccessful synthesis of the ion sensitive coordination monomer APTRZAAM **19** via EDC coupling.

EDC coupling: The APTRZ (100 mg, 1.03 mmol) was added to dichloromethane (100 mL) solution containing the excesses of 66% EDC (297 mg, 1.55 mmol) and 10% acrylic acid (74 mg, 1.03 mmol) under argon flux. 4-(Dimethylamino)-pyridine (126 mg, 1.03 mmol) was added to the above reaction mixture and stirred for 24 hours at room temperature. The conversion was investigated by TLC (Cell-300, EtOH:Hex:AcOH=200:100:1, iodine and FeBr₂ indication). The reaction was quenched after 48 hours. The purification was not enabled.

Yield: 0 mg (0%).



Scheme 21: The unsuccessful synthesis of the ion sensitive coordination monomer APTRZAAM **19** via the active ester NAS.

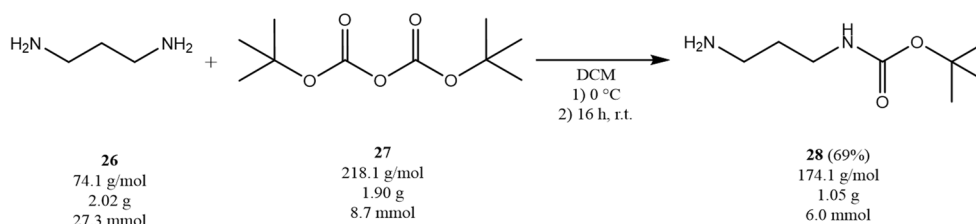
Active ester: 2,5-Dioxopyrrolidin-1-yl acrylate (100 mg, 0.59 mmol) was dissolved in dry EtOAc (or CHCl₃) (12 mL) containing K₂CO₃ (270 mg, 1.95 mmol). A solution of APTRZ (50 mg, 0.39 mmol) in CHCl₃ (10.5 mL) was added dropwise under vigorous stirring and formation of precipitation. The reaction mixture was diluted with dry EtOAc (10 mL) after 30 minutes reaction time. The conversion was investigated by TLC (Al₂O₃-N, CH₂Cl₂:MeOH:NH₃=45:7:1, iodine and FeBr₂ indication). After 45 hours the mixture was concentrated via rotary evaporation and concentrated under vacuum. The remaining gel was diluted in DCM and filtered to remove the K₂CO₃ and concentrated to dryness. Afterwards the slightly brownish oil was dissolved in water and freeze dried. The target product could not be obtained.

Yield: 0 mg (0%).

Amine-functionalized and Boc-protected DNA-binding Monomer *tert*-Butyl-(3-acrylamidopropyl)carbamate (APAAm-Boc).

tert-Butyl(3-acrylamidopropyl)carbamate (APAAm-Boc) was synthesized according to a modified procedure of Mateescu et al.²⁵⁹ The synthesis was performed in the Macromolecular Chemistry working group by Niklas Jung. The synthesis was divided into two steps.

Step 1: Introduction of the protection group.

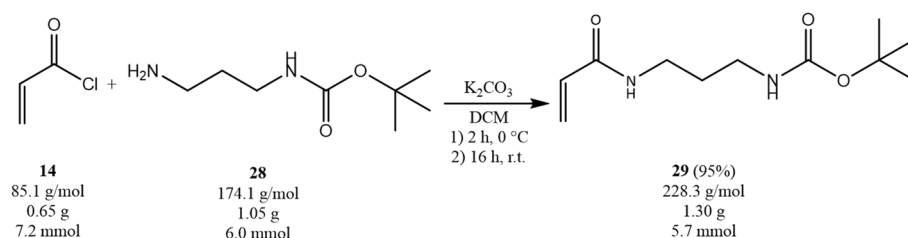


Scheme 22: The asymmetrical Boc-protection of the propylendiamine **26** for the precursor *tert*-butyl(3-aminopropyl)carbamate **28**.

1,3-Propylenediamine (2.02 g, 27.3 mmol, 2.3 mL) was dissolved in CH₂Cl₂ (35 mL) and cooled to 0 °C. A mixture of di-*tert*-butyl dicarbonate (1.90 g, 8.7 mmol, 2.00 mL) was dissolved in CH₂Cl₂ (15 mL) and added dropwise. The reaction mixture was stirred for 16 hours at room temperature. Subsequently, the reaction mixture was concentrated to dryness and the residue dissolved in CH₂Cl₂ (25 mL). The organic phase was washed with saturated NaHCO₃ solution (3 x 30 mL), dried over anhydrous Na₂SO₄ and the solvent was removed under reduced pressure to yield the colourless, sticky product. The neglectable impurities of the double protected conjugate is not reacting in the subsequent coupling.

¹H NMR (500 MHz, CDCl₃) δ (ppm): 0.87 (s, 2H, NH₂-CH₂-CH₂-CH₂-NH-Boc), 1.41 (s, 9H, NH₂-CH₂-CH₂-CH₂-NH-Boc), 1.58 (p, *J*=6.6 Hz, 2H, NH₂-CH₂-CH₂-CH₂-NH-Boc), 2.74 (t, *J*=6.6 Hz, 2H, NH₂-CH₂-CH₂-CH₂-NH-Boc), 3.19 (m, 2H, NH₂-CH₂-CH₂-CH₂-NH-Boc) and 4.94 (br. s, 1H, -NH-Boc).

¹³C NMR (126 MHz, CDCl₃) δ (ppm): 28.5 (NH₂-CH₂-CH₂-CH₂-NH-Boc), 33.6 (NH₂-CH₂-CH₂-CH₂-NH-Boc), 38.6 (NH₂-CH₂-CH₂-CH₂-NH-Boc), 39.8 (NH₂-CH₂-CH₂-CH₂-NH-Boc), 79.1 (NH₂-CH₂-CH₂-CH₂-NH-Boc), 156.3 (NH₂-CH₂-CH₂-CH₂-NH-Boc).

Step 2: Acrylation of the mono-protected propyl diamine.

Scheme 23: The synthesis of the Boc-protected amine-modified and DNA-binding monomer APAAm-Boc **29**.

tert-Butyl-*N*-(3-aminopropyl)carbamate (1.05 g, 6.0 mmol) was dissolved in dichloromethane (35 mL) and cooled to 0 °C. Anhydrous potassium carbonate (0.99 g, 7.2 mmol) was added and the solution was stirred for 1 hour. Acryloyl chloride (0.65 g, 7.2 mmol, 580 μ l), dissolved in dichloromethane (10 ml), was added dropwise at 0 °C under vigorous stirring. The reaction was further continued for 16 hours at room temperature. Dichloromethane (8 ml) was added to the reaction mixture, and the precipitates were filtered-off. The organic phase was extracted with saturated sodium bicarbonate (2 \times 25 mL) and saturated brine solution (2 \times 25 mL). The organic product phase was dried with anhydrous sodium sulfate, filtered and concentrated to dryness.

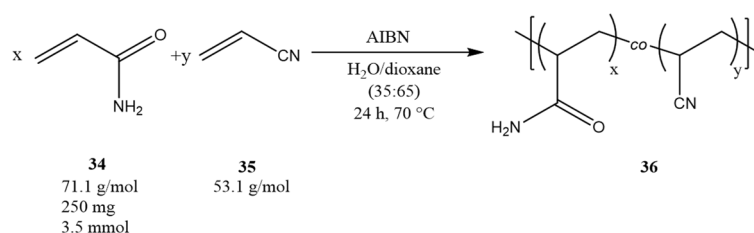
Yield: 1.30 g (95%).

1H NMR (500 MHz, $CDCl_3$, shown in the appendix, Figure S16) δ ppm: 1.42 (s, 9H, -NH-Boc), 1.63 (p, $J=6.2$ Hz, 2H, -CONH-CH₂-CH₂-CH₂-NH-Boc), 3.16 (m, 2H, -CONH-CH₂-CH₂-CH₂-NH-Boc), 3.36 (q, $J=6.2$ Hz, 2H, -CONH-CH₂-CH₂-CH₂-NH-Boc), 4.92 (br. s, 1H, -CONH-CH₂-CH₂-CH₂-NH-Boc), 5.60 (dd, $J=1.9/10.5$, 1H, H₂C=CH-CONH-), 6.09 (dd, $J=10.0/17.2$, 1H, H₂C=CH-CONH-), 6.24 (dd, $J=1.5/17.2$, 1H, H₂C=CH-CONH-) and 6.49 (br. s, 1H, -CONH-CH₂-CH₂-CH₂-NH-Boc).

^{13}C NMR (125 MHz, $CDCl_3$, shown in the appendix, Figure S16), δ ppm: 28.4 (-NH-Boc), 30.2, (-CONH-CH₂-CH₂-CH₂-NH-Boc), 35.8 (-CONH-CH₂-CH₂-CH₂-NH-Boc), 37.0 (-CONH-CH₂-CH₂-CH₂-NH-Boc), 79.4 (-CONH-CH₂-CH₂-CH₂-NH-Boc), 126.1 (H₂C=CH-CONH-), 131.1 (H₂C=CH-CONH-), 156.8 (-CONH-CH₂-CH₂-CH₂-NH-Boc) and 165.9 (H₂C=CH-CONH-)

14.3.3. Adjustable UCST by Copolymerization of AAm and AN

General Procedure for the Free-Radical Copolymerization of Tuneable Poly(AAm_x-co-AN_y) (FRP15%-50%).



Scheme 24: The free radical copolymerization of the tuneable thermoresponsive UCST copolymer poly(AAm-co-AN) **36** (FRP15-50%).

AAm (250 mg, 3.52 mmol), AN and AIBN (according to Table 12) were dissolved in the mixture of water/dioxane (35:65) (4 mL). The polymerization mixture was degassed by three freeze-thaw cycles. The reaction was started in a preheated sample holder at 70 °C and quenched after 24 hours by air after liquid nitrogen cooling. The product was precipitated twice in ice-cold MeOH (100 mL), dissolved in distilled water and freeze dried. The cloud points and molar mass distributions were determined (Table 12 and in the appendix, Table S3).

Table 12: The feed ratios of AAm (250 mg, 3.52 mmol), AN and AIBN, resulting cloud points, glass transition temperatures and yields for the general free-radical copolymerization of poly(AAm-co-AN).

Sample Code	[M]/[I]	AN		AIBN ^[a] m/ mg (μmol)	<i>T_g</i> / °C	<i>T_c</i> ^[b] / °C	Yield / % (mg)
		m/ mg (mmol)	V/ μL				
FRP15%	200	33	41	3.4	177.1	- ^[c]	57
		(0.62)		(20.7)			(162)
FRP20%	200	47	58	3.6	175.1	- ^[c]	63
		(0.88)		(21.9)			(188)
FRP25%	200	62	78	3.8	168.4	<6	48
		(1.17)		(23.1)			(150)
FRP30%	200	80	100	4.1	166.0	12	44 ^[d]
		(1.51)		(25.0)			(146)
FRP35%	200	101	126	4.4	162.6	26.8	53
		(1.90)		(26.8)			(187)
FRP40%	200	125	156	4.8	156.7	42.6	37 ^[d]
		(2.35)		(29.2)			(138)
FRP45%	200	153	191	5.2	152.8	61.1	51
		(2.88)		(31.7)			(209)
FRP50%	200	187	234	5.4	150.9	73.8	54
		(3.52)		(32.9)			(229)

^[a] The initiator was added *via* stock solution.

^[b] Cloud points (UCST) determined at the half height of the cooling cycle.

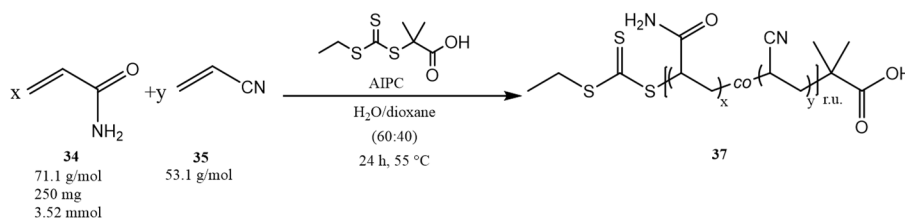
^[c] Cloud points (UCST) lay below 0 °C.

^[d] Losses during the purification procedure.

Exemplary ¹H NMR (400 MHz, D₂O/MeCN-d₃ (85:15), shown in the appendix, Figure S17a), δ ppm: 1.40-3.40 (backbone).

Exemplary ¹H NMR (500 MHz, DMSO-d₆, shown in the appendix, Figure S17b), δ ppm: 1.20-3.40 (backbone), 6.50-8.00 (amide of AAm).

General Procedure for the RAFT Copolymerization of Asymmetric and Tuneable Poly(AAm_x-co-AN_y)-EMP (CRP25.0%-55.0%, CRP3k-29k and CRP0h-24h).



Scheme 25: The RAFT copolymerization of the tuneable thermoresponsive UCST copolymer poly(AAm-co-AN)-EMP 37 (CRP25%-50%, CRP3k-29k and CRP0h-24h).

Variation of the Acrylonitrile Fraction

AAm (250 mg, 3.52 mmol) and various feed ratios of AN, EMP and AIPC (Table 13) were dissolved in the mixture of water/dioxane (60:40) (2.5 mL). The polymerization mixture was degassed by three freeze-thaw cycles. The polymerization was started in a preheated sample holder at 55 °C and quenched after 24 hours by air after cooling with liquid nitrogen. The product was precipitated twice in ice-cold MeOH (100 mL), dissolved in distilled water and freeze dried. The cloud points and molar mass distributions were determined (in the appendix, Table S5).

Table 13: The feed ratios of the acrylamide (250 mg, 3.52 mmol), acrylonitrile, EMP and AIPC, resulting glass transition temperatures, cloud points and yields for the general RAFT copolymerization of poly(AAm-co-AN)-EMP with various AN fraction.

Sample Code	[M]/ [CTA]	AN		EMP n/ μmol (mg)	AIPC ^[a] n/ μmol (mg)	<i>T_g</i> / °C	<i>T_c</i> ^[b] / °C	Yield / % (mg)
		n/ mmol (mg)	V/ μL					
CRP25.0%	200	1.17 (62)	78	23 (5.28)	4.7 (1.52)	- ^[d]	- ^[c]	- ^[c]
CRP27.5%	200	1.34 (71)	89	24 (5.46)	4.9 (1.57)	- ^[d]	- ^[c]	- ^[c]
CRP30.0%	200	1.51 (80)	100	25 (5.66)	5.0 (1.62)	162.9	1.6	69 (231)
CRP32.5%	200	1.70 (90)	113	26 (5.87)	5.2 (1.68)	161.3	8.7	82 (284)
CRP35.0%	200	1.90 (101)	126	27 (6.09)	5.4 (1.75)	158.2	16.0	83 (295)
CRP37.5%	200	2.11 (112)	140	28 (6.34)	5.6 (1.82)	158.2	28.0	73 (269)
CRP40.0%	200	2.35 (125)	156	29 (6.60)	5.9 (1.90)	152.7	32.3	58 (220)
CRP41.0%	200	2.45 (130)	162	30 (6.71)	6.0 (1.93)	- ^[d]	37.5	45.2 ^[e] (176)
CRP45.0%	200	2.88 (153)	191	32 (7.20)	6.4 (2.07)	152.7	52.0	48 ^[e] (195)
CRP50.0%	200	3.52 (187)	234	35 (7.92)	7.0 (2.27)	- ^[d]	72.5	40 ^[e] (174)
CRP55.0%	200	4.30 (228)	286	39 (8.80)	7.8 (2.53)	- ^[d]	78.8	24 ^[e] (114)

^[a] The initiator was added *via* stock solution.

^[b] Cloud points (UCST) determined at the half height of the cooling cycle.

^[c] The yields and *T_c* were not further determined due to non-existent thermoresponsive properties.

^[d] The values were not determined.

^[e] Yield lowered due to losses caused by the high UCST.

Variation of the Chain Length

The educts AAm (250 mg, 3.52 mmol), AN (112 mg, 2.11 mmol, 140 μ L), EMP and AIPC (Table 14) were applied according to the procedure above. The cloud points and molar mass distributions were determined (in the appendix, Table S6).

Table 14: The feed ratios of the monomers AAm (250 mg, 3.52 mmol) and AN (112 mg, 2.11 mmol, 140 μ L), EMP and AIPC, resulting cloud points and yields for the general RAFT copolymerization of poly(AAm-co-AN)-EMP with various chain lengths.

Sample Code	[M]/[CTA]	EMP ^[a] n/ μ mol (mg)	AIPC ^[a] n/ μ mol (mg)	T_c ^[b] / $^{\circ}$ C	Yield / % (mg)
CRP3k	50	112.6 (25.2)	22.5 (7.3)	9.5	56 (216)
CRP6k	100	56.3 (12.6)	11.3 (3.6)	23.2	53 (198)
CRP11k	200	28.2 (6.3)	5.6 (1.8)	24.9	57 (208)
CRP16k	300	18.8 (4.2)	3.8 (1.2)	27.9	52 (189)
CRP21k	400	14.1 (3.2)	2.8 (0.9)	34.2	29 (105)
CRP29k	500	11.3 (2.5)	2.3 (0.7)	24.8	50 (180)

^[a] The initiator and chain transfer agent were added *via* stock solution.

^[b] Cloud points (UCST) determined at the half height of the cooling cycle.

Investigation of Copolymerization Kinetic

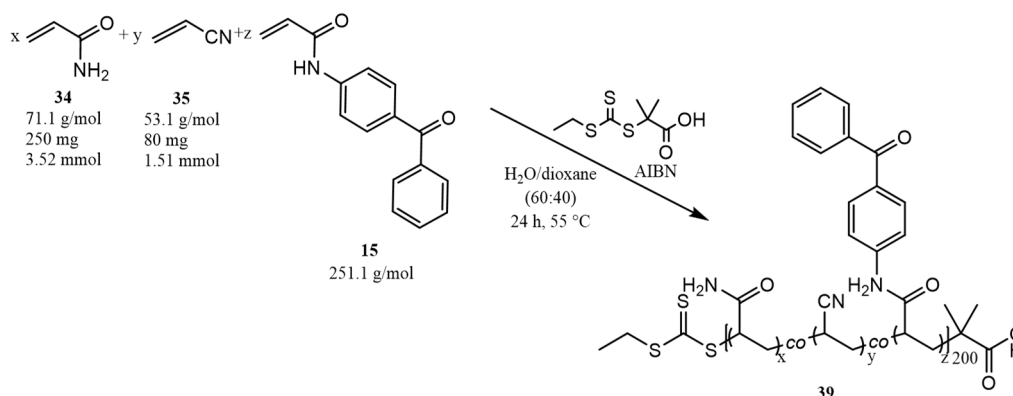
AAm (1500 mg, 21 mmol), AN (748 mg, 14 mmol, 748 μ L), EMP (39 mg, 176 μ mol) and AIPC (11 mg, 35 μ mol) were dissolved in a mixture of deuterated D₂O and non-deuterated dioxane (15 mL) (60:40). The mixture was further used as stock solution, separated into six reaction mixtures (2.5 mL) and applied according to the procedure above. After 1 hours, 2 hours, 4 hours, 6 hours and 24 hours, one reaction batch was quenched by air after cooling with liquid nitrogen. The ¹H NMR measurement was prepared from a reaction mixture aliquot (160 μ L), which was filled up to 640 μ L with deuterated water (480 μ L).

The reaction mixtures were characterized with respect to the consumption of monomers, conversion and chain growth by ¹H NMR (recorded in D₂O, integration normalized with respect to dioxane as internal standard, shown in the appendix, Figure S20 and Figure S21) and gel-permeation chromatography (in the appendix, Table S4). The purified product was additionally characterized with respect to the monomer incorporation by ¹H NMR (recorded in DMSO-d₆, shown in the appendix, Table S6).

Exemplary ¹H NMR (400 MHz, D₂O/MeCN-d₃ (85:15), shown in the appendix, Figure S19a), δ ppm: 1.40 (br. t, J=6.7, 3H, $\text{CH}_3\text{-CH}_2\text{-CS}_3\text{-R}$), 1.50-3.35 (backbone) and 3.49 (br. q, J=7.0, 2H, $\text{CH}_3\text{-CH}_2\text{-CS}_3\text{-R}$).

Exemplary ¹H NMR (400 MHz, DMSO-d₆, shown in the appendix, Figure S19b), δ ppm: 1.28 (br. t, J=6.7, 3H, $\text{CH}_3\text{-CH}_2\text{-CS}_3\text{-R}$), 1.30-3.00 (backbone), 3.32 (br. q, J=7.0, 2H, $\text{CH}_3\text{-CH}_2\text{-CS}_3\text{-R}$) and 6.50-7.70 (m, $\text{NH}_2\text{-R}$ of acrylamide).

General Procedure for the Free-Radical Copolymerization of Tuneable and Photo-Crosslinkable Poly(AAm_x-co-AN_y-co-BPAAm_z) (FRP-BP0.5%-5.0%).



Scheme 26: The free-radical copolymerization of the tuneable and photo-crosslinkable UCST copolymer poly(AAm-co-AN-co-BPAAm) **38** (FRP-BP0.5%-5.0%).

AAm (250 mg, 3.52 mmol), AN (80 mg, 1.51 mmol), BPAAm (Table 15) and AIBN (Table 15) were dissolved in mixture of water/dioxane (35:65) (4mL). The polymerization mixture was degassed by three freeze-thaw cycles. The polymerization was started in a preheated sample holder at 70 °C and quenched after 24 hours by air after liquid nitrogen cooling. The product was precipitated twice in ice-cold MeOH (100 mL), dissolved in distilled water and freeze dried. The cloud points and molar mass distributions were determined (in the appendix, Table S7).

Table 15: The feed ratios of the AAm (250 mg, 3.52 mmol), AN (80 mg, 1.51 mmol), photo-crosslinkable monomer BPAAm, AIPC, resulting cloud points and yields for the general FRP copolymerization of poly(AAm-co-AN-co-BPAAm) with various BPAAm fractions.

Sample Code	[M]/ [I]	BPAAm n/ μ mol (mg)	AIBN ^[a] n/ μ mol (mg)	T_g / °C	T_c ^[b] / °C	Yield / % (mg)
FRP-BP0.5%	200	25.3 (6)	25.3 (4.15)	171.6	9.0	42 (141)
FRP-BP1.0%	200	50.3 (13)	25.4 (4.16)	171.2	25.8	43 (146)
FRP-BP1.3%	200	65.8 (17)	25.5 (4.18)	171.6	36.2	68.2 (265)
FRP-BP2.0%	200	102.7 (26)	25.6 (4.20)	175.2	55.9	54 (190)
FRP-BP5.0%	200	264.7 (67)	26.5 (4.35)	173.8	>90 ^[c]	53 (209)

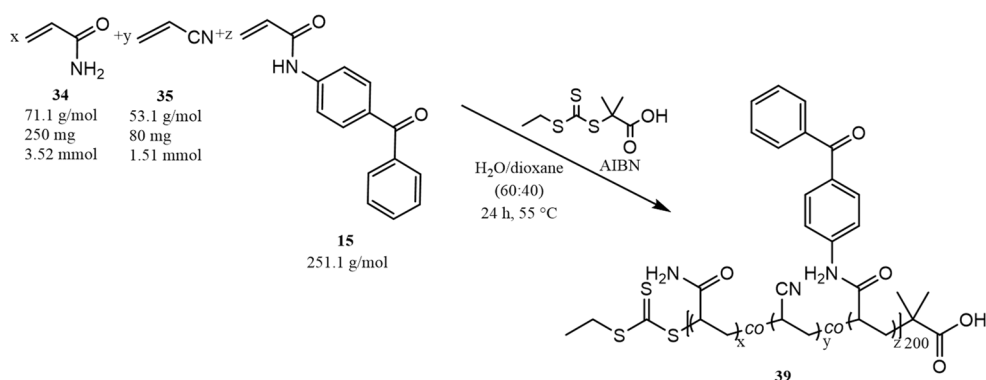
^[a] The chain transfer agent and initiator were added *via* stock solution.

^[b] Cloud points (UCST) determined at the half height of the cooling cycle.

^[c] Cloud point lay above the detectable temperature. Value is calculated theoretically.

Exemplary ¹H NMR (400 MHz, D₂O/MeCN-d₃ (85:15), shown in the appendix, Figure S26), δ ppm: 1.40-3.40 (backbone) and 7.50-8.00 (aromatic proton of the BP side group units).

General Procedure for the RAFT Copolymerization of Asymmetric, Tuneable and Photo-Crosslinkable Poly(AAm_x-co-AN_y-co-BPAAm_z)-EMP (CRP-BP0.5%-2.5%).



Scheme 27: The RAFT copolymerization of the tuneable and photo-crosslinkable UCST copolymer poly(AAm-co-AN-co-BPAAm)-EMP **39** (CRP-BP0.5-2.5%).

AAm (250 mg, 3.52 mmol), AN (80 mg, 1.5 mmol) and various feed ratios of BPAAm, EMP and AIPC (Table 16) were dissolved in mixture of water/dioxane (60:40) (2.5 mL). The polymerization mixture was degassed by three freeze-thaw cycles. The polymerization was started in a preheated sample holder at 55 °C and quenched after 24 hours by air after cooling with liquid nitrogen. The product was precipitated twice in ice-cold MeOH (100 mL), dissolved in distilled water and freeze dried. The cloud points and molar mass distributions were determined (in the appendix, Table S8).

Table 16: The feed ratios of the AAm (250 mg, 3.52 mmol), AN (80 mg, 1.5 mmol), the photo-crosslinkable monomer BPAAm, AIPC, EMP, resulting cloud points and yields for the general RAFT copolymerization of poly(AAm-co-AN-co-BPAAm)-EMP with various BPAAm fractions.

Sample Code	[M]/ [CTA]	BPAAm n/ μmol (mg)	EMP ^[a] n/ μmol (mg)	AIBN ^[a] n/ μmol (mg)	<i>T</i> _c ^[b] / °C	Yield /% (mg)
CRP-BP0.5%	200	25 (6)	25.3 (5.7)	5.1 (1.6)	18.8	75 (255)
CRP-BP1.0%	200	51 (13)	25.4 (5.7)	5.1 (1.6)	33.5	71 (247)
CRP-BP1.3%	200	77 (19)	25.5 (5.7)	5.1 (1.7)	45.5	73 (258)
CRP-BP2.0%	200	103 (26)	25.7 (5.8)	5.1 (1.7)	56.4	62 (222)
CRP-BP2.5%	200	129 (32)	25.8 (5.8)	5.2 (1.7)	71.0	58 (198)

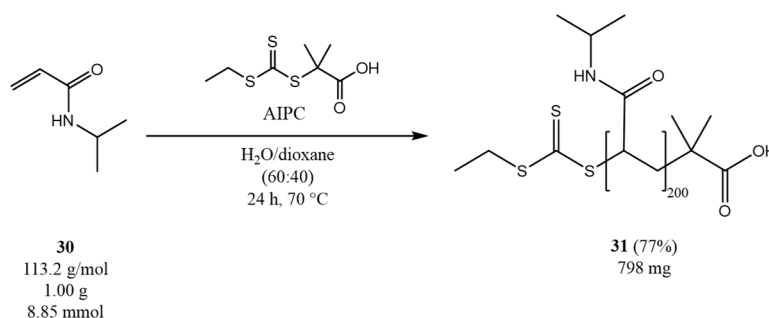
^[a] The chain transfer agent and initiator were added *via* stock solution.

^[b] Cloud points (UCST) determined at the half height of the cooling cycle.

¹H NMR (400 MHz, D₂O/MeCN-*d*₃ (85:15), shown in the appendix, Figure S28a), δ ppm: 1.40 (br. t, 3H, CH₃-CH₂-CS₃-), 1.45-3.40 (backbone), 3.49 (br. q, 2H, CH₃-CH₂-CS₃-) and 7.50-8.00 (aromatic proton of the BP side group units).

14.3.4. Photo-Crosslinkable NIPAAm-Based LCST Copolymers

RAFT Polymerization of the Reference Homopolymer Poly(NIPAAm)-EMP (R1).



Scheme 28: The RAFT polymerization of the reference homopolymer poly(NIPAAm)-EMP **31**.

NIPAAm (1.00 g, 8.86 mmol), EMP (34 mg, 94 μ mol) and a stock solution of AIPC (1.4 mg, 4.4 μ mol) were dissolved in a mixture of water/dioxane (60:40) (10 mL). The polymerization mixture was degassed by threefold circles of freeze-thaw. The polymerization was started in a preheated sample holder at 55 °C and quenched after 24 hours by air under ice cooling. The polymer was precipitated in ice cooled diethyl ether twice, extracted *via* stirring in diethyl ether over 2 d and dried under reduced pressure. The cloud points and molar mass distributions were determined (shown in the appendix, Figure S31).

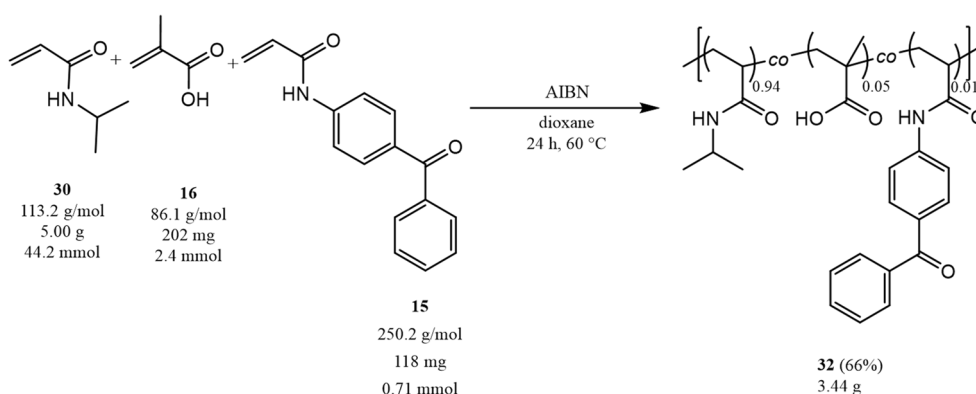
Yield: 0.80 g (77%).

¹H NMR (400 MHz, CDCl₃, shown in the appendix, Figure S30), δ ppm: 0.94-3.40 (backbone), 3.83-4.27 (br. s, isopropyl of NIPAAm), 3.33 (CH₃-CH₂-CS₃-backbone), 5.60-7.20 (br. s, amides of the side chains) and 7.42-7.87 (m, BP protons).

Cloud point (recorded at 1.0 wt% aqueous solution, shown in the appendix, Figure S31):

$T_c=33.0$ °C

Free Radical Copolymerization of the Photo-Crosslinkable Poly(NIPAAm-co-MAA-co-BPAAm) (94:5:1) (FRP-MAA).



Scheme 29: The free-radical copolymerization of the photo-crosslinkable poly(NIPAAm) **32**.

NIPAAm (5.00 g, 44 mmol), MAA (203 mg, 2.35 mmol, 198 μ L), BPAAm (118 mg, 0.71 mmol) were dissolved in freshly distilled dioxane (40 mL). The stabilizer of MAA was removed *via* short column chromatography (aluminium oxide, neutral). The polymerization mixture was degassed by threefold cycles of vacuum (10 s) and argon purge, before AIBN (6.8 mg, 41.0 μ mol) was added under argon stream. Finally, the mixture was degassed again by five cycles of vacuum (10 s) and argon purge. The polymerization was started in a preheated sample holder at 60 °C and quenched after 24 hours by air under ice cooling. The polymer was precipitated three times in ice cooled diethyl ether and dried under reduced pressure. The cloud points and molar mass distributions were determined (shown in the appendix, Figure S33). The availability of the BPAAm unit was determined by ^1H NMR measurements.

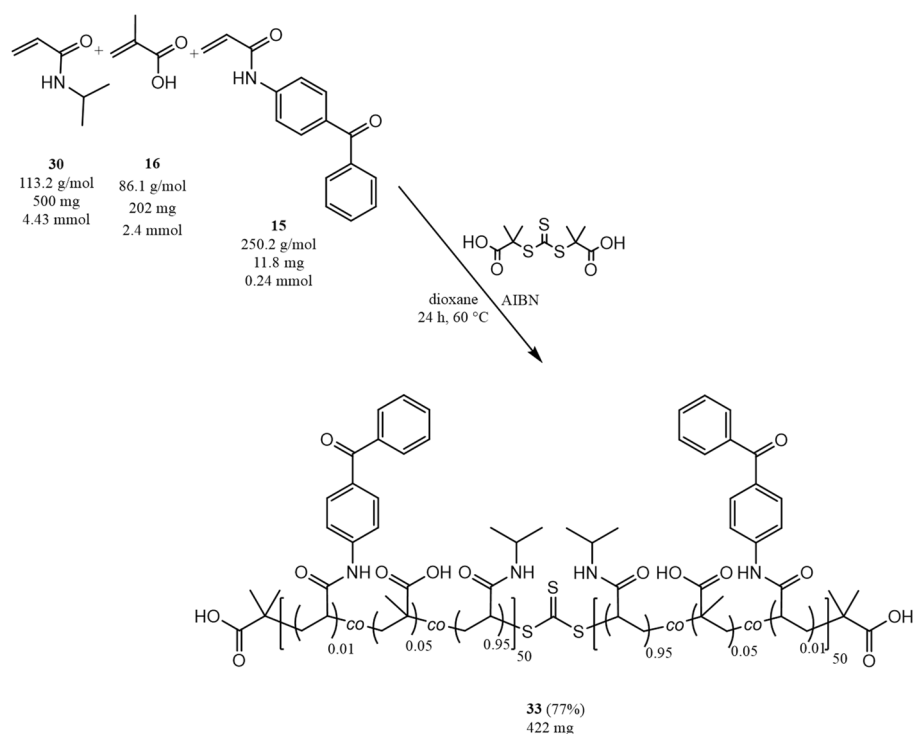
Yield: 3.44 g (66%).

^1H NMR (400 MHz, CDCl_3 , shown in the appendix, Figure S32), δ ppm: 0.94-3.65 (backbone), 3.83-4.27 (br. s, isopropyl of NIPAAm), 5.60-7.20 (br. s, amides of the side chains) and 7.42-7.87 (aromatic benzophenone protons).

Cloud point (recorded at 1.0 wt% aqueous solution, shown in the appendix, Figure S33):

$T_c=33.6$ °C

RAFT Copolymerization of the Symmetric and Photo-Crosslinkable Poly(NIPAAm-co-MAA-co-BPAAm)-BIT (94:5:1) (CRP-MAA-BIT).



Scheme 30: The RAFT copolymerization of the symmetric and photo-crosslinkable poly(NIPAAm)-BIT **33**.

NIPAAm (500 mg, 4.43 mmol), MAA (20 mg, 0.24 mmol, 20 μ L), BPAAm (12 mg, 47 μ mol) and BIT (13 mg, 47 μ mol) were dissolved in freshly distilled dioxane (10 mL). The polymerization mixture was degassed by three circles of vacuum (10 s) and argon purge, before AIBN (0.39 mg, 24 μ mol) was added under argon stream *via* stock solution. Finally, the mixture was degassed again by five cycles of vacuum (10 s) and argon purge. The polymerization was started in a preheated sample holder at 70 °C and quenched after 24 hours by air under ice cooling. The polymer was precipitated three times in ice cooled diethyl ether and dried under reduced pressure. The cloud points and molar mass distributions were determined (shown in the appendix, Figure S35). The availability of the BPAAm unit and the chain length of the polymer were determined by ^1H NMR measurements.

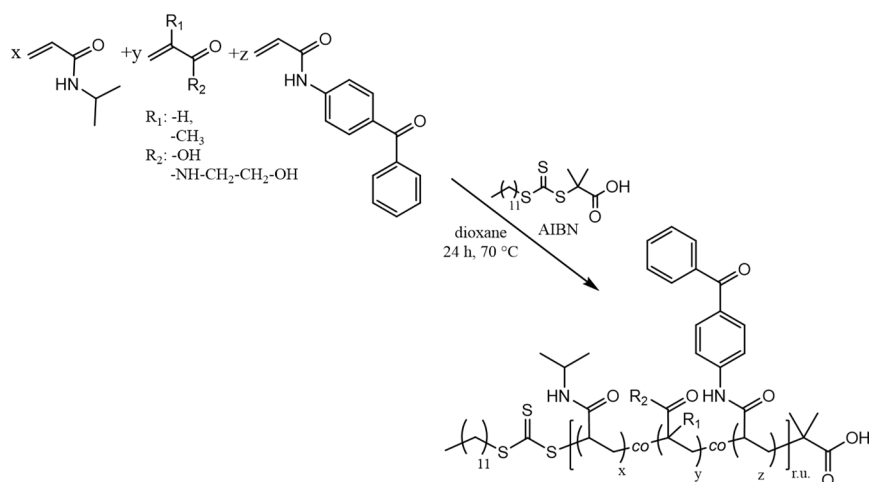
Yield: 422 mg (77%).

^1H NMR (400 MHz, CDCl_3 , shown in the appendix, Figure S34), δ ppm: 0.94-3.50 (backbone), 3.70-4.00 (br. s, isopropyl of NIPAAm), 5.60-7.20 (br. s, amides of the side chains) and 7.42-7.80 (aromatic benzophenone protons).

Cloud point (recorded at 1.0 wt% aqueous solution, shown in the appendix, Figure S35):

$T_c=25.3$ °C

General Procedure for the RAFT Copolymerization of Asymmetric and Photo-Crosslinkable Poly(NIPAAm-co-X-co-BPAAm)-DMP.



Scheme 31: The general procedure for the RAFT copolymerization of asymmetric and photo-crosslinkable poly(NIPAAm)-DMP.

NIPAAm, BPAAm, the varied monomer (AA, MAA or HEAAm) and DMP were dissolved in freshly distilled dioxane (10 mL). The polymerization mixtures were degassed by three circles of vacuum (10 s) and argon purge, before AIBN was added under argon stream. Finally, the mixtures were degassed again by five cycles of vacuum (10 s) and argon purge. The polymerization was started in a preheated sample holder at 70 °C and quenched after 24 hours by air under ice cooling. The polymer was precipitated three times in ice cooled diethyl ether and dried under reduced pressure. The cloud points and molar mass distributions were determined (shown in the appendix, Table S9). The availability of the BPAAm units and chain length were determined by ^1H NMR. The turbidity and ^1H NMR measurements of the synthesized copolymers are shown in the appendix, Figure S36 - Figure S48.

Table 17: The feed ratios of monomers, DMP and AIBN, resulting yields and cloud points for the general RAFT copolymerization of an asymmetric and photo-crosslinkable PNIPAAm-DMP.

Sample Code	[M]/[CTA]	R ₁	R ₂	NIPAAm m/ g (mmol)	Monomer m/ mg (μmol)	BPAAm m/ mg (μmol)	DMP m/ mg (μmol)	AIBN ^[b] m/ mg (μmol)	T _c ^[c] / °C	Yield / % (mg)
CRP-AA	100	-H	-	1.00 (8.85)	33.9 (471)	23.6 (94)	34.2 (94)	0.8 (4.8)	29.1	67 (711)
CRP-MAA	100	-CH ₃	-	0.50 (4.43)	20.3 (240)	11.8 (47)	17.1 (47)	0.4 (24)	28.5	77 (422)
CRP-AA-DMP-EA	100	-H	-	0.50 (4.43)	17.0 (240)	11.8 (47)	19.1 (47) ^[a]	0.4 (24)	27.0	61 (359)
CRP-HEAAm	100	-H	EA	0.50 (4.43)	27.1 (240)	11.8 (47)	17.1 (47)	0.4 (24)	27.7	75 (417)
CRP-HEAAm 10%16k	100	-H	EA	0.47 (418)	54.2 (470)	11.8 (47)	17.1 (47)	0.4 (24)	28.8	75 (410)
CRP-HEAAm 10%26k	200	-H	EA	0.47 (418)	54.2 (470)	11.8 (47)	8.6 (24)	0.2 (12)	30.6	68 (369)

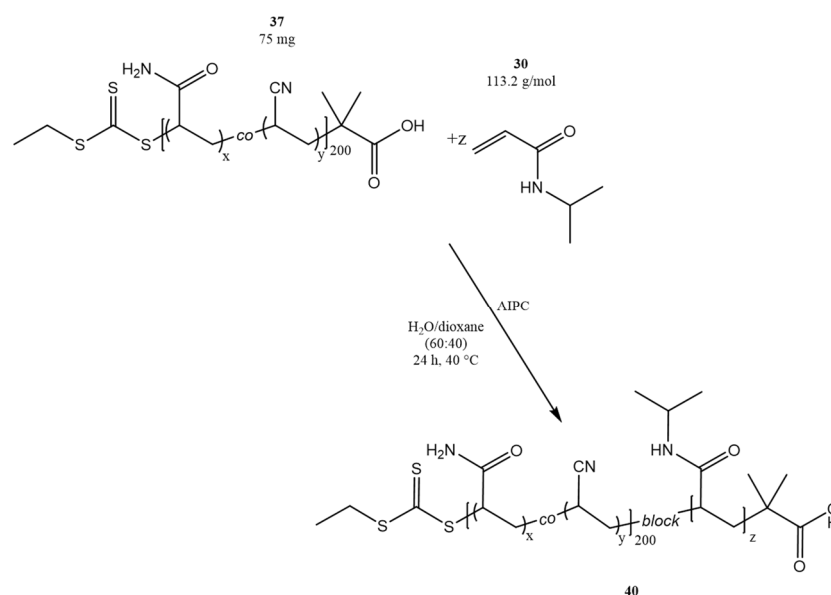
^[a] DMP-EA was used instead of DMP. Ethanolamine is assigned by the abbreviation EA

^[b] The initiator was added *via* stock solution.

^[c] Cloud points (LCST) determined at the half height of the heating cycle.

Exemplary ^1H NMR (400 MHz, CDCl_3 , shown in the appendix, Figure S36 - Figure S48), δ ppm: 0.88 (br. t, 3 H, $\text{H}_3\text{C-DMP-}$), 0.94-3.65 (backbone), 3.83-4.27 (br. s, isopropyl of NIPAAm), 5.60-7.20 (br. s, amides of the side-chains), 7.42-7.87 (aromatic benzophenone protons).

14.3.5. Double Thermoresponsive LCST-UCST Block Copolymers



Scheme 32: The RAFT block copolymerization of the double thermoresponsive LCST- UCST block copolymer poly[(AAm_x-co-AN_y)₂₀₀-block-(NIPAAm)₂₀₀]-EMP **40** (BCU30.0%L-BCU55.0%L).

The purified macroCTA poly(AAm_x-co-AN_y)-EMP (synthesized according to the UCST copolymer systems CRP25.0%-55.0%), NIPAAm and AIPC (Table 18) were dissolved in a mixture of water/dioxane (60:40) (2.5 mL). The reaction mixture was degassed by five freeze-thaw cycles. The polymerization was started in a preheated sample holder at 40 °C and quenched by air after cooling with liquid nitrogen. The cold product mixture was homogenized and precipitated twice in ice-cold EtOAc (100 mL). The obtained precipitates were freeze-dried. The cloud points and molar mass distributions were determined (in the appendix, Table S10).

Table 18: The feed ratios of the macroCTA poly(AAm_x-co-AN_y)₂₀₀-EMP, NIPAAm, AIPC and resulting yields for the general RAFT block copolymerization of poly[(AAm_x-co-AN_y)₂₀₀-block-(NIPAAm)₂₀₀]-EMP with various fractions of the hydrophobic component AN in the macroCTA.

Sample Code	[AN] _{CTA} / mol%	[M] / [CTA]	macroCTA		NIPAAm	AIPC ^[a]	Yield
			/ kg·mol ⁻¹	/ mg (μmol)	/ mg (mmol)	/ mg (μmol)	/ % (mg)
BCU30.0%L	30.0	200	13.4	75	127	1.12	69
				(5.60)	(1.12)	(0.36)	(138)
BCU32.5%L	32.5	200	13.4	75	127	1.12	75
				(5.60)	(1.12)	(0.36)	(150)
BCU35.0%L	35.0	200	14.0	75	121	1.07	82
				(5.36)	(1.07)	(0.35)	(155)
BCU37.5%L	37.5	200	13.6	75	125	1.10	87
				(5.51)	(1.10)	(0.36)	(172)
BCU40.0%L	40.0	200	12.9	75	131	1.16	81
				(5.81)	(1.16)	0.38	(162)
BCU45.0%L	45.0	200	14.1	75	120	1.06	79
				(5.32)	(1.06)	0.34	(163)
BCU50.0%L	50.0	200	12.3	75	138	1.22	75
				(6.10)	(1.22)	(0.39)	(159)
BCU55.0%L	55.0	200	12.0	75	141	1.25	69
				(6.25)	(1.25)	(0.40)	(149)

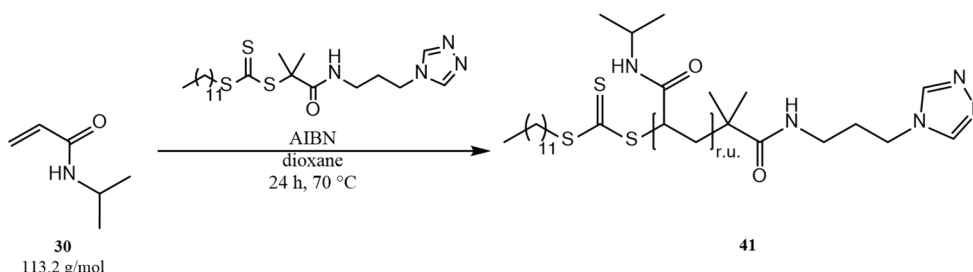
^[a] The initiator was added *via* stock solution.

^1H NMR (400 MHz, D_2O , shown in the appendix, Figure S49), δ ppm: 0.95-3.20 (m, CH_3 - CH_2 - CS_3^- , backbone), 3.39 (br. q, 2H, CH_3 - CH_2 - CS_3^-) and 3.70-4.00 (br. s, isopropyl of NIPAAm).

14.3.6. Iron Ion Sensitive Macromolecular Coordination Ligands

Hemi-Telechelic Macromolecular Coordination Ligands

General Procedure for the RAFT Polymerization of the LCST-Typed Thermoresponsive Hemi-Telechelic Macromolecular Coordination Ligand Poly(NIPAAm)-DMP-APTRZ (P2k-25k)



Scheme 33: The RAFT polymerization of the LCST-typed hemi-telechelic polymer ligand poly(NIPAAm)-DMP-APTRZ **41** (P2k-25k) with various chain lengths.

The starting precursors DMP-APTRZ, AIBN and NIPAAm were dissolved in freshly distilled dioxane (15 mL) and placed in a Schlenk-tube in the molar ratios of [DMP-APTRZ]:[AIBN]:[NIPAAm] according to Table 19. The reaction mixtures were degassed by five cycles of vacuum and argon flux. The reactions were performed in a preheated sample holder at a temperature of 70 °C and quenched after 24 hours by air and cooling with ice. The polymers were precipitated from ice cold diethyl ether or hexane. The solid products were collected using centrifugation and dried under reduced pressure. Cloud points and molar mass distributions of the polymers were determined (in the appendix, Table S15). The existence of the end groups was controlled by ¹H NMR measurements (in the appendix, Figure S57).

Table 19: Feed of AIBN, DMP-APTRZ and NIPAAm in the performed RAFT polymerizations of the LCST-typed hemi-telechelic MCL poly(NIPAAm)-DMP-APTRZ with various chain lengths.

Sample Code	[M] ₀ : [CTA ₀ : [I] ₀	AIBN ^[b] / mg (μmol)	DMP-APTRZ / mg (μmol)	NIPAAm / mg (mmol)	T _c ^[c] / °C	Yield / % (mg)
P3k	15: 1: 0.05	4.3 (26.4)	250 (529)	896 (7.98)	34.7	68 (782)
P4k	25: 1: 0.05 ^[a]	1.3 (7.9)	75 (159)	448 (3.97)	33.4	94 (493)
P7k	25: 1: 0.05	2.6 (15.9)	150 (317)	896 (7.98)	32.9	92 (961)
P12k	50: 1: 0.05 ^[a]	0.4 (2.6)	25 (53)	298 (2.64)	34.1	87 (281)
P23k	100: 1: 0.05 ^[a]	0.4 (2.6)	25 (53)	600 (5.28)	34.8	86 (538)
P25k	150: 1: 0.05 ^[a]	0.4 (2.6)	25 (53)	900 (7.92)	- ^[d]	60 (555)
P25k	150: 1: 0.05	0.9 (5.3)	50 (106)	1793 (15.95)	34.7	68 (1270)

^[a] Polymers were precipitated in hexane instead of diethyl ether.

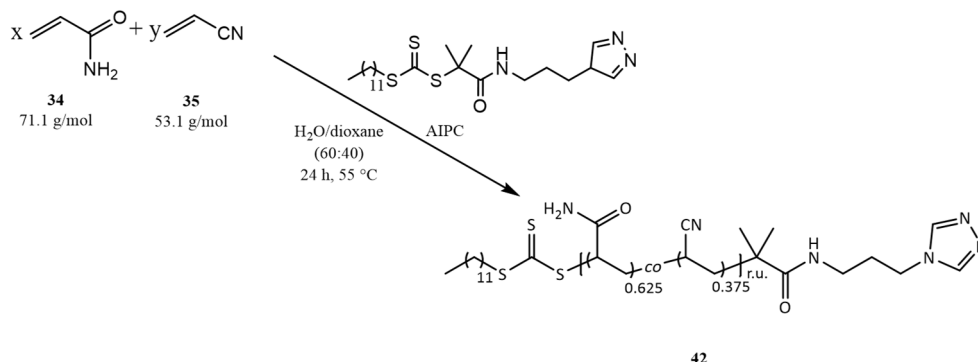
^[b] The initiator was added *via* stock solution.

^[c] Cloud points (LCST) determined at the half height of the heating cycle.

^[d] Values not determined.

¹H NMR (400 MHz, CDCl₃, shown in the appendix, Figure S57), δ ppm: 0.87 (t, 3 H, CH₃-(CH₂)₁₁-CS₃-), 1.13-3.30 (backbone), 4.00 (br. s, -CONH-CH₂-(CH₃)₂ of NIPAAm), 6.40 (amide of NIPAAm), 8.48 (br. s, 2 H, -TRZ).

General Procedure for the RAFT Copolymerization of UCST-Typed Thermoresponsive Hemi-Telechelic Macromolecular Coordination Ligand Poly(AAm-co-AN)-DMP-APTRZ (UCP4k-UCP27k)



Scheme 34: The RAFT polymerization of the UCST-typed hemi-telechelic copolymer ligand poly(AAm_{0.625}-AN_{0.375})-DMP-APTRZ **42** (UCP4k-UCP27k) with various chain lengths.

The starting precursors AAm, AN, DMP-APTRZ and AIPC (according to Table 20) were dissolved in a mixture of water/dioxane (60:40) (2.5 mL). The mixture was degassed by three freeze-thaw cycles. The reactions were performed in a preheated sample holder at a temperature of 55 °C and quenched after 24 hours by air and ice cooling. The cold reaction mixtures were homogenized and precipitated twice in ice-cold MeOH (100 mL). Afterwards the purified products were dissolved in distilled water and freeze dried. Cloud points and molar mass distributions of the polymers were determined (in the appendix, Table S17). The existence of the end groups was controlled by ¹H NMR measurements (appendix Figure S65).

Table 20: Feed of AIBN, DMP-APTRZ, AAm and AN in the performed RAFT copolymerizations of the UCST-typed hemi-telechelic coordinating copolymer ligand poly(AAm_{0.625}-AN_{0.375})-DMP-APTRZ with various chain lengths.

Sample Code	[M] ₀ : [CTA] ₀ : [I] ₀	AIPC ^[a] / μmol (mg)	DMP-APTRZ / μmol (mg)	AAm / mmol (mg)	AN / mmol (mg)	T _c ^[b] / °C	Yield / % (mg)
UCP3k	30: 1: 0.1	11.0 (3.6)	112.5 (53.2)	2.1 (150)	1.3 (67)	11.5	37 (101) ^[c]
UCP7k	60: 1: 0.1	5.6 (1.8)	56.3 (26.6)	2.1 (150)	1.3 (67)	-	46 (113) ^[c]
UCP8k	100: 1: 0.1	3.4 (1.1)	33.8 (16.0)	2.1 (150)	1.3 (67)	3.0	51 (125) ^[c]
UCP16k	200: 1: 0.1	2.8 (0.9)	28.1 (13.3)	3.5 (250)	2.1 (112)	19.9	73 (275)
UCP27k	400: 1: 0.1	1.4 (0.5)	14.2 (6.7)	3.5 (250)	2.1 (112)	34.8	60 (222)

^[a] The initiator was added *via* stock solution.

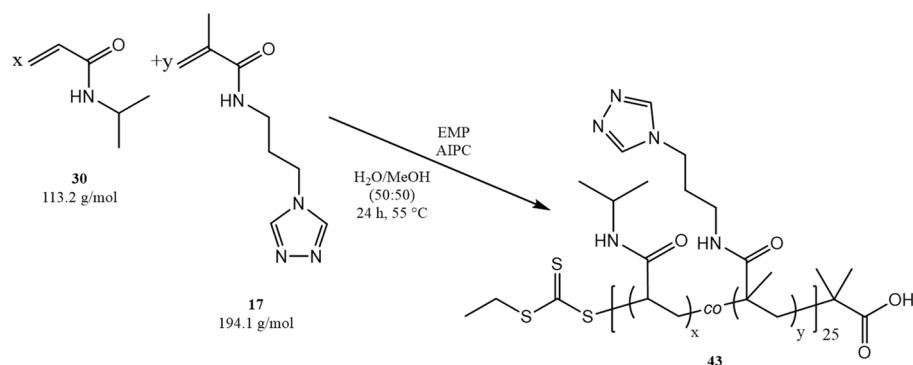
^[b] Cloud points (UCST) determined at the half height of the cooling cycle.

^[c] Yields reduced due to the losses during precipitation process the amphiphilic character of low molecular weight copolymers.

¹H NMR (400 MHz, D₂O/MeCN-d₃ (85:15), shown in the appendix, Figure S65), δ ppm: 0.97 (t, 3 H, CH₃-(CH₂)₁₁-CS₃-), 1.23-3.50 (backbone), 4.26 (q, 2 H, -(CH₂)₂-CH₂-TRZ.) and 8.64 (br. s, 2 H, -TRZ).

Multidentate Macromolecular Coordination Ligands

General Procedure for the RAFT Copolymerization of LCST-Typed Thermoresponsive Multidentate Coordination Copolymer Ligand Poly(NIPAAm_x-co-APTRZMAAm_y)-EMP (C4.8k5%-C4.6k15%)



Scheme 35: The RAFT polymerization of the LCST-typed multidentate coordination copolymer ligand poly(NIPAAm-co-APTRZMAAm)₂₅-EMP **43** (C4.8k5%-C4.6k15%) with various APTRZMAAm fractions.

The precursors AIPC, EMP and NIPAAm were dissolved in a mixture of water/methanol (1:1) (1 mL) and placed in a Schlenk-tube with a molar ratio of [monomers]₀: [EMP]₀: [AIPC]₀ = 25:1:0.1 (according to Table 21). The APTRZMAAm was added to the reaction mixtures in the solvent mixture (1.5 mL). The reaction mixtures were degassed by five freeze-thaw cycles. The polymerizations were performed in a preheated sample holder at a temperature of 55 °C and quenched after 24 hours by air and ice cooling. The polymers were precipitated twice in ice cold EtOAc. The solid products were collected using centrifugation, dissolved in distilled water and freeze-dried. The cloud points and molar mass distributions were determined (in the appendix, Table S19). The quantification of the APTRZ units was determined by ¹H NMR measurements (in the appendix, Figure S70).

Table 21: Feed of AIPC, EMP, NIPAAm and the ion-sensitive APTRZMAAm in the performed RAFT copolymerizations of the LCST-typed multidentate coordination copolymer ligand poly(NIPAAm-co-APTRZMAAm)₂₅-EMP with various molar fractions of APTRZMAAm.

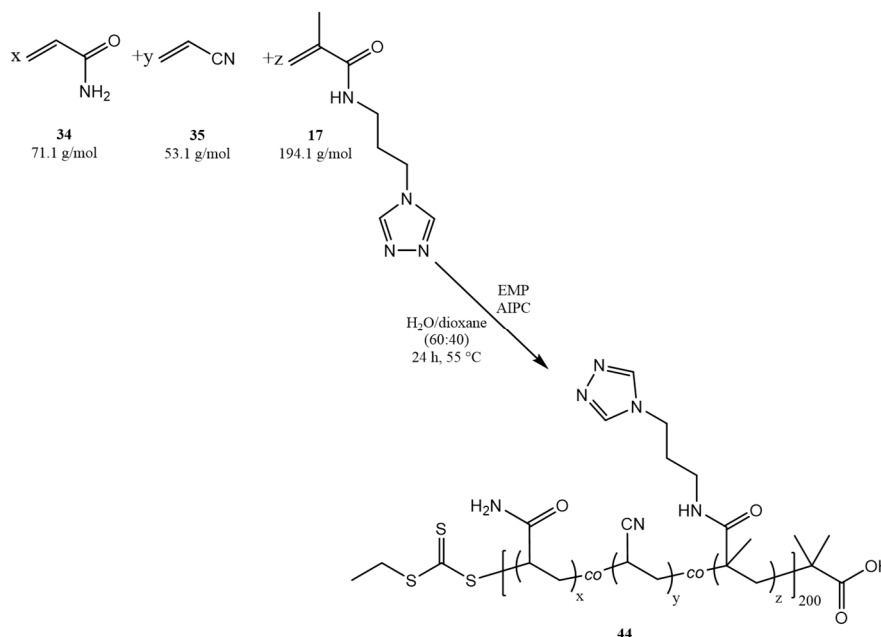
Sample Code	[M] / [CTA]	[APTRZMAAm] _{feed} / mol%	AIPC ^[a] / mg (μmol)	EMP / mg (μmol)	APTRZMAAm / mg (mmol)	NIPAAm / mg (mmol)	T _c ^[b] / °C	Yield / % (mg)
C4.8k5%	25	5.0	2.38 (7.4)	17 (73.5)	17 (0.09)	197 (1.74)	36.6	69 (160)
C4.9k10%	25	10.0	2.38 (7.4)	16.5 (73.5)	34 (0.17)	188 (1.66)	39.1	60 (145)
C4.6k15%	25	15.0	2.38 (7.4)	16.5 (73.5)	50 (0.26)	177 (1.57)	44.7	55 (136)

^[a] The initiator was added *via* stock solution.

^[b] Cloud points (LCST) determined at the half height of the heating cycle.

¹H NMR (500 MHz, CDCl₃, shown in the appendix, Figure S70), δ ppm: 0.88-3.55 (CTA, backbone), 3.99 (br. s, isopropyl of NIPAAm -CH₂-(CH₃)₂), 4.19 (br. s, -CH₂-TRZ), 5.75-7.25 (amide of NIPAAm) and 8.55 (br. s, -APTRZMAAm).

General Procedure for the RAFT Copolymerization of UCST-Typed Thermoresponsive Multidentate Coordination Copolymer Ligand Poly(AAm_x-co-AN_y-co-APTRZMAAm_z) - EMP (UCP11.6k2.5%-UCP13.7k10%)



Scheme 36: The RAFT polymerization of the UCST-typed multidentate coordination copolymer ligand poly(AAm-co-AN-co-APTRZMAAm)₂₀₀-EMP **44** (UCP11.6k2.5%-UCP13.7k10%) with various APTRZMAAm fractions.

AAm (100 mg, 1.41 mmol), AN (75 mg, 1.41 mmol, 93.4 μ L), the triazole monomer APTRZMAAm, EMP and the AIPC with a molar ratio of [monomers]₀:[EMP]₀:[AIPC]₀=200:1:0.1 (according to Table 22) were dissolved in a mixture of water/dioxane (60:40) (2.5 mL). The ice-cold mixture was degassed by three freeze-thaw cycles. The reactions were performed in a preheated sample holder at a temperature of 55 °C and quenched after 24 hours by air and ice cooling. The cold reaction mixtures were homogenized and precipitated twice in ice-cold MeOH (100 mL). Afterwards the purified products were dissolved in distilled water and freeze dried. The cloud points and molar mass distribution of the polymers were determined (in the appendix, Table S21). The existent end group was controlled by ¹H NMR measurements (in the appendix, Figure S72).

Table 22: Feed of AIPC, EMP, AAm (100 mg, 1.41 mmol), AN (75 mg, 1.41 mmol, 93.4 μ L) and the ion-sensitive APTRZMAAm in the performed RAFT copolymerizations of the UCST-typed multidentate coordination copolymer ligand poly(AAm-co-AN-co-APTRZMAAm)₂₀₀-EMP with various molar fractions of APTRZMAAm.

Sample Code	[M] / [CTA]	[APTRZMAAm] _{feed} / mol%	AIPC ^[a] / mg (μ mol)	EMP ^[a] / mg (μ mol)	APTRZMAAm / mg (mmol)	T _c ^[b] / °C	Yield / % (mg)
UCP11.6k2.5%	200	2.5	0.93	3.25 (14.4)	14 (0.07)	49.7	65 (125)
UCP14.9k5.0%	200	5.0	0.96	3.33 (14.8)	29 (0.15)	41.3	61 (127)
UCP13.7k10.0%	200	10.0	1.01	3.52 (15.6)	60 (0.31)	34.7	58 (138)

^[a] The initiator and CTA were added *via* stock solution.

^[b] Cloud points (UCST) determined at the half height of the cooling cycle.

^1H NMR (500 MHz, $\text{D}_2\text{O}/\text{MeCN-d}_3$ (85:15), shown in the appendix, Figure S72), δ ppm:
1.45 (br.t, 3H, $\text{CH}_3\text{-CH}_2\text{-CS}_3^-$), 1.50-3.45 (CTA, backbone), 3.52 (q, 2H, $\text{CH}_3\text{-CH}_2\text{-CS}_3^-$),
4.25 (br. s, $-\text{CONH}(\text{CH}_2)_2\text{-CH}_2\text{-TRZ}$) and 8.63 (br. s, $-\text{APTRZMAAm}$).

Complexation Procedures for Macromolecular Coordination Ligands

General Complexation Procedure for DLS:

A 0.1 wt% aqueous solution for hemi-telechelic ligands of the LCST-type and 1.0 wt% for the other copolymer ligands was prepared. Unless specified otherwise, for the investigation of the complexation process a tenfold molar excess of $\text{Fe}(\text{BF}_4)_2 \cdot 6\text{H}_2\text{O}$ stock-solution with ascorbic acid (1 mol%) was added to the polymeric solutions and mixed homogeneously. The hydrodynamic radius of the (co-)polymers was analyzed by DLS *via* the correlation curve and additionally the number by intensity fit (when less than three existent aggregation species). Depending on the cloud points of the polymers and complexes the temperatures of the measurement were adjusted to study the aggregation below and above their critical solution temperature. By default, for hemi-telechelic ligands of the LCST-type $T=22\text{ }^\circ\text{C}$ and $T=35\text{ }^\circ\text{C}$, and $T=2\text{ }^\circ\text{C}$ and $50\text{ }^\circ\text{C}$ for the UCST-type were adjusted. For multidentate copolymers of the LCST-type $T=20\text{ }^\circ\text{C}$ and $T=60\text{ }^\circ\text{C}$, and $T=20\text{ }^\circ\text{C}$ and $T=60\text{ }^\circ\text{C}/70\text{ }^\circ\text{C}$ for UCST-typed were adjusted. The copolymer solutions were heated above their cloud point and cooled down before the measurement.

General Complexation Procedure for Turbidity Measurements:

A 0.1 wt% aqueous solution for hemi-telechelic ligands of the LCST-type and 1.0 wt% for the other copolymer ligands was prepared. Unless specified otherwise, for the investigation of the complexation process a tenfold molar excess of $\text{Fe}(\text{BF}_4)_2 \cdot 6\text{H}_2\text{O}$ stock-solution with ascorbic acid (1 mol%) was added to the polymeric solutions and mixed homogeneously. The cloud points from the turbidity curves of the polymeric solutions was analyzed by a non-linear curve fit. The measurement was started out of the homogeneous mixing phase (heating cycle for LCST and cooling cycle for UCST systems). The measurements in the different media were performed by addition of divalent iron salt to the already measured pure aqueous polymer solutions. The absorption wavelength for measurements in presence of Fe^{2+} was adjusted to higher wavelength ($\lambda=740\text{ nm}$).

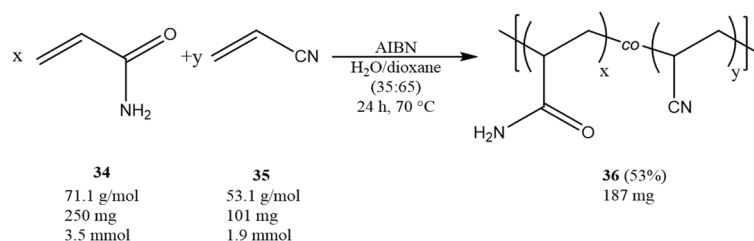
General Complexation Procedure for Shorter Polymers:

A 3.0 wt% solution of a polymer sample ($\bar{M}_n < 5\text{ kg}\cdot\text{mol}^{-1}$) was prepared in absolute ethanol under inert conditions. A tenfold molar excess of ethanolic $\text{Fe}(\text{BF}_4)_2 \cdot 6\text{H}_2\text{O}$ stock-solution with traces of ascorbic acid was added to the polymeric solutions and mixed homogeneously. The precipitate was collected *via* centrifugation, washed three times with absolute ethanol and dried under reduced pressure.

14.3.7. Thermoresponsive Copolymer Vectors for Gene Delivery

Syntheses of the Reference Copolymers Poly(AAm_x-co-AN_y) and Poly(AAm_x-co-AN_y)-EMP (R1 and R2)

Free-radical Copolymerization of the Reference Poly(AAm_{0.65}-co-AN_{0.35}) (R1)



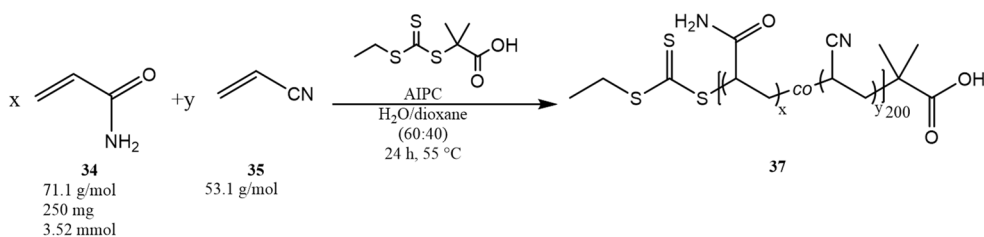
Scheme 37: The free radical copolymerization of the reference copolymer poly(AAm-co-AN) **36** (R1) without amine side groups and CS₃ moiety.

AAm (250 mg 3.52 mmol), AN (101 mg, 1.90 mmol) and AIBN (4.4 mg, 26.8 μmol) were dissolved in a mixture of water/dioxane (35:65) (4mL). The polymerization mixture was degassed by three freeze-thaw cycles. The polymerization was started in a preheated sample holder at 70 °C and quenched by air after liquid nitrogen cooling after 24 hours. The product was precipitated twice from ice-cold MeOH (100 mL), dissolved in distilled water and freeze dried four times. The cloud points and molar mass distributions were determined (in the appendix, Table S23).

Yield: 355 mg (53%).

¹H NMR (400 MHz, DMSO-d₆, shown in the appendix, Figure S75), δ ppm: 1.40-3.40 (backbone).

General Procedure for the RAFT Copolymerization of the Reference poly(AAm_x-co-AN_y)-EMP (R2-R4)



Scheme 38: The RAFT copolymerization of the reference copolymers poly(AAm-co-AN)-EMP **37** (R2-R4) without amine side groups.

AAm (250 mg, 3.52 mmol) and various feed ratios of AN, EMP and AIPC (Table 23) were dissolved in a mixture of water/dioxane (60:40) (2.5 mL). The polymerization mixture was degassed by three freeze-thaw cycles. The polymerization was started in a preheated sample holder at 55 °C and quenched after 24 hours by air after cooling with liquid nitrogen. The product was precipitated twice in ice-cold MeOH (100 mL), dissolved in distilled water and freeze dried four times. The cloud points and molar mass distributions were determined (in the appendix, Table S23).

Table 23: Feed ratios of the AIPC, EMP, AAm (250 mg, 3.52 mmol) and AN, resulting cloud points and yields for the general RAFT copolymerization of the reference copolymers and their subsequent sample code.

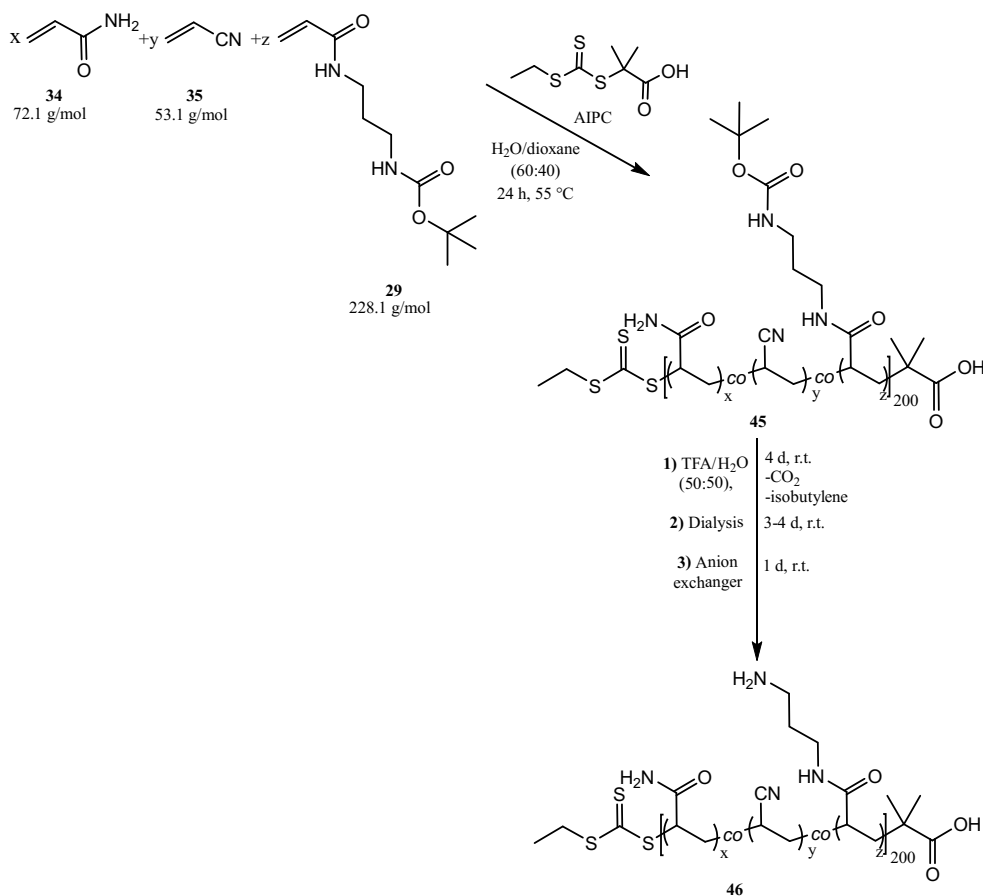
Sample Code	[M]/ [CTA]	[AN] / mol%	AN / mmol (mg)	V(AN) / μL	EMP ^[a] / μmol (mg)	AIPC ^[a] / μmol (mg)	T_c ^[b] / $^\circ\text{C}$	Yield / % (mg)
R2	200	32.5	1.70 (90)	113	26.1 (5.87)	5.2 (1.68)	17.0	82 (284)
R3	200	41.0	2.45 (130)	162	29.8 (6.71)	6.0 (1.93)	37.5	46 (176)
R4	200	45.0	2.88 (153)	191	32.0 (7.20)	6.4 (2.07)	44.0	63 (259)

^[a] Initiator/CTA added *via* stock solution.

^[b] Cloud points (UCST) determined at the half height of the cooling cycle.

^1H NMR (400 MHz, DMSO- d_6 , "R2" shown in the appendix, Figure S75), δ ppm: 1.40 (br. t, $J=6.7$, 3H, $\text{CH}_3\text{-CH}_2\text{-CS}_3\text{-R}$), 1.50-3.35 (backbone), 3.49 (br. q, $J=7.0$, 2H, $\text{CH}_3\text{-CH}_2\text{-CS}_3\text{-R}$).

General Procedure for the Syntheses of the pDNA-Binding Copolymer Vectors Poly(AAm_x-co-AN_y-co-APAAM_z)-EMP (C30%Boc, C30% and C10%AN)



Scheme 39: The RAFT copolymerization and deprotection process of the pDNA-binding copolymer vectors poly(AAm-co-AN-co-APAAM)-EMP **46** (C10%-C40%).

Various feed ratios of AAm, AN, APAAM-Boc, EMP and AIPC (Table 24) were dissolved in a mixture of water/dioxane (60:40) (2.5 mL). The polymerization mixture was degassed by three freeze-thaw cycles. The polymerization was started in a preheated sample holder at 55 °C and quenched after 24 hours by air after cooling with liquid nitrogen. The reaction mixture was concentrated to dryness. The solid product was dissolved in distilled water (2 mL), mixed with TFA (50:50 vol%) and stirred for 2-3 days. Afterwards, the solvent was removed again, before the product was dissolved in distilled water and dialyzed against water for 3-4 days. The obtained purified product was stirred in presence of freshly regenerated weakly basic anion exchanger for an additional day. The filtered polymer solution was freeze dried three times. The cloud points and molar mass distributions were determined (appendix Table S23).

¹H NMR (500 MHz, D₂O, "C10%" and "C30%" shown in the appendix, Figure S76), δ ppm: 1.17 (br. t, 3H, CH₃-CH₂-CS₃-R), 1.20-3.20 (backbone, NH₂-CH₂-CH₂-CH₂-amide of APAAM) and 3.20-3.60 (br. s, NH₂-CH₂-CH₂-CH₂-amide of APAAM side group).

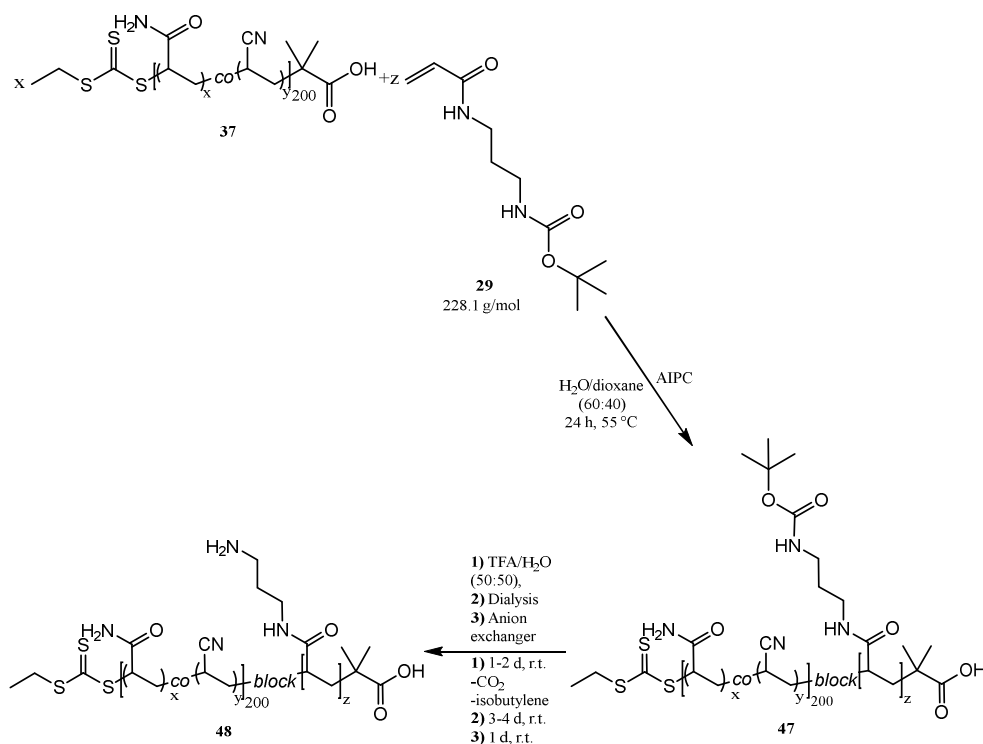
Table 24: Feed ratio of AAm, AN, AIPC, EMP and the DNA-binding APAAm, with resulted yields for the general procedure of the RAFT copolymerizations of pDNA binding vectors and their subsequent sample code.

Sample Code	[APAAm] / mol%	APAAm-Boc / mmol (mg)	[AN] / mol%	AN / mmol (mg)	V(AN) / μ L	AAm / mmol (mg)	EMP ^[a] / μ mol (mg)	AIPC ^[a] / μ mol (mg)	Yield / % (mg)
C10%	10	0.26 (60)	49.0	1.29 (69)	86	1.06 (75)	13.0 (2.93)	2.6 (0.85)	85.7 (154)
C10%AN	10	0.33 (77)	59.0	1.96 (104)	130	1.06 (75)	16.7 (3.77)	3.3 (1.08)	21.7 (49) ^[b]
C20%	20	0.75 (172)	52.0	1.96 (104)	130	1.06 (75)	18.8 (4.24)	3.8 (1.22)	57.9 (162)
C30%	30	0.57 (131)	45.5	0.87 (46)	58	0.47 (33)	9.6 (2.15)	1.9 (0.62)	47.7 (74)
C40%	40	0.63 (143)	39.0	0.61 (32)	41	0.33 (23)	7.8 (1.76)	1.6 (0.51)	56.7 (78)

^[a] Initiator/CTA added *via* stock solution.

^[b] Yields lowered due to purification errors.

General Procedure for Syntheses of the pDNA-Binding Block Copolymer Vectors Poly[(AAM_x-co-AN_y)-*block*-(APAAm)_z]-EMP (BC40Boc, BC40 and BC60)



Scheme 40: The RAFT block copolymerization and deprotection process of the pDNA-binding block copolymer vectors poly[(AAM_x-co-AN_y)-*block*-(APAAm)_z]-EMP **48** (BC20-BC60).

The macroCTA (synthesized according to reference polymers R2-R4 or CRP25.0%-CRP55.0%), APAAm-Boc and AIPC (Table 25) were dissolved in a mixture of water/dioxane (60:40) (2.0 mL). The polymerization mixture was degassed by five freeze-thaw cycles. The polymerization was started in a preheated sample holder at 55 °C and quenched after 24 hours by air after cooling with liquid nitrogen. The reaction mixture was concentrated to dryness. The solid product was dissolved in distilled water (2 mL), mixed with TFA (50:50 vol%) and stirred for 1-2 days. Afterwards, the solvent was removed again, before the product was dissolved in distilled water and dialyzed against water for 3-4 days. The obtained purified product was stirred in presence of freshly regenerated weakly basic anion exchanger for an additional day. The filtered polymer solution was freeze dried three times. The cloud points and molar mass distributions were determined (in the appendix, Table S23).

¹H NMR (500 MHz, D₂O, "BC40" and "BC60%" shown in the appendix, Figure S77), δ ppm: 1.16 (br. t, 3H, CH₃-CH₂-CS₃-R), 1.20-3.20 (backbone, NH₂-CH₂-CH₂-CH₂-amide of APAAm side group) and 3.20-3.40 (br. s, NH₂-CH₂-CH₂-CH₂-amide of APAAm side group).

Table 25: Feed ratio of AIPC, the macroCTA and the DNA-binding APAAm with the resulted yields for the general procedure of the RAFT block copolymerizations of pDNA binding vectors and their subsequent sample code.

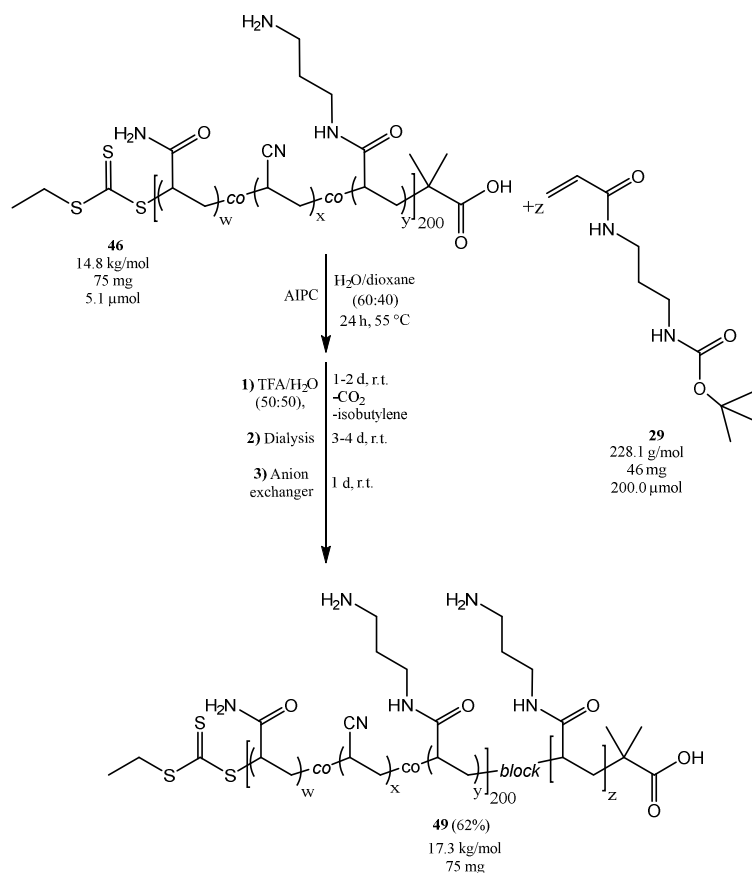
Sample Code	[APAAm] / r.u.	\bar{M}_n (macroCTA) / kg·mol ⁻¹	macroCTA / μ mol (mg)	APAAm-Boc / mmol (mg)	AIPC ^[c] / μ mol (mg)	Yield / %(mg)
BC20 ^[a]	20	13.2	4.5 (60)	0.09 (21)	0.9 (0.29)	63 (51)
BC40 ^[a]	40	13.2	5.7 (75)	0.23 (52)	1.14 (0.37)	52 (66)
BC60 ^[a]	60	13.2	5.7 (75)	0.34 (78)	1.14 (0.37)	71 (108)
BC60AN ^[b]	60	12.4	5.9 (75)	0.35 (80)	0.38 (0.33)	68 (105)

^[a] Poly(AAm_{0.65}-co-AN_{0.35})-EMP was used as macroCTA (according to CRP35.0%, \bar{M}_n = 13.2 kg·mol⁻¹, D =1.40, T_c [UCST]=16.0 °C).

^[b] Poly(AAm_{0.45}-co-AN_{0.55})-EMP (according to CRP55.0%, \bar{M}_n =12.4 kg·mol⁻¹, D =1.34, T_c [UCST]=78.8 °C) was used as macroCTA.

^[c] Initiator added *via* stock solution.

Synthesis of the Dual pDNA-Binding Copolymer Vector Poly[(AAm_{0.28}-co-AN_{0.52}-co-APAAm_{0.20})₂₀₀-*block*-(APAAm)₄₀]-EMP (BC20%40).



Scheme 41: The RAFT block copolymerization and deprotection process of the dual pDNA-binding block copolymer vector poly[(AAm-co-AN-co-APAAm)-*block*-(APAAm)]-EMP **49** (BC20%40).

The macroCTA poly(AAm_{0.28}-co-AN_{0.52}-co-APAAm_{0.20})-EMP (synthesized according to copolymer vector C20%, 75 mg, 5.1 μmol), the monomer APAAm-Boc (46 mg, 200.0 μmol) and AIPC (0.33 mg, 1.0 μmol) *via* stock solution were dissolved in a mixture of water/dioxane (60:40) (2.5 mL). The mixture was degassed by five freeze-thaw cycles. The polymerization was started in a preheated sample holder at 55 °C and quenched after 24 hours by air after cooling with liquid nitrogen. The reaction mixture was concentrated to dryness. The solid product was dissolved in distilled water (2 mL), mixed with TFA (50:50 vol%) and stirred for 1-2 days. Afterwards, the solvent was removed again, before the product was dissolved in distilled water and dialyzed against water for 3-4 days. The obtained purified product was stirred in presence of freshly regenerated weakly basic anion exchanger for an additional day. The filtered polymer solution was freeze dried three times. The cloud point and molar mass distribution were determined (in the appendix, Table S23).

Yield: 76 mg (62%).

^1H NMR (500 MHz, D_2O , "BC20%40" shown in the appendix, Figure S78), δ ppm: 1.16 (br. t, 3H, $\text{CH}_3\text{-CH}_2\text{-CS}_3\text{-R}$), 1.20-3.20 (backbone, $\text{NH}_2\text{-CH}_2\text{-CH}_2\text{-CH}_2\text{-amide}$ of APAAM side group) and 3.20-3.50 (br. s, $\text{NH}_2\text{-CH}_2\text{-CH}_2\text{-CH}_2\text{-amide}$ of APAAM side group).

15. References

- 1 M. R. Aguilar and J. S. Román, *Smart Polymers and Their Applications*, Woodhead Publishing, 2019.
- 2 E. Gomes and J. Shorter, *J. Biol. Chem.*, 2019, **294**, 7115–7127.
- 3 A. K. Rai, J.-X. Chen, M. Selbach and L. Pelkmans, *Nature*, 2018, **559**, 211–216.
- 4 H. Zhang, S. Elbaum-Garfinkle, E. Langdon, N. Taylor, P. Occhipinti, A. Bridges, C. P. Brangwynne and A. S. Gladfelter, *Mol. Cell*, 2015, **60**, 220–230.
- 5 E. W. Martin and T. Mittag, *Biochemistry*, 2018, **57**, 2478–2487.
- 6 S. C. Weber and C. P. Brangwynne, *Curr. Biol. CB*, 2015, **25**, 641–646.
- 7 S. Alberti, *Curr. Biol.*, 2017, **27**, R1097–R1102.
- 8 Y. Zhao, F. Sakai, L. Su, Y. Liu, K. Wei, G. Chen and M. Jiang, *Adv. Mater.*, 2013, **25**, 5215–5256.
- 9 H. Zhang, Y. Tian and L. Jiang, *Nano Today*, 2016, **11**, 61–81.
- 10 C. de las H. Alarcón, S. Pennadam and C. Alexander, *Chem Soc Rev*, 2005, **34**, 276–285.
- 11 D. Roy, W. L. A. Brooks and B. S. Sumerlin, *Chem. Soc. Rev.*, 2013, **42**, 7214.
- 12 Y.-J. Kim and Y. T. Matsunaga, *J. Mater. Chem. B*, 2017, **5**, 4307–4321.
- 13 H. Feil, Y. H. Bae, J. Feijen and S. W. Kim, *Macromolecules*, 1993, **26**, 2496–2500.
- 14 J. Seuring and S. Agarwal, *Macromolecules*, 2012, **45**, 3910–3918.
- 15 B. A. Pineda-Contreras, H. Schmalz and S. Agarwal, *Polym. Chem.*, 2016, **7**, 1979–1986.
- 16 S. Chen, X. Jiang and L. Sun, *J. Appl. Polym. Sci.*, 2013, **130**, 1164–1171.
- 17 S. Furyk, Y. Zhang, D. Ortiz-Acosta, P. S. Cremer and D. E. Bergbreiter, *J. Polym. Sci. Part Polym. Chem.*, 2006, **44**, 1492–1501.
- 18 F. Liu, S. Jiang, L. Ionov and S. Agarwal, *Polym Chem*, 2015, **6**, 2769–2776.
- 19 M. Ahmed and R. Narain, *Prog. Polym. Sci.*, 2013, **38**, 767–790.
- 20 M. Chipper, D. Fournier, R. Hoogenboom and U. S. Schubert, *Macromol. Rapid Commun.*, 2008, **29**, 1640–1647.
- 21 G. Moad, E. Rizzardo and S. H. Thang, *Aust. J. Chem.*, 2005, **58**, 379–410.
- 22 H. Feng, X. Lu, W. Wang, N.-G. Kang and J. W. Mays, *Polymers*, 2017, **9**, 494.
- 23 G. Moad, E. Rizzardo and S. H. Thang, *Aust. J. Chem.*, 2009, **62**, 1402.
- 24 P. Nesvadba, in *Encyclopedia of Radicals in Chemistry, Biology and Materials*, eds. C. Chatgililoglu and A. Studer, John Wiley & Sons, Ltd, Chichester, UK, 2012.
- 25 K. Matyjaszewski, S. Gaynor, D. Greszta, D. Mardare and T. Shigemoto, *J. Phys. Org. Chem.*, 1995, **8**, 306–315.
- 26 M. J. Monteiro and J. de Barbeyrac, *Macromolecules*, 2001, **34**, 4416–4423.
- 27 M. K. Georges, R. P. N. Veregin, P. M. Kazmaier and G. K. Hamer, *Macromolecules*, 1993, **26**, 2987–2988.
- 28 B. Tieke, *Makromolekulare Chemie: Eine Einführung*, Wiley-VCH Verlag GmbH & Co. KGaA, 3. vollst. überarb. u. erw. Auflage., 2014.
- 29 W. A. Braunecker and K. Matyjaszewski, *Prog. Polym. Sci.*, 2007, **32**, 93–146.
- 30 E. Rizzardo and D. H. Solomon, *Aust. J. Chem.*, 2012, **65**, 945.
- 31 J.-S. Wang and K. Matyjaszewski, *J. Am. Chem. Soc.*, 1995, **117**, 5614–5615.
- 32 G. Moad, J. Chiefari, (Bill) Y?K Chong, J. Krstina, R. T. Mayadunne, A. Postma, E. Rizzardo and S. H. Thang, *Polym. Int.*, 2000, **49**, 993–1001.
- 33 O. W. Webster, *Science*, 1991, **251**, 887–893.
- 34 S. Perrier and P. Takolpuckdee, *J. Polym. Sci. Part Polym. Chem.*, 2005, **43**, 5347–5393.
- 35 C. Barner-Kowollik and S. Perrier, *J. Polym. Sci. Part Polym. Chem.*, 2008, **46**, 5715–5723.
- 36 C. Boyer, V. Bulmus, T. P. Davis, V. Ladmiraal, J. Liu and S. Perrier, *Chem. Rev.*, 2009, **109**, 5402–5436.
- 37 H. Willcock and R. K. O'Reilly, *Polym. Chem.*, 2010, **1**, 149–157.
- 38 R. T. A. Mayadunne, E. Rizzardo, J. Chiefari, Y. K. Chong, G. Moad and S. H. Thang, *Macromolecules*, 1999, **32**, 6977–6980.
- 39 D. B. Thomas, A. J. Convertine, R. D. Hester, A. B. Lowe and C. L. McCormick, *Macromolecules*, 2004, **37**, 1735–1741.
- 40 R. Wang, C. L. McCormick and A. B. Lowe, *Macromolecules*, 2005, **38**, 9518–9525.

- 41R. T. A. Mayadunne and E. Rizzardo, *MECHANISTIC AND PRACTICAL ASPECTS OF RAFT POLYMERIZATION*, 2006.
- 42D. J. Keddie, G. Moad, E. Rizzardo and S. H. Thang, *Macromolecules*, 2012, **45**, 5321–5342.
- 43G. Moad, E. Rizzardo and S. H. Thang, *Polym. Int.*, 2011, **60**, 9–25.
- 44) Y. K. Chong, J. Krstina, T. P. T. Le, G. Moad, A. Postma, E. Rizzardo and S. H. Thang, *Macromolecules*, 2003, **36**, 2256–2272.
- 45A. Favier and M.-T. Charreyre, *Macromol. Rapid Commun.*, 2006, **27**, 653–692.
- 46J. Xu, J. He, D. Fan, X. Wang and Y. Yang, *Macromolecules*, 2006, **39**, 8616–8624.
- 47F. Eeckman, A. J. Moës and K. Amighi, *Int. J. Pharm.*, 2002, **241**, 113–125.
- 48A. A. Koffi, F. Agnely, G. Ponchel and J. L. Grossiord, *Eur. J. Pharm. Sci.*, 2006, **27**, 328–335.
- 49X. Wang, X. Qiu and C. Wu, *Macromolecules*, 1998, **31**, 2972–2976.
- 50M. Karg, I. Pastoriza-Santos, J. Pérez-Juste, T. Hellweg and L. M. Liz-Marzán, *Small*, 2007, **3**, 1222–1229.
- 51T. Okano, N. Yamada, M. Okuhara, H. Sakai and Y. Sakurai, in *The Biomaterials: Silver Jubilee Compendium*, ed. D. F. Williams, Elsevier Science, Oxford, 1995, pp. 109–115.
- 52A. Chunder, K. Etcheverry, G. Londe, H. J. Cho and L. Zhai, *Colloids Surf. Physicochem. Eng. Asp.*, 2009, **333**, 187–193.
- 53D. Schmaljohann, *Adv. Drug Deliv. Rev.*, 2006, **58**, 1655–1670.
- 54S. T. Hemp, A. E. Smith, W. C. Bunyard, M. H. Rubinstein and T. E. Long, *Polymer*, 2014, **55**, 2325–2331.
- 55I. Galaev and B. Mattiasson, Eds., *Smart Polymers for Bioseparation and Bioprocessing*, CRC Press, London ; New York, 2001.
- 56I. Tan, F. Roohi and M.-M. Titirici, *Anal Methods*, 2012, **4**, 34–43.
- 57M. A. Ward and T. K. Georgiou, *Polymers*, 2011, **3**, 1215–1242.
- 58Z. Shen, B. Shi, H. Zhang, J. Bi and S. Dai, *Soft Matter*, 2012, **8**, 1385–1394.
- 59J. Seuring and S. Agarwal, *Macromol. Rapid Commun.*, 2012, **33**, 1898–1920.
- 60J. Zhao and H. Wang, *J. Polym. Sci. Part B Polym. Phys.*, 2016, **54**, 1869–1877.
- 61J. Seuring, F. M. Bayer, K. Huber and S. Agarwal, *Macromolecules*, 2012, **45**, 374–384.
- 62J. Niskanen and H. Tenhu, *Polym Chem*, 2017, **8**, 220–232.
- 63R. J. Young and P. A. Lovell, *Introduction to Polymers, Third Edition*, Routledge, Boca Raton, 3rd edn., 2011.
- 64Y. Ono and T. Shikata, *J. Am. Chem. Soc.*, 2006, **128**, 10030–10031.
- 65T. E. de Oliveira, C. M. Marques and P. A. Netz, *Phys. Chem. Chem. Phys.*, 2018, **20**, 10100–10107.
- 66E. C. Cho, J. Lee and K. Cho, *Macromolecules*, 2003, **36**, 9929–9934.
- 67Q. Zhang, C. Weber, U. S. Schubert and R. Hoogenboom, *Mater. Horiz.*, 2017, **4**, 109–116.
- 68H. A. Gaballa, L. M. Geever, J. A. Killion and C. L. Higginbotham, *J. Polym. Sci. Part B Polym. Phys.*, 2013, **51**, 1555–1564.
- 69D. R. Baughman and Y. A. Liu, in *Neural Networks in Bioprocessing and Chemical Engineering*, eds. D. R. Baughman and Y. A. Liu, Academic Press, Boston, 1995, pp. 365–433.
- 70L. M. Geever, D. M. Devine, M. J. D. Nugent, J. E. Kennedy, J. G. Lyons, A. Hanley and C. L. Higginbotham, *Eur. Polym. J.*, 2006, **42**, 2540–2548.
- 71X. Qiu, C. M. S. Kwan and C. Wu, *Macromolecules*, 1997, **30**, 6090–6094.
- 72Y. Hiruta, Y. Nagumo, A. Miki, T. Okano and H. Kanazawa, *RSC Adv.*, 2015, **5**, 73217–73224.
- 73A. Asadujjaman, B. Kent and A. Bertin, *Soft Matter*, 2017, **13**, 658–669.
- 74A. Gandhi, A. Paul, S. O. Sen and K. K. Sen, *Asian J. Pharm. Sci.*, 2015, **10**, 99–107.
- 75J. Zhang, *Switchable and Responsive Surfaces and Materials for Biomedical Applications*, Elsevier, 2014.
- 76S. Reinelt, D. Steinke and H. Ritter, *Beilstein J. Org. Chem.*, 2014, **10**, 680–691.
- 77K. Jain, R. Vedarajan, M. Watanabe, M. Ishikiriya and N. Matsumi, *Polym. Chem.*, 2015, **6**, 6819–6825.

- 78D. Crespy and R. M. Rossi, *Polym. Int.*, 2007, **56**, 1461–1468.
- 79W.-F. Lee and Y.-C. Yeh, *Eur. Polym. J.*, 2005, **41**, 2488–2495.
- 80K. S. Soppimath, D. C.-W. Tan and Y.-Y. Yang, *Adv. Mater.*, 2005, **17**, 318–323.
- 81Y. Zhang, S. Furyk, L. B. Sagle, Y. Cho, D. E. Bergbreiter and P. S. Cremer, *J. Phys. Chem. C*, 2007, **111**, 8916–8924.
- 82D. Fournier, R. Hoogenboom, H. M. L. Thijs, R. M. Paulus and U. S. Schubert, *Macromolecules*, 2007, **40**, 915–920.
- 83H. Okamura, Y. Morihara, S. Masuda, K. Minagawa, T. Mori and M. Tanaka, *J. Polym. Sci. Part Polym. Chem.*, 2002, **40**, 1945–1951.
- 84D. N. Schulz, D. G. Peiffer, P. K. Agarwal, J. Larabee, J. J. Kaladas, L. Soni, B. Handwerker and R. T. Garner, *Polymer*, 1986, **27**, 1734–1742.
- 85H. Zhang, S. Guo, W. Fan and Y. Zhao, *Macromolecules*, 2016, **49**, 1424–1433.
- 86H. Willcock, A. Lu, C. F. Hansell, E. Chapman, I. R. Collins and R. K. O'Reilly, *Polym. Chem.*, 2013, **5**, 1023–1030.
- 87† Pascaline Mary, * Denis D. Bendejacq, ‡ and Marie-Pierre Labeau and P. Dupuis, Reconciling Low- and High-Salt Solution Behavior of Sulfobetaine Polyzwitterions, <https://pubs.acs.org/doi/pdf/10.1021/jp071995b>, (accessed 19 May 2020).
- 88S. Jiang and Z. Cao, *Adv. Mater.*, 2010, **22**, 920–932.
- 89Z. Zhang, T. Chao, S. Chen and S. Jiang, *Langmuir*, 2006, **22**, 10072–10077.
- 90B. A. Pineda-Contreras, F. Liu and S. Agarwal, *J. Polym. Sci. Part Polym. Chem.*, 2014, **52**, 1878–1884.
- 91Y. Zhao, T. Bai, Q. Shao, S. Jiang and A. Q. Shen, *Polym. Chem.*, 2015, **6**, 1066–1077.
- 92D. Quémener, T. P. Davis, C. Barner-Kowollik and M. H. Stenzel, *Chem. Commun.*, 2006, **0**, 5051–5053.
- 93L. Barner, T. P. Davis, M. H. Stenzel and C. Barner-Kowollik, *Macromol. Rapid Commun.*, 2007, **28**, 539–559.
- 94A. Gregory and M. Stenzel, *Prog. Polym. Sci.*, 2012, **37**, 38–105.
- 95M. Arotçaréna, B. Heise, S. Ishaya and A. Laschewsky, *J. Am. Chem. Soc.*, 2002, **124**, 3787–3793.
- 96S. Eggers, T. Eckert and V. Abetz, *J. Polym. Sci. Part Polym. Chem.*, 2018, **56**, 399–411.
- 97N. S. Vishnevetskaya, V. Hildebrand, B.-J. Niebuur, I. Grillo, S. K. Filippov, A. Laschewsky, P. Müller-Buschbaum and C. M. Papadakis, *Macromolecules*, 2016, **49**, 6655–6668.
- 98F. Käfer, F. Liu, U. Stahlschmidt, V. Jérôme, R. Freitag, M. Karg and S. Agarwal, *Langmuir*, 2015, **31**, 8940–8946.
- 99H.-Y. Tian, J.-J. Yan, D. Wang, C. Gu, Y.-Z. You and X.-S. Chen, *Macromol. Rapid Commun.*, 2011, **32**, 660–664.
- 100 C. M. Papadakis, P. Müller-Buschbaum and A. Laschewsky, *Langmuir*, 2019, **35**, 9660–9676.
- 101 G. Wu, Z.-S. Wang and Q.-Y. Bai, *Macromolecules*, 2019, **52**, 5907–5916.
- 102 H. Sun, X. Chen, X. Han and H. Liu, *Langmuir*, 2017, **33**, 2646–2654.
- 103 Y. Kotsuchibashi, M. Ebara, T. Aoyagi and R. Narain, *Polymers*, 2016, **8**, 380.
- 104 F. D. Jochum, P. J. Roth, D. Kessler and P. Theato, *Biomacromolecules*, 2010, **11**, 2432–2439.
- 105 C. Cummings, H. Murata, R. Koepsel and A. J. Russell, *Biomacromolecules*, 2014, **15**, 763–771.
- 106 Y.-J. Shih, Y. Chang, A. Deratani and D. Quemener, *Biomacromolecules*, 2012, **13**, 2849–2858.
- 107 H. Zhang, X. Tong and Y. Zhao, *Langmuir*, 2014, **30**, 11433–11441.
- 108 A. Can, Q. Zhang, T. Rudolph, F. H. Schacher, J.-F. Gohy, U. S. Schubert and R. Hoogenboom, *Eur. Polym. J.*, 2015, **69**, 460–471.
- 109 L. H. Gade, *Koordinationschemie*, John Wiley & Sons, 2012.
- 110 R. Tsuchida, *Bull. Chem. Soc. Jpn.*, 1938, **13**, 388–400.
- 111 C. Janiak, H.-J. Meyer, D. Gudat and R. Alsfasser, *Riedel Moderne Anorganische Chemie*, Walter de Gruyter, 2012.
- 112 O. Roubeau, *Chem. Weinh. Bergstr. Ger.*, 2012, **18**, 15230–15244.

- 113 P. Gütllich, Y. Garcia and H. A. Goodwin, *Chem. Soc. Rev.*, 2000, **29**, 419–427.
- 114 S. Decurtins, P. Gütllich, C. P. Köhler, H. Spiering and A. Hauser, *Chem. Phys. Lett.*, 1984, **105**, 1–4.
- 115 M. Milek, F. W. Heinemann and M. M. Khusniyarov, *Inorg. Chem.*, 2013, **52**, 11585–11592.
- 116 A. Bousseksou, G. Molnár, L. Salmon and W. Nicolazzi, *Chem. Soc. Rev.*, 2011, **40**, 3313.
- 117 G. I. Dzhardimalieva and I. E. Uflyand, *ChemistrySelect*, 2018, **3**, 13234–13270.
- 118 G. I. Dzhardimalieva and I. E. Uflyand, *Chemistry of Polymeric Metal Chelates*, Springer, 2018.
- 119 A. S. Abd-El-Aziz, C. E. C. Jr, C. U. P. Jr and M. Zeldin, *Macromolecules Containing Metal and Metal-Like Elements, Volume 5: Metal-Coordination Polymers*, John Wiley & Sons, 2005.
- 120 X. Wu and C. L. Fraser, *Macromolecules*, 2000, **33**, 4053–4060.
- 121 H. Zhen, C. Luo, W. Yang, W. Song, B. Du, J. Jiang, C. Jiang, Y. Zhang and Y. Cao, *Macromolecules*, 2006, **39**, 1693–1700.
- 122 G. R. Whittell, M. D. Hager, U. S. Schubert and I. Manners, *Nat. Mater.*, 2011, **10**, 176–188.
- 123 F. Peng, G. Li, X. Liu, S. Wu and Z. Tong, *J. Am. Chem. Soc.*, 2008, **130**, 16166–16167.
- 124 N. A. A. Rossi, I. Mustafa, J. K. Jackson, H. M. Burt, S. A. Horte, M. D. Scott and J. N. Kizhakkedathu, *Biomaterials*, 2009, **30**, 638–648.
- 125 N. Bertrand, M. A. Gauthier, C. Bouvet, P. Moreau, A. Petitjean, J.-C. Leroux and J. Leblond, *J. Controlled Release*, 2011, **155**, 200–210.
- 126 J. M. Bryson, J. W. Reineke and T. M. Reineke, *Macromolecules*, 2012, **45**, 8939–8952.
- 127 W. Li, Y. Kim, J. Li and M. Lee, *Soft Matter*, 2014, **10**, 5231–5242.
- 128 L. Munuera and R. K. O'Reilly, *Dalton Trans.*, 2009, **39**, 388–391.
- 129 A. O. Moughton and R. K. O'Reilly, *Macromol. Rapid Commun.*, 2010, **31**, 37–52.
- 130 J.-F. Gohy, B. G. G. Lohmeijer and U. S. Schubert, *Macromol. Rapid Commun.*, 2002, **23**, 555–560.
- 131 T. Liu and S. Liu, *Anal. Chem.*, 2011, **83**, 2775–2785.
- 132 Y. Chujo, K. Sada and T. Saegusa, *Macromolecules*, 1993, **26**, 6320–6323.
- 133 J.-F. Gohy, B. G. G. Lohmeijer, S. K. Varshney, B. Décamps, E. Leroy, S. Boileau and U. S. Schubert, *Macromolecules*, 2002, **35**, 9748–9755.
- 134 H. Ohashi, Y. Hiraoka and T. Yamaguchi, *Macromolecules*, 2006, **39**, 2614–2620.
- 135 H. Ohashi, T. Abe, T. Tamaki and T. Yamaguchi, *Macromolecules*, 2012, **45**, 9742–9750.
- 136 T. Kaliyappan and P. Kannan, *Prog. Polym. Sci.*, 2000, **25**, 343–370.
- 137 U. S. Schubert and C. Eschbaumer, *Angew. Chem. Int. Ed.*, 2002, **41**, 2892–2926.
- 138 O. Roubeau, *Chem. - Eur. J.*, 2012, **18**, 15230–15244.
- 139 M. A. Trojer, A. Movahedi, H. Blanck and M. Nydén, *J. Chem.*, 2013, **2013**, Art. no. 946739.
- 140 D. Gupta and D. K. Jain, *J. Adv. Pharm. Technol. Res.*, 2015, **6**, 141–146.
- 141 E. Kılıç and N. P. Bayramgil, *Polym. Int.*, 2013, **62**, 621–628.
- 142 M. Ramamoorth and A. Narvekar, *J. Clin. Diagn. Res. JCDR*, 2015, **9**, GE01–GE06.
- 143 S. A. Rosenberg, P. Aebersold, K. Cornetta, A. Kasid, R. A. Morgan, R. Moen, E. M. Karson, M. T. Lotze, J. C. Yang and S. L. Topalian, *N. Engl. J. Med.*, 1990, **323**, 570–578.
- 144 K. Culver, K. Cornetta, R. Morgan, S. Morecki, P. Aebersold, A. Kasid, M. Lotze, S. A. Rosenberg, W. F. Anderson and R. M. Blaese, *Proc. Natl. Acad. Sci. U. S. A.*, 1991, **88**, 3155–3159.
- 145 N. Nayerossadat, T. Maedeh and P. A. Ali, *Adv. Biomed. Res.*, , DOI:10.4103/2277-9175.98152.
- 146 F. P. Polack, S. J. Thomas, N. Kitchin, J. Absalon, A. Gurtman, S. Lockhart, J. L. Perez, G. Pérez Marc, E. D. Moreira, C. Zerbini, R. Bailey, K. A. Swanson, S. Roychoudhury, K. Koury, P. Li, W. V. Kalina, D. Cooper, R. W. Frenck, L. L. Hammitt, Ö.

- Türeci, H. Nell, A. Schaefer, S. Ünal, D. B. Tresnan, S. Mather, P. R. Dormitzer, U. Şahin, K. U. Jansen and W. C. Gruber, *N. Engl. J. Med.*, 2020, **383**, 2603–2615.
- 147 M. J. Mulligan, K. E. Lyke, N. Kitchin, J. Absalon, A. Gurtman, S. Lockhart, K. Neuzil, V. Raabe, R. Bailey, K. A. Swanson, P. Li, K. Koury, W. Kalina, D. Cooper, C. Fontes-Garfias, P.-Y. Shi, Ö. Türeci, K. R. Tompkins, E. E. Walsh, R. Frenck, A. R. Falsey, P. R. Dormitzer, W. C. Gruber, U. Şahin and K. U. Jansen, *Nature*, 2020, **586**, 589–593.
- 148 N. Pardi, M. J. Hogan, F. W. Porter and D. Weissman, *Nat. Rev. Drug Discov.*, 2018, **17**, 261–279.
- 149 V. A. Bloomfield, *Biopolymers*, 1997, **44**, 269–282.
- 150 C. H. Jones, C.-K. Chen, M. Jiang, L. Fang, C. Cheng and B. A. Pfeifer, *Mol. Pharm.*, 2013, **10**, 1138–1145.
- 151 C. H. Jones, C.-K. Chen, A. Ravikrishnan, S. Rane and B. A. Pfeifer, *Mol. Pharm.*, 2013, **10**, 4082–4098.
- 152 E. S. Robertson, T. Ooka and E. D. Kieff, *Proc. Natl. Acad. Sci. U. S. A.*, 1996, **93**, 11334–11340.
- 153 S. Zhang, Y. Xu, B. Wang, W. Qiao, D. Liu and Z. Li, *J. Control. Release Off. J. Control. Release Soc.*, 2004, **100**, 165–180.
- 154 S. Shukla, A. Singh, A. Pandey and A. Mishra, *Biochem. Eng. J.*, 2012, **65**, 70–81.
- 155 R. Kircheis, A. Kichler, G. Wallner, M. Kursa, M. Ogris, T. Felzmann, M. Buchberger and E. Wagner, *Gene Ther.*, 1997, **4**, 409–418.
- 156 M.-A. Zanta, O. Boussif, A. Adib and J.-P. Behr, *Bioconjug. Chem.*, 1997, **8**, 839–844.
- 157 M. A. Mintzer and E. E. Simanek, *Chem. Rev.*, 2009, **109**, 259–302.
- 158 M. T. Calejo, S. A. Sande and B. Nyström, *Expert Opin. Drug Deliv.*, 2013, **10**, 1669–1686.
- 159 M. Kurisawa, M. Yokoyama and T. Okano, *J. Controlled Release*, 2000, **69**, 127–137.
- 160 F. J. Xu and W. T. Yang, *Prog. Polym. Sci.*, 2011, **36**, 1099–1131.
- 161 B. J. Berne and R. Pecora, *Dynamic Light Scattering: With Applications to Chemistry, Biology, and Physics*, Courier Corporation, 2000.
- 162 J. Stetefeld, S. A. McKenna and T. R. Patel, *Biophys. Rev.*, 2016, **8**, 409–427.
- 163 D. E. Koppel, *J. Chem. Phys.*, 1972, **57**, 4814–4820.
- 164 I. D. Morrison, E. F. Grabowski and C. A. Herb, *Langmuir*, 1985, **1**, 496–501.
- 165 C. Schick, *Anal. Bioanal. Chem.*, 2009, **395**, 1589.
- 166 R. Jose, V. Thavasi and S. Ramakrishna, *J. Am. Ceram. Soc.*, 2009, **92**, 289–301.
- 167 J. M. Barton, in *Epoxy Resins and Composites I*, Springer, Berlin, Heidelberg, 1985, pp. 111–154.
- 168 M. J. Starink, *Int. Mater. Rev.*, 2004, **49**, 191–226.
- 169 A. F. Barnes, M. J. Hardy and T. J. Lever, *J. Therm. Anal.*, 1993, **40**, 499–509.
- 170 G. Bruylants and J. W. and C. Michaux, *Differential Scanning Calorimetry in Life Science*, <http://www.eurekaselect.com/61425/article>, (accessed 5 May 2020).
- 171 C. G. Biliaderis, *Food Chem.*, 1983, **10**, 239–265.
- 172 E. Verdonck, K. Schaap and L. C. Thomas, *Int. J. Pharm.*, 1999, **192**, 3–20.
- 173 A. F. Abdelkader and J. R. White, *J. Mater. Sci.*, 2005, **40**, 1843–1854.
- 174 H. Wang and K. S. Siow, *Polym. Eng. Sci.*, 1999, **39**, 422–429.
- 175 S. Kasap, J. Málek and R. Svoboda, in *Springer Handbook of Electronic and Photonic Materials*, eds. S. Kasap and P. Capper, Springer International Publishing, Cham, 2017, pp. 1–1.
- 176 M. Reading, A. Luget and R. Wilson, *Thermochim. Acta*, 1994, **238**, 295–307.
- 177 G. H. Lathe and C. R. J. Ruthven, *Biochem. J.*, 1956, **62**, 665–674.
- 178 J. Cazes, *Analytical Instrumentation Handbook*, CRC Press, 2004.
- 179 B. Trathnigg, *Prog. Polym. Sci.*, 1995, **20**, 615–650.
- 180 G. Schwedt, *Analytische Chemie: Grundlagen, Methoden und Praxis*, Wiley-VCH Verlag GmbH & Co. KGaA, Weinheim, 2. vollständig überarbeitete Auflage., 2008.
- 181 M. Hesse, H. Meier and B. Zeeh, *Spektroskopische Methoden in der organischen Chemie*, Thieme, Stuttgart; New York, Auflage: 7., überarbeitete Auflage 247 Abbildungen, 304 Formbilder und Schemata, 102 Tab., 2005.
- 182 C. Hofmann and M. Schönhoff, *Colloid Polym. Sci.*, 2009, **287**, 1369–1376.

- 183 H. G. Schild, *Prog. Polym. Sci.*, 1992, **17**, 163–249.
- 184 G. Odian, *Principles of Polymerization*, Wiley-Interscience, Hoboken, N.J., 4., 2004.
- 185 L. Hou and P. Wu, *Soft Matter*, 2015, **11**, 7059–7065.
- 186 S. Y. Lin, K. S. Chen and L. Run-Chu, *Biomaterials*, 2001, **22**, 2999–3004.
- 187 S. Lanzalaco and E. Armelin, *Gels*, DOI:10.3390/gels3040036.
- 188 P. Matricardi, C. Di Meo, T. Coviello, W. E. Hennink and F. Alhaique, *Adv. Drug Deliv. Rev.*, 2013, **65**, 1172–1187.
- 189 U. Ritz, P. Kögler, I. Höfer, P. Frank, S. Klees, S. Gebhard, C. Brendel, K. Kaufmann, A. Hofmann, P. M. Rommens and U. Jonas, *J. Mater. Chem. B*, 2016, **4**, 6552–6564.
- 190 P. W. Beines, I. Klosterkamp, B. Menges, U. Jonas and W. Knoll, *Langmuir*, 2007, **23**, 2231–2238.
- 191 J. Virtanen, M. Arotçaréna, B. Heise, S. Ishaya, A. Laschewsky and H. Tenhu, *Langmuir*, 2002, **18**, 5360–5365.
- 192 L. Mäkinen, D. Varadharajan, H. Tenhu and S. Hietala, *Macromolecules*, 2016, **49**, 986–993.
- 193 W. Wang, L. Tetley and I. F. Uchegbu, *Langmuir*, 2000, **16**, 7859–7866.
- 194 H. Mori, I. Kato, S. Saito and T. Endo, *Macromolecules*, 2010, **43**, 1289–1298.
- 195 A. Gandhi, A. Paul, S. O. Sen and K. K. Sen, *Asian J. Pharm. Sci.*, 2015, **10**, 99–107.
- 196 R. Plummer, D. J. T. Hill and A. K. Whittaker, *Macromolecules*, 2006, **39**, 8379–8388.
- 197 A. M. Md Jani, D. Losic and N. H. Voelcker, *Prog. Mater. Sci.*, 2013, **58**, 636–704.
- 198 G. W. Preston and A. J. Wilson, *Chem. Soc. Rev.*, 2013, **42**, 3289–3301.
- 199 V. B. Schwartz, F. Thétiot, S. Ritz, S. Pütz, L. Choritz, A. Lappas, R. Förch, K. Landfester and U. Jonas, *Adv. Funct. Mater.*, 2012, **22**, 2376–2386.
- 200 P.-F. Li, R. Xie, J.-C. Jiang, T. Meng, M. Yang, X.-J. Ju, L. Yang and L.-Y. Chu, *J. Membr. Sci.*, 2009, **337**, 310–317.
- 201 W. J. Stępniewski and Z. Bojar, *Surf. Coat. Technol.*, 2011, **206**, 265–272.
- 202 A. Li, F. Müller, A. Birner, K. Nielsch and U. Gösele, DOI:10.1063/1.368911.
- 203 K. Nielsch, J. Choi, K. Schwirn, R. B. Wehrspohn and U. Gösele, *Nano Lett.*, 2002, **2**, 677–680.
- 204 R. C. Furneaux, W. R. Rigby and A. P. Davidson, *Nature*, 1989, **337**, 147–149.
- 205 B. Lee, S. Hyun, G. Jeon, E. Y. Kim, J. Kim, W. J. Kim and J. K. Kim, *ACS Appl. Mater. Interfaces*, 2016, **8**, 11758–11764.
- 206 M. Liu, J. Zhang, Y. Qiao, T. Ye, N. Liu, X. Xu, C. Zou and S. Huang, *J. Phys. Chem. C*, 2019, **123**, 12500–12504.
- 207 C. Dekker, *Nat. Nanotechnol.*, 2007, **2**, 209–215.
- 208 S. S. Patel, B. J. Belmont, J. M. Sante and M. F. Rexach, *Cell*, 2007, **129**, 83–96.
- 209 F. Chen, X. Jiang, T. Kuang, L. Chang, D. Fu, Z. Yang, J. Yang, P. Fan, Z. Fei and M. Zhong, *RSC Adv.*, 2015, **5**, 70204–70210.
- 210 R. K. Joshi, P. Carbone, F. C. Wang, V. G. Kravets, Y. Su, I. V. Grigorieva, H. A. Wu, A. K. Geim and R. R. Nair, *Science*, 2014, **343**, 752–754.
- 211 S. P. Surwade, S. N. Smirnov, I. V. Vlassiuk, R. R. Unocic, G. M. Veith, S. Dai and S. M. Mahurin, *Nat. Nanotechnol.*, 2015, **10**, 459–464.
- 212 J. He, H. Liu, P. Pang, D. Cao and S. Lindsay, *J. Phys. Condens. Matter Inst. Phys. J.*, 2010, **22**, 454112.
- 213 I. Vlassiuk, P. Y. Apel, S. N. Dmitriev, K. Healy and Z. S. Siwy, *Proc. Natl. Acad. Sci. U. S. A.*, 2009, **106**, 21039–21044.
- 214 X. Liu, T. Xiao, F. Wu, M.-Y. Shen, M. Zhang, H. Yu and L. Mao, *Angew. Chem. Int. Ed.*, 2017, **56**, 11802–11806.
- 215 G. Pérez-Mitta, J. S. Tuninetti, W. Knoll, C. Trautmann, M. E. Toimil-Molares and O. Azzaroni, *J. Am. Chem. Soc.*, 2015, **137**, 6011–6017.
- 216 I. M. Salin and J. C. Seferis, *J. Appl. Polym. Sci.*, 1993, **47**, 847–856.
- 217 J. Zhao and H. Wang, *J. Polym. Sci. Part B Polym. Phys.*, 2016, **54**, 1869–1877.
- 218 L. H. Gade, *Koordinationschemie*, Wiley, Weinheim, 2010.
- 219 A. Y. Robin and K. M. Fromm, *Coord. Chem. Rev.*, 2006, **250**, 2127–2157.
- 220 W. L. Leong and J. J. Vittal, *Chem. Rev.*, 2011, **111**, 688–764.

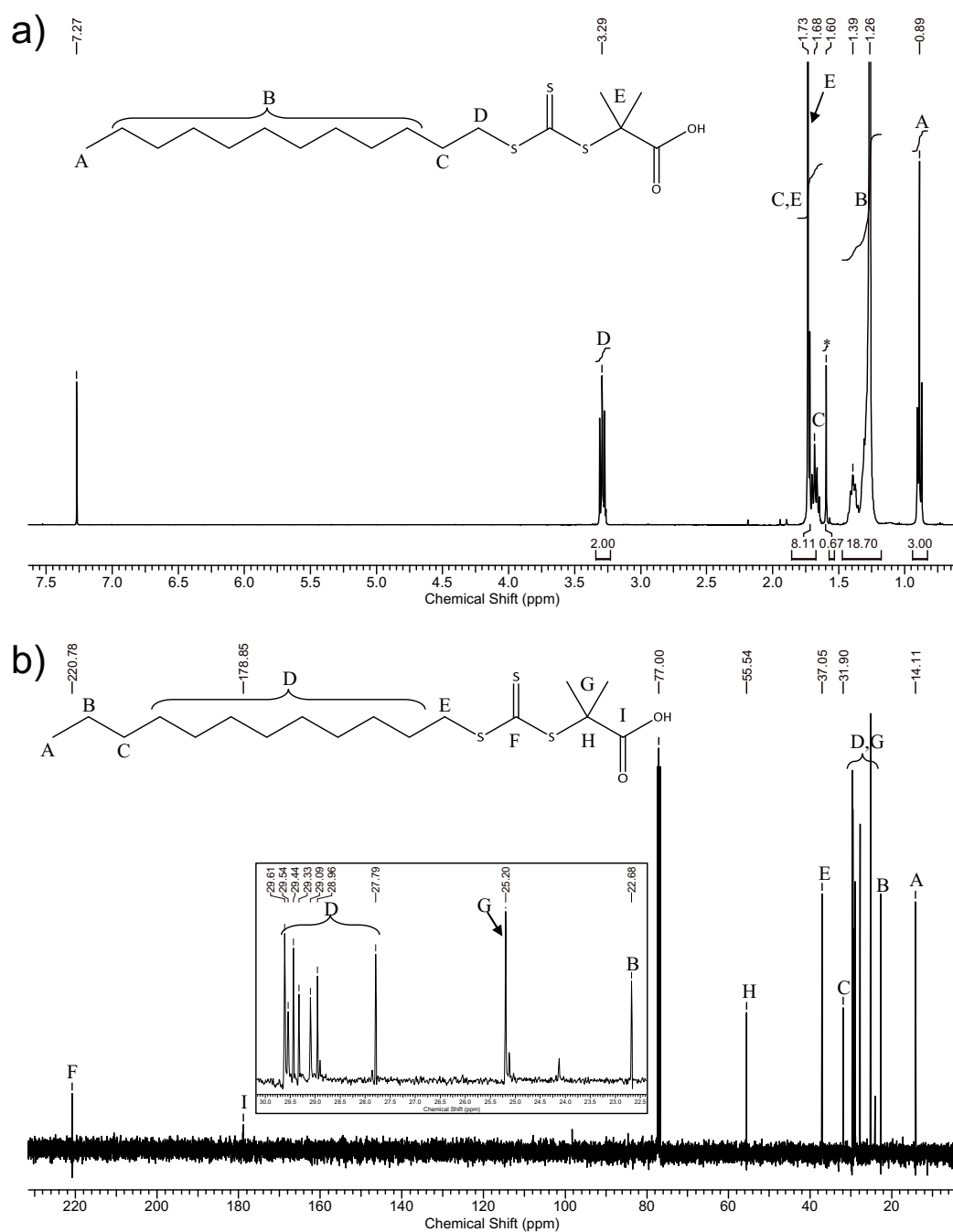
- 221 C. Rüttiger, H. Hübner, S. Schöttner, T. Winter, G. Cherkashinin, B. Kuttich, B. Stühn and M. Gallei, *ACS Appl. Mater. Interfaces*, 2018, **10**, 4018–4030.
- 222 K. Zhang, S. Liu, Q. Zhao and W. Huang, *Coord. Chem. Rev.*, , DOI:10.1016/j.ccr.2016.03.016.
- 223 G. R. Whittell and I. Manners, *Adv. Mater.*, 2007, **19**, 3439–3468.
- 224 C. Janiak, *Dalton Trans.*, 2003, 2781–2804.
- 225 D. W. R. Balkenende, S. Coulibaly, S. Balog, Y. C. Simon, G. L. Fiore and C. Weder, *J. Am. Chem. Soc.*, 2014, **136**, 10493–10498.
- 226 B. Sandmann, B. Happ, S. Kupfer, F. H. Schacher, M. D. Hager and U. S. Schubert, *Macromol. Rapid Commun.*, 2015, **36**, 604–609.
- 227 W.-X. Feng, S.-Y. Yin, M. Pan, H.-P. Wang, Y.-N. Fan, X.-Q. Lü and C.-Y. Su, *J. Mater. Chem. C*, 2017, **5**, 1742–1750.
- 228 M. Freund, *Berichte Dtsch. Chem. Ges.*, 1896, **29**, 2483–2490.
- 229 J. G. Haasnoot, *Coord. Chem. Rev.*, 2000, **200–202**, 131–185.
- 230 B. Pergolese, M. Muniz-Miranda and A. Bigotto, *J. Phys. Chem. B*, 2004, **108**, 5698–5702.
- 231 W. Ye, Q. Yao, S. Yu, P. Gong and M. Qin, *Molecules*, 2017, **22**, 1759.
- 232 S. R. Singer and C. N. McDaniel, *Plant Physiol.*, 1982, **69**, 1382–1386.
- 233 M. Erfantalab and H. Khanmohammadi, *Spectrochim. Acta. A. Mol. Biomol. Spectrosc.*, 2014, **125**, 345–352.
- 234 Y. Boland, P. Hertsens, J. Marchand-Brynaert and Y. Garcia, *Synthesis*, 2006, **2006**, 1504–1512.
- 235 Y. Ono and T. Shikata, *J. Am. Chem. Soc.*, 2006, **128**, 10030–10031.
- 236 D. Roy, W. L. A. Brooks and B. S. Sumerlin, *Chem. Soc. Rev.*, 2013, **42**, 7214–7243.
- 237 M. A. Ward and T. K. Georgiou, *Polymers*, 2011, **3**, 1215–1242.
- 238 A. J. Convertine, N. Ayres, C. W. Scales, A. B. Lowe and C. L. McCormick, *Biomacromolecules*, 2004, **5**, 1177–1180.
- 239 G. Zhou and I. I. Harruna, *Macromolecules*, 2005, **38**, 4114–4123.
- 240 M. F. T. Meier, F. Thetiot, N. Pittala, I. Lieberwirth, C. Kunzler, S. Triki and U. Jonas, *Polym. Chem.*, 2021, **12**, 5598–5612.
- 241 S. Furryk, Y. Zhang, D. Ortiz-Acosta, P. S. Cremer and D. E. Bergbreiter, *J. Polym. Sci. Part Polym. Chem.*, 2006, **44**, 1492–1501.
- 242 J. G. Haasnoot, G. Vos and W. L. Groeneveld, *Z. Für Naturforschung B*, 2014, **32**, 1421–1430.
- 243 A. K. Tucker and M. J. Stevens, *Macromolecules*, 2012, **45**, 6697–6703.
- 244 J.-J. Li, Y.-N. Zhou, Z.-H. Luo and S. Zhu, *Polym. Chem.*, 2018, **10**, 260–266.
- 245 G. D. Schmidt-Wolf and I. G. H. Schmidt-Wolf, *Trends Mol. Med.*, 2003, **9**, 67–72.
- 246 H. Yin, R. L. Kanasty, A. A. Eltoukhy, A. J. Vegas, J. R. Dorkin and D. G. Anderson, *Nat. Rev. Genet.*, 2014, **15**, 541–555.
- 247 M. Ahmed and R. Narain, *Biomaterials*, 2011, **32**, 5279–5290.
- 248 M. A. Mintzer and E. E. Simanek, *Chem. Rev.*, 2009, **109**, 259–302.
- 249 M. Huang, C.-W. Fong, E. Khor and L.-Y. Lim, *J. Controlled Release*, 2005, **106**, 391–406.
- 250 A. A. Eltoukhy, D. J. Siegwart, C. A. Alabi, J. S. Rajan, R. Langer and D. G. Anderson, *Biomaterials*, 2012, **33**, 3594–3603.
- 251 R. N. Johnson, D. S. H. Chu, J. Shi, J. G. Schellinger, P. M. Carlson and S. H. Pun, *J. Control. Release Off. J. Control. Release Soc.*, 2011, **155**, 303–311.
- 252 W. T. Godbey, K. K. Wu and A. G. Mikos, *J. Biomed. Mater. Res.*, 1999, **45**, 268–275.
- 253 O. Boussif, F. Lezoualc'h, M. A. Zanta, M. D. Mergny, D. Scherman, B. Demeneix and J. P. Behr, *Proc Natl Acad Sci U A*, 1995, **92**, 7297–301.
- 254 W. T. Godbey, K. K. Wu and A. G. Mikos, *J. Control. Release Off. J. Control. Release Soc.*, 1999, **60**, 149–160.
- 255 Z. Mao, L. Ma, J. Yan, M. Yan, C. Gao and J. Shen, *Biomaterials*, 2007, **28**, 4488–4500.
- 256 M. Kurisawa, M. Yokoyama and T. Okano, *J. Control. Release Off. J. Control. Release Soc.*, 2000, **69**, 127–137.

- 257 B. R. Twaites, C. de Las Heras Alarcón, M. Lavigne, A. Saulnier, S. S. Pennadam, D. Cunliffe, D. C. Górecki and C. Alexander, *J. Control. Release Off. J. Control. Release Soc.*, 2005, **108**, 472–483.
- 258 M. Karimi, P. Sahandi Zangabad, A. Ghasemi, M. Amiri, M. Bahrami, H. Malekzad, H. Ghahramanzadeh Asl, Z. Mahdieh, M. Bozorgomid, A. Ghasemi, M. R. Rahmani Taji Boyuk and M. R. Hamblin, *ACS Appl. Mater. Interfaces*, 2016, **8**, 21107–21133.
- 259 M. Mateescu, I. Nuss, A. Southan, H. Messenger, S. V. Wegner, J. Kupka, M. Bach, G. E. M. Tovar, H. Boehm and S. Laschat, *Synthesis*, 2014, **46**, 1243–1253.
- 260 R. R. B. Makarand V. Risbud, *Drug Deliv.*, 2000, **7**, 69–75.
- 261 H. Gin, B. Dupuy, D. Bonnemaïson-Bourignon, L. Bordenave, R. Bareille, M. J. Latapie, C. Baquey, J. H. Beziau and D. Ducassou, *Biomater. Artif. Cells. Artif. Organs*, 1990, **18**, 25–42.
- 262 W. Li, L. Huang, X. Ying, Y. Jian, Y. Hong, F. Hu and Y. Du, *Angew. Chem. Int. Ed.*, 2015, **54**, 3126–3131.
- 263 M. Kokkinopoulou, J. Simon, K. Landfester, V. Mailänder and I. Lieberwirth, *Nanoscale*, 2017, **9**, 8858–8870.
- 264 P. Renz, M. Kokkinopoulou, K. Landfester and I. Lieberwirth, *Macromol. Chem. Phys.*, 2016, **217**, 1879–1885.
- 265 M. E. Nash, W. M. Carroll, P. J. Foley, G. Maguire, C. O. Connell, A. V. Gorelov, S. Beloshapkin and Y. A. Rochev, *Soft Matter*, 2012, **8**, 3889–3899.
- 266 A. Postma, T. P. Davis, G. Li, G. Moad and M. S. O'Shea, *Macromolecules*, 2006, **39**, 5307–5318.
- 267 J. T. Lai, D. Filla and R. Shea, *Macromolecules*, 2002, **35**, 6754–6756.
- 268 United States, US8791286B2, 2014.
- 269 B. V. K. J. Schmidt, M. Hetzer, H. Ritter and C. Barner-Kowollik, *Macromolecules*, 2011, **44**, 7220–7232.
- 270 N. Pittala, F. Thétiot, S. Triki, K. Boukheddaden, G. Chastanet and M. Marchivie, *Chem. Mater.*, 2017, **29**, 490–494.
- 271 1971.
- 272 S. C. Hyde, I. A. Pringle, S. Abdullah, A. E. Lawton, L. A. Davies, A. Varathalingam, G. Nunez-Alonso, A. M. Green, R. P. Bazzani, S. G. Sumner-Jones, M. Chan, H. Li, N. S. Yew, S. H. Cheng, A. C. Boyd, J. C. Davies, U. Griesenbach, D. J. Porteous, D. N. Sheppard, F. M. Munkonge, E. W. Alton and D. R. Gill, *Nat. Biotechnol.*, 2008, **26**, 549–51.
- 273 T. Le Gall, I. Baussanne, S. Halder, N. Carmoy, T. Montier, P. Lehn and J. L. Decout, *Bioconj. Chem.*, 2009, **20**, 2032–2046.
- 274 T. Le Gall, D. Loizeau, E. Picquet, N. Carmoy, J.-J. Yaouanc, L. Burel-Deschamps, P. Delépine, P. Giamarchi, P.-A. Jaffrès, P. Lehn and T. Montier, *J. Med. Chem.*, 2010, **53**, 1496–1508.

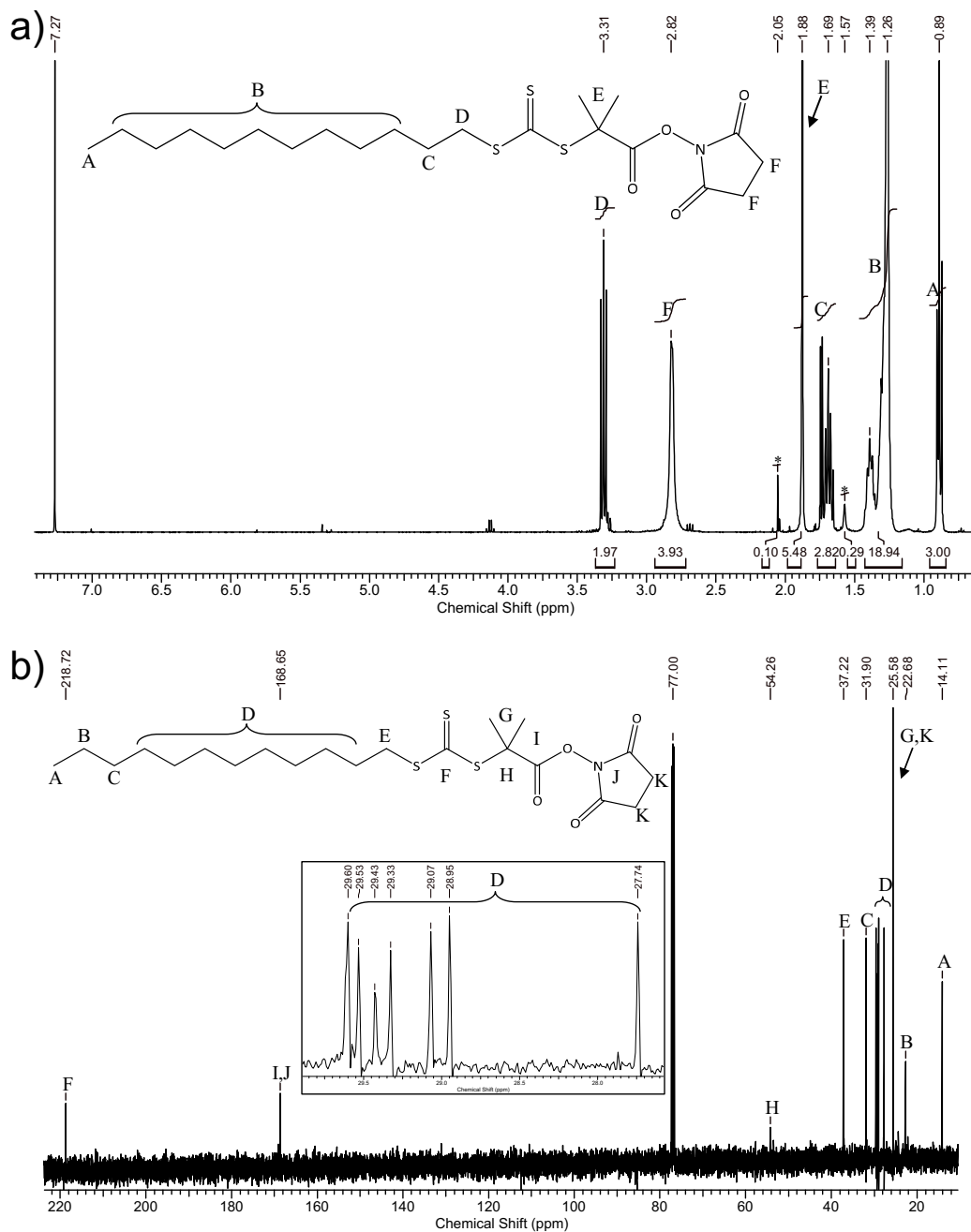
16. Appendix

16.1. Chain Transfer Agents

16.1.1. Carboxyl-terminated Asymmetric Chain Transfer Agent 2- {[(Dodecylthio)-carbothiyl]thio}-2-methylpropanoic Acid (DMP)



16.1.2. Ester Activated Chain Transfer Agent 2,5-Dioxopyrrolidin-1-yl-2-[[[(dodecylthio)-carbonothioyl]thio]-2-methylpropanoate (DMP-NHS)



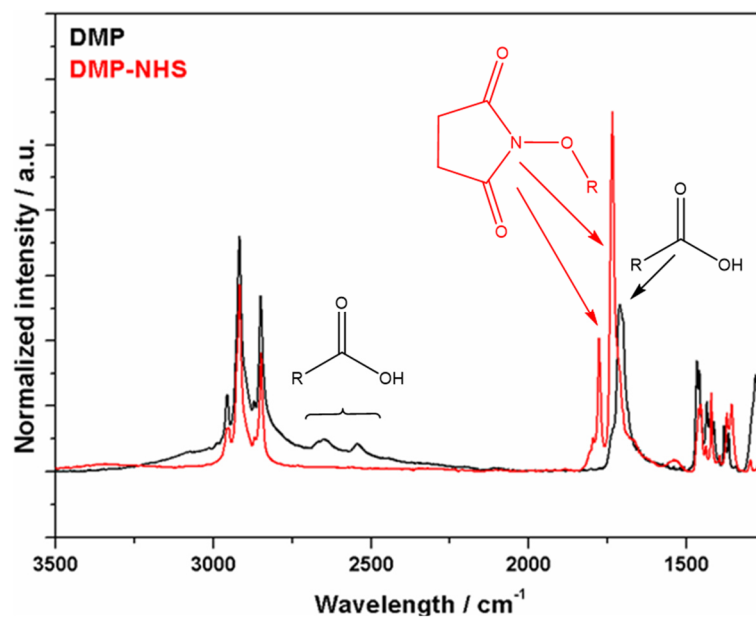
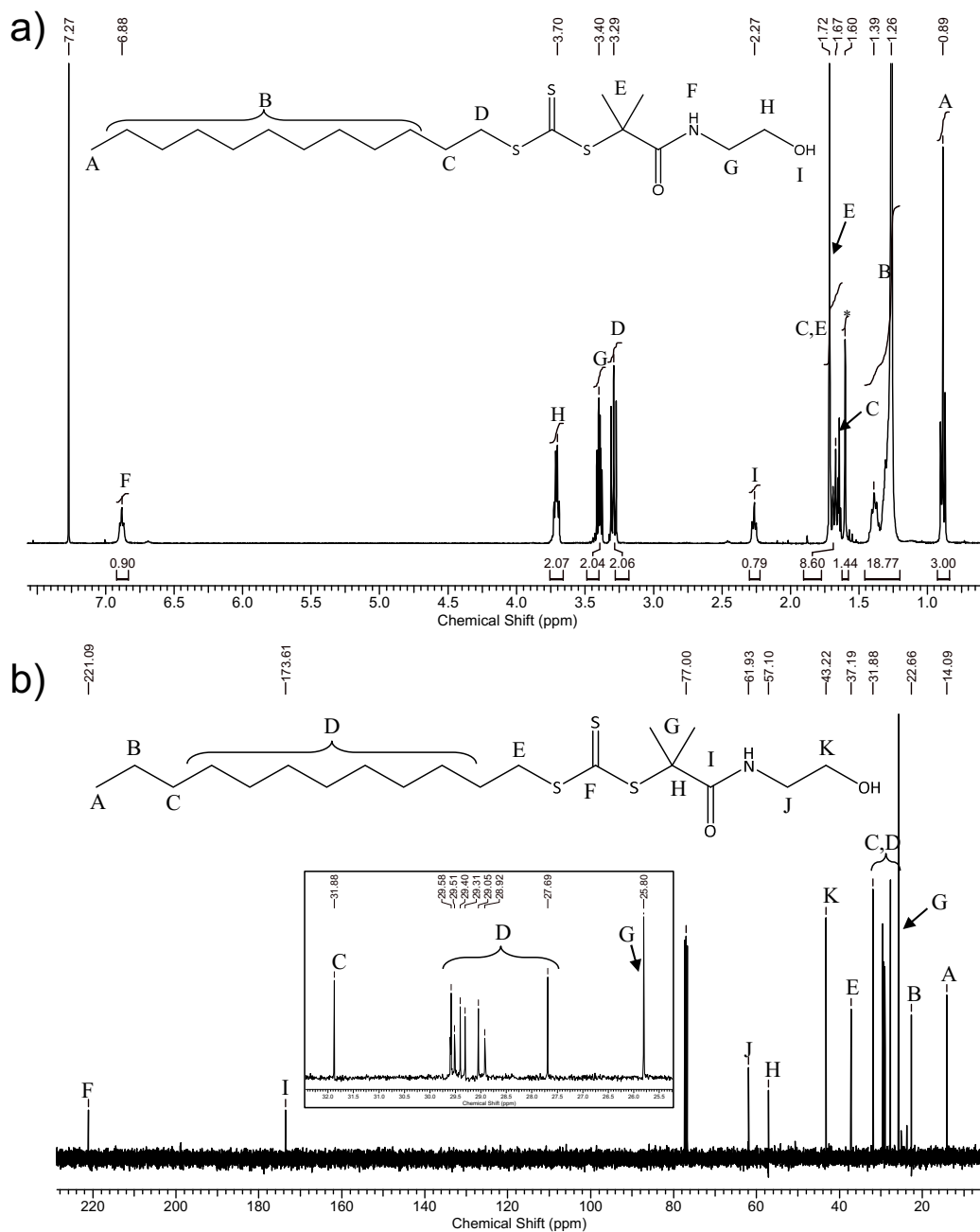


Figure S3: ATR-IR spectra of the educt DMP (black) and the activated chain transfer agent DMP-NHS (red).

16.1.3. Hydroxy End-functionalized Chain Transfer Agent Dodecyl-{1-[(2-hydroxyethyl)-amino]-2-methyl-1-oxopropan-2-yl}carbonotrithioate (DMP-EA)



16.1.4. Triazole End-functionalized Chain Transfer Agent 1-[[3-(4*H*-1,2,4-triazol-4-yl)propyl]amino]-2-methyl-1-oxopropan-2-yl-dodecyl-carbonotrithioate (DMP-APTRZ)

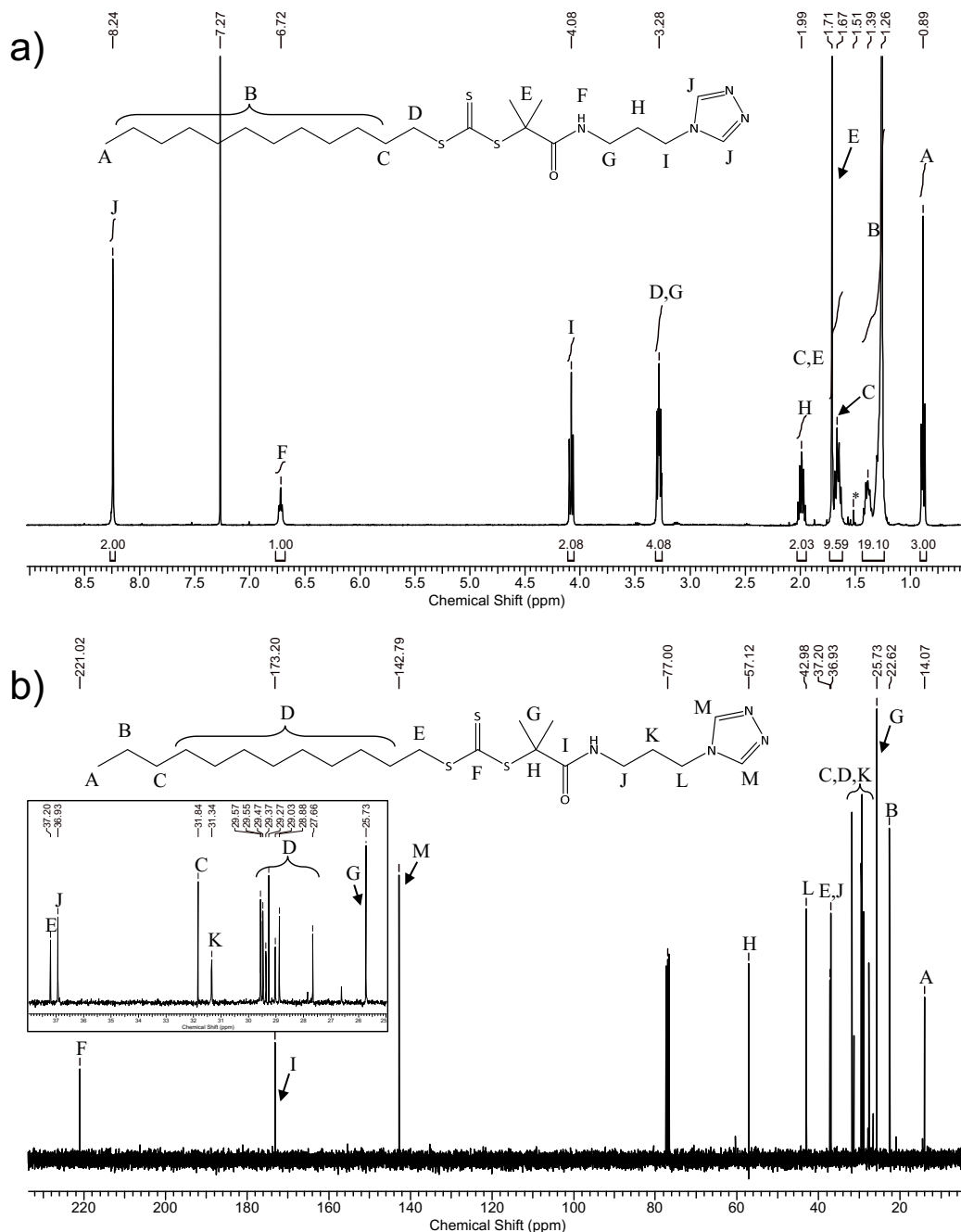


Figure S5: a) ^1H NMR (400 MHz) and b) ^{13}C NMR (101 MHz) spectra of the triazole end-functionalized chain transfer agent DMP-APTRZ, recorded in CDCl_3 .

The success of the end group modification of the chain transfer agent by the coordination moiety APTRZ was additionally proved by 2D NMR spectroscopy (COSY and HMBC) in Figure S6 and Figure S7.

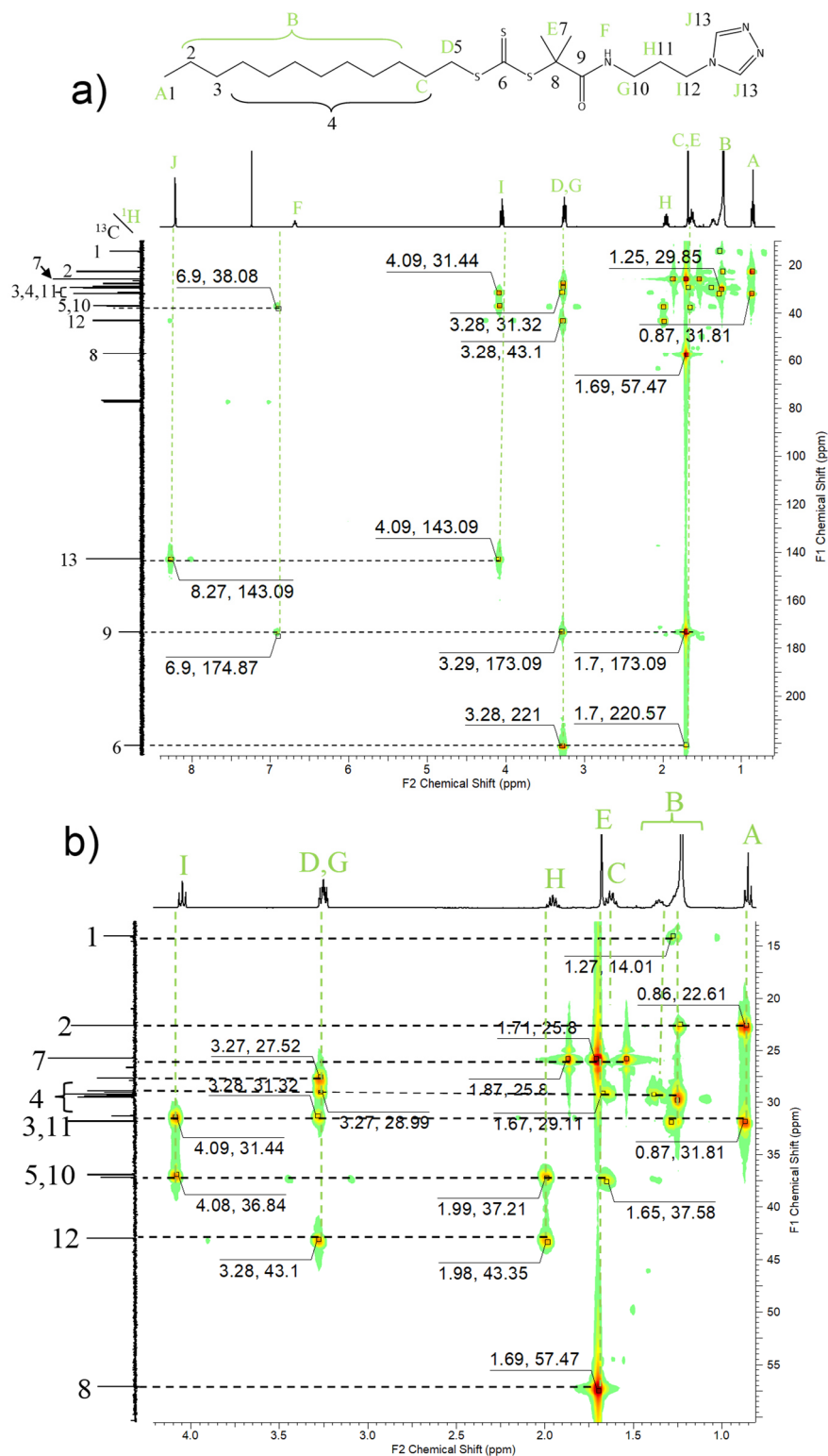


Figure S7: a) HMBC spectrum and b) its excerpt of the triazole end-functionalized chain transfer agent DMP-APTRZ, recorded in CDCl_3 .

The signals and coupling partners from the 2D HMBC NMR spectrum are summarized in the table below (Table S2).

16.1.5. Carboxyl-terminated Symmetric Chain Transfer Agent 2,2'-[Thio-carbonyl-bis-(sulfanediyl)]-bis-(2-methylpropanoic acid) (BIT)

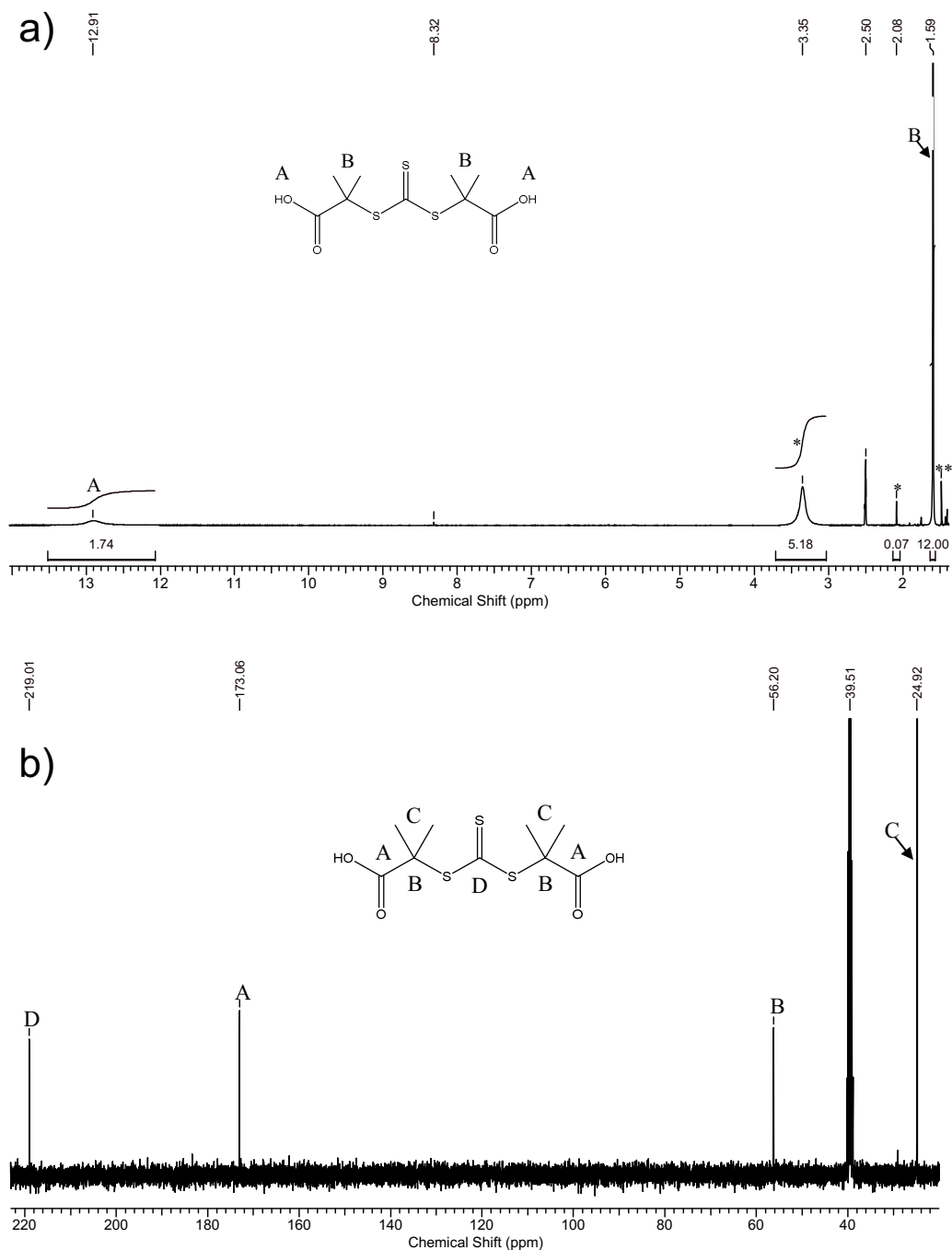
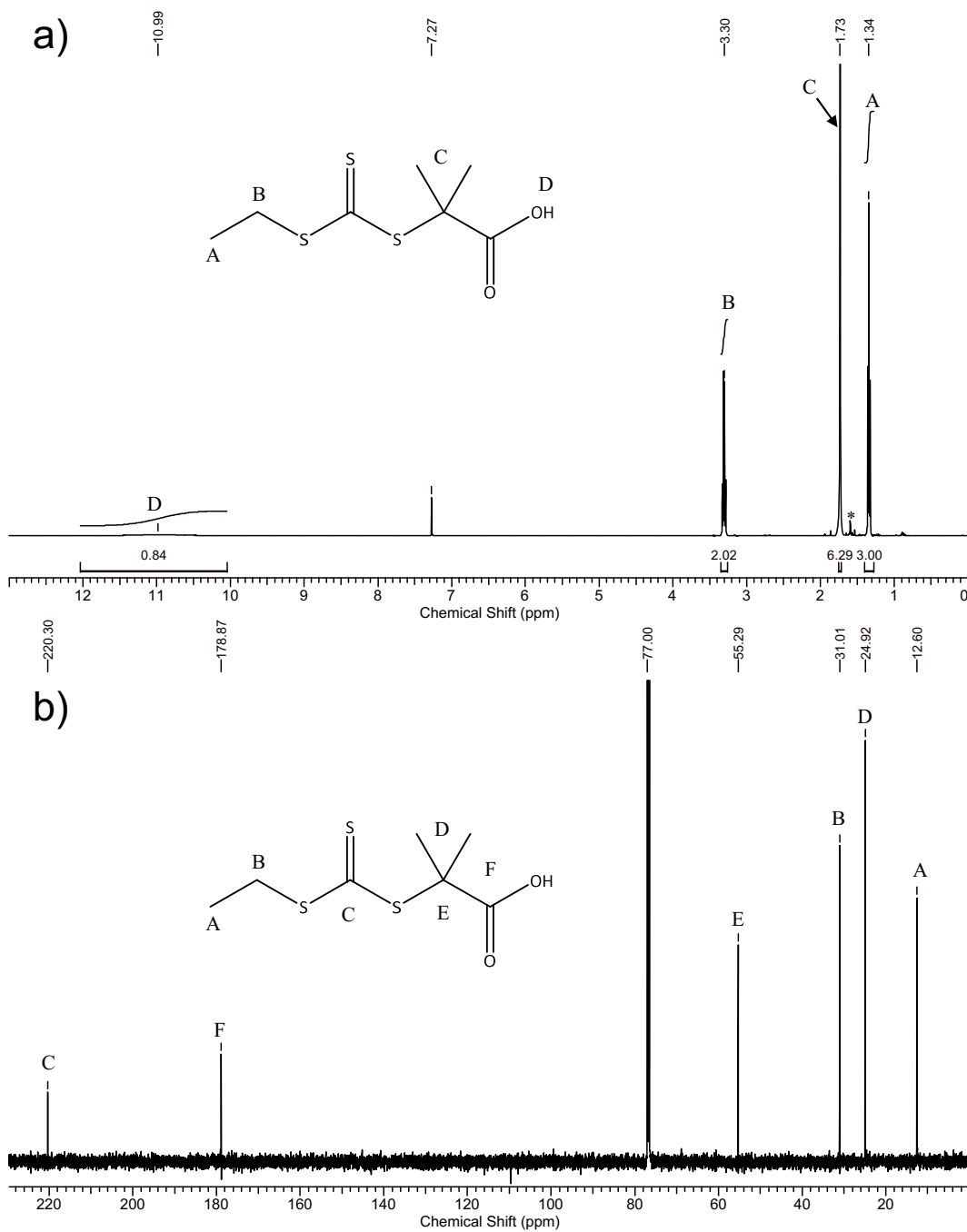
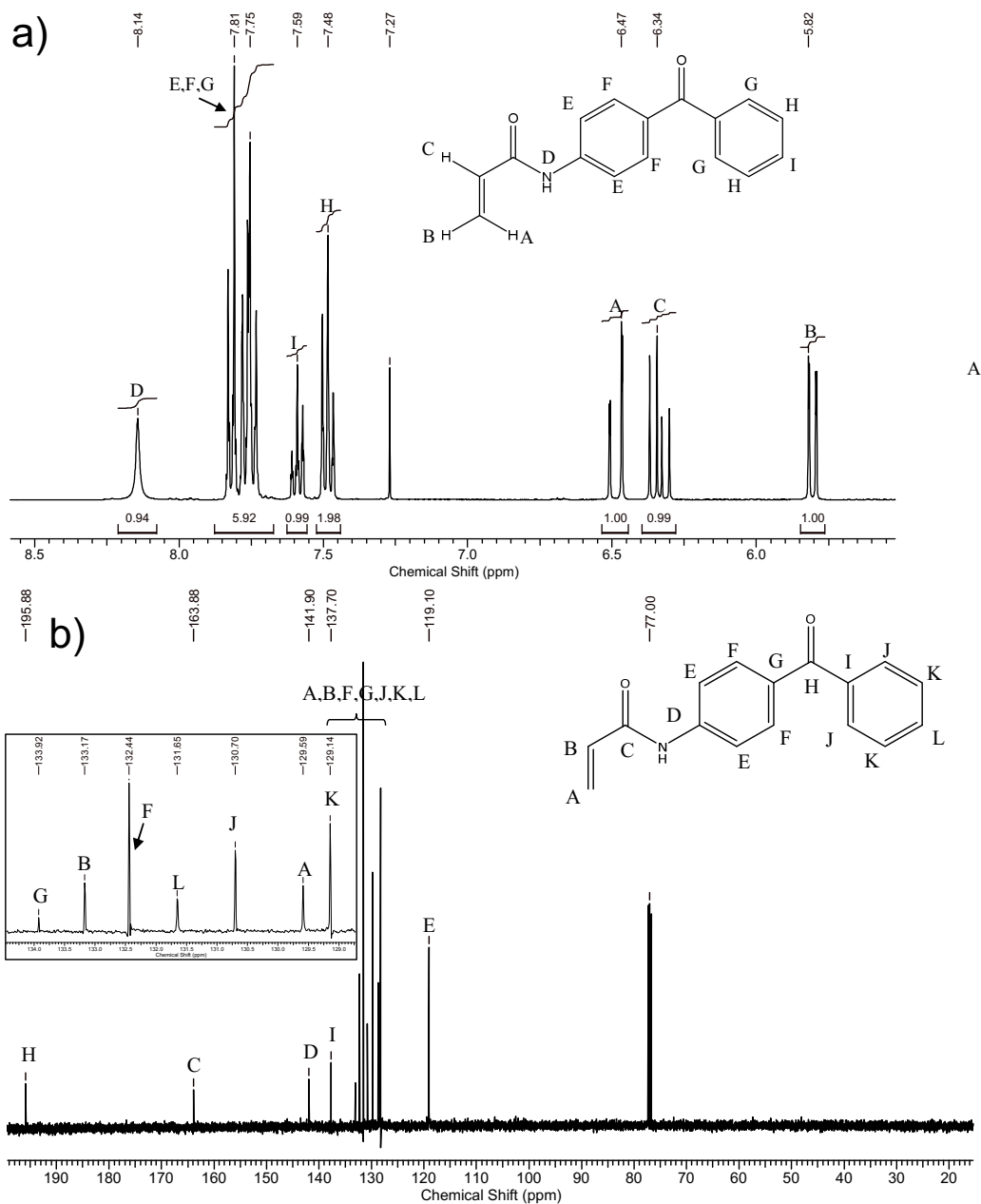


Figure S8: a) ^1H NMR (400 MHz) and b) ^{13}C NMR (101 MHz) spectra of the symmetric chain transfer agent BIT, recorded in CDCl_3 . Asterisks mark solvent residues (water, acetone).

16.1.6. Carboxyl-terminated Asymmetrical Hydrophilic Chain Transfer Agent 2-[[Ethylthio]-carbothioyl]thio}-2-methylpropanoic Acid (EMP)

16.2. Monomers

16.2.1. Photo-crosslinkable Monomer *N*-(4-Benzoylphenyl)acrylamide (BPAAm)



16.2.2. Ion Sensitive Coordination Monomer *N*-[3-(4*H*-1,2,4-triazol-4-yl)propyl]-methacrylamide (APTRZMAAm)

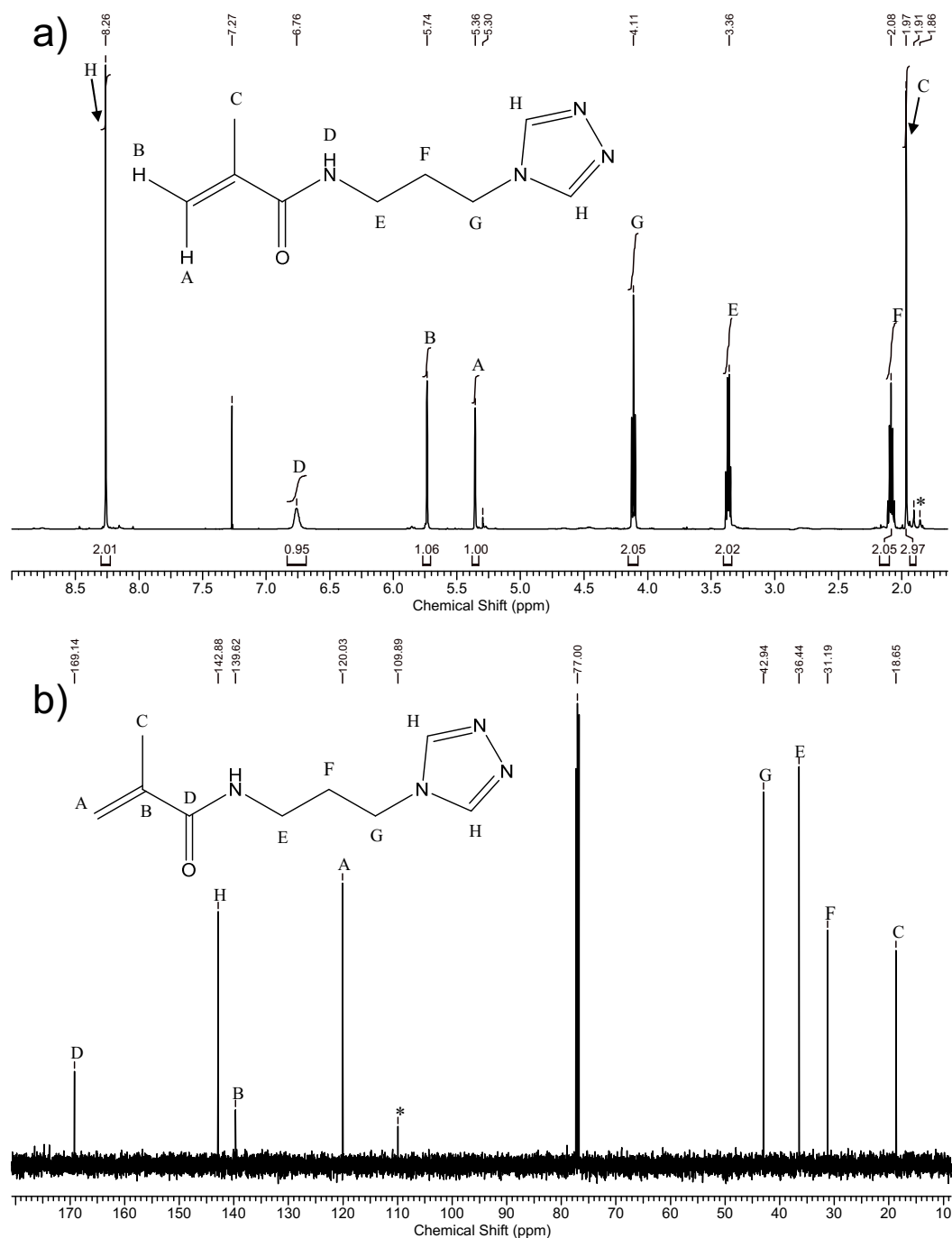


Figure S11: a) ^1H NMR (500 MHz) and b) ^{13}C NMR (125 MHz) spectra of the ion sensitive coordination monomer APTRZMAAm, recorded in CDCl_3 .

The purity of the product was investigated *via* HPLC-MS to ensure the validity of its formation (Figure S12).

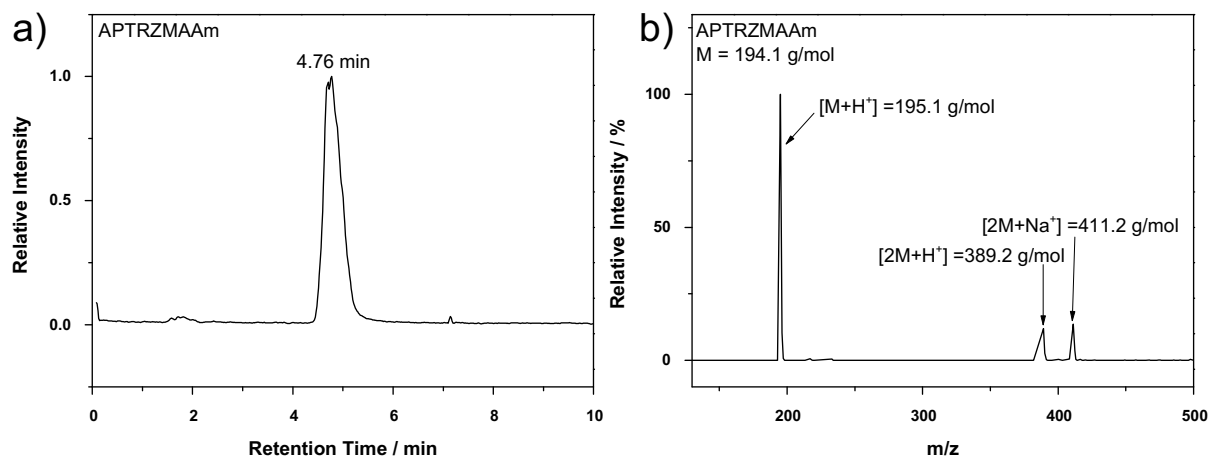


Figure S12: a) HPLC-MS chromatogram and b) its corresponding mass spectrum of the monomer APTRZMAAm.

16.2.3. Unsuccessful Pathways within the Syntheses of Ion Sensitive Coordination Monomers

Pathway 1: Acrylation via Acryloyl Chloride

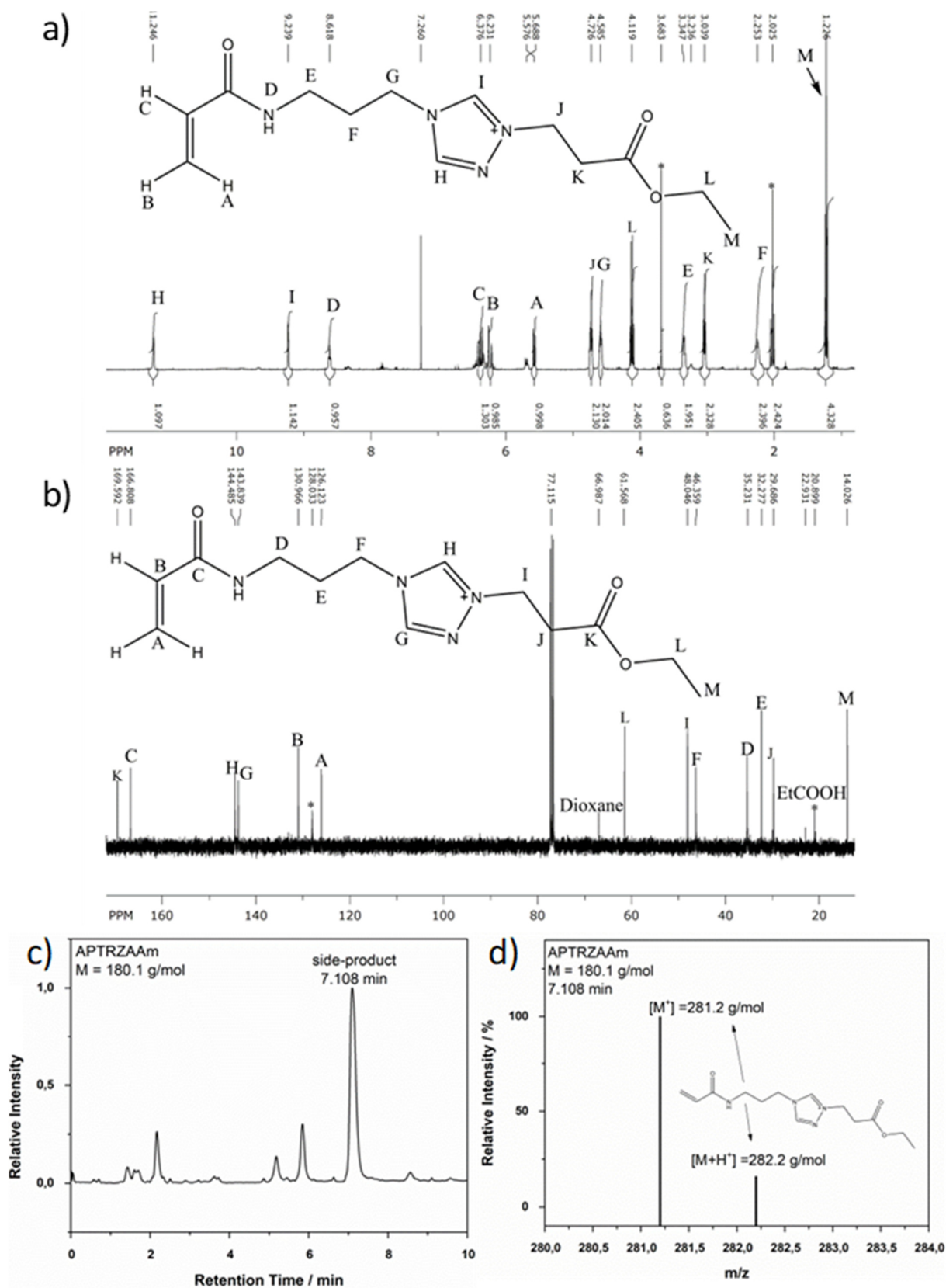


Figure S13: a) ^1H (400 MHz) and b) ^{13}C NMR (101 MHz) spectra of the Michael addition side product within the synthesis in chloroform of the monomer APTRZAAM, recorded in CDCl_3 . Asterisks marks solvent residues (H_2O). c) HPLC-MS chromatogram and d) mass spectrum of the corresponding side product.

The main product (yield: 24-35%) of the synthesis of APTRZAAm performed in chloroform is shown above (Figure S13). A quarterisation process of the nitrogen is suggested. The targeted monomer APTRZAAm underwent a Michael addition reaction *via* the triazolyl group. A propionyl acetate rest added to the five-membered triazole ring.

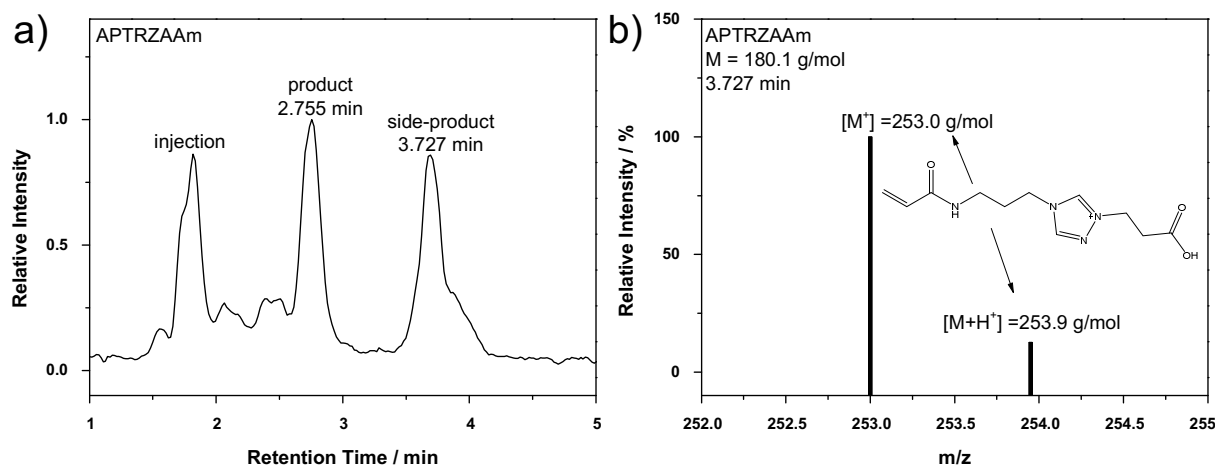


Figure S14: a) HPLC-MS chromatogram and b) mass spectrum of the Michael addition side product within the synthesis in dioxane of the monomer APTRZAAm after short-column chromatography with acidic eluent.

The complete conversion of the educt APTRZ was not reached despite varied excesses of acryloyl chloride. The remaining APTRZ had to be separated.

The complete purification of the product APTRZAAm *via* extraction was not enabled due to the common water-solubility of the educts K_2CO_3 , AA, APTRZ and the product APTRZAAm. Column chromatography was not successful independent of the applied stationary phases (Al_2O_3-N , cellulose Cell300, silica) and neutral eluent mixtures due to the similar retention times and/or coordinative interactions (between compound and stationary phase).

The applications of acidic eluents enabled the removal of APTRZ, but led to a formation of the Michael addition derivate from the addition of APTRZAAm and free acryloyl chloride. The assumption of an added propionyl acetate moiety was confirmed by TLC, HPLC-MS and NMR measurements (shown in Figure S13).

This side product is formed under reaction conditions in dependence of the solvent. Chloroform led to the formation of the pseudo-Michael addition product with a high conversion (visible in Figure S13), while acetonitrile seemed to react further with this side-product. In freshly distilled dioxane the product APTRZAAm is obtained (chemical equivalent triazolyl protons visible in 1H NMR), but could not be purified (suggested side-product shown in Figure S14). During the separation of product and impurities *via* column chromatography (cellulose, EtOH:Hex:AcOH=200:100:1) the pure product underwent the previous described side-reaction. The use of different bases (e.g., DMAP/TEA) complicated the purification dramatically. The synthesis routes above *via* acryloyl chloride provoked the formation of untargeted side products (shown in Figure S13, Figure S14). Therefore, the synthesis *via* DCC coupling was chosen (illustrated in Figure S11 and Figure S12).

Pathway 2: CDI Coupling

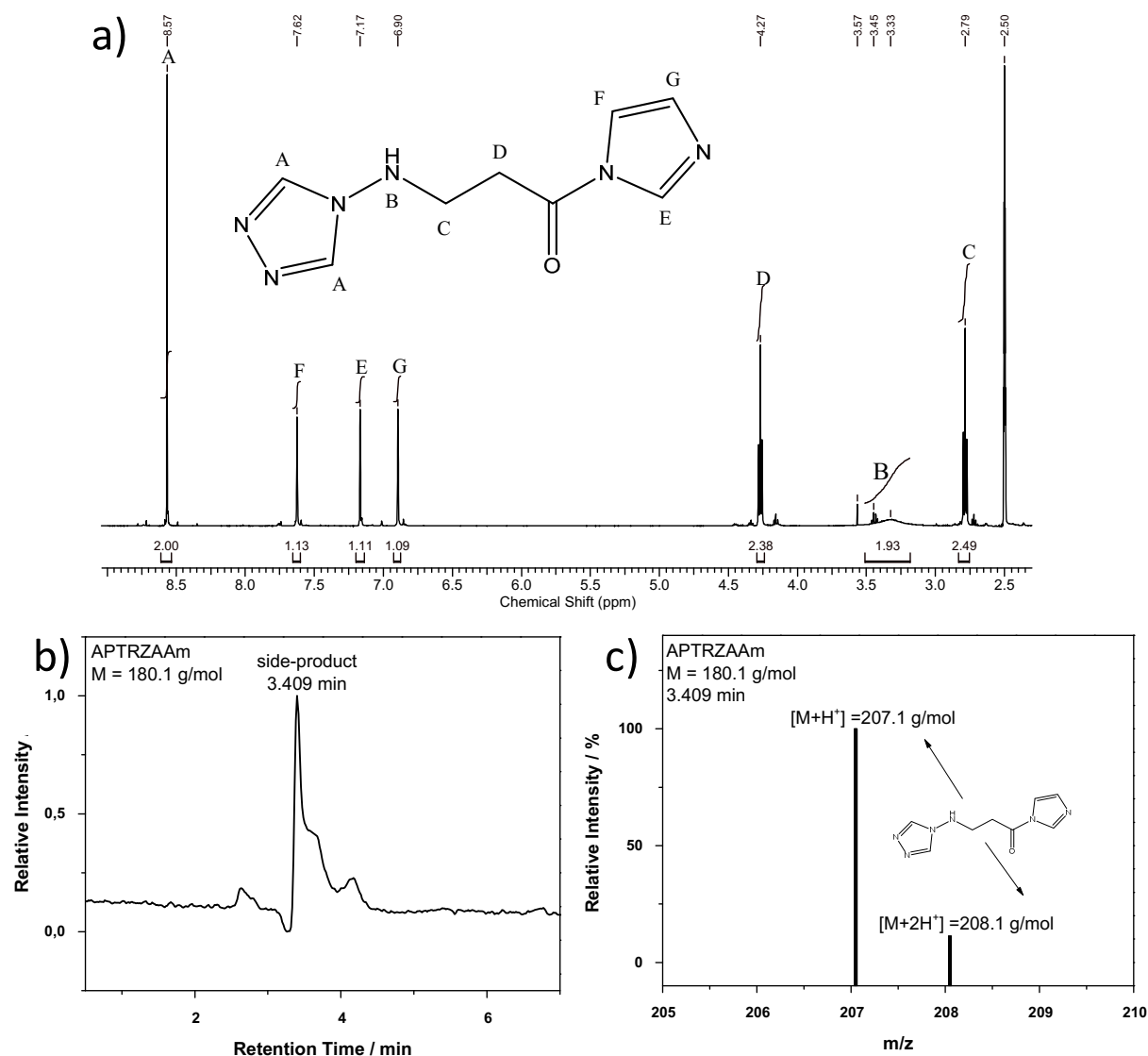
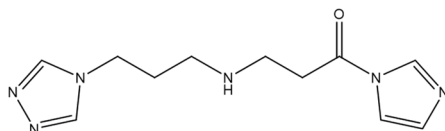


Figure S15: a) ¹H NMR (400 MHz) spectra of the Michael addition product within the synthesis of the comparable monomer NH₂-TRZAAM with NH₂-TRZ as coordinating functionality, recorded in DMSO-d₆. b) HPLC-MS chromatogram and c) mass spectrum of the corresponding side product.

4*H*-1,2,4-triazol-4-amine was applied in the beginning as equivalent of the coordination moiety APTRZ. Secondly, the experiments were performed repeatedly with APTRZ, but they delivered similar results. The syntheses were performed with various mole equivalents of the educts in differing solvents and with different bases.



Scheme S1: Anticipated side product of the failed synthesis of APTRZAAM *via* CDI coupling in accordance with its ¹H NMR with impurities (not shown) and the shown purified analogue *via* NH₂-TRZ coupling.

The CDI forms an activated imidazolid species of AA as intermediate, which is supposed to react with amines under cleavage of an imidazole rest. The found product corresponds to the

Michael addition-like product of this activated intermediate of the CDI coupling reaction (shown Figure S15). After addition of the triazole the side product precipitates and forms a whitish solid, which is insoluble in the most organic solvents. Further post-reactions of the side product in order to an acrylation were not successful. The obtained purified side product belongs to the suggested Michael addition product (Figure S15).

On the basis of this discussed analogue, the synthesis progress (and appearance) and its ^1H NMR with impurities (not shown) the Michael addition side product of APTRZ (Scheme S1) was anticipated.

Pathway 3: EDC Chemistry / Active Ester Coupling

The applied synthesis routes revealed the main difficulties of the synthesis of a triazole functionalized monomer based on APTRZ. The main educts and side products of the chosen routes are water-soluble, so that separation of the product was disabled. The incomplete conversion of the educt APTRZ to product APTRZAAm (similar solubilities) demanded a separation by column chromatography.

A potential acidic eluent (protonation of the amine APTRZ) led to the Michael addition of the product. The product was not purifiable. The application of a methacrylic derivate (instead of AA) avoided this addition. The classic coupling with DCC forms water-insoluble dicyclohexyl urea, which simplifies the work-up. Consequently, the route of APTRZMAAm *via* DCC coupling was chosen.

16.2.4. Amine-functionalized and Boc-protected DNA-binding Monomer *tert*-Butyl-(3-acrylamidopropyl)carbamate (APAAm-Boc)

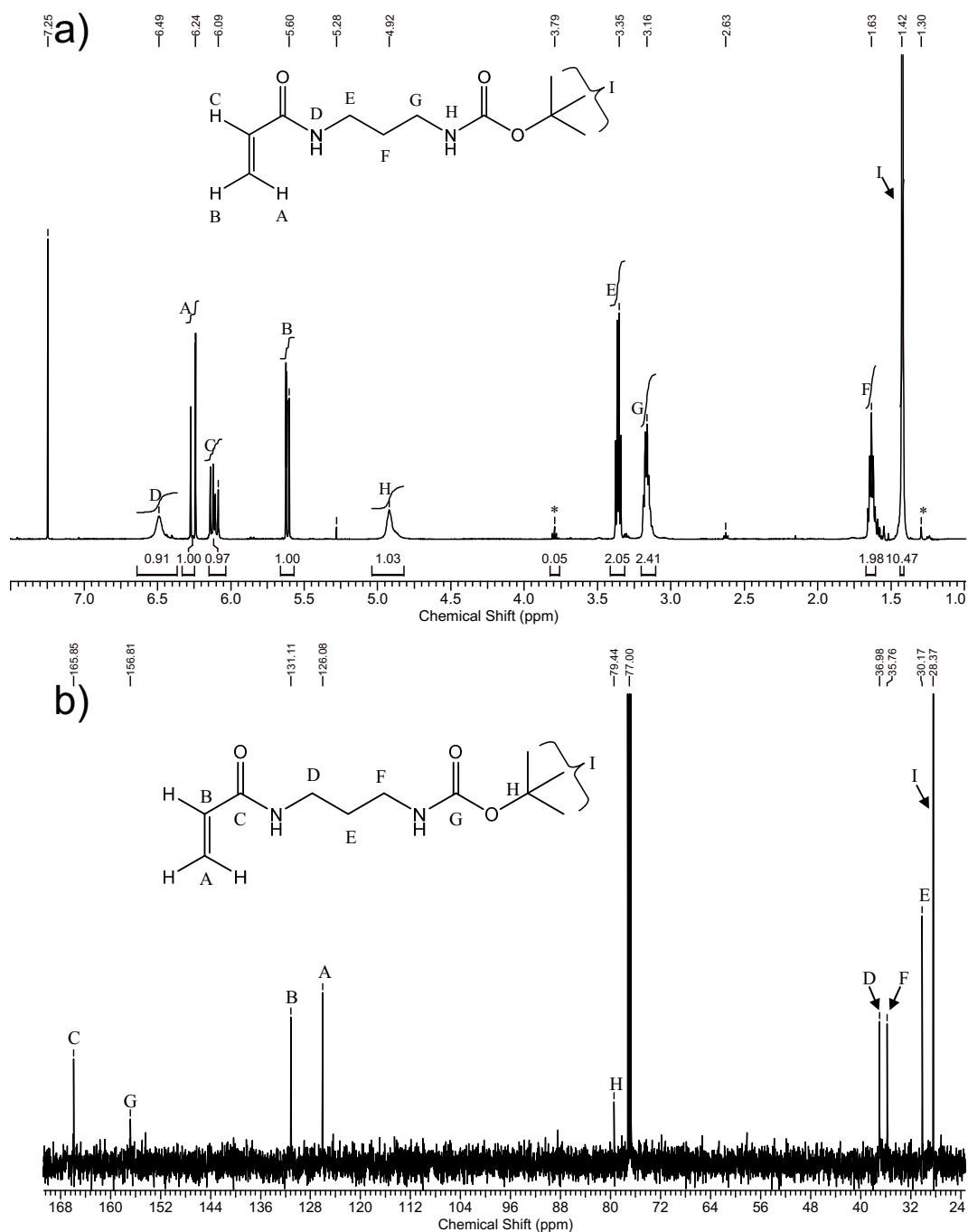


Figure S16: a) ^1H NMR (500 MHz) and b) ^{13}C NMR (125 MHz) spectra of the amine-functionalized and Boc-protected DNA-binding monomer APAAm, recorded in CDCl_3 .

16.3. Adjustable UCST by Copolymerization of AAm and AN

16.3.1. General Procedure for the Free-Radical Copolymerization of Tuneable Poly(AAm_x-co-AN_y) (FRP25%-50%)

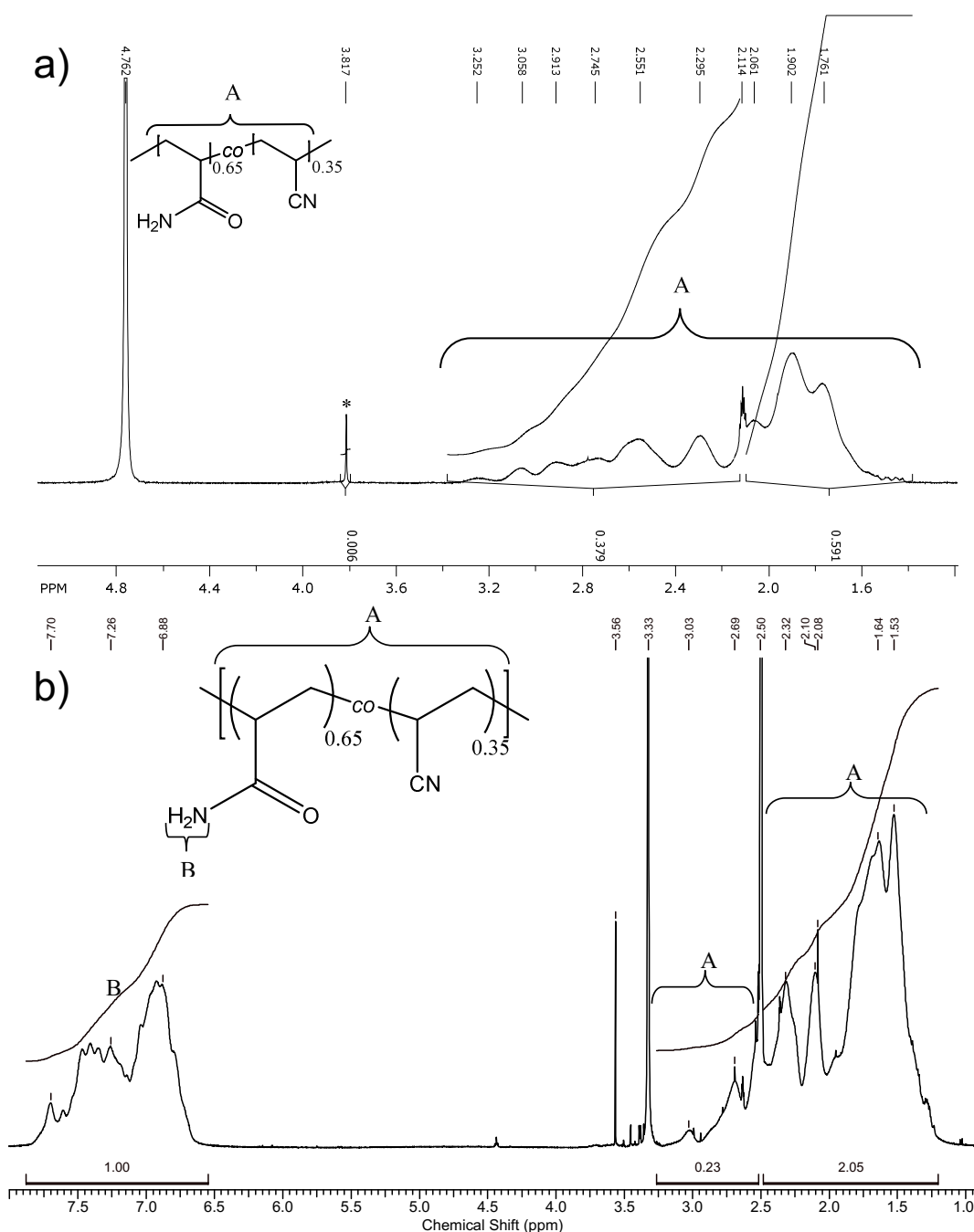


Figure S17: ¹H NMR spectra (500 Hz) of the free-radical polymerized and thermoresponsive tuneable UCST copolymer poly(AAm-co-AN) (FRP35%), recorded in a) D₂O/MeCN-d₃ (85:15) and in b) DMSO-d₆ for the determination of the incorporation ratio of AAm. Asterisks mark solvent residues.

The elugram (shown in the appendix, Figure S18) of the free-radical polymerization product (FRP40%) is illustrated in comparison to the RAFT conjugate (CRP40%) as universal example for the following experimental series. The extracted values of the molar mass distributions from all copolymers are presented in the corresponding tables.

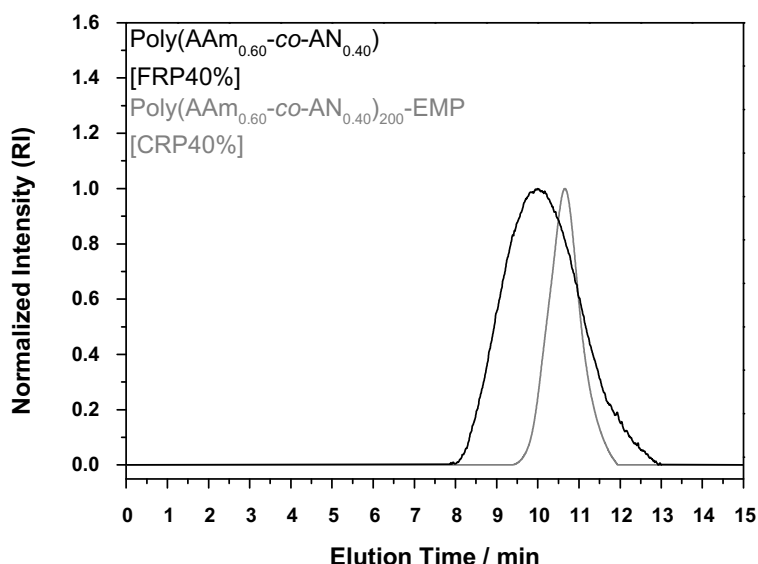


Figure S18: Exemplary elugrams of a) the free radical copolymer poly(AAm-co-AN) (FRP40%) in comparison with b) the RAFT copolymer poly(AAm-co-AN)-EMP (CRP40%) *via* gel-permeation chromatography in water/MeCN (85:15) with NaNO₃.

The macromolecular properties of *via* the general procedure synthesized UCST copolymers with varied AN fraction are summarized in the table below (Table S3).

Table S3: The summarized experimental data of the free-radical polymerized tuneable UCST copolymers poly(AAm-co-AN) with various AN fraction. The sample code of the copolymers, experimental molar masses (\bar{M}_n), dispersities (\bar{D}), incorporation ratio of the hydrophobic component monomer AN and resulting cloud points of heating/cooling cycle are shown.

Sample Code	FRP15%	FRP20%	FRP25%	FRP30%	FRP35%	FRP40%	FRP45%	FRP50%
$\bar{M}_{n,GPC}^{[b]}$ / kg·mol ⁻¹	17.3	24.5	21.5	22.4	24.3	17.1	–[a]	–[a]
$\bar{D}^{[b]}$	3.99	2.90	2.87	2.61	2.61	2.28	–[a]	–[a]
[AN] ^{feed} / mol%	15	20	25	30	35	40	45	50
[AN] ^{incorporated} ^[c] / mol%	–[d]	–[d]	22.2	29.4	35.0	38.5	45.0	–[d]
$T_{c,heat}^{[e]}$ / °C	–[f]	–[f]	<6	15.3	29.3	44.0	61.7	73.8
$T_{c,cool}^{[e]}$ / °C	–[f]	–[f]	<6	12.1	26.8	42.6	61.1	71.1

[a] The molar mass determination *via* GPC was not enabled due to the UCST-driven precipitation of the polymer in the eluent mixture.

[b] Molar mass determined *via* gel-permeation chromatography in H₂O/MeCN (85:15) with NaNO₃.

[c] Incorporation ratio determined *via* ¹H NMR.

[d] Values were not determined.

[e] Cloud point determined *via* turbidity measurement by UV-Vis spectroscopy.

[f] Cloud points lay below 0 °C.

16.3.2. General Procedure for the RAFT Copolymerization of Asymmetric and Tuneable Poly(AAm_x-co-AN_y)-EMP (CRP25.0%-55.0%, CRP3k-26k and CRP0h-24h)

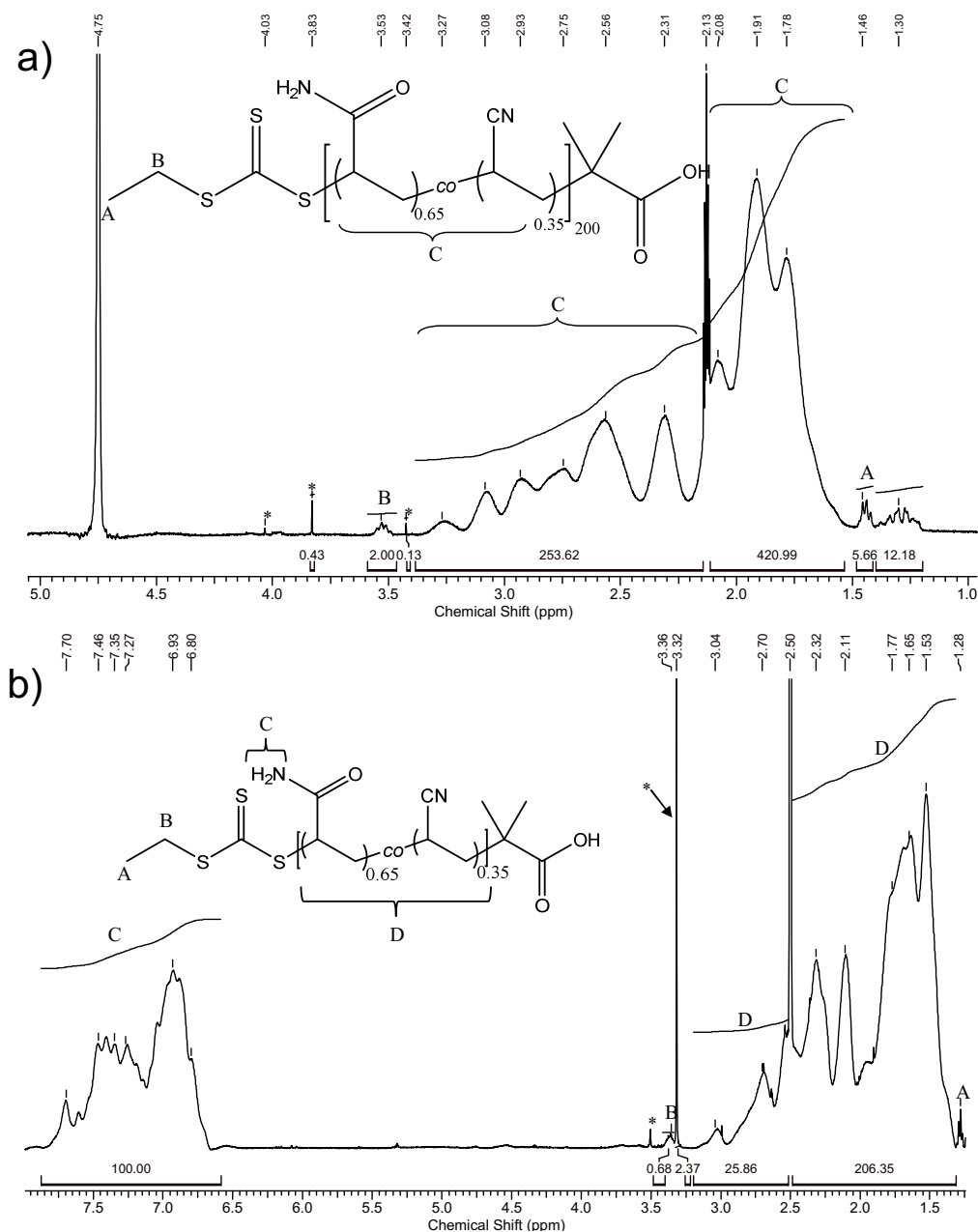


Figure S19: ¹H NMR spectra (400 Hz) of the RAFT polymerized, thermoresponsive and tuneable UCST copolymer poly(AAm-co-AN)-EMP (CRP35%), recorded in a) D₂O/MeCN-d₃ (85:15) and in b) DMSO-d₆ for the determination of the incorporation ratio of AAm. Asterisks mark solvent residues.

The incorporation ratio of the monomer AAm was calculated from the ¹H NMR spectra. The integrals of the amide protons were referred to the integrals of the backbone of the copolymers.

$$[AAm]_{\text{incorporated}}[\text{in}\%] = \frac{\int_{6.6\text{ppm}}^{8.2\text{ppm}} [AAm]}{2\text{protons}} \bigg/ \frac{\int_{1.3\text{ppm}}^{3.2\text{ppm}} [\text{backbone}]}{3\text{protons}} \cdot 100 \quad (13)$$

The RAFT copolymerization of acrylamide and acrylonitrile was investigated within the kinetic study *via* ¹H NMR and GPC measurement (Figure S20, Figure S21 and Table S4).

Kinetic Study of the Copolymerization of AAm and AN

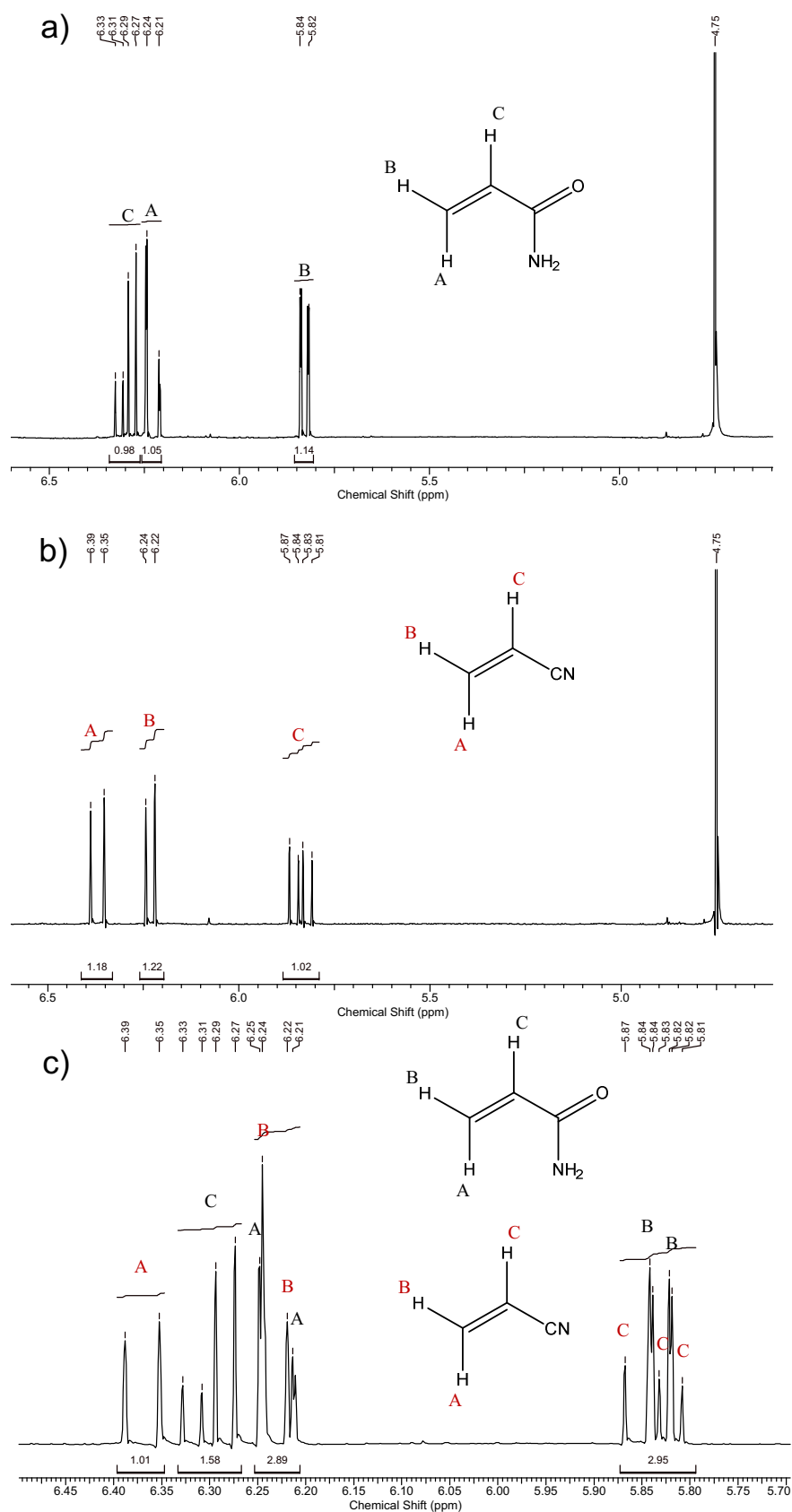


Figure S20: Excerpt of the ^1H NMR spectra (500 Hz) for the investigation of the reaction kinetics of the copolymerization of poly(AAm_{0.60}-co-AN_{0.40})-EMP, recorded in D_2O . The analyte was taken from the reaction mixture of D_2O /dioxane (85:15). The spectra show the monomers a) acrylamide, b) acrylonitrile and c) the resulted reaction mixture for the quantification of the monomer fractions (AN: A, 6.35-6.39 ppm, red and AAm: C, 6.27-6.33 ppm, black).

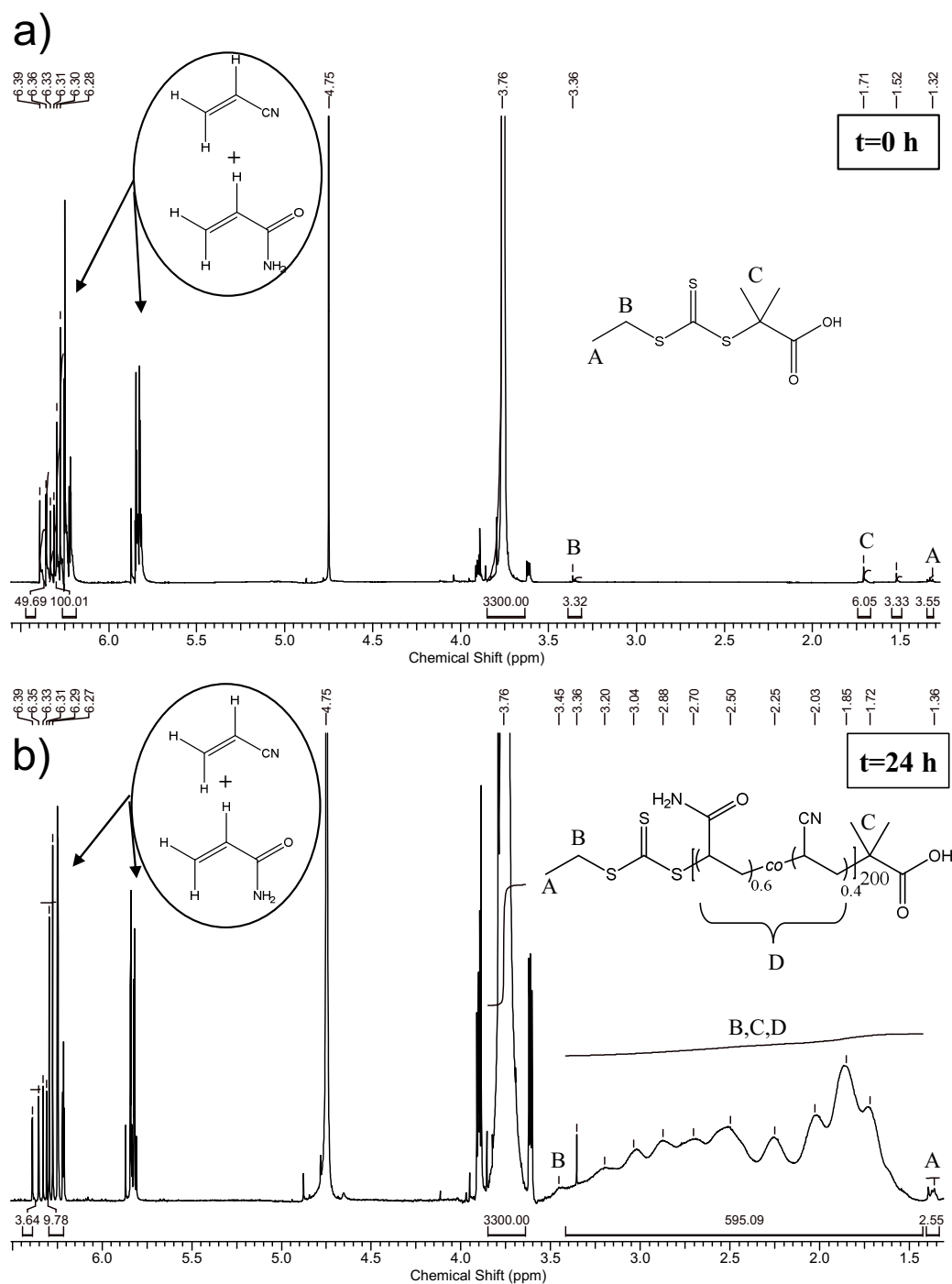


Figure S21: Excerpt of the ¹H NMR spectra (500 Hz) for the investigation of the reaction kinetics of the copolymerization of poly(AAm_{0.60}-co-AN_{0.40})-EMP, recorded in D₂O. The analyte was taken from the reaction mixture of D₂O/dioxane (85:15). The spectra show the progress of the polymerization reaction at a) the start (0 h) and b) at the end (24 h) of reaction used for the subsequent quantification of the monomer fractions, the resulting conversion (p) and the growth of the polymer chain (r.u.) at various reaction times.

The kinetic study was performed *via* time dependent ¹H NMR observation of the polymerization reaction in D₂O/dioxane (60:40). The non-deuterated dioxane represents the internal standard (fixed concentration in reaction mixture), which was used for the normalization of the integrals for the quantification of the monomer concentration in the reaction mixture. The conversion was visualized by the shrinking (baseline separated) integrals of AAm (indicated as black “C” in Figure S20, 6.35 ppm) and AN (indicated as red

“A” in Figure S20, 6.39 ppm) and were calculated by the degree of polymerization X_n based on both the molar mass of the measurement *via* gel-permeation chromatography and ^1H NMR spectroscopy. The growth of the copolymeric chain is indicated above (Figure S21) and can be determined by the relation between backbone protons and the z-group of the chain transfer agent EMP (1.36 ppm). The dispersities and molar mass distributions of the precipitated products were determined *via* gel-permeation chromatography in water/MeCN (85:15) with NaNO_3 . The incorporation ratio of the monomer acrylamide was quantified by the ^1H NMR measurement of the purified products, recorded in DMSO-d_6 .

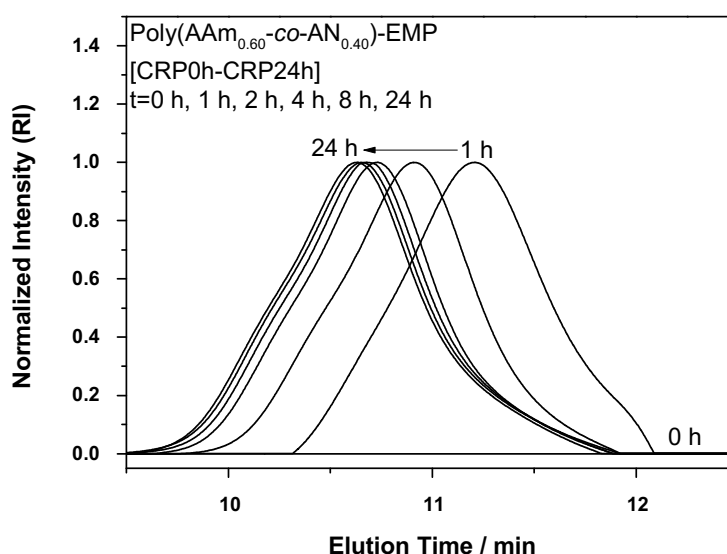


Figure S22: Elugrams of the obtained products after 1 h, 2 h, 4 h, 6 h, 8 h and 24 h (CRP0h-CRP24h) from the RAFT copolymerization of AAm and AN *via* gel-permeation chromatography in water/MeCN (85:15) with NaNO_3 .

The macromolecular properties from the kinetic investigation of the UCST copolymers with varied chain lengths are summarized below (Table S4).

Table S4: The summarized experimental data of the kinetic investigation of the RAFT polymerized tuneable UCST copolymers poly(AAm_{0.60}-co-AN_{0.40})-EMP. The sample code of the copolymers, experimental molar masses (\bar{M}_n), corresponding degree of polymerization (X_n), dispersities (\bar{D}), incorporation ratio of the hydrophobic component monomer AN and the conversions (p) are shown.

Sample Code	CRP0h	CRP1h	CRP2h	CRP4h	CRP6h	CRP8h	CRP24
$\bar{M}_{n,NMR}$ / $\text{kg}\cdot\text{mol}^{-1}$	0.2	5.0	9.1	11.3	12.1	12.6	12.8
$X_{n,NMR}$ / a.u.	0	71	140	174	186	194	197
$\bar{M}_{n,GPC}^{[a]}$ / $\text{kg}\cdot\text{mol}^{-1}$	0.2	5.5	9.0	11.1	12.0	12.4	13.1
$X_{n,GPC}$ / a.u.	0	78	139	171	185	191	202
$\bar{D}^{[a]}$	1.40	1.35	1.38	1.39	1.36	1.38	1.37
$[\text{AN}]^{\text{feed}}$ / mol%	40.0	40.0	40.0	40.0	40.0	40.0	40.0
$[\text{AN}]^{\text{incorporated}^{[b]}}$ / mol%	0	47.7	46.4	44.9	40.9	40.9	39.5
P / %	0	35	70	87	93	97	98

^[a] Molar mass determined *via* gel-permeation chromatography in $\text{H}_2\text{O}/\text{MeCN}$ (85:15) with NaNO_3 .

^[b] Incorporation ratio determined *via* ^1H NMR.

Variation of the Acrylonitrile Fraction

The shift of the cloud point in aqueous solution of the linear copolymer with respect to the molar acrylonitrile fraction is shown below (Figure S23). The cloud points of the copolymers correlate linearly with increasing fraction of AN in the chain.

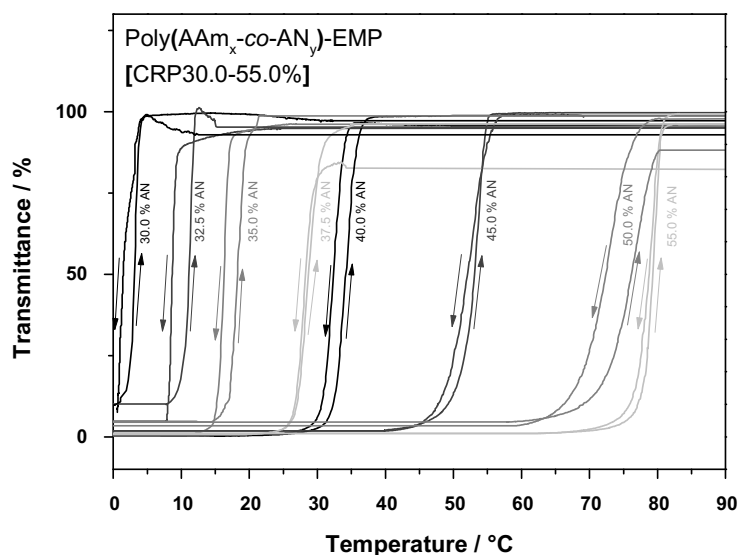


Figure S23: Cloud point determination of the tuneable thermoresponsive UCST copolymer poly(AAm-co-AN)-EMP with various AN fraction (CRP30-55%), recorded from 1.0 wt% aqueous solution (at $\nu=650$ nm).

The macromolecular properties of *via* the general procedure synthesized UCST copolymers with varied AN fraction are summarized in the table below (Table S5).

Table S5: The summarized experimental data of the RAFT polymerized tuneable UCST copolymers poly(AAm-co-AN)-EMP with various AN fraction. The sample code of the copolymers, experimental molar masses (\bar{M}_n), dispersities (\bar{D}), incorporation ratio of the hydrophobic component monomer AN and resulting cloud points of heating/cooling cycle are shown.

Sample Code	CRP30.0%	CRP32.5%	CRP35.0%	CRP37.5%	CRP40%	CRP45%	CRP50%	CRP55%
$\bar{M}_{n,theo.}$ / $\text{kg}\cdot\text{mol}^{-1}$	13.3	13.3	13.2	13.1	13.0	12.8	12.6	12.4
$\bar{M}_{n,NMR}$ / $\text{kg}\cdot\text{mol}^{-1}$	13.4	13.4	14.0	13.6	12.9	14.1	12.3	11.0
$\bar{M}_{n,GPC}^{[b]}$ / $\text{kg}\cdot\text{mol}^{-1}$	12.8	14.2	14.0	14.2	13.0	11.1 ^[a]	6.4 ^[a]	5.0 ^[a]
$\bar{D}^{[b]}$	1.39	1.39	1.40	1.34	1.39	1.42	1.43	1.34
$[\text{AN}]_{\text{feed}}$ / mol%	30.0	32.5	35.0	37.5	40.0	45.0	50.0	55.0
$[\text{AN}]_{\text{incorporated}}^{[c]}$ / mol%	29.8	31.0	35.1	37.3	40.9	45.5	- ^[d]	- ^[d]
$T_{c,heat}^{[e]}$ / °C	3.2	11.2	18.3	28.6	34.1	53.0	76.4	79.2
$T_{c,cool}^{[e]}$ / °C	1.6	8.7	16.3	28.0	32.3	52.1	72.5	78.8

^[a] The molar mass determination *via* GPC shows major deviations due to the high cloud point (coiling state).

^[b] Molar mass determined *via* gel-permeation chromatography in $\text{H}_2\text{O}/\text{MeCN}$ (85:15) with NaNO_3 .

^[c] Incorporation ratio determined *via* ^1H NMR.

^[d] Values were not determined.

^[e] Cloud point determined *via* turbidity measurement by UV-Vis spectroscopy.

Variation of the Chain Length

The macromolecular properties of *via* the general procedure synthesized UCST copolymers with varying chain lengths and the turbidity curves with respect to variation of the copolymer concentration in aqueous solution is illustrated and summarized below (Figure S24 and Table S6).

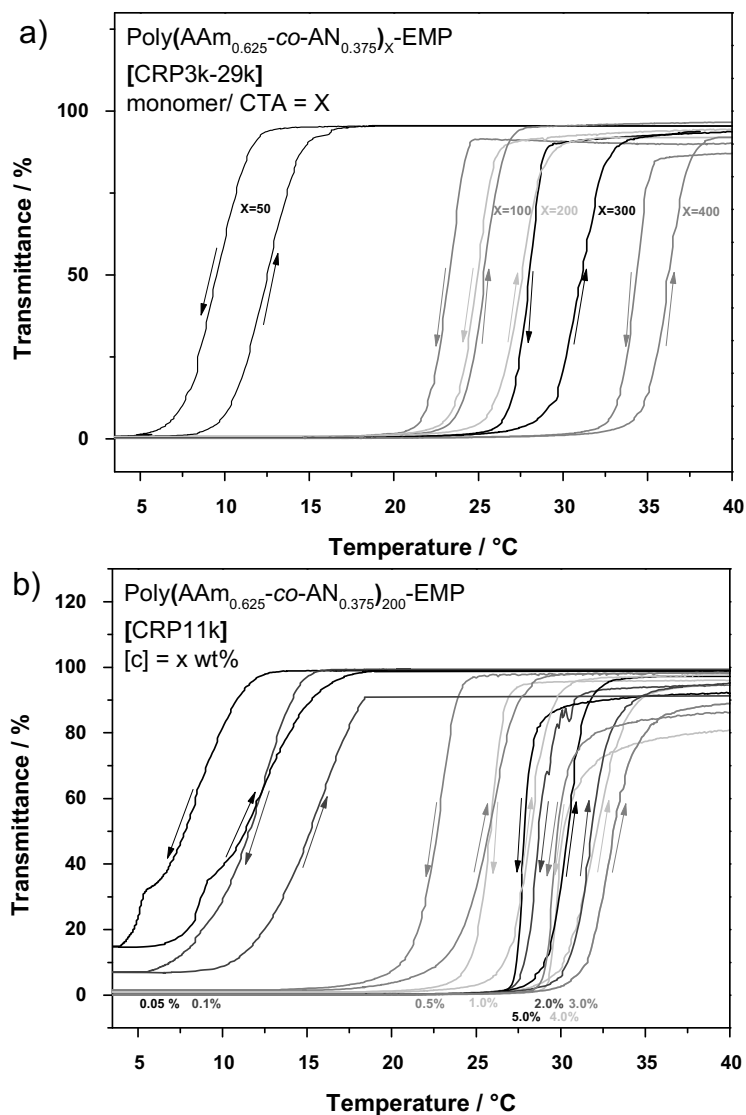


Figure S24: a) Cloud point determination of the tuneable thermoresponsive UCST copolymers poly(AAm_{0.625}-co-AN_{0.375})-EMP with various repeat unit numbers (CRP3k-29k), recorded from 1.0 wt% aqueous solution (at $\nu=650$ nm). b) The cloud points of CRP11k measured at various copolymer concentrations (0.05-5.00 wt%) for a phase diagram illustration in aqueous solution (at $\nu=650$ nm).

The uniform molecular mass distributions are shown below in the elugrams of the synthesized UCST copolymers with varied chain lengths (Figure S25).

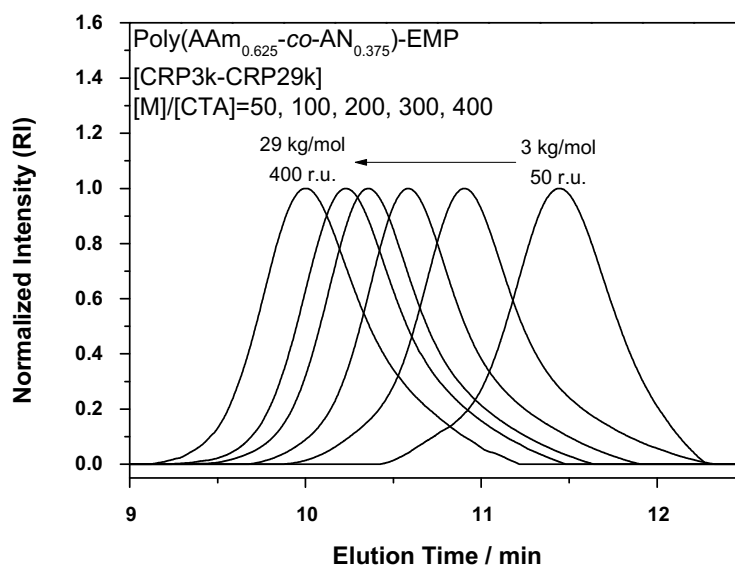


Figure S25: Elugrams of the copolymers with varied chain lengths (CRP3k-CRP29k) from the RAFT copolymerization of AAm and AN *via* gel-permeation chromatography in water/MeCN (85:15) with NaNO₃.

The macromolecular properties of *via* the general procedure synthesized UCST copolymers with varied chain lengths are summarized in the table below (Table S6).

Table S6: The summarized experimental data of the RAFT polymerized tuneable UCST copolymers poly(AAm_{0.625}-co-AN_{0.375})-EMP with various chain lengths. The sample code of copolymers, experimental molar masses (\bar{M}_n), dispersities (\bar{D}) and resulting cloud points of heating/cooling cycle are shown.

Sample Code	CRP3k	CRP6k	CRP11k	CRP16k	CRP21k	CRP29k
$\bar{M}_{n,theo.}$ / kg·mol ⁻¹	3.4	6.7	13.1	19.5	26.0	32.4
$\bar{M}_{n,NMR}^{[a]}$ / kg·mol ⁻¹	3.6	7.5	12.8	18.1	22.8	29.5
$\bar{M}_{n,GPC}^{[b]}$ / kg·mol ⁻¹	2.7	6.1	11.2	16.1	21.0	28.7
$\bar{D}^{[b]}$	1.34	1.42	1.28	1.28	1.20	1.21
$T_{c,heat}^{[c]}$ / °C	12.4	25.3	27.5	31.0	36.1	27.5
$T_{c,cool}^{[c]}$ / °C	9.5	23.2	24.9	27.9	34.2	24.8

^[a] Molar mass determined *via* ¹H NMR.

^[b] Molar mass determined *via* gel-permeation chromatography in H₂O/MeCN (85:15) with NaNO₃.

^[c] Cloud point determined *via* turbidity measurement by UV-Vis spectroscopy.

16.3.3. General Procedure for the Free-Radical Copolymerization of Tuneable and Photo-Crosslinkable Poly(AAm_x-co-AN_y-co-BPAAm_z) (FRP-BP0.5-5.0%)

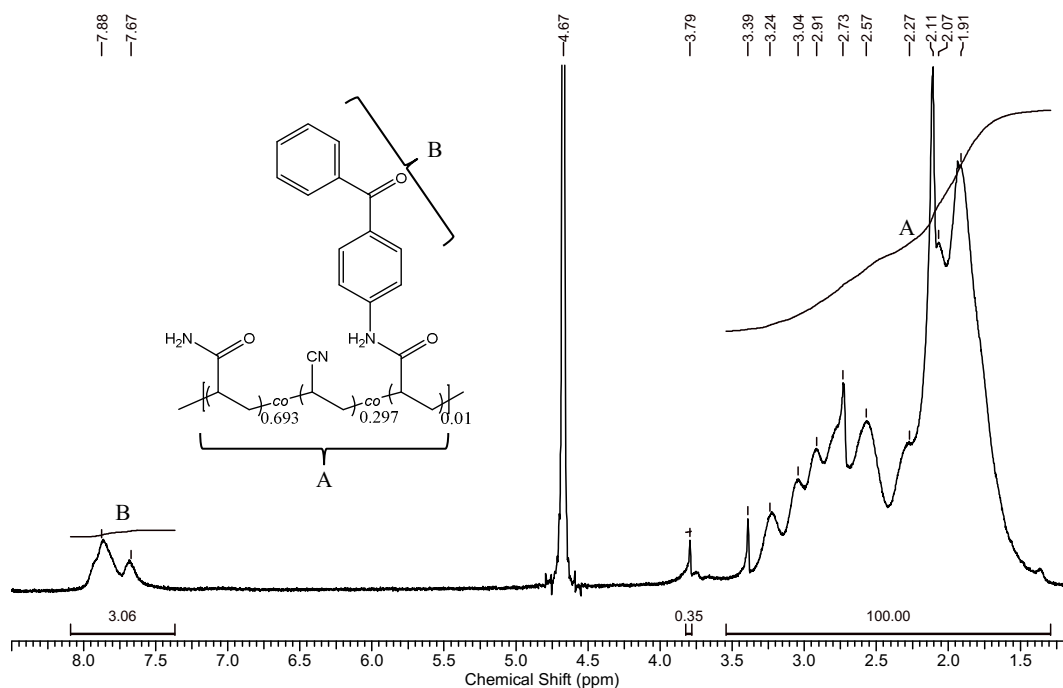


Figure S26: ^1H NMR spectrum (400 Hz) of the thermoresponsive, photo-crosslinkable and tuneable UCST copolymer poly(AAm-co-AN-co-BPAAm) (FRP-BP1%), recorded in D_2O .

The incorporation ratio of the photo-crosslinkable monomer BPAAm was calculated by the means of the ^1H NMR spectra.

$$[\text{BPAAm}]_{\text{incorporated}} [\text{in}\%] = \frac{\int_{7.4\text{ppm}}^{8.2\text{ppm}} [\text{BPAAm}]}{\frac{9\text{protons}}{\int_{1.3\text{ppm}}^{3.2\text{ppm}} [\text{backbone}]}} \cdot 100 \quad (14)$$

The integrals of the aromatic protons (benzophenone side group) were referred to the integrals of the backbone of the copolymers to determine the molar fraction of BPAAm.

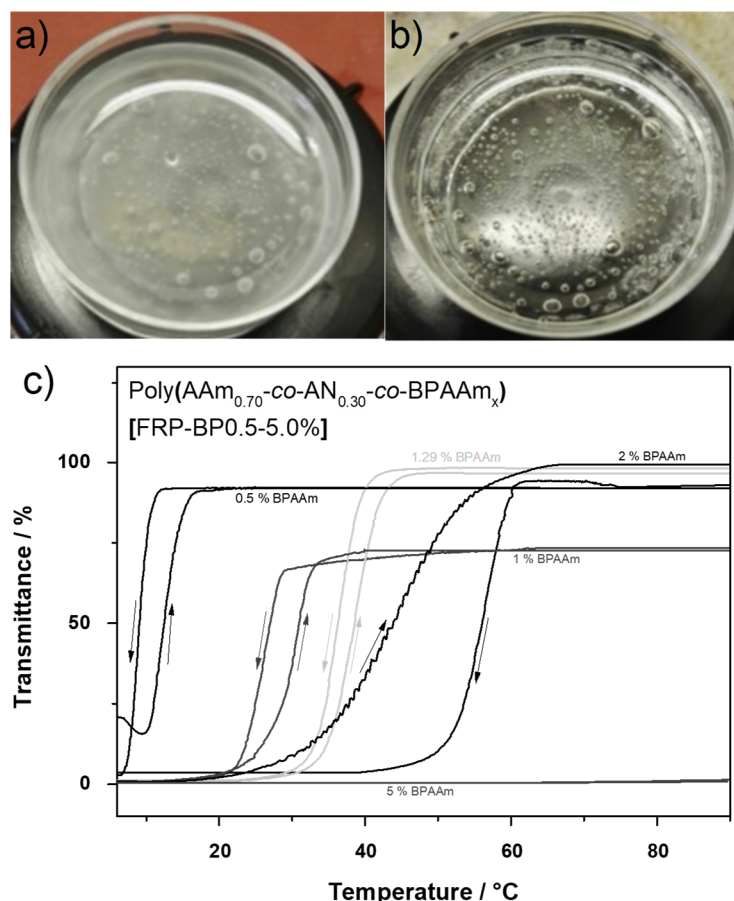


Figure S27: The visual appearance of a hydrated and photo-crosslinked hydrogel network from a thermoresponsive polymer with UCST behaviour a) below and b) above the cloud point. c) The cloud point determination of the copolymers poly(AAm-co-AN-co-BPAAm) (FRP-BP0.5%-5.0%) with various fractions of BPAAm, recorded from 1.0 wt% aqueous solution (at $\nu=650$ nm).

The macromolecular properties of *via* the general procedure synthesized photo-crosslinkable UCST copolymers with varied chain lengths are summarized in the table below (Table S7).

Table S7: The summarized experimental data of the free-radical polymerized and photo-crosslinkable UCST copolymers poly(AAm-co-AN-co-BPAAm) with various BPAAm fractions. The sample code of the copolymers, experimental molar masses (\bar{M}_n), dispersities (\bar{D}), glass transition temperatures (T_g), incorporation ratio of the photo-crosslinkable monomer BPAAm and resulting cloud points of heating/cooling cycle are shown.

Sample Code	FRP-BP0.5%	FRP-BP1.0%	FRP-BP1.3%	FRP-BP2.0%	FRP-BP5.0%
$\bar{M}_n, GPC^{[a]}$ / kg·mol ⁻¹	17.6	17.7	16.7	15.1	15.6
$\bar{D}^{[a]}$	2.60	3.12	2.84	3.15	2.70
[BPAAm] _{feed} / mol%	0.50	1.00	1.29	2.00	5.00
[BPAAm] _{incorporated} ^[b] / mol% ^[b]	0.49	0.99	1.28	1.95	4.70
Film Stability ^[d]	0	+	++	++	++
$T_{c,heat}^{[c]}$ / °C	12.7	29.7	38.4	43.9	> 90 ^[e]
$T_{c,cool}^{[c]}$ / °C	9.0	25.8	36.3	55.9	> 90 ^[e]

^[a] Molar mass determined *via* gel-permeation chromatography in H₂O/MeCN (85:15) with NaNO₃.

^[b] Incorporation ratio determined *via* ¹H NMR.

^[c] Cloud point determined *via* turbidity measurement by UV-Vis spectroscopy.

^[d] Film stability was tested qualitatively by optical impression (e.g., film formation, solubility, swelling and turbidity point) and summarized by hypothetical values (0-++).

^[e] The precise cloud point was not determinable technically due to high temperatures.

16.3.4. General Procedure for the RAFT Copolymerization of Asymmetric, Tuneable and Photo-Crosslinkable Poly(AAm_x-co-AN_y-co-BPAAm_z)-EMP (CRP-BP0.5%-2.5%)

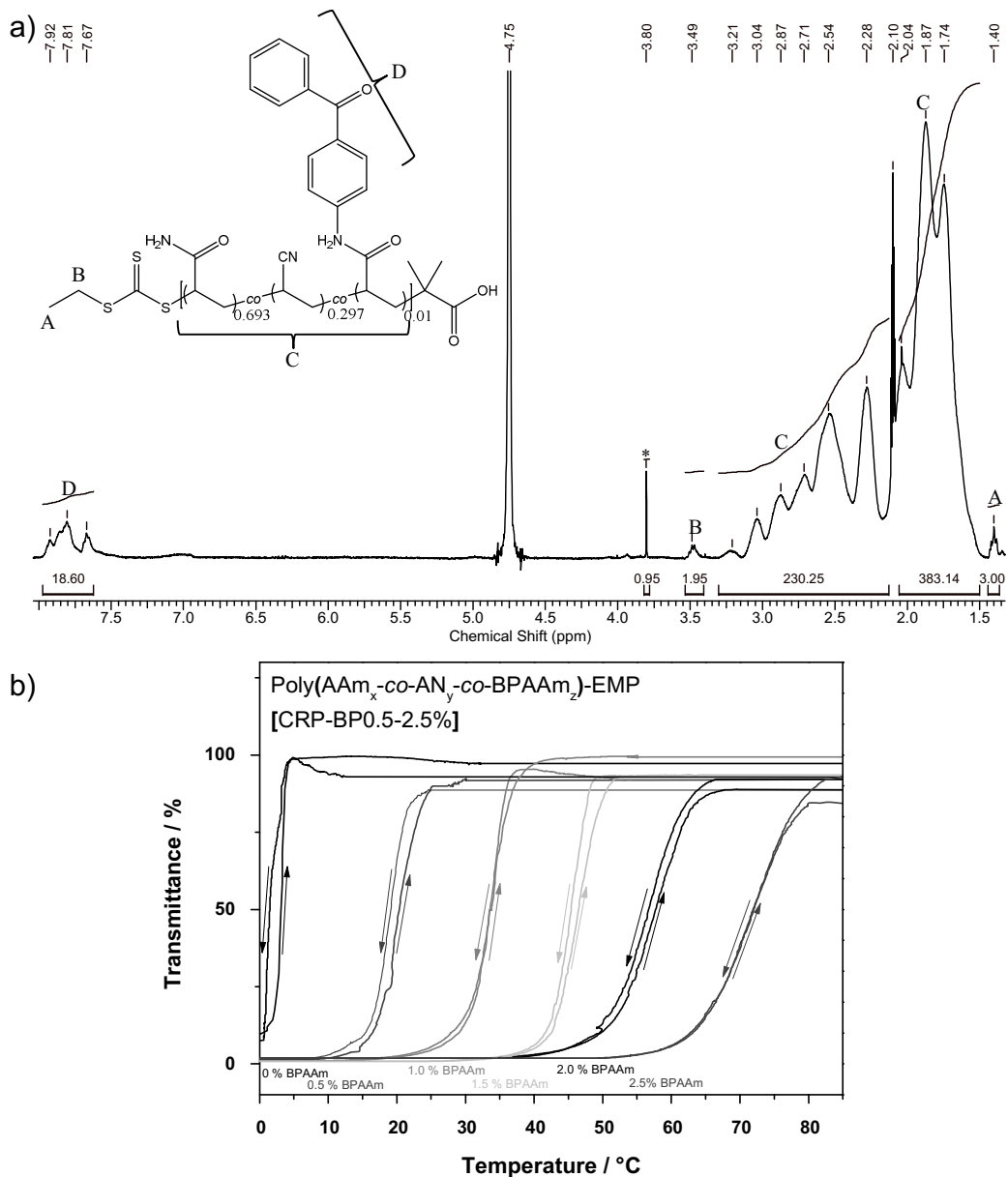


Figure S28: a) ¹H NMR spectrum (400 Hz) of the RAFT polymerized, photo-crosslinkable and tuneable UCST copolymer poly(AAm-co-AN-co-BPAAm)-EMP (CRP-BP0.5%-2.5%), recorded in D₂O/MeCN-d₃ (85:15). Asterisks mark solvent residues. b) The cloud point determination of the copolymers poly(AAm-co-AN-co-BPAAm)-EMP (CRP-BP0.5%-2.5%) with various BPAAm fractions, recorded from 1.0 wt% aqueous solution (at $\nu=650$ nm).

The macromolecular properties of the *via* general procedure synthesized photo-crosslinkable UCST copolymers with varied BPAAm fraction are summarized below (Table S8).

Table S8: The summarized experimental data of the RAFT polymerized and photo-crosslinkable UCST copolymers poly(AAm-co-AN-co-BPAAm)-EMP with various BPAAm fractions. The sample code of copolymers, experimental molar masses (\bar{M}_n), dispersities (\bar{D}), incorporation ratio of the photo-crosslinkable monomer BPAAm and resulting cloud points of heating/cooling cycle are shown.

Sample Code	CRP-BP0.5%	CRP-BP1.0%	CRP-BP1.5%	CRP-BP2.0%	CRP-BP2.5%
$\bar{M}_{n,theo.}$ / kg·mol ⁻¹	13.5	13.7	13.9	14.1	14.3
$\bar{M}_{n,NMR}$ / kg·mol ⁻¹	12.8	13.7	13.4	8.9 ^[a]	8.8 ^[a]
$\bar{M}_{n,GPC}^{[b]}$ / kg·mol ⁻¹	12.6	10.8	11.1	9.1 ^[a]	8.8 ^[a]
$\bar{D}^{[b]}$	1.41	1.36	1.34	1.34	1.27
[BPAAm] _{feed} / mol%	0.50	1.00	1.50	2.00	2.50
[BPAAm] _{incorporated} ^[c] / mol%	0.49	0.99	1.49	1.84	2.02
Film Stability ^[d]	0	0	+	++	++
$T_{c,heat}^{[e]}$ / °C	20.1	33.7	46.3	57.1	71.7
$T_{c,cool}^{[e]}$ / °C	18.8	33.5	45.5	56.4	71.0

^[a] The molar mass determination *via* GPC (coiling state) and ¹H NMR (broad signals) was not enabled due to the high cloud point.

^[b] Molar mass determined *via* gel-permeation chromatography in H₂O/MeCN (85:15) with NaNO₃.

^[c] Incorporation ratio determined *via* ¹H NMR.

^[d] Film stability was tested qualitatively by optical impression (e.g., film formation, solubility, swelling and turbidity point) and summarized by hypothetical values (0-++).

^[e] Cloud point determined *via* turbidity measurement by UV-Vis spectroscopy.

16.4. Photo-Crosslinkable NIPAAm-Based LCST Copolymers

The copolymers were designed to offer tuneable, but robust thermoresponsive properties in combination with an accessible hydrogel formation *via* photo-crosslinking. The photo-crosslinking was succeeded *via* the BPAAm unit. The shifting of the cloud point was performed *via* copolymerization with polar side groups (e.g., AA, MAA, HEAAm) and functionalization's (e.g., DMP, EMP, BIT and DMP-EA).

The elugram (shown in the appendix, Figure S29) of the free-radical polymerization product (FRP-MAA) is illustrated in comparison to the RAFT conjugate (CRP-MAA) as universal example for the following experimental series. The extracted values of the molar mass distributions from all copolymers are presented in the corresponding tables.

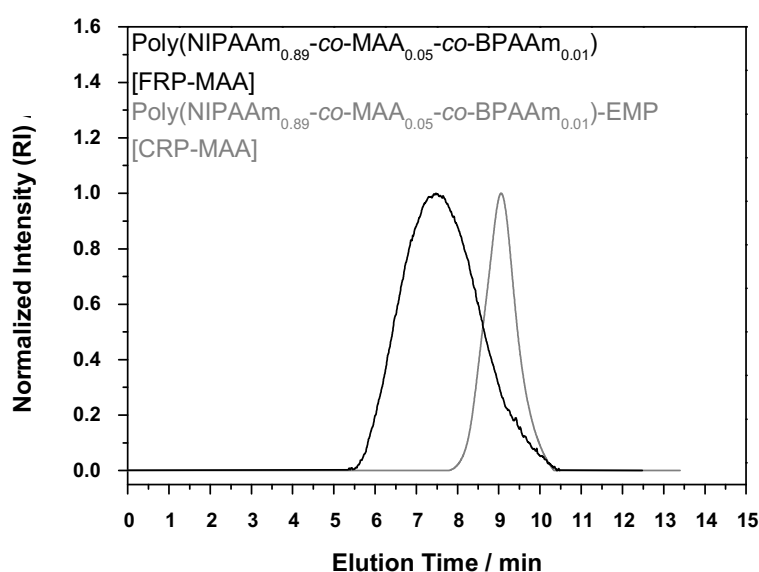


Figure S29: Exemplary elugrams of a) the free radical copolymer FRP-MAA in comparison with b) the RAFT copolymer CRP-MAA *via* gel-permeation chromatography in DMAc with LiBr.

The experimental data of the syntheses are shown below (Table S9).

Table S9: The summarized experimental data of the synthesized LCST copolymer systems. The sample code of the copolymers, theoretical and experimental (via ^1H NMR and GPC) molar masses (\bar{M}_n), dispersities (\mathcal{D}), incorporation ratio of the photo-crosslinkable monomer unit BPAAm and resulting cloud points of the heating/cooling cycle are shown.

Sample Code	R1	FRP-MAA	CRP-MAA-BIT	CRP-AA	CRP-MAA	CRP-AA-DMP-EA	CRP-HEAAm	CRP-HEAAm 10%16k	CRP-HEAAm 10%26k
$\bar{M}_{n,theo}$ / $\text{kg}\cdot\text{mol}^{-1}$	23.8	– ^[a]	11.6	11.5	11.7	11.6	11.8	11.6	23.3
$\bar{M}_{n,NMR}$ ^[b] / $\text{kg}\cdot\text{mol}^{-1}$	25.1	– ^[a]	– ^[a]	12.8	12.3	11.0	12.9	11.8	22.8
$\bar{M}_{n,GPC}$ ^[c] / $\text{kg}\cdot\text{mol}^{-1}$	29.9	138.2	11.4	10.3	14.9	16.4	15.7	16.2	26.1
\mathcal{D} ^[c]	1.14	2.33	1.26	1.10	1.25	1.17	1.23	1.19	1.29
$[\text{BPAAm}]_{\text{feed}}$ / mol%	0	1.00	1.00	1.00	1.00	1.00	1.00	1.00	1.00
$[\text{BPAAm}]_{\text{incorporated}}$ ^[d] / mol%	0	0.96	1.02	0.90	1.19	1.08	0.97	1.04	0.96
$T_{c,heat}$ ^[e] / $^{\circ}\text{C}$	33.0	33.6	25.3	29.1	28.5	27.0	27.7	28.8	30.6
$T_{c,cool}$ ^[e] / $^{\circ}\text{C}$	28.5	27.3	21.6	26.2	24.9	24.1	24.9	23.7	28.7

^[a] The molar mass determination *via* ^1H NMR and its theoretical prediction was not enabled due to FRP or not baseline separated integral of the end group.

^[b] Molar mass determined *via* ^1H NMR normalization of the end group from the chain transfer agent.

^[c] Molar mass determined *via* gel-permeation chromatography in DMAc with LiBr.

^[d] Incorporation ratio determined *via* ^1H NMR.

^[e] Cloud point determined *via* turbidity measurement by UV-Vis spectroscopy.

16.4.1. RAFT Polymerization of the Reference Homopolymer Poly(NIPAAm)-EMP (R1)

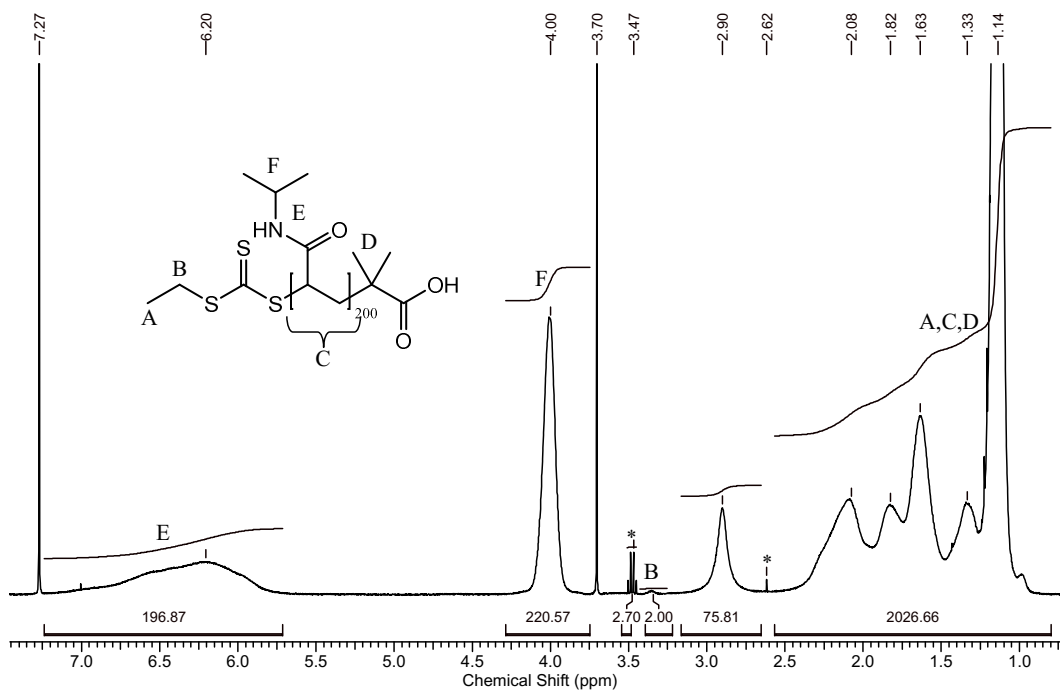


Figure S30: ¹H NMR spectrum (400 Hz) of the reference homopolymer PNIPAAm-EMP (R1), recorded in CDCl₃. Asterisks mark solvent residues.

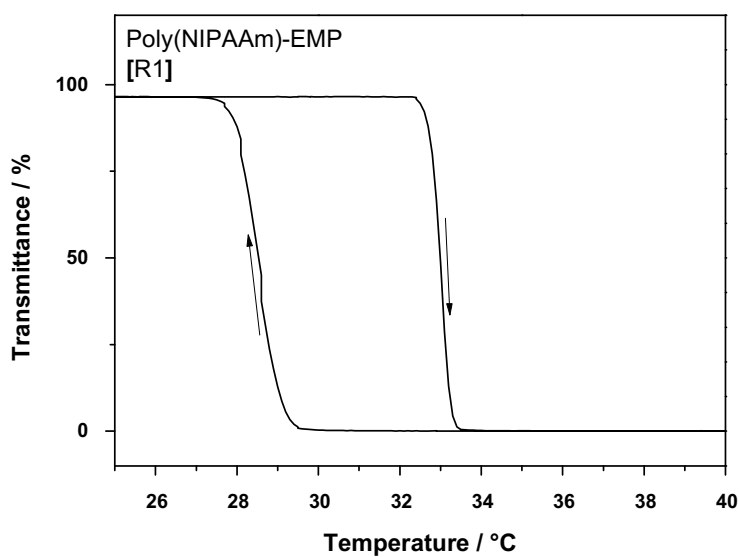


Figure S31: Cloud point determination of the reference homopolymer PNIPAAm-EMP (R1), recorded from 1.0 wt% aqueous solution (at $\lambda=650$ nm).

16.4.2. Free Radical Copolymerization of the Photo-Crosslinkable Poly(NIPAAm-co-MAA-co-BPAAm) (94:5:1) (FRP-MAA)

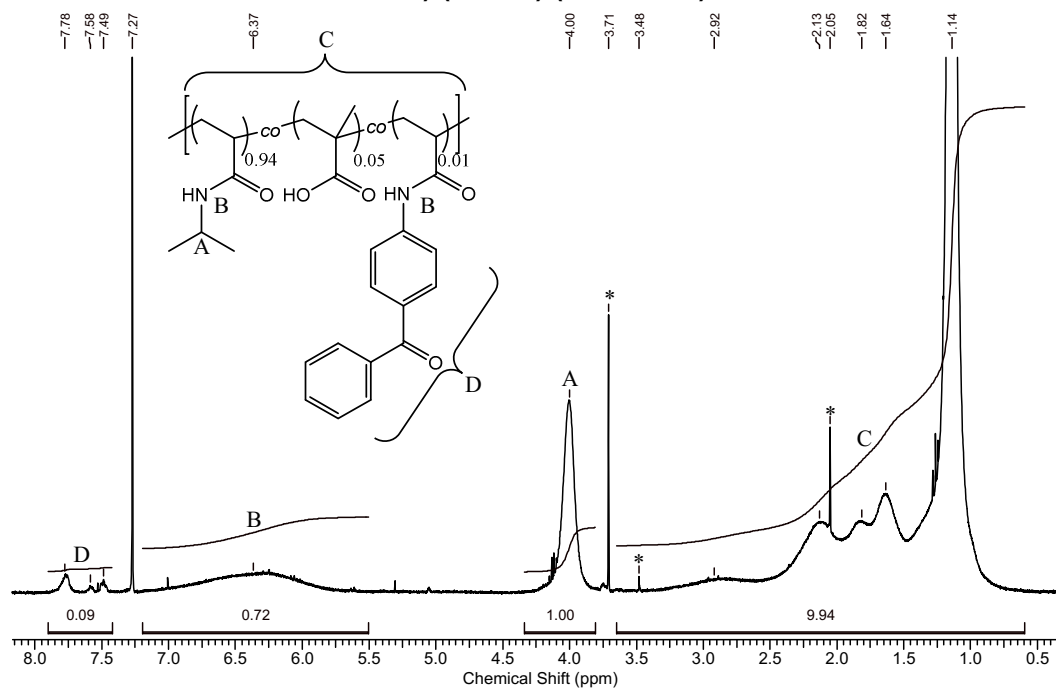


Figure S32: ^1H NMR spectrum (400 Hz) of the photo-crosslinkable PNIPAAm (FRP-MAA), recorded in CDCl_3 . Asterisks mark solvent residues.

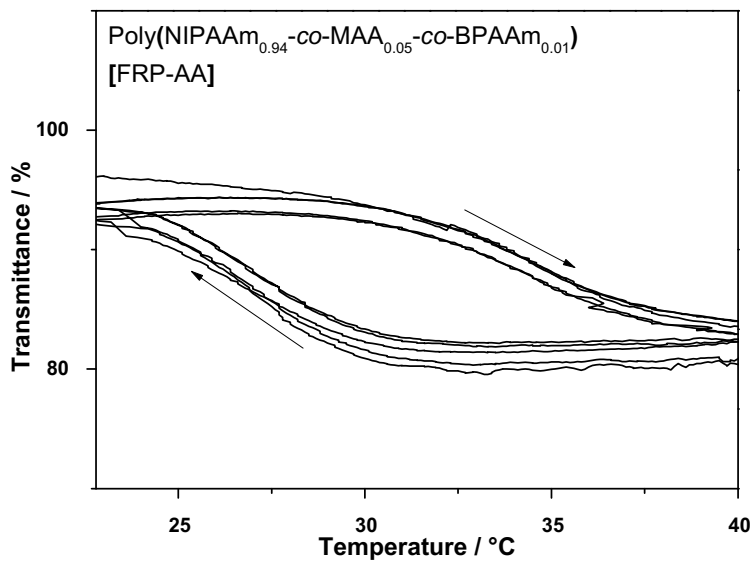


Figure S33: Cloud point determination of the photo-crosslinkable PNIPAAm (FRP-MAA), recorded with five cycles from 1.0 wt% aqueous solution (at $\nu=650$ nm).

16.4.3. RAFT Copolymerization of the Symmetric and Photo-Crosslinkable Poly(NIPAAm-co-MAA-co-BPAAm)-BIT (94:5:1) (CRP-MAA-BIT)

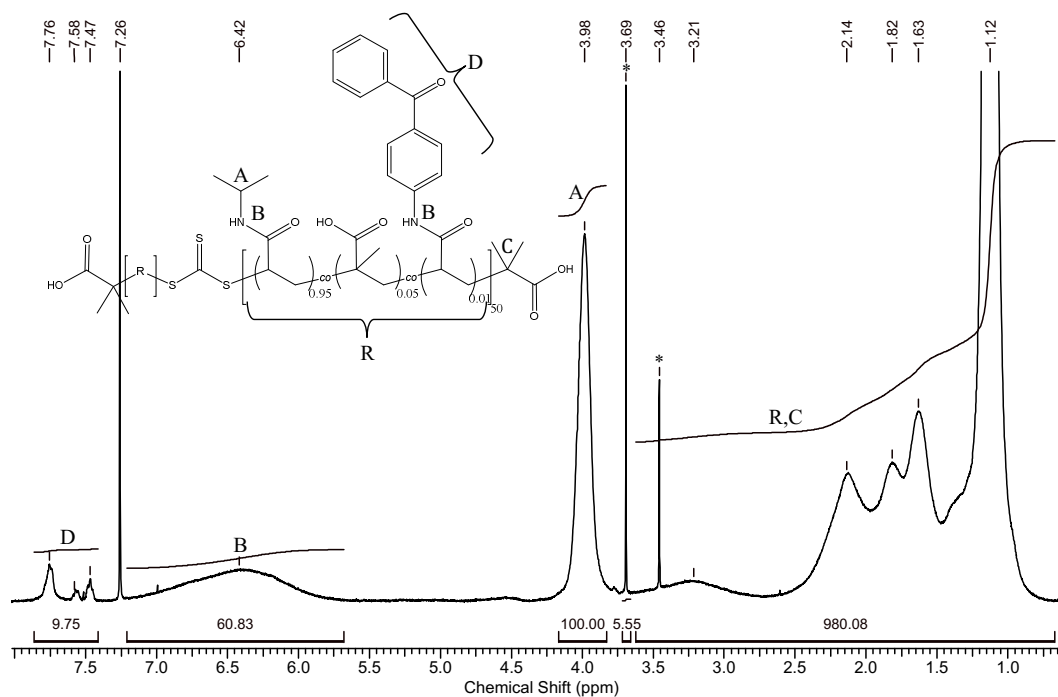


Figure S34: ¹H NMR spectrum (400 Hz) of the symmetric and photo-crosslinkable PNIPAAm (CRP-MAA-BIT), recorded in CDCl₃. Asterisks mark solvent residues.

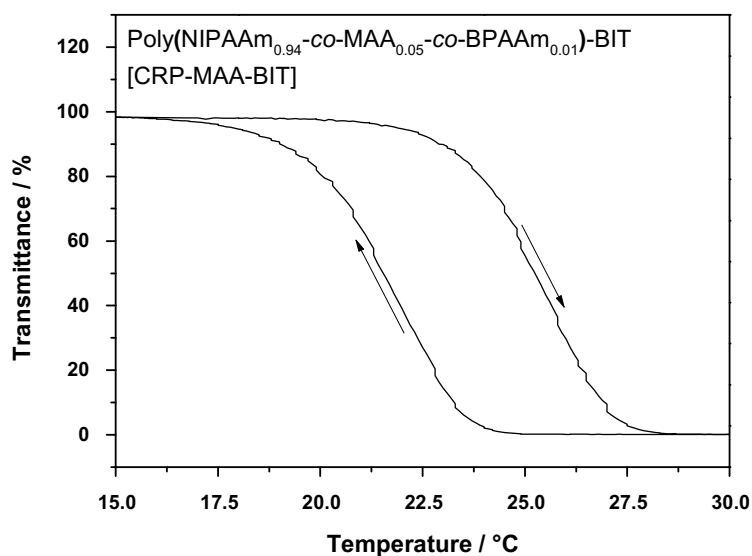


Figure S35: Cloud point determination of the symmetric and photo-crosslinkable PNIPAAm (CRP-MAA-BIT), recorded from 1.0 wt% aqueous solution (at $\nu=650$ nm).

16.4.4. General Procedure for the RAFT Copolymerization of Asymmetric and Photo-Cross-linkable Poly(NIPAAm-co-X-co-BPAAm)-DMP

Copolymer Poly(NIPAAm-co-AA-co-BPAAm)-DMP (94:5:1) (CRP-AA)

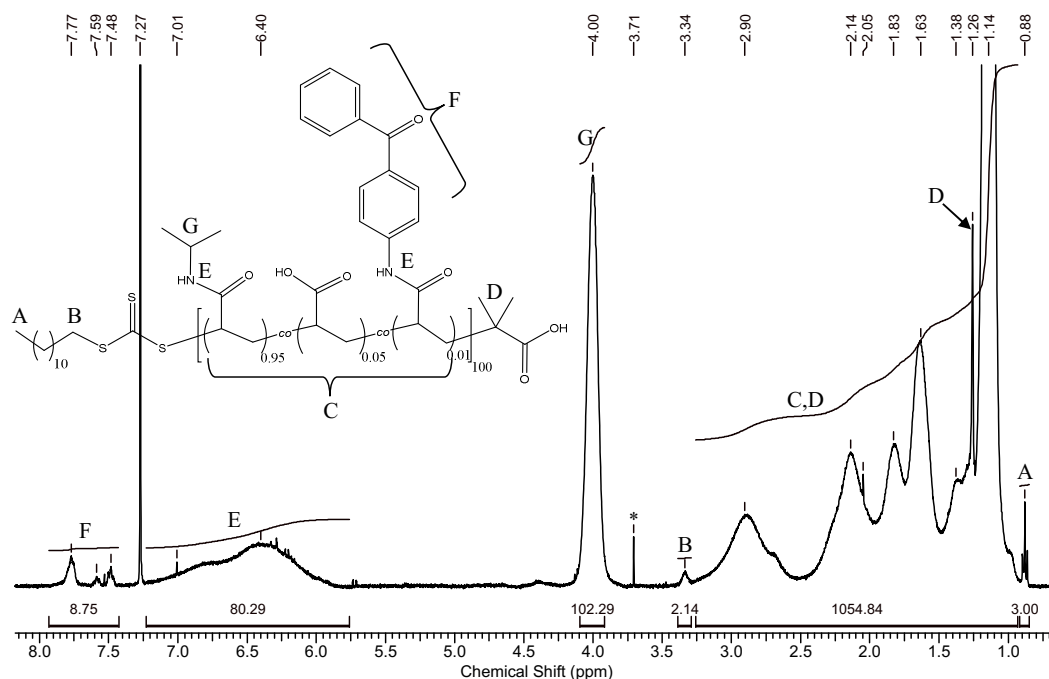


Figure S36: ¹H NMR spectrum (400 Hz) of the asymmetric and photo-crosslinkable PNIPAAm (CRP-AA), recorded in CDCl₃. Asterisks mark solvent residues.

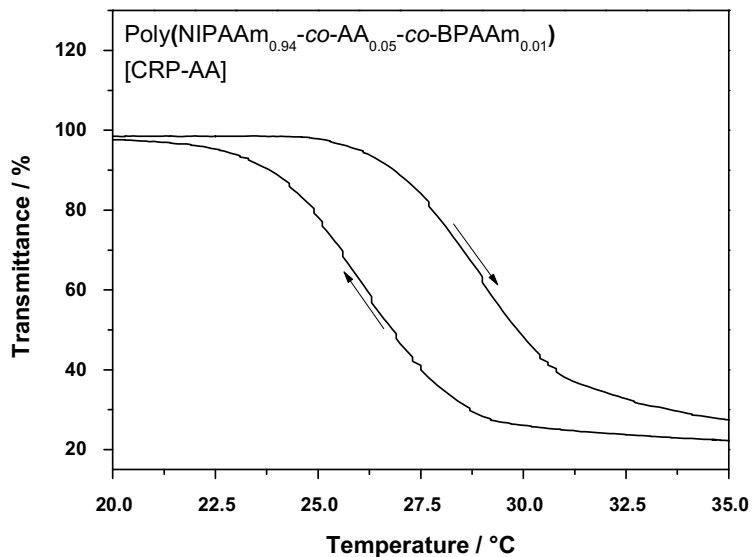


Figure S37: Cloud point determination of the asymmetric and photo-crosslinkable PNIPAAm (CRP-AA), recorded from 1.0 wt% aqueous solution (at $\nu=650$ nm).

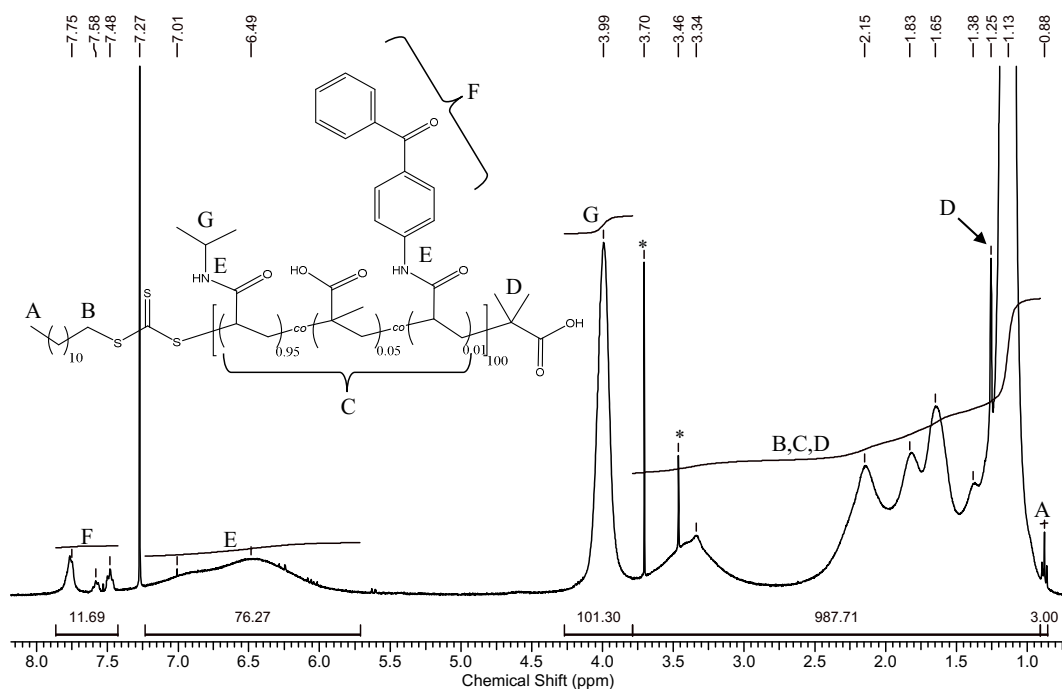
Copolymer Poly(NIPAAm-co-MAA-co-BPAAm)-DMP (94:5:1) (CRP-MAA)

Figure S38: ^1H NMR spectrum (400 Hz) of the asymmetric and photo-crosslinkable PNIPAAm (CRP-MAA), recorded in CDCl_3 . Asterisks mark solvent residues.

The thermoresponsive properties of the copolymer were applied in the project of “nanopores” and further investigated regarding their concentration dependence (phase diagram). It was recorded *via* turbidity measurement by UV-Vis spectroscopy and T1/T2 time study by ^1H NMR.

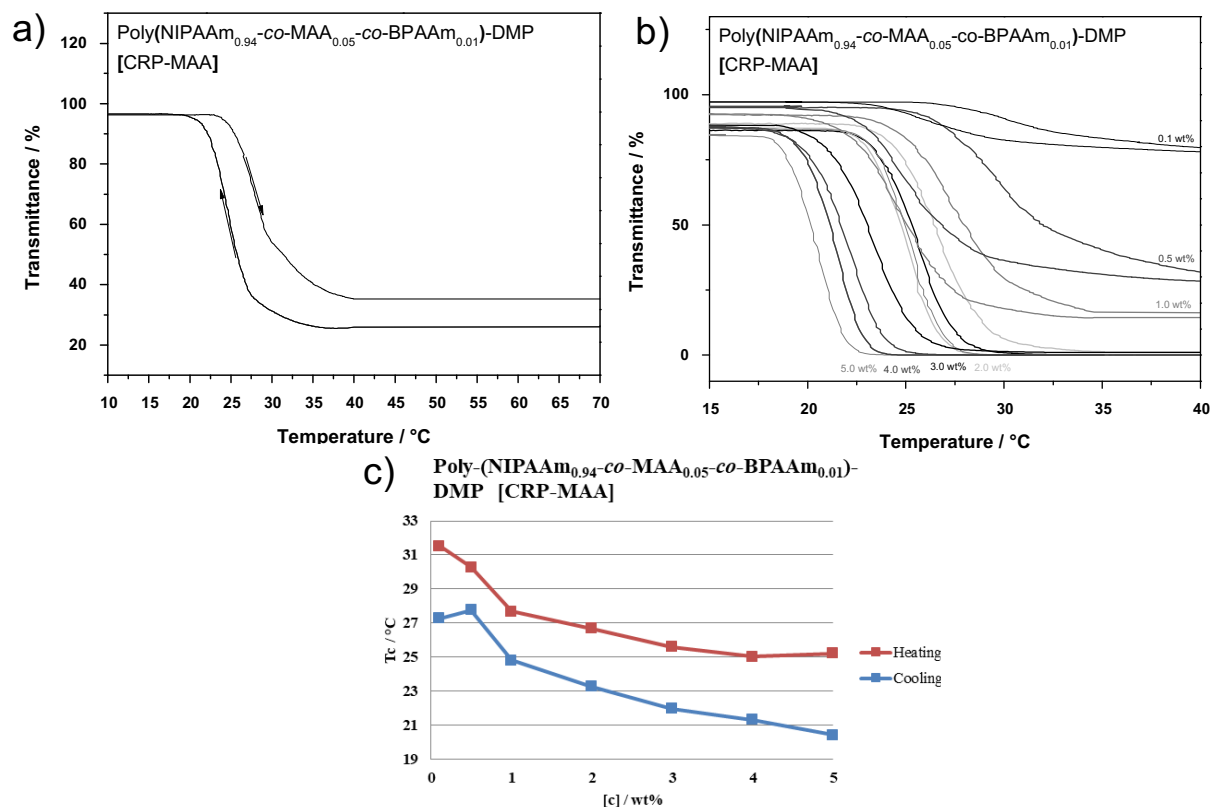


Figure S39: Cloud point determination of the asymmetric and photo-crosslinkable PNIPAAm (CRP-MAA), recorded from a) 1.0 wt% aqueous solution (at $\nu=650$ nm), b) from various concentrations and c) the resulting phase diagram of the LCST polymer system.

The phase transition of CRP-AA was further investigated *via* T1/T2 relaxation time measurements by NMR. The measurements were performed by MSc. Jan Wied from the inorganic working group of Prof. Dr. Schmedt auf der Günne.

The polymer was dissolved in a mixture of D₂O/H₂O=60:40. The solution was degassed *via* argon stream for 1 h, filled without bubbles into a glass capillary and sealed. The variable temperature measurements were performed within the range of 10 to 40 °C with an applied 1H T1 inversion recovery at every $\Delta T=2$ K. The temperature was adjusted and equilibrated for 40 min. The signals were fitted in the deconv2Dxy software.

$$f(x) = a \cdot (1 - d \cdot \exp(-(x/b)^c)) \quad (15)$$

The T₁-times were calculated by the equation with integral signal A, the T₁ time B, Kohlrauschfaktor C and Fit parameter D (~2).

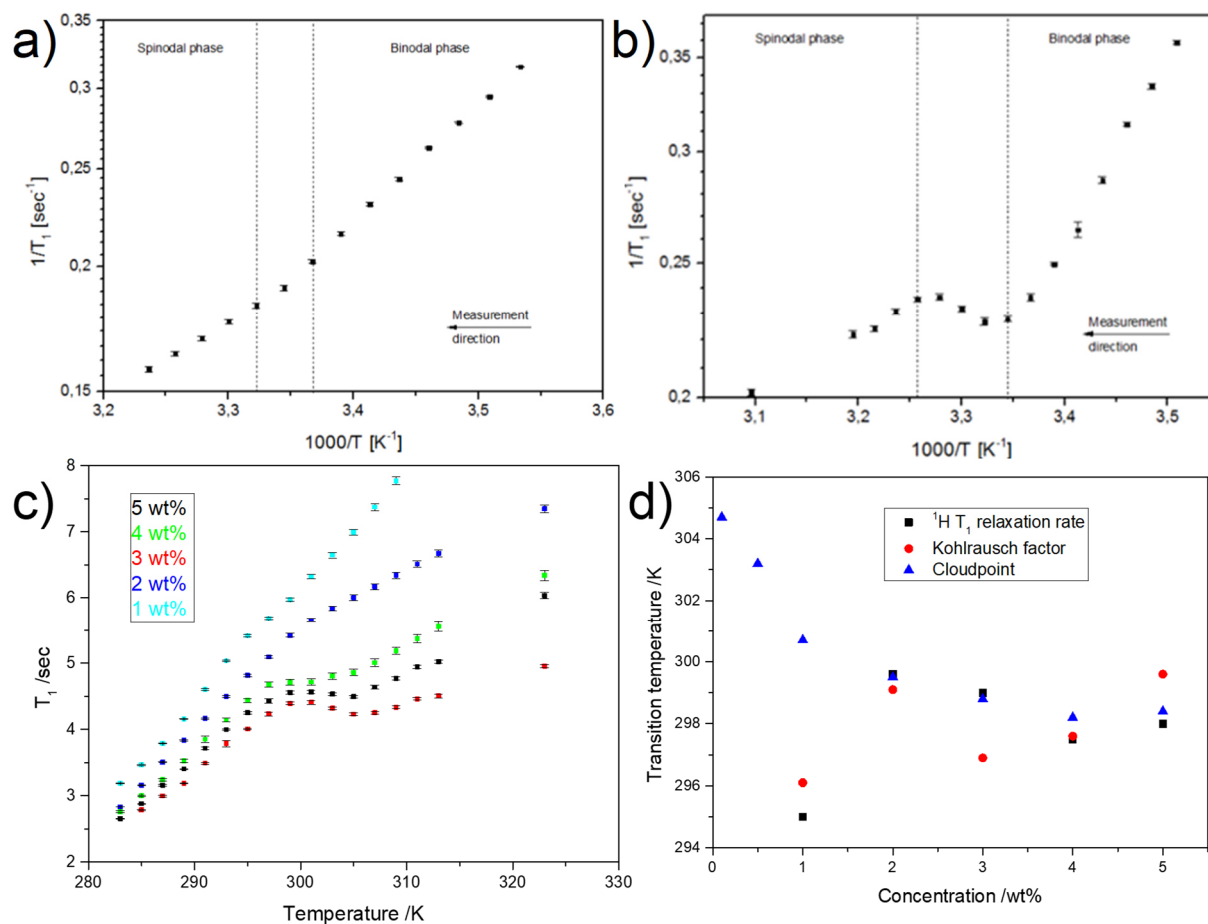


Figure S40: Cloud point determination of the asymmetric and photo-crosslinkable PNIPAAm (CRP-MAA) via T_1/T_2 NMR studies, recorded from a) 1.0 wt% and b) 5.0 wt% solution ($\text{D}_2\text{O}/\text{H}_2\text{O}=60:40$). c) shows the overview of the concentration dependent measurements and d) illustrates the corresponding phase diagram with its relaxation rates, Kohlrausch factors and corresponding cloud points.

Copolymer Poly(NIPAAm-co-AA-co-BPAAm)-DMP-EA (94:5:1) (CRP-AA-DMP-EA)

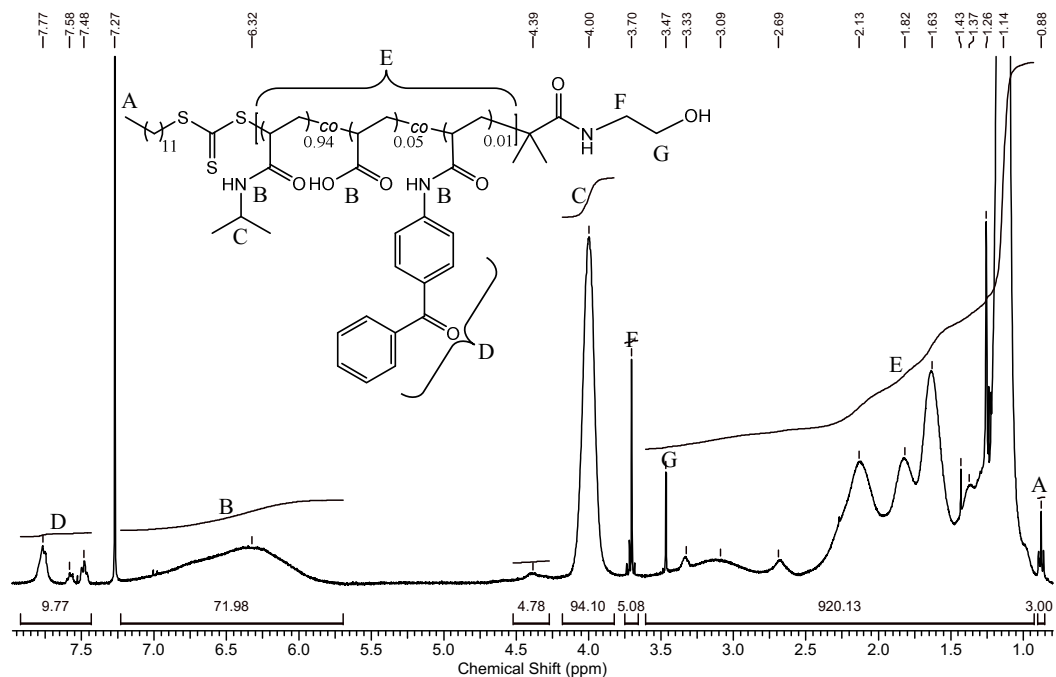


Figure S41: ^1H NMR spectrum (400 Hz) of the asymmetric and photo-crosslinkable PNIPAAm (CRP-AA-DMP-EA), recorded in CDCl_3 . Asterisks mark solvent residues.

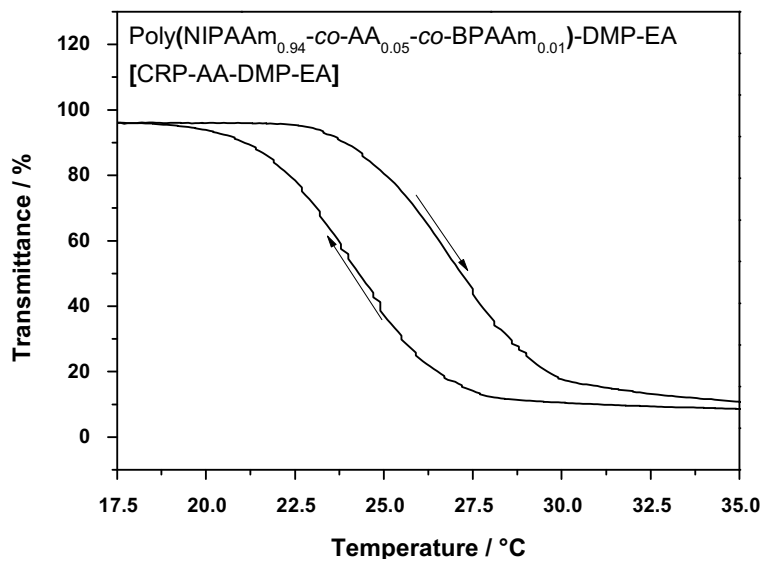


Figure S42: Cloud point determination of the asymmetric and photo-crosslinkable PNIPAAm (CRP-AA-DMP-EA), recorded from 1.0 wt% aqueous solution (at $\nu=650$ nm).

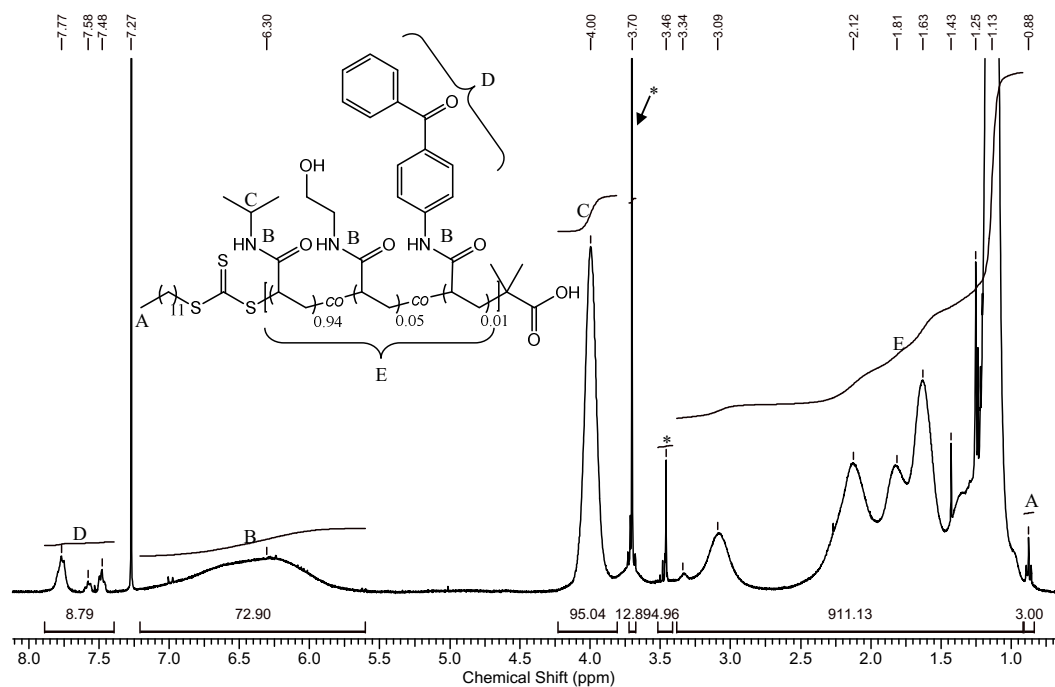
Copolymer Poly(NIPAAm-co-HEAAm-co-BPAAm)-DMP (94:5:1) (CRP-HEAAm)

Figure S43: ^1H NMR spectrum (400 Hz) of the asymmetric and photo-crosslinkable PNIPAAm (CRP-HEAAm), recorded in CDCl_3 . Asterisks mark solvent residues.

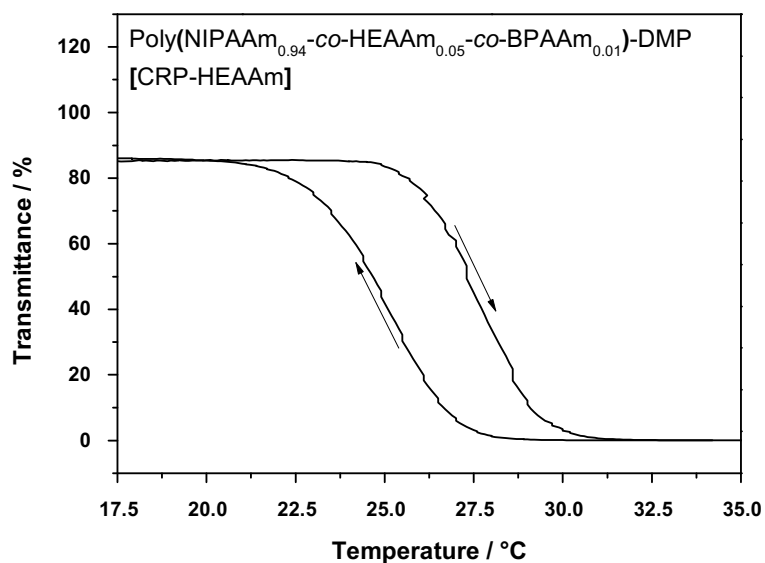


Figure S44: Cloud point determination of the asymmetric and photo-crosslinkable PNIPAAm (CRP-HEAAm), recorded from 1.0 wt% aqueous solution (at $\nu=650$ nm).

Copolymer Poly(NIPAAm-co-HEAAm-co-BPAAm)-DMP (89:10:1) (CRP-HEAAm10%16k)

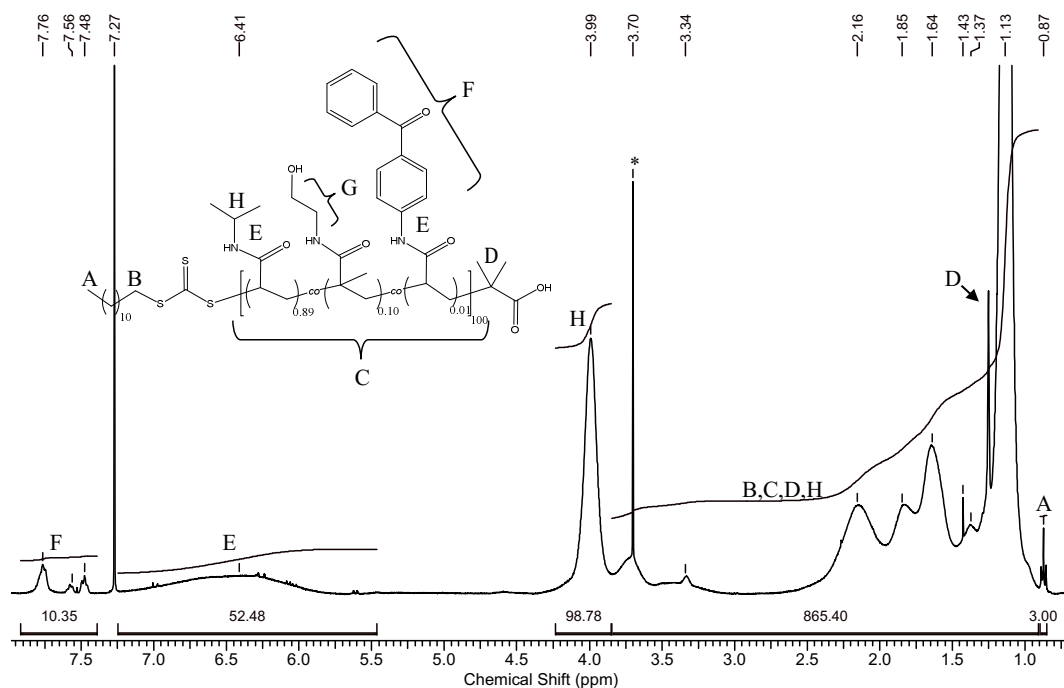


Figure S45: ^1H NMR spectrum (400 Hz) of the asymmetric and photo-crosslinkable PNIPAAm (CRP-HEAAm10%16k), recorded in CDCl_3 . Asterisks mark solvent residues.

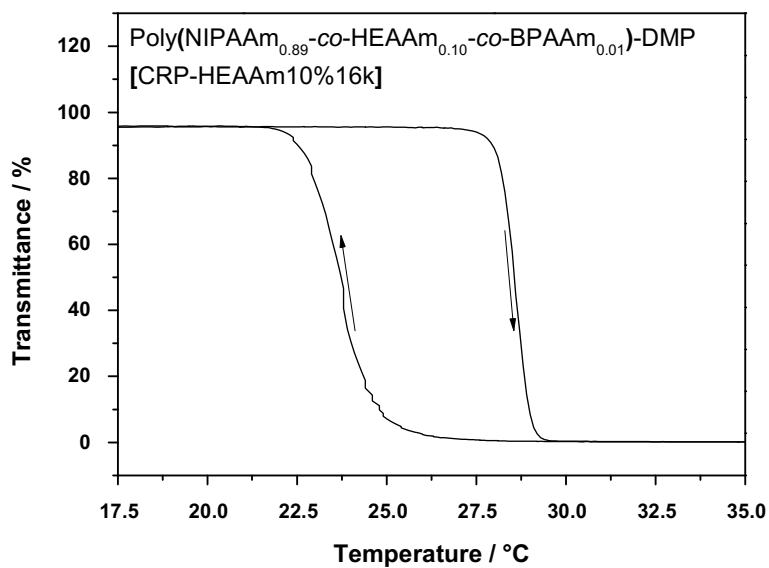


Figure S46: Cloud point determination of the asymmetric and photo-crosslinkable PNIPAAm (CRP-HEAAm10%16k), recorded from 1.0 wt% aqueous solution (at $\nu=650$ nm).

Copolymer Poly(NIPAAm-co-HEAAm-co-BPAAm)-DMP (89:10:1) (CRP-HEAAm10%26k)

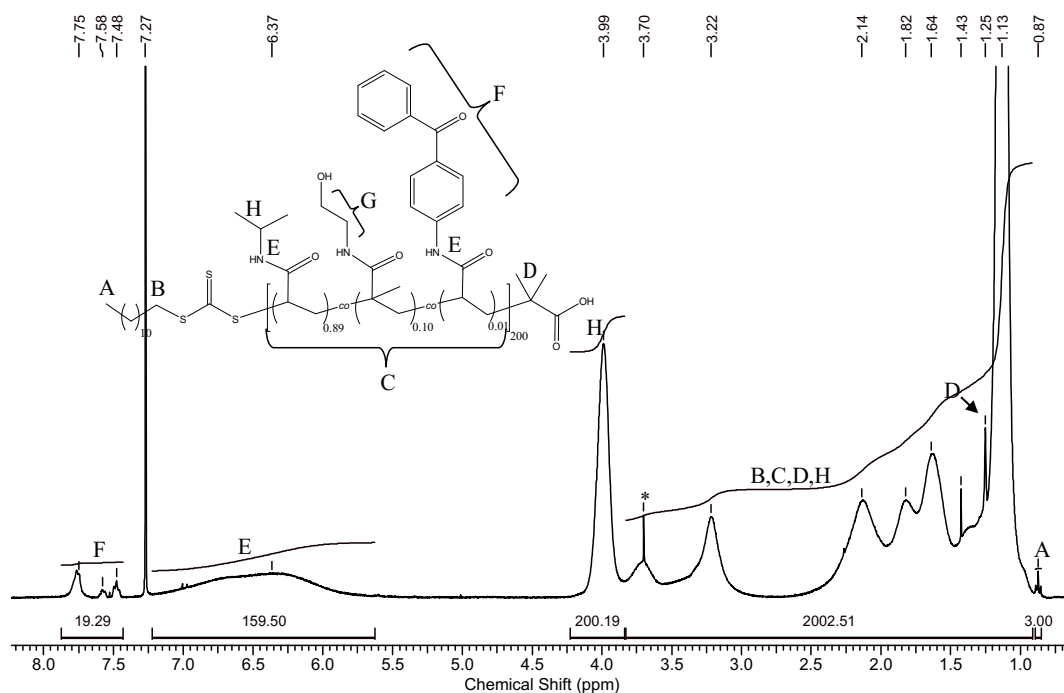


Figure S47: ^1H NMR spectrum (400 Hz) of the asymmetric and photo-crosslinkable PNIPAAm (CRP-HEAAm10%26k), recorded in CDCl_3 . Asterisks mark solvent residues.

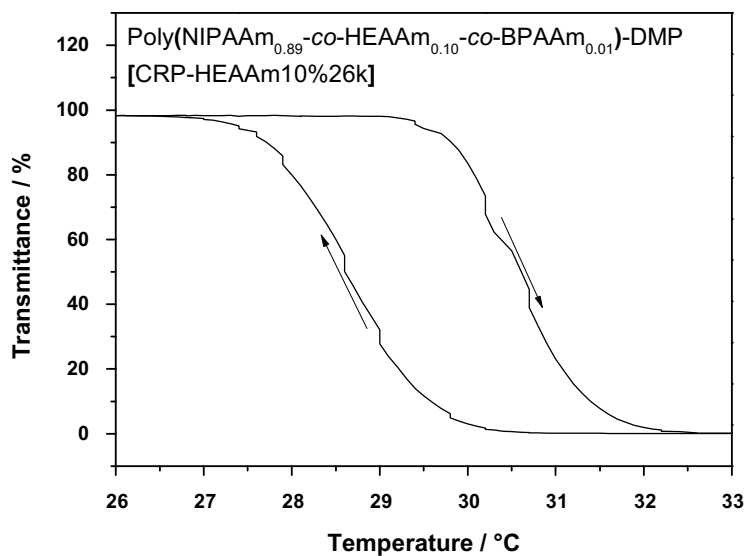


Figure S48: Cloud point determination of the asymmetric and photo-crosslinkable PNIPAAm (CRP-HEAAm10%26k), recorded from 1.0 wt% aqueous solution (at $\nu=650$ nm).

16.5. Double Thermoresponsive LCST-UCST Block Copolymers

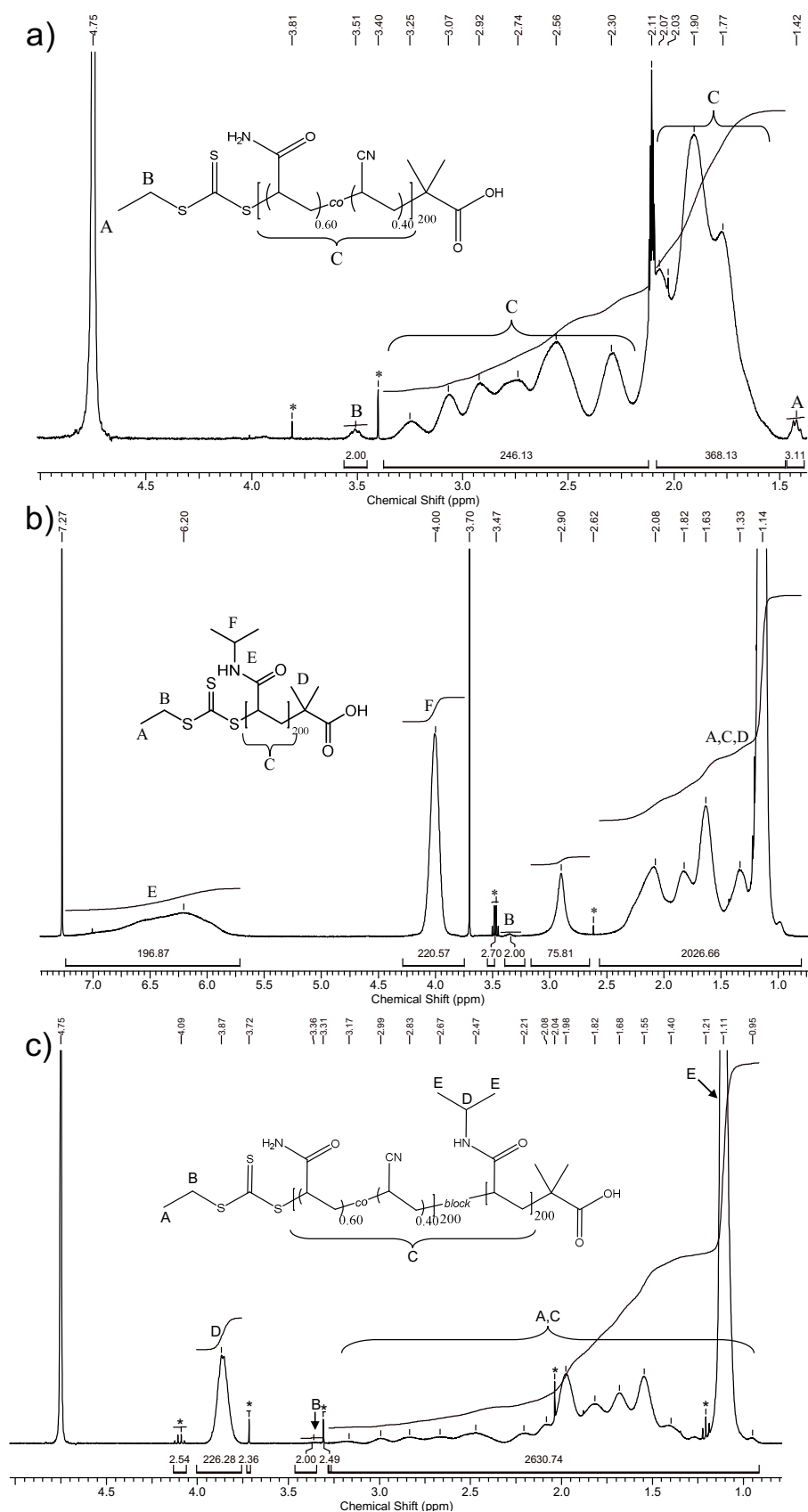


Figure S49: ^1H NMR spectra (400 Hz) of a) the applied thermoresponsive macroCTA and UCST block poly(AAm_{0.60}-co-AN_{0.40})₂₀₀-EMP (CRP40.0%), recorded in $\text{D}_2\text{O}/\text{MeCN-}d_3$ (85:15), b) a reference for the LCST block homopolymer poly(NIPAAm)₂₀₀-EMP, recorded in CDCl_3 , and c) the resulting double thermoresponsive UCST-LCST block copolymer poly[(AAm_{0.60}-co-AN_{0.40})₂₀₀-block-(NIPAAm)₂₀₀]-EMP, recorded in D_2O . Asterisks mark solvent residues.

The exemplary elugram of the precursor macroCTA poly(AAm-co-AN)-EMP in comparison with the final block copolymer poly[(AAm-co-AN)-*block*-(NIPAAm)]-EMP is shown in Figure S50. The elugrams are recorded in different eluents to prove the formation of block copolymers. While the molar mass distribution does not vary in water/MeCN (presumably due to the coiling state), the eluent DMAc allows the detection of the targeted molar mass of the block copolymers. The theoretical prediction of the molar masses aligns with the experimental data. While product is soluble in the eluent DMAc, the precursor does not possess any solubility (high polarity). Despite the same flow rate (1 mL/min), the elution times are not comparable precisely and are used indicatively to prove the success of the block copolymerization.

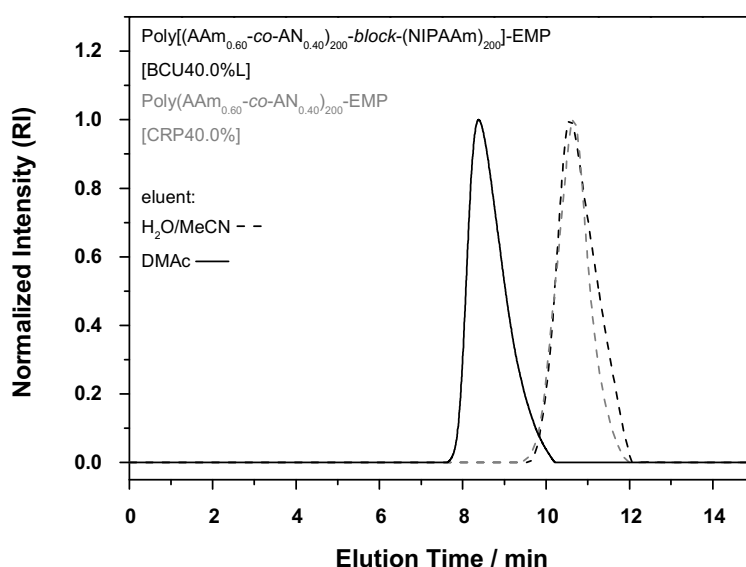


Figure S50: Elugrams in the RAFT block copolymerization of a) the applied UCST-starting block poly(AAm_{0.60}-co-AN_{0.40})₂₀₀-EMP (CRP40.0%) and b) the resulting double thermoresponsive LCST-UCST-block copolymer poly[(AAm_{0.60}-co-AN_{0.40})₂₀₀-*block*-(NIPAAm)₂₀₀]-EMP recorded *via* gel-permeation chromatography in both eluents DMAc with LiBr (dashed) and H₂O/MeCN (85:15) with NaNO₃ (solid).

The elugrams show the success of the proceeded block copolymerization by the means of the macroCTA pathway. The double thermoresponsive LCST-UCST block copolymer is shown in comparison to its precursor, the UCST-starting block (Figure S50).

The resulted thermoresponsive properties of the LCST-UCST block copolymers are represented in the modulated DSC measurements (Figure S51) in comparison with the turbidity curves of the cooling cycle measured by UV-Vis spectroscopy. The total heat flow conforms to the result of a conventional measurements, while the modulated mode separates the signal into the reversing (thermodynamic) and non-reversing (kinetic) components.

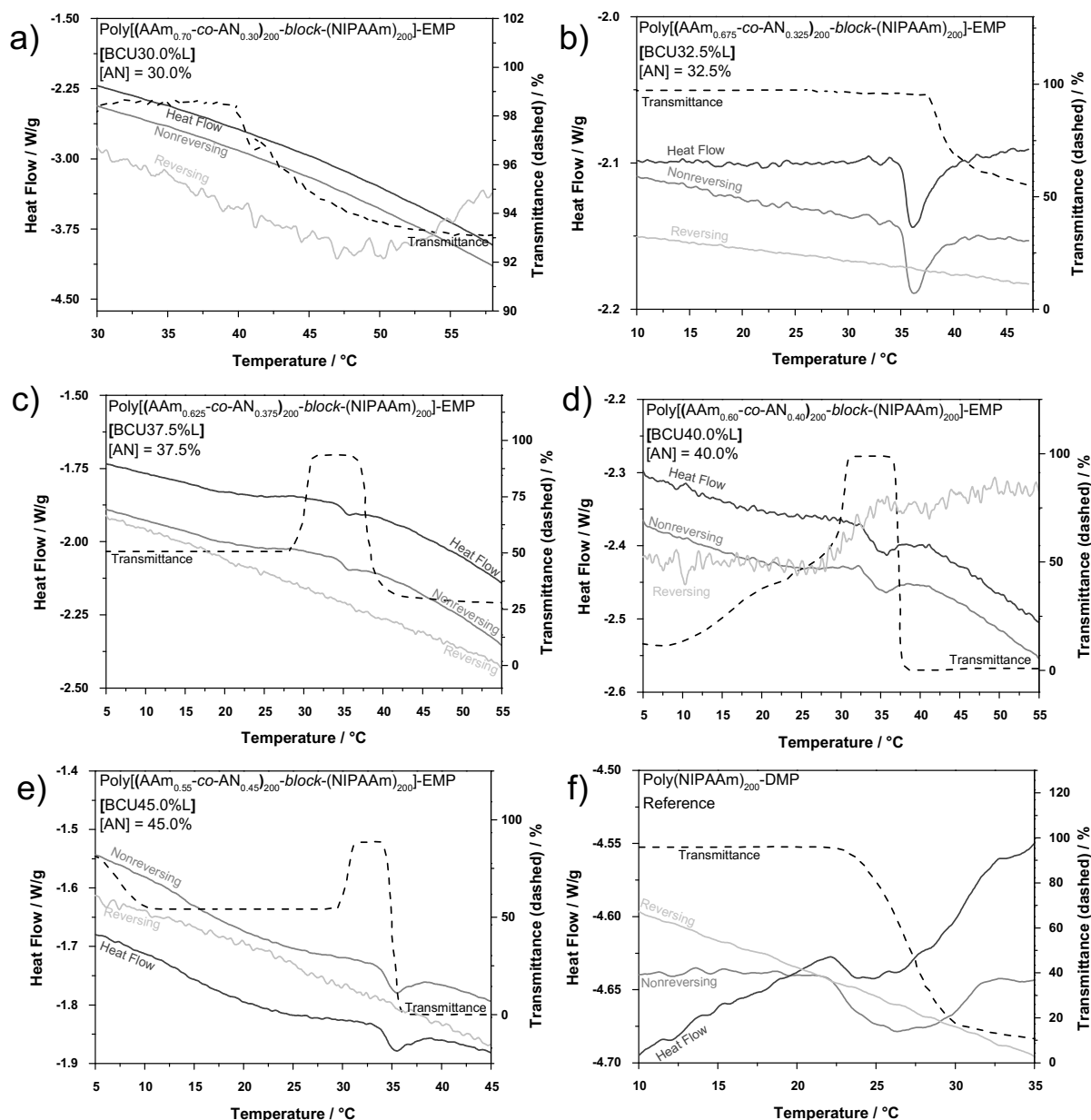


Figure S51: Modulated DSC measurements in comparison with the corresponding turbidity curves (via UV-Vis spectroscopy) of the double thermoresponsive LCST-UCST-block copolymers poly[(AAm-co-AN)₂₀₀-block-(NIPAAm)₂₀₀]-EMP with varied molar fraction of AAm/AN of a) (70.0:30.0), b) (67.5:32.5), c) (62.5:37.5), d) (60.0:40.0) and e) (55.0:45.0) in the precursor starting block. f) represents a reference polymer of poly(NIPAAm)₂₀₀-DMP. The measurements were recorded in the heat-only mode (15 s, 1.5 K/min, 2-50 °C, ±0.06) by a heating cycle of an 1.0 wt% aqueous solution.

The anomalous thermoresponsive behaviour of the double thermoresponsive LCST-UCST block copolymers was additionally studied by dynamic light scattering measurements of the thermoresponsive states at different temperatures (Figure S52). The aggregation behaviour of the characteristic temperatures was analysed. The aggregation sizes were taken indicatively for changes of the object's dimensions and not as precise values due to the multi dimensions of scattering species. The aggregation sizes become reliable for less than a twofold decay.

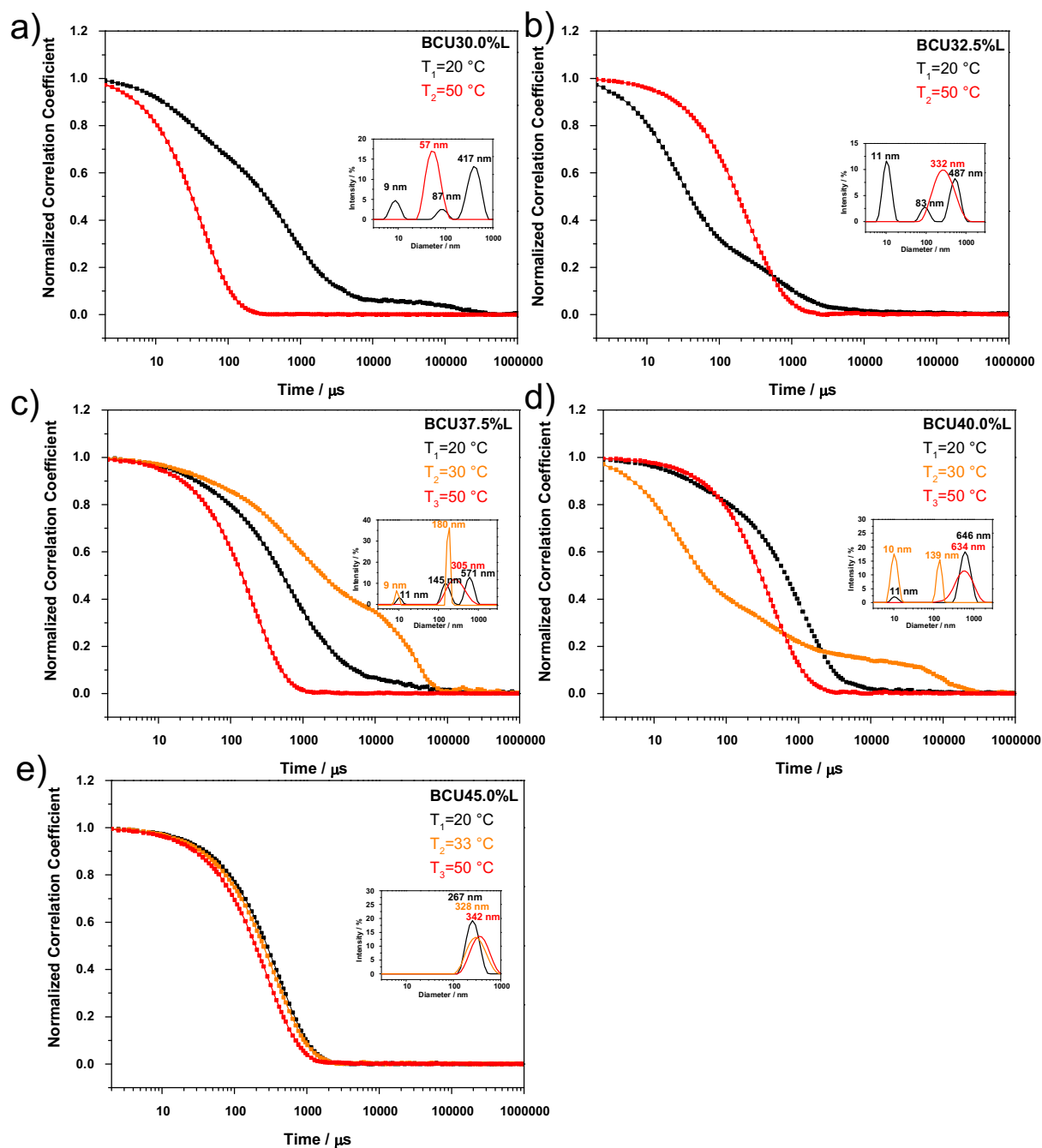


Figure S52: DLS measurement of a 1.0 wt% polymer solution for the aggregation study of the double thermoresponsive LCST-UCST-block copolymers poly[(AAm-co-AN)₂₀₀-*block*-(NIPAAm)₂₀₀]-EMP with varied molar fraction of AAm/AN of a) (70.0:30.0), b) (67.5:32.5), c) (62.5:37.5), d) (60.0:40.0) and e) (55.0:45.0) in the starting block. The measurements were performed with respect to the thermoresponsive states (extracted from the turbidity curves) of the samples at T₁=20 °C, T₂=30/33 °C and T₃=50 °C. The aggregation sizes are analyzed by intensity.

The macromolecular and thermoresponsive properties of the UCST-LCST block copolymers are summarized below (Table S10). The block copolymers with varied molar fraction of AN in the UCST-starting block are compared with the corresponding original UCST-starting blocks (described further in 13.3.4 according to CRP30%-CRP55%).

Table S10: The summarized experimental data of the RAFT polymerized and double thermoresponsive LCST-UCST block copolymers poly[(AAm-co-AN)-*block*-(NIPAAm)]-EMP with molar various fractions of AN in the UCST-starting block. The sample code of copolymers and their corresponding comparable UCST-starting block poly(AAm-co-AN)-EMP, experimental molar masses (\bar{M}_n), dispersities (\mathcal{D}), yields and the resulting cloud points of the heating/cooling cycle are shown.

Sample Code		BCU 30.0%L	BCU 32.5%L	BCU 35.0%L	BCU 37.5%L	BCU 40.0%L	BCU 45.0%L	BCU 50.0%L	BCU 55.0%L	R1 ^[f]
[AN] _{feed} ^[c] / mol%		30.0	32.5	35.0	37.5	40.0	45.0	50.0	55.0	0%
Starting Block ^[a]	$\bar{M}_{n,theo}$ / kg·mol ⁻¹	13.3	13.3	13.2	13.1	13.0	12.8	12.6	12.4	23.3
	$\bar{M}_{n,NMR}$ / kg·mol ⁻¹	13.4	13.4	14.7	13.6	12.9	14.1	12.3	12.0	22.8
	$\bar{M}_{n,GPC}$ ^[d] / kg·mol ⁻¹	12.8	14.2	14.0	14.2	13.0	11.1 ^[e]	6.4 ^[e]	5.0 ^[e]	26.1
	\mathcal{D} ^[d]	1.39	1.39	1.48	1.40	1.34	1.39	1.42	1.42	1.29
	$T_{c,cool}$ / °C	1.6	8.7	14.7	28.0	32.3	52.1	72.5	78.8	28.5
	$T_{c,heat}$ / °C	3.2	11.2	16.0	28.6	34.1	53.0	76.4	79.2	33.0
Final Block Copolymer ^[b]	$\bar{M}_{n,theo}$ / kg·mol ⁻¹	36.0	36.0	37.3	36.2	35.5	36.7	34.9	34.6	-
	$\bar{M}_{n,NMR}$ / kg·mol ⁻¹	29.1	33.7	26.9	36.9	37.7	33.6	33.1	25.9	-
	$\bar{M}_{n,GPC}$ ^[d] / kg·mol ⁻¹	31.3	36.2	24.7	36.3	36.6	37.9	38.3	43.9	-
	\mathcal{D} ^[d]	1.15	1.38	1.21	1.42	1.44	1.36	1.32	1.22	-
	$T_{c,cool}$ / °C	39.5	36.1	35.7 36.9	7.5 34.2	15.6 32.9	> 90 29.4	29.8	30.6	-
	$T_{c,heat}$ / °C	43.9	40.8	40.9 44.0	30.1 38.1	30.9 37.3	7.5 30.5 35.0	34.6	35.0	-
	Yield / % (mg)	69 (138)	75 (150)	82 (155)	87 (172)	81 (162)	79 (163)	75 (159)	69 (149)	-

^[a] The UCST-starting block poly(AAm_x-co-AN_y)₂₀₀-EMP (according to CRP30%-CRP55%) represents the precursor of the block copolymerization.

^[b] The final LCST-UCST block copolymer poly[(AAm_x-co-AN_y)₂₀₀-*block*-(NIPAAm)₂₀₀]-EMP (BCU30.0%L-BCU55.0%L) from the RAFT block copolymerization.

^[c] The molar fraction of the monomer acrylonitrile in the precursor UCST-starting block.

^[d] The values determined by gel-permeation chromatography in H₂O/MeCN (85:15) with NaNO₃.

^[e] Values are deviating due to the hydrophobic coiling states in the eluent caused by a high cloud point.

^[f] The reference for the LCST-block represents poly(NIPAAm)₂₀₀-EMP.

16.6. Thermoresponsive Switching States in Nanopore Membranes

The applied LCST copolymers are described with their macromolecular and thermoresponsive properties in the previous chapters (according to 13.3.3 and 15.3).

The most important chemical data are summarized repeatedly below in Table S11. The GPC measurements delivered the molar mass distributions ($\bar{M}_{n,GPC}$) and dispersities (\mathcal{D}) of the polymer systems. The molar masses ($\bar{M}_{n,NMR}$) of the RAFT polymers and the incorporation ratio of the photocrosslinker benzophenone acrylamide in the polymer chains were derived from ^1H NMR measurements.

Table S11: The experimental number-average molar mass (\bar{M}_n) the dispersity (\mathcal{D}) and the incorporation ratio of BPAAm ([BPAAm]) of the used copolymers (FRP-MAA, CRP-HEAAm, CRP-AA-DMP-EA).

Copolymer System	CRP-HEAAm	FRP-MAA	CRP-AA-DMP-EA
$\bar{M}_{n,NMR}$ / kg·mol ⁻¹	12.9	- [a]	11.0
$\bar{M}_{n,GPC}$ / kg·mol ⁻¹	15.7	138.2	16.4
\mathcal{D}	1.23	2.31	1.17
[BPAAm] _{incorporated} / mol%	0.98	1.00	1.08

[a] The molar mass of FRP polymers is not determinable *via* ^1H NMR

The thermoresponsive properties of the polymers determined by turbidity (heating and cooling cycle) and modulated DSC measurements (heating cycle) are summarized below (Table S12).

Table S12: The determination of the thermoresponsive properties, the used copolymers (FRP-MAA, CRP-HEAAm, CRP-AA-DMP-EA) *via* UV-Vis spectroscopy and MDSC in polymeric solution and in filled AAO.

Copolymer System		CRP-HEAAm	FRP-MAA	CRP-AA-DMP-EA
Turbidity ^[a]	$T_{c,heat}$ / °C	27.7	33.6	27.0
	$T_{c,cool}$ / °C	24.9	27.3	24.1
Calorimetric [in Solution]	$T_{c,heat}$ / °C	- [b]	31.2	28.7
Calorimetric [in AAO]	$T_{c,heat}$ / °C	- [b]	32.4	26.8

[a] Values determined *via* turbidity measurement

[b] Not determined values.

16.6.1. Quantification of the Copolymer Filling by HEAAm/DMP-EA inside the Nanopores

The control of the polymerization and the narrow dispersity ($\mathcal{D}=1.23$) underlines the successful process of a RAFT-polymerization. The benzophenone moiety (shown as “D” in Figure S43) is incorporated completely. The cloud point (shown in Figure S44, $T_c=27.7$ °C) is slightly lowered by hydrophilic influence of the HEAAm-units and the carboxylic acid end-groups. The molar fraction of polymer inside the pores is measured by TGA in comparison

with the calculated values (Table S14). The TGA delivers convincing results in the range of the theoretical values (Table S13).

The theoretical mass of the polymer filled in the nanopores correlates with the occupied volume of the pores V_{AAO} (porosity, length of pores L_{AAO} , area of the substrate A_{AAO}) of a substrate and the concentration of polymer in the stock solution $[c]_{polymer}$ during the filling process. The mass m is corrected by the experimental value of the density of ethanolic solution $\rho_{solution}$.

$$m_{polymer} = V_{AAO} \cdot [c]_{polymer} \cdot \rho_{solution} = P \cdot L_{AAO} \cdot A_{AAO} \cdot [c]_{polymer} \cdot \rho_{solution} \quad (16)$$

Table S13: The theoretical calculated polymer mass based on the experimental determined values of the substrate porosity, pore length (L_{AAO}), substrate area (A_{AAO}), concentration of the polymer solution during the filling process of pores ($[c]_{polymer}$) and density of the solution ($\rho_{solution}$).

$[c]_{polymer}$ / wt%	Porosity	L_{AAO} / μm	A_{AAO} / mm^2	V_{AAO} / mm^3	V_{AAO} / μL	$\rho_{solution}$ / $\text{g}\cdot\text{cm}^{-3}$	m / $\text{g}\cdot\text{ml}^{-1}$	$m_{polymer}$ / μg
1.0	0.4	100	50.27	2.01	2.01	0.794	1.60	15.97
2.0	0.4	100	50.27	2.01	2.01	0.80	1.60	32.09
3.0	0.4	100	50.27	2.01	2.01	0.80	1.61	48.25

The experimental mass of the polymer in the substrates is determined in dependence of polymer fraction in the stock solution during the filling process of the pores ($[c]$). It is described by the experimental absolute mass of the substrate (m_{AAO}), its measured relative and absolute weight loss (Δm_{Loss}) in the thermo-gravimetric measurement. The subtracted weight losses of filled and empty AAO are defined as absolute mass of polymer inside the pores $\Delta m[\text{AAO-Blank}]$ in comparison to the theoretical calculated values $\Delta m[\text{theoretical}]$.

Table S14: The measured initial mass of the substrates (m_{AAO}), absolute and relative mass loss (m_{AAO}) of the thermogravimetric measurements, determination of the experimental mass loss of polymer inside the nanopores ($\Delta m[\text{AAO-bank}]$) in comparison to the theoretical values ($\Delta m[\text{Theoretical}]$).

$[c]_{polymer}$ / wt%	AAO type	m_{AAO} / mg	Δm_{Loss} / %	Δm_{Loss} / μg	Δm [AAO-Blank] / μg	Δm [theoretical] / μg
1.0	Sample	7.455	0.362	26.98	13.53	15.97
	Blank	7.398	0.182	13.45		
2.0	Sample	6.786	0.790	53.58	40.38	32.09
	Blank	6.711	0.197	13.21		
3.0	Sample	5.312	1.216	64.59	50.83	48.26
	Blank	5.220	0.264	13.76		

16.6.2. Thermoresponsive Switching of the LCST Copolymer FRP-MAA inside the Nanopores

The polymerization was successful. The benzophenone moiety (indicated as “D” in Figure S32) is incorporated completely. The cloud point (shown in Figure S33, $T_c=33.6$ °C) lies constantly for many cycles in the typical range of pure PNIPAAm ($T_c\sim 32$ °C). The calorimetric measurement of this polymer system underlines the reliability of the method. The transition temperatures were obtained by the fitting of the heat flow curve minima. The modulated calorimetric measurement (Figure S53a) in solution (1.0 wt%) proves the applicability of the method. The coil-to-globule transition in pure polymeric solution is visible in the non-reversing signal of the measurement ($T_{c,DSC}[\text{solution}]=31.0$ °C) and fits to the corresponding turbidity measurement in solution ($T_{c,UV}[\text{solution}]=33.6$ °C). The transition temperature inside the nanopores (Figure S53b) is determinable ($T_c[\text{AAO}]=32$ °C).

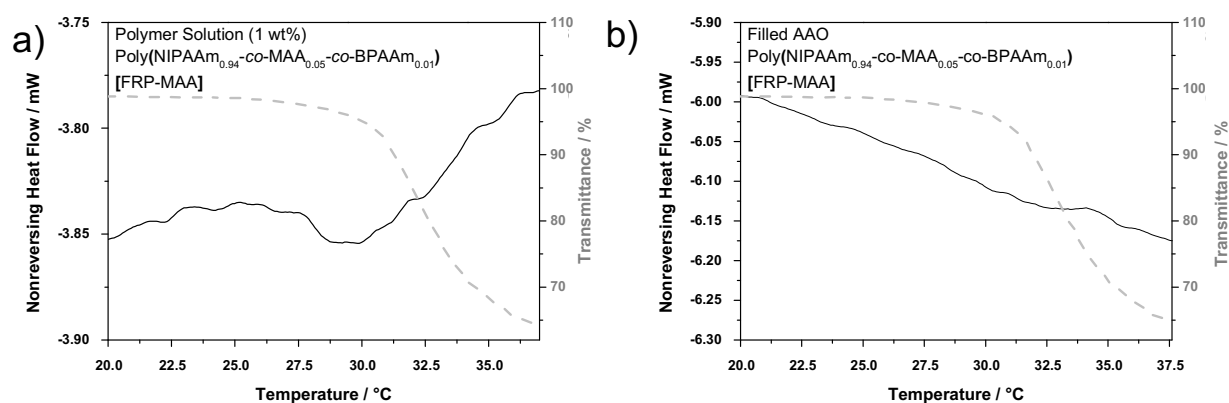


Figure S53: LCST determination via modulated DSC of poly(NIPAAm-co-MAA-co-BPAAm) (94:5:1) (FRP-MAA) of a) as 1.0 wt% aqueous solution (black) and b) as copolymeric film inside the nanopores (black) in comparison with the corresponding turbidity measurement (dashed grey) in solution (1.0 wt%).

16.6.3. Thermoresponsive Switching of the LCST Copolymer CRP-AA-DMP-EA inside the Nanopores

The control of the polymerization and the narrow dispersity ($\mathcal{D}=1.17$) underlines the successful process of RAFT polymerization. The benzophenone moiety (shown as “D” in Figure S41) is incorporated completely. The cloud point (shown in Figure S42, T_c [solution]=27.0 °C) is slightly lowered by hydrophilic influence of the AA-units and the carboxylic acid end-groups. The modulated calorimetric measurement (Figure S54a) in solution (1 wt%) proves the applicability of the method. The coil-to-globule transition in pure polymeric solution is visible in the non-reversing signal of the measurement ($T_{c,DSC}$ [solution]=29 °C) and fits to the corresponding turbidity measurement in solution ($T_{c,UV}$ [solution]=27.0 °C). The transition temperature inside the nanopores (Figure S54b) is determinable (T_c [AAO]=27 °C). The measurement of this polymer system underlines the reliability of the method.

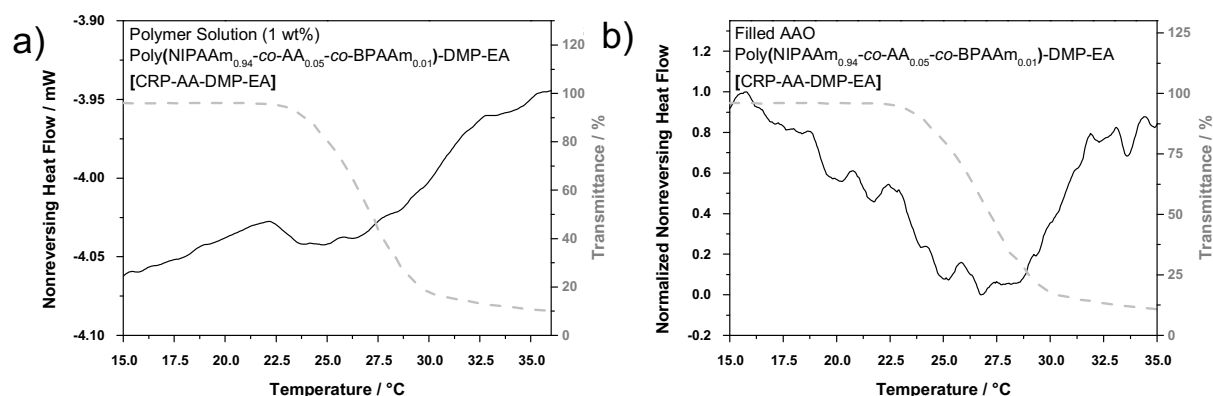


Figure S54: LCST determination *via* modulated DSC of poly(NIPAAm-co-AA-co-BPAAm)-DMP-EA (94:5:1) (CRP-AA-DMP-EA) a) as 1.0 wt% aqueous solution (black) and b) as copolymeric film inside the nanopores (black) in comparison with the corresponding turbidity measurement (dashed grey) in solution (1.0 wt%).

16.7. Iron Ion Sensitive Macromolecular Coordination Ligands

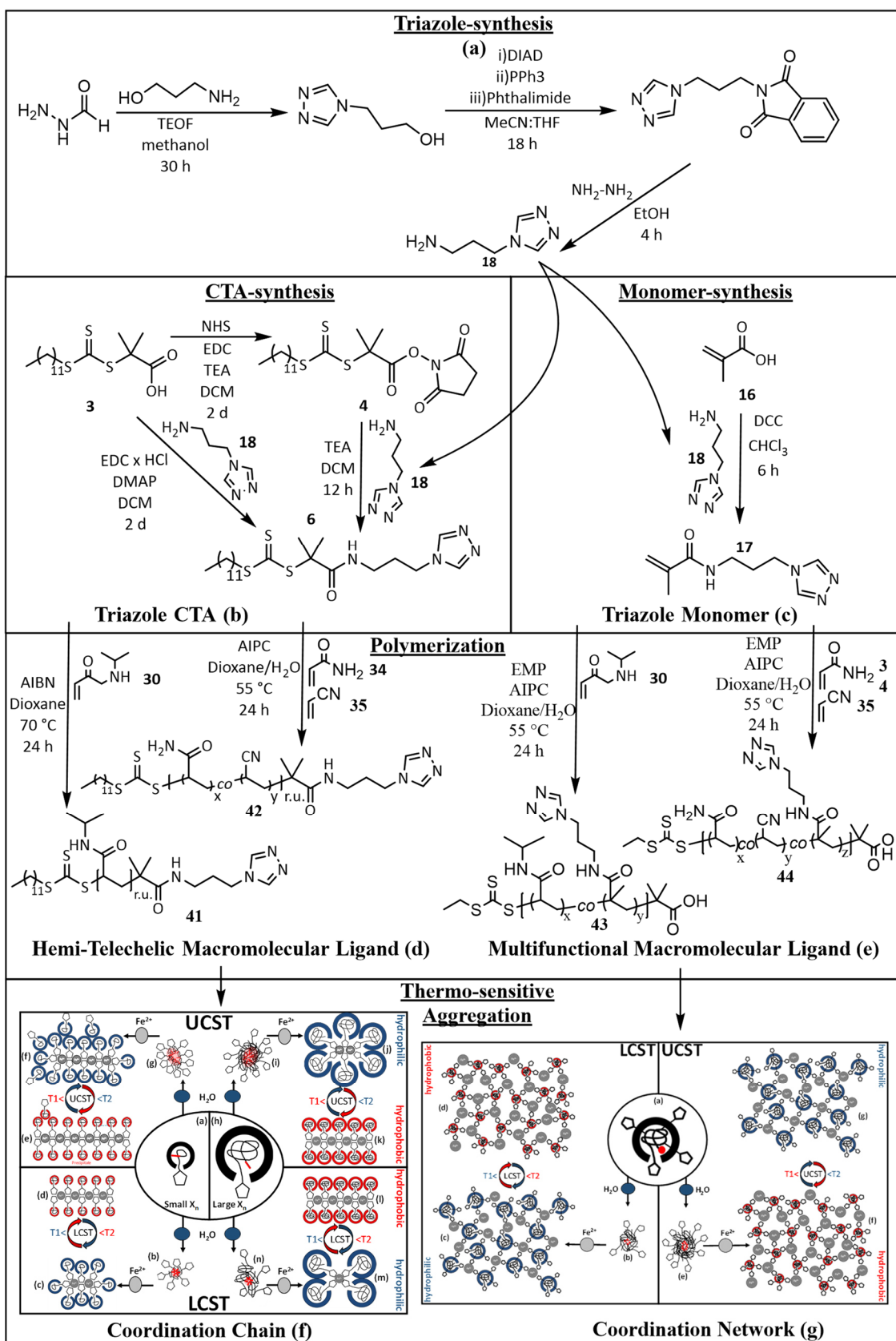


Figure S55: Flow diagram of the performed syntheses and the corresponding aggregation studies of the MCLs.

16.7.1. Coordination Moiety for the Functionalization of Polymers

Synthesis of [1,2,4]-Triazole-1-yl-propylamine (APTRZ)

The ion sensitive chain transfer agent DMP-APTRZ was end-functionalized with a [1,2,4]-triazole-1-yl-propylamine (APTRZ) moiety, which was synthesized by the collaboration partners Franck Thetiot and Narsimhulu Pittala from the inorganic working group of Prof. Dr. Smail Triki of the University of Brest.

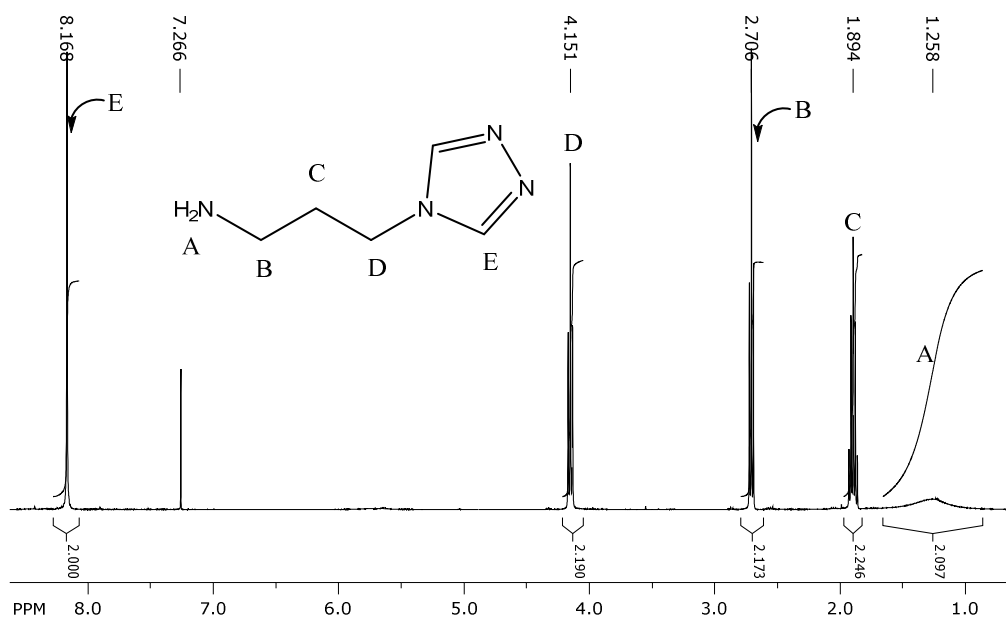


Figure S56: ¹H NMR (400 MHz) spectrum of the coordination moiety [1,2,4]-triazole-1-yl-propylamine **18** (APTRZ), recorded in CDCl₃.

The 4-*R*-1,2,4-triazole derivative 3-(4*H*-1,2,4-triazol-4-yl)propan-1-amine (APTRZ) was synthesized *via* a three-step route inspired from previously reported protocols^{234,270,271}, but with impactful modifications to improve the purification and the yield. In the first step, the intermediate 3-(4*H*-1,2,4-triazol-4-yl)propan-1-ol (HYPTRZ) is synthesized through a modified Bayer synthesis^{270,271}, followed in the second step 2-(3-(4*H*-1,2,4-triazol-4-yl)propyl)isoindoline-1,3-dione (PHTPTRZ) by a modified Mistunobu reaction.²³⁴ In the final step, the deprotection of PHTPTRZ by hydrazine led to the free amine 3-(4*H*-1,2,4-triazol-4-yl)propan-1-amine (APTRZ).²³⁴

Step 1: (4*H*-1,2,4-triazol-4-yl)propan-1-ol (HYPTRZ). A mixture of triethyl orthoformate (18 mL, 108 mmol) and formyl hydrazine (5.4 g, 90 mmol) in dry methanol (100 mL) is refluxed for 6 hours under nitrogen atmosphere. Then 3-aminopropanol (6.9 mL, 90 mmol) is added and the resulting solution is refluxed for additional 24 h. Subsequently, the mixture is allowed to cool down to room temperature, and the resulting crude product is recrystallized from dry ethanol and diethyl ether mixture at low temperature (-32 °C). Finally, the moisture sensitive

white crystalline product is filtered off, washed with cold diethyl ether, and dried under vacuum.

Yield: 8.25 g (72%).

^1H NMR (300 MHz, MeOD), δ ppm: 8.56 (s, 2H, -N-CH=N), 4.27 (t, 2H, trz-CH₂-), 3.56 (t, 2H, -CH₂-OH), 2.04 (m, 2H, CH₂-CH₂-OH), ^{13}C NMR (101 MHz, MeOD), δ ppm: 144.8 (-N-CH=N), 58.9 (trz-CH₂-), 43.3 (-CH₂-OH), 33.0 (-CH₂-CH₂-OH).

Step 2: 2-[3-(4*H*-1,2,4-triazol-4-yl)propyl]iso-indoline-1,3-dione (PHTPTRZ). Diisopropyl azodicarboxylate (DIAD) (9.7 mL, 49.45 mmol, 1.23 equivalent) is added with stirring in small portions to a solution of triphenylphosphine (PPh₃) (12.98 g, 49.45 mmol, 1.23 equiv.) in dry THF (60 mL) at 0 °C under argon, and the mixture is stirred for 10 min. A suspension of phthalimide (5.89 g, 40 mmol, 1 equiv.) and 4-(3-hydroxypropyl)-1,2,4-triazole (HYPTRZ) (5.08 g, 40 mmol, 1 equivalent) in dry acetonitrile (60 mL) is added to the reaction mixture at 0 °C, and the resulting mixture is stirred overnight at room temperature. The white precipitate formed was collected using sintered funnel, washed with cold THF and acetonitrile to obtain a white crystalline powder.

Yield: 82% (8.45 g).

^1H NMR (500 MHz, DMF-*d*₇), δ ppm: 8.62 (s, 2H, -N-CH=N-), 7.91-7.89 (m, 4H, H_{Ar}), 4.27 (t, 2H, trz-CH₂-), 3.69 (t, 2H, -CH₂-Pth), 2.23 (qi, 2H, -CH₂-CH₂-Pth), ^{13}C NMR (101 MHz, DMF-*d*₇), δ ppm: 168.9 (-C=O), 143.9 (-N-CH=N-), 134.9 (-C_{Ar}), 132.8 (-C_{Ar}), 123.5 (-C_{Ar}), 42.8 (trz-CH₂-), 35.4 (-CH₂-Pth), 30.5 (-CH₂-CH₂-Pth).

Step 3: 3-(4*H*-1,2,4-triazol-4-yl)propan-1-amine (APTRZ). Triazole derivative 2-[3-(4*H*-1,2,4-triazol-4-yl)propyl]iso-indoline-1,3-dione (PHTPTRZ) (5 g, 19.51 mmol) and NH₂NH₂·H₂O (5 mL, 103.17 mmol) in 100 mL of ethanol were heated to reflux for 4 hours. After removal of the phthalhydrazide by filtration at room temperature, the solvent was removed under reduced pressure to give pale-yellow oil. To ensure that all phthalhydrazide was removed, 50 mL of acetonitrile was added and kept at -32 °C overnight, the resulting precipitate was filtered, and the filtrate concentrated to afford the pure oil.

Yield: 1.98 g (81%).

^1H NMR (300 MHz, CDCl₃, shown in Figure S56), δ ppm: 8.17 (s, 2H, -N-CH=N-), 4.15 (t, 2H, trz-CH₂-), 2.71 (t, 2H, -CH₂-NH₂), 1.89 (m, 2H, -CH₂-CH₂-NH₂), 1.26 (br s, 2H, NH₂); ^{13}C NMR (300 MHz, CDCl₃), δ ppm: 143.0 (-N-CH=N-), 42.5 (trz-CH₂-), 38.3 (-CH₂-NH₂), 33.7 (-CH₂-CH₂-NH₂).

16.7.2. Hemi-Telechelic Macromolecular Coordination Ligands

General Procedure for the RAFT Polymerization of the LCST-typed Thermoresponsive Hemi-Telechelic Macromolecular Coordination Ligand Poly(NIPAAm)-DMP-APTRZ (P2k-P25k)

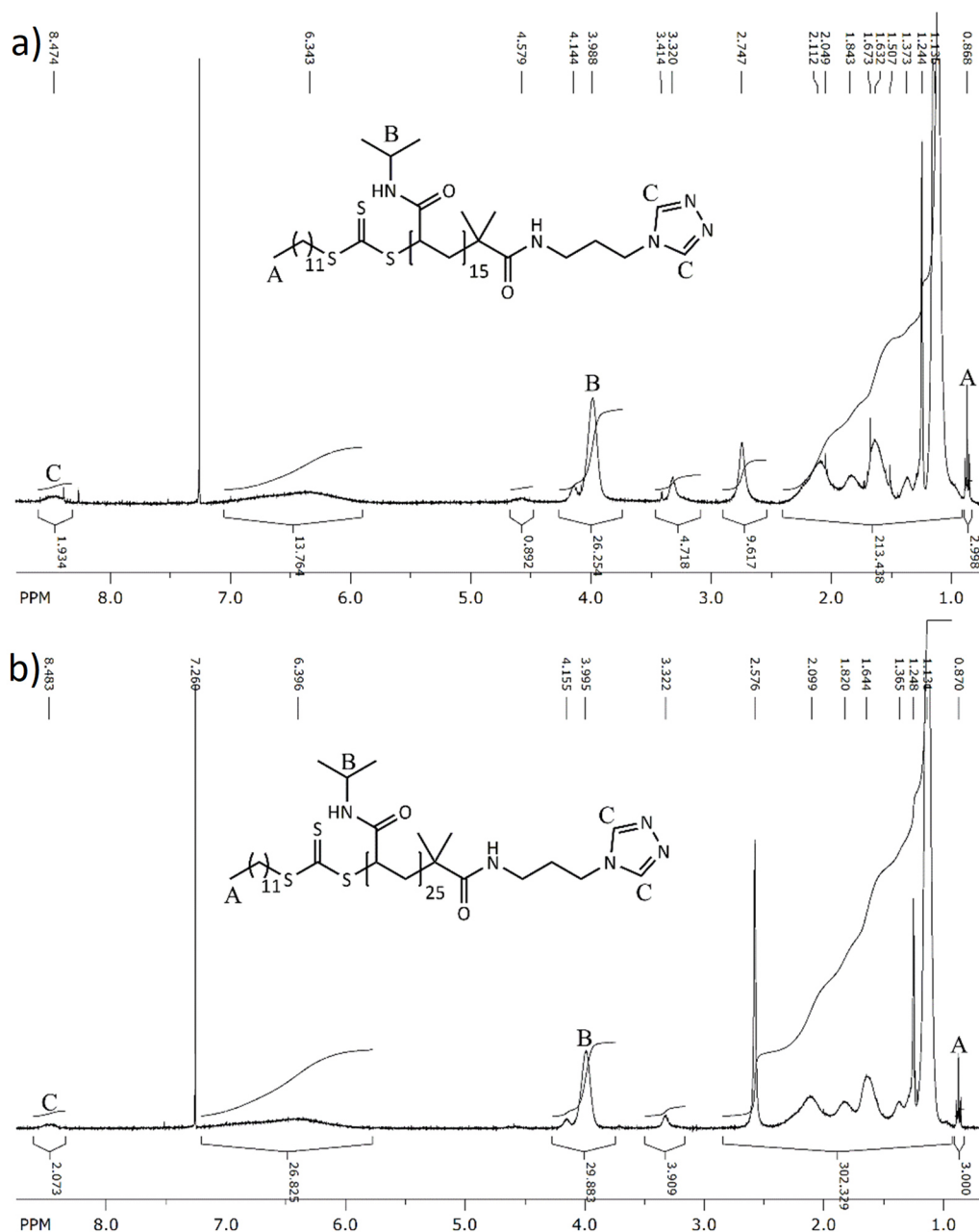


Figure S57: ^1H NMR spectra (400 Hz) of the LCST-typed hemi-telechelic MCL poly(NIPAAm)-DMP-APTRZ a) P3k and b) P4k, recorded in CDCl_3 .

The macromolecular properties of *via* the general procedure synthesized macromolecular hemi-telechelic coordination polymers with varied chain lengths are summarized below (Table S15).

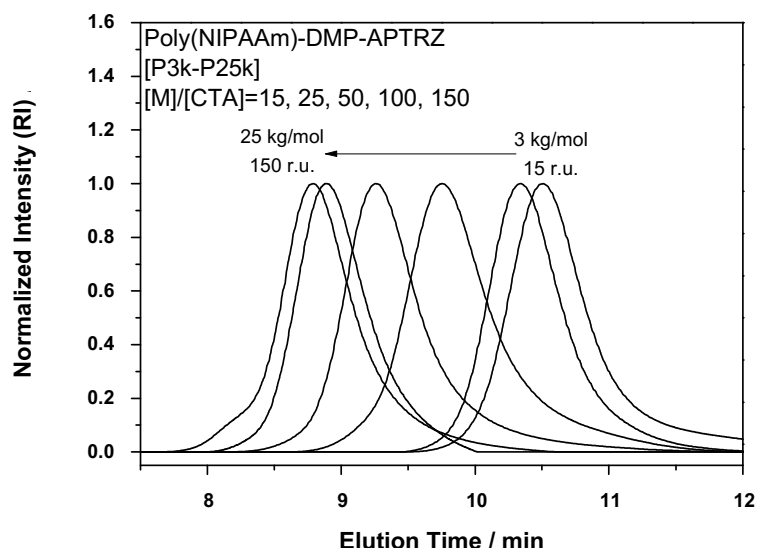


Figure S58: Elugrams of the hemi-telechelic macromolecular coordination polymers (P3k-P25k) with LCST behaviour from the RAFT polymerization with chain transfer agent DMP-APTRZ *via* gel-permeation chromatography in DMAc with LiBr.

Table S15: The summarized experimental data of the LCST-typed hemi-telechelic polymer ligands poly(NIPAAm)-DMP-APTRZ with various chain lengths. The sample code of the polymers, experimental molar masses (\bar{M}_n) with corresponding degree of polymerization (X_n), dispersities (\bar{D}) and resulting cloud points of heating/cooling cycle in water with and without iron ions are shown.

Sample Code	P3k	P4k	P7k	P12k	P23k	P25k	
$\bar{M}_{n,theo}$	2.2	3.3	6.1	11.8	17.5	17.5	
/ kg·mol ⁻¹ (X_n)	(15)	(25)	(50)	(100)	(150)	(150)	
$\bar{M}_{n,NMR}$	3.8	4.0	..[b]	..[b]	..[b]	21.2	
/ kg·mol ⁻¹ (X_n)	(26)	(30)	..[b]	..[b]	..[b]	(183)	
$\bar{M}_{n,GPC}^{[a]}$	3.1	3.9	6.9	12.3	23.3	24.8	
/ kg·mol ⁻¹ (X_n)	(21)	(30)	(57)	(104)	(199)	(212)	
$\bar{D}^{[a]}$	1.38	1.27	1.38	1.34	1.12	1.19	
$T_{c,heat}^{[c]}$ / °C	H ₂ O	34.5	33.4	32.9	34.1	34.8	..[b]
$T_{c,cool}^{[c]}$ / °C		32.9	31.5	30.1	31.3	32.0	..[b]
$T_{c,heat}^{[c]}$ / °C	Fe ²⁺ _{aq.}	30.2 ^[d]	32.2 ^[d]	31.5 ^[d]	33.2 ^[d]	33.4 ^[d]	..[b]
$T_{c,cool}^{[c]}$ / °C		27.0 ^[d]	30.6 ^[d]	28.8	30.4	31.2	..[b]

[a] Molar mass determined *via* gel-permeation chromatography in DMAc with LiBr.

[b] Values not determined.

[c] Cloud point determined *via* turbidity measurement by UV-Vis spectroscopy.

[d] Formation of precipitates due to the addition of iron salt above/below the cloud point.

The influence of the molar mass on the thermoresponsive behaviour of the ligands is shown in Figure S59 for samples P4k and P12k by the turbidity measurement in aqueous medium (1.0 wt%) with and without iron ions.

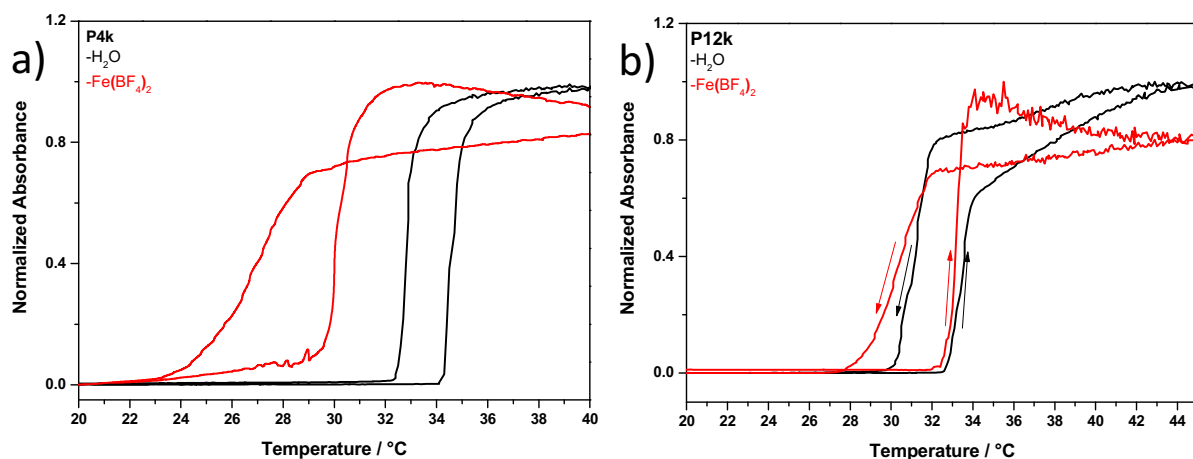


Figure S59: Turbidity measurement for the cloud point determination of the LCST-typed hemi-telechelic polymer ligand poly(NIPAAm)-DMP-APTRZ a) (P4k) and b) (P12k) as 1.0 wt% aqueous polymer solution of ($v=550$ nm) and after the addition of tenfold molar excess of $\text{Fe}(\text{BF}_4)_2$ ($v=740$ nm) by UV-Vis spectroscopy.

The influence of the iron ions on the aggregation behaviour of the bare polymer without triazole moiety poly(NIPAAm)-DMP (P25kCOOH) is shown in Figure S60 by the comparison between the aggregation sizes in aqueous medium with and without Fe^{2+} . PNIPAAm possesses a minor concentration dependency with respect to the aggregation behaviour, so that a diluted solution was studied in DLS (more precision).

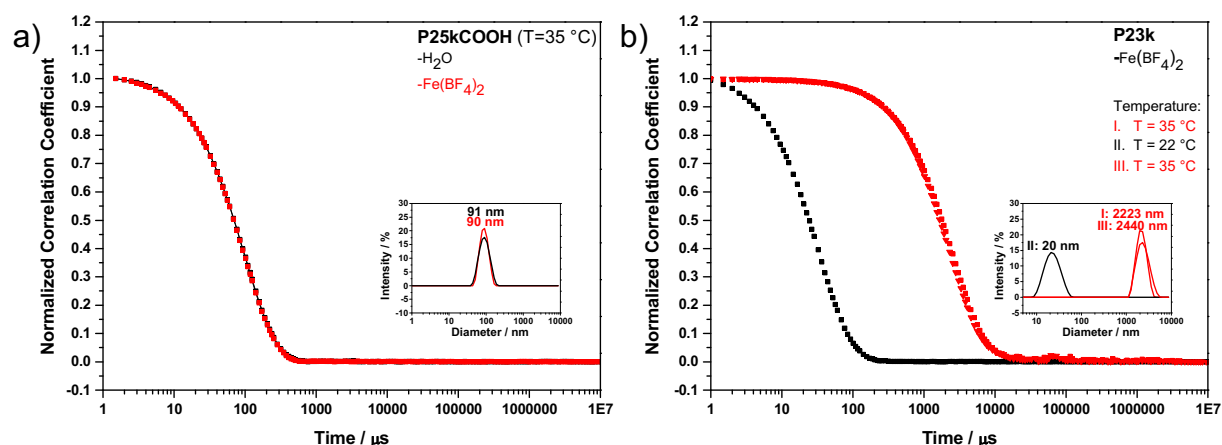


Figure S60: DLS measurement for a) the reference study of the iron-ion influence of the aggregation behaviour of a bare polymer without triazolyl moiety poly(NIPAAm)-DMP (P25kCOOH) in aqueous solution (0.1 wt%) with and without iron ions at 35 °C and b) the study of the reversibility of the switchable aggregation states of the long macromolecular hemi-telechelic ligand poly(NIPAAm)-DMP-APTRZ (P23k) in aqueous solution (0.1 wt%) in presence of Fe^{2+} in dependence of the temperature variation. The aggregation sizes are analyzed by intensity.

The aggregation behaviour with the apparent aggregation sizes of the hemi-telechelic MCL with varying chain lengths below and above the critical solution temperature (22 °C and 35 °C) in aqueous media (0.1 wt%) in dependence of the presence of iron ions is studied by DLS measurements in Figure S61. Although the provided DLS data of precipitating samples are not appropriate, they are illustrated just as temporal snapshot to confirm the macroscopic growth of the complexation. Both the analyses and the resulted data are shown as indicative values and are not used as such.

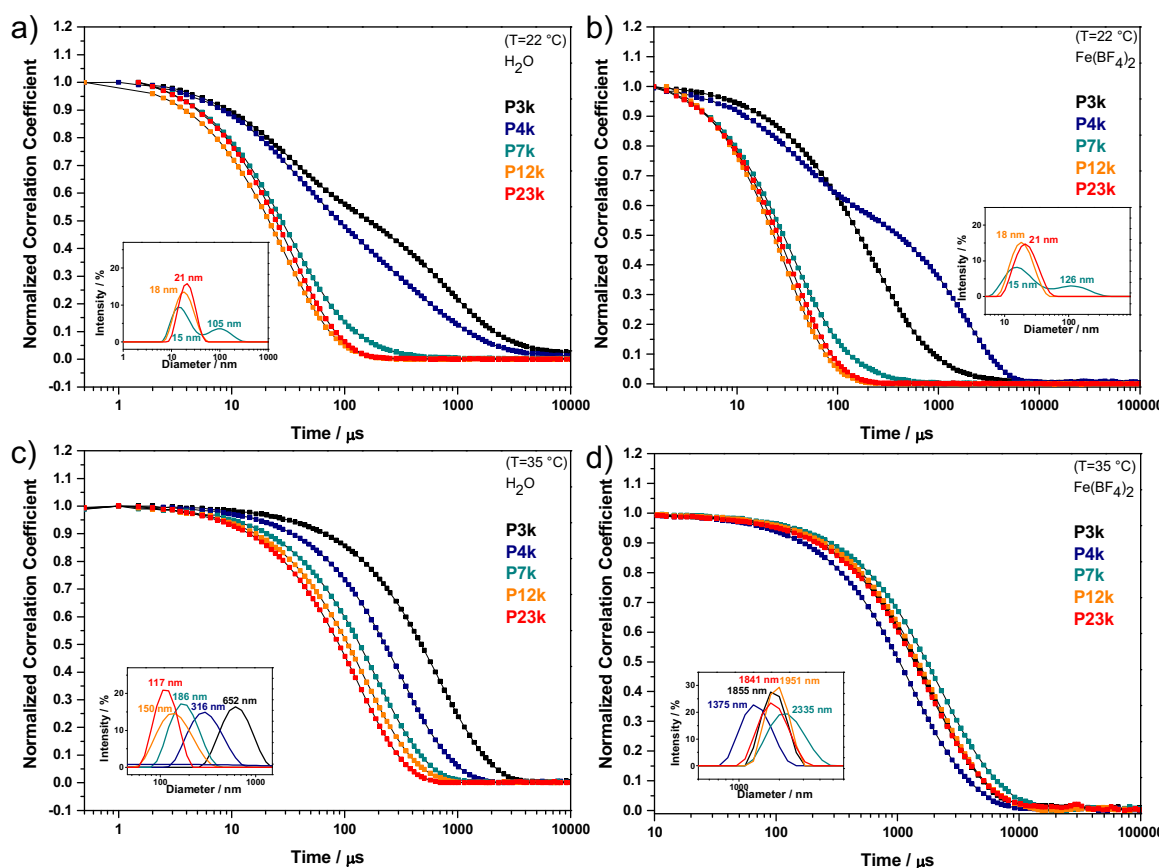


Figure S61: DLS measurement for the study of the iron-ion-sensitive aggregation behaviour of the LCST-typed macromolecular hemi-telechelic ligands poly(NIPAAm)-DMP-APTRZ (P3k-P23k) in dependence of the molar mass of the ligands with their (apparent) hydrodynamic diameter in aqueous solution without (a, c) and with present iron ions (b, d) in a tenfold excess, below (a-b) and above (c-d) the T_c of a 0.1 wt% polymer solution. P3k and P4k precipitated after addition of iron even below the cloud point at 22 °C (variable aggregation sizes). The aggregation sizes are analyzed by intensity.

The data of the aggregation behaviour of *via* the general procedure synthesized macromolecular hemi-telechelic coordination polymers with varied chain lengths are summarized below (Table S16). As discussed above, the data of precipitating samples are simply shown to corroborate the substantial growth of the scattering objects and are not used as precise values.

Table S16: Aggregation and thermoresponsive behaviour in dependence of molar mass (\bar{M}_n), cloud point (T_c) and hydrodynamic diameter at 22 and 35 °C of the LCST-typed hemi-telechelic polymer ligand poly(NIPAAm)-DMP-APTRZ and the reference poly(NIPAAm)-DMP in water with and without iron ions as determined *via* DLS. Aggregation sizes in Fe²⁺-solution described as apparent values. The aggregation sizes are analyzed by intensity.

Sample Code	\bar{M}_n [a] / kg·mol ⁻¹	H ₂ O		Fe ²⁺ _{aq}			
		T_c [d] / °C	$D_{h,22\text{ °C}}$ / nm	$D_{h,35\text{ °C}}$ / nm	T_c [d] / °C	$D_{h,22\text{ °C}}$ / nm	$D_{h,35\text{ °C}}$ / nm
P3k ^[b]	3.1	34.7	md. ^[c]	652	30.2	md. ^[c]	1860
P4k ^[b]	3.9	33.4	md. ^[c]	316	32.2	15 1110	1380
P7k	6.9	32.9	18 108	186	31.5	20 126	2340
P12k	12.3	34.1	20	150	33.2	20	1950
P23k	23.3	34.8	21	117	33.4	21	1990
P25kCOOH	25.3	31.0	md. ^[c]	90	36.0	md. ^[c]	90

[a] Molar mass determined *via* gel-permeation chromatography in DMAc with LiBr.

[b] Formation of precipitates due to the addition of iron salt.

[c] Multiple aggregation size distributions were observed.

[d] The values were extracted from the heating cycle.

The chain length influences the size of the scattering objects of the hemi-telechelic ligands in pure aqueous medium below the T_c . The size of the oligomeric aggregation clusters decreases with rising chain length Figure S62.

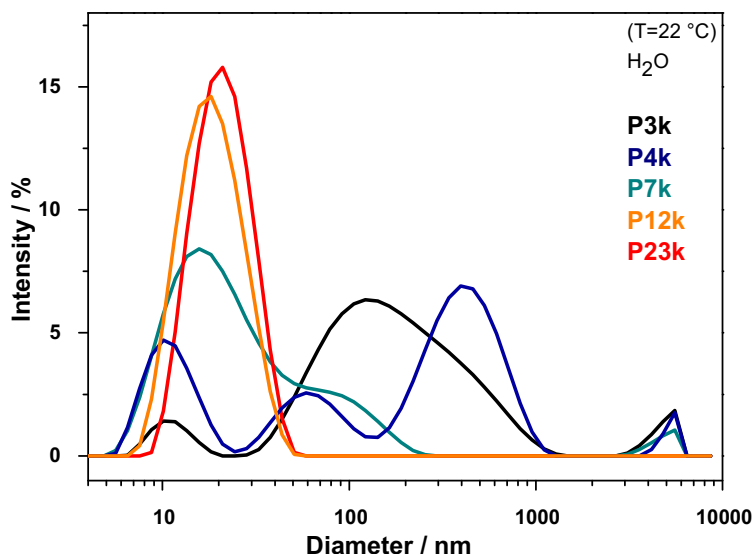


Figure S62: The chain length dependence of the formed aggregation objects of the hemi-telechelic polymer ligands poly(NIPAAm)-DMP-APTRZ (P3k-P23k) in pure aqueous solution in a 0.1 wt% polymer solution below (22 °C) the T_c . The aggregation sizes are represented by intensity.

The influence of the anion and cation type on the aggregation size was investigated by the DLS measurement of the long hemi-telechelic ligand in aqueous solution by addition of different salts above the T_c . The apparent aggregation size is supposed to correlate with the coordination strength between macromolecular ligand and the corresponding ion. The series underlines the exposing properties of divalent iron ions (as attractive driving force) for the formation of expanded complexes.

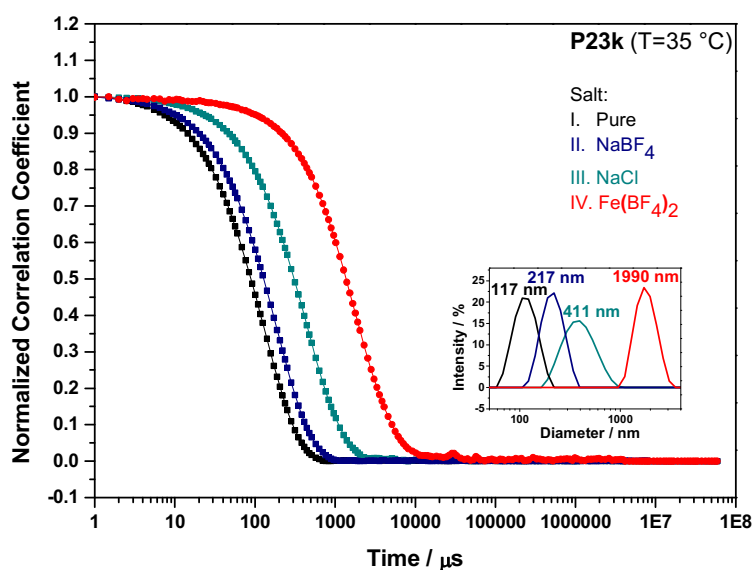


Figure S63: Salt-dependent aggregation behaviour of the LCST-typed hemi-telechelic polymer ligand (P23k) with its (apparent) hydrodynamic diameter in water with and without iron ions with a tenfold excess above (35 °C) the T_c of a 0.1 wt% polymer solution and tenfold excess of corresponding salt. The aggregation sizes are analyzed by intensity.

In addition to the previous DLS studies, the aggregation behaviour of the long hemi-telechelic MCL (P23k) was imaged by TEM measurement (Figure S64) of a trehalose matrix dried from a 0.1 wt% polymer solution at the certain temperature below and above the critical solution temperature (22 °C and 40 °C) with and without iron ions in aqueous media (0.1 wt%).

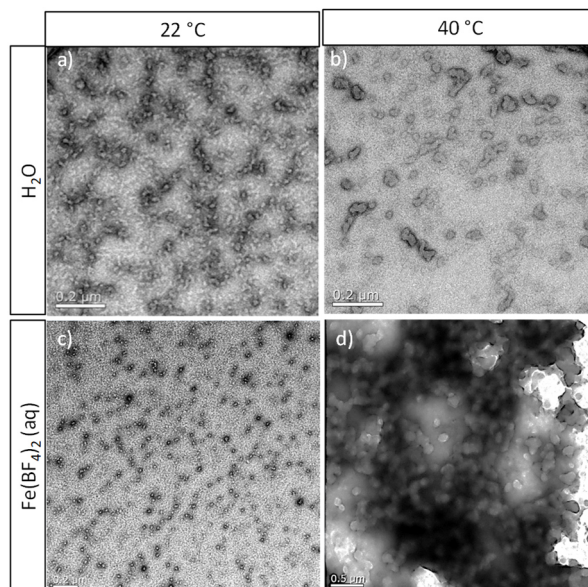


Figure S64: TEM images of the long LCST-typed hemi-telechelic MCL (P23k) prepared in a trehalose matrix and dried from a 0.1 wt% aqueous solution without (a-b) and with present iron ions (c-d) in a tenfold excess, below (a, c) and above (b, d) the T_c .

In pure water below the critical solution temperature ($T=22$ °C) P23k forms truncated wormlike aggregates of 10 nm diameter and length of up to 50 nm (similar range to DLS data, Figure 36b), with very broad length distribution and irregular shape (Figure S64a).

Above the cloud point ($T=40$ °C), globular aggregates with increased dimensions (average around 100 nm, broad distribution, matching DLS data, Figure 36d) and irregular shape are formed, which tend to cluster (Figure S64). An increased hydrophobicity of and stronger affinity between the polymer chains above T_c would explain this behaviour. In solution with iron ions ($T=22$ °C) below the T_c , the long polymer P23k forms highly spherical aggregates with highly spherical geometry and diameters of about 10 nm (Figure S64c, congruent with DLS data, Figure 36b). Probably, Fe^{2+} addition leads to a slight compaction of the aggregates from pure water, but probably due to the large polymer chain, extended 1D complexes cannot form under these conditions. Above T_c (at $T=37$ °C) in presence of iron ions, P23k forms larger, slightly elongated aggregates with globular shape of 100-600 nm diameter and strong tendency to cluster (Figure S64d, note the larger scale bar of 0.5 μ m), explaining also the large increase in correlation time in DLS (Figure 36d). Here, the collapsed polymer chains have less space requirement and may facilitate Fe^{2+} coordination to larger structures.

General Procedure for the RAFT Copolymerization of the UCST-typed Thermoresponsive Hemi-Telechelic Macromolecular Coordination Ligand Poly(AAm-co-AN)-DMP-APTRZ (UCP4k-UCP27k)

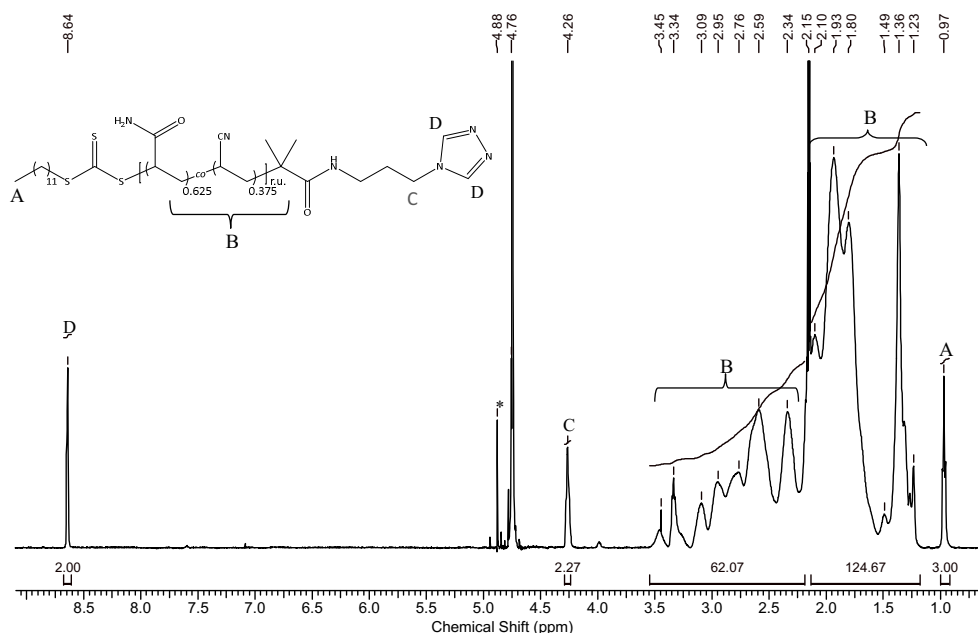


Figure S65: ^1H NMR spectrum (400 Hz) of the UCST-typed hemi-telechelic MCL poly(AAm-co-AN)-DMP-APTRZ (UCP4k), recorded in $\text{D}_2\text{O}/\text{MeCN-d}_3$ (85:15).

The macromolecular properties of *via* the general procedure synthesized macromolecular hemi-telechelic coordination copolymers with varied chain lengths are summarized below (Table S17).

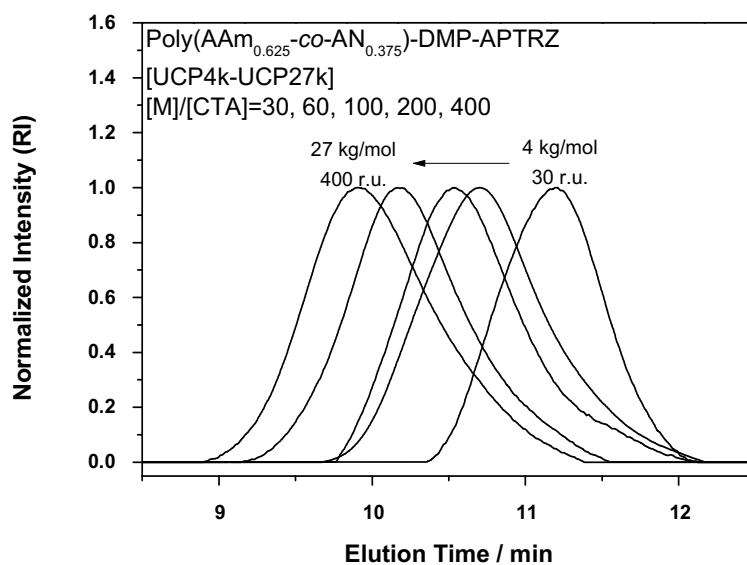


Figure S66: Elugrams of the hemi-telechelic macromolecular coordination polymers (UCP4k-UCP27k) with UCST behaviour from the RAFT polymerization with chain transfer agent DMP-APTRZ *via* gel-permeation chromatography in water/MeCN with NaNO_3 .

Table S17: The summarized experimental data of the UCST-typed hemi-telechelic copolymer ligands poly(AAm_{0.625}-co-AN_{0.375})-DMP-APTRZ with various chain lengths. The sample code of copolymers, experimental molar masses (\bar{M}_n) with corresponding degree of polymerization (X_n), dispersities (\bar{D}) and the resulting cloud points of heating/cooling cycle in water with and without iron ions are shown.

Sample Code	UCP4k	UCP7k	UCP8k	UCP16k	UCP27k	UCP14kCOOH	UCP16kCOOH	
$\bar{M}_{n,theo.}$	2.4	4.3	6.9	13.3	26.2	13.1	19.5	
/ kg·mol ⁻¹ (X_n)	(30)	(60)	(100)	(200)	(400)			
$\bar{M}_{n,NMR}$	4.5	8.3	8.8	15.4	21.2	13.6	18.1	
/ kg·mol ⁻¹ (X_n)	(56)	(116)	(127)	(232)	(324)			
$\bar{M}_{n,GPC}^{[a]}$	4.2	6.5	8.4	15.6	26.8	14.2	16.1	
/ kg·mol ⁻¹ (X_n)	(53)	(91)	(122)	(232)	(409)			
$\bar{D}^{[a]}$	1.36	1.44	1.63	1.72	1.52	1.40	1.28	
$T_{c,heat}^{[c]}$ / °C	H ₂ O	16.2	-	25.3	25.3	40.7	28.6	28.1
$T_{c,cool}^{[c]}$ / °C		11.5	-	18.8	19.9	34.8	28.0	26.3
$T_{c,heat}^{[c]}$ / °C	Fe ²⁺ _{aq.}	34.0 ^[e]	14.3	30.0	31.4	43.5	.. ^[d]	15.2
$T_{c,cool}^{[c]}$ / °C		21.2 ^[e]	6.7 ^[e]	26.1 ^[e]	25.7 ^[e]	37.0 ^[e]	.. ^[d]	25.4

^[a] Molar mass determined *via* gel-permeation chromatography in H₂O/MeCN (85:15) with NaNO₃.

^[b] Incorporation ratio determined *via* ¹H NMR.

^[c] Cloud point determined *via* turbidity measurement by UV-Vis spectroscopy.

^[d] Precise values not determined.

^[e] Formation of precipitates due to the addition of iron salt above/below the cloud point.

The influence of the molar mass on the thermoresponsive behaviour of the ligands is shown in Figure S67 for samples UCP4k and UCP16k by the turbidity measurement in aqueous medium (1.0 wt%) with and without iron ions.

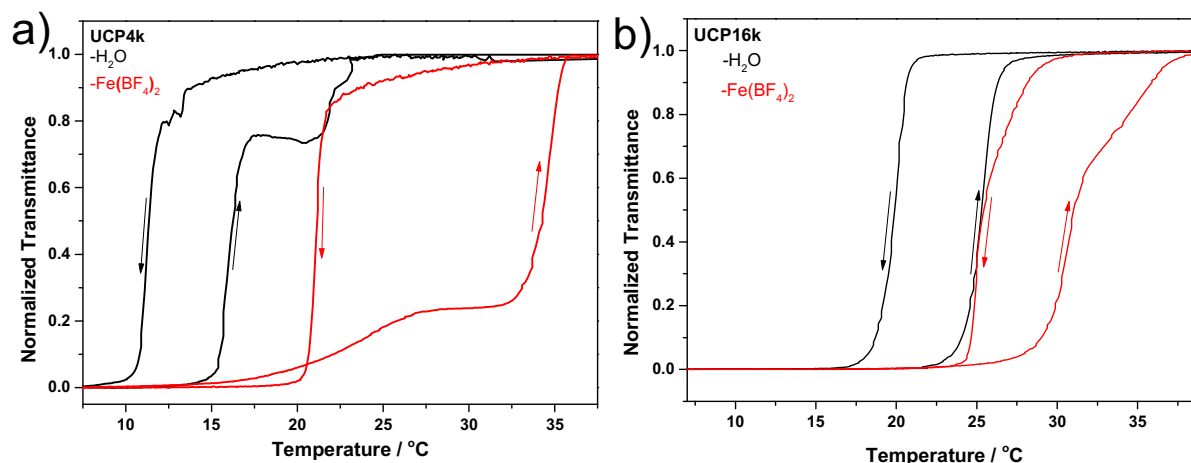


Figure S67: Turbidity measurement for the cloud point determination of the UCST-typed hemi-telechelic polymer ligands poly(AAm_{0.625}-co-AN_{0.375})-DMP-APTRZ with varying molar mass of a) UCP4k and b) UCP16k as 1.0 wt% aqueous polymer solution of ($\nu=550$ nm) and after the addition of tenfold molar excess of Fe(BF₄)₂ ($\nu=740$ nm) by UV-Vis spectroscopy.

The influence of the iron ions on the aggregation behaviour of the bare polymer without triazole moiety poly(AAm_{0.625}-co-AN_{0.375})-EMP (UCP14kCOOH) is shown in Figure S68 by the comparison of the aggregation sizes between aqueous medium with and without iron ions.

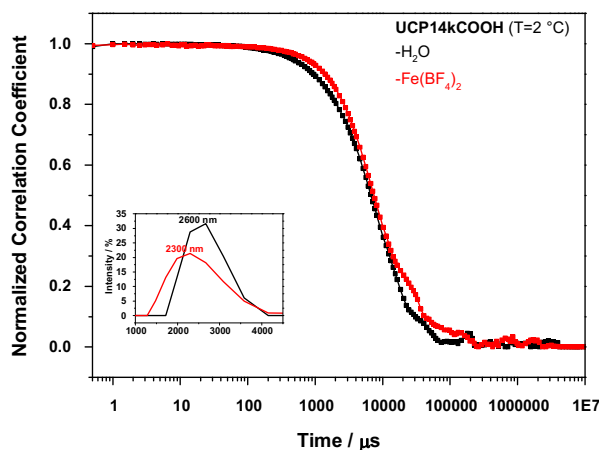


Figure S68: DLS measurement for the reference study of the iron-ion influence of the aggregation behaviour of a bare polymer without triazolyl moiety poly(AAm_{0.625}-co-AN_{0.375})-EMP (UCP14kCOOH) in aqueous solution (1.0 wt%) at 2 °C with and without iron ions by the (apparent) hydrodynamic diameter. The aggregation sizes are analyzed by intensity.

The data of the aggregation behaviour of *via* the general procedure synthesized macromolecular hemi-telechelic coordination polymers with varied chain lengths are summarized below (Table S18). As discussed below, the data of precipitating samples are simply shown to corroborate the substantial growth of the scattering objects and are not used as precise values.

Table S18: Aggregation and thermoresponsive behaviour in dependence of molar mass (\bar{M}_n), cloud point (T_c) and hydrodynamic diameter at 2 and 50 °C of the UCST-typed hemi-telechelic copolymer ligand poly(AAm_{0.625}-co-AN_{0.375})-DMP-APTRZ and the reference poly(AAm_{0.625}-co-AN_{0.375})-EMP in pure aqueous solution with and without iron ions as determined *via* DLS. Aggregation sizes in Fe²⁺-solution described as apparent values. Aggregation sizes in brackets represent neglectable species. The aggregation sizes are analyzed by intensity.

Sample Code	\bar{M}_n ^[a] / kg·mol ⁻¹	H ₂ O			Fe ²⁺ _{aq}		
		T_c ^[d] / °C	$D_{h,2\text{ °C}}$ / nm	$D_{h,50\text{ °C}}$ / nm	T_c ^[d] / °C	$D_{h,2\text{ °C}}$ / nm	$D_{h,50\text{ °C}}$ / nm
UCP4k ^[b]	4.2	11.5	955 (5560)	14 458	21.2	3090 ^[b]	9 18 ^[b]
UCP7k ^[b]	6.5	-	md. ^[c]	14 295	6.7	1990 ^[b]	18 295
UCP8k	8.4	18.8	295 (5560)	21 122	26.1	3580 ^[b]	24
UCP16k	15.6	19.9	220	16 220	25.7	3600 ^[b]	38
UCP27k	26.8	34.8	164 825	21 122	37.0	1990 ^[b]	(10) 68
UCP16kCOOH	16.1	26.3	2305	(10) 68	25.4	2310	4

^[a] Molar mass determined *via* gel-permeation chromatography in H₂O/MeCN (85:15) with NaNO₃.

^[b] Formation of precipitates due to the addition of iron salt.

^[c] Multiple aggregation size distributions were observed.

^[d] The values were extracted from the cooling cycle.

The aggregation behaviour with the apparent aggregation sizes of the hemi-telechelic MCLs with varying chain lengths below and above the critical solution temperature (2 °C and 50 °C) in aqueous solution (1.0 wt%) with and without present iron ions is studied by DLS measurements in Figure S69. Although the provided DLS data of precipitating samples are not valid, they are illustrated just as temporal snapshot to confirm the macroscopic growth of

the complexation. Both the analyses and the resulted data are shown as indicative values and are not used as such.

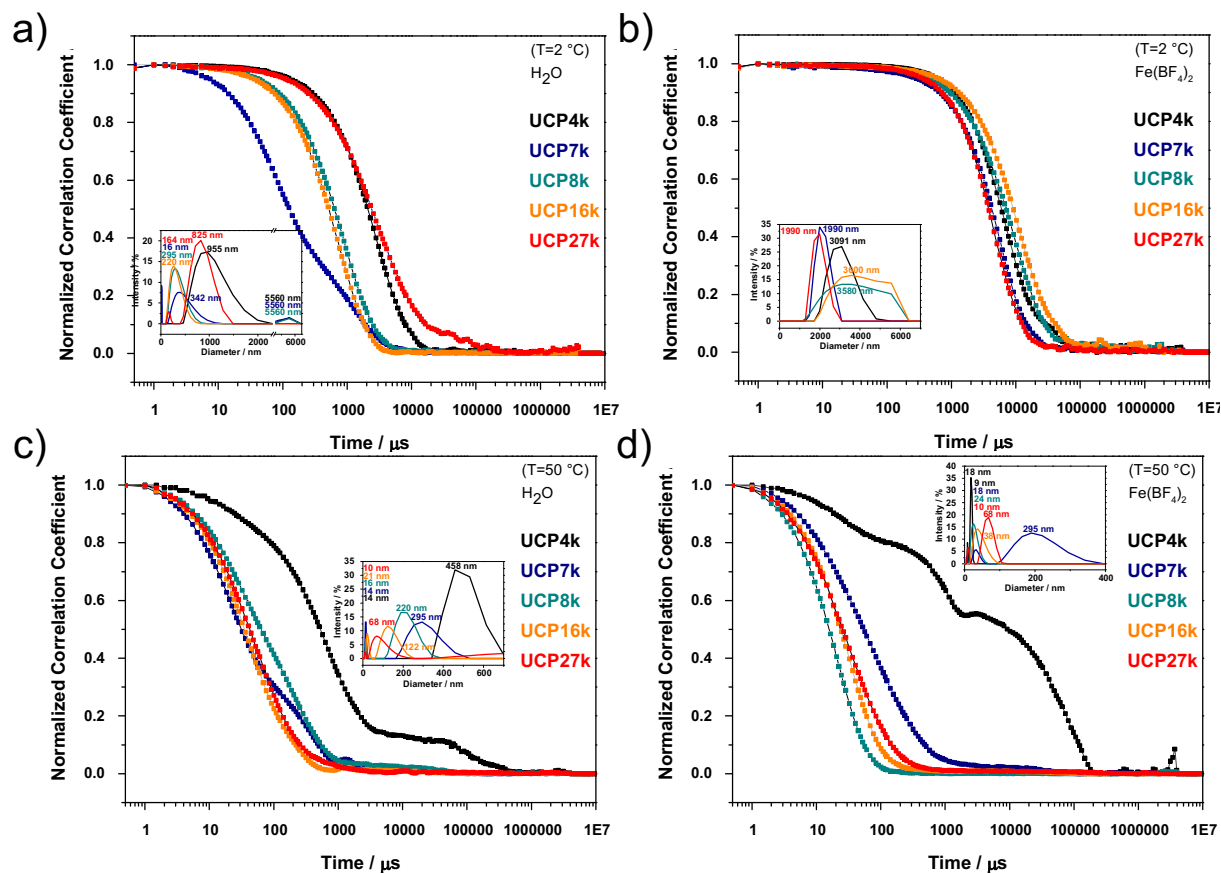


Figure S69: DLS measurement for the study of the iron-ion-sensitive aggregation behaviour of the UCST-typed macromolecular hemi-telechelic ligands poly(AAm-co-AN)-DMP-APTRZ (UCP4k-UCP27k) in dependence of the molar mass of the ligands with their (apparent) hydrodynamic diameter in aqueous solution without (a, c) and with iron ions (b, d) in a tenfold excess, below (a-b) and above (c-d) the T_c of a 1.0 wt% polymer solution. P4k precipitated after addition of iron even above the cloud point at 50 °C (variable aggregation sizes). The aggregation sizes are analyzed by intensity.

16.7.3. Multidentate Macromolecular Coordination Ligands

General Procedure for the RAFT Copolymerization of the LCST-typed Thermo-responsive Multidentate Coordination Copolymer Poly(NIPAAm_x-co-APTRZMAAm_y)-EMP (C4.8k5%-C4.6k15%)

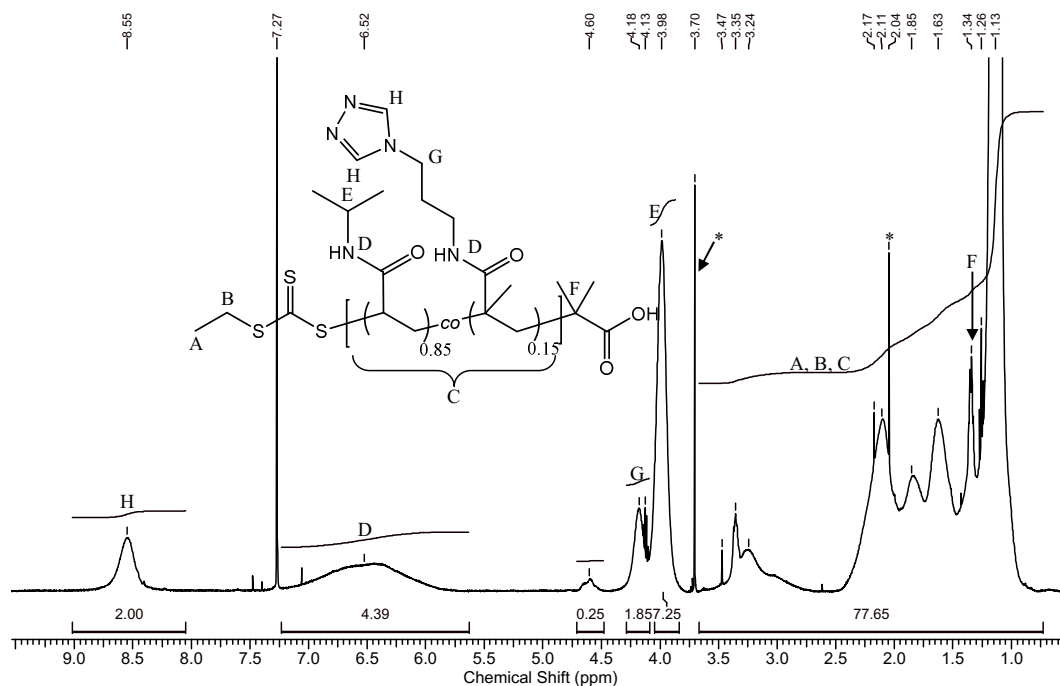


Figure S70: ^1H NMR spectrum (500 Hz) of the LCST-typed multidentate MCL poly(NIPAAm-co-APTRZMAAm)-EMP (C4.6k15%), recorded in CDCl_3 .

Table S19: The summarized experimental data of the LCST-typed multidentate copolymer ligands poly(NIPAAm-co-APTRZMAAm)₂₅-EMP with various molar fractions of the triazole monomer APTRZMAAm. The sample code of copolymers, experimental molar masses (\bar{M}_n) with corresponding degree of polymerization (X_n), dispersities (\mathcal{D}), incorporation ratio of the APTRZMAAm and the resulting cloud points of heating/cooling cycle in water with and without iron ions are shown.

Sample Code	C4.8k5%	C4.9k10%	C4.6k15%
$\bar{M}_{n,theo}$	3.2	3.3	3.4
/ $\text{kg}\cdot\text{mol}^{-1}$ (X_n)	(25)	(25)	(25)
$\bar{M}_{n,NMR}$..[d]	..[d]	..[d]
/ $\text{kg}\cdot\text{mol}^{-1}$ (X_n)			
$\bar{M}_{n,GPC}^{[a]}$	4.8	4.9	4.6
/ $\text{kg}\cdot\text{mol}^{-1}$ (X_n)	(36)	(33)	(33)
$\mathcal{D}^{[a]}$	1.07	1.08	1.10
$[\text{APTRZMAAm}]_{\text{feed}}$ / mol%	5.0	10.00	15.00
$[\text{APTRZMAAm}]_{\text{incorporated}}$ / mol% ^[b]	4.1	7.6	13.8
$T_{c,heat}^{[c]}$ / °C	H ₂ O	36.6	39.1
$T_{c,cool}^{[c]}$ / °C			
$T_{c,heat}^{[c]}$ / °C	Fe ²⁺ -aq	25.4 ^[e]	29.1 ^[e]
$T_{c,cool}^{[c]}$ / °C			

^[a] Molar mass determined *via* gel-permeation chromatography in DMAc with LiBr.

^[b] Incorporation ratio determined *via* ^1H NMR.

^[c] Cloud point determined *via* turbidity measurement by UV-Vis spectroscopy.

^[d] Molar masses not determinable *via* ^1H NMR.

^[e] Formation of precipitates due to the addition of iron salt above/below the cloud point.

The macromolecular properties of *via* the general procedure synthesized macromolecular multidentate coordination copolymers with molar fractions of the triazole monomer APTRZMAAm are summarized above (Table S19).

The aggregation behaviour with the apparent aggregation sizes of the multidentate MCLs with varying molar fraction of the triazole monomer APTRZMAAm below and above the critical solution temperature (20 °C and 60 °C) in aqueous media (1.0 wt%) with and without present iron ions is studied by DLS measurements in Figure S71. Although the provided DLS data of precipitating samples are not appropriate, they are illustrated just as temporal snapshot to confirm the macroscopic growth of the complexation. Both the analyses and the resulted data are shown as indicative values and are not used as such.

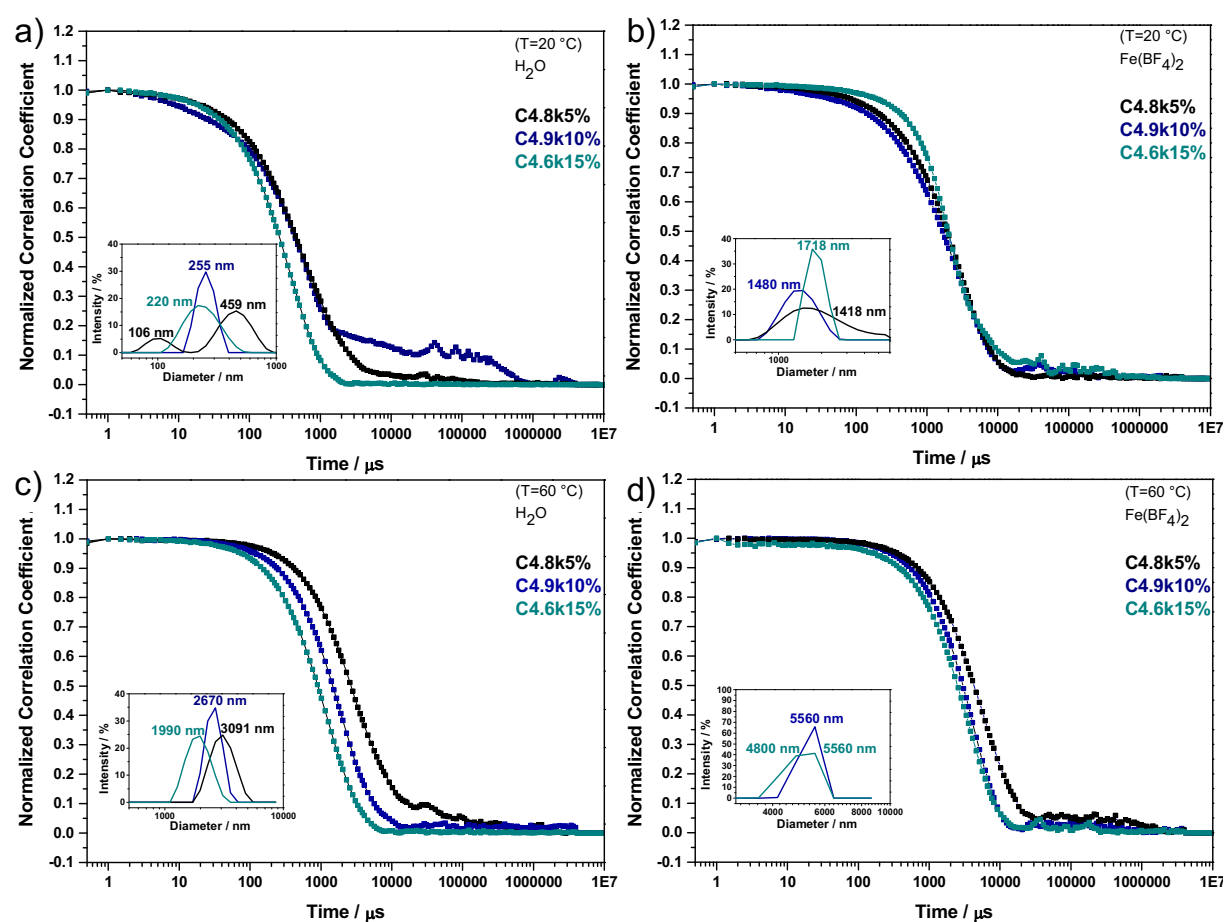


Figure S71: DLS measurement for the study of the iron-ion-sensitive aggregation behaviour of the LCST-typed macromolecular multidentate ligands poly(NIPAAm-co-APTRZMAAm)-EMP (C4.8k5%-C4.6k15%) in dependence of the molar fraction of the triazole monomer APTRZMAAm in the copolymer chain with their (apparent) hydrodynamic diameter in aqueous media without (a, c) and with present iron ions (b, d) in a tenfold excess, below (a-b) and above (c-d) the T_c of a 1.0 wt% polymer solution. The samples precipitated after addition of iron (b, d) even below the cloud point at 20 °C (variable aggregation sizes). The aggregation sizes are analyzed by intensity.

The data of the aggregation behaviour of *via* the general procedure synthesized macromolecular multidentate coordination polymers with varied fractions of the triazole monomer APTRZMAAm are summarized below (Table S20). As discussed above, the data

of precipitating samples are simply shown to corroborate the substantial growth of the scattering objects and are not used as precise values.

Table S20: Aggregation and thermoresponsive behaviour in dependence of the molar fraction of the triazole monomer APTRZMAAm, cloud point (T_c) and hydrodynamic diameter at 20 and 60 °C of the LCST-typed multidentate copolymer ligand poly(NIPAAm-co-APTRZMAAm)₂₅-EMP in pure aqueous solution with and without iron ions as determined *via* DLS. Aggregation sizes in Fe²⁺-solution described as apparent values. The aggregation sizes are analyzed by intensity.

Sample Code	[APTRZMAAm] / mol%	H ₂ O			Fe ²⁺ _{aq}		
		$T_{c, heat}^{[b]}$ / °C	$D_{h, 20 °C}$ / nm	$D_{h, 60 °C}$ / nm	$T_{c, heat}^{[b]}$ / °C	$D_{h, 20 °C}$ / nm	$D_{h, 60 °C}$ / nm
C4.8k5%	5.0	36.6	459 106	3091	35.9	1420	9450 ^[a]
C4.9k10%	10.0	39.1	255	2670	33.1	1480	5560 ^[a]
C4.6k15%	15.0	44.7	220	1990	32.4	1720 ^[a]	4800 ^[a]

^[a] Formation of precipitates due to the addition of iron salt.

^[b] The values were extracted from the heating cycle.

General Procedure for the RAFT Copolymerization of the UCST-typed Thermo-responsive Multidentate Coordination Copolymer Poly(AAm_x-co-AN_y-co-APTRZMAAm_z)-EMP (UCP11.6k2.5%-UCP13.7k10%)

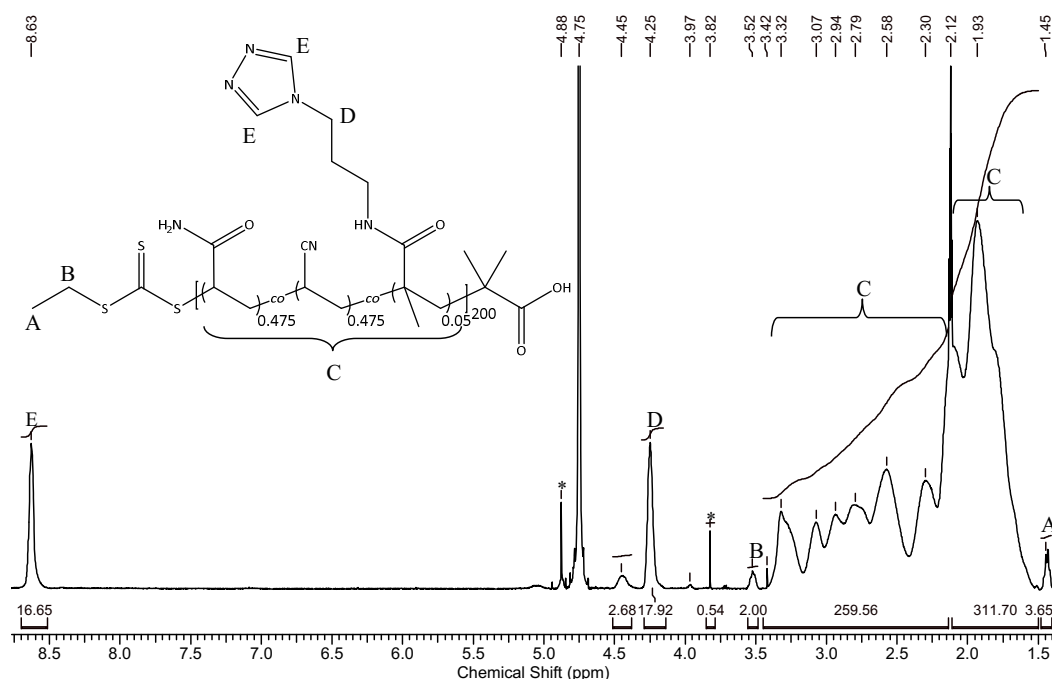


Figure S72: ^1H NMR spectrum (500 Hz) of the UCST-typed multidentate MCL poly(AAm-co-AN-co-APTRZMAAm)-EMP (UCP14.9k5%), recorded in $\text{D}_2\text{O}/\text{MeCN-d}_3$ (85:15).

Table S21: The summarized experimental data of the UCST-typed multidentate copolymer ligands poly(AAm-co-AN-co-APTRZMAAm)₂₀₀-EMP with various molar fractions of the triazole monomer APTRZMAAm. The sample code of copolymers, experimental molar masses (\bar{M}_n) with corresponding degree of polymerization (X_n), dispersities (D), incorporation ratio of the APTRZMAAm and resulting cloud points of heating/cooling cycle in water with and without iron ions are shown.

Sample Code		UCP11.6k2.5%	UCP14.9k5.0%	UCP13.7k10.0%
$\bar{M}_{n,theo.}$		13.3	13.9	15.6
/ $\text{kg}\cdot\text{mol}^{-1}$ (X_n)		(200)	(200)	(200)
$\bar{M}_{n,NMR}$		11.6	14.9	13.7
/ $\text{kg}\cdot\text{mol}^{-1}$ (X_n)		(175)	(214)	(176)
$\bar{M}_{n,GPC}^{[a]}$		12.2	8.3 ^[d]	6.4 ^[d]
/ $\text{kg}\cdot\text{mol}^{-1}$ (X_n)		(184)	(119)	(82)
$D^{[a]}$		1.11	1.21	1.24
$[\text{APTRZMAAm}]_{\text{feed}}$		2.5	5.0	10.0
/ mol%				
$[\text{APTRZMAAm}]_{\text{incorporated}}$		2.5	4.4	7.4
/ mol% ^[b]				
$T_{c,heat}^{[c]}$	H_2O	49.7	41.3	34.7
/ $^\circ\text{C}$				
$T_{c,cool}^{[c]}$	$\text{Fe}^{2+}_{\text{aq}}$	50.5	45.2	35.6
/ $^\circ\text{C}$				
$T_{c,heat}^{[c]}$	$\text{Fe}^{2+}_{\text{aq}}$	19.8 ^[e]	22.9 ^[e]	36.5 ^[e]
/ $^\circ\text{C}$				
$T_{c,cool}^{[c]}$	$\text{Fe}^{2+}_{\text{aq}}$	56.2 ^[e]	46.4 ^[e]	48.7 ^[e]
/ $^\circ\text{C}$				

^[a] Molar mass determined *via* gel-permeation chromatography in DMAc with LiBr.

^[b] Incorporation ratio determined *via* ^1H NMR.

^[c] Cloud point determined *via* turbidity measurement by UV-Vis spectroscopy.

^[d] Molar masses determined *via* gel-permeation chromatography affected by varying coiling of copolymers in eluent DMAc.

^[e] Formation of precipitates due to the addition of iron salt above/below the cloud point.

The macromolecular properties of *via* the general procedure synthesized macromolecular multidentate coordination copolymers with molar fractions of the triazole monomer APTRZMAAm are summarized above (Table S21).

The aggregation behaviour with the apparent aggregation sizes of the multidentate MCLs with varying molar fraction of the triazole monomer APTRZMAAm below and above the critical solution temperature (20 °C and 60 °C / 70 °C) in aqueous media (1.0 wt%) with and without iron ions is studied by DLS measurements in Figure S73. Although the provided DLS data of precipitating samples are not appropriate, they are illustrated just as temporal snapshot to confirm the macroscopic growth of the complexation. Both the analyses and the resulted data are shown as indicative values and are not used as such.

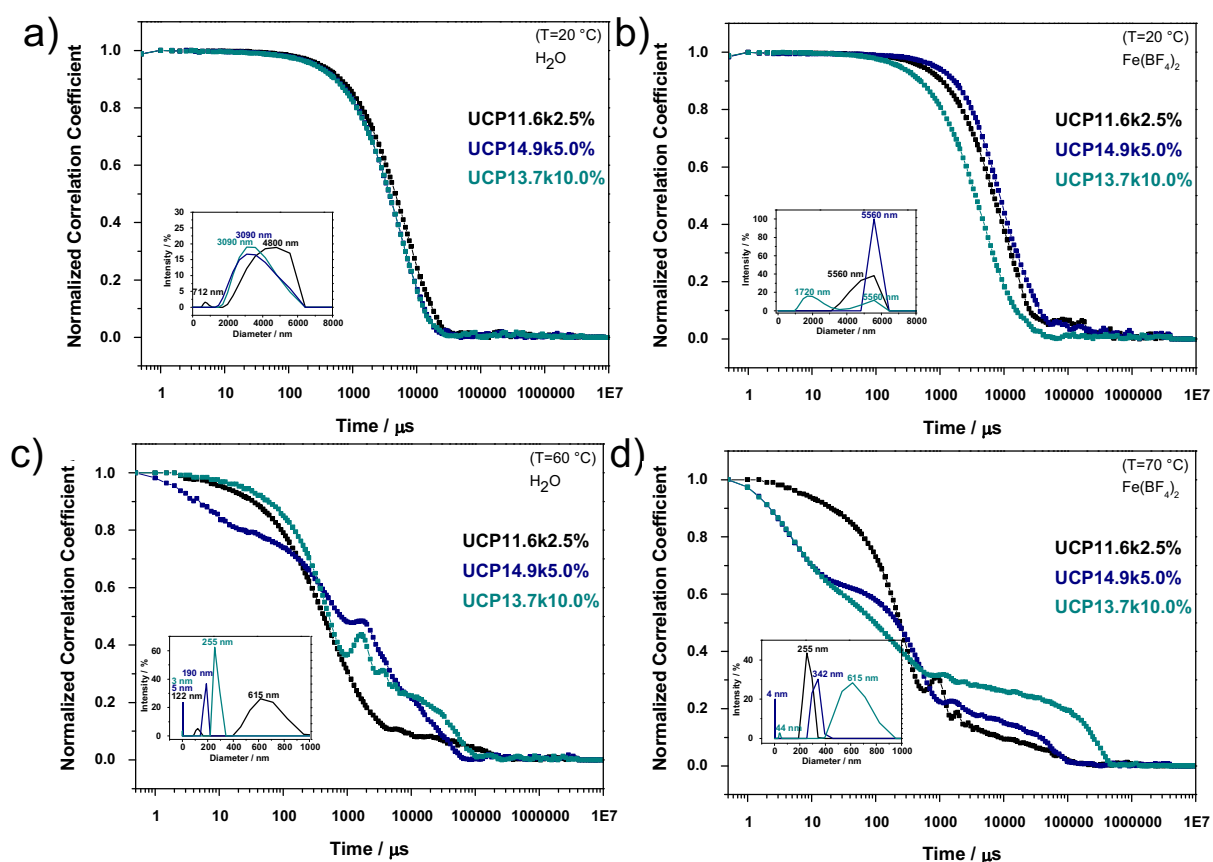


Figure S73: DLS measurement for the study of the iron-ion-sensitive aggregation behaviour of the UCST-typed macromolecular multidentate ligands poly(AAm-*co*-AN-*co*-APTRZMAAm)-EMP (UCP11.6k2.5%-UCP13.7k10.0%) in dependence of the molar fraction of the triazole monomer APTRZMAAm in the copolymer chain with their (apparent) hydrodynamic diameter in aqueous media without (a, c) and with present iron ions (b, d) in a tenfold excess, below (a-b) and above (c-d) the T_c of a 1.0 wt% polymer solution. The samples precipitated after addition of iron (b, d) even above the cloud point at 70 °C (variable aggregation sizes). The aggregation sizes are analyzed by intensity.

The data of the aggregation behaviour of *via* the general procedure synthesized macromolecular multidentate coordination polymers with varied fractions of the triazole monomer APTRZMAAm are summarized below (Table S22). As discussed above, the data of precipitating samples are simply shown to corroborate the substantial growth of the scattering objects and are not used as precise values.

Table S22: Aggregation and thermoresponsive behaviour in dependence of the molar fraction of the triazole monomer APTRZMAAm, cloud point (T_c) and hydrodynamic diameter at 20 and 60 °C (in presence of Fe^{2+} : 70 °C) of the UCST-typed multidentate copolymer ligand poly(AAm-co-AN-co-APTRZMAAm)₂₀₀-EMP in pure aqueous solution with and without iron ions as determined *via* DLS. Aggregation sizes in Fe^{2+} -solution described as apparent values. The aggregation sizes are analyzed by intensity.

Sample Code	[APTRZMAAm] / mol%	H ₂ O			Fe ²⁺ _{aq}		
		$T_{c, \text{heat}}^{[b]}$ / °C	$D_h, 20\text{ °C}$ / nm	$D_h, 60\text{ °C}$ / nm	$T_{c, \text{heat}}^{[b]}$ / °C	$D_h, 20\text{ °C}$ / nm	$D_h, 70\text{ °C}$ / nm
UCP11.6k2.5%	2.5	50.5	(712) 4800	122 615	56.2	5560 ^[a]	260 ^[a]
UCP14.9k5.0%	5.0	45.2	3090	5 615	46.2	5560 ^[a]	4 ^[a] 340 ^[a]
UCP13.7k10%	10.0	35.6	3090	(3) 255	48.7	1720 ^[a] 5560 ^[a]	(44) ^[a] 620 ^[a]

^[a] Formation of precipitates due to the addition of iron salt.

^[b] The values were extracted from the cooling cycle.

16.8. Thermoresponsive Copolymer Vectors for Gene Delivery

16.8.1. Biochemical Experimental Part

The copolymers were applied as non-viral copolymer vectors in the research field of gene delivery. The biological tests were performed mainly by the collaboration partners assistant Prof. Dr. Tony Le Gall and Dr. Yann Le Guen from the working group of Prof. Dr. Tristan Montier in medical faculty in the University of Brest (F). The experiments were done under my observation and the duplicates of the complexation assays were reperformed by myself practically.

For the sake of completeness, the following procedures, instrumentation and assays are noted below.

Materials: The plasmid DNA pGM144²⁷² (3.7 kb) was used for the tests. It was amplified and purified by Aldevron (production lot # 83649). Three cell lines were used i.e. A549 (ATCC® CCL-185™, human epithelial lung carcinoma cells), HeLa (ATCC® CCL-2™, human epithelial ovarian carcinoma cells) and C2C12 (ATCC® CRL-1772™, murine myoblast cells).

Polymer Stock Solutions Preparation: Stock solution of the vectors were prepared in concentration of 5 mg/mL. These were stored not longer than a month in the dark and cold at T=-20 °C.

Polyplexes Preparation: Polymer/DNA mixtures i.e., polyplexes were prepared either in 20 mM HEPES or in 0.9% NaCl solution. Various concentrations of the vectors were added to a fixed amount of pDNA in solution. The mass ratio (MR) was used to define the ratio between the mass of a given copolymer and the mass of pDNA (polymer/DNA). The resulted mixture was kept at r.t. for at least 15 min before subsequent uses (detailed hereafter). Branched PEI (Sigma) was used as reference.

Fluorescence Measurements: The aromatic dye ethidium bromide (EtBr) was used to evaluate the condensation of the pDNA in the polyplexes (as described in literature ²⁷³). This DNA-intercalating stain emits under excitation (λ_{exc} =530 nm) a fluorescence at 590 nm. The analyses were done by a Mithras2 multiplate reader (Berthold) or a 7300 Real Time PCR System (Applied Biosystems).

Gel Retardation Assay: Polyplexes were assayed using electrophoresis in EtBr-stained agarose gel (0.8%). After 30 min at 100 V/90 mA, the gel was imaged using an UV transilluminator (Fisher Bioblock).

Cell Culture: Every cell line was grown in Dulbecco's Modified Eagle Medium (DMEM) supplemented with 10% heat inactivated fetal bovine serum (FBS), 1.0% L-glutamine and

1.0% antibiotics (100 units/mL penicillin, 100 µg/mL streptomycin). Incubations were carried out at T=37 °C (unless otherwise stated), in a humidified atmosphere containing 5% CO₂. DMEM, FBS, penicillin, and streptomycin were purchased from Invitrogen.

Cell Transfection: The transfection experiments were performed as reported before.²⁷⁴ The day before the experiments the cells were seeded into 96-well plates with a density of 25 000 cells per well. Naked pDNA and polyplexes were added dropwise into each well (0.25 µg of DNA per well). After 36 h at T=37 °C, the culture medium was removed, and the cells were lysed by adding 0.5 X Passive Lysis Buffer (Promega) into each well. The chemiluminescence Luciferase Assay System (Promega) was carried out for all lysates to determine luciferase expression, while the BC Assay kit (Uptima) was used to quantify the total protein content. Finally, data were expressed as relative light units (RLU) per milligram of total proteins (mean ± SD with n=3).

Cell Viability: The number of living cells being present in each well (resulting from both cell proliferation and cell death that occurred during the experiment) was determined using the ViaLight kit (Lonza) after 24 hours (as recommended by the manufacturer). The results were expressed as percentages relative to the signal intensity measured with non-transfected cells used as reference (100% cell viability).

16.8.2. The Macromolecular Properties of the Copolymer Vectors

The experimental data of the macromolecular properties are summarized below in Table S23 and Table S24. The sample codes of the copolymer vectors, the theoretical and experimental molar masses, the corresponding dispersities, the resulting cloud points and the yields are shown below.

Table S23: The comparison of the theoretical and experimental (*via* GPC and ^1H NMR) molar masses of references and copolymer vectors for gene delivery including dispersities (\mathcal{D}), cloud points (T_c) and yields.

Sample Code	Type	\bar{M}_{theo} / $\text{kg}\cdot\text{mol}^{-1}$	\bar{M}_{NMR} / $\text{kg}\cdot\text{mol}^{-1}$	$\bar{M}_{n,GPC}^{[i]}$ / $\text{kg}\cdot\text{mol}^{-1}$	$\mathcal{D}^{[i]}$	$T_c^{[c]}$ / $^{\circ}\text{C}$	Yield / % (mg)
R1	Reference	- [a]	- [a]	24.3	2.62	26.8	53 (187)
R2		13.3	11.6	12.8	1.30	17.0	69 (240)
R3		13.0	11.3	13.7	1.40	37.5	45 (176)
R4		12.8	13.8	10.9	1.50	44.0	63 (259)
C10%	Copolymer	13.8	13.2	12.1	1.39	3.5	86 (154)
C10%AN		13.5	12.4	12.9	1.40	35.8	22 (49) ^[h]
C20%		14.8	13.8	15.9	1.46	- [d]	58 (162)
C30%Boc		22.2	21.3	18.9	1.24	- [e]	- [f]
C30%		16.2	14.2	- [b]	- [b]	- [d]	48 (74)
C40%		17.6	17.6	- [b]	- [b]	- [d]	57 (78)
BC20	Block Copolymer	15.7	15.9	19.5	1.20	5.6	63 (51)
BC40Boc		22.3	25.8	22.6	1.25	- [e]	- [f]
BC40		18.3	17.3	- [b]	- [b]	- [d]	52 (66)
BC60		20.9	17.5	- [b]	- [b]	- [d]	71 (108)
BC60AN		20.2	17.9	18.9	1.22	58.2 ^[g]	68 (105)
BC20%40		20.0	17.3	- [b]	- [b]	- [d]	62 (75)

[a] Values were not determinable due to the FRP.

[b] GPC measurement was not recorded due to the low solubility in the eluent DMAc.

[c] Cloud points of the cooling process determined *via* turbidity measurements in a 1.0 wt% aqueous solution.

[d] Cloud points not determinable ($T_c < 5^{\circ}\text{C}$) due to the high [APAAm].

[e] Cloud points not determinable ($T_c > 85^{\circ}\text{C}$) due to the high [APAAm-Boc].

[f] Values were not determined.

[g] Cloud points determined in 0.1 wt% aqueous solution due to the high UCST.

[h] Yields lowered due to purification errors.

[i] Molar mass determined *via* gel-permeation chromatography in DMAc with LiBr (except R1-R4 due to solubility in $\text{H}_2\text{O}/\text{MeCN}$ (85:15) with NaNO_3).

The results of the copolymerization are analyzed by the comparison of the feed and incorporation ratios of the applied monomers AN and APAAm. The AN adjusts the hydrophobicity and the solvent interaction of the copolymer and was calculated reversely by the AAm content in the copolymer. The DNA-coordinating APAAm enlarges the strength of the interaction with the positively charged pDNA and was quantified *via* ^1H NMR of the signals of the aminopropyl spacer (see in the appendix, Table S24).

Table S24: The determination of the incorporation ratios of the monomers AN and APAAm in the copolymer vectors for gene delivery via ^1H NMR measurements.

Sample Code	Type	Feed Ratio		Incorporation Ratio	
		[AN] / mol%	[APAAm] / mol%	[AN] ^[b] / mol%	[APAAm] ^[c] / mol%
R1	Reference	35.0	0	34.2	0
R2		32.5	0	33.0	0
R3		41.0	0	41.4	0
R4		45.0	0	46.6	0
C10%	Copolymer	49.0	10.0	- ^[a]	11.7
C10%AN		59.0	10.0	- ^[a]	11.0
C20%		52.0	20.0	- ^[a]	20.7
C30%Boc		45.5	30.0	45.5	31.0
C30%		45.5	30.0	- ^[a]	28.6
C40%		39.0	40.0	- ^[a]	38.2
BC20	Block Copolymer	31.8	9.1	- ^[a]	8.2
BC40Boc		29.2	16.7	32.5	14.0
BC40		29.2	16.7	- ^[a]	16.8
BC60		26.9	23.1	- ^[a]	23.7
BC60AN		42.3	23.1	- ^[a]	22.7
BC20%40		43.3	33.3	- ^[a]	34.0

^[a] The molar fraction of AAm/AN were not determinable in the solvent D₂O via ^1H NMR.

^[b] The molar fraction extracted from the ^1H NMR measurement, recorded in DMSO-d₆.

^[c] The molar fraction extracted from the ^1H NMR measurement, recorded in D₂O.

The exemplary elugram of the vectors confirmed the successful block copolymerization. The precursor macroCTA poly(AAm-co-AN)-EMP in comparison with the final block copolymer poly[(AAm-co-AN)-block-(APAAm)]-EMP is shown in Figure S74. The elugrams are recorded in different eluents due to the complimentary solubility of the analytes in the eluents and the interaction of the product in with the GPC-column (in water/MeCN). Despite the same flow rate (1 mL/min), the elution times are not comparable precisely and are used indicatively to prove the success of the block copolymerization. While the measurement in H₂O/MeCN indicated strong interaction with the column material, the measurement with the setup with the eluent DMAc allows the detection of the desired molar mass of the block copolymers. The theoretical prediction of the molar masses aligns with the experimental data.

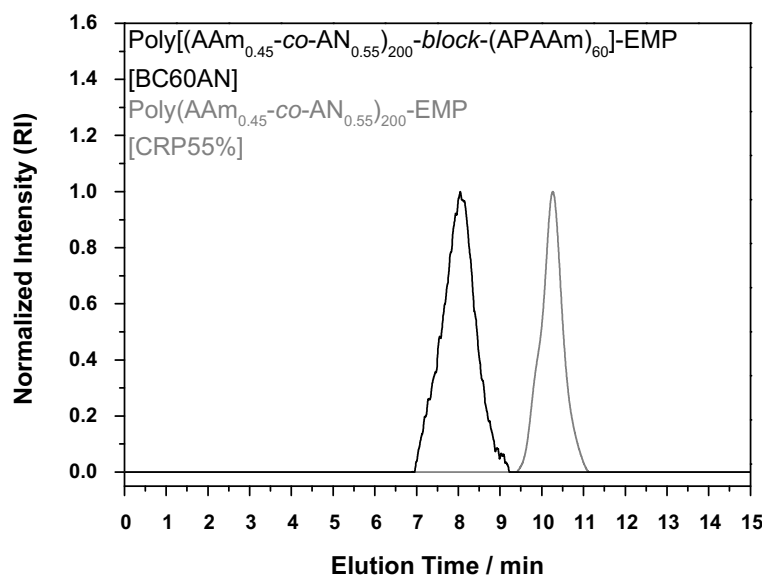


Figure S74: Elugrams in the RAFT block copolymerization of the copolymeric vectors. a) The applied UCST-starting block poly(AAm_{0.45}-co-AN_{0.55})₂₀₀-EMP (CRP55.0%) and b) the resulting DNA-binding block copolymer poly[(AAm_{0.45}-co-AN_{0.45})₂₀₀-block-(APAAm)₆₀]-EMP (BC60AN) recorded *via* gel-permeation chromatography in different eluents DMAc with LiBr (black) and H₂O/MeCN (85:15) with NaNO₃ (grey).

16.8.3. Syntheses of the Reference Copolymers Poly(AAm_x-co-AN_y) and Poly(AAm_x-co-AN_y)-EMP (R1 and R2)

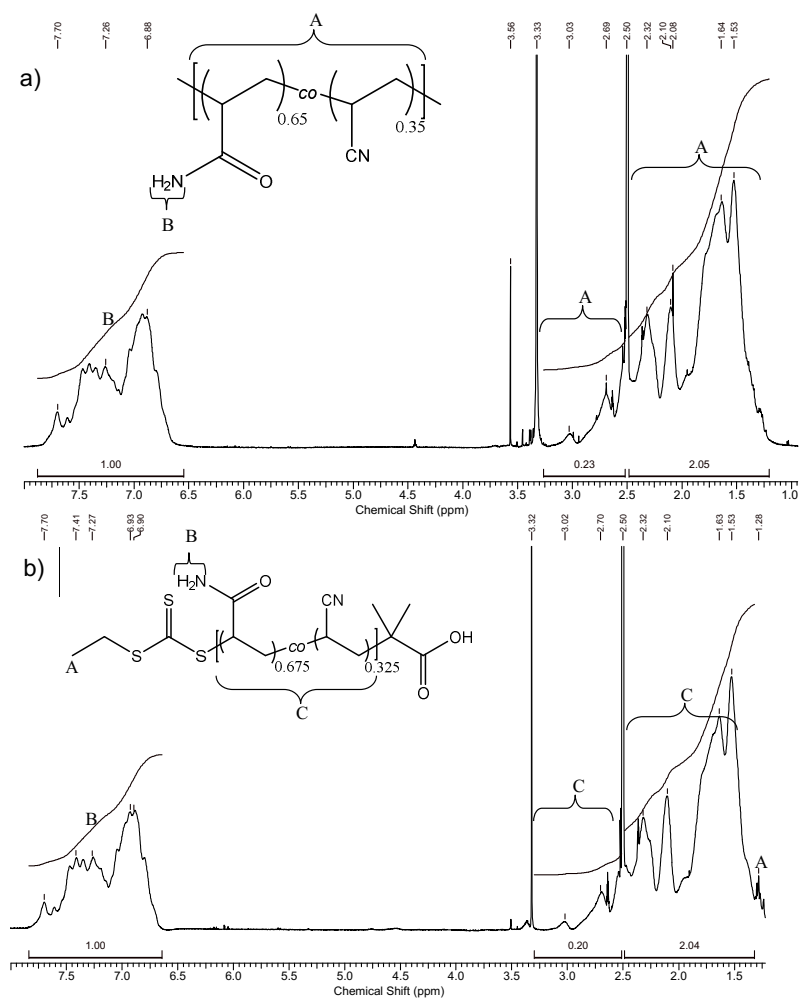


Figure S75: ¹H NMR spectra (400 MHz) of the thermoresponsive reference copolymers a) R1 and b) R2, recorded in DMSO-d₆ before the fourfold cycle of freeze-drying. Asterisks marks solvent residues (dioxane, methanol).

16.8.4. General Procedure for the Syntheses of the pDNA-Binding Copolymer Vectors Poly(AAm_x-co-AN_y-co-APAAM_z)-EMP (C30%Boc, C30% and C10%AN)

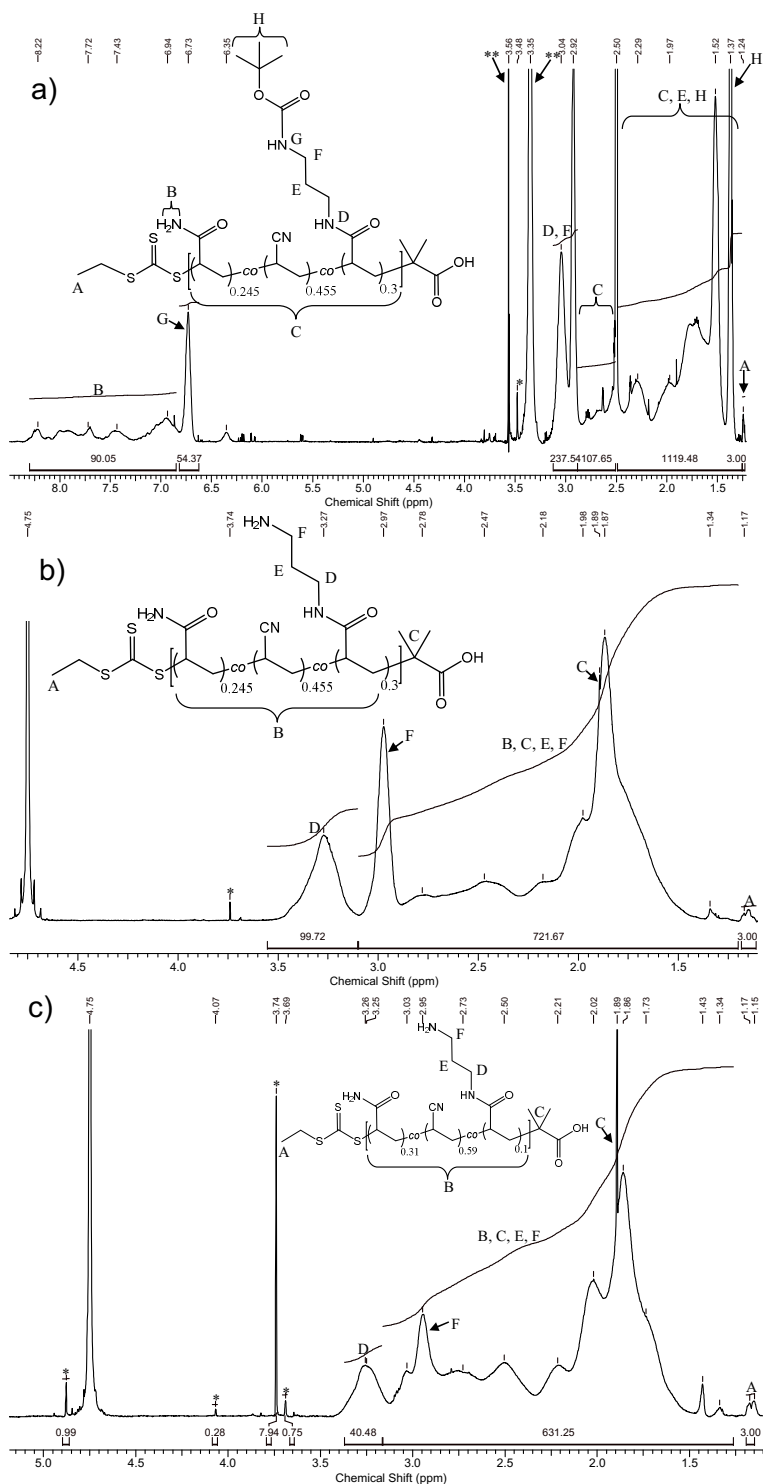


Figure S76: ¹H NMR spectra (500 MHz) of a) the synthesized pDNA-binding copolymer vectors C30%Boc before the removal of the amine protection group, recorded in DMSO-d₆, b) its deprotected equivalents C30% and c) C10%AN, recorded in D₂O before the threefold cycle of freeze-drying. Asterisks marks solvent residues (dioxane, water).

16.8.5. General Procedure for Syntheses of the pDNA-Binding Block Copolymer Vectors Poly[(AAm_x-co-AN_y)-block-(APAAm)_z]-EMP (BC40Boc, BC40 and BC60)

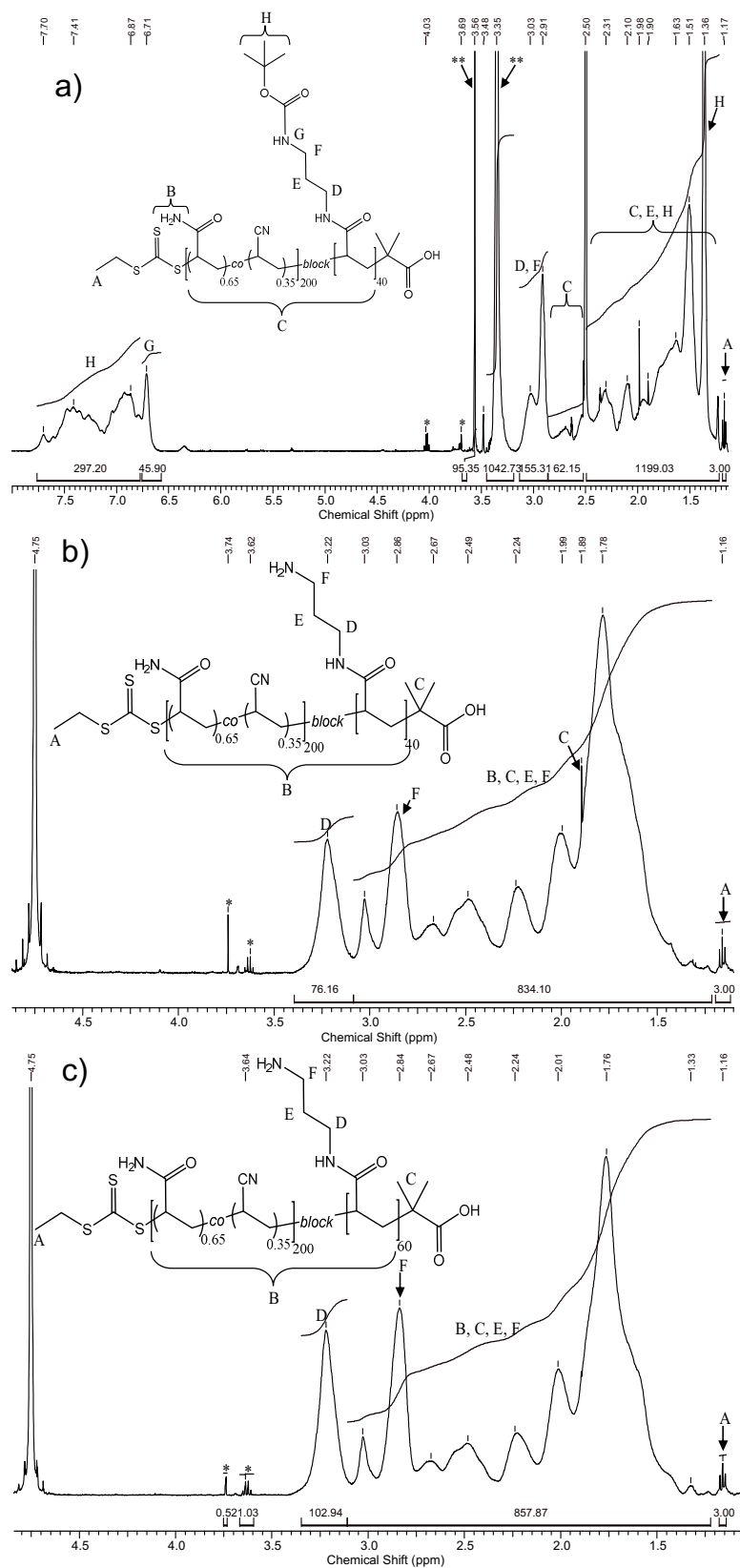


Figure S77: ¹H NMR spectra (500 MHz) of a) the synthesized pDNA-binding block copolymer vectors BC40Boc before the removal of the amine protection group, recorded in DMSO-d₆, b) its deprotected equivalents BC40 and c) BC60, recorded in D₂O before the threefold cycle of freeze-drying. Asterisks marks residues (dioxane, water).

16.8.6. Synthesis of the Dual pDNA-Binding Copolymer Vector Poly[(AAm_{0.28}-co-AN_{0.52}-co-APAAm_{0.20})₂₀₀-*block*-(APAAm)₄₀]-EMP (BC20%40)

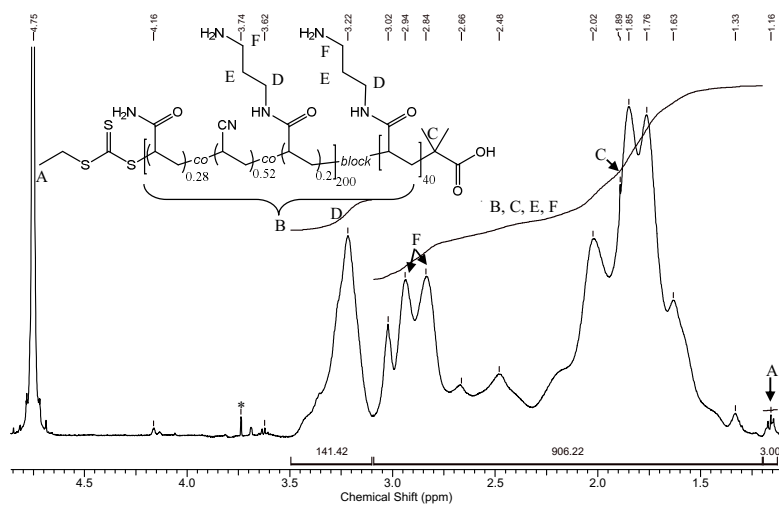


Figure S78: ¹H NMR spectra (500 MHz) of the synthesized dual pDNA-binding block copolymer vector BC20%40, recorded in D₂O before the threefold cycle of freeze-drying. Asterisks marks solvent residues (dioxane).

16.8.7. Determination of the Experimental Molar Masses and APAAm Contents of the Copolymer Vectors

The experimental data of the copolymer syntheses (e.g., ^1H NMR and GPC) were verified by the comparison with the theoretical values in the appendix, Table S23.

The theoretical molar masses of the copolymers were calculated by the number of targeted repeat units in the copolymers ($N_{r.u./polymer}$), the feed ratios of the monomers and their corresponding molar masses (including the single mass of the CTA).

$$\bar{M}_{theo} = N_{r.u./polymer} \cdot ([AAm]_{feed} \cdot M_{AAm} + [AN]_{feed} \cdot M_{AN} + [APAAM]_{feed} \cdot M_{APAAM}) + M_{EMP} \quad (17)$$

The approximate experimental molar masses of the copolymers (represented in the appendix, Table S23) were calculated by the absolute number of the repeat units in the copolymers, derived from the ^1H NMR spectra. The absolute number of repeat units is defined by the integral of the backbone protons ($I_{H,backbone}$) divided by the number of protons per single monomer unit - excluding the overlapping integral of ethylene APAAm rests as part of its propylene spacer ($\text{NH}_2\text{-CH}_2\text{-CH}_2\text{-CH}_2\text{-NHOC-R}$, indicated as "E/F" in the ^1H NMR spectra) laying below the backbone signal of the copolymer. The experimental molar masses were determined by the number of repeat units in the copolymers $\frac{1}{3}(I_{H,backbone} - 2 \cdot I_{H,APAAM})$, the feed ratios of the monomers and their corresponding molar masses.

$$\bar{M}_{NMR} = \frac{1}{3}(I_{H,backbone} - 2 \cdot I_{H,APAAM})([AAm]_{feed} \cdot M_{AAm} + [AN]_{feed} \cdot M_{AN} + [APAAM]_{feed} \cdot M_{APAAM}) + M_{EMP} \quad (18)$$

The approximate molar incorporation ratio of the APAAm (represented in the appendix, Table S24) unit is derived from the almost baseline separated signal of its methylene group as part of the APAAm propylene spacer ($\text{NH}_2\text{-CH}_2\text{-CH}_2\text{-CH}_2\text{-NHOC-R}$, indicated as "D" in the ^1H NMR spectra) in relation to the absolute number of repeat units $\frac{1}{3}(I_{H,backbone} - 2 \cdot I_{H,APAAM})$.

$$[APAAM]_{mol\%} = \frac{\frac{1}{2}[APAAM]}{\frac{1}{3}(I_{H,backbone} - 2 \cdot I_{H,APAAM})} \cdot 100 \quad (19)$$

16.8.8. Determination of the Experimental Molar Masses and Composition of the Boc-Protected Copolymer Vector Precursors

For the complete characterization of the copolymers, the analyses were performed for the Boc-protected copolymers. The copolymers with Boc-protected amine side groups represent the copolymeric precursors of the final products.

The theoretical molar masses of the copolymers before the removal of the Boc-protection group (represented in the appendix, Table S23) were calculated by the number of targeted repeat units in the copolymers ($N_{r.u./polymer}$), the feed ratios of the monomers and their corresponding molar masses.

$$\bar{M}_{theo} = N_{r.u./polymer} \cdot ([AAm]_{feed} \cdot M_{AAm} + [AN]_{feed} \cdot M_{AN} + [APAAm - Boc]_{feed} \cdot M_{APAAm-Boc}) + M_{EMP} \quad (20)$$

The approximate experimental molar masses of the copolymers before the removal of the Boc-protection group were calculated by the absolute number of the repeat units in the copolymers, derived from the 1H NMR spectra. The absolute number of repeat units $\frac{1}{3} \left(I_{H,backbone} - \frac{9}{2} I_{H,APAAm} - I_{H,APAAm} \right)$ is defined by the integral of backbone protons ($I_{H,backbone}$) divided by the number of protons per monomer unit - excluding the number of protons of the APAAm-Boc moiety (indicated as "E/F" and "H" in the 1H NMR spectra) laying below the backbone signal of the copolymer. The experimental molar masses were determined by the number of repeat units in the copolymers, the feed ratios of the monomers and their corresponding molar masses.

$$\bar{M}_{NMR} = \frac{1}{3} \left(I_{H,backbone} - \frac{9}{2} I_{H,APAAm} - I_{H,APAAm} \right) ([AAm]_{feed} \cdot M_{AAm} + [AN]_{feed} \cdot M_{AN} + [APAAm - Boc]_{feed} \cdot M_{APAAm-Boc}) + M_{EMP} \quad (21)$$

The approximate molar incorporation ratio of the Boc-protected APAAm unit (represented in the appendix, Table S24) was determined (in accordance to the previous copolymers) and the appearing changes of the integration limits.

$$[APAAm]_{mol\%} = \frac{\frac{1}{2}[APAAm]}{\frac{1}{3} \left(I_{H,backbone} - \frac{9}{2} I_{H,APAAm} - I_{H,APAAm} \right)} \cdot 100 \quad (22)$$

Due to the hydrophobic effect of the Boc-protection moiety, the protected copolymers were analysed in DMSO- d_6 . Consequently, the incorporation ratio of the AAm (represented in the appendix, Table S24) is additionally determinable by the integral of AAm in the relation to the absolute number of repeat units $\frac{1}{3} \left(I_{H,backbone} - \frac{9}{2} I_{H,APAAm} - I_{H,APAAm} \right)$.

$$[AAm]_{mol\%} = \frac{\frac{1}{2}[AAm]}{\frac{1}{3} \left(I_{H,backbone} - \frac{9}{2} I_{H,APAAm} - I_{H,APAAm} \right)} \cdot 100 \quad (23)$$

16.8.9. Gene Delivery Properties of the Copolymer Vectors

The complexation assay and the subsequent electrophoresis corroborates the formation of polyplex of the tested vectors and used pDNA (Figure S79). The molar fraction and the skeletal architecture of the vector had major influence on the efficiency and the needed mass ratio (MR) between vector and pDNA.

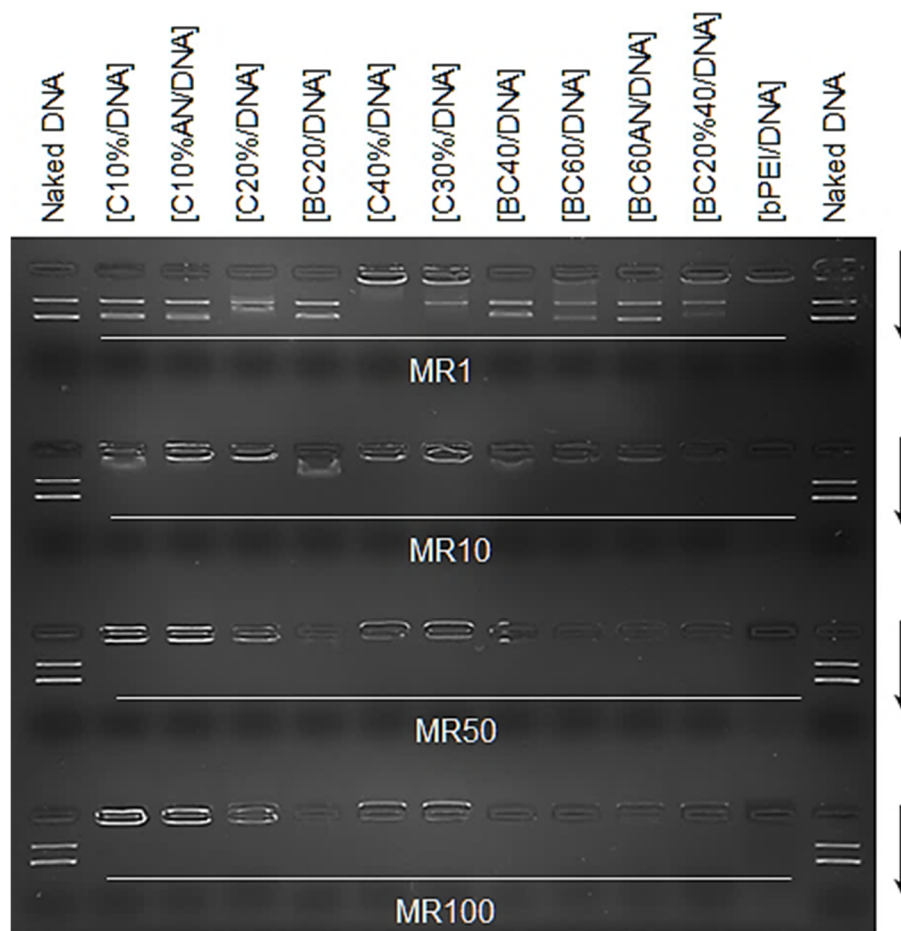


Figure S79: DNA retardation assay using copolymers and block copolymers. The samples were subjected to agarose gel electrophoresis. The vertical arrows denote the direction of electrical current.

The following flow diagram (Figure S80) sketches the procedure for the preparation of a transfection assay. The vectors were weighted and diluted in HEPES or saline to prepare the working solutions (2.0 wt%). The working solution were further diluted according to the targeted concentration series (MR=0.1-128 or [c]=12.5-1600 $\mu\text{g}/\text{mL}$). The polyplexes were prepared by addition of pDNA, before the transfection tests were started with the desired number of cells (25,000 cells/well) belonging to the cell lines (A549, C2C12 and HeLa). After the transfection process the transfection, viability and protein dosage experiments were performed simultaneously.

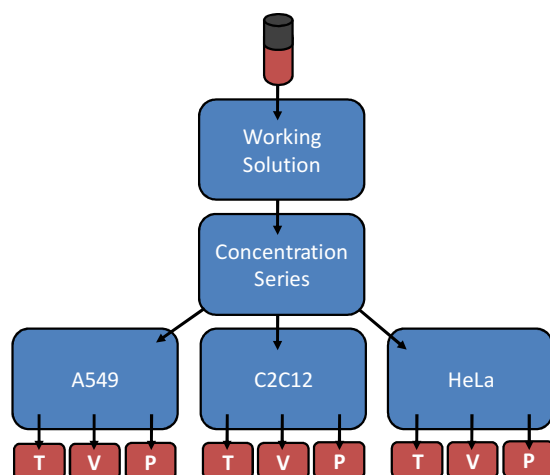


Figure S80: Exemplary working step procedure for the transfection assay with the transfection (T), cell viability (V) and protein dosage (P) experiments for the cell lines A549, C2C12 and HeLa.

The microscope images (Figure S81) of the performed transfection assay visualise the low cytotoxicity of the vectors in comparison to the standard PEI for the mass ratios MR=64 and MR=128. The visual impression correlates reasonable with the luciferase assay. The cells possess a high viability even at high vector dosages, while the standard PEI already shows a very low viability for mass ratios MR<16. The vector poly[(AAm_{0.65}-co-AN_{0.35})₂₀₀-*block*-(APAAm)₂₀]-EMP (BC20) represents an exemplary vector of the tested series.

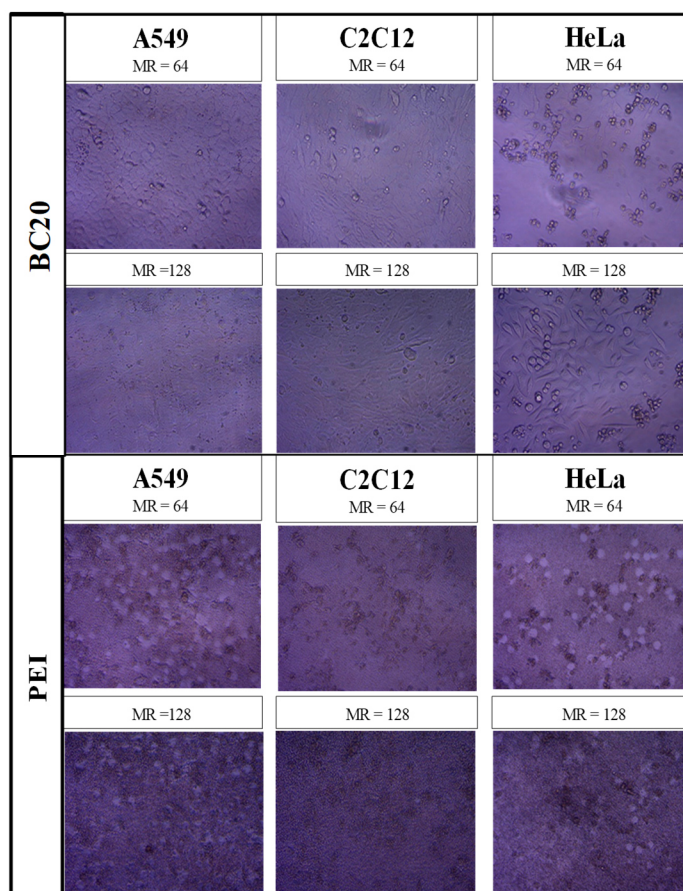


Figure S81: Microscope images of the transfection experiment with the cell lines (A549, C2C12 and HeLa) at high mass ratios between pDNA and block copolymer BC20 (MR=64 and MR128) in comparison to the reference PEI.

The transfection efficiency in combination with the viability of the copolymeric vectors is shown below (Figure S82). The optimal doses of a vector are the specific mass ratio with the highest efficiency of transfection. Those are illustrated in Figure 47 (of chapter 13.3.7).

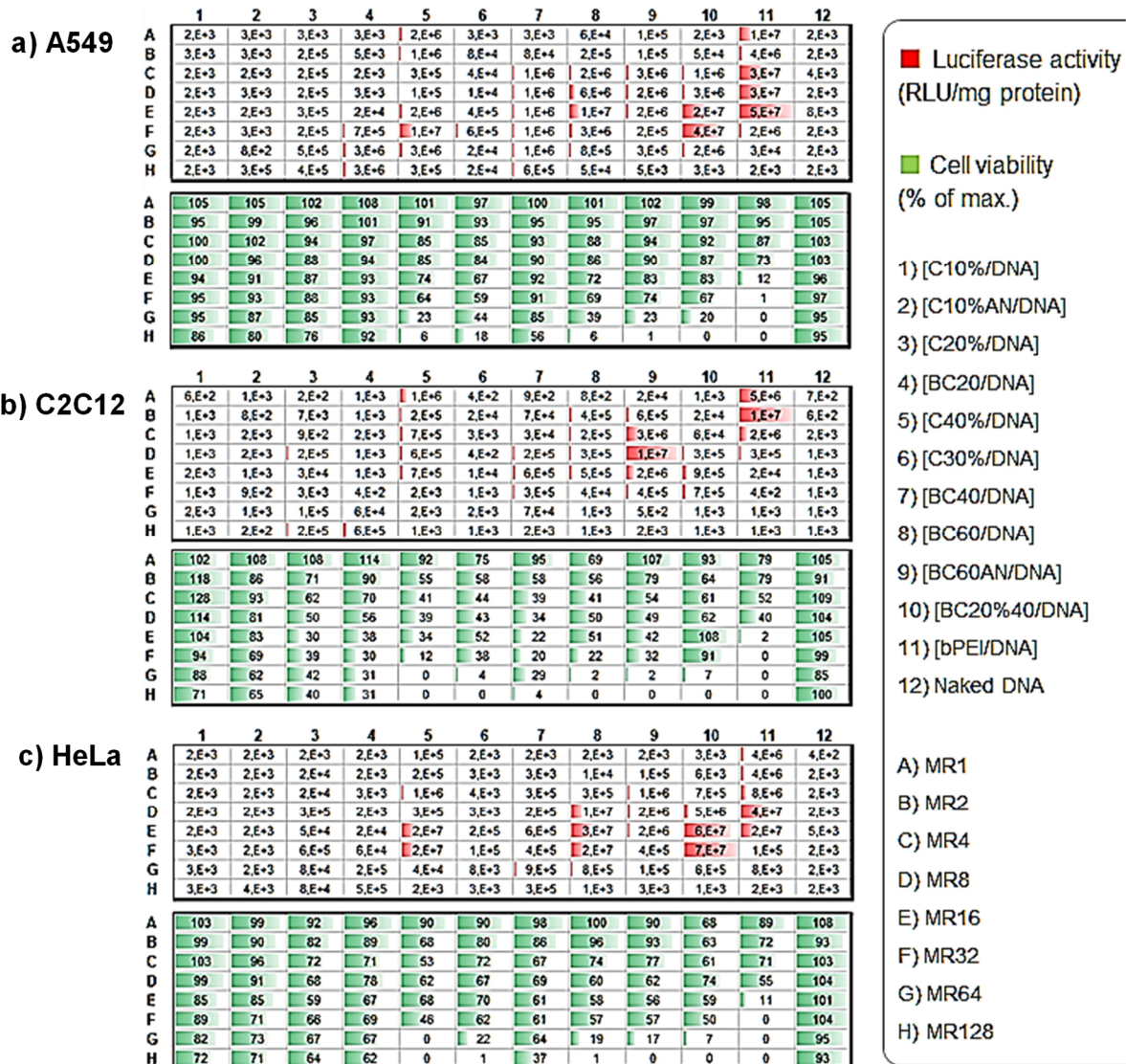


Figure S82: Transfection efficiency and associated cell viability using the copolymers and block copolymers in A549, C2C12 and HeLa. For each cell line, the top and bottom tables correspond to luciferase activity and cell viability measurements.

16.8.10. Calculation of the N/P the Copolymer Vectors

The N/P ratio describes the ratio between the number of amine coordination sites of the (copolymeric) vector (N_N) and the phosphate backbone binding sites of the DNA (N_P). It can be used to improve the comparability of the transfection efficiency values of different vectors. When a vector with lower N/P ratio delivers a comparable transfection efficiency, it is more effective and presumably less cytotoxic (less amine functionalities).

$$\frac{N}{P} \text{ ratio} = \frac{N_N}{N_P} \quad (24)$$

The number of amine coordination sites (N_N) is given by the used mass (m_V) of copolymeric vector, its molar mass distribution (\bar{M}_n), its percentual fraction of the monomer with amine site group ($[APAAm]_{\%}$) and the degree of polymerization X_n (or number of total repeat units).

$$N_N = \frac{m_V}{\bar{M}_n} \cdot [APAAm]_{\%} \cdot X_n \quad (25)$$

The number of phosphate sites (N_P) in a pDNA with 3.7 kb (kilo base pairs) is given by the averaged molar mass per base pair ($M_b=660$ g/mol) and the used mass (m_{pDNA}) for the experiment.

$$N_P = 3.7kb \cdot \frac{m_{pDNA}}{M_b} = 3.03 \cdot 10^{-3} P \text{ (per g)} \quad (26)$$

The N/P ratios for the applied mass ratios of the synthesized vectors (MR) are below in Table S25. The values are based on the theoretical feed ratios for the copolymerization.

Table S25: Theoretical N/P ratios in dependence of the applied mass ratios (MR) of varied copolymer vectors based on theoretical feed ratios of monomers and molecular masses of synthesized copolymer vectors.

Sample Code	MR1	MR2	MR4	MR8	MR16	MR32	MR64	MR128
R1 ^[a]	-	-	-	-	-	-	-	-
R2 ^[a]	-	-	-	-	-	-	-	-
R3 ^[a]	-	-	-	-	-	-	-	-
R4 ^[a]	-	-	-	-	-	-	-	-
C10%	0.48	0.96	1.91	3.83	7.65	15.30	30.61	61.22
C10%AN	0.49	0.98	1.96	3.91	7.82	15.64	31.29	62.58
C20%	0.89	1.78	3.57	7.14	14.27	28.54	57.08	114.16
C30%Boc	0.89	1.78	3.57	7.14	14.27	28.54	57.08	114.16
C30%	1.22	2.44	4.89	9.78	19.56	39.11	78.22	156.44
C40%	1.50	3.00	6.00	12.00	24.00	48.00	96.00	192.00
BC20	0.42	0.84	1.68	3.37	6.73	13.47	26.93	53.86
BC40Boc	0.59	1.19	2.37	4.74	9.49	18.98	37.96	75.92
BC40	0.72	1.45	2.89	5.78	11.56	23.13	46.26	92.51
BC60	0.95	1.90	3.79	7.59	15.17	30.35	60.69	121.38
BC60AN	0.98	1.96	3.92	7.85	15.70	31.40	62.80	125.59
BC20%40	1.32	2.64	5.27	10.55	21.10	42.20	84.40	168.79

^[a] Reference copolymers (R1-R4) do not contain APAAm repeat units.

The experimental refined N/P ratios of the applied mass ratios of the synthesized vectors (MR) are below in the appendix, Table S26. The experimental incorporation ratio of the monomer APAAm and molar mass of the vector are considered.

Table S26: Experimental N/P ratios in dependence of the applied mass ratios (MR) of varied copolymer vectors based on experimental incorporation ratios of monomers and molecular masses of synthesized copolymers. The experimental data (incorporation ratio of APAAm and \bar{M}_n of copolymer vectors) were derived *via* ^1H NMR spectroscopy.

Sample Code	MR1	MR2	MR4	MR8	MR16	MR32	MR64	MR128
R1 ^[a]	-	-	-	-	-	-	-	-
R2 ^[a]	-	-	-	-	-	-	-	-
R3 ^[a]	-	-	-	-	-	-	-	-
R4 ^[a]	-	-	-	-	-	-	-	-
C10%	0.56	1.12	2.24	4.48	8.95	17.91	35.81	71.62
C10%AN	0.54	1.08	2.15	4.30	8.60	17.21	34.42	68.84
C20%	0.92	1.85	3.69	7.38	14.77	29.54	59.08	118.16
C30%Boc	0.92	1.84	3.69	7.37	14.75	29.49	58.98	117.97
C30%	1.17	2.33	4.66	9.32	18.64	37.29	74.57	149.14
C40%	1.43	2.87	5.73	11.46	22.92	45.84	91.68	183.36
BC20	0.38	0.76	1.52	3.03	6.07	12.13	24.27	48.54
BC40Boc	0.50	0.99	1.99	3.98	7.96	15.91	31.82	63.64
BC40	0.73	1.45	2.91	5.82	11.63	23.27	46.53	93.07
BC60	0.97	1.95	3.89	7.78	15.57	31.13	62.27	124.54
BC60AN	0.96	1.93	3.86	7.71	15.43	30.85	61.71	123.42
BC20%40	1.35	2.69	5.39	10.77	21.54	43.08	86.17	172.34

^[a] Copolymer vectors do not contain APAAm repeat units.